

ABSTRACT

In a bus air conditioning system, the working load is relatively high in comparison to a passenger car. As such, the size of the compressor used is also relatively large due to high refrigerant flow rate required to meet the demand for high cooling capacity. For high refrigerant flow rate, reciprocating piston-cylinder concept has been known to operate successfully. The present work carried out is also based on the piston-cylinder compression concept but attempt was made to reduce the size of the compressor so that it is more compact and stable. This thesis reports the actual effort of introducing a novel concept of compression mechanism of the refrigerant compressor for a bus air conditioning system. The development of prototypes is based on experience and knowledge gained through reverse engineering on several existing compressor models in the market such as the swash plate compressor and the wobble plate compressor. Literature reviews were carried out to keep up with the latest technology that is available in the market and to acquire more state of the art knowledge required to design a better compressor. In parallel, an experimental rig was developed based on international standard to test and evaluate both existing and newly developed compressors. Tests were conducted by varying the compressor speed from 800rpm to 1800rpm. The performance of the compressors were studied in terms of coefficient of performance (COP), volumetric efficiency (η_v) and mechanical efficiency (η_{mech}). For the existing compressor model, the highest COP obtained was 4.1 at 800rpm while the highest volumetric and mechanical efficiencies are 71% at 1400 rpm and 74% at 800 rpm. Similar data were planned to be obtained from the test of the newly developed prototypes. However, the new prototypes were not fully developed and data obtained from the test carried out were not enough to make a conclusive comparison with the performance of the existing model. The compressor managed to get a pressure ratio of 3 which was enough for an air conditioning system to work. The shortfalls and the source of the failure have been identified and recommendations for improvement have been made.

ABSTRAK

Di dalam sebuah sistem hawa dingin bas, beban penyejukan adalah lebih tinggi berbanding sistem hawa dingin kereta. Ini bermakna, saiz pemampat yang digunakan juga lebih besar disebabkan lebih banyak aliran refrigeran diperlukan untuk memenuhi kapasiti yang besar. Untuk kadar alir refrigeran yang besar, konsep pemampat salingan biasanya digunakan. Kerja kerja yang dijalankan untuk kajian ini turut berkait rapat dengan pemampat salingan, akan tetapi percubaan dibuat untuk mengurangkan saiz pemampat supaya ia lebih stabil dan padat. Tesis ini melaporkan usaha yang dilakukan bagi memperkenalkan konsep mekanisma pemampatan efrigeran baru untuk sistem hawa dingin bas. Pembangunan prototaip adalah berdasarkan pengalaman dan pengetahuan yang didapati melalui proses kejuruteraan semula terhadap pemampat sedia ada iaitu pemampat plat wobal satu sisi dan plat *swash*. Kajian literatur turut dijalankan bagi memastikan penyelidik tidak ketinggalan dalam teknologi baru di dalam pasaran dan juga menambah lebih pengetahuan dalam kaedah membangunkan pemampat. Sebuah pelantar ujikaji juga dibangunkan dalam masa yang sama, berdasarkan piawai antarabangsa bertujuan untuk menguji pemampat sedia ada dan juga pemampat yang baru dibangunkan. Ujikaji dilakukan dengan pelbagai laju putaran dengan halaju minimum 800 ppm dan maksimum 1800 ppm. Prestasi pemampat dilihat dari sudut kecekapan prestasi (COP), kecekapan isipadu (η_v) dan kecekapan mekanikal (η_{mech}). Bagi pemampat sedia ada, nilai kecekapan prestasi paling tinggi direkodkan adalah 4.1 pada halaju 800 ppm manakala kecekapan isipadu dan mekanikal tertinggi adalah 71% pada 1400 rpm dan 74% pada 800 ppm. Walaubagaimanapun, hasil ujikaji ini tidak dapat dibandingkan dengan pemampat yang baru dibangunkan kerana pemampat tersebut gagal berfungsi selama masa minimum yang diperlukan untuk bacaan ujikaji diambil. Akan tetapi, nisbah mampatan minimum sebanyak 3 dapat dicapai yang mana ia boleh diterima pakai untuk sistem hawa dingin. Kekurangan dan punca kegagalan telah dikenal pasti dan cadangan untuk meningkat taraf konsep telah dibuat.

TABLE OF CONTENTS

CHAPTER	TITLE	PAGE
	DECLARATION	ii
	ABSTRACT	iii
	ABSTRAK	iv
	TABLE OF CONTENT	v
	LIST OF TABLES	ix
	LIST OF FIGURES	x
	LIST OF SYMBOLS	xii
	LIST OF APPENDICES	xviii
1	INTRODUCTION	
	1.1 Overview	1
	1.2 Problem Statement	2
	1.3 Significant of Research	3
	1.4 Research Objective	4
	1.5 Scope of Work	4
	1.6 Research Methodology	4
	1.6.1 Reverse Engineering	5
2	THEORY AND LITERATURE REVIEW	7
	2.1 Introduction	7
	2.2 Refrigeration Process	7
	2.3 Compressors	8

2.4	Compression Concept	11
2.4.1	Reciprocating Compressor	11
2.4.2	Wobble Plate Compressor	12
2.4.3	Variable Displacement Wobble Plate Compressor	13
2.4.4	Swash Plate Compressor	14
2.4.5	Radial Motion Piston Compressors	15
2.4.6	Rotary and Orbital Compressors	16
2.5	Current State of Art	18
2.5.1	Design and Development	19
2.5.2	Experimental and Analytical Work	22
2.5	Conclusion	24
3	PRELIMINARY DESIGN AND ANALYSIS	25
3.1	Introduction	25
3.2	Description of Technology	26
3.3	Preliminary Design	27
3.3.1	Determination of Compressor Specification	28
3.3.2	Valve System	31
3.3.3	Piston and Piston Rings	37
3.3.4	Lubrication System	38
3.3.5	Material Selection	39
3.4	Compressor Kinematics Analysis	40
3.5	Compressor Static Analysis	41
3.5.1	Piston free Body Diagram	42
3.5.2	Connecting Rod Free Body Diagram	44
3.5.3	Wobble Plate Free Body Diagram	45
3.5.4	Ball Mount Free Body Diagram	52
3.5.5	Rotor Free Body Diagram	53
3.5.6	Shaft Free Body Diagram	57

3.7	Experimental Setup	59
3.7.1	Experimental Rig	59
3.7.2	Test Condition	61
3.7.3	Test Rig Preparation	62
3.7.4	Experimental procedure	63
3.7.5	Compressor Performance Analysis	63
3.7.6	Pressure Test Rig	64
4	EXPERIMENTAL RESULTS AND DISCUSSIONS	66
4.1	Introduction	66
4.2	Pressure Test Experiment Result	66
4.3	Compressor Test on Air Conditioning Experimental Rig	67
4.3.1	Results and Performance Characteristic of New Compressor Model	67
4.3.3	Comparison Between Swash Plate and Symmetrical Wobble Plate Compressor	70
4.4	Compressor Post Mortem	70
4.4.1	Machining Tolerances	71
4.4.2	Oil Lubrication System	71
4.4.3	Oscillating Shaft Assembly	72
4.5	Summary	73
5	CONCLUSION AND SUGGESTIONS FOR FUTURE WORK	74
5.1	Conclusions	74
5.2	Suggestions For Future Research	75
	REFERENCES	77

LIST OF TABLES

TABLE	TITLES	<u>PAGE</u>
Table 2.1	Rotary and Orbital Compressors Operating Concept	17
Table 3.1	Mean Piston Speed for Multiple Piston Configurations	32
Table 3.2	Valve Geometry	38
Table 6.1	Pressure Test Data	103

LIST OF FIGURES

FIGURE	TITLES	PAGE
1.1	Methodology Flow Chart	5
2.1 (a)	Schematic Diagram of Refrigerant Components and System	9
2.1 (b)	T-S diagram Showing Each Process in the Cycle	9
2.2	Category of Refrigerating and Air Conditioning Compressors	10
2.3	Suction and Discharge Processes in a Reciprocating Compressor	13
2.4	Wobble Plate Compression Process	14
2.5	Variable Displacement Wobble Plate Compressor	15
2.6	Swash Plate Operating Concept	16
2.7	Scotch Yoke Compressor	17
3.1	New Design of Symmetrical Wobble Plate Compressor	27
3.2	New Compressor Working Step	28
3.3	Design and Development Sequences	30
3.4	Typical P-V Diagram	34
3.5	Pressure Versus Shaft Angle Position	34
3.6	Tilting Angle Versus Shaft Angle of Rotation	42
3.7	Piston Stroke Versus Shaft Angle of Rotation	42
3.8	Variation of Pressure on Piston with Shaft Rotation Angle	44
3.9	Piston Free Body Diagram	44
3.10	Connecting Rod Position	45
3.11	Connecting Rod Free Body Diagram	46
3.12	Wobble Plate Position Coordinate System	47
3.13	Wobble Plate Free Body Diagram on Y-Z Plane	48

FIGURE	TITLES	PAGE
3.14	Wobble Plate Free Body Diagram on Y-Z Plane at $\alpha=0$	49
3.15	Wobble Plate Free Body Diagram on X-Z Plane	50
3.16	Wobble Plate Free Body Diagram on the X-Y Plane	51
3.17	Variation of Ball Mount Reaction Force (F_{wb}) with Shaft Rotation Angle	52
3.18	Variation of Guide Rod Reaction Force (F_{wgx}) with Shaft Rotation	53
3.19	Ball Mount Free Body Diagram	53
3.20	Rotor Position	54
3.21	Rotor Free Body Diagram on the X-Z Plane	55
3.22	Rotor Free Body Diagram on the Y-Z Plane	56
3.23	Shaft Rotor Assembly with Moment Reaction	56
3.24	Variation of Rotor-Shaft Reaction Force (F_{rs}) with Shaft Rotation	57
3.25	Variation of Centre Rotor Moment Reaction (M_t) with Shaft Rotation	58
3.26	Shaft Free Body Diagram on the X-Z Plane	58
3.27	Shaft Free Body Diagram on the Y-Z Plane	59
3.28	Variation of Shaft-Bearing Reaction Force (F_{sbf}/F_{sbr}) with Shaft Rotation	60
5.1	Compressor Test Bench Facility	94
5.2	Schematic Diagram of Experimental Rig with Temperature and Pressure Measurement Points	95
5.3	Flow Meter	96
5.4	Method of Temperature Measurement	97
6.1	Pressure Ratio Versus Time	106
6.2	Pressure Versus Time	106
6.3	Shaft power Consumption Versus Shaft Speed	107

LIST OF SYMBOLS

A_d	-	Discharge Port Area
A_{ef}	-	Effective Port Area
A_v	-	Area loaded by pressure
b_v	-	Valve width
C_{cir}	-	Circumferences
C_m	-	Mean Piston Speed
c	-	Speed of Sound
cc	-	Centimetre Cubic
COP	-	Coefficient of performance
COP_a	-	Actual coefficient of performance
D_p	-	Piston diameter
D_{dp}	-	Discharge ports diameter
F	-	Force
F_{np}	-	Pressure force
F_{nbmcbx}	-	Ball Mount reaction force from cylinder block at x-axis
F_{nbmcbx}	-	Ball Mount reaction force from cylinder block at y-axis
F_{nbmcbz}	-	Ball Mount reaction force from cylinder block at z-axis
F_{nbmwx}	-	Ball Mount reaction force from wobble plate at x-axis
F_{nbmwy}	-	Ball Mount reaction force from wobble plate at y-axis
F_{nbmwz}	-	Ball Mount reaction force from wobble plate at z-axis
F_{ncrpx}	-	Connecting rod reaction force from piston at x-axis

F_{ncrpy}	-	Connecting rod reaction force from piston at y-axis
F_{ncrpz}	-	Connecting rod reaction force from piston at z-axis
F_{ncrwx}	-	Connecting rod reaction force from wobble plate at x-axis
F_{ncrwy}	-	Connecting rod reaction force from wobble plate at y-axis
F_{ncrwz}	-	Connecting rod reaction force from wobble plate at z-axis
F_{np}	-	Gas pressure force
F_{npcbx}	-	Piston reaction force from the cylinder block at x-axis
F_{npcby}	-	Piston reaction force from the cylinder block at y-axis
F_{npcrx}	-	Piston reaction force from the connecting rod at x-axis
F_{npcry}	-	Piston reaction force from the connecting rod at y-axis
F_{npcrz}	-	Piston reaction force from the connecting rod at z-axis
F_{nrwfx}	-	Rotor reaction force from front wobble plate at x-axis
F_{nrwfy}	-	Rotor reaction force from front wobble plate at y-axis
$F_{nrw fz}$	-	Rotor reaction force from front wobble plate at z-axis
F_{nrwrx}	-	Rotor reaction force from rear wobble plate at x-axis
F_{nrwry}	-	Rotor reaction force from rear wobble plate at y-axis
F_{nrwrz}	-	Rotor reaction force from rear wobble plate at z-axis
$F_{nr sx}$	-	Rotor reaction force from shaft at x-axis
$F_{nr sy}$	-	Rotor reaction force from shaft at y-axis
$F_{nsbf x}$	-	Shaft reaction force from front cylinder block at x-axis
$F_{nsbf y}$	-	Shaft reaction force from front cylinder block at y-axis
$F_{nsbr x}$	-	Shaft reaction force from rear cylinder block at x-axis
$F_{nsbr y}$	-	Shaft reaction force from rear cylinder block at y-axis
$F_{nsr x}$	-	Shaft reaction force from rotor at x-axis
$F_{nsr y}$	-	Shaft reaction force from rotor at y-axis

$F_{nw\text{bmx}}$	-	Wobble plate reaction force from ball mount at x-axis
$F_{nw\text{bmy}}$	-	Wobble plate reaction force from ball mount at y-axis
$F_{nw\text{bmz}}$	-	Wobble plate reaction force from ball mount at z-axis
$F_{nw\text{crx}}$	-	Wobble plate reaction force from connecting rod at x-axis
$F_{nw\text{cry}}$	-	Wobble plate reaction force from connecting rod at y-axis
$F_{nw\text{crz}}$	-	Wobble plate reaction force from connecting rod at z-axis
$F_{nw\text{gx}}$	-	Wobble plate reaction force from guide rod at x-axis
$F_{nw\text{rx}}$	-	Wobble plate reaction force from rotor at x-axis
$F_{nw\text{ry}}$	-	Wobble plate reaction force from rotor at y-axis
$F_{nw\text{rz}}$	-	Wobble plate reaction force from rotor at z-axis
F_v	-	Force required to lift valve to opening height
h	-	Enthalpy
h_v	-	Valve lift height
h_1	-	Enthalpy at compressor suction
h_2	-	Enthalpy at compressor discharge
h_3	-	Enthalpy at condenser
h_4	-	Enthalpy at compressor discharge
I	-	Second moment of area
K	-	Specific heat ratio
k	-	Spring Constant
k_s	-	Contraction Coefficient
L_v	-	Valve length
L_p	-	Piston Stroke
l_{cr}	-	Connecting rod length

l_{nwcrx}	-	Coordinate of connecting rod of the n'th piston at wobble plate on the x-axis
l_{nwcry}	-	Coordinate of connecting rod of the n'th piston at wobble plate on the y-axis
l_{nwrx}	-	Coordinate of rotor of the n'th piston at wobble plate on the x-axis
l_{nwry}	-	Coordinate of rotor of the n'th piston at wobble plate on the y-axis
M	-	Mach number
m	-	mass (kg)
\dot{m}	-	refrigerant mass flowrate
N	-	rotational speed
P	-	Compressor power
P	-	Pressure
P_1	-	Pressure at compressor suction
P_2	-	Pressure at compressor discharge
P_3	-	Pressure after condenser
P_4	-	Pressure after thermostatic expansion valve (TXV)
ΔP	-	Pressure difference at valve ports
Q	-	Flowrate at valve ports
Q_d	-	Flowrate at discharge ports
R	-	Ideal gas constant
rpm	-	rotation per minute
T	-	Temperature
T_1	-	Suction temperature

T_2	-	Discharge Temperature
T_3	-	Condensing temperature
T_4	-	Temperature after thermostatic expansion valve (TXV)
T_{evap}	-	Temperature at evaporator
T_{cond}	-	Temperature at condenser
t	-	Time
t_v	-	Valve Thickness
t_{v1}	-	Time at suction valve closed
t_{v2}	-	Time at discharge valve opened
t_{v3}	-	Time at discharge valve closed
t_{v4}	-	Time at suction valve opened
V	-	Volume
V_d	-	Displacement volume
V_p	-	Volume of one piston
V_{actual}	-	Actual Flowrate
V_{dis}	-	Theoretical Flowrate
V_I	-	Suction volume
V_o	-	Input voltage
V_{V2}	-	Starting discharge volume in piston
V_{V3}	-	End of discharge volume in piston
v	-	Velocity
v_d	-	Velocity at discharge port
I_o	-	Input current
\dot{W}_{vapor}	-	Indicated power

\dot{W}_{shaft}	-	Input power by motor
X_{np}	-	X coordinate of ball joint connection for n'th piston on cylinder block
X_{nw}	-	X coordinate of ball joint connection for n'th piston on wobble plate
Y_{np}	-	Y coordinate of ball joint connection for n'th piston on cylinder block
Y_{nw}	-	Y coordinate of ball joint connection for n'th piston on wobble plate
μ	-	Micron (10^{-6})
η	-	Efficiency
η_{mech}	-	Mechanical efficiency
η_{motor}	-	Motor efficiency
η_v	-	Volumetric efficiency
θ_o	-	Power factor
θ	-	Angle of rotating shaft to reference
θ_{v1}	-	Shaft angle at suction valve closed
θ_{v2}	-	Shaft angle at discharge valve opened
θ_{v3}	-	Shaft angle at discharge valve closed
θ_{v4}	-	Shaft angle at suction valve opened
α	-	Tilting angle of wobble plate at Y-Z plane
γ	-	Tilting angle of wobble plate at X-Z plane
ω	-	Angular velocity

ζ	-	Damping Coefficient
ρ	-	Density of gas

LIST OF APPENDICES

APPENDIX	TITLES	PAGE
A	BOM data of Wobble Plate Compressor and Swash Plate Compressor	119
B	Discharge Port Calculation	123
C	Piston Rings Data and Selection	130
D	Cycloid Profile Generation Via Vector Method	134
E	Kinematics Analysis	137
F	Static Analysis Results	148
G	Third Prototype BOM Data of New Symmetrical Wobble Plate Compressor	161
H	Figures and Information of Experimental Setup and Equipments	167
I	Figures and Information of Pressure Test Setup and Equipments	179
J	Experimental Results For DKS 32 and New Compressor	183
K	Results and Performance Characteristic of Swash Plate Compressor Model (ZEXEL)	185
L	Parts Figures of New Compressor After Test	190
M	List of Papers	192

CHAPTER 1

INTRODUCTION

1.1 Overview

The highly competitive nature of the refrigeration and air-conditioning industry creates an atmosphere in which systems manufacturers must continuously improve the quality and capability of their products in order to maintain or increase their current market shares. Environmental concerns and higher energy costs persuade governments in many parts of the world for their country to develop more efficient systems. Thus, customers demand systems that cost less to purchase and to operate than that already existed in the market. The challenge faced by compressor manufacturers is to meet this demands and this requires aggressive R&D work. Therefore it is not surprised to see records of product development work when one looks at the history of compressors like Matshushita or Sanden which are actively filing patents to every improvement made on their compressor models.

With the evolution of compressor technology beginning from late 19 century, hundreds of manufactures have emerged throughout the world producing various models to compress various type of gases at different capacities. Majority of these models are develop to compress air and the application of the technology is also adaptable for compressing refrigerant and other industrial gases. This thesis focuses on the development of a refrigerant compressor for the bus air conditioning system.

Compressors are usually classified based on their characteristics such as working concept, drive arrangement, and capacity. In addition to these various characteristics the positive displacement compressors can be categorized based on its motion [1] as; rotary, reciprocating and orbital. Each of these compressors has their advantages and disadvantages which are discussed later in the thesis.

Currently, some local air conditioning system suppliers for buses obtained their compressor from APM (Automotive Parts Malaysia Sdn. Bhd.) which manufactures the product under license from Zexel [2]. The technology is therefore foreign and all development work are carried out at their parent company. Other air conditioning systems are using conventional reciprocating BOCK compressors [3] which are imported from Germany. These compressors are bulky, heavy and costly. These two branded models are common amongst the air conditioning suppliers although that there are still other models available in the market. On the other hand, wobble plate type compressors produced by SANDEN are installed in a compact but low capacity systems and used mainly in cars air conditioning system. As outlined by Hiroshi Toyoda [4], the history of the wobble plate compressor begun from 1955 and the compressors were manufactured by General Motors and continued by SANDEN at 1971 to date. They have successfully redesigned and improved the compressor to a stage that the performance surpasses most of the other types of compressor available at that time. Even now, the design (1971) is still applied especially to third world countries, such as Malaysia where demands are still high. With these arguments, it is imperative that we have our own compressor developed to reduce our country dependence on foreign technologies and also creating new job opportunities.

Based on the existing design, a new concept is introduced and developed. The concept introduced has better characteristic while maintaining some of the good features of the existing design which will be discussed later in the thesis.

1.2 Problem Statement

The work carried out is to develop an alternative refrigerant gas compressor with a better characteristic on certain aspect such as less vibration while operating at high speed and comes in smaller durable packages. On top of it, the market demands smaller and better efficiency compressors to reduce cost as well as increasing their product features. Originally it was planned to acquire the compressor technology through patent review, reverse engineering and examination of the existing designs

without any intention to improve the performance. However today's refrigeration industry is very demanding requiring a tight specification, as such that the designed compressor should be capable of operating at low noise and vibration levels while running at high speed which contributes to smaller overall size. In the process of reverse engineering, literature study and problem solving it is found that the vibration can be reduced by introducing a new concept and thus achieving the above said criteria. The whole process involved a new concept development and thus treated as problems to be solved in the present work and therefore create opportunity to set a clear and achievable objective with a reasonable scope of work specified.

1.3 Significant of research

Air conditioning system mainly comprises of four major components [5] that is; the compressor, evaporator, condenser and the expansion valve. The compressor is considered as the "heart" of the air conditioning system and it is also difficult to manufacture due to its precision machining requirement. The aim of the research is to acquire the compressor technology which comprised of several elements such as the lubrication system, material selection, tribology, heat transfer, and others. It is imperative that the designed compressor met the high demand of today's requirement such as compactness, lightweight yet simple and easy to manufacture. The success of the research work will help in reducing the monopoly of the companies that produce these compressors using the technologies they developed.

In the existing swash plate type compressor used in the bus air-conditioning system, the swash mechanism creates unbalanced forces to the compressor which contributes to vibration and noise. However, these effects are not relevant since the engine that drives the compressor is already noisy. If this issue can be technically addressed, it will open up to more innovative possibilities in designing the air conditioning system layout. For example a more compact air conditioning system for bus can be developed with all of the components placed on the roof including the compressor which is to be driven by a motor, the design would at least improve accessibility to the system during maintenance which in turn reduces maintenance

and thus bus down time which is commercially crucial especially on city shuttle or commuter busses.

1.4 Research Objective

To design and develop a new symmetrical single acting wobble plate refrigerant gas compressor for mass transit air conditioning system.

1.5 Scope of Work

- i. To conduct literature study on the existing refrigerant gas compressor that is currently used on automobiles air conditioning system.
- ii. To develop new compressor concept followed by engineering analysis
- iii. To produce engineering drawings and fabricate prototype for testing
- iv. To design an experimental rig and conduct performance testing on existing swash plate compressor and on the new wobble plate compressor
- v. To analyze data and compare results obtained on the performance of the two different compressors

1.6 Research Methodology

The research was carried according to the methodology flow chart as depicted in Figure 1.1.

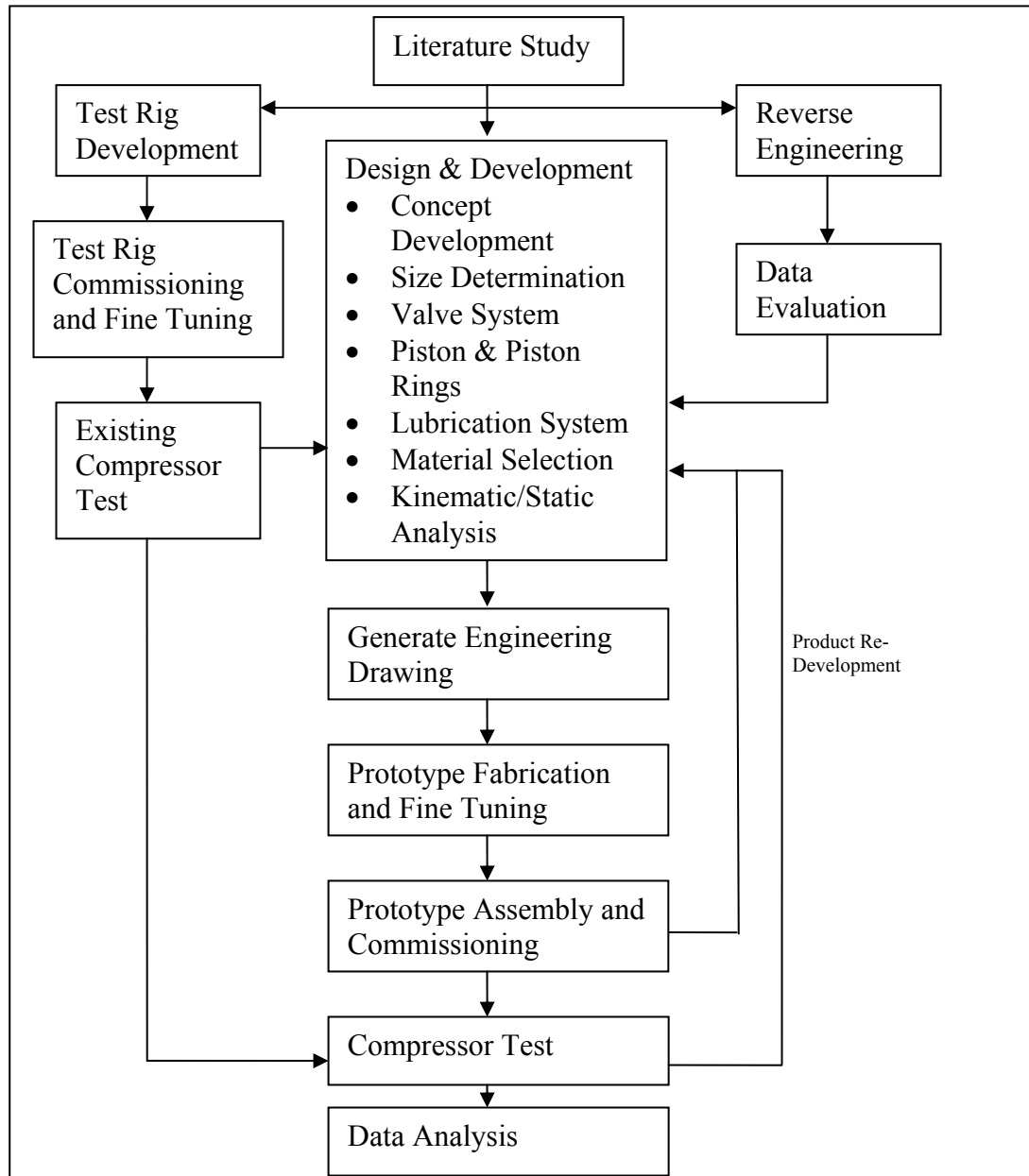


Figure 1.1 Methodology Flow Chart

Reverse Engineering

Reverse engineering was done basically to develop or to improve based on an existing product. According to Ingle [6], reverse engineering is a four stage process which includes data evaluation, data generation, design verification and design implementation. Alternatively as outlined by Otto and Wood [7], the four stage process is further detailed into several processes. Critical data of the existing

product is recorded in BOM document where it may contain information such as the physical appearances, design, function, dimension, reliability, reproducibility and ability to be remanufactured. Then, the data obtained is used as basic parameters and modifications were made where necessary.

However, in the current work reverse engineering plays an important role by giving the researcher a head start in the compressor technology especially in understanding on how the wobble plate concept work. Since that the technology is considered secret by its manufacturer, it is imperative for the researcher to learn the basic design of compressor, suitable sizes and material used in order to produce a good compressor. Hence, an existing single sided wobble plate compressor and double acting swash plate compressor which is already established technology and available in the market for quite some time is reverse engineered. The weakness of the reverse engineered compressor are also identified thru the reverse engineering done and is discussed briefly in chapter 2.3.2 and 2.3.4. The detailed BOM and component pictures are available in appendix A.

CHAPTER 2

THEORY AND LITERATURE REVIEW

2.1 Introduction

The vapor-compression cycle is the most widely used refrigeration cycle in practice. Its range of application covers from small refrigerator to building and automobile air conditioning for human comfort. It consists of four major components that are the compressor, condenser, expander (expansion valve) and evaporator. Research work and improvement are still being made on this system to improve the performance as well as reducing the overall cost. The operating concept of the system, currently available compressor concept and current research work with emphasize on piston compressors are highlighted in the literature review. All information and data gained through literature study are then extracted to formulate a proper methodology in designing and developing the newly proposed compressor.

2.2 Refrigeration Process

A complete vapor compression cycle [8] is shown on the T-s diagram in Figure 2.1 (b) and shown schematically in Figure 2.1 (a). The refrigerant evaporates entirely in the evaporator and produces a refrigerating effect. It is then induced by the compressor at state point 1, and is compressed isentropically to point 2. It is next condensed to liquid in the condenser, and the latent heat of condensation is rejected to the atmosphere as the heat sink. The liquid refrigerant, at state point 3, flows through an expansion valve, which reduces the pressure to that of the evaporator. In the ideal vapor compression cycle, the throttling process in the expansion valve is the only irreversible process, usually indicated by a dotted line. Some of the liquid flashes into vapor and enters the evaporator at state point 4. The remaining liquid portion evaporates at the evaporating temperature thus completing the cycle.

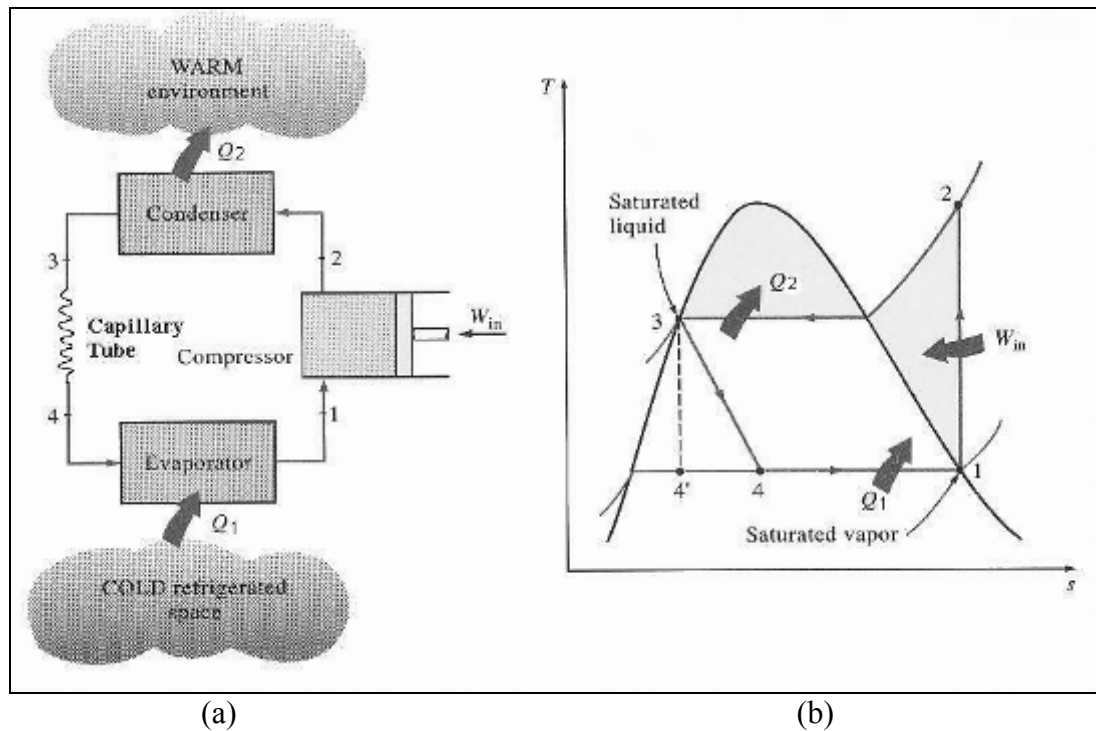


Figure. 2.1 (a) Schematic diagram of refrigeration components and system, (b) T-s diagram showing each process in the cycle. [9]

2.3 Compressors

In the case of an air conditioning system, the compressors [10] main function is to raise the pressure of the refrigerant and provide the primary force to circulate the refrigerant. At low pressure and temperature heat is transfused to the refrigerant by an evaporation process and at high pressure and temperature heat is rejected by the refrigerant by a condensation process.

Compressors can be classified into two major groups based on the characteristics [9]. The first one is a positive displacement compressors, it increases the pressure of the vapor refrigerant by reducing the internal volume of the compression chamber through mechanical force applied to the compressor. The reciprocating, scroll, screw and rotary compressors fall into this category. The second type of compressors is the non-positive displacement refrigerant compressors which increases the refrigerant pressures by depending on the conversion of

dynamic pressures to static pressures. The centrifugal compressors fall into this category.

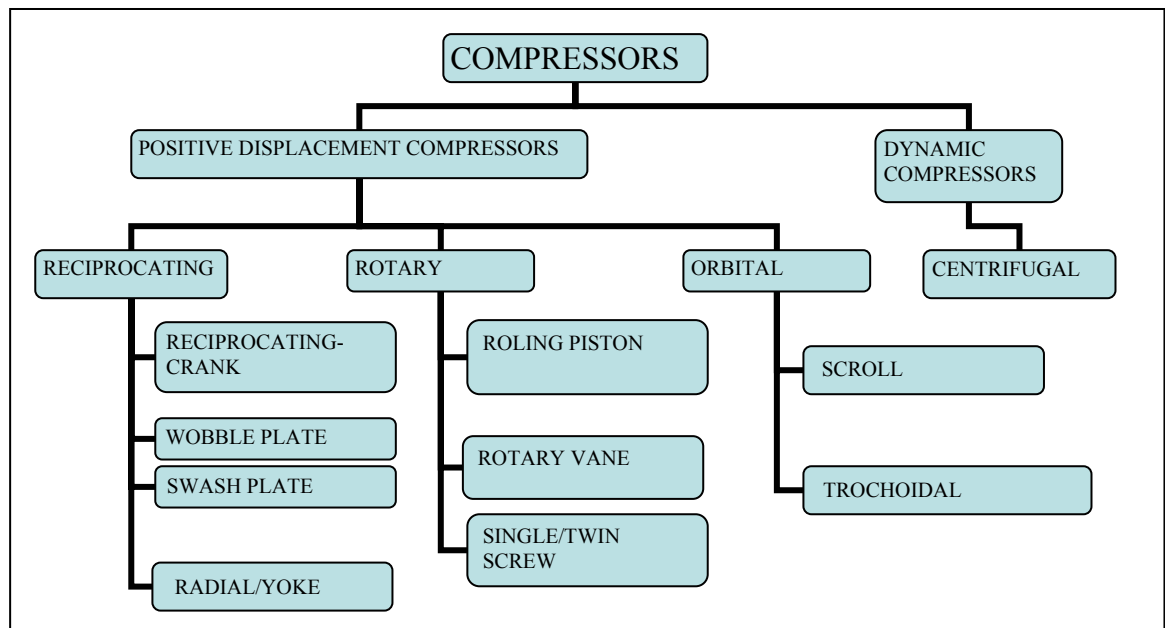


Figure. 2.2 Category of refrigerating and air conditioning compressors

Another classification exists that differentiate between compressors, pumps and blowers [11]-all these serve to create gas flows. The criterion used in the classification is the suction or delivery pressure. The ratio of discharge pressure to suction pressure is termed the compression ratio. The value of this ratio provides distinction between the three devices:-

- i. Machines operating with suction below atmospheric pressure and compressing the gas to equal or slightly higher pressure are termed as vacuum pumps.
- ii. Multi-blade machines which are designed and used to increase flow of gases with no pressure rise are termed as fans.
- iii. Machines with suction at approximately atmospheric pressure compression ratio less than 3 and with high discharge velocity are normally termed as blowers
- iv. Machines with high suction pressure and low compression ratio may be termed as circulation pump or circulator

Only machines for a final discharge pressure of 2.0265 to 506.625 bars are considered compressors. They may be further subdivided into:-

- i. Low pressure compressors for a final discharge pressure of up to 25.33 Bar
- ii. Medium pressure compressor for a final discharge pressure of from 25.33 to 101.33 Bar
- iii. High pressure compressors for a final discharge pressure of from 101.33 to 506.63 Bar

A classification of compressor size is, based on the gas flow rates:-

- i. Small – compressor handling up to 160 m³/hr
- ii. Medium – compressor handling between 160 m³/hr to 4000 m³/hr
- iii. Large – compressor handling more than 4000 m³/hr

Most compressors are driven by motors. Recent development in refrigerant compressor has produced an almost leak free hermetic compressor [8]. This hermetic compressor is sealed or welded in the same housing as the motor. The advantage of this system is that it can minimize leakage of gas refrigerant and the motor can be cooled by the low suction temperature gas flowing through the motor windings. When not fully sealed the compressor is called semi hermetic which is also known as accessible hermetic compressors. The semi hermetic type allows accessibility for maintenance or repairs thus saving operating and capital cost. The third which is the older model is an open compressor. The compressor and the motor are in two separate housing. However the combination requires that the compressor has a special shaft seal to prevent refrigerant leakage. External fan may be installed to cool down the motor.

Hermetic compressors are driven by motor directly or driven by gear trains. Semi-hermetic and open type compressors on the other hand can be driven directly, gear trains or driven by motor or other type of drivers like steam turbine, gas turbine

or diesel engine using belt and pulley. Gear train can be used to increase the speed of the compressor. However it requires about 3 percent more power input compares to that of the direct drive system [11].

2.4 Compression Concept

There many types of air conditioning compressor available in the market with each compressor have their own advantages as well as limitations. As discussed in last chapter, the compressor can be divided into two major groups; positive displacement and dynamic compressor. Positive displacement compressor can be further subdivided into three major groups; reciprocating, rotary and orbital compressors. The following section discusses in brief the working concept and its current applications.

2.4.1 Reciprocating Compressor – Crank

One of the oldest compressor concept (1865) that resembles a steam engine [12] is still in use today, not only for refrigeration and air conditioning systems but also for other applications to produce pressurized fluids such as air, natural gas and other industrial gases. A crank mechanism converts rotary motion into rectilinear reciprocating motion. An example of a reciprocating compressor is shown at Figure 2.3. A single acting piston in a cylinder is driven by a crankshaft with a connecting rod. At the top of the cylinder are a suction valve and a discharge valves. Refrigerant vapor is drawn through the suction valve into the cylinder until the piston reaches its lowest position. As the piston is forced upward by the crankshaft, it compresses the vapor to a pressure slightly higher then that of the discharge pressure. The superheated high pressure refrigerant gas opens the discharge valve and goes out of the cylinder. The gaseous refrigerant in a reciprocating compressor is compressed by the change of internal volume of the compression chamber caused by the power exerted on the piston in the cylinder. However, the crankshaft assembly requires

spaces which makes reciprocating compressors usually comes in large sizes compared to other type of compressors. This makes the concept unsuitable on certain applications where a smaller package is preferred such as in automobile air conditioning system.

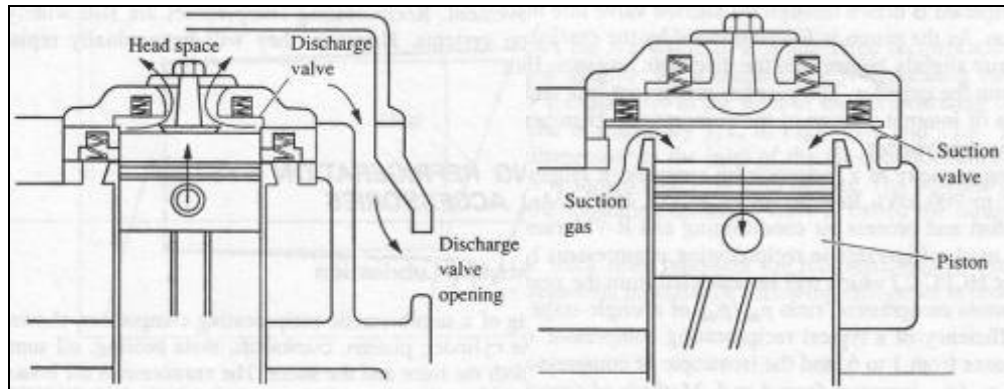


Figure. 2.3 Suction and discharge processes in a reciprocating compressor [13]

2.4.2 Wobble Plate Compressor

A wobble plate compressor drives all the pistons through an angle plate that looks like a swash plate, but the wobble plate does not rotate and drives every single piston which is connected to the wobble plate by a rod [13]. Bearings are used between the rotating rotor and the wobble plate. Usually, a five or seven cylinders single sided compressors are available for the automotive market.

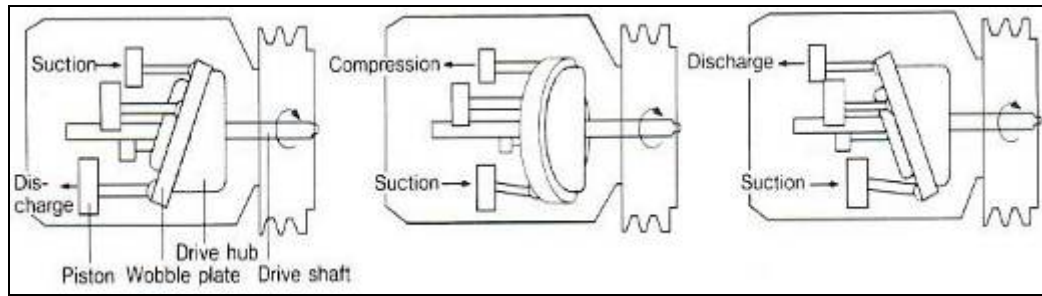


Figure. 2.4 Wobble plate compression process [13]

A closer look on the compressor through reverse engineering shows that the compressor has its advantages and disadvantages. The horizontal design of the compressor allows it to fit on small spaces compared to its much larger counterparts such as the reciprocating compressor. The design allows it to be widely used on automobiles where the compressor is placed in the engine compartment. Here, the unbalanced force originated from the compressor single plate design is negated due to the vibration generated by the engine. However, such design flaw limits the compressor application where otherwise could have been a robust compressor.

2.4.3 Variable Displacement Wobble Plate Compressor

Improved wobble plate designs have the ability to control the compressor displacement [13]. When there is low cooling load at the evaporator, the tilting angle of the wobble plate is reduced. By doing so, the compressor is more efficient as it reduces the drive load when it is not needed. It also eliminates the need to cycle the compressor off and on.

Wobble plate angle is determined by the relative pressures at each end of the piston. When cooling load calls for high output and maximum displacement, the crankcase pressure is kept low by allowing valve bleeds crankcase pressure into the suction line. When cooling demand lessens, the control valve closes the bleed to the suction cavity and opens a passage between the discharge line and the crankcase, thus raising the pressure. By doing so, the pressure at the bottom side of the piston is

increased causing the wobble plate moving to low angle and reducing the compressor displacement.

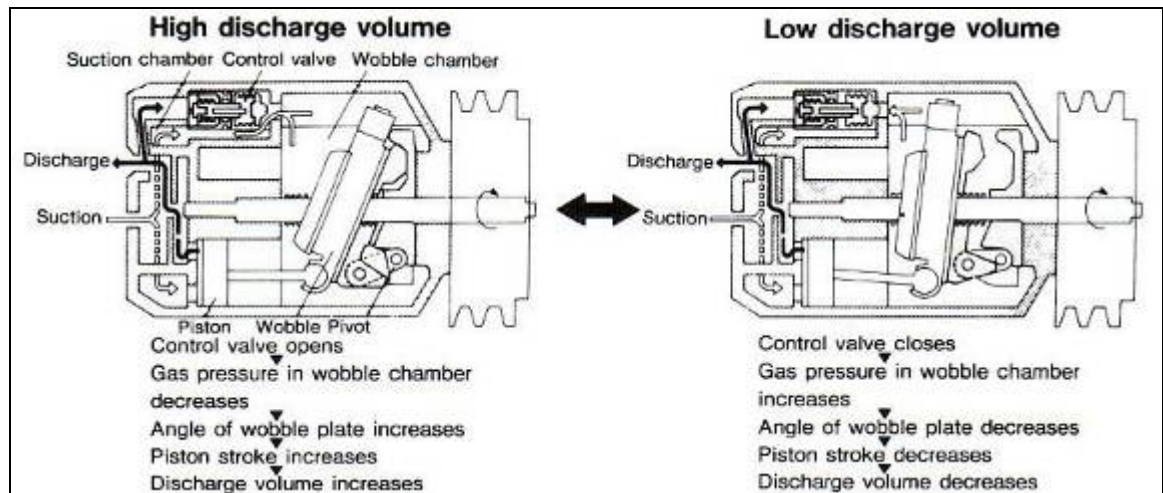


Figure. 2.5 Variable displacement wobble plate compressor operating concept [13]

A comprehensive paper is written by Skinner [14] on their V-5 Automotive variable displacement compressor. According to him, the compressor has several features and advantages compared to the old clutch pulley system. The concept offers smooth continuous compressor operation eliminating engine cycling, no discharge temperature swings due to compressor cycling and improve the fuel economy.

2.4.4 Swash Plate Compressor

In this compressor, the swash plate [13] which is attached to the device shaft drives the pistons. The swash plate is mounted at a certain angle to the shaft so it also wobbles and causes the reciprocating action of the pistons. The swash plate revolves with shaft; each piston has a pair of shoe which acts as bearings that can pivot accordingly as the swash plate slides through them. Since that each piston is double ended and arranged parallel to and around the shaft, it has a double acting effect which means that as one side of the piston is in compression mode, the other will be in suction mode. One drive shaft revolution causes each piston end to move through a complete pumping cycle.

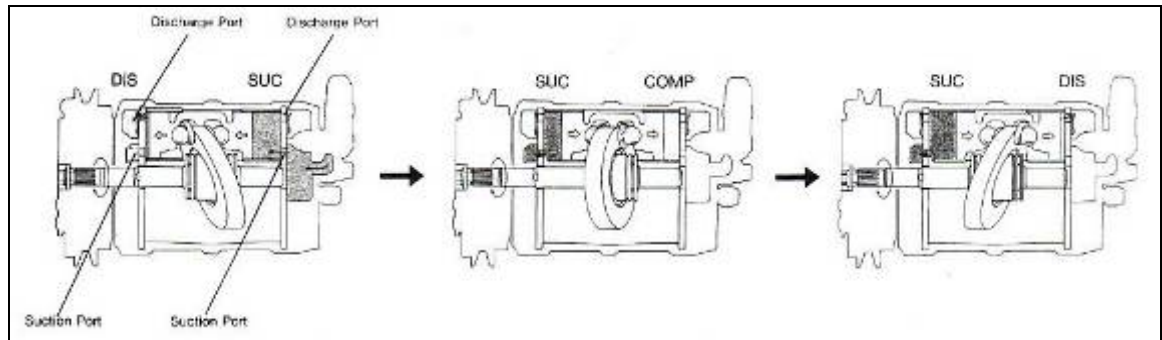


Figure. 2.6 Swash plate operating concept [13]

The double acting concept enables the compressor to come in a small package with high capacity. The number of components involve are small making it one of the cheap compressor to manufacture. Despite all the advantage this compressor has, the compressor also suffers vibration problems. The double acting piston generates unbalance moments when it operates and on investigation through reverse engineering, there was no components functioned as a counter balance for the unbalance force. The sliding shoes also generate frictions and contribute to an increase in compressor power consumption.

2.5 Radial Motion Piston Compressors

Radial compressors [13] use two double ended pistons that cross at the rotating block and scotch yoke crankshaft. Radial compressors are fairly compact and are much smaller then the in-line compressors. Usually available in intercontinental cars, the compressors have drawbacks such as complex mechanism which ultimately increases manufacturing cost and will be higher compared to that of the other reciprocating compressors.

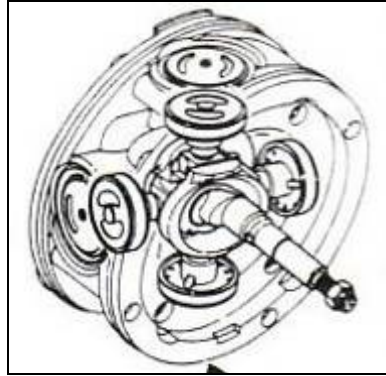
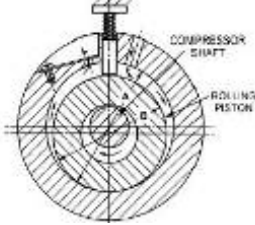


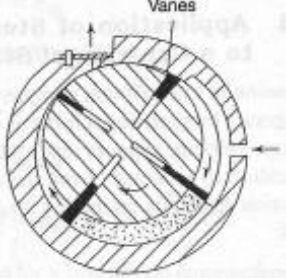
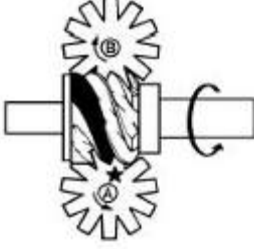
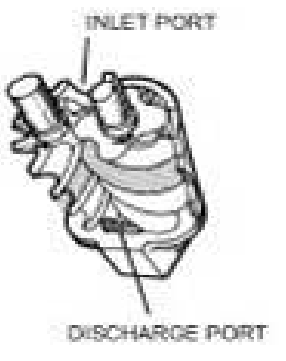
Figure.2.7 Scotch Yoke compressor [13]

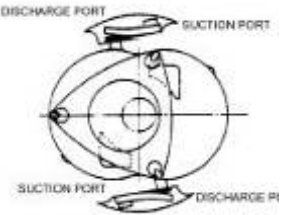
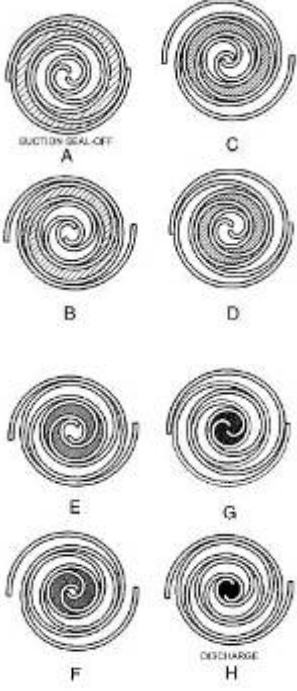
2.5.1 Rotary and Orbital Compressors

In general, there are a wide variety of rotary compressors available in the market. Listed on table 2.1 are some of the common concepts commonly used for domestic, commercial, automotive and industrial applications.

Table 2.1 Rotary and Orbital Compressors operating Concept

Concept Name/Figureures	Description	Applications
Rolling Piston [9] 	This type of compressor uses a roller mounted on an eccentric cam of a shaft with a single vane or blade suitably positioned in the non-rotating cylindrical housing, generally called the cylinder block. The blade reciprocates in a slot machined in the cylinder block. This reciprocating motion is caused by the eccentrically moving roller which pushes the vane at one end and pushed out of the slot by an opposing spring	-Household refrigerators, freezers and air conditioning system up to 2 Kw
Rotary Vane [9]	In the rotating vane type, the rotor is concentric with the shaft. Each vane slides within the rotor but is kept in contact with the inner cylinder wall due to centrifugal force. The assembly of rotor and vanes is off centre with respect to the cylinder. Rotary vane compressors have a low mass to	-Automobile a/c system with various sizes and number of vanes

	<p>displacement ratio, which in combination with compact size make them suitable for transportation air conditioning application.</p>	
<p>Single Screw [9]</p> 	<p>The single-screw compressor consists of a single cylindrical main rotor that works with a pair of gate rotors. The main rotor has helical grooves, with a cylindrical periphery and a globoid (or hourglass shape) root profile. The two identical gate rotors are located on opposite sides of the main rotor. The casing enclosing the main rotor has two slots, which allow the teeth of the gate rotors to pass through them. Two diametrically opposed discharge ports use a common discharge manifold located in the casing. The compressor is driven through the main rotor shaft, and the gate rotors follow by direct meshing action with the main rotor.</p>	<p>-Commonly used on centralized a/c system</p>
<p>Twin Screw [9]</p> 	<p>Twin screw compressors are more widely used because their isentropic efficiency is slightly higher than the single screw compressors. A typical twin screw compressor consists of a male and female lobes rotor, suction and discharge ports. When the lobes are separated at the suction port, vapor refrigerant is drawn in and the intake process continues until the interlobe space is out of contact within the suction port. The volume of gas trapped in the interlobe space within the meshing point is compressed during successive rotation of the rotor. When the interlobes space makes contact with the discharge port, the compressed gas discharges through the outlet.</p>	
<p>Trochoidal [9]</p>	<p>The trochoidal compressor is a small, rotary, positive-displacement compressor which can run at high speed up to 9000 rpm. They are manufactured in various configurations.</p>	

	<p>Trochoidal curvatures can be produced by the rolling motion of one circle outside or inside the circumference of a basic circle, producing either epitrochoids or hypotrochoids, respectively.</p>	
<p>Scroll [9]</p> 	<p>Scroll compressors are orbital motion, positive-displacement machines that compress with two inter-fitting, spiral-shaped scroll members. Compression is accomplished by sealing suction gas in pockets of a given volume at the outer periphery of the scrolls and progressively reducing the size of those pockets as the scroll relative motion moves them inwards toward the discharge port. The Figureure on the left shows the sequence of suction, compression, and discharge phases. As the outermost pockets are sealed off, the trapped gas is at suction pressure and has just entered the compression process. At stages B through F, orbiting motion moves the gas toward the center of the scroll pair, and pressure rises as pocket volumes are reduced. At stage G, the gas reaches the central discharge port and begins to exit from the scrolls. Stages A through H in the Figureure show that two distinct compression paths operate simultaneously in a scroll set. The discharge process is nearly continuous, since new pockets reach the discharge stage very shortly after the previous discharge pockets have been evacuated.</p>	<p>-Currently used on residential and commercial a/c system -Automobile a/c system</p>

2.6 Current State of Art

This section looks at the current state of art involving previous work in compressor design, development, experiment and analysis. The literature review is divided into two subtopics, design & development and experiment & analysis of a compressor. Only sources that cover related topics to reciprocating and wobble plate compressors are discussed in the chapter.

2.6.1 Design and Development

Marcos Giovani [15] presented the main advantages of using an integrated CAE/CAD/CAM system in the development of compressor for refrigeration. One of the compressor parts was selected and developed to illustrate the work which consisted of several developments phase; modeling (CAD), functional analysis (FEA), manufacture of the cast tool rack, casting of the crankcase, machining the crankcase, experimental test and final approval. The three dimensional model is the basic link among all the development phase and permits great interaction of information to several disciplines involved in the process. This prevents reworks and ambiguous information. At the end of the process, significant increase in the quality of the model and productivity in development was observed and achieved.

Suction and discharge valves must work reliably under conditions of high cyclic stresses from bending and impact. The allowable bending stress and impact velocity for the valve material are limiting factors and thus compressor manufacturers are interested in maximizing the fatigue strength of the valves. Bjorn Auren[16] was one such researcher where he described fatigue testing that had been performed on a martensitic stainless valve steel (modified AISI 420) that is commonly used in compressors. Strip steel samples with different mechanical properties were tested for bending and impact fatigue. The investigation showed that surface treatment of standard stainless flapper valve steel by tumbling and shot peening increased the compressive residual stresses and reduced stress relaxation which also led to an increase in fatigue strength. It can be further utilized to improve the efficiency in future compressor designs, as well as solve existing reliability problems.

The benefits of analytical models for developing compressor is quite obvious, parameter studies can easily be performed in order to optimize the compressor design and its use in a given refrigeration system. Because of these benefits many researchers have worked on trying to develop a completely general theoretical model. Schwerzler and Hamilton [17] were such researchers who were working on simulation and design studies of multiple cylinder refrigeration

compressor. One of the issues that were investigated in their research work is the effect of small discharge plenum on multiple cylinder compressors. This effect caused the compressor to operate inefficiently and creating pressure fluctuation in the discharge lines. A compressor designed for efficient operation at one speed or set of operating conditions of pressure may be quite inefficient at a different speed or set of operating conditions. Each of these affects are studied using the analytical model developed.

Zair Asrar et. al. [18] studied the kinematics of the wobble plate compressor. In order to understand more of the wobble plate concepts, the study was needed as it involved the characteristic of the piston movement that could help in designing and in the material selection for the compressor. Although that there are previous design concerning the wobble plate compressor kinematics, different approach was used in developing the kinematics equation. From the developed models, the force behavior for each piston can be calculated and the overall torque of the compressor was obtained.

In 1984, the variable wobble plate compressor was first introduced in the market. The variable displacement compressor automatically changed the displacement volume to match the system air conditioning requirements, allowing smooth continuous operation and thus gave a better drive ability, lower fuel consumption, and improved durability. Kenji Tojo [19] outlined the analytical model for evaluating the dynamic behavior of the variable displacement compression mechanism. The models developed gives detailed geometric and kinematic information regarding each element. It also calculated gas torque fluctuation, nutating motion of the wobble plate, constraint forces of each pair of machine elements and unbalanced forces of inertia. The research showed that because of the design concept, compromise between perfect balance , space, weight, maximum nutating angle and shaft rotating speed must be determined properly.

Another group of researchers that are taken interest in the behavior of variable displacement compressors was Ishii [20]. Their group comprised of academia and engineers from Panasonic works together in examining the

compressor dynamic behavior which enables it to control the cooling capacity continuously. They've taken step by step procedure starting by calculating the inertial forces and moments of the moving components, followed by the constraint force at each pair of compressor elements and the frictional forces generated. They have concluded that the inertial and frictional forces have significant effect upon the ability to control cooling load, quiet operation and durability while running at high speed.

There are two types of well known horizontal air conditioning compressor, one is the single side wobble plate compressor, and the other is double sided swash plate compressor. Due to the increasing demand for high speed, high performance, quiet compressor, Naoki Jingu [21] developed a swash plate compressor with a fixed displacement. The advantage and disadvantage of the existing compressor were analyzed and positive attributes were combined in the new developed compressor. However, the single sided compressor was facing problem with the lubrication oil where there was a possibility of oil loss through the piston ring into the system and unable to return to the crankcase. In order to solve the problem, new arrangement of piston rings was introduced to the compressor. Experiment conducted on single sided swash plate showed improvements over its predecessor, in addition it also easily adapted for variable displacement compressor.

David M. Ebbing [22] started the research on the control stability and NVH (Noise and Vibration Harshness) of a variable displacement swash plate compressor. As previously mentioned, the swash plate compressor offers much better running speed, NVH and displacement control which is slowly replacing the variable wobble plate compressor. Comparison was made between 6cvc125 swash plate compressor and V-5 wobble plate compressor. The swash plate compressor has several advantages compared to the existing wobble plate compressor, the obvious one is the speed capability that can reach up to 8500 rpm where as a wobble plate compressor will need an over speed protection at 5000 rpm although the maximum speed can be increase by using mechanical de-strokers. The structural noise of swash plate compressor is also much more stable due to the evenly positioned pistons which contributes to evenly distribute torque compared to a wobble plate compressor

where as the anti rotation mechanism cause the cylinder bore pattern not evenly spaced. Ebbing concluded in the end that the variable swash plate compressor design allowed it to run at high speed without affecting the durability and thus allowing for a more compact design to replace a larger wobble plate compressor.

Gabriella [23] describes the methods of measurement and data post-processing methods implemented at one compressor manufacturer to assess and evaluate the sound quality of compressors. Sounds quality is measured by computing metrics which represent the objective data. In parallel, the sound quality is assessed by jurors where different compressor sounds presented to them preferably in a control environment to ensure consistency and reliability.

2.6.2 Experiment and Analytical Work

Kaynakli and Horuz [24] investigated an automotive air conditioning system in detail by conducting experiments on such system. Certain parameters of the system such as the temperature of ambient, the evaporator and condenser and the speed of the compressor were varied and the corresponding system performance was investigated. Recorded data such as the cooling load, compressor power consumption, refrigerant mass flow rate, COP value, fluctuation of the minimum and maximum system pressures were analyzed and optimum operation conditions were determined. They concluded that the cooling capacity increases with the increase of condenser temperature and compressor speed but the COP of the system decreases in conjunction with the increase of compressor power consumption. The refrigerant flow rate was more affected by the compressor speed compared to temperature variation on the condenser, evaporator and ambient temperature.

A compressor performance if can be predicted in the early stage, the information would be very helpful for a design engineer in designing a compressor. Grolier [25] proposed a method of evaluating the performance of a reciprocating compressor using an analytical formula of the volumetric efficiency. The developed formula took account of important factors which exist during the compression

process and affect the overall refrigeration performance. Among those well known factors are like back flow through ports, valves leakage, blow by between piston and cylinder and oil mixed with refrigerant. To get a good agreement between theory and experiment, knowledge of the suction gas temperature in the cylinder and the clearance volume of the compressor are required. The results obtain based on the develop equations were compared with experimental data obtained from calorimeter test. The results agree within +/-10%.

Current air conditioning system using the variable displacement compressor has the advantage of reduced engine disturbances, smooth continues compressor operation, comfortable environment inside the vehicle passage compartment and improved fuel economy compared to the more common system where the compressor is controlled by switching on or off of the magnetic pulley. However, coupled with a thermal expansion valve the system is troubled with instability or also known as the hunting phenomenon which lead to a lower safety level, shortened life span and higher energy consumption. Changqing Tian et. al [26] conducted an experiment to find out the dynamic characteristic of the variable displacement compressor mainly on the compressor speed, discharge pressure and the cooling load effect on the piston stroke length and refrigerant mass flow rate. Several conclusions have been made; First, the discharge pressure and case pressure were found to increase together with the compressor speeds. Second, the difference between the suction and case pressures was influenced by the compressor speed and cooling load, and third there was an oscillation in the adjusting process of the piston stroke length.

During the last two decades, air conditioning system experienced significant advances along with growing popularity among auto users. Two technology advances that are noteworthy are the variable displacement compressor and parallel flow micro channel condensers. Saiz Jabardo [27] built a model as well as conducting an experimental evaluation of air conditioning system utilizing the above said technology. The objective of the models was to understand the cabin thermal control much better as there are many aspects that affect the system such as thermal load variations and stringent working conditions. An experimental rig was built to

test and check system and components performances and to obtain support data for a computer simulation program of the refrigeration circuit. In the experiment; the compressor speed, evaporator return air and condensing air temperature are varied and the corresponding results was plotted on a graph and discussed. He concluded that; variables parameters such as the compressor speed and condensing air temperature do not affect the refrigerating capacity because of the capacity control mechanism of the compressor; the refrigerating capacity is significantly affected by the evaporator return air temperature; refrigerating capacity, mass flow rate, and COP varied linearly with condensing and return air temperatures and compressor speed. The simulations results are also comparable with the experimental ones with the maximum deviations within the range of 20%.

2.7 Conclusion

There are lots of useful information that were collected from the study which have been conducted. This information were considered in order to produce a good design of a new vapor compressor such as the concept of existing refrigerant compressors, current research work on compressors as well as the proper method of conducting experiments on air conditioning systems. From the reviews of the compressor concepts, it is found that the existing compressor concept suffers design problem such as sizes, vibration and complex crank mechanism. Thus, it is imperative to design better compressors in term of the said criteria

CHAPTER 3

METHODOLOGY

3.1 Introduction

This chapter discusses the preliminary consideration of the new double sided wobble plate compressor which includes technology description, preliminary design and static analysis. The compressor is designed based on an existing double acting swash plate compressor which is widely used on a mini bus air conditioning system. The compressor is designed at 310 cc per revolution operating at a nominal speed of 1450 rpm. Further discussion on capacity of the compressor is included later in the thesis.

3.2 Description of Technology

The new compressor is an improvement of the linear reciprocating compressor otherwise also known as the double acting swash plate compressor. Additional features are introduced to increase the overall performance while maintaining its small size as against that of the common reciprocating compressors which are bulky, heavy and relatively tall.

The new invented compressor is named as Symmetrical Single Acting Wobble Plate compressor (SSAWP). The novelty of this invention is that the compression mechanism is set on both sides of the pistons. The compressor has each pair of piston-cylinder assembly of opposing forces cancelled, both during suction and compression, creating a dynamically balanced machine. Whereas in the existing swash plate compressor, while cylinder at one end is in compression mode the cylinder at the other end is in suction mode, as describe earlier in section 2.5.4 and illustrated in Figure 2.6. Such movement of each reciprocating piston creates the

unbalance force and the combined movement of all pistons will create instability to the machine. Figure 3.1 shows the cross section of the new symmetrical wobble plate compressor.

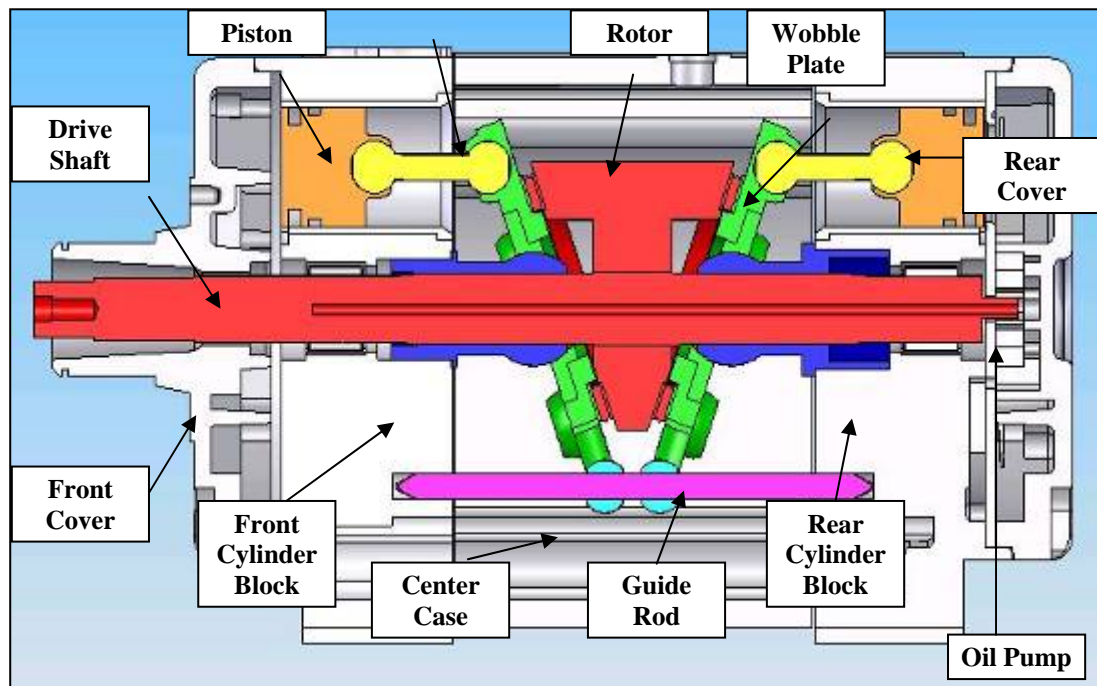


Figure 3.1 New Design of Symmetrical Wobble Plate Compressor

Referring to Figure 3.1, the pistons and the wobble plate are connected by a connecting rod employing a ball joint assembly. Each wobble plate assembly is sandwiched between a rotor and a supporting sphere through which the shaft passes. As the shaft and rotor rotates, it acts like a cam mechanism driving the wobble plate in a nutating path. This will produce a reciprocating motion at one point of the wobble plate and transmitted to the piston via the connecting rod. A guide rod or an anti rotating mechanism is required to prevent the wobble plate from rotating together with the rotor. The wobble plate assemblies are symmetrical to each other and this means that the motion of each pair of opposing pistons is the same in magnitude but opposite in direction. Thus, theoretically all dynamic forces caused by the reciprocating movement of piston on the horizontal axis are cancelled. This yield a balance and less vibration compressor while operating at higher speed.

Figure 3.2 shows the cross section view and the compression step of the proposed new concept. The first half shaft rotation was the suction mode where gas is being induced into the compression chamber. The second half shaft rotation was the compression mode where gas is being compressed and discharge to the discharge manifold.

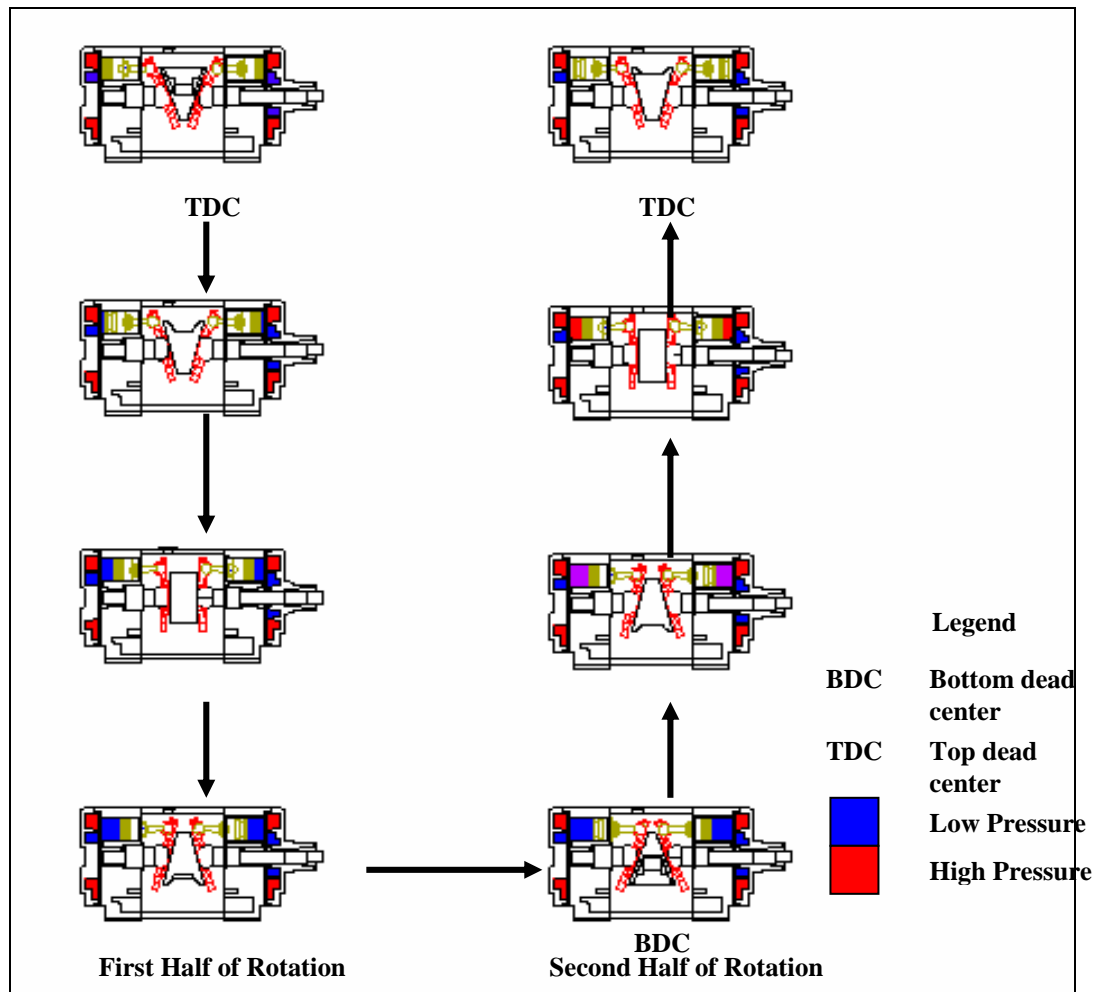


Figure 3.2 New Compressor Working Step

3.3 Preliminary Design

Once a concept is finalised the next thing to do is to list all the design considerations and technical specification. Tothero [28] ruled out a few significant considerations that must be taken into account, which are: description of the design, displacement/ capacity, materials, valves and lubrication. The design and development sequences are as shown in Figure 3.3.

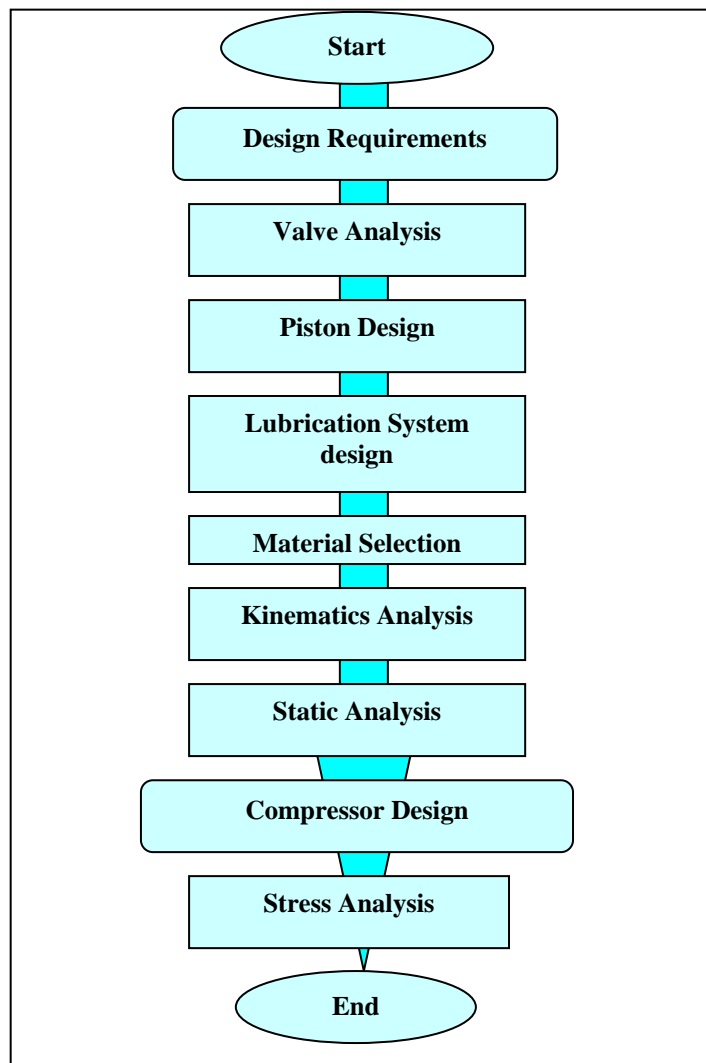


Figure 3.3 Design and Development Sequences

3.3.1 Determination of Compressor Specification

In determining the principal dimensions of the compressor, the displacement required for the application selected must first be known. Since that the compressor will be used for a mini bus air conditioning system, the existing information of the compressor that is currently used on the bus is then taken as a reference for the new compressor. The displacement for the existing swash plate compressor is 313 cm^3/rev [2], and this value is taken as the displacement of the new compressor to be designed.

An optimum number of pistons have to be selected to deliver the capacity required. In doing so, the appropriate speed N and a satisfactory stroke piston diameter ratio, v and the mean piston speed, C_m will be designed. To simplify the design process, several piston diameters which come in standard size are considered, analyzed and the piston is selected if found. Standard size piston [29] is selected because the piston which is readily available comes with piston rings and thus will cut down on the manufacturing cost. Having fixed the displacement and diameter of piston, the number of piston required and the stroke can also be determined. The stroke ratio v [911] depends not only on the delivery pressure of the compressor but also the speed of the reciprocating machine. Vacuum pumps and high speed air compressors for example has $v \geq 0.5$, for fluorocarbon compressors usually $v \approx 0.8$, for ammonia compressors $v \approx 1$ and for high pressure compressors $v \approx 4$ to 6. The stroke [911] of a compressor for a given piston diameter can be calculated using equation 3.1.

$$L_p = \frac{4V_p}{\pi D_p^2} \quad (3.1)$$

The compressor rotating speed, N is the main factor in determining the dimensions and number of cylinders for a given flow-rate of refrigerant in a compressor. The mean piston speed C_m of the compressors can be calculated using the following equation:-

$$C_m = \frac{L_p N}{30} \quad (3.2)$$

For all types of compressor, high piston speeds with high rpm cause considerable wear of pistons, piston rings and cylinders. High mean piston speed will result in higher rate of rubbing of piston parts and the frictions generates heat and wear thus contaminates the lubrication oil requiring the oil filter to be replaced very often. Other disadvantages of high compressor speeds are the valve lift design is smaller to coop with the fast suction discharge process resulting in an increase in losses due to throttling. The volumetric efficiency is also affected as the valve port

diameter and clearance volume are proportionally larger to allow more gas to pass through due to high speed. The valve plate is subject to vibration when operating at high speed which in turn affects the overall compressor operation. The present tendency is to limit the mean piston speed. The mean piston speed [911] is normally:-

Small compressors	$C_m \leq 2$ m/sec
Medium compressors	$C_m \leq 3$ m/sec
Large compressors	$C_m \leq 5$ m/sec

Total swept volume specified is $313 \text{ cm}^3/\text{rev}$. There are three standard diameters of piston to be chosen depending on the numbers of cylinders that the block can accommodate to give $313 \text{ cm}^3/\text{rev}$ of refrigerant gas. The computation is shown in table 3.1.

Based on the data in table 3.1, piston sets with stroke ratio larger than 0.9 and lesser than 0.7 are not considered. This involved piston sets with diameters of 32 mm and parts of piston sets with diameters of 36 and 42. Only sets with number of piston 10 and 6 with diameters of 36 mm and 42 mm respectively are found to be within criteria considered as stated previously. The next parameter that is considered is the mean piston speed, it clearly shows that piston sets of diameter 36 mm with number of piston 10 have better attributes than the other sets and thus selected for the prototype.

Table 3.1 Mean Piston Speed for Multiple Piston Configuration ratios

Piston Dia. (mm)	No. of Piston	Swept Volume for one Piston	Stroke /Dia Ratio	Mean Piston Speed (m/s)	
				1250 rpm	3000 rpm
32	6	64.24223	2.00757	2.67676	6.424223
	8	48.18167	1.505677	2.00757	4.818167
	10	38.54534	1.204542	1.606056	3.854534
36	6	50.75929	1.40998	2.114971	5.075929

	8	38.06947	1.057485	1.586228	3.806947
	10	30.45558	0.845988	1.268982	3.045558
42	6	37.29254	0.887918	1.553856	3.729254
	8	27.96941	0.665938	1.165392	2.796941
	10	22.37552	0.532751	0.932314	2.237552

3.3.2 Valve System

Suction and discharge valves are two important parts in a reciprocating compressor. Successful valve design will provide long life and low pressure lost while on the other hand, a poorly designed valve which handles a high gas velocity and poor mechanical action resulting in high pressure lost and an increase in power consumption. Such event occurs when the valve failed to open or close at the precise discharge point resulting in unnecessary pressure build up and gas backpressure. As outlined by ASHRAE [89], a valve should meet the following requirements :-

- i. Large and straight flow areas with short travel distance
- ii. Symmetric design low valve mass with small lift for quick action
- iii. Minimum clearance volume
- iv. Durable yet low cost
- v. Tight sealing at ports with minimum valve flutter

Valve in use nowadays usually falls in the free-floating reed valve, reed clamped at one end, ring valve, or valve formed as a ring. In case of the new proposed compressor, the valve is designed based on free floating reed valve for the suction port and reed clamped at one end for the discharge port. This is based on the existing simple valve design and the valves produced are cheap and found installed on most air conditioning compressor.

After the required displacement has been determined the design of the compressor valve was embarked upon. Wernel [30] have constructed step by step method to design the valve ports and plates. A detail step by step calculation is outlined by Appendix B in order to produce a good working valve. The method is rewritten in the thesis and applied for the valve port design in the new compressor.

The first step in designing the valve system is to determine the average flow velocity particularly at the discharge port since that it operates at higher pressure and velocity. Since the design has the resemblance of a reciprocating compressor, a generous amount of clearance volume is allocated first to accommodate the valve operation.

A typical p-v diagram is then constructed as shown in Figure 3.4. At position 1, the piston is at bottom dead center. Both valves are close as the piston starts to compress the gas. At point 2, the discharge valve opens and the gas is pushed out at constant pressure until point 3. The volume of the suction gas is V_1-V_4 at pressure P_1 or P_4 .

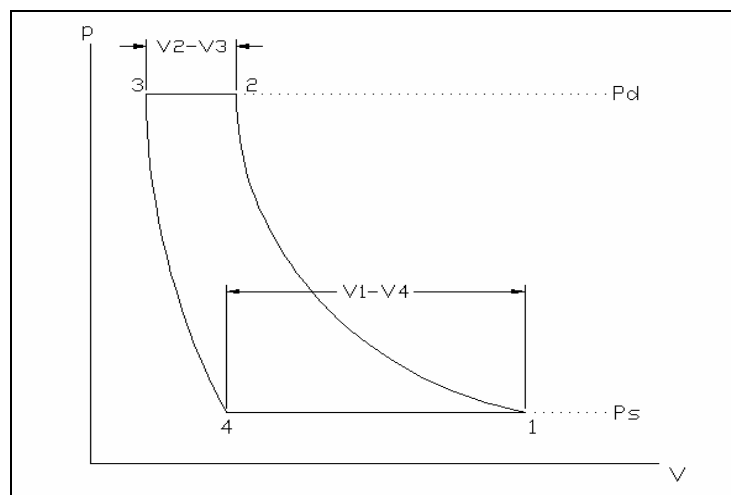


Figure 3.4 Typical P-V diagram [30]

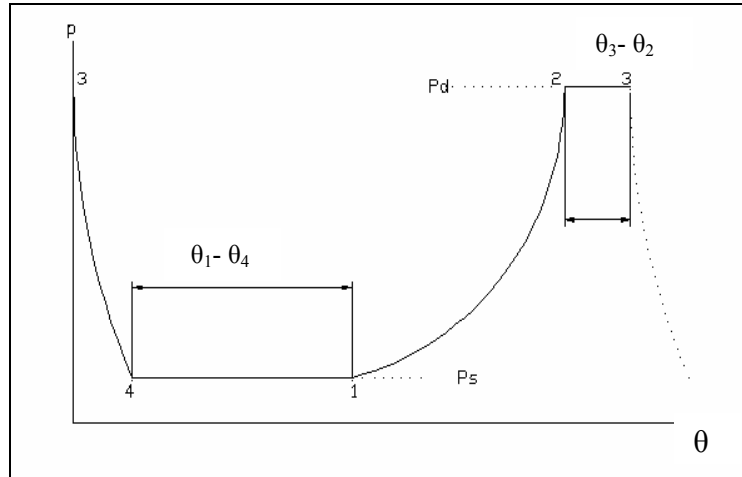


Figure 3.5 Pressure versus Shaft Angle Position [30]

Next, we establish a relationship between volume and time or preferably shaft (crank) angle since that the idealized indicator diagrams is independent on the shaft speed. For a reciprocating compressor, the related diagram is shown in 3.5. $\theta_1 - \theta_4$ is the crank angle where the suction valve is open and the discharge valve open at $\theta_3 - \theta_2$. These angles can be converted into opening times assuming that the compressor runs at constant speed of w (rad/s).

$$t_{v1} - t_{v4} = \frac{1}{w} (\theta_{v1} - \theta_{v4}) \quad (3.3)$$

$$t_{v3} - t_{v2} = \frac{1}{w} (\theta_{v3} - \theta_{v2}) \quad (3.4)$$

From the diagram it is learned that the duration of the valve opening is proportional to shaft speed, the faster the shaft rotates the duration of valve opening becomes shorter. For convenience, only the discharge port was calculated as it is more critical then the suction port. Thus, the average flow velocity of an ideal discharge valve of flow area A_d is

$$v_d = \frac{V_2 - V_3}{(t_3 - t_2)A_d} = \frac{Q_d}{A_d} \quad (3.5)$$

It is important to realize that this is only an average value since that in the actual valve the volume pushed out per unit time is not constant and dependent on the kinematics. Also, the inability of the valve to open instantly is not considered in the equation. The same equation can be used to calculate the average speed of the suction valve under the same condition.

Based on experience and the theoretical argument [30] that pressure drops and flow losses in a valve are a function of the square of the flow velocity according to

$$\Delta p = \zeta \frac{\rho v^2}{2} = \zeta \frac{\rho (Mc)^2}{2} = \zeta \frac{\rho}{2} kRTM^2 \quad (3.6)$$

Based on equation 3.6, it shows that the Mach number is important or the deciding factor. At a given temperature and mass density, it is recommended that $M \leq 0.2$ [30]. The allowable flow velocity is, therefore,

$$v = Mc \quad (3.7)$$

where,

$$c = \sqrt{kRT} \quad (3.8)$$

The required effective flow area is, therefore,

$$A_{ef} = \frac{Q_d}{v_d} = \frac{Q_d}{M_d c_d} \quad (3.9)$$

The valve opening lift height is established by dividing the port area by the effectively available circumferences of the covering plate or reed. However, for a flexible ring valve the gap area is not simply the circumference times the lift height.

Rather, h_v is interpreted as an average value. For a reed valve, the available circumference is equal to

$$C = \pi D \quad (3.11)$$

Thus, the average required valve lift height is

$$h_v = \frac{A_{ef}}{C} \quad (3.12)$$

A valve stop is introduced to the design so that the valve will rest against this stop during most of its opening time. If not, the valve will overshoot its equilibrium position and flutter is introduced as the valve will not return to its original closed position slowly as it overshoots the opposite direction. The valve stop will not only prevent flutter but also to some extent reduce noise, gas pulsation and preventing high impact stresses on the valve.

The effective stiffness of the valve whether it is provided by a spring or by flexural resistance of a reed valve is determined by the maximum required valve lift, h_v . As a rough approximation, we estimate the stiffness from the momentum impulse law, ignoring Bernoulli effects due to wide valve seats, stream line detachment and reattachment. Thus, the average force required to reach the opening height, h_v is,

$$F_v = \rho A_{ef} v^2 \quad (3.13)$$

From equation 3.7, we now have,

$$F_v = k A_{ef} p M^2 \quad (3.14)$$

For a spring loaded plate valve,

$$K_s = \frac{F_v}{h_v} \quad (3.15)$$

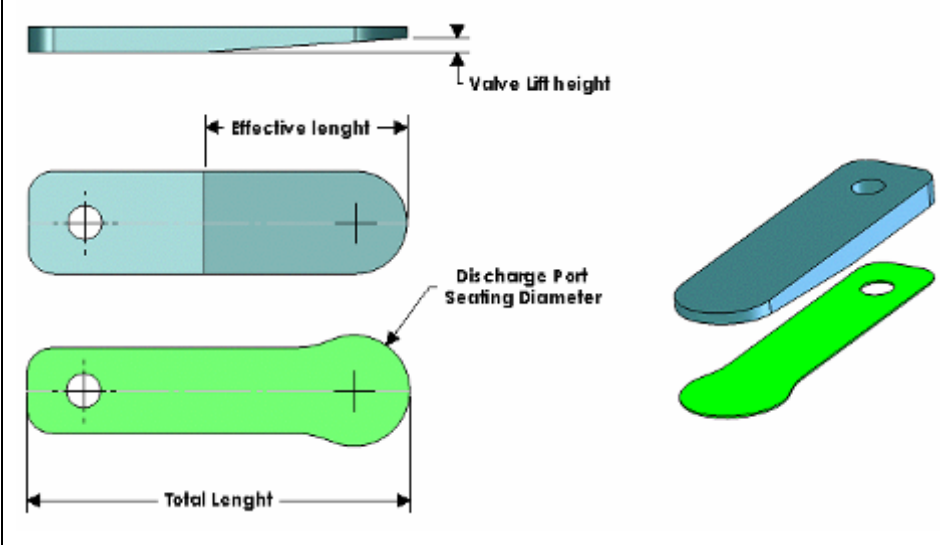
For a reed valve, the force given by this approach represents an approximate value only because of the flexure and expressed in term of resultant. In a case of a cantilever beam type reed, the width b based on the seat area and the thickness, t as

$$t_v = L_v \sqrt[3]{\frac{4K_s}{Eb_v}} \quad (3.16)$$

Assuming that a proper material has been selected, two parameters that should be that we may look at are the width, b and length, L .

The spring stiffness is important to assist a valve in closing at the proper time. However, if the stiffness is too high it will retard the opening which contributes to flow losses. With these important effects discussed, it is important that the valve is carefully designed to obtain maximum efficiency possible. All of the above calculations are included in Appendix B. The final design data of the valve are presented in table 3.2.

Table 3.2 Valve Geometry



Discharge Port Diameter	9 mm
Discharge Port Seating Diameter	12 mm
Effective Length of Reed Valve	24.65 mm
Valve Lift Height	2.5 mm
Total Length of Reed Valve	30 mm
Valve Thickness	0.3 mm

3.3.3 Piston and Piston Rings

The main requirement of a good piston is good sealing and lightweight [13]. A properly design piston will increased the mechanical efficiency of the compressor by reducing the inertia forces and delivering more gas to the system. Usually, pistons are made of cast iron, cast steel with thin walls and other non ferrous metal such as silumin and aluminum. One good example is an effort by Lee [31] who investigated the fabrication process and the material properties of SiC_p/Al-Si metal matrix (mmc) pistons. According to him, a good aluminum based piston should have high strength, good wear resistance and light. As for the new compressor, early prototypes were using existing piston used for small lawn mower engine. Later in the development stage, a custom made piston using aluminum as the material was introduced. The main purpose of the new piston is to adopt a design that is more

suitable for compressing gas. The previous piston had bigger clearance volume and using scarf joint rings which may cause leakage in the compressor. Hence a new full circle type piston ring with special properties was selected. Detail on the material and size of the piston rings are included in Appendix C.

3.3.4 Lubrication system

Basically, there are two types; oil flooded system and oil force feed lubrication system. A flooded system depends on the compressor own devices such as the crankshaft or the wobble plate to lift the lubrication oil to the shaft level, bearings or piston rings. There was no pressure developed by this system so it is not considered as force feed as it only requires splashes caused by the moving component inside the crankcase. A force feed system may include a pump gear or plunger which develops pressure to deliver lubrication oil to the designated parts of the compressor.

In the proposed new compressor, both systems are applied. A small portion of the wobble plate and guide rod is submerged in the lubrication oil. When the compressor operates, the movement of the wobble plate and guide rod will splash the oil inside the crankcase and lubricate ball joints, thrust bearings and piston rings. The force feed system is needed to lubricate journal bearings where the splashed oil cannot reach. A cycloidal pump [32] is selected to force feed the oil from the oil sump to the thrust bearings, needle bearings, ball joints, ball mounts and other rubbing components thru a series of passages interconnecting from the oil sump, cylinder block and shaft. As the shaft rotates, it act as the driver for the pump internal rotor sucking oil from the bottom oil sump and pushing it through the small hole passage inside the shaft. Also, the discharge oil acted as a sprinkler inside the crankcase simultaneously sending oil to rubbing components at the top level of the compressor which flooded system may not reach. Detail calculation on generation of the cycloidal profile via vector generation is included in Appendix D. Detail design is described in sub-section 4.3.5. As for the lubrication oil, similar type of oil that is currently used with the existing swash plate compressor is selected. Since that both

mechanism are almost identical and using refrigerant R134a as well, the oil selected should perform without any problem in the new compressor.

3.3.5 Materials Selection

Since that the compressor is designed for automobile use and in this case for bus air conditioning system, a light weight and compact compressor is preferred. Existing model such as the reciprocating compressor have a bulky and heavy design thus limiting the available space inside the engine and hard to move during maintenance. The material selected should have the strength to withstand long hour's operation while at the same time relatively cheap to produce. Trade offs between durability and lightweight is an important criteria that is considered during the design process. Based on the criteria mentioned as well as on experience with other types of compressors readily available in the market for similar operation, suitable material is none other then aluminum alloy. However, it is well known that shelf grade aluminum alloy have a low strength and vulnerable to friction compared to other metal. This however will limits the material usage on the new compressor where only none or low friction components such as the pistons, wobble plates, and rotor can be used.

On other parts which is exposed to frictions and stresses, extra strength materials are used. Steel's versatility lends itself well to the production of parts that must possess high strength or hardness. Thus, steel is the material of choice for the compressor shaft, guide rods and mating adaptors such as the ball mount and slide ball adaptors.

The new compressor also used casting method [33] for the cylinder blocks and crankcase. The method used was known as CO_2 sand cast using silicate of soda as the binders. A small amount of silicate of soda is mixed on the sand that is going to be used for the sand moulds, CO_2 gas is then introduced into the sand. When CO_2 contacts water in silicate of soda, carbonic acid is formed and neutralizes the silicate

of soda forming a glass bond for the molding sand. It only requires about 2.5 to 4 percent depend on the mass involved and the whole process requires short time and save cost to complete. In the case of the existing compressor, most of the compressor casings used are found to be Aluminum LM-25 [34] based. However the actual percentage of other components in the alloy such as Titanium, Zink, Silicon and Iron was not precisely determined. Even if it was, it may not be available in the market and it will be difficult and too expensive to produce the alloy in-house.

3.4 Compressor Kinematics Analysis

The reciprocating motion of the piston is achieved when the rotation of the shaft is converted to a wobbling motion of the wobble plate. It is of utmost importance for the designer to understand how such motion is achieved. Comprehensive kinematic analysis has been carried out for the mechanism and the reciprocating piston by Zair [16]. Based on the analysis, the tilting angle of the wobble plate and the displacement of pistons relative to shaft rotation can be studied in greater detail. Detailed calculation to determine the piston tilting angle and displacement were obtained by Zair [16] and are included in Appendix E.

Figure 3.6 shows the tilting angle of wobble plate with respect to shaft rotation and Figure 3.7 shows the displacement of the pistons also with respect to shaft rotation. By understanding the wobble plate and piston stroke movement with respect to shaft rotation angle, the static analysis of the compressor was calculated and included in sub-section 3.5.

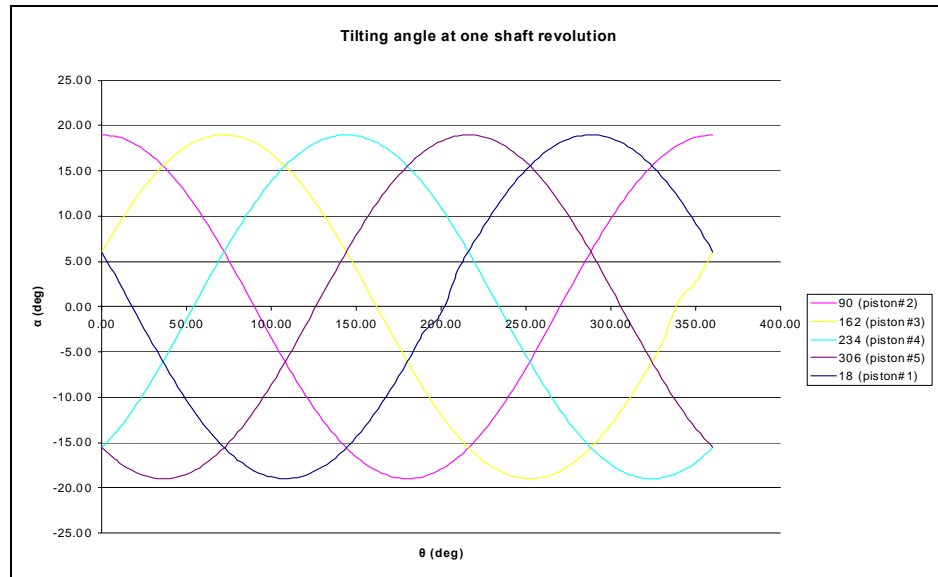


Figure 3.6 Tilting Angle versus Shaft Angle of Rotation

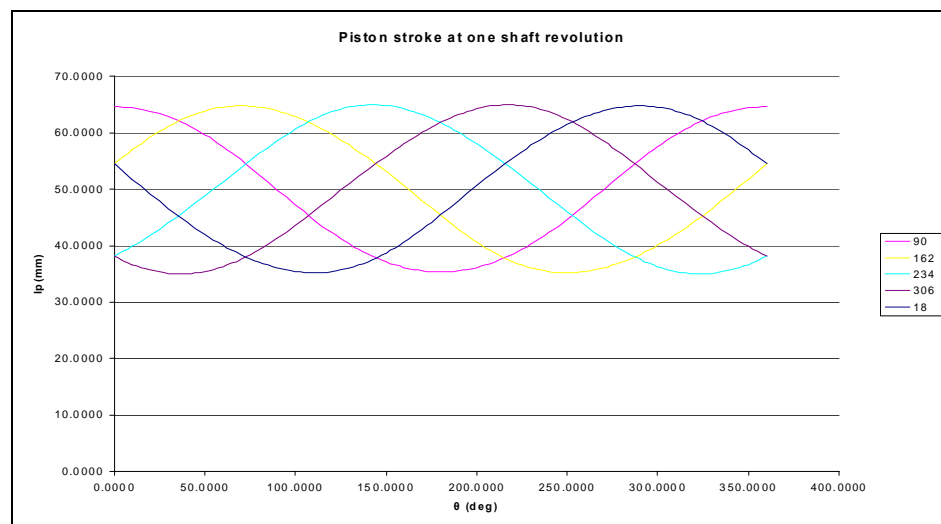


Figure 3.7 Piston Stroke versus Shaft Angle of Rotation

3.5 Compressor Static Analysis

Only static analysis was conducted for the prototype as a quick solution to determine the forces that are involved in the critical components considering that this is the preliminary work in developing the compressor based on the new concept. Detailed dynamic and kinematics analysis are conducted and prepared by a fellow

research member as another master degree project on the development on a similar concept but for a very high pressure (230 bar) multi stage compressor.

The static stress analysis is basically to estimate the safety factor of critical parts in the compressor. These are parts that are subjected to high loads due to the gas pressure which may result in deformation and failure during operation. The critical parts are the piston, wobble plate and shaft assembly. The derived equations are then solved based on operating pressure of 20 bar at the discharge area and 3 bar at suction area. Using this approach, initial design of the compressor is made simple and safe as the shape and sizes of the compressor with the corresponding stresses analyzed using finite element method software such as COSMOS. All of the forces calculated in the following chapter are presented in Appendix F.

3.5.1 Piston free body diagram

The static analysis is started at the pistons where pressure force is exerted on the piston cylinder surface. This force is same for to each compression stage but varies as the shaft turns. By using simple thermodynamic analysis and the piston position obtained from the kinematics analysis, the variations of gas pressure for a particular piston with the shaft rotation angle are given in Figure 3.8 respectively. Figure 3.9 represents the piston model in general and is not specific in design. Actual design may vary from initial prototypes to the final design.

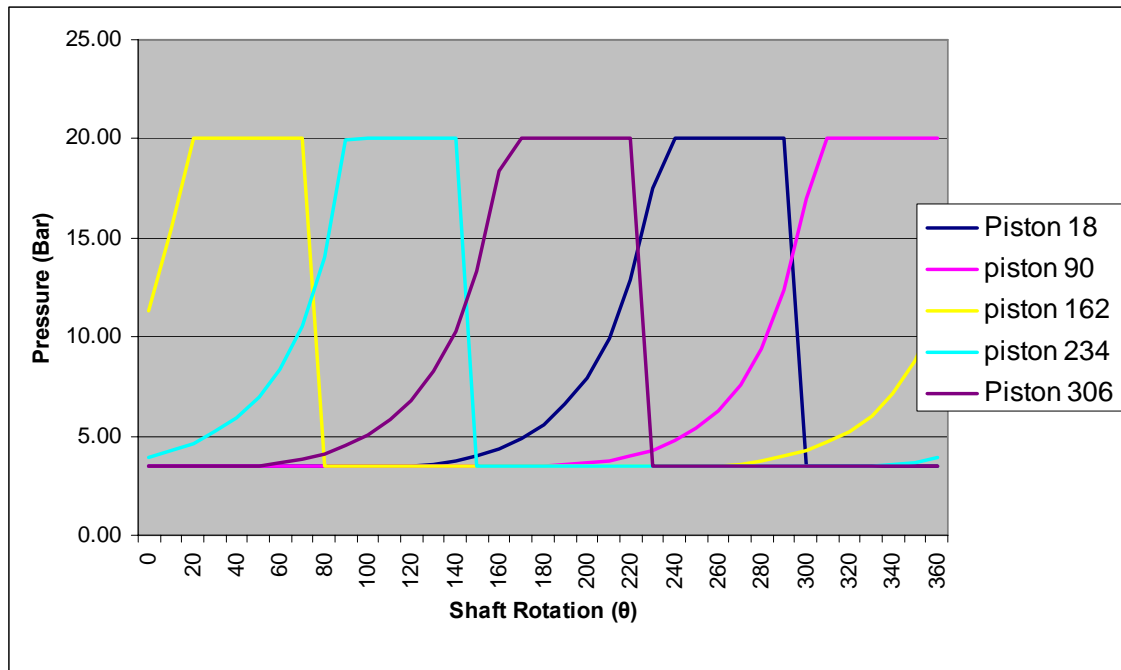


Figure 3.8 Variation of Pressure on Piston with Shaft Rotation Angle

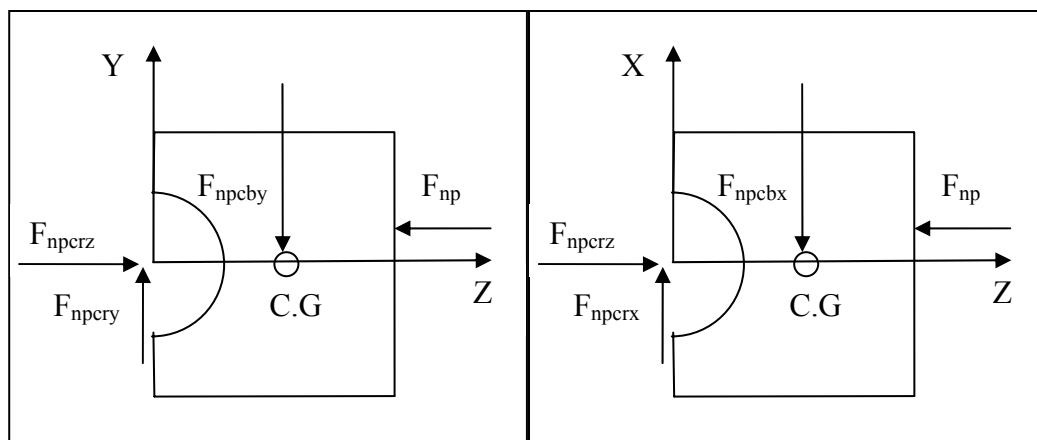


Figure 3.9 Piston Free Body Diagram

Forces acting on a single piston are connecting rod reaction force (F_{npcr}), gas pressure force (F_{np}) and cylinder block reaction force (F_{npcb}). With the aid of Figure 3.9, the analysis is done in 2-D for easier calculation. The force equation can be written as;

$$\begin{aligned} \sum F_y &= 0 \\ F_{npcry} + F_{npcby} &= 0 \end{aligned} \quad (3.18)$$

$$\begin{aligned}\sum F_x &= 0 \\ F_{npcrx} + F_{npcbx} &= 0\end{aligned}\quad (3.19)$$

$$\begin{aligned}\sum F_z &= 0 \\ F_{npcrz} + F_{np} &= 0\end{aligned}\quad (3.20)$$

3.5.2 Connecting Rod Free Body Diagram

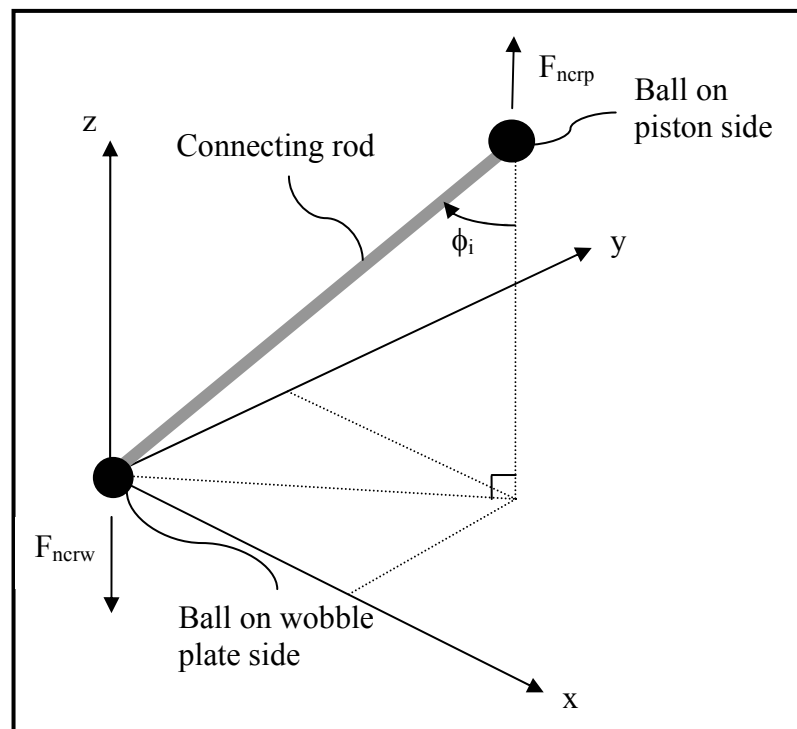


Figure 3.10 Connecting Rod Position

Connecting rod is used to transfer the plate wobbling motion into piston reciprocating motion in the cylinder. The forces acting on a single connecting rod are piston reaction force (F_{ncrp}) and wobble plate reaction force (F_{ncrw}) as shown in Figure 3.10. The force generated on the piston by the connecting rod also exerts an equal but opposite force on the wobble plate which is known as a two force body problem.

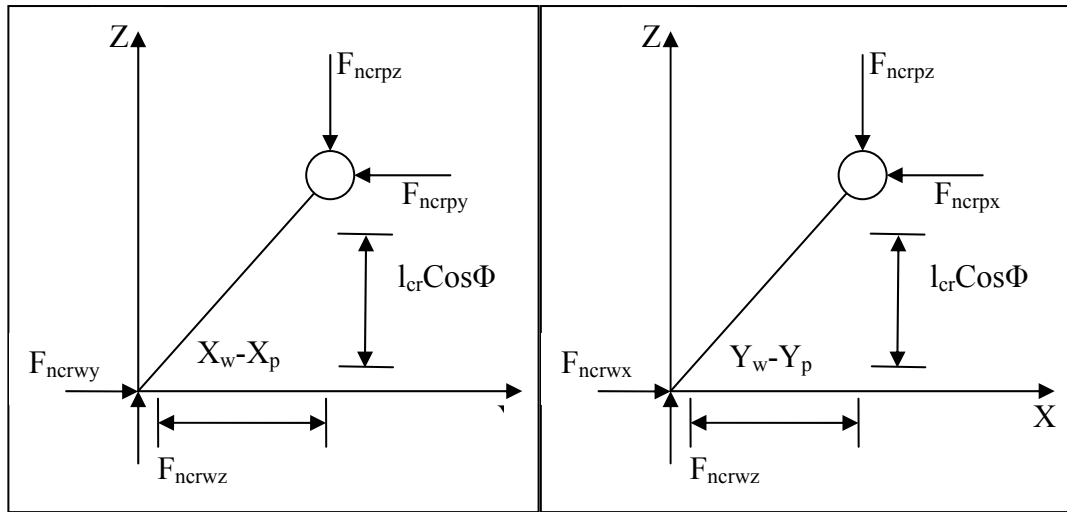


Figure 3.11 Connecting Rod FBD

Figure 3.11 shows the piston force components x, y and z and can be written as:-

$$F_{ncrpy} = \frac{F_{ncrpz} (X_{nw} - X_{np})}{l_{cr} \cos \phi} \quad (3.21)$$

$$F_{ncrpx} = \frac{F_{ncrpz} (Y_{nw} - Y_{np})}{l_{cr} \cos \phi} \quad (3.22)$$

Thus;

$$\begin{aligned} F_{ncrpx} &= -F_{ncrwx} \\ F_{ncrpy} &= -F_{ncrwy} \\ F_{ncrpz} &= -F_{ncrwz} \end{aligned} \quad (3.23)$$

3.5.3 Wobble plate free body diagram

At the centre of the wobble plate is a hole on which a female spherical profile shoe is fitted tightly. In the analysis, the wobble plate and the shoe are assumed as a single body. It is sandwiched between the rotor and a male ball mount. The shaft passes through the rotor, the spherical shoe and the ball mount. The rotor

caused the plate to wobble about the ball mount. The frictional force exerted by the rotor on the wobble plate is counteracted by the anti rotating mechanism installed at the lower part of the wobble plate preventing it from rotating along. To simplify the process, the guide rod reaction force, F_{grx} was assumed acting on the x-axis only. Simple approach was taken by Tian [35] in developing their mathematical model for the variable displacement compressor. In this prototype there are five pistons/cylinder pairs on each side of the rotor. Each piston is assembled to the wobble plate by a connecting rod which has a spherical ball welded to each end. During compression, the pressure forces are acting on the wobble plate through the connecting rods. For simplicity, each connecting rod is analyzed using a general equation which has a different value due to different location of the connecting rods at any given time. As a note, each of the equation presented in this chapter presented a single connecting rod affecting the wobble plate assembly. The total of each connecting rod forces affecting the male ball mount and the anti rotation mechanism is computed in MS Excel and presented in Appendix F.

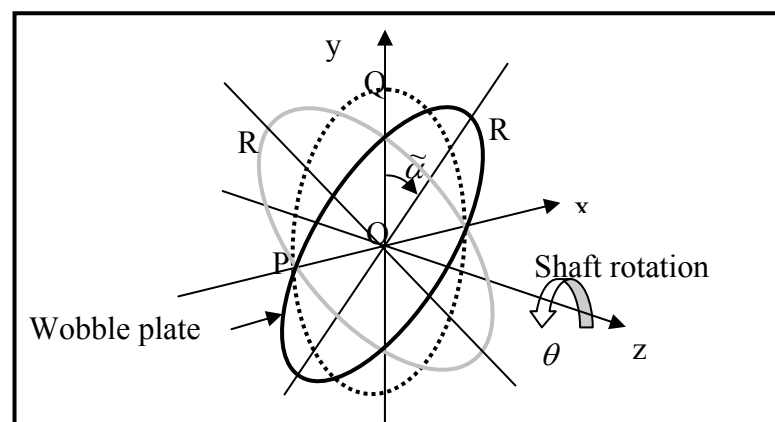


Figure 3.12 Wobble Plate Position Coordinate System

Using coordinates such as shown in Figure 3.12, the force analysis is first conducted on a y-z plane.

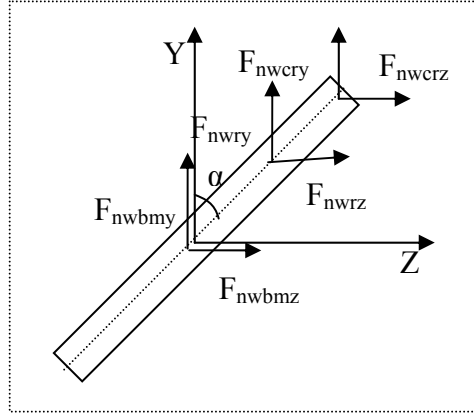


Figure 3.13 Wobble Plate Free Body Diagram on Y-Z Plane

Based on Figure 3.13, force equations on y-z plane are derived;

$$\begin{aligned}\sum F_{ny} &= 0 \\ F_{nwcry} + F_{nwry} + F_{nwbmy} &= 0\end{aligned}\quad (3.24)$$

$$\begin{aligned}\sum F_{nz} &= 0 \\ F_{nwcrcz} + F_{nwrcz} + F_{nwbmz} &= 0\end{aligned}\quad (3.25)$$

$$\begin{aligned}\sum M_{x-x} &= 0 \\ F_{nwcry} \cdot l_{nwcrcz} + F_{nwry} \cdot l_{nwrcz} - F_{nwcrcz} \cdot l_{nwcry} - F_{nwrcz} \cdot l_{nwry} &= 0\end{aligned}\quad (3.26)$$

Since force F_r is always perpendicular with wobble plate plane (thrust bearing), F_{nwrcz} can be written as;

$$F_{nwrcz} = \frac{F_{nwry}}{\tan(\alpha)}\quad (3.27)$$

By inserting equation 3.27 into 3.26, we have;

$$F_{nwry} = \frac{F_{nwcrcz} \cdot l_{nwcry} - F_{nwcry} \cdot l_{nwcrcz}}{l_{nwrcz} - \frac{l_{nwry}}{\tan(\alpha)}}\quad (3.28)$$

Solving equation 3.24, we have;

$$F_{nwbmy} = -(F_{nwcry} + F_{nwry}) \quad (3.29)$$

Solving Equation 3.25, we have;

$$F_{nwbmz} = -(F_{nwcrz} + F_{nwrz}) \quad (3.30)$$

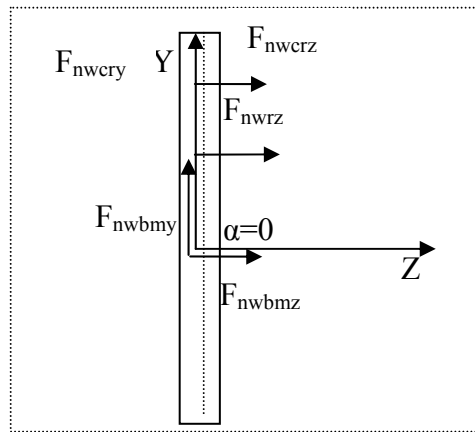


Figure 3.14 Wobble Plate Free Body Diagram on Y-Z Plane at $\alpha=0$

However based on Figure 3.11, at $\alpha=0$ force F_{nwry} is equal to 0 and equation 3.26 is written as;

$$\begin{aligned} \sum M_{x-x} &= 0 \\ F_{nwcry} \cdot l_{nwcrz} - F_{nwrz} \cdot l_{nwry} &= 0 \end{aligned}$$

$$F_{nwrz} = \frac{F_{nwcry} \cdot l_{nwcrz}}{l_{nwry}} \quad (3.31)$$

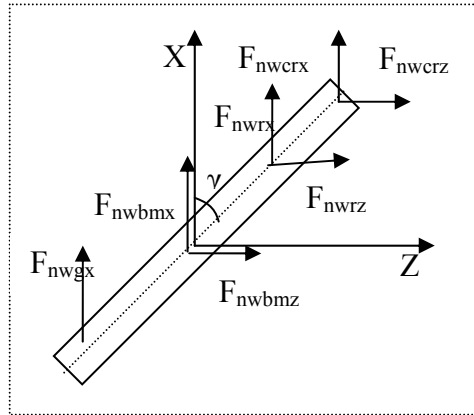


Figure 3.15 Wobble Plate Free Body Diagram on the X-Z Plane

Based on Figure 3.15, force equations on x-z plane are derived;

$$\begin{aligned} \sum F_{nx} &= 0 \\ F_{nwcx} + F_{nwx} + F_{nwbmx} + F_{nwgx} &= 0 \end{aligned} \quad (3.32)$$

However, force component F_{nwgx} is not on the same plane with the rest of the forces as it is fixed at the guide rod position.

$$\begin{aligned} \sum F_{nz} &= 0 \\ F_{nwcz} + F_{nwx} + F_{nwbmz} &= 0 \end{aligned} \quad (3.33)$$

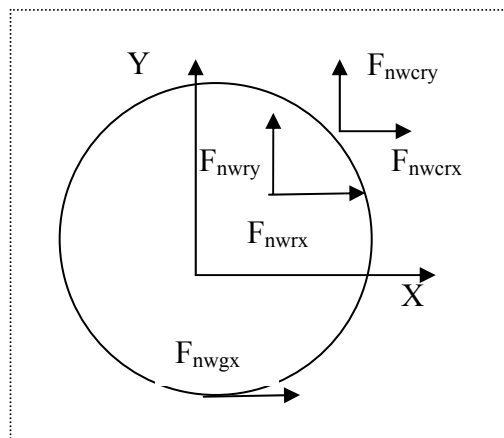


Figure 3.16 Wobble Plate Free Body Diagram on the X-Y Plane

To calculate force component F_{nwgx} , moment acting on Z-axis is written instead of moment acting on Y-axis as shown in Figure 3.16.

$$\begin{aligned} \sum M_{z-z} &= 0 \\ F_{nwcx} \cdot l_{ncy} + F_{nwrx} \cdot l_{nwy} - F_{nwcx} \cdot l_{nwcx} - F_{nwy} \cdot l_{nwrx} - F_{nwgx} \cdot l_{nwy} &= 0 \end{aligned} \quad (3.34)$$

Also;

$$\begin{aligned} \tan(\gamma) &= \frac{F_{nwrx}}{F_{nwrz}} \\ F_{nwrx} &= F_{nwrz} \tan(\gamma) \end{aligned} \quad (3.35)$$

By inserting equation 3.35 into 3.34, we have

$$F_{nwgx} = - \left(\frac{F_{nwcx} \cdot l_{ncy} + F_{nwrx} \cdot l_{nwy} - F_{nwcx} \cdot l_{nwcx} - F_{nwy} \cdot l_{nwrx}}{l_{nwy}} \right) \quad (3.36)$$

Solving equation 3.32, we have;

$$\begin{aligned} \sum F_{nx} &= 0 \\ F_{nwcx} + F_{nwrx} + F_{nwbmx} + F_{nwgx} &= 0 \\ F_{nwbmx} &= -(F_{nwcx} + F_{nwrx} + F_{nwgx}) \end{aligned} \quad (3.37)$$

Thus, from the equations generated above the magnitude of reaction force of the ball mount (F_{wb}), and the guide rod (F_{wgx}) was calculated and presented in Figure 3.17 and figure 3.18.



Figure 3.17 Variation of Ball Mount Reaction Force (F_{wb}) with Shaft Rotation Angle

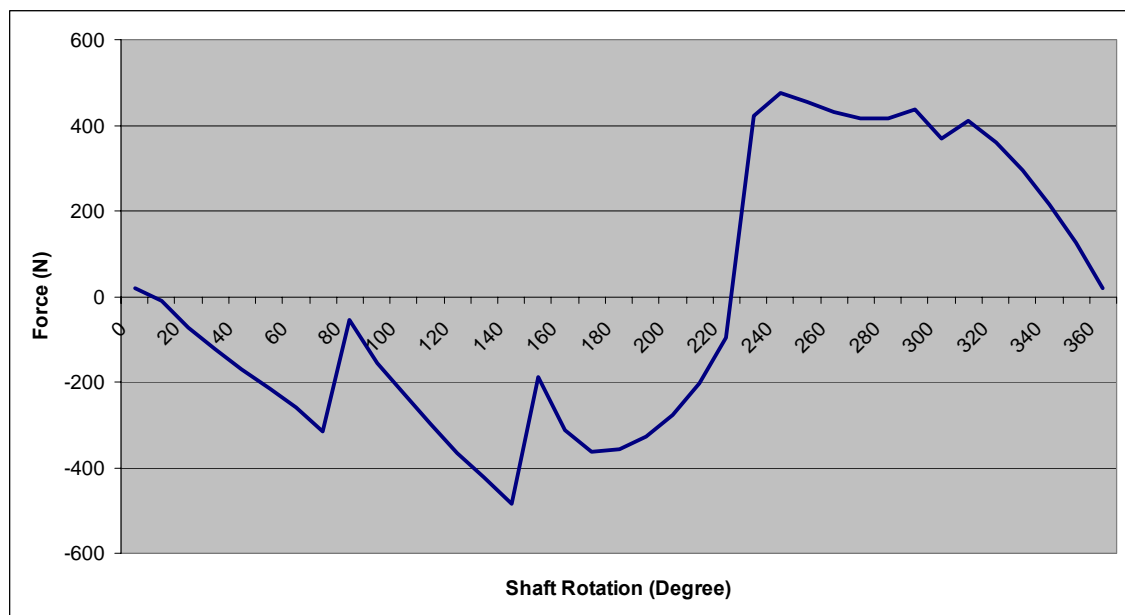
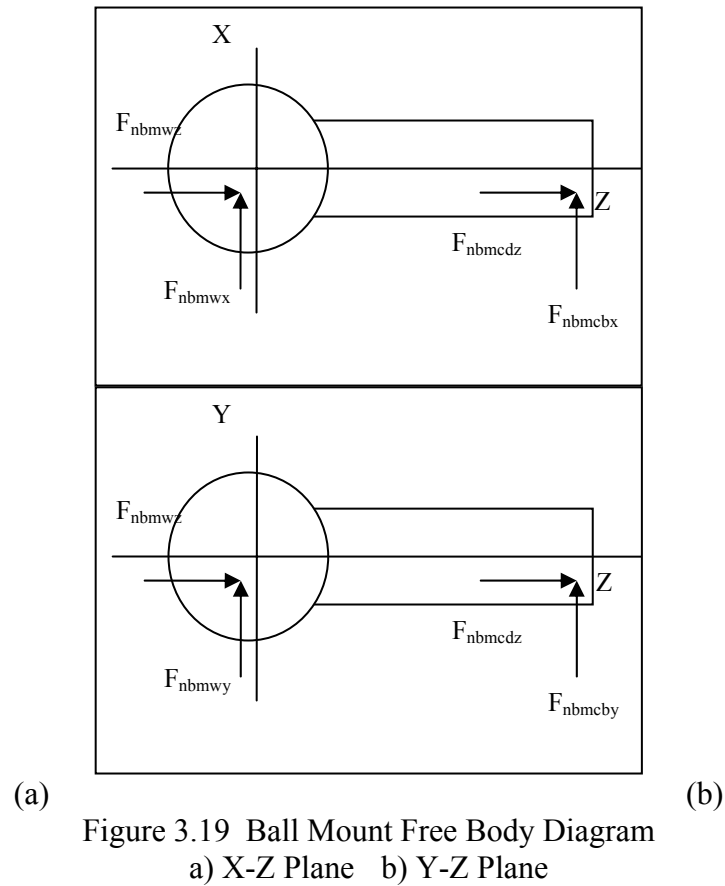


Figure 3.18 Variation of Guide Rod Reaction Force (F_{wgx}) with Shaft Rotation

3.5.4 Ball Mount Free Body Diagram

The force acting on the ball mount consist of two sources. One is reaction force from the wobble plate, F_{nbmw} and the other is the reaction force from cylinder block, F_{nbmcb} . Figure 3.19 shows the general free body diagram of the ball mount employed in the compressor.



The force acting on the ball mount is a two force-body diagram problem, the reaction force from the cylinder, F_{nbmcb} block is the same but on opposite direction of the force exerted on the ball mount surface by the wobble plate, F_{nbmw} .

$$F_{nbmw_x} + F_{nbmcb_x} = 0 \quad (3.38)$$

$$F_{nbmw_y} + F_{nbmcb_y} = 0 \quad (3.39)$$

$$F_{nbmw_z} + F_{nbmcb_z} = 0 \quad (3.40)$$

3.5.5 Rotor Free Body Diagram

The force acting on the rotor comes from both sides of the rotor. Although that the shaft and rotor are of two different components, however the rotor is tight fitted to the shaft.

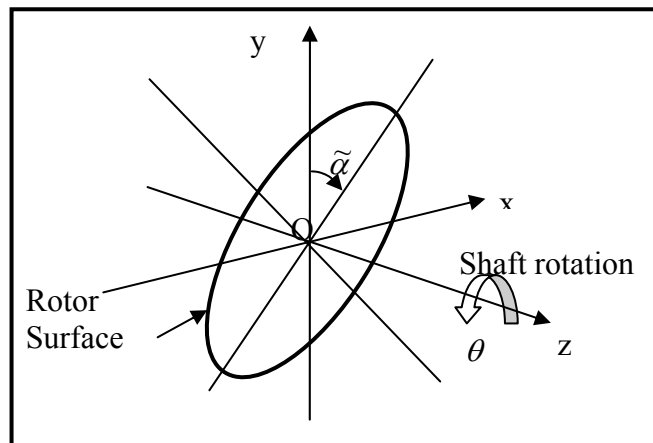


Figure 3.20 Angular Positions of Rotor

Figure 3.20 shows the coordinate system used on the shaft-rotor assembly. The coordinate system is further divided into two planes; x-z plane and y-z plane.

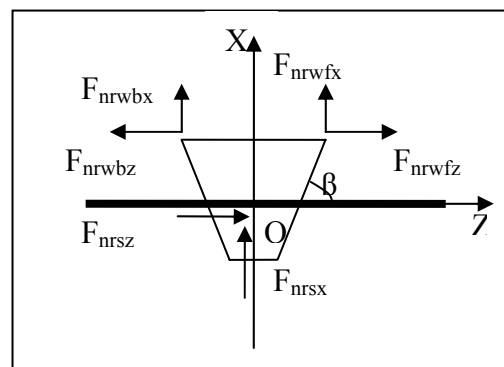


Figure 3.21 Rotor Free Body Diagram on the X-Z Plane

Based on Figure 3.21, force equations on x-z plane derived;

$$\begin{aligned}\sum F_{nz} &= 0 \\ F_{nrwfz} + F_{nrwbz} &= 0\end{aligned}\quad (3.41)$$

However, F_{nrwfz} is equal but opposite to F_{nrwbz} and are therefore cancelled. There are no other forces acting on the z-axis, allowing the compressor to operate with less vibration.

$$\begin{aligned}\sum F_{nx} &= 0 \\ F_{nrwfx} + F_{nrwbx} + F_{rsx} &= 0\end{aligned}\quad (3.42)$$

It is known that F_{nrwf} is equal to F_{nrwbx} due to mirror image arrangement. Solving equation 3.42, gives;

$$F_{rsx} = 2F_{nrwfx}\quad (3.43)$$

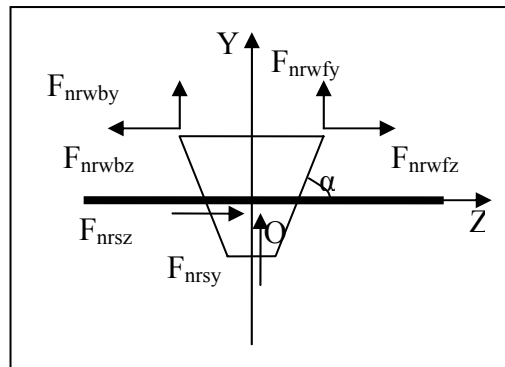


Figure 3.22 Rotor Free Body Diagram on the Y-Z Plane

Based on Figure 3.22, force equation on y-z plane is derived as;

$$\begin{aligned}\sum F_{ny} &= 0 \\ F_{nrwfy} + F_{nrwby} + F_{rsy} &= 0\end{aligned}\quad (3.44)$$

The same rules apply with equation 3.42, thus solving equation 3.44, gives;

$$F_{rsy} = 2F_{nrwfy} \quad (3.45)$$

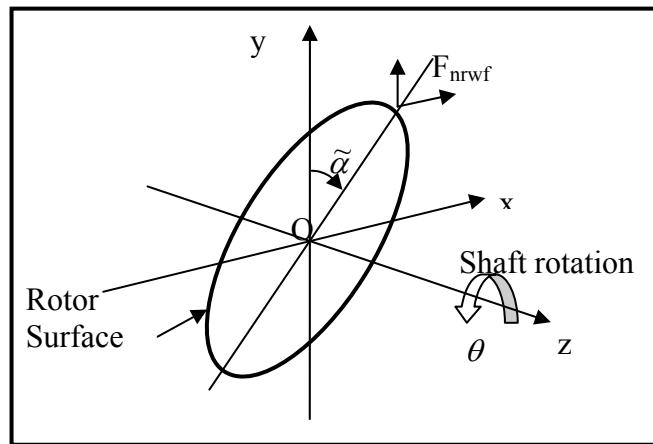


Figure 3.23 Shaft Rotor Assembly with Moment Reaction

Based on Figure 3.23, force component acting on x-axis and y-axis on the rotor on each side yields moment on z-axis which is equal to the compressor static torque;

$$\begin{aligned} \sum M_{z-z} &= 0 \\ \sum [2(F_{nrwfy} \cdot l_{nrwfx} + F_{nrwfx} \cdot l_{nrwfy})] + M_T &= 0 \end{aligned} \quad (3.46)$$

The magnitude of rotor-shaft reaction force is shown in figure 3.24 and the magnitude of center rotor moment reaction is shown in figure 3.25.

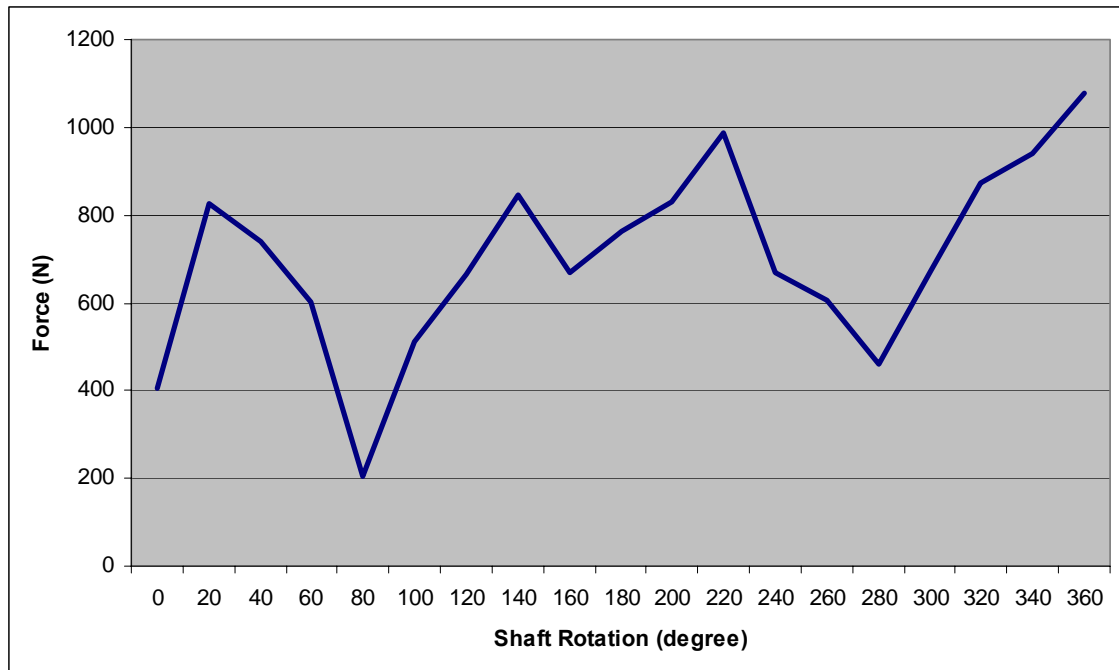


Figure 3.24 Variation of Rotor-Shaft Reaction Force (F_{rs}) with Shaft Rotation

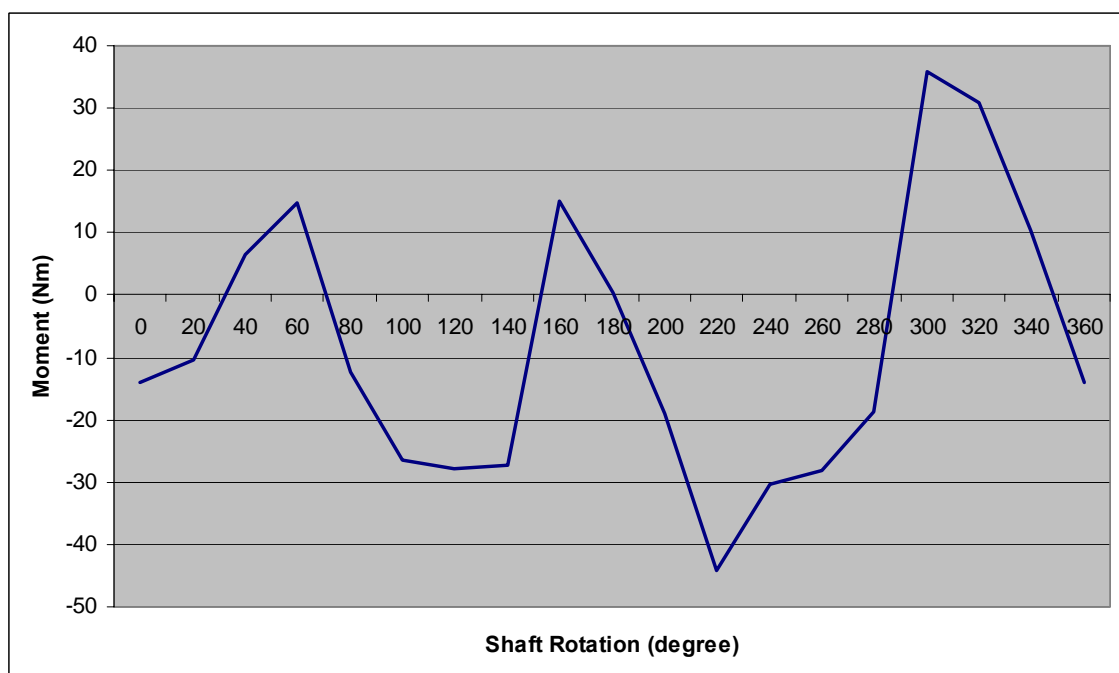


Figure 3.25 Variation of Centre Rotor Moment Reaction (M_t) with Shaft Rotation

3.5.6 Shaft Free Body Diagram

The shaft of the compressor in general comprises of a cylindrical beam with reaction force coming from the two bearings supporting the shaft, and the tight fitted rotor. Figure 3.26 shows the reaction forces on X-Z plane and Figure 3.20 shows the reaction forces on Y-Z plane.

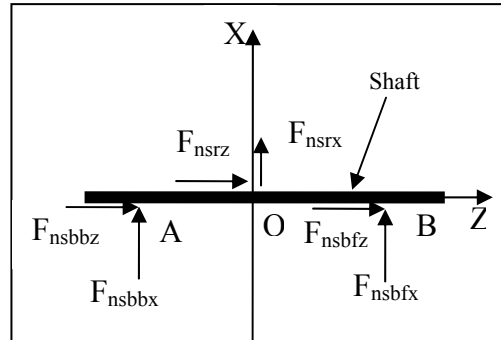


Figure 3.26 Shaft Free Body Diagram on the X-Z Plane

The only forces acting on the center of the shaft is the rotor reaction force, F_{sr} and can be written as;

$$\begin{aligned}\sum F_{nx} &= 0 \\ F_{srx} + F_{sbrx} + F_{sbf_x} &= 0\end{aligned}\quad (3.47)$$

Since F_{sbrx} is equal to F_{sbf_x} , equation 3.47 is written as;

$$F_{sbf_x} = -\frac{F_{srx}}{2}\quad (3.48)$$

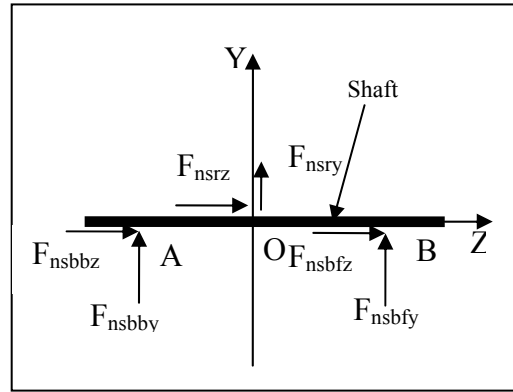


Figure 3.27 Shaft Free Body Diagram on the Y-Z Plane

Using the same method to obtain equation 3.48, F_{sbfy} is written as;

$$F_{sbfy} = -\frac{F_{sry}}{2} \quad (3.49)$$

The magnitude of bearing reaction force (F_{sbf}/F_{sbr}) is shown in figure 3.28.

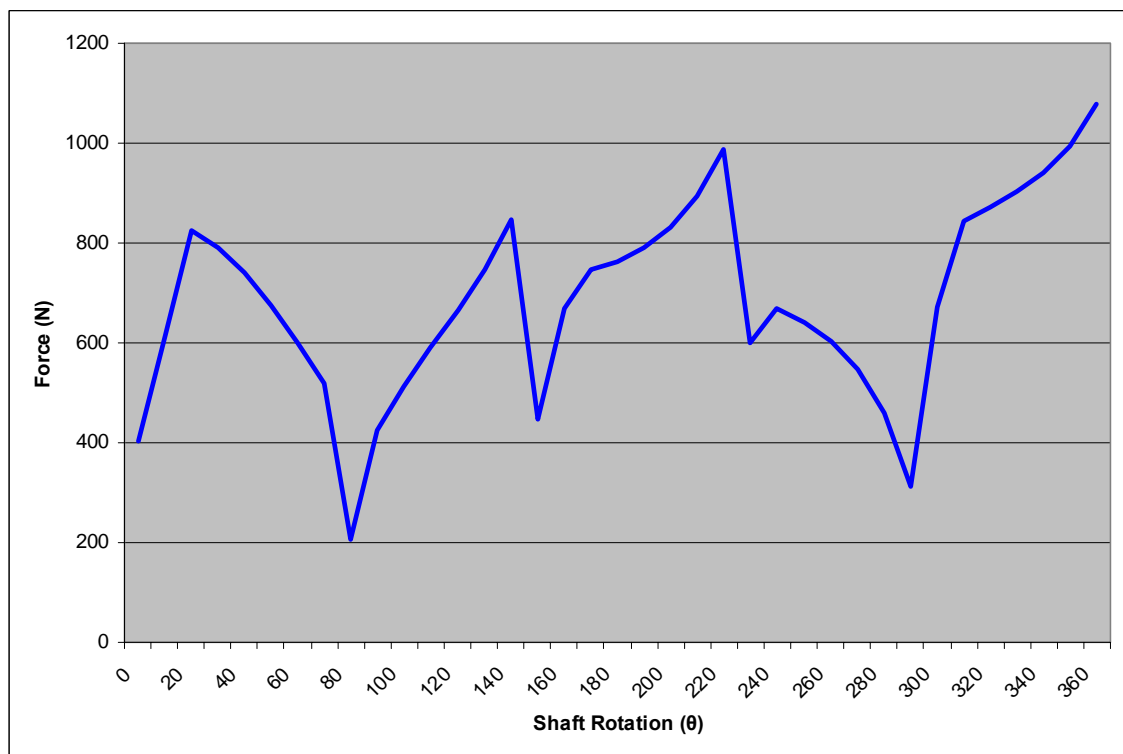


Figure 3.28 Variation of Shaft-Bearing Reaction Force (F_{sbf}/F_{sbr}) with Shaft Rotation

3.7 Experimental Setup

This chapter describes the development of an experimental setup which was aimed to study performance characteristic of refrigerant compressors. It is very important to ensure instrumentation and methods used for testing the compressors are reliable and according to international standards. By doing so, the data obtained during the test procedure are also reliable.

3.7.1 Experimental Rig

The experimental rig which comprised of components from existing mini bus air conditioning system was rearranged in such a way that the instrumentation can be properly installed and the measurement of important parameters can be made using a data acquisition system. The experimental rig was developed based on British Standard, BS 3122- Part1: 1990- *Refrigerant Compressors: Methods of Test for Performance* [39]. This standard describes several methods of evaluating a compressor performance. From eight methods available in BS 3122, method F (Flow-meter method) was selected as it was the easiest method to implement without changing the current system. It was also cheaper and easier to set up as the original piping was retained while additional piping was only added for the flow meter. However, in the current work, additional features were introduced to the basic design of experimental set-up as in Method F. Pressure of the refrigerant were measured not only at compressor suction and discharge (P_1 and P_2) as shown in figure 5.2, but also after the condenser and expansion valve (P_3 and P_4). As for the refrigerant temperature, six measurement points were introduced although only four of them were significant (T_1 , T_2 , T_3 and T_4). The other two points (T_5 and T_6) were meant to monitor the effect of sub-cooling. Both additional measurement points for pressure and temperature were crucial in order to plot a P-h diagram and to estimate the enthalpy values at the respective state points. The photograph of the experimental rig is as shown in figure 5.1. Additional photographs of the experimental rigs are shown in Appendix H.

Instead of a cooling compartment, an air circulation system was introduced to the experimental set up. Fresh and cooled air mixture was circulated through the evaporator which enabled the air temperature and flow rate to be controlled and ultimately controlled the cooling load of the evaporator. If more heat is required by the system, a butterfly valve installed at the end of the ducting system will control the air mixture and more fresh air is allowed to flow to the evaporator thereby increases the air temperature. Additional fan was mounted at the exhaust duct to enhance the air circulation. Air flow mixer was installed between the gating system and the temperature measurement point to allow for a uniform measurement of the air flow rate. Method from BS 5141:Part 1:1975 [40] was adopted in designing the ducting system.

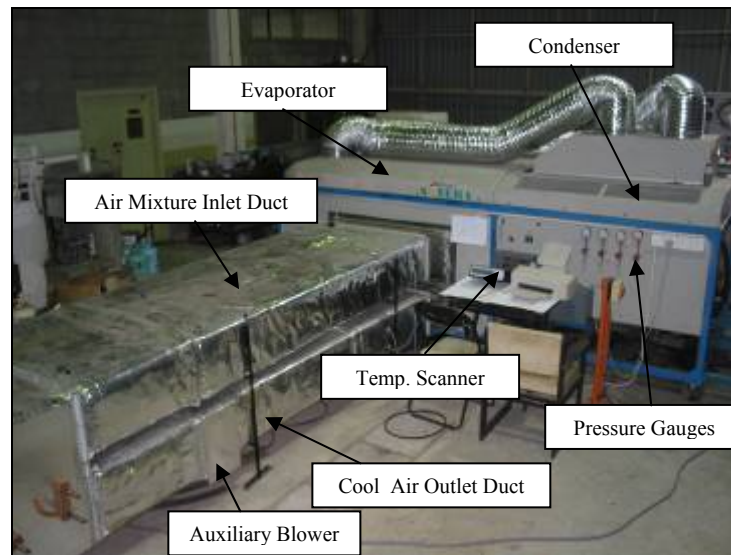


Figure 3.29 Compressor Test Bench Facility

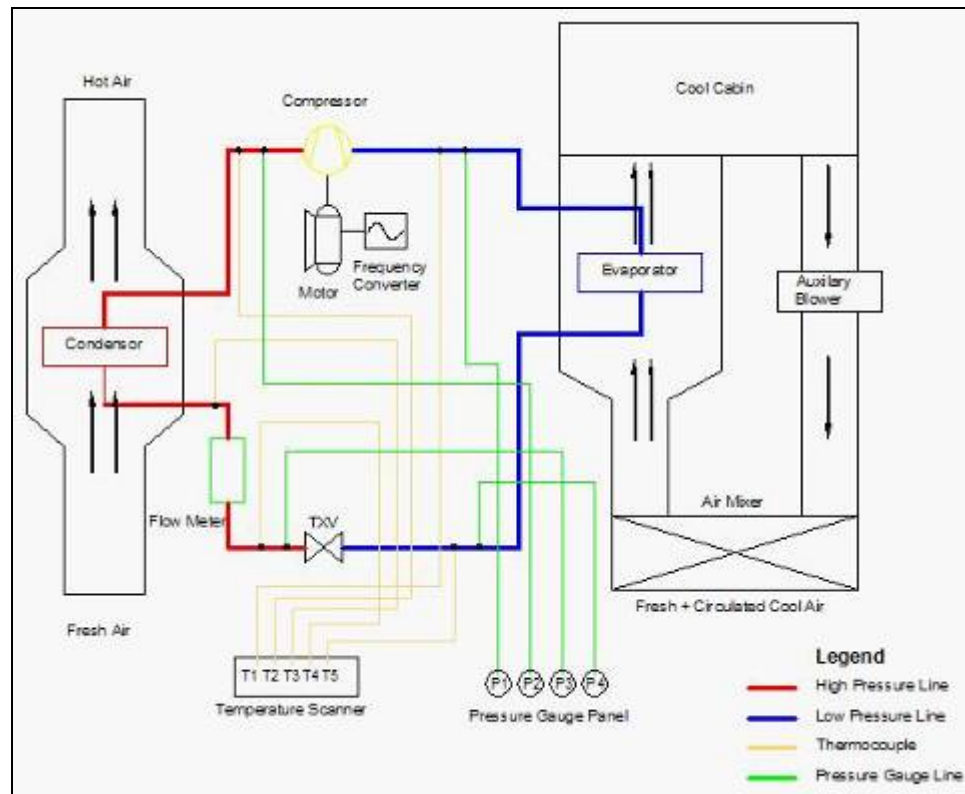


Figure 3.30 Schematic Diagram of Experimental Rig with Temperature and Pressure Measurement Points

3.7.2 Test Condition

The tests were conducted at several different speeds ranging from 800 rpm to 1800 rpm. Normally a sub engine drive compressor runs at 1450 rpm while for a direct drive compressor varies from 800 rpm to 3000 rpm, however due to the motor capacity used in the experiments a lower speed would have to be used. Several tests were conducted repeatedly in order to obtain accurate and reliable data. Data was recorded when the system reached steady state and suction pressure was maintained at 3.8 bar since that the only adjustable value is the temperature inlet to the evaporator. This was confirmed by taking readings three times with an interval of 15 minutes where the three readings should have identical data. Also, the system showed sign of steady state as indicated by the flow meter and bubble free liquid refrigerant flow as seen through the system sight glass. The parameters recorded

were temperature, mass flow rate of liquid refrigerant, voltage and current supplied to the motor, power factor and the actual compressor speed.

3.7.3 Test Rig Preparation

Test rig preparation is an important step in preparing the air conditioning system for the experiments. The procedure is necessary as it confirms whether the test bench is ready and able to provide data within an acceptable range for a typical compressor speed. It was during this stage that the air conditioning system was tested to ensure that it is not facing any problems like leaking, insufficient refrigerants or malfunctioning data acquisition equipments. Stated below are the procedures involved for the test bench commissioning:-

- i. Suck out all gases from inside the system using a vacuum pumps
- ii. Charge refrigerant gas into the system through the compressor suction and discharge hose around 5 to 7 bar
- iii. Test all connections and data measurement points for leakage
- iv. Switch on the motor and set the compressor speed to 800 rpm
- v. As the compressor runs, monitor the refrigerant condition by observing through the sight glass
- vi. The air conditioning system will be fully charged when the refrigerant observed is in complete liquid state (this is further confirmed with the flow meter which should give stable readings)
- vii. Disconnect the refrigerant charging kit from the system
- viii. Switch off all data acquisition system, blowers and motor
- ix. Leave the system idle for three to four days and observe for any pressure drop and leakage
- x. The system is ready for the experiment if there is no problem detected during the pre start-up procedures

3.7.4 Experimental Procedure

To carry out the experiment, it was imperative that a procedure be developed to ensure a smooth running of all system, equipment and instrumentation. A detail data collecting procedure was developed by taking account the pressure and temperature measurement intervals, speed steps and circulated air mixture. Stated below are the procedures:

- i. Record ambient temperature and pressure
- ii. Switched on motor and set the compressor speed to a designated value
- iii. Adjust the damper so that the suction pressure is maintained at 3.8 bar
- iv. Record pressure and temperature on designated points on the system after a stable readings is observed
- v. Record the flow rate of the refrigerant
- vi. Record the voltage and current supplied to the motor
- vii. Each reading is to be recorded every 10 minutes up to three times
- viii. Increase the speed of the compressor to the next set value
- ix. Repeat the procedure from (iii) to (vii), the speeds are to be varied from 800 rpm to 1800 rpm

3.7.5 Compressor performance Analysis

These are the parameters that are analyzed using the collected experimental data.

a) Actual Coefficient of Performance, COP_a

$$COP_a = \frac{\text{Cooling} \cdot \text{Capacity}}{\text{Compressor} \cdot \text{Power}}$$

$$\begin{aligned}
& \frac{\dot{m}(h_1 - h_4)}{\dot{m}(h_2 - h_1)} \\
& = \frac{(h_1 - h_4)}{(h_2 - h_1)}
\end{aligned} \tag{3.1}$$

b) Volumetric Efficiency, η_v

$$\begin{aligned}
\eta_v &= \frac{V_{actual}}{V_{displacement}} \\
&= \frac{m_{actual}}{m_{displacement}} \\
&= \frac{\dot{m}_{actual} / N}{P_1 V_1 / RT_1}
\end{aligned} \tag{5.2}$$

c) Mechanical Efficiency, η_{mech}

$$\begin{aligned}
\eta_{mech} &= \frac{\dot{W}_{vapor(indicated)}}{\dot{W}_{shaft(motor)}} \\
&= \frac{\dot{m}(h_2 - h_1)}{MotorPower \times \eta_{motor}}
\end{aligned} \tag{5.3}$$

Motor Power = $V_o I_o \cos \theta_o$ and η_{motor} is assumed to be at typical value of 89.5%.

3.7.6 Pressure Test Rig

The new compressor was first tested on a pressure test rig before it was installed on the actual experimental rig. The pressure test rig was developed and set up by other

researcher based on BSI 1571-2:1975 [42]. The test rig figures and experimental procedure are included in Appendix I. The result of the pressure test is included in 6.2.

CHAPTER 4

EXPERIMENTAL RESULTS AND DISCUSSIONS

4.1 Introduction

This chapter presents experimental results and findings of the current work, followed by relevant discussions. The discussions are based on performance characteristics at different compressor speeds for both existing compressor model (ZEXEL) and the newly developed compressor.

4.2 Pressure Test Experiment Result

As a precaution, the third prototype was tested on a simple pressure test rig first to determine the compressor capability. Table 6.1 shows the experimental data collected with an interval of 10 minutes for each data set.

Table 4.1 Pressure Test Data

Pd(bar)	Tin (°c)	Tout (°c)	m (g/s)	Speed (rpm)	Torque (Nm)	Shaft Pow. (KW)
4	23.4	28.7	5	300	11.88	0.46
7	23.2	28.9	5	300	16.2	0.63
8	23.8	28.9	2	300	19.8	0.77

The data obtained shows that the compressor was able to achieve up to a pressure ratio of 8 which is more than enough to achieve proper air conditioning system pressure. With the above achievement, the prototype was moved to the actual experimental rig for actual testing.

4.3 Compressor Test on Air Conditioning Experimental Rig

The following results are divided into two parts as the experiments were conducted for two different compressors. The first compressor performance test was for the existing swash plate compressor acted as base data and is included in Appendix K while the second performance test result was for the new compressor. Both results are analyzed and plotted on graphs.

4.3.1 Results and Performance Characteristics of New Compressor Model

Current research and development work managed to design and fabricate three prototypes. Out of the three units, the final prototype was almost complete as all the necessary features and design improvements were integrated. However, due to some unfortunate circumstances data produced fall short of what was intended to be obtained. However, commissioning data is available for analysis.

The third prototype was initially running smoothly and commissioning was well underway. Experimental data was recorded during the whole procedures and the compressor continued to run for 30 minutes, then the compressor suffered mechanical failures and stalled. The time was not enough for a proper data extraction as experiment procedures and commissioning usually require at least two hours of refrigerant charging running at 1200 rpm. As commissioning data shows, flow-rate of the refrigerant was unreadable as the dial gauge was unstable for proper readings which generally showed insufficient refrigerant in the system. Still, the compressor shows same behavior with swash plate compressor during initial commissioning. The only readable information are the value of compression ratio, shaft power consumption, suction and discharge pressures which indicated the capability of the double sided wobble plate compressor to compressed gas. The maximum speed tested on these prototypes was only 900 rpm. The results are as in Appendix J. The relation between pressure ratio, pressure and speed are shown in Figures 4.1 and 4.2.

The experiment data obtained was taken during the commissioning procedures. As stated in the commissioning procedures as well as considering that the prototype is still new, the compressor was switched on at a lower speed and increased over time. At minute 15 and 20, the compressor was left running at 800 rpm. The speed was increased further at around minute 25 and maintained at 900 rpm. A short while after minute 30, the compressor jammed. Figure 6.6 shows that the suction pressures drop from their initial values, this shows that as the compressor was switched on, the wobble plate mechanism was put to work inside the compressor creating vacuum inside the compression chamber during piston expansion, and therefore drawing the refrigerant gas inside. The suction effect could be seen more clearly at higher operating speeds since more vacuum was created at these speeds. The suction pressure appears to be constant at 900 rpm, it is to be noted that during the whole experiments refrigerant gas was being charged to the system at the suction port of the compressor at 5 bar. The Figure also shows that the discharge values increased against time to a maximum of 12 bar. This behavior was normal as from experience and observation the existing swash plate compressor behaved the same way during the commissioning process. Thus, the pressure ratio increased almost linearly against the compressor speed and time, as indicated in Figure 6.2. The absence of cooling effect in this cycle could be explained by the fact that the system starved of refrigerant. Only small amount of refrigerant induced throughout the testing, since the commissioning process only lasted 30 minutes where normally it should have lasted for two hours running at 1400 rpm. Figure 6.3 shows the shaft power consumption versus speed and it shows that as the speed is increased the shaft power consumption is also increased linearly.

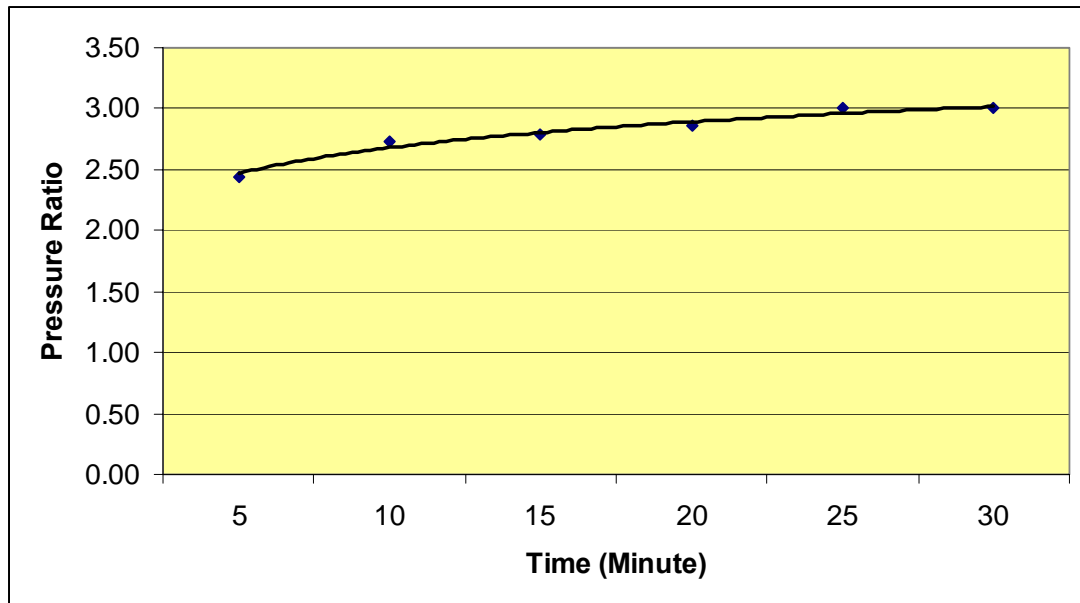


Figure 4.1 Pressure Ratio Versus Time

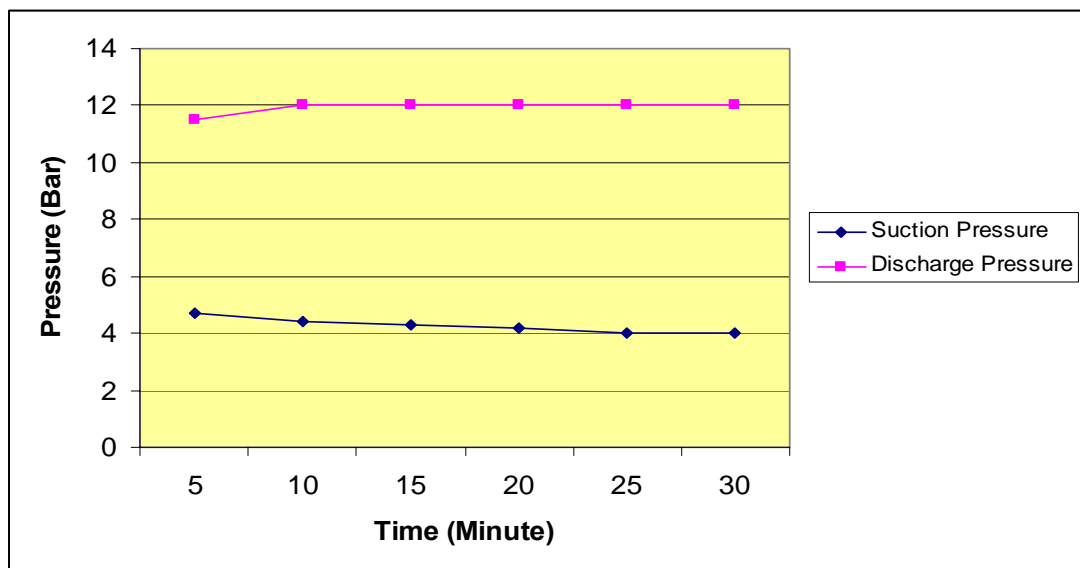


Figure 4.2 Pressure Versus Time

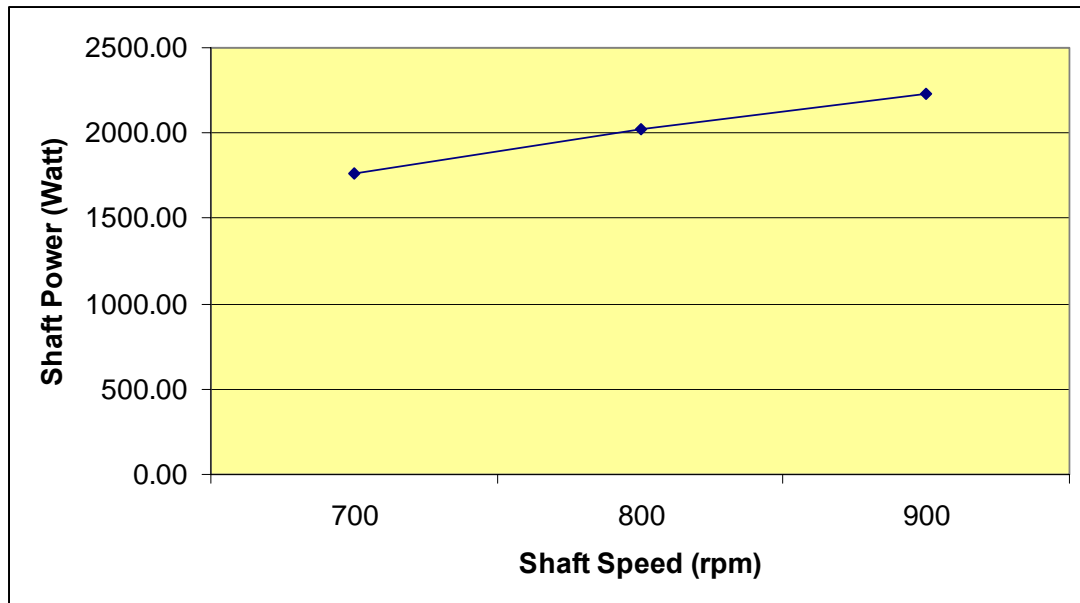


Figure 4.3 Shaft power Consumption Versus Shaft Speed

4.3.2 Comparison between Swash Plate and Symmetrical wobble Plate Compressor

An equal comparison between compressors performances could not be established due to the exact performance of the new wobble plate compressor cannot be measured. Since that only a maximum speed of 900 rpm was achieved running for 30 minutes and the refrigerant failed to reach to an adequate mass flow rate, proper experiment data retrieval was unsuccessful.

4.4 Compressor Post Mortem

As discussed in previous chapter, the compressor suffered mechanical failures and forced to a halt after running for about 30 minutes at 900 rpm. The compressor was then dismantled to observe the damage components inside the compressor. Generally, observation showed that the shaft and the ball mount were physically tight fitted together and after rotating for some time stalled the whole compressor. Such failures had never been encountered on test of previous prototypes

which ultimately a proof that it was not caused by the kinematics of the wobble plate compressor. It also shows that the problem does not relate with component failure as none of the component seems to be broken. The following chapters discuss in brief the criteria and combinations of them that may lead to the said prototype failure. Photographs of damage parts are included in Appendix L.

4.4.1 Machining Tolerances

The third prototypes critical components such as the wobble plate assembly have to undergo several corrections and re-machining due to wrong dimensions and tolerances. However since there was time and cost constraints, a total rework on some of the components were impossible and only substantial corrections were made. An example of such action taken was the machining of the hemispheric adaptor in the wobble plate assembly. Before that the hemispheric slot did not fit the ball mount very well. Due to the machinist limited equipment and knowledge, only estimated tolerances were added. Other reasons that may cause the tolerances to deviate from its original specified values were that the hard chrome plating coated on the adaptor may produce a layer of uneven coating inside the hemispheric surface which increase frictions and produce metallic chips at the sliding surfaces when operating at high speed. Such event is beyond the control of the designer due to the limitation in the machining process, measuring equipment and operator's skills.

4.4.2 Oil Lubrication System

One of the significant improvements made to the third prototypes is on the lubrication system. As previously discussed function of the system is to distribute lubrication oil onto the rubbing faces; ball joint connection, rotor and wobble plate surfaces, and ball mount-wobble plate-shaft sliding surfaces. However, one of the weaknesses of the lubrication system which was overlooked by the designer is the

absent of oil filter at the suction port of the oil pump. If further study is to be conducted on the compressor this oil filter should be installed.

Several parts of the compressor are newly made and running for the first time on the compressor. A good example of such components is the wobble plate itself where during the fabrication process, the whole assembly was heat treated. Although, the end results had improved the strength of the aluminum made components, the heat treatment had degraded the surface roughness of the inner side of the ball joint. Running at high speed, would eventually produce fine metallic powder that settled down into the oil sump. Other particles may also be produced from pistons which slide against the carbon steel liners causing continuous wear and tear of the VITON piston rings.

The contaminated unfiltered oil is pumped back to the critical sliding surfaces through the shaft as shown in Figure 4.15. It only took a fine metallic chips to get between the sliding surfaces on the ball mount causing the shaft assembly to jam and wobbling motion to stop. This was evident from the damage observed on the rubbing components, as shown in Appendix L.

4.4.3 Oscillating Shaft Assembly

Although great care was taken in designing the shaft and rotor assembly accompanied by adequate analysis, the dimensions of the finished product may be different from that of the engineering drawing due to unforeseen circumstances. Such event may happen to the shaft assembly where the rotor is very complex to be machined. Although the rotor is designed dynamically balanced with the aid of Autocad, an undetectable off set of even a few millimeters will unbalance the whole assembly. This is proven true as if the prototype shaft is left on a flat table, it will roll to its heavier side. Thus when running at high speed there exist an oscillation on the shaft which causes the wobbled plate surfaces to be subjected to severe frictions. However the probability of such event is very small at the relatively low operating speed of both tests on air conditioning system and pressure test rig during which the

vibrations were not significant. Hence oscillation was thought not to be the main cause but may contribute a little to the failure of the compressor.

4.5 Summary

The final prototype of the newly developed compressor was tested on an actual air conditioning system which formed part of the experimental rig. The results and data analysis of the existing model and that of the new compressor have been presented. Since the new compressor could not deliver the expected results due to the fact that the compressor failed to run at sufficient period to enable a reasonably adequate measurement to be taken, a real meaningful comparison could not be made between the performances of the two compressor models. However, the failure had been physically analyzed and the probable cause had been identified. Although addressed, the problem could not be rectified due to time and financial constraints. More refined works certainly needs to be done on the new compressor to further improve its performance.

CHAPTER 5

CONCLUSIONS AND SUGGESTIONS FOR FUTURE RESEARCH WORK

5.1 Conclusions

A compact and stable new compressor based on a symmetrical wobble plate concept was successfully developed. The kinematics and graphical simulation were studied thoroughly to understand the concept working mechanism. The capacity of the new designed compressor is equivalent to that of an existing swash plate compressor that was used on a mini bus air conditioning system.

An engineering analysis was carried out before each prototype was produced. Three prototypes were designed, fabricated and tested on a pressure test rig. The result shows that the second and third prototype was able to achieve the compression ratio of more than 4 which is the minimum pressure ratio required for an actual air conditioning system to work.

Air Conditioning experimental rig was designed, built and successfully tested and commissioned. The rig was designed according to international standard and using standard components used on a mini bus air conditioning system. Test on existing mini bus refrigerant gas compressor were conducted to produce some base data intended to be used for comparison against the performance of the newly developed compressor. The final prototype of the newly developed compressor was tested on an actual air conditioning system which formed the experimental rig. The results and data analysis of the existing model and the new compressor have been presented. Since the new compressor could not deliver the expected results due to the fact that the compressor failed to run at sufficient time for a reasonably adequate measurement to be taken, a real meaningful comparison could not be made between the performances of the two compressor model. However, the failure had been physically analyzed and the probable cause had been identified. Although addressed,

the problem could not be rectified due to time and financial constraints. Out of the research work done, the writer have produced a total of three papers as listed in appendix M.

5.2 Suggestions for Future Research

The following recommendations are the scopes of work suggested for future research:

- i. Understanding the kinematics and dynamics of the double sided wobble plate compressor will help in designing the compressor much faster, easier and safer. The establishment of a complete dynamic analysis would help further in realizing a vibration free compressor.
- ii. Material selection should be conducted based on the fact that the designed compressor is to be used for mobile air conditioning system for a bus. This will require light materials used on a compact design usually runs at high speed. To further increase the market value of the concept, a light-reliable-small compressor should be designed. This can be achieved by implementing individual cylinder block concept using alternative material such as the light magnesium alloy employing a simple assembly of these blocks to the compressor casing.
- iii. Lubrication system should be improved by introducing other features such as oil filter at the inlet oil passage and oil cooling system by using cool gas into the crankcase. A good lubrication system would reduce heat build up on sliding components and thus reducing friction and ensuring longer lifetime of the part.
- iv. Valve mechanics and gas ports should be studied thoroughly as the affect of superheating, volumetric efficiency and valve backflow can influence the compressor overall performance. Correct sizing of gas ports and proper design of reed valves will substantially increase the flow efficiency, operating range and will also reduce noise. The positioning of the suction and discharge ports should also be considered at the rear side

away from the rotating pulley to minimize the risk of pulley clashing with the refrigerant hose.

- v. Conduct testing in wider range of speeds, especially at higher speeds up to 4000rpm. This may help to characterize the compressor performance in a similar condition to that of the actual operation in an automobile air-conditioning system.
- vi. A compressor is actually a universal pump with a wide range of applications; hydraulic pumps, air compressors, high pressure natural gas compressors or vacuum pump. This symmetrical wobble plate compressor can be studied further for these type of applications.

REFERENCES

1. Chang, K.Y. *A Theoretical and Experimental Study of an Oil-Flooded Rotary Sliding-Vane Compressor*. Ph.D. University of Strathclyde; 1983.
2. ZEXEL. *DKS-16H, DKS-26, DKS-32 for Bus Air Conditioner*. Singapore. 2002
3. BOCK. *FK: Vehicle Compressors*. Germany. 2002
4. Toyoda, H. and Hiraga, M. Historical Review of the wobble-plate and scroll type compressors. *SAE Paper*. 1990. No. 901737.
5. O'Neil, D. L., Bryant, J. A. Air Conditioning System. In: Kreider, J. F. *Handbook of Heating, Ventilation and Air Conditioning*. Boca Raton: CRC Press LLC. 31; 2001
6. Ingle, K. *Reverse Engineering*. New York. Usa: McGraw-Hill. 1994]
7. Otto, K. and Wood, K. *Product Evaluation: A Reverse Engineering and Redesign Methodology*. USA: Massachusetts Institute of Technology (MIT). 1998]
8. Stoecker, W. F. and Jones, J.W. *Refrigeration & Air Conditioning*. 2nd. Ed. Singapore: McGraww-Hill. 1982. 187.
9. ASHRAE. *ASHRAE: HVAC System and Equipment*. New York: American Society of Heating, Refrigerating and Air Conditioning Engineers, Inc, 2000.
10. Trott, A. R. *Refrigeration and Air Conditioning*. England. McGraw-Hill. 1981

11. Chlumsky, V. *Reciprocating and Rotary Compressors*. Prague: Publisher of Technical Literature. 1965.
12. King, G.R. *Basic Refrigeration*. USA: Nickerson and Collins Co.1979
13. Birch, T. W. *Automotive Heating and Air Conditioning, 3rd ed.* Upper Saddle River, N.J: Prentice Hall. 2003
14. Skinner, T. J. and Swadner, R. L. V-5 Automotive Variable Displacement Air Conditioning Compressor. *SAE Paper*. 1986. No. 850040.
15. Marcus Giovanni Dropa de Bortoli (2002). The use of Integrated CAE/CAD/CAM System During the Compressor Design. *2002 Proceedings of International Compressor Conference*, Purdue University, USA.
16. Bjorn Auren (2002). Effect of Material Properties and Surface Treatment on the Performance of Stainless Flapper Valve Steel for Compressors. *2002 Proceedings of International Compressor Conference*, Purdue University, USA.
17. Schwerzler and Hamilton- simulation and design studies of multiple cylinder refrigeration compressor
18. Zair, A. A., Ardiyansyah S., Ainullotfi A. L. and Md N. M. Study on the Stressing of a New Symmetrical Wobble Plate Compressor : Kinematic and Forces. *Malaysia S & T Congress*. September 2003. Kuala Lumpur. 2003.
19. Tojo, K. Takao, K. and Nakamura, Y. A Study on the Kinematics of a Variable Displacement Compressor for Automotive Air Conditioners. *Proc. Of International Compressor Conference*. 1988. USA. Purdue University. 1988.

20. Ishii, N., Abe, Y., Taguchi, T., Maruyama, T. and Kitamura, T. Dynamic Behaviour of Variable Displacement Wobble Plate Compressor for Automotive Air Conditioners. *Proc. Of International Compressor Conference*. 1990. USA. Purdue University. 1990.
21. Jingu, J., Fukai, I., Kurihara, M., and Keiji, S. The development of a Fixed Displacement Single Sided Swash Plate A/C Compressor. *SAE Paper*. 2000. No. 2000-01-0971.
22. Ebbing, D. M. Control Stability and NVH Improvements of the Variable Displacement Swash plate Compressor. *Society of Automotive Engineers, Inc.* 2001. No. 2001-01-3837.
23. Gabriella, C. and Lowery, D. C. Sound Quality Evaluation of Compressors. *Proc. Of International Compressor Conference*. 2002. USA. Purdue University. 1990. C14-3
24. Kaynakli, Ö, and Horuz, I. An Experimental Analysis of Automotive Air Conditioning System. *International Comm. Heat Mass Transfer*. 2003. Vol.30. 273-284.
25. Grolier, P. A Method to Estimate the Performance of Reciprocating Compressor. *Proc. Of International Compressor Conference*. 2002. USA. Purdue University. 2002. C4-5
26. Tian, Q. Dou, C. Yang, C. Li, X. Yan, Q. Dynamic Behaviour of a Variable Displacement Compressor for Automotive Air Conditioning. *Proc. Of International Compressor Conference*. 2002. USA. Purdue University. 2002. C3-3
27. Jabardo, J.M., Mamani, J.G., Ianella, M.R. Modeling and experimental evaluation of an automotive air conditioning system with a variable capacity compressor. *International Journal of Refrigeration*. 2002. Vol 25:1157-1172

28. Tothero, D.L. and Keeney, D.F. A Rotary Vane Compressor for Automotive Air Conditioning Applications. 1978. USA: *Proc. of International Compressor Conference*, Purdue University.1978
29. SAE International. *Internal Combustion Engines- Piston Rings Grooves*. Warrendale, J2275. 1996
30. Soedel, W. *Design and Mechanics of Compressor Valves*. West Lafayette, USA: Office of Publications.3-13:1984
31. Lee, H. S., Yeo, J. S., and Hong, S. H. The Fabrication Process and Mechanical properties SiCp/Al-Si Metal Matrix for Automobile Air Conditioner Compressor Pistons. *Journal of Material Properties*. 2001. 113: 202-208
32. Holmes, W. T. *Plane Geometry of Rotors in Pumps and Gears*. Manchester: The Scientific Publishing Company. 1-20: 1978
33. Ammen, C. W. *Metal Castings*. New York: McGraw-Hill.4:1998
34. Tian, C. Dou, C. Yang, X. and Li, X. A Mathematical Model of Variable Displacement Wobble Plate Compressor for Automotive Air Conditioning System. *Applied Thermal Engineering*. 2004. 24: 2467-2486
35. Mohd Faizal bin Mohideen Batcha. *Design and Development of a New Multi-Vane Rotary Compressor for Automobile Air Conditioning System*. MSC Thesis. Universiti teknologi Malaysia: 2005
36. Hareo, T. *Wobble Plate Compressor*. GB2199903. 1988
37. Ono, T. *Supporting Mechanism for a Wobble Plate and Method of Making Same*. 5415077. 1995

38. Peng, Y. H. *Automotive Refrigerant Wobble Plate Type Compressor Piston with Improved Ball and Socket Joint*. 6006652. 1999.
39. British Standards Institution. *Refrigerant Compressors. Part 1. Methods of Test for Performance*. London. BS 3122:Part 1.1990
40. British Standards Institution. *Air Heating and Cooling Coils. Part 1: Method of Testing for rating of Cooling Coils*. London. BS 5141-1.1975
41. Brooks Instrument. *Installation and Operation Manual: Models MT 3809 and MT 3819*. UK: Installation Manual. 2002
42. British Standards Institution. *Testing Positive Displacement Compressor and Exhausters- Part 2: Method for Simplified Acceptance Testing for Air Compressors and Exhausters*. London. BS 1571-2. 1975

Appendix A

BOM data of Wobble Plate Compressor and Swash Plate Compressor

BILL OF MATERIAL

PAGE: 01/02

Product : Wobble Plate Compressor Manufacturer : SANDEN Displacement : 138 cc/rev
 Model : 4506 Lubricant : SP20

PART NO.	ITEM	FUNCTIONS	QTY	MATERIAL	DIMENSION (mm)	REMARKS
01	Front end plate (casted)	- Valve enclosure - Suction and discharge gas enclosure	1	Aluminum Alloy	Ø125 x 23(t)	- Pressure die cast component - Suction and discharge port are placed here
02	Front cylinder block (casted)	- Piston Enclosure - Crank mechanism housing	1	Aluminum Alloy	Ø125 x 98(t)	- Pressure die cast component - Have bolt points to mount in engine compartments
03	Rear end plate (casted)	- Cylinder block endplate - Magnetic pulley mount	1	Aluminum Alloy	Ø128 x 8(t)	- Pressure die cast component
04	Front valveplate	- Valve seat	1	Aluminum Alloy	Ø118 x 4(t)	- Holes are drilled according to suction and discharge ports
05	Discharge valve	- Discharge gas valve	1	SPRING STEEL		- Clover profile attached at center - Covers five discharge port in one single plate
06	Valve retainer	- Valve height limiter	1	MILD STEEL		- Clover profile attached on top of valve plate
07	Suction valve	- Suction gas valve	1	SPRING STEEL	Ø118 x 1(t)	- One single plate with valve profile - Sandwiched between valve plate and cylinder block

Table A.1 BOM Data for Wobble plate Compressor

BILL OF MATERIAL

PAGE: 02/02

Product : Wobble Plate Compressor		Manufacturer : SANDEN				
Model : 4506		Lubricant : SP 20				
PART NO.	ITEM	FUNCTIONS	QTY	MATERIAL	DIMENSION (mm)	REMARKS
08	Upper thrust bearing	- to support rotor at endplate	1	Standart Part	Ø88(OD) x Ø78 (ID) x 2(t)	
09	Rotor shaft	- deliver rotating motion to rotor	1	MACHINERY STEEL	Ø17 x 75(l)	- Shaft have uneven diameter on certain location - Uses key slot for pulley mount
10	Rotor	- to drive the wobble in nutating motion	1	Aluminum Alloy	Ø91 x 30(th)/8(tl) Tilting angle = 19	- Wedge shape rotor - Have special profiles to reduce weight
11	Rotor thrust washer	- protect the rotor surface	1	STEEL	Ø76 x Ø56 x 1(t)	- Simple round thin plate simply keyed at edge of rotor
12	Lower Thrust bearing	- to allow rotation of the rotor at the wobble plate surface	1	Standart Part	Ø76 x Ø56 x 2(t)	
13	Ball Bearing	- Hold wobble plate in place	1	STEEL	Ø22	- Placed on a hemispherical slot in ball mount

Table A.2 BOM Data for Wobble plate Compressor

BILL OF MATERIAL

PAGE: 02/02

Product		: Wobble Plate Compressor		Manufacturer : SANDEN		
Model		: 4506		Lubricant : SP 20		
PART NO.	ITEM	FUNCTIONS	QTY	MATERIAL	DIMENSION (mm)	REMARKS
14	Rear ball mount with spring and Anti Rotation Gear	- Hold wobble plate in place	1	Aluminum Alloy STEEL	Ø20 x 45(l)	- Ball mount allow the wobble plate to tilt in certain angle at y and x axis - Anti rotation mechanism are in a form of mating gears
15	Wobble plate with anti rotation gear mechanism	- Convert rotating motion to reciprocating motion	1	Aluminum Alloy STEEL	Ø82 x 5(t)	- Five connecting rods connected via ball joint concept - Mating gears in the center
16	Connecting rod	- Transfer reciprocating motion to piston	5	STEEL	Rods - Ø4 x 44 Ball - Ø14	- Connects wobble plate and piston - Both ends used ball joint method
17	Piston	- Compress gas	5	Aluminum Alloy	Ø36 x 17(t)	- Use ball joint method to connect to connecting rod
18	Retaining spring	- Acting as a damper device for crank assem	1	CARBON STEEL		-Standart Part
19	Shaft Needle Bearing	- Shaft support	2	Standart Part	Ø24(OD) x Ø17(ID) x 15(L)	- Ensure smooth shaft rotation

Table A.3 BOM Data for Wobble plate Compressor



(a) (b)
Figure A.1 Sanden Wobble Plate Compressor
a) Compressor b) Components

<p>Wobble Plate Type Compressor Model No.: 8D5H14 Product Specifications</p>		
<p>For full size cars, mini buses, vans, ambulances. Suitable for 1600cc - 3500cc engines. Available in DC12 & DC24volt only.</p>		
Bore	: 35mm	
Stroke	: 28.6mm	
Displacement per Revolution	: 138cc/rev.	
Number of Cylinders	: 5	
Maximum Allowable Continuous RPM	: 6000	
Refrigerant	: HFC134a	
Oil (SAN DEN SP-20)	: (175cc)	
Total Weight (with clutch and oil)	: (7.6kg)	

Figure A.2 Wobble Plate Compressor Specification

Appendix B
Discharge Port Calculation

B.1 Valve Port Design

Table B.1 shows the conditions that are used in determining the valve port dimensions.

Table B.1 Compressor Sizes and Operating Parameters

Displacement Volume / Cylinder	31.3 cm ³
Bore	36 mm
Stroke	30.5 mm
Suction Pressure	3.8 bar
Suction Temperature	11
Discharge Pressure	20 bar
Discharge Temperature	76.79
n Constant	1.14

A Typical P-V diagram is sketched as shown in figure B.1.

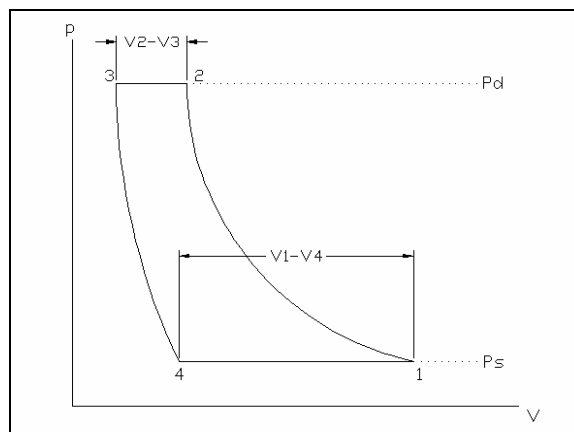


Figure B.1 Pressure Versus Volume

Each point condition is calculated with relevant equation:-

$$P_d = P_s \left(\frac{V_s}{V_d} \right)^n \quad (\text{B.1})$$

$$V_1 = 31.3 \text{ cm}^3$$

$$V_2 = V_1 \left(\frac{P_1}{P_2} \right)^{\frac{1}{n}}$$

$$V_2 = 31.3 \left(\frac{3.8}{20} \right)^{\frac{1}{1.14}}$$

$$V_2 = 7.2923 \text{ cm}^3$$

$$V_3 = 0.03\% \times V_1$$

$$V_3 = 0.0939 \text{ cm}^3$$

$$V_4 = V_3 \left(\frac{P_3}{P_4} \right)^{\frac{1}{n}}$$

$$V_4 = 0.0939 \left(\frac{20}{3.8} \right)^{\frac{1}{1.14}}$$

$$V_4 = 0.4048 \text{ cm}^3$$

Next, a relation between volume and shaft angle is sketched as shown in figure B.2.

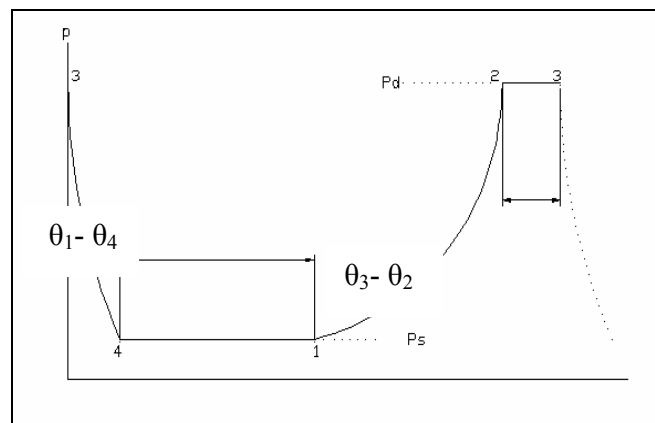


Figure B.2 Pressure Versus Shaft Rotation

Since discharge port is critical compared to suction port, only discharge port is calculated using from equation 3.3 and rewritten here for convenience.

$$t_3 - t_2 = \frac{1}{w}(\theta_3 - \theta_2) \quad (\text{B.2})$$

Assuming the compressor runs at a constant speed of 2000 rpm

$$w = \frac{2\pi(2000)}{60}$$

$$w = 209.44 \text{ rad/s}$$

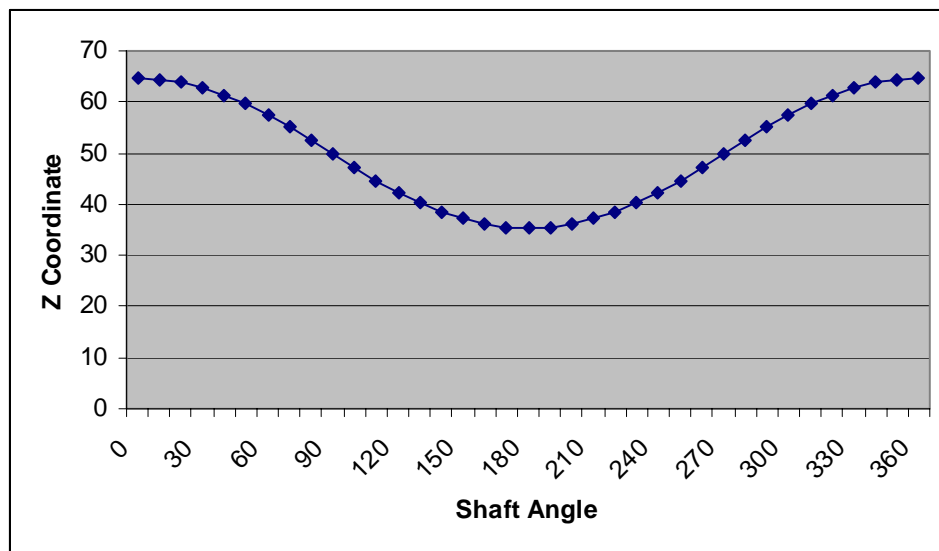


Figure B.3 Piston Position on Z-axis Versus Shaft Angle

θ_2 is estimated using equation B.1 and figure B.3.

$$V_2 = \frac{\pi D^2 l}{4}$$

$l = 9.4 \text{ mm}$ (from top dead centre)

Since the calculated piston movement is reference at center of wobble plate, then :-

$$\begin{aligned} L_{zp} &= 64.65 - 9.4 \\ &= 55.25 \text{ mm} \end{aligned}$$

The value of L_{zp} is compared with corresponding shaft angle and estimated as;

$$\theta_2 \approx 4.9742 \text{ rad (289 o)}$$

$$\theta_3 = 6.2834 \text{ rad (360 o)}$$

Using equation B.2, we have;

$$\begin{aligned} t_3 - t_2 &= \frac{1}{w}(\theta_3 - \theta_2) \\ &= \frac{1}{209.44}(6.2834 - 4.9742) \\ &= 6.251 \times 10^{-3} \text{ second} \end{aligned}$$

As the recommended Mach number is, $M \leq 0.2$. The allowable flow velocity is calculated using equation 3.7.

$$v = M.c$$

Where as,

$$\begin{aligned} c &= \sqrt{k.R.T} \\ &= \sqrt{1.3077 \times 0.0813 \times 1000 \times 361} \\ &= 195.91 \text{ms}^{-1} \end{aligned}$$

$$\begin{aligned} v &= Mc \\ &= 0.2 \times 195.91 \\ &= 39.182 \text{ms}^{-1} \end{aligned}$$

Affective flow area is calculated using equation 3.7.

$$\begin{aligned} A &= \frac{Q}{v} \\ A_d &= \frac{V_2 - V_3}{(t_3 - t_2)v_d} \\ &= \frac{(31.3 - 0.0939) \times 10^{-6}}{(6.251 \times 10^{-3})39.182} \\ &= 1.2741 \times 10^{-4} \text{ m}^2 \end{aligned}$$

$$\begin{aligned}
 A_d &= \frac{\pi D^2}{4} \\
 D &= \sqrt{\frac{4A_d}{\pi}} \\
 &= \sqrt{\frac{4 \times 1.2741 \times 10^{-4}}{\pi}} \\
 &= 0.013m \\
 &= 13mm
 \end{aligned}$$

However, since that we require a smaller discharge port due to the discharge velocity will not exceed Mach number 0.2. The discharge port is designed smaller with a diameter of $D = 9$ mm instead of 13. This is proven thru the following calculation.

$$\begin{aligned}
 v_d &= \frac{V_2 - V_3}{(t_3 - t_2)A_d} = \frac{Q_d}{A_d} \\
 &= \frac{(7.2923 - 0.0939) \times 10^{-6}}{(6.251 \times 10^{-3} \times 63.6173 \times 10^{-6})} \\
 &= 18.1ms^{-1}
 \end{aligned}$$

$$\begin{aligned}
 M &= \frac{v}{c} \\
 &= \frac{18.1}{195.91} \\
 &= 0.09
 \end{aligned}$$

B.2 Valve Geometry

The available circumference is calculated using equation (based on designed port size);

$$\begin{aligned} C &= \pi D \\ &= \pi \times 0.009 \\ &= 0.0283 \text{ m} \end{aligned}$$

The average required lift height is found as

$$\begin{aligned} h &= \frac{A_e}{C} \\ h &= \frac{63.6173 \times 10^{-6}}{0.0283} = 2.248 \times 10^{-3} \text{ m} \end{aligned}$$

Using above values and equation 3.13, the available average force to reach opening height h ;

$$\begin{aligned} F &= \rho \cdot A \cdot v^2 \\ F &= 89.73 \times 63.6173 \times 10^{-6} \times (18.1)^2 = 1.87 \text{ N} \end{aligned}$$

The spring rate, K can be written as;

$$\begin{aligned} K &= \frac{F}{h} \\ &= \frac{1.87}{2.248 \times 10^{-3}} \\ &= 831 \text{ N/m} \end{aligned}$$

The thickness value of the plate is determined at 0.3 mm using ASTM a154 and the length of the valve is calculated using;

$$t = L^3 \sqrt{\frac{4K}{Eb}}$$

$$0.0003 = L \sqrt{\frac{4 \times 831}{205e^9 \times 0.009}}$$

$$L = 0.02465m$$

C.1 Piston Rings Properties and Dimension

The piston rings are selected from a brand named Eriks. The following figures and diagrams are scanned from Eriks Pte Ltd catalogue book.

ERIKS fluid sealing		Algemene eigenschappen van elastomeren		General properties of Elastomers		Allgemeine Eigenschaften von Elastomeren												
Dit handboek bevat hoofdzakelijk afdichtingselementen die vervaardigd zijn uit elastomeren. Het probleemloos functioneren van de afdichting staat of valt dus met de bestendigheid van het elastomeer. Om U behulpzaam te zijn bij het selecteren van het juiste elastomeermateriaal treft U onderstaand overzicht aan.		This handbook mainly describes sealing elements made of elastomers. Their trouble-free operation largely depends on the resistance of the relevant elastomer. To help you select the appropriate type of elastomer, please find below a condensed material selection guide.		In diesem Katalog werden hauptsächlich aus Elastomeren hergestellte Dichtungselemente beschrieben. Dabei wird das einwandfreie Funktionieren der Dichtung also durch die Beständigkeit des betreffenden Elastomers bedingt. Die nachstehende Übersicht kann Ihnen bei der Wahl des jeweiligen Elastomers behilflich sein.		Natural rubber	Buna S	Buna N Nitril	Ethylene Propylene	Butyl	Neoprene	Urethane	Tripol	Silicone	Fluorocarbon	Fluoro-elastamer (Viton)	Polycrylat	Kautschuk
DIN/ISO 1829	NR	SBR	NBR	EPDM	IR	CR	AU	T	MVD	FMVC	PPM	ACM	PPM					
Hardness (shore A)	30-90	40-90	40-95	40-80	20-80	20-90	50-80	50-80	10-90	40-80	60-90	50-90	80-90					
Tensile strength (p.s.i.)	3000	3000	2500	2500	2000	3000	5000	1000	1400	900	2000	2000	2000					
Tearing strength	U	ZG	G	G	ZG	ZG	U	R	N	N	G	G	G					
Wear resistance	U	U	G	G	G	G	ZG	R	N	N	G	G	G					
Fireproof hydraulic fluids	N	N	N	ZG	ZG	R	N	R	G	ZG	R to U	N	U					
Lubricating oils	N	N	G	N	N	G	ZG	U	U	U	U	ZG	U					
Fuel oils	N	N	G	N	N	R	ZG	U	R	U	U	ZG	U					
Hydraulic oils	N	N	U	N	N	G	ZG	U	G	U	U	U	U					
Vegetable oils	N	R	U	R	U	G	ZG	R	G	U	U	U	U					
Animal fats	N	R	U	R	U	G	ZG	R	G	U	U	U	U					
Petrol (normal)	N	N	ZG	N	N	R	ZG	U	R	U	U	ZG	U					
Petrol (high octane)	N	N	G	N	N	N	ZG	U	N	U	U	G	U					
Kerosene	N	N	ZG	N	N	R	ZG	U	R	U	U	ZG	U					
Aromatic hydrocarbons	N	N	R	N	N	N	G	U	N	U	U	R	U					
Aliphatic hydrocarbons	N	N	ZG	N	N	G	ZG	U	R	U	U	ZG	U					
Water (under 80°C)	G	ZG	ZG	U	U	R	R to N	R	U	U	U	U	N					
Water (above 80°C)	N	R	R	U	G	N	N	N	U	ZG	G	N	U					
Alcohols	G	G	ZG	U	U	U	R	R	U	U	U	N	U					
Ketones	N	N	N	G	ZG	N	N	ZG	G	N	N	N	U					
Concentrated acids	N	N	N	R	G	N	N	R	G	ZG	G	ZG	N					
Diluted acids	R	R	R	G	U	G	N	R	G	ZG	U	N	U					
Alkalis	G	G	R	ZG	U	G	N	N	G	R	U	G	N					
Chlorinated solvents	N	N	R	N	N	N	R	ZG	N	U	U	R	U					
Ozone and sunlight	R	R	R	U	U	ZG	ZG	ZG	U	U	U	ZG	U					
Max. temperature at continuous service	70°C	105°C	105°C	135°C	120°C	105°C	70°C	65°C	230°C	205°C	200°C	175°C	280°C					
Electrical properties	U	ZG	N	U	U	ZG	G	R	U	U	U	N	U					
Compression set	ZG	ZG	ZG	G	G	ZG	N	N	U	ZG	R	G	G					
Flame resistant	-	-	-	-	-	+	-	-	-	-	+	-	+					

U = Uitstekend	U = Excellent	U = Ausgezeichnet
ZG = Zeer goed	ZG = Very good	ZG = Sehr gut
G = Goed	G = Good	G = Gut
R = Redelijk	R = Reasonable	R = Ziemlich gut
N = Niet aanbevolen	N = Unsuitable	N = Nicht empfohlen
- = Nee	- = No	- = Nein
+ = Ja	+ = Yes	+ = Ja

Figure C.1 Piston Rings Properties

	Recommended for the following media	Remarks
	<p>NBR, Nitrile, Buna-N, Perbunan</p> <p>Petroleum-based hydraulic and lubricating oils, animal and vegetable oils, acetylene, alcohols, water, air, alkalis, fuel oils and many other media.</p>	
	<p>FPM, Viton®, Fluorcarbon Elastomers</p> <p>High-quality compounds for high temperatures. Synthetic and hydraulic fluids; a wide range of chemicals, heavily oxidizing acids, suitable for vacuum.</p>	

Figure C.2 Piston Rings Properties

Based on the above data, Viton based material is selected as the material for the piston rings. The following diagram shows the requirements for the bore inner surface roughness.

Ruwhheid	Roughness	Rauhgkeit	Ra	Rt
Stang/cilinderwand	Cylinder walstroed	Zylinderwand/Stange	$\leq 0,3 \mu\text{m}$	$\leq 3 \mu\text{m}$
Afdichtingsgroef	Collar/o-ring groove	Manschette/o-Ringnut		
Groefbodem	Groove bottom	Nutgrond	$\leq 1,8 \mu\text{m}$	$\leq 10 \mu\text{m}$
Groefflank	Groove wall	Nutflanke	$\leq 3 \mu\text{m}$	$\leq 16 \mu\text{m}$
Afstrijkergroef	Wiper groove	Abstreifernut		
Groefbodem	Groove bottom	Nutgrond	$\leq 2,5 \mu\text{m}$	$\leq 16 \mu\text{m}$
Groefflank	Groove wall	Nutflanke	$\leq 4 \mu\text{m}$	$\leq 20 \mu\text{m}$
Oliekeerring	Rotary shaft seals	Radial-Wellendichtringe		
As	Shaft	Welle	$\leq 0,3 \mu\text{m}$	$\leq 3 \mu\text{m}$
Boring	Bore	Bohrung	$\leq 2,5 \mu\text{m}$	$\leq 12 \mu\text{m}$

<p>Afchuiningen aan stang- en cilinderinvoeringen 15° à 20° over 5 à 7 mm.</p> <p>Voor de opgegeven waarden als druk, temperatuur en snelheid geldt, dat maximale waarden niet in combinatie mogen voorkomen. Vraag in speciale gevallen ons advies.</p>	<p>The rods and cylinders should have 5-7 mm long lead-in chamfers of 15-20°.</p> <p>The maximum values specified for pressure, temperature and speed should not be applied in conjunction with each other. Please consult us for special applications.</p>	<p>Abschrägungen an Stangen- und Zylindereinführungen 15 bis 20° über 5 bis 7 mm.</p> <p>Für die angegebenen Werte wie Druck, Temperatur und Geschwindigkeit gilt, daß Höchstwerte nicht in Kombination vorkommen dürfen. In Sonderfällen fragen Sie bitte unsere Spezialisten!</p>
--	---	---

Figure C.3 Piston Rings Surface Finishing and Tolerances

Piston rings set with a diameter of 36 are selected from the catalogue as shown in figure C.5.

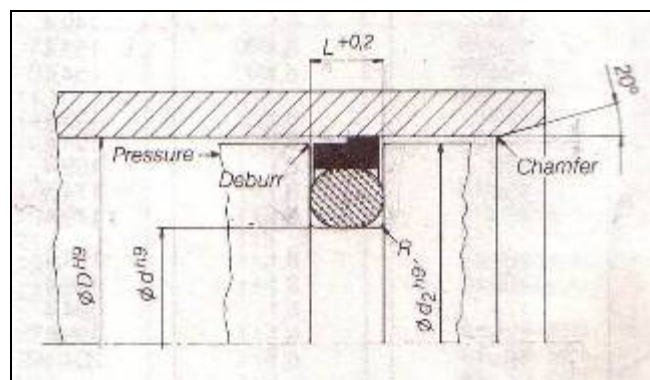


Figure C.4 Piston Rings Cross Section

AFMETINGEN ERIFLON single-acting piston seal 850			ERIFLON Einfachwirkenden Kolbendichtung 850		
Afmetingen Dimensions Abmessungen			Ø d _h	O-Ring nr. AS	Bestelnummer Order number Bestellnummer
Ø D	Ø d	L			
8	3,1	2,2	7,7	006	ER-39-850- 8-006
10	5,1	2,2	9,7	009	ER-39-850- 10-009
12	7,1	2,2	11,7	011	ER-39-850- 12-011
15	10,1	2,2	14,7	012	ER-39-850- 15-012
16	11,1	2,2	15,7	013	ER-39-850- 16-013
18	10,7	3,2	17,8	111	ER-39-850- 18-111
20	12,7	3,2	19,6	112	ER-39-850- 20-112
22	14,7	3,2	21,6	113	ER-39-850- 22-113
25	17,7	3,2	24,6	115	ER-39-850- 25-115
28	17,3	4,2	27,5	209	ER-39-850- 28-209
30	19,3	4,2	29,5	210	ER-39-850- 30-210
32	21,3	4,2	31,5	211	ER-39-850- 32-211
35	24,3	4,2	34,5	213	ER-39-850- 35-213
36	25,3	4,2	35,5	214	ER-39-850- 36-214
38	27,3	4,2	37,5	215	ER-39-850- 38-215
39	28,3	4,2	38,5	215	ER-39-850- 39-215
40	29,3	4,2	39,5	216	ER-39-850- 40-216
42	31,3	4,2	41,5	217	ER-39-850- 42-217
45	34,3	4,2	44,5	219	ER-39-850- 45-219
48	37,3	4,2	47,5	221	ER-39-850- 48-221
50	39,3	4,2	49,5	222	ER-39-850- 50-222
52	41,3	4,2	51,5	223	ER-39-850- 52-223
55	44,3	4,2	54,5	224	ER-39-850- 55-224
56	45,3	4,2	55,5	224	ER-39-850- 56-224
60	44,9	6,3	59,4	327	ER-39-850- 60-327
63	47,9	6,3	62,4	328	ER-39-850- 63-328
64	48,9	6,3	63,4	328	ER-39-850- 64-328
65	49,9	6,3	64,4	328	ER-39-850- 65-328
70	54,9	6,3	79,4	330	ER-39-850- 70-330
75	59,9	6,3	74,4	332	ER-39-850- 75-332
80	64,9	6,3	79,4	333	ER-39-850- 80-333
85	69,9	6,3	84,4	335	ER-39-850- 85-335
89	73,9	6,3	88,4	336	ER-39-850- 89-336
90	74,9	6,3	89,4	336	ER-39-850- 90-336
95	79,9	6,3	94,4	337	ER-39-850- 95-337
100	84,9	6,3	99,4	340	ER-39-850-100-340
105	89,9	6,3	104,4	341	ER-39-850-105-341
110	94,9	6,3	109,4	343	ER-39-850-110-343
115	99,9	6,3	114,4	344	ER-39-850-115-344
120	104,9	6,3	119,4	345	ER-39-850-120-345
125	109,9	6,3	124,4	347	ER-39-850-125-347
127	111,9	6,3	126,4	348	ER-39-850-127-348
130	114,9	6,3	129,4	349	ER-39-850-130-349
132	116,9	6,3	131,4	349	ER-39-850-132-349
133	117,9	6,3	132,4	350	ER-39-850-133-350
135	119,9	6,3	134,4	351	ER-39-850-135-351
140	124,9	6,3	139,4	352	ER-39-850-140-352
145	129,9	6,3	144,4	353	ER-39-850-145-353
150	134,9	6,3	149,4	355	ER-39-850-150-355
154	138,9	6,3	153,4	356	ER-39-850-154-356
155	139,9	6,3	154,4	356	ER-39-850-155-356
160	144,9	6,3	159,4	358	ER-39-850-160-358
165	149,9	6,3	164,4	360	ER-39-850-165-360
170	154,9	6,3	169,4	361	ER-39-850-170-361
175	159,9	6,3	174,4	362	ER-39-850-175-362
180	164,9	6,3	179,4	363	ER-39-850-180-363
190	174,9	6,3	189,4	364	ER-39-850-190-364
200	179,5	8,1	194,4	441	ER-39-850-200-441
210	189,5	8,1	209,4	443	ER-39-850-210-443
220	199,5	8,1	219,4	444	ER-39-850-220-444
225	204,5	8,1	224,4	445	ER-39-850-225-445
230	209,5	8,1	229,4	445	ER-39-850-230-445

• = Stocked size
 • = Abmessungen auf Lager
 Andere afmetingen op aanvraag leverbaar. Other sizes are available upon request. Andere Abmessungen sind auf Anfrage lieferbar.
 O-ring nr. volgens AS 568A AS = O-ring to AS Standard 568A AS = O-Ring gemäß AS-Normen 568A.

Figure C.5 Piston Rings Dimension

Appendix C

Piston Rings Data and Selection

D.1 Vector Generation of Cycloidal Profile

A Lily pump consist of a wheel with a number (n) of cycloid gear tooth geared with an internal gear wheel with plus one number (n+1) of cycloid gear with the tooth form such that contacts between teeth are never broken as the wheels rotate. By this means, spaces between the profiles expand and contract with rotation creating working spaces of suction and discharge effect making it suitable to work as a pump for the compressor.

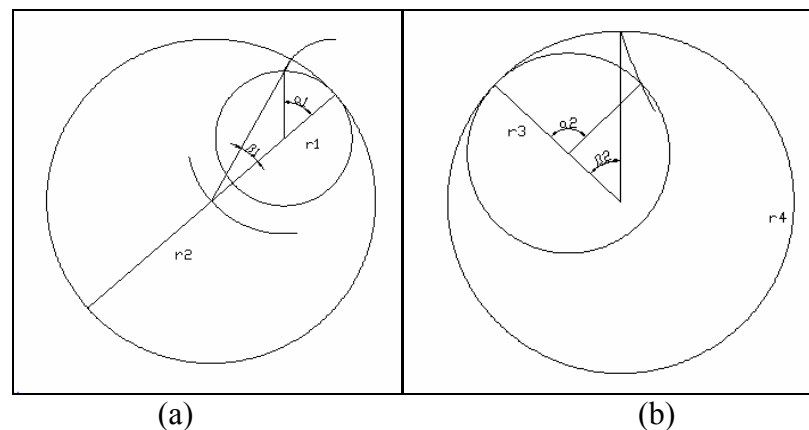


Figure D.1 Vector Diagram
a) Epicycloid Generation b) hypocycloid Generation

The gear and internal gear wheel are consist of Epicycloid and Hypocycloid placed each at addendum and dedendum of each wheels and are identical. To generate the cycloids on an engineering drawing, an alternative generation method using vectors description is used. Equation D.1 and D.2 is used to generate epicycloids loop and equation D.3 and D.4 is used to generate hypocycloids loop with n is the number of gear tooth with figure D.1 shows the value of r_1 , r_2 , r_3 , r_4 , $\alpha_{1,2}$ and $\beta_{1,2}$. Figure D.2 and D.3 shows the initial generation vectors of epicycloids and hypocycloids for rotor and internal gear respectively. Figure D.4 shows the cycloids generated on Autocad before full solid 3D drawing is drawn. Lastly, table D.1 shows calculated $\alpha_{1,2}$ and $\beta_{1,2}$ for generating the cycloids diagram.

$$r_1 \alpha_1 = r_2 \beta_1 \quad (D.1)$$

$$n + 1 = \frac{r_2}{r_2 - r_1} \quad (D.2)$$

$$r_3\alpha_2 = r_4\beta_2 \quad (\text{D.3})$$

$$n-1 = \frac{r_3}{r_4 - r_3} \quad (\text{D.4})$$

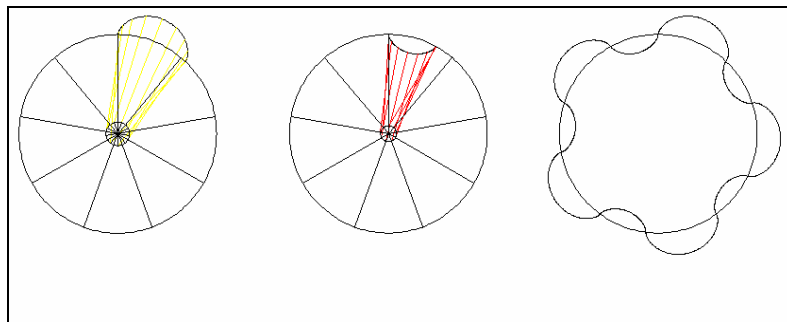


Figure D.2 Internal Gear Generations via Vector Method

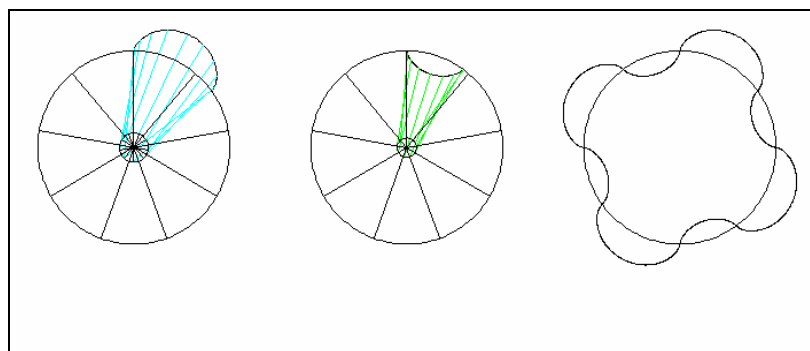


Figure D.3 Rotor Generations via Vector Method

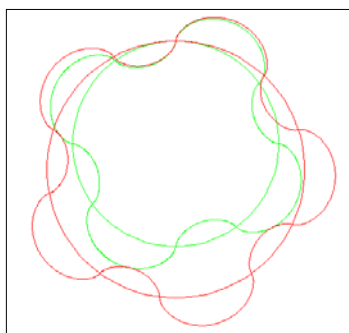


Figure D.4 Matched Rotor and Internal Gear

Table D.1 Calculated α and β

Epicycloid with pitch diameter 50		Hypocycloid with pitch diameter 50		Epicycloid with pitch diameter 40		Hypocycloid with pitch diameter 40	
r1	25	r3	20	r1	20	r3	15
r2	30	r4	25	r2	25	r4	20
n	5	n	5	n	4	n	4
a	2	b	3	a	2	b	3
r2'	28	r3'	23	r2'	23	r3'	18
α -1	β -1	β -2	α -2	α -1	β -1	β -2	α -2
0.00	0.00	0.00	0.00	0.00	0.00	0.00	0.00
40.00	35.71	40.00	43.48	40.00	34.78	40.00	44.44
80.00	71.43	80.00	86.96	80.00	69.57	80.00	88.89
120.00	107.14	120.00	130.43	120.00	104.35	120.00	133.33
160.00	142.86	160.00	173.91	160.00	139.13	160.00	177.78
200.00	178.57	200.00	217.39	200.00	173.91	200.00	222.22
240.00	214.29	240.00	260.87	240.00	208.70	240.00	266.67
280.00	250.00	280.00	304.35	280.00	243.48	280.00	311.11
320.00	285.71	320.00	347.83	320.00	278.26	320.00	355.56
360.00	321.43	360.00	391.30	360.00	313.04	360.00	400.00
400.00	357.14	400.00	434.78	400.00	347.83	400.00	444.44
440.00	392.86	440.00	478.26	440.00	382.61	440.00	488.89
480.00	428.57	480.00	521.74	480.00	417.39	480.00	533.33
520.00	464.29	520.00	565.22	520.00	452.17	520.00	577.78
560.00	500.00	560.00	608.70	560.00	486.96	560.00	622.22
600.00	535.71	600.00	652.17	600.00	521.74	600.00	666.67

Appendix D

Cycloid Profile Generation Via Vector Method

E.1 Kinematics Analysis

The following kinematic calculation and equation were extracted from Zair [16] and included in the appendix for reader convenience. The first step in analyzing the motion of wobble plate is to find the relationship between shaft angles of rotation, θ and wobble plate tilting angle, α . All the piston and wobble plate movements start from the shaft rotation. From Figure E.1, taking the shaft rotation angle clockwise, for every shaft rotation, wobble plate will move from point R to point R' and return back to point R. The geometrical representation of this relationship is obtained from Figure E.2. Maximum wobble plate tilting angle is given by $\tilde{\alpha}$ which is determined by the inclination angle of rotor. From Figure E.2, we know that;

$$m = \frac{\ell}{\tan \theta} \quad (\text{E.1})$$

$$x = R \cos \alpha \quad (\text{E.2})$$

$$\ell = x \sin \theta \quad (\text{E.3})$$

Substitute equation (D.2) into equation (D.3), we get;

$$\ell = R \cos \alpha \sin \theta \quad (\text{E.4})$$

And substitute equation (D.4) into equation (D.1), we get;

$$m = \frac{R \cos \alpha \sin \theta}{\tan \theta} = R \cos \alpha \cos \theta \quad (\text{E.5})$$

By using ellipse relationship;

$$\frac{m^2}{R^2} + \frac{\ell^2}{R^2 \cos^2 \tilde{\alpha}} = 1 \quad (\text{E.6})$$

Substitute equation (E.4) and equation (E.5) into equation (E.6) and rearranging, the relationship between θ and α is obtained as;

$$\therefore \alpha = \cos^{-1} \left[\frac{A}{\sin^2 \theta + A \cos^2 \theta} \right]^{1/2}$$

Where;

$$A = \cos^2 \tilde{\alpha} \quad (\text{E.7})$$

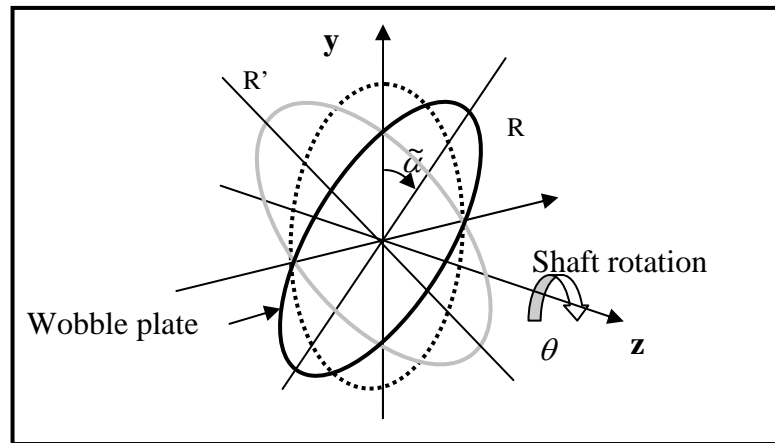


Figure E.1 Relationship between θ and α

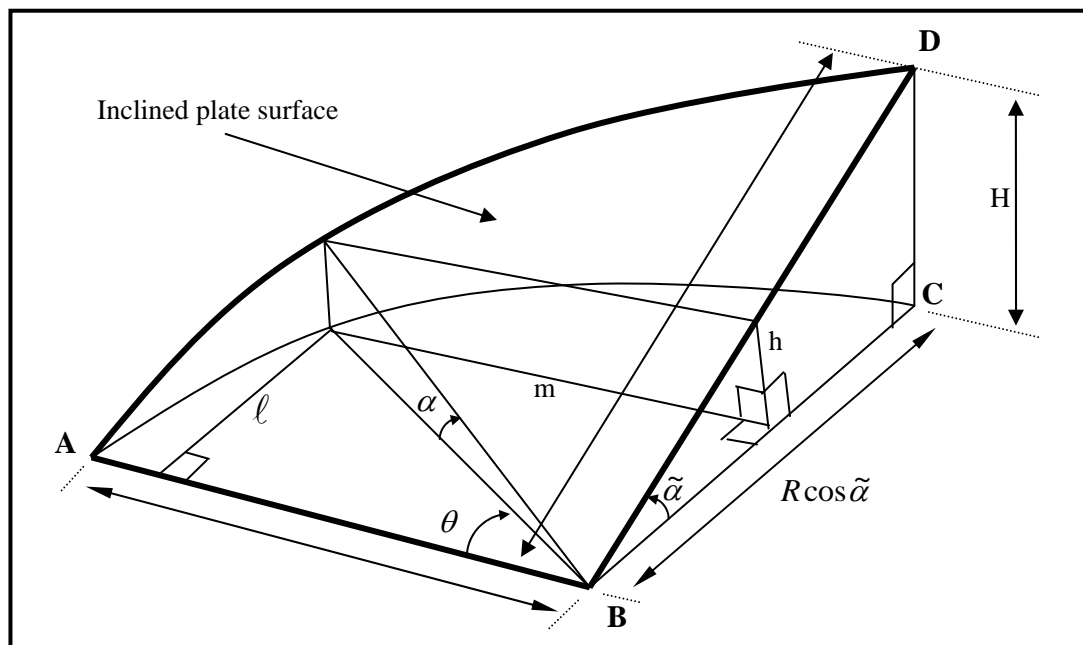


Figure E.2 Geometrical model to obtain the relationship between θ and α

Using the above equation and compressor parameters, the shaft rotation and tilting angle is calculated and tabulated in table E.1.

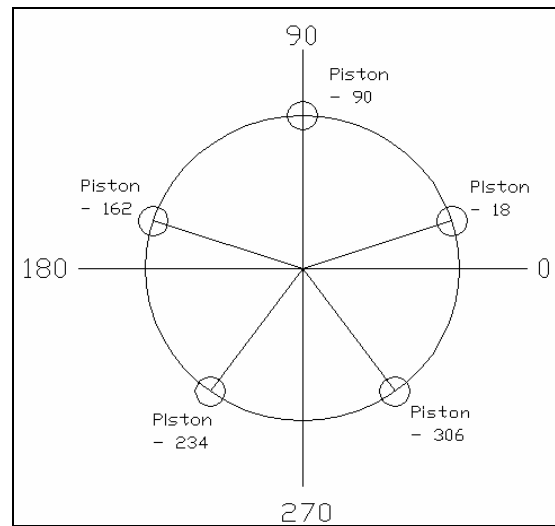


Figure E.3 Piston Position

Table E.1 Tilting angle of each piston position

θ	α				
	$\theta-18$	$\theta-90$	$\theta-162$	$\theta-234$	$\theta-306$
0.00	6.07	19.00	6.07	15.57	-15.57
10.00	9.18	18.73	2.74	-17.20	-13.45
20.00	11.97	17.93	-0.69	-18.31	-10.90
30.00	14.35	16.60	-4.09	-18.90	-7.97
40.00	16.28	14.78	-7.35	-18.96	-4.76
50.00	17.71	12.48	-10.34	-18.47	-1.38
60.00	18.61	9.77	-12.97	-17.46	2.06
70.00	18.99	6.72	-15.18	-15.93	5.42
80.00	18.83	3.42	-16.91	-13.91	8.58
90.00	18.13	0.00	-18.13	-11.44	11.44
100.00	16.91	-3.42	-18.83	-8.58	13.91
110.00	15.18	-6.72	-18.99	-5.42	15.93
120.00	12.97	-9.77	-18.61	-2.06	17.46
130.00	10.34	-12.48	-17.71	1.38	18.47
140.00	7.35	-14.78	-16.28	4.76	18.96
150.00	4.09	-16.60	-14.35	7.97	18.90
160.00	0.69	-17.93	-11.97	10.90	18.31
170.00	-2.74	-18.73	-9.18	13.45	17.20

180.00	-6.07	-19.00	-6.07	15.57	15.57
190.00	-9.18	-18.73	-2.74	17.20	13.45
200.00	-11.97	-17.93	-0.69	18.31	10.90
210.00	-14.35	-16.60	4.09	18.90	7.97
220.00	-16.28	-14.78	7.35	18.96	4.76
230.00	-17.71	-12.48	10.34	18.47	1.38
240.00	-18.61	-9.77	12.97	17.46	-2.06
250.00	-18.99	-6.72	15.18	15.93	-5.42
260.00	-18.83	-3.42	16.91	13.91	-8.58
270.00	-18.13	0.00	18.13	11.44	-11.44
280.00	-16.91	3.42	18.83	8.58	-13.91
290.00	-15.18	6.72	18.99	5.42	-15.93
300.00	-12.97	9.77	18.61	2.06	-17.46
310.00	-10.34	12.48	17.71	-1.38	-18.47
320.00	-7.35	14.78	16.28	-4.76	-18.96
330.00	-4.09	16.60	14.35	-7.97	-18.90
340.00	0.69	17.93	11.97	-10.90	-18.31
350.00	2.74	18.73	9.18	-13.45	-17.20
360.00	6.07	19.00	6.07	-15.57	-15.57

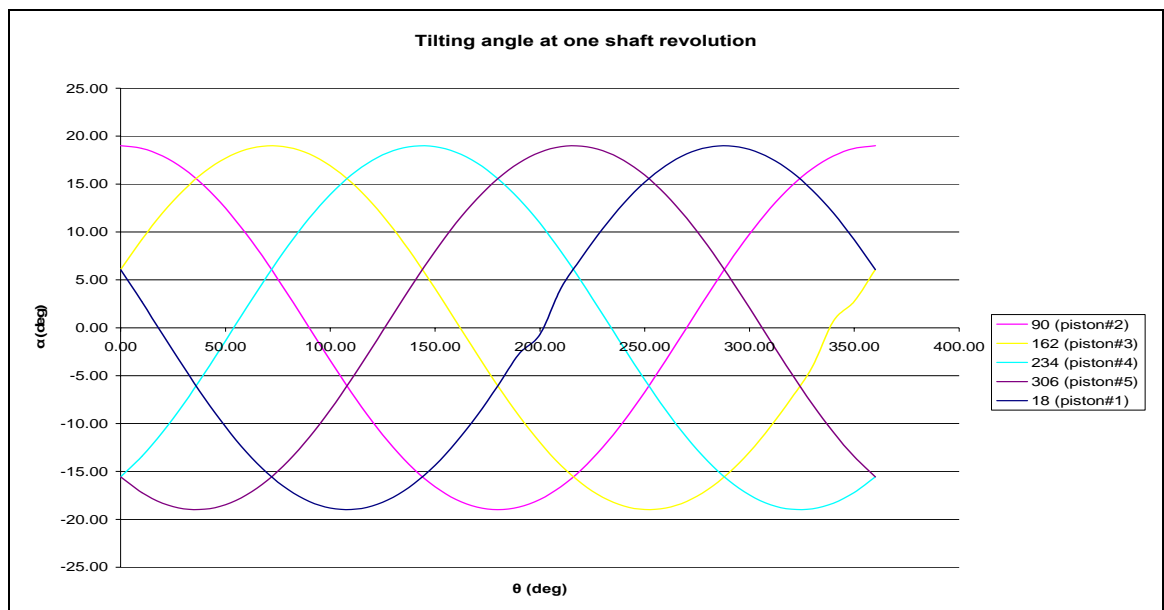


Figure E.4 Tilting angle at one shaft revolution

E.2 Movement of Connecting Rod Ball at Wobble Plate Side

Movement of connecting rod ball at wobble plate side, s will be obtained using coordinate transformation method. Shaft rotation is taken to be clockwise with $\alpha = \tilde{\alpha}$ at $\theta = 90^\circ$. Assume that one guide rod ball is used at the plate periphery to prevent plate from moving with the rotor rotation at $\theta = 4/3 \pi$ radian. z-axis is taken to be coincident with shaft; y-axis and x-axis are also as shown in Figure E.5. At the guide rod location, wobble plate movement is restricted to movement along plane y-z only with angle α from Y-axis.

From Figure E.6; with shaft rotation, θ , y-axis will moves to y_α -axis while z-axis moves to z_α -axis. This coordinate transformation can be written as;

$$\begin{aligned} x_s &= x_\alpha \\ y_s &= y_\alpha \cos \alpha - z_\alpha \sin \alpha \\ z_s &= z_\alpha \cos \alpha + y_\alpha \sin \alpha \end{aligned} \tag{E.8}$$

Wobble plate also rotate at y_α -axis with angle γ . x_α -axis and z_α -axis will move to x_γ -axis and z_γ -axis correspondingly. This coordinate transformation can be written as;

$$\begin{aligned} x_\alpha &= x_\gamma \cos \gamma - z_\gamma \sin \gamma \\ y_\alpha &= y_\gamma \\ z_\alpha &= z_\gamma \cos \gamma + x_\gamma \sin \gamma \end{aligned} \tag{E.9}$$

Substitute sets of equation (E.9) into sets of equation (E.8), we get the movement of connecting rod ball at wobble plate side as;

$$x_s = x_\gamma \cos \gamma - z_\gamma \sin \gamma$$

$$\begin{aligned}
 y_s &= y_\gamma \cos \alpha - (z_\gamma \cos \gamma + x_\gamma \sin \gamma) \sin \alpha \\
 z_s &= (z_\gamma \cos \gamma + x_\gamma \sin \gamma) \cos \alpha + y_\gamma \sin \alpha
 \end{aligned} \tag{E.10}$$

Relationship for angle γ and angle β is then obtained from Figure E.6 as;

$$\gamma = \tan^{-1} \left[\frac{\tan \beta}{\cos \alpha} \right] \tag{E.11}$$

β is lagging α by 90° and given as;

$$\beta = \cos^{-1} \left[\frac{A}{\sin^2(\theta - 90) + A \cos^2(\theta - 90)} \right]^{\frac{1}{2}} \tag{E.12}$$

The value of x_γ , y_γ , z_γ can be obtained from Figure E.7 as follows;

$$\begin{aligned}
 x_\gamma &= R_w \sin \theta_i \\
 y_\gamma &= R_w \cos \theta_i \\
 z_\gamma &= t_w
 \end{aligned} \tag{E.13}$$

Using equation E.13 and E.10, the motion of ball joint on wobble plate side for n^{th} piston can be written as;

$$\begin{aligned}
 x_s &= (R_w \sin \theta_i) \cos \gamma - (t_w) \sin \gamma \\
 y_s &= (R_w \cos \theta_i) \cos \alpha - ((t_w) \cos \gamma + (R_w \sin \theta_i) \sin \gamma) \sin \alpha \\
 z_s &= ((t_w) \cos \gamma + (R_w \sin \theta_i) \sin \gamma) \cos \alpha + (R_w \cos \theta_i) \sin \alpha
 \end{aligned} \tag{E.14}$$

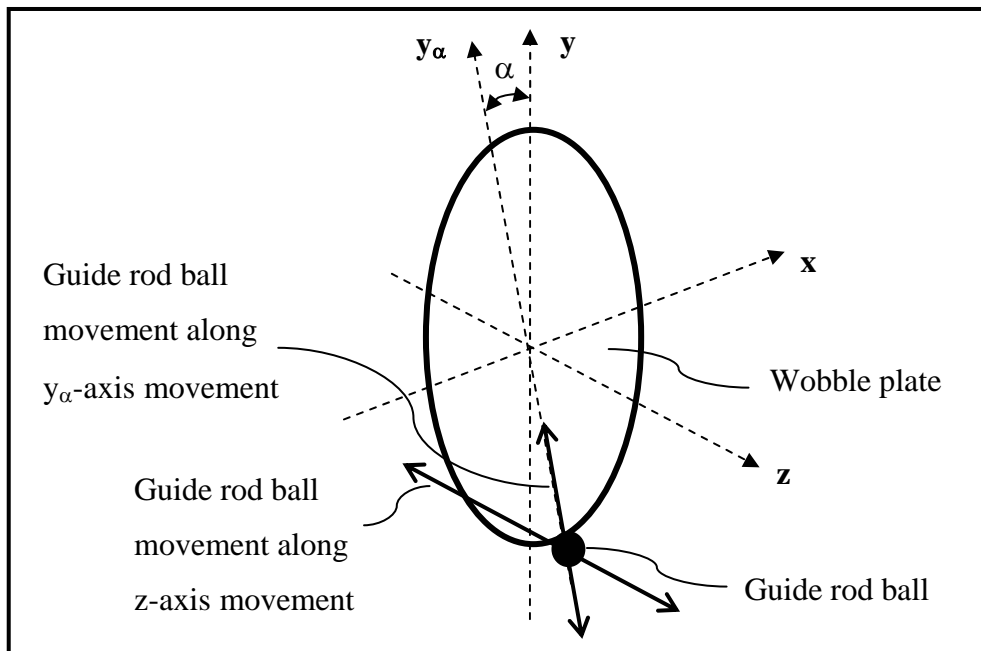


Figure E.5 Location of guide rod ball on wobble plate

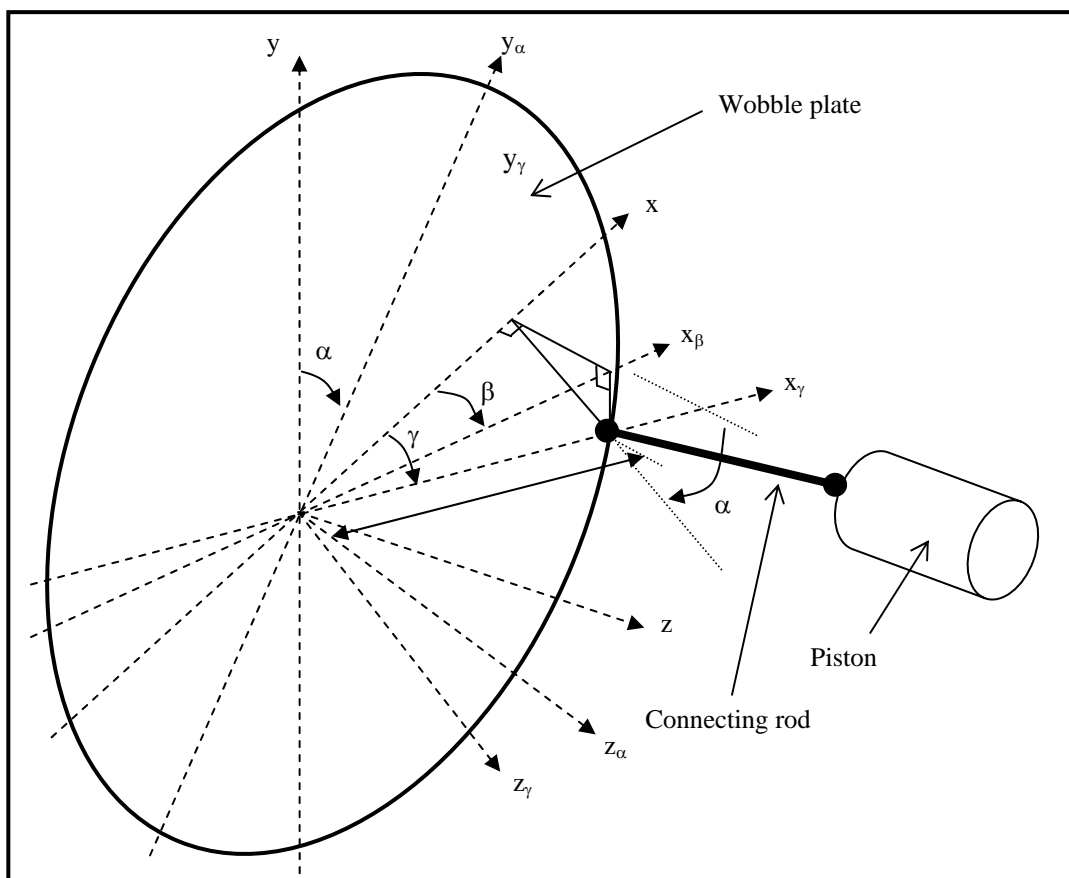


Figure E.6 Geometric relationship that exist in wobble plate

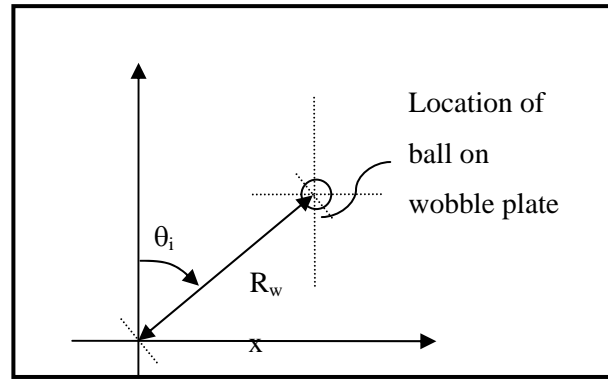


Figure E.7 Location of connecting rod ball on wobble plate in $Y\gamma$ - $X\gamma$ plane

E.3 Movement of Connecting Rod Ball at Piston Side

From Figure E.8 and Figure E.9, the coordinate of connecting rod ball on piston side, t is represented by:

$$x_t = R_p \sin \theta_i$$

$$y_t = R_p \cos \theta_i$$

$$z_t = z_s + l_{cr} \cos \phi_i \quad (\text{E.15})$$

Substitute z_s term in the equation E.14 in equation E.15, the z-axis position of connecting rod ball at piston side can be obtain as;

$$z_t = ((t_w) \cos \gamma + (R_w \sin \theta_i) \sin \gamma) \cos \alpha + (R_w \cos \theta_i) \sin \alpha + l_{cr} \cos \phi_i \quad (\text{E.16})$$

The ϕ_i angle is the angle between the connecting rod and piston's z-axis given as;

$$\phi_i = \sin^{-1} \left[\left\{ (x_s - x_t)^2 + (y_s - y_t)^2 \right\}^{1/2} / l_{cr} \right] \quad (\text{E.17})$$

Value of x_t and y_t in equation E.25 is a constant for each θ_i . Only position of ball joint at piston side in z-axis, z_t changes during shaft revolution.

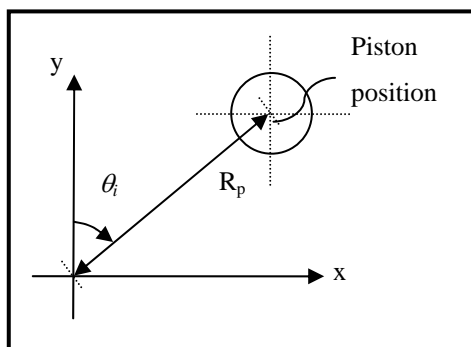


Figure E.8 Location of connecting rod ball on piston side

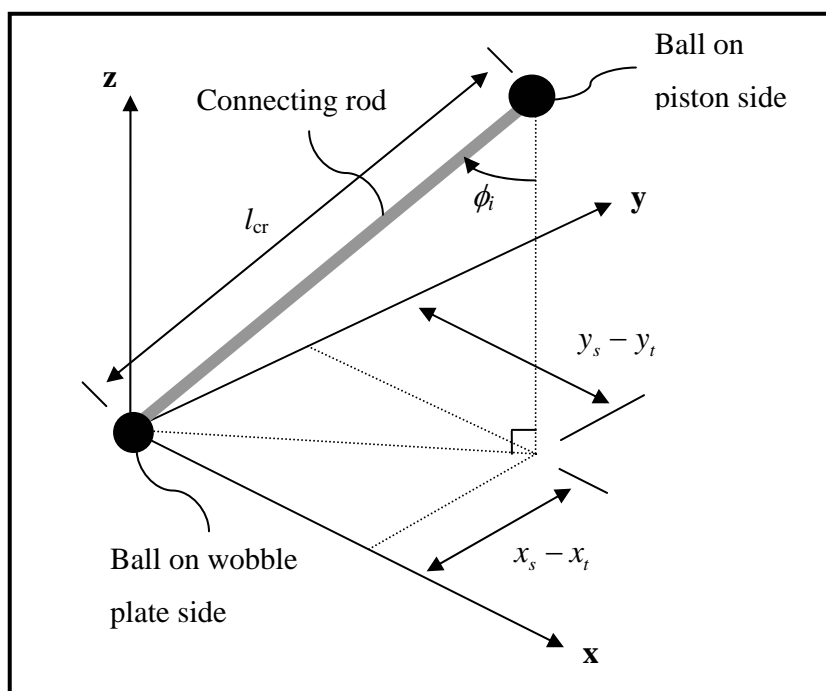


Figure E.9 Location of connecting rod ball on piston side and wobble plate side

Using the above equations, the compressor stroke are calculated and presented in table for each piston position

Table E.2 Piston Position on the Z Axis for Each Position

θ	Z_t				
	0-18	0-90	0-162	0-234	0-306
0.00	54.47	64.65	54.47	38.13	38.13
10.00	56.96	64.45	51.85	36.71	39.86
20.00	59.22	63.85	49.21	35.68	41.85
30.00	61.16	62.86	46.64	35.10	44.03
40.00	62.72	61.47	44.22	35.00	46.36
50.00	63.86	59.70	42.02	35.39	48.79
60.00	64.55	57.60	40.07	36.27	51.29
70.00	64.78	55.22	38.41	37.60	53.80
80.00	64.57	52.63	37.06	39.31	56.26
90.00	63.93	49.94	36.06	41.35	58.57
100.00	62.89	47.26	35.43	43.62	60.64
110.00	61.49	44.69	35.20	46.05	62.39
120.00	59.78	42.33	35.40	48.55	63.72
130.00	57.80	40.25	36.05	51.06	64.60
140.00	55.59	38.51	37.16	53.52	64.98
150.00	53.19	37.14	38.71	55.88	64.87
160.00	50.65	36.15	40.65	58.08	64.28
170.00	48.03	35.55	42.92	60.09	63.25
180.00	45.42	35.35	45.42	61.83	61.83
190.00	42.92	35.55	48.03	63.25	60.09
200.00	40.65	36.15	50.65	64.28	58.08
210.00	38.71	37.14	53.19	64.87	55.88
220.00	37.16	38.51	55.59	64.98	53.52
230.00	36.05	40.25	57.80	64.60	51.06
240.00	35.40	42.33	59.78	63.72	48.55
250.00	35.20	44.69	61.49	62.39	46.05
260.00	35.43	47.26	62.89	60.64	43.62
270.00	36.06	49.94	63.93	58.57	41.35
280.00	37.06	52.63	64.57	56.26	39.31
290.00	38.41	55.22	64.78	53.80	37.60
300.00	40.07	57.60	64.55	51.29	36.27
310.00	42.02	59.70	63.86	48.79	35.39
320.00	44.22	61.47	62.72	46.36	35.00
330.00	46.64	62.86	61.16	44.03	35.10
340.00	49.21	63.85	59.22	41.85	35.68
350.00	51.85	64.45	56.96	39.86	36.71
360.00	54.47	64.65	54.47	38.13	38.13

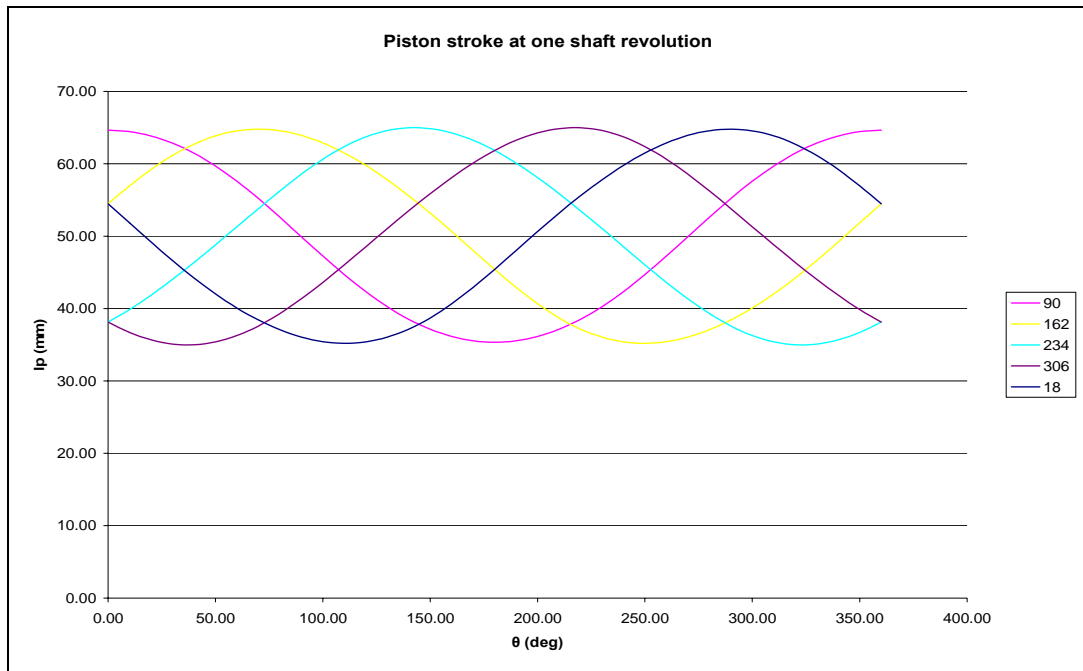


Figure E.10 Piston Stroke for Each Piston

Appendix E

Kinematics Analysis

Appendix F
Static Analysis Results

F.1 Forces Acting on the Piston

Table F.1: Forces Acting on Piston 1

$\theta_n =$	18							
θ	zp	Prs (Bar)	Fpp (N)	Fpcrx	Fpcry	Fpcrz	Fpcbx	Fpcby
0.00	54.47	3.50	0.00	0.00	0.00	0.00	0.00	0.00
20.00	49.21	3.50	0.00	0.00	0.00	0.00	0.00	0.00
40.00	44.22	3.50	0.00	0.00	0.00	0.00	0.00	0.00
60.00	40.07	3.50	0.00	0.00	0.00	0.00	0.00	0.00
80.00	37.06	3.50	0.00	0.00	0.00	0.00	0.00	0.00
100.00	35.43	3.50	0.00	0.00	0.00	0.00	0.00	0.00
120.00	35.40	3.51	-1.34	-0.01	0.04	1.34	0.01	-0.04
140.00	37.16	3.76	-26.92	-0.70	1.14	26.92	0.70	-1.14
160.00	40.65	4.38	-89.54	-3.68	2.73	89.54	3.68	-2.73
180.00	45.42	5.60	-213.95	-10.19	-0.06	213.95	10.19	0.06
200.00	50.65	7.97	-454.89	-18.71	-15.63	454.89	18.71	15.63
220.00	55.59	12.90	-956.63	-24.89	-52.68	956.63	24.89	52.68
240.00	59.78	20.00	-1679.50	-18.28	-89.95	1679.50	18.28	89.95
260.00	62.89	20.00	-1679.50	-3.47	-52.74	1679.50	3.47	52.74
280.00	64.57	20.00	-1679.50	-3.47	2.48	1679.50	3.47	-2.48
300.00	64.55	3.50	0.00	0.00	0.00	0.00	0.00	0.00
320.00	62.72	3.50	0.00	0.00	0.00	0.00	0.00	0.00
340.00	59.22	3.50	0.00	0.00	0.00	0.00	0.00	0.00
360.00	54.47	3.50	0.00	0.00	0.00	0.00	0.00	0.00

Table F.2: Forces Acting on Piston 2

$\theta_n =$	90							
θ	zp	Prs	Fpp (N)	Fpcrx	Fpcry	Fpcrz	Fwcrx	Fwcry
0.00	64.65	3.50	0.00	0.00	0.00	0.00	0.00	0.00
20.00	63.85	3.50	0.00	0.00	0.00	0.00	0.00	0.00
40.00	61.47	3.50	0.00	0.00	0.00	0.00	0.00	0.00
60.00	57.60	3.50	0.00	0.00	0.00	0.00	0.00	0.00
80.00	52.63	3.50	0.00	0.00	0.00	0.00	0.00	0.00
100.00	47.26	3.50	0.00	0.00	0.00	0.00	0.00	0.00
120.00	42.33	3.50	0.00	0.00	0.00	0.00	0.00	0.00
140.00	38.51	3.50	0.00	0.00	0.00	0.00	0.00	0.00
160.00	36.15	3.50	0.00	0.00	0.00	0.00	0.00	0.00
180.00	35.35	3.50	0.00	0.00	0.00	0.00	0.00	0.00
200.00	36.15	3.62	-11.80	0.00	-0.07	-11.80	0.00	0.07
220.00	38.51	3.98	-49.11	0.00	-0.99	-49.11	0.00	0.99
240.00	42.33	4.75	-127.01	0.00	-4.70	-127.01	0.00	4.70
260.00	47.26	6.26	-281.32	0.00	-13.63	-281.32	0.00	13.63
280.00	52.63	9.43	-603.87	0.00	-29.26	-603.87	0.00	29.26
300.00	57.60	16.99	-1372.82	0.00	-50.76	-1372.82	0.00	50.76
320.00	61.47	20.00	-1679.50	0.00	-33.99	-1679.50	0.00	33.99
340.00	63.85	20.00	-1679.50	0.00	-10.57	-1679.50	0.00	10.57
360.00	64.65	20.00	-1679.50	0.00	-1.62	-1679.50	0.00	1.62

Table F.3: Forces Acting on Piston 3

$\theta_n =$	162							
θ	zp	Prs, Vlvd 2	Fpp (N)	Fpcrx	Fpcry	Fpcrz	Fwcrx	Fwcry
0.00	54.47	11.34	-797.74	37.98	-0.24	797.74	-37.98	0.24
20.00	59.22	20.00	-1679.50	69.07	51.16	1679.50	-69.07	-51.16
40.00	62.72	20.00	-1679.50	43.68	71.40	1679.50	-43.68	-71.40
60.00	64.55	20.00	-1679.50	18.26	51.49	1679.50	-18.26	-51.49
80.00	64.57	3.50	0.00	0.00	0.00	0.00	0.00	0.00
100.00	62.89	3.50	0.00	0.00	0.00	0.00	0.00	0.00
120.00	59.78	3.50	0.00	0.00	0.00	0.00	0.00	0.00
140.00	55.59	3.50	0.00	0.00	0.00	0.00	0.00	0.00
160.00	50.65	3.50	0.00	0.00	0.00	0.00	0.00	0.00
180.00	45.42	3.50	0.00	0.00	0.00	0.00	0.00	0.00
200.00	40.65	3.50	0.00	0.00	0.00	0.00	0.00	0.00
220.00	37.16	3.50	0.00	0.00	0.00	0.00	0.00	0.00
240.00	35.40	3.50	0.00	0.00	0.00	0.00	0.00	0.00
260.00	35.43	3.52	-1.75	0.00	0.00	1.75	0.00	0.00
280.00	37.06	3.75	-25.47	0.05	-0.80	25.47	-0.05	0.80
300.00	40.07	4.26	-77.80	0.85	-4.17	77.80	-0.85	4.17
320.00	44.22	5.24	-176.98	4.61	-9.75	176.98	-4.61	9.75
340.00	49.21	7.15	-371.34	15.27	-12.76	371.34	-15.27	12.76
360.00	54.47	11.34	-797.74	37.98	-0.24	797.74	-37.98	0.24

Table F.4: Forces Acting on Piston 4

$\theta_n =$	234							
θ	zp	Prs, Vlvd 2	Fpp (N)	Fpcrx	Fpcry	Fpcrz	Fwcrx	Fwcry
0.00	38.13	3.92	-42.53	1.25	0.03	42.53	-1.25	-0.03
20.00	41.85	4.64	-115.73	2.94	2.91	115.73	-2.94	-2.91
40.00	46.36	5.92	-246.77	3.97	11.48	246.77	-3.97	-11.48
60.00	51.29	8.40	-498.31	3.35	27.89	498.31	-3.35	-27.89
80.00	56.26	14.03	-1071.54	1.37	52.90	1071.54	-1.37	-52.90
100.00	60.64	20.00	-1679.50	2.15	48.72	1679.50	-2.15	-48.72
120.00	63.72	20.00	-1679.50	11.28	6.55	1679.50	-11.28	-6.55
140.00	64.98	20.00	-1679.50	26.97	-23.07	1679.50	-26.97	23.07
160.00	64.28	3.50	0.00	0.00	0.00	0.00	0.00	0.00
180.00	61.83	3.50	0.00	0.00	0.00	0.00	0.00	0.00
200.00	58.08	3.50	0.00	0.00	0.00	0.00	0.00	0.00
220.00	53.52	3.50	0.00	0.00	0.00	0.00	0.00	0.00
240.00	48.55	3.50	0.00	0.00	0.00	0.00	0.00	0.00
260.00	43.62	3.50	0.00	0.00	0.00	0.00	0.00	0.00
280.00	39.31	3.50	0.00	0.00	0.00	0.00	0.00	0.00
300.00	36.27	3.50	0.00	0.00	0.00	0.00	0.00	0.00
320.00	35.00	3.50	0.00	0.00	0.00	0.00	0.00	0.00
340.00	35.68	3.55	-5.20	0.13	-0.08	5.20	-0.13	0.08
360.00	38.13	3.92	-42.53	1.25	0.03	42.53	-1.25	-0.03

Table F.5: Forces Acting on Piston 5

$\theta_n =$	306							
θ	zp	Prs, Vlvd 2	Fpp (N)	Fpcrx	Fpcry	Fpcrz	Fwcrx	Fwcry
0.00	38.13	3.50	0.00	0.00	0.00	0.00	0.00	0.00
20.00	35.68	3.50	0.00	0.00	0.00	0.00	0.00	0.00
40.00	35.00	3.50	0.00	0.00	0.00	0.00	0.00	0.00
60.00	36.27	3.63	-13.63	-0.09	0.05	13.63	0.09	-0.05
80.00	39.31	4.12	-63.40	-0.08	1.84	63.40	0.08	-1.84
100.00	43.62	5.07	-160.06	-0.20	7.90	160.06	0.20	-7.90
120.00	48.55	6.82	-338.38	-2.28	18.94	338.38	2.28	-18.94
140.00	53.52	10.27	-689.17	-11.08	32.07	689.17	11.08	-32.07
160.00	58.08	18.36	-1512.77	-38.42	37.99	1512.77	38.42	-37.99
180.00	61.83	20.00	-1679.50	-49.38	1.31	1679.50	49.38	-1.31
200.00	64.28	20.00	-1679.50	-42.65	-25.06	1679.50	42.65	25.06
220.00	64.98	20.00	-1679.50	-26.97	-23.07	1679.50	26.97	23.07
240.00	63.72	3.50	0.00	0.00	0.00	0.00	0.00	0.00
260.00	60.64	3.50	0.00	0.00	0.00	0.00	0.00	0.00
280.00	56.26	3.50	0.00	0.00	0.00	0.00	0.00	0.00
300.00	51.29	3.50	0.00	0.00	0.00	0.00	0.00	0.00
320.00	46.36	3.50	0.00	0.00	0.00	0.00	0.00	0.00
340.00	41.85	3.50	0.00	0.00	0.00	0.00	0.00	0.00
360.00	38.13	3.50	0.00	0.00	0.00	0.00	0.00	0.00

F.2 Forces Acting on the Wobble Plate

Table F.6 Reaction Forces on Wobble Plate Due to Piston 1

SET 1													
$\theta_n =$	18												
θ	zp	Prs (Bar)	Fp (N)	Fwcrx	Fwcry	Fwcrz	Fwry	Fwrx	Fwrz	Fwbmy	Fwbmx	Fwbmz	Fwgrx
0.00	54.47	3.50	0.00	0.00	0.00	0.00	0.00	0.00	0.00	0.00	0.00	0.00	0.00
20.00	49.21	3.50	0.00	0.00	0.00	0.00	0.00	0.00	0.00	0.00	0.00	0.00	0.00
40.00	44.22	3.50	0.00	0.00	0.00	0.00	0.00	0.00	0.00	0.00	0.00	0.00	0.00
60.00	40.07	3.50	0.00	0.00	0.00	0.00	0.00	0.00	0.00	0.00	0.00	0.00	0.00
80.00	37.06	3.50	0.00	0.00	0.00	0.00	0.00	0.00	0.00	0.00	0.00	0.00	0.00
100.00	35.43	3.50	0.00	0.00	0.00	0.00	0.00	0.00	0.00	0.00	0.00	0.00	0.00
120.00	35.40	3.51	1.34	-0.01	0.04	-1.34	0.31	0.36	1.36	-0.35	-0.50	-0.01	0.16
140.00	37.16	3.76	26.92	-0.70	1.14	-26.92	3.89	9.70	30.13	-5.03	-10.82	-3.21	1.82
160.00	40.65	4.38	89.54	-3.68	2.73	-89.54	1.41	40.30	117.10	-4.13	-33.92	-27.56	-2.70
180.00	45.42	5.60	213.95	-10.19	-0.06	-213.95	-31.98	98.99	300.60	32.05	-54.05	-86.65	-34.75
200.00	50.65	7.97	454.89	-18.71	-15.63	-454.89	-128.96	168.73	608.35	144.59	-31.45	-153.46	-118.58
220.00	55.59	12.90	956.63	-24.89	-52.68	-956.63	-335.52	218.41	1149.02	388.20	83.99	-192.38	-277.51
240.00	59.78	20.00	1679.50	-18.28	-89.95	-1679.50	-611.56	137.17	1815.79	701.51	324.67	-136.29	-443.55
260.00	62.89	20.00	1679.50	-3.47	-52.74	-1679.50	-580.00	-86.12	1700.99	632.74	438.97	-21.49	-349.38
280.00	64.57	20.00	1679.50	-3.47	2.48	-1679.50	-516.86	-287.24	1700.05	514.37	527.66	-20.56	-236.95
300.00	64.55	3.50	0.00	0.00	0.00	0.00	0.00	0.00	0.00	0.00	0.00	0.00	0.00
320.00	62.72	3.50	0.00	0.00	0.00	0.00	0.00	0.00	0.00	0.00	0.00	0.00	0.00
340.00	59.22	3.50	0.00	0.00	0.00	0.00	0.00	0.00	0.00	0.00	0.00	0.00	0.00
360.00	54.47	3.50	0.00	0.00	0.00	0.00	0.00	0.00	0.00	0.00	0.00	0.00	0.00

Table F.7 Reaction Forces on Wobble Plate Due to Piston 2

SET 2													
$\theta_n =$	90												
θ	z _p	Prs	F _{piston} (N)	F _{wcrx}	F _{wcry}	F _{wcrz}	F _{wry}	F _{wrx}	F _{wrz}	F _{wbmy}	F _{wbmx}	F _{wbmz}	F _{wgrx}
0.00	64.65	3.50	0.00	0.00	0.00	0.00	0.00	0.00	0.00	0.00	0.00	0.00	0.00
20.00	63.85	3.50	0.00	0.00	0.00	0.00	0.00	0.00	0.00	0.00	0.00	0.00	0.00
40.00	61.47	3.50	0.00	0.00	0.00	0.00	0.00	0.00	0.00	0.00	0.00	0.00	0.00
60.00	57.60	3.50	0.00	0.00	0.00	0.00	0.00	0.00	0.00	0.00	0.00	0.00	0.00
80.00	52.63	3.50	0.00	0.00	0.00	0.00	0.00	0.00	0.00	0.00	0.00	0.00	0.00
100.00	47.26	3.50	0.00	0.00	0.00	0.00	0.00	0.00	0.00	0.00	0.00	0.00	0.00
120.00	42.33	3.50	0.00	0.00	0.00	0.00	0.00	0.00	0.00	0.00	0.00	0.00	0.00
140.00	38.51	3.50	0.00	0.00	0.00	0.00	0.00	0.00	0.00	0.00	0.00	0.00	0.00
160.00	36.15	3.50	0.00	0.00	0.00	0.00	0.00	0.00	0.00	0.00	0.00	0.00	0.00
180.00	35.35	3.50	0.00	0.00	0.00	0.00	0.00	0.00	0.00	0.00	0.00	0.00	0.00
200.00	36.15	3.62	11.80	0.00	-0.07	-11.80	-5.78	2.21	17.87	5.86	-0.89	-6.07	-1.32
220.00	38.51	3.98	49.11	0.00	-0.99	-49.11	-18.94	16.44	71.82	19.94	-6.47	-22.71	-9.97
240.00	42.33	4.75	127.01	0.00	-4.70	-127.01	-30.69	53.94	178.27	35.39	-20.59	-51.26	-33.35
260.00	47.26	6.26	281.32	0.00	-13.63	-281.32	-22.91	130.17	383.20	36.54	-48.65	-101.89	-81.52
280.00	52.63	9.43	603.87	0.00	-29.26	-603.87	48.90	277.82	817.83	-19.64	-103.84	-213.96	-173.98
300.00	57.60	16.99	1372.82	0.00	-50.76	-1372.82	327.55	575.67	1902.52	-276.78	-219.76	-529.70	-355.92
320.00	61.47	20.00	1679.50	0.00	-33.99	-1679.50	640.94	556.21	2429.93	-606.95	-218.81	-750.43	-337.40
340.00	63.85	20.00	1679.50	0.00	-10.57	-1679.50	819.79	313.61	2533.63	-809.22	-126.42	-854.13	-187.19
360.00	64.65	20.00	1679.50	0.00	-1.62	-1679.50	887.64	0.00	2577.88	-886.01	0.00	-898.39	0.00

Table F.8 Reaction Forces on Wobble Plate Due to Piston 3

SET 3

$\theta_n =$	162												
θ	z _p	Prs, Vlvd 2	F _{piston} (N)	F _{wcrx}	F _{wcry}	F _{wcrz}	F _{wry}	F _{wrx}	F _{wrz}	F _{wbmy}	F _{wbmx}	F _{wbmz}	F _{wgrx}
0.00	54.47	11.34	797.74	37.98	-0.24	-797.74	119.23	-369.04	1120.59	-119.00	343.78	-322.85	-12.73
20.00	59.22	20.00	1679.50	69.07	51.16	-1679.50	-27.71	-793.66	2306.20	-23.45	635.84	-626.71	88.76
40.00	62.72	20.00	1679.50	43.68	71.40	-1679.50	-267.59	-667.80	2074.55	196.20	431.25	-395.06	192.87
60.00	64.55	20.00	1679.50	18.26	51.49	-1679.50	-421.78	-480.71	1830.66	370.30	187.62	-151.16	274.83
80.00	64.57	3.50	0.00	0.00	0.00	0.00	0.00	0.00	0.00	0.00	0.00	0.00	0.00
100.00	62.89	3.50	0.00	0.00	0.00	0.00	0.00	0.00	0.00	0.00	0.00	0.00	0.00
120.00	59.78	3.50	0.00	0.00	0.00	0.00	0.00	0.00	0.00	0.00	0.00	0.00	0.00
140.00	55.59	3.50	0.00	0.00	0.00	0.00	0.00	0.00	0.00	0.00	0.00	0.00	0.00
160.00	50.65	3.50	0.00	0.00	0.00	0.00	0.00	0.00	0.00	0.00	0.00	0.00	0.00
180.00	45.42	3.50	0.00	0.00	0.00	0.00	0.00	0.00	0.00	0.00	0.00	0.00	0.00
200.00	40.65	3.50	0.00	0.00	0.00	0.00	0.00	0.00	0.00	0.00	0.00	0.00	0.00
220.00	37.16	3.50	0.00	0.00	0.00	0.00	0.00	0.00	0.00	0.00	0.00	0.00	0.00
240.00	35.40	3.50	0.00	0.00	0.00	0.00	0.00	0.00	0.00	0.00	0.00	0.00	0.00
260.00	35.43	3.52	1.75	0.00	0.00	-1.75	0.54	0.30	1.76	-0.54	0.06	-0.02	-0.36
280.00	37.06	3.75	25.47	0.05	-0.80	-25.47	9.30	1.38	27.26	-8.50	3.50	-1.79	-4.94
300.00	40.07	4.26	77.80	0.85	-4.17	-77.80	30.29	-6.79	89.93	-26.12	18.78	-12.13	-12.83
320.00	44.22	5.24	176.98	4.61	-9.75	-176.98	64.57	-42.03	221.12	-54.82	59.38	-44.14	-21.96
340.00	49.21	7.15	371.34	15.27	-12.76	-371.34	105.63	-138.20	498.27	-92.87	150.92	-126.93	-27.99
360.00	54.47	11.34	797.74	37.98	-0.24	-797.74	119.23	-369.04	1120.59	-119.00	343.78	-322.85	-12.73

Table F.9 Reaction Forces on Wobble Plate Due to Piston 4

SET 4

$\theta_n =$	234												
θ	zp	Prs, Vlvd 2	Fpiston (N)	Fwcrx	Fwcry	Fwcrz	Fwry	Fwrx	Fwrz	Fwbmy	Fwbmx	Fwbmz	Fwgrx
0.00	38.13	3.92	42.53	1.25	0.03	-42.53	1.71	-16.20	58.17	-1.74	22.56	-15.63	-7.61
20.00	41.85	4.64	115.73	2.94	2.91	-115.73	5.67	-30.58	158.82	-8.58	44.37	-43.09	-16.73
40.00	46.36	5.92	246.77	3.97	11.48	-246.77	16.60	-28.08	337.11	-28.08	47.29	-90.34	-23.18
60.00	51.29	8.40	498.31	3.35	27.89	-498.31	37.87	24.17	671.61	-65.76	-15.72	-173.30	-11.81
80.00	56.26	14.03	1071.54	1.37	52.90	-1071.54	70.42	215.22	1425.85	-123.32	-278.53	-354.31	61.93
100.00	60.64	20.00	1679.50	2.15	48.72	-1679.50	64.87	553.35	2234.07	-113.59	-787.71	-554.57	232.21
120.00	63.72	20.00	1679.50	11.28	6.55	-1679.50	17.57	711.69	2262.51	-24.12	-1064.09	-583.01	341.11
140.00	64.98	20.00	1679.50	26.97	-23.07	-1679.50	47.87	778.21	2265.59	-24.80	-1181.91	-586.10	376.74
160.00	64.28	3.50	0.00	0.00	0.00	0.00	0.00	0.00	0.00	0.00	0.00	0.00	0.00
180.00	61.83	3.50	0.00	0.00	0.00	0.00	0.00	0.00	0.00	0.00	0.00	0.00	0.00
200.00	58.08	3.50	0.00	0.00	0.00	0.00	0.00	0.00	0.00	0.00	0.00	0.00	0.00
220.00	53.52	3.50	0.00	0.00	0.00	0.00	0.00	0.00	0.00	0.00	0.00	0.00	0.00
240.00	48.55	3.50	0.00	0.00	0.00	0.00	0.00	0.00	0.00	0.00	0.00	0.00	0.00
260.00	43.62	3.50	0.00	0.00	0.00	0.00	0.00	0.00	0.00	0.00	0.00	0.00	0.00
280.00	39.31	3.50	0.00	0.00	0.00	0.00	0.00	0.00	0.00	0.00	0.00	0.00	0.00
300.00	36.27	3.50	0.00	0.00	0.00	0.00	0.00	0.00	0.00	0.00	0.00	0.00	0.00
320.00	35.00	3.50	0.00	0.00	0.00	0.00	0.00	0.00	0.00	0.00	0.00	0.00	0.00
340.00	35.68	3.55	5.20	0.13	-0.08	-5.20	0.21	-2.35	7.09	-0.13	3.27	-1.88	-1.05
360.00	38.13	3.92	42.53	1.25	0.03	-42.53	1.71	-16.20	58.17	-1.74	22.56	-15.63	-7.61

Table F.10 Reaction Forces on Wobble Plate Due to Piston 5

SET 5

$\theta_n =$	306												
θ	zp	Prs, Vld 2	Fpiston (N)	Fwcrx	Fwcry	Fwcrz	Fwry	Fwrx	Fwrz	Fwbmy	Fwbmx	Fwbmz	Fwgrx
0.00	38.13	3.50	0.00	0.00	0.00	0.00	0.00	0.00	0.00	0.00	0.00	0.00	0.00
20.00	35.68	3.50	0.00	0.00	0.00	0.00	0.00	0.00	0.00	0.00	0.00	0.00	0.00
40.00	35.00	3.50	0.00	0.00	0.00	0.00	0.00	0.00	0.00	0.00	0.00	0.00	0.00
60.00	36.27	3.63	13.63	-0.09	0.05	-13.63	0.67	-6.42	18.74	-0.73	9.40	-5.11	-2.89
80.00	39.31	4.12	63.40	-0.08	1.84	-63.40	13.68	-28.36	90.62	-15.52	37.02	-27.22	-8.58
100.00	43.62	5.07	160.06	-0.20	7.90	-160.06	56.51	-56.22	228.15	-64.41	61.98	-68.09	-5.56
120.00	48.55	6.82	338.38	-2.28	18.94	-338.38	146.05	-68.17	464.29	-164.99	46.77	-125.91	23.67
140.00	53.52	10.27	689.17	-11.08	32.07	-689.17	308.59	-22.82	898.40	-340.66	-73.29	-209.23	107.18
160.00	58.08	18.36	1512.77	-38.42	37.99	-1512.77	626.55	189.25	1892.96	-664.54	-467.12	-380.19	316.30
180.00	61.83	20.00	1679.50	-49.38	1.31	-1679.50	577.61	435.64	2073.50	-578.92	-776.89	-394.01	390.64
200.00	64.28	20.00	1679.50	-42.65	-25.06	-1679.50	407.11	614.65	2114.36	-382.05	-969.75	-434.87	397.75
220.00	64.98	20.00	1679.50	-26.97	-23.07	-1679.50	183.69	739.30	2205.17	-160.62	-1097.29	-525.67	384.96
240.00	63.72	3.50	0.00	0.00	0.00	0.00	0.00	0.00	0.00	0.00	0.00	0.00	0.00
260.00	60.64	3.50	0.00	0.00	0.00	0.00	0.00	0.00	0.00	0.00	0.00	0.00	0.00
280.00	56.26	3.50	0.00	0.00	0.00	0.00	0.00	0.00	0.00	0.00	0.00	0.00	0.00
300.00	51.29	3.50	0.00	0.00	0.00	0.00	0.00	0.00	0.00	0.00	0.00	0.00	0.00
320.00	46.36	3.50	0.00	0.00	0.00	0.00	0.00	0.00	0.00	0.00	0.00	0.00	0.00
340.00	41.85	3.50	0.00	0.00	0.00	0.00	0.00	0.00	0.00	0.00	0.00	0.00	0.00
360.00	38.13	3.50	0.00	0.00	0.00	0.00	0.00	0.00	0.00	0.00	0.00	0.00	0.00

F.3 Forces Acting on the Ball Mounts

Table F.11: Forces Acting on Ball Mounts

θ	$\Sigma bmwz$	$\Sigma bmwy$	$\Sigma bmwx$	Magnitud	$\Sigma bmc bz$	$\Sigma bmc by$	$\Sigma bmc bx$
0.00	338.49	120.74	-366.35	513.19	-338.49	-120.74	366.35
20.00	669.79	32.03	-680.21	955.16	-669.79	-32.03	680.21
40.00	485.40	-168.12	-478.54	702.05	-485.40	168.12	478.54
60.00	329.58	-303.81	-181.31	483.52	-329.58	303.81	181.31
80.00	381.53	138.83	241.50	472.40	-381.53	-138.83	-241.50
100.00	622.66	178.00	725.73	972.66	-622.66	-178.00	-725.73
120.00	708.94	189.47	1017.81	1254.76	-708.94	-189.47	-1017.81
140.00	798.53	370.49	1266.01	1541.98	-798.53	-370.49	-1266.01
160.00	407.76	668.67	501.04	929.75	-407.76	-668.67	-501.04
180.00	480.66	546.87	830.95	1104.80	-480.66	-546.87	-830.95
200.00	588.33	237.46	1001.20	1185.29	-588.33	-237.46	-1001.20
220.00	718.06	-227.58	1013.31	1262.61	-718.06	227.58	-1013.31
240.00	136.29	-701.51	-324.67	784.92	-136.29	701.51	324.67
260.00	21.51	-632.20	-439.03	769.99	-21.51	632.20	439.03
280.00	22.35	-505.88	-531.16	733.86	-22.35	505.88	531.16
300.00	12.13	26.12	-18.78	34.38	-12.13	-26.12	18.78
320.00	44.14	54.82	-59.38	92.09	-44.14	-54.82	59.38
340.00	128.82	93.00	-154.19	221.40	-128.82	-93.00	154.19
360.00	338.49	120.74	-366.35	513.19	-338.49	-120.74	366.35

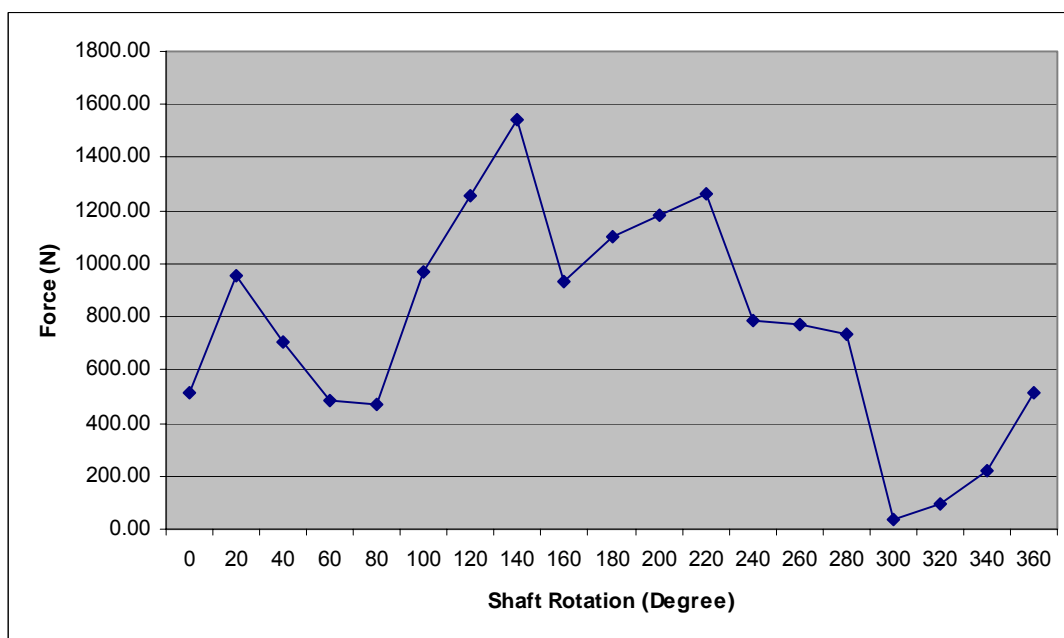


Figure F.1: Force Magnitude Acting on the Ball Mount

F.4 Forces Acting on Guide Rod

Table F.12: Forces Acting on the Guide Rod

θ	ΣF_{gwx}	Z_w	$\Sigma F_{gcbfx/rx}$
0.00	20.34	-17.26	-20.34
20.00	-72.03	-16.32	72.03
40.00	-169.69	-13.52	169.69
60.00	-260.13	-8.99	260.13
80.00	-53.35	-3.16	53.35
100.00	-226.65	3.16	226.65
120.00	-364.93	8.99	364.93
140.00	-485.74	13.52	485.74
160.00	-313.60	16.32	313.60
180.00	-355.88	17.26	355.88
200.00	-277.85	16.32	277.85
220.00	-97.49	13.52	97.49
240.00	476.90	8.99	-476.90
260.00	431.26	3.16	-431.26
280.00	415.87	-3.16	-415.87
300.00	368.75	-8.99	-368.75
320.00	359.36	-13.52	-359.36
340.00	216.23	-16.32	-216.23
360.00	20.34	-17.26	-20.34

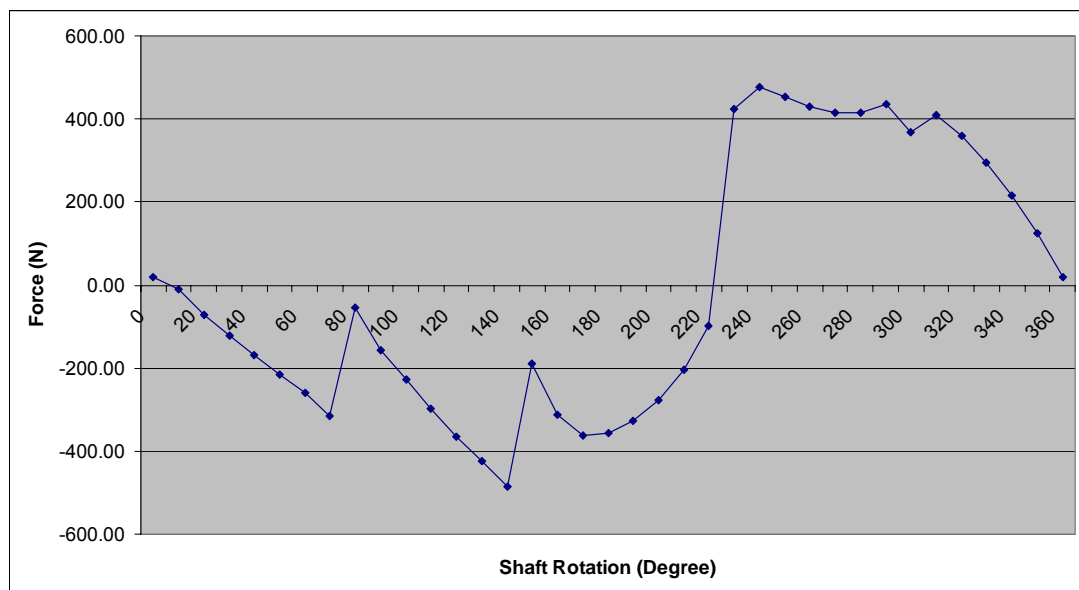


Figure F.2: Total Force F_{gwx} acting on the Guide Rod

F.5 Forces Acting on Rotor

Table F.13: Forces Reaction on Center of Rotor

θ	Σr_{sx}	Σr_{sy}	Magnitud
0.00	385.24	-120.95	403.78
20.00	824.24	22.04	824.54
40.00	695.88	251.00	739.76
60.00	462.96	383.24	601.01
80.00	-186.86	-84.09	204.91
100.00	-497.13	-121.38	511.74
120.00	-643.88	-163.93	664.42
140.00	-765.09	-360.35	845.70
160.00	-229.55	-627.96	668.60
180.00	-534.63	-545.62	763.89
200.00	-785.60	-272.37	831.47
220.00	-974.15	170.77	989.00
240.00	-191.11	642.25	670.08
260.00	-44.35	602.37	604.00
280.00	8.04	458.66	458.73
300.00	-568.88	-357.83	672.06
320.00	-514.18	-705.51	873.00
340.00	-173.06	-925.62	941.66
360.00	385.24	-1008.58	1079.65

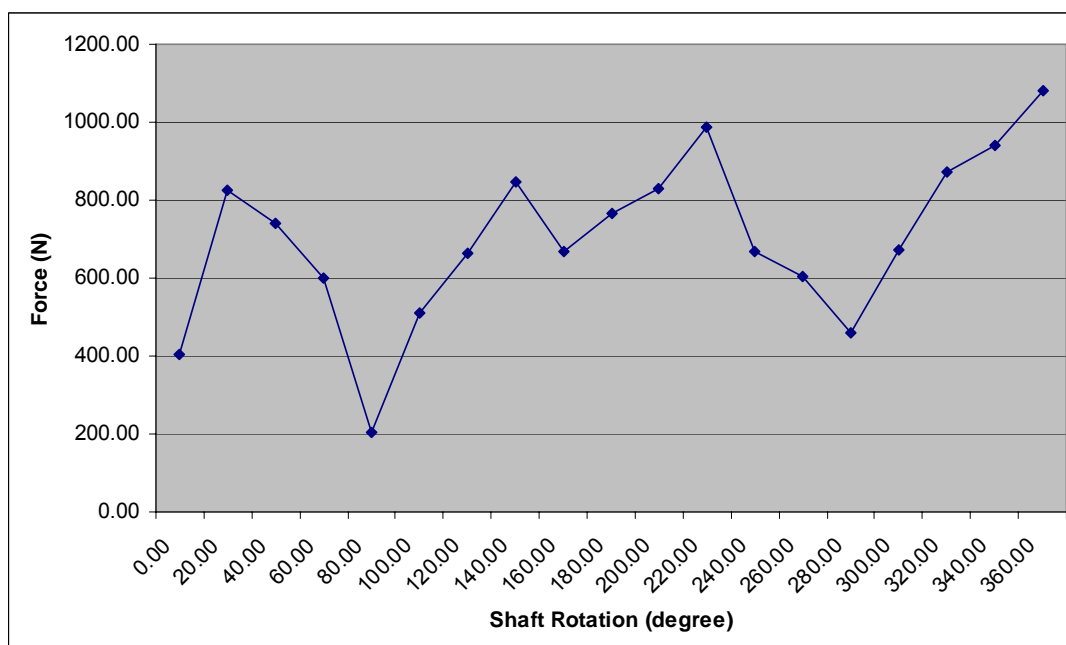


Figure F.3: Magnitude Force Reaction on Center of Rotor

F.6 Moments Acting on Center of Rotor (Tight Fit Assembly)

Table F.14: Total Moments Exerted on Center of Rotor

θ	Moment (Nm)					Moment
	Piston 1	Piston 2	Piston 3	Piston 4	Piston 5	
0.00	0.00	0.00	-14.71	0.76	0.00	-13.95
20.00	0.00	0.00	-11.88	1.39	0.00	-10.49
40.00	0.00	0.00	5.63	0.89	0.00	6.52
60.00	0.00	0.00	17.29	-2.74	0.35	14.90
80.00	0.00	0.00	0.00	-14.33	2.01	-12.32
100.00	0.00	0.00	0.00	-31.70	5.15	-26.55
120.00	0.03	0.00	0.00	-37.02	9.21	-27.79
140.00	0.40	0.00	0.00	-40.58	13.00	-27.18
160.00	0.78	0.00	0.00	0.00	14.34	15.12
180.00	-0.10	0.00	0.00	0.00	0.42	0.32
200.00	-4.39	0.14	0.00	0.00	-14.76	-19.01
220.00	-15.56	1.06	0.00	0.00	-29.81	-44.32
240.00	-33.82	3.54	0.00	0.00	0.00	-30.28
260.00	-36.60	8.64	-0.03	0.00	0.00	-27.99
280.00	-36.49	18.44	-0.53	0.00	0.00	-18.58
300.00	0.00	37.73	-1.99	0.00	0.00	35.73
320.00	0.00	35.76	-4.97	0.00	0.00	30.80
340.00	0.00	19.84	-9.66	0.11	0.00	10.29
360.00	0.00	0.00	-14.71	0.76	0.00	-13.95

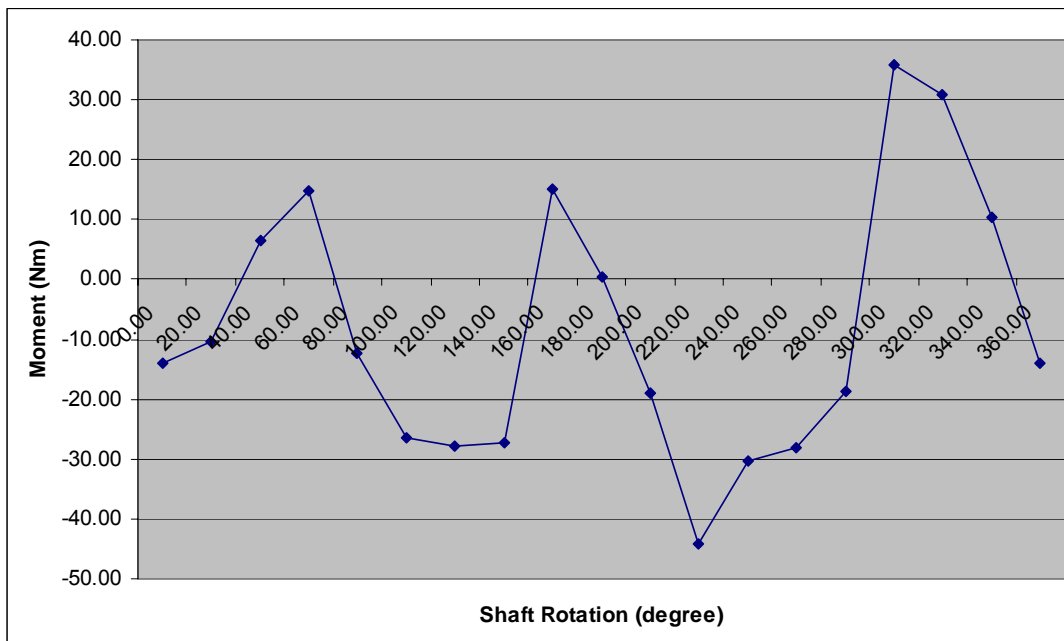


Figure F.4: Total Moment Acting at the Center of Rotor

F.7 Forces Acting on the Shaft

Table F.15: Forces Acting on the Shaft

θ	Σs_{rx}	Σs_{ry}	$\Sigma s_{bfx}/s_{brx}$	$\Sigma s_{bfy}/s_{bry}$
0.00	-385.24	120.95	-192.62	60.47
20.00	-824.24	-22.04	-412.12	-11.02
40.00	-695.88	-251.00	-347.94	-125.50
60.00	-462.96	-383.24	-231.48	-191.62
80.00	186.86	84.09	93.43	42.05
100.00	497.13	121.38	248.57	60.69
120.00	643.88	163.93	321.94	81.97
140.00	765.09	360.35	382.54	180.17
160.00	229.55	627.96	114.77	313.98
180.00	534.63	545.62	267.31	272.81
200.00	785.60	272.37	392.80	136.18
220.00	974.15	-170.77	487.07	-85.39
240.00	191.11	-642.25	95.55	-321.13
260.00	44.35	-602.37	22.18	-301.19
280.00	-8.04	-458.66	-4.02	-229.33
300.00	568.88	357.83	284.44	178.92
320.00	514.18	705.51	257.09	352.76
340.00	173.06	925.62	86.53	462.81
360.00	-385.24	1008.58	-192.62	504.29

Appendix G

Third Prototype BOM Data of New Symmetrical Wobble Plate Compressor

Table G.1 BOM Data

BILL OF MATERIAL PAGE: 01/02 Product : Symmetrical Wobble Plate Compressor Model : 3P410P-310 Lubricant : ZXL 100 PG						
PART NO.	ITEM	FUNCTIONS	QTY	MATERIAL	DIMENSION (mm)	REMARKS
HOUSING						
3P410P-310-01	Center/rotor housing (casting)	- Crank mechanism enclosure	1	LM-25		
3P410P-310-02	Front end plate (casting)	- Valve Enclosure	1	LM-25		
3P410P-310-03	Rear end plate (casting)	- Valve Enclosure	1	LM-25		
3P410P-310-04	Front cylinder block (casting)	- Piston Enclosure	1	LM-25		
3P410P-310-05	Rear cylinder block (casting)	- Piston Enclosure	1	LM-25		
3P410P-310-08	Cylinder lining	- Increase durability due to frictions	10	G 2500a		
VALVE PARTS						
3P410P-310-09	Front valveplate	- Valve mechanism seats	1	MILD STEEL		
3P410P-310-10	Rear valveplate	- Valve mechanism seats	1	MILD STEEL		
3P410P-310-11	Discharge valve #1	- Discharge gas valve	4	ASTM a154		
3P410P-310-12	Discharge valve #2	- Discharge gas valve	2	ASTM a154		
3P410P-310-13	Valve retainer #1	- Valve height limiter	4	MILD STEEL		
3P410P-310-14	Valve retainer #2	- Valve height limiter	2	MILD STEEL		
3P410P-310-15	Front suction valve	- Suction gas valve	1	ASTM a154		
3P410P-310-16	Rear suction valve	- Suction gas valve	2	ASTM a155		

Table G.2 BOM Data

BILL OF MATERIAL						PAGE: 01/02
Product		: Symmetrical Wobble Plate Compressor				
Model		:3P410P-310	Lubricant	:ZXL 100 PG		
PART NO.	ITEM	FUNCTIONS	QTY	MATERIAL	DIMENSION (mm)	REMARKS
WOBBLE PLATE						
3P410P-310-24	Front supporting ball	- Hold wobble plate in place	1	AISI 4140		
3P410P-310-25	Rear supporting ball with spring	- Hold wobble plate in place	1	AISI 4140		
3P410P-310-26	Wobble plate	- Convert rotating motion	2	AL 5454 H32		
3P410P-310-27	Supporting ball mount	- Protect wobble plate inner surface	2	AISI 4140		
3P410P-310-28	Wobble plate thrust washer	- Protect wobble plate surface	2	SKF-AS 5578 (55x78x1)		
3P410P-310-29	Guide rod ball holder	- Anti rotating ball adaptor	2	AISI 4140		
3P410P-310-30	connecting rod	- Transfer reciprocating motion to piston	10	AISI 4141		
3P410P-310-31	Piston	- Compress gas	10	Al 2024-T3		
3P410P-310-35	Guide rod	- Guide the guide ball in in one direction only	1	AISI 4140		
3P410P-310-36	Guide ball	- Linkage between guide and wobble plate	2	AISI 4141		
OIL PUMP COMPONENTS						
3P410P-310-37	Reversing ring	- Oil pump compnents	1	AISI 4142		
3P410P-310-38	Outer rotor oil pump	- Oil pump compnents	1	AISI 4143		
3P410P-310-39	Inner rotor oil pump	- Oil pump compnents	1	AISI 4144		
DRIVE PARTS						
3P410P-310-20	Rotor shaft	- deliver rotating motion to rotor	1	AISI 4140		
3P410P-310-21	Rotor	- to drive the wobble in nutating motion	1	AL 5454 H32		
3P410P-310-22	Rotor thrust washer	- protect the rotor surface	2			Standart with thrust bearing

Table G.3 BOM Data

BILL OF MATERIAL						PAGE: 01/02
Product		: Symmetrical Wobble Plate Compressor				
Model		:3P410P-310		Lubricant	:ZXL 100 PG	
PART NO.	ITEM	FUNCTIONS	QTY	MATERIAL	DIMENSION (mm)	REMARKS
STANDART PART						
	Retaining spring	- Acting as a damper	1	CARBON STEEL		Standart part
	Heavy hex flange screw				M12x1.75x80	Standart part
	Hex flange screw				M8x1.25x45	Standart part
	Hex flange screw				M8x1.25x40	Standart part
	Needle Roller Bearing		2		20x28x20	NK 20/20 (SKF)
	Shaft seal - 20x30x7		1		20x30x7	Standart part
	Needle roller thrust bearing		2		55x78x3	AXK5578 (SKF)
	Cylinder block gasket		2			TOMBO 1304
	Dowel pin		6		Ø 5	Standart part
	Rotor thrust washer		2			SKF-AS 5578 (55x78x1)
	Needle roller thrust bearing		2			SKF-AXK 5578 (55x78x3)
	Piston ring (top)		10			ER-39-850-36-214
	Guide Strip (bottom)		10			ER-39-214-4.0-2.5
	Dowel pin		1		Ø 2	Standart part
	Valve rivet		6		Ø4	Standart part
	Valve plate gasket		2			TOMBO 1304



(a) (b)
Figure G.1 New Symmetrical Compressor
a) Front View b) Rear View



(a) (b)
Figure G.2 Front End Plate
a) Front View b) Rear View



(a) (b)
Figure G.3 Rear End Plate
a) Front View b) Rear View



(a)

(b)

Figure G.3 Cylinder Block

a) Front View b) Rear View with Attached Wobble Plate

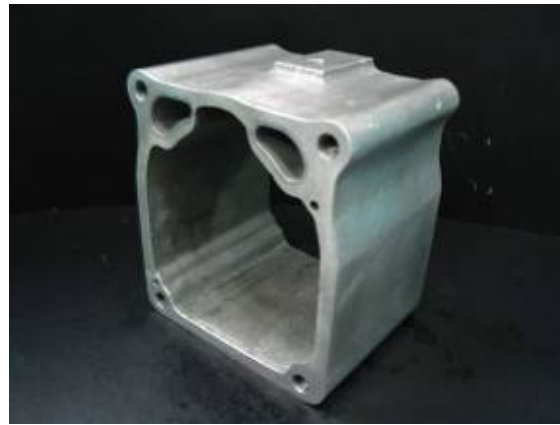


Figure G.4 Crankcase



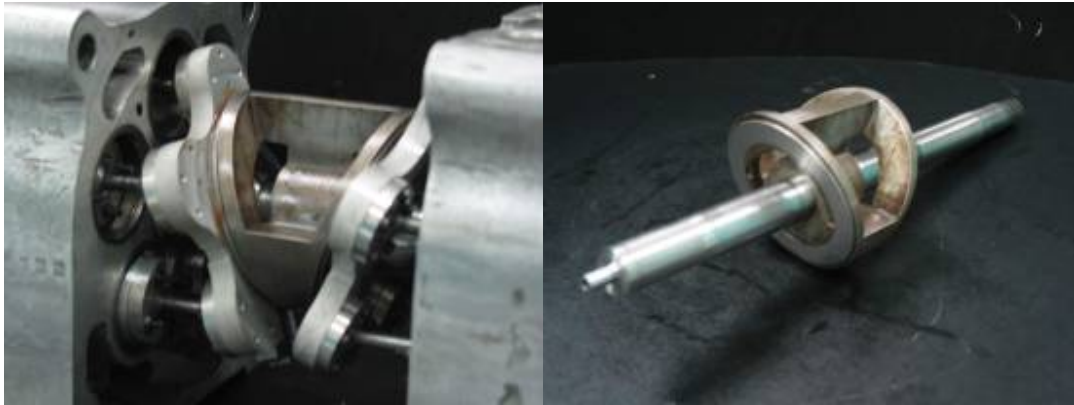
(a)

(b)

Figure G.5 Valve Plates

a) Suction Valve Plate

b) Discharge Valve Plate with Retainer



(a)

(b)

Figure G.6 Crank Mechanism

a) Wobble Plate Assembly b) Shaft Assembly

H.1 Test Rig and Equipment Data



Figure H.1 Test Rig Setup



Figure H.2 Charging Equipment



Figure H.3 Refco Pressure Gauges

Table H.1 Pressure Gauge Specification

	Low Pressure Gauge	High Pressure Gauge
Min. Pressure (Bar)	-1	9
Max Pressure (Bar)	-1	30



Figure H.4 Flow Meter

Table H.2 Flow Meter Specification

Model	MT3809
Medium	Liquid
Min Flowrate	19 g/s
Max Flowrate	190 g/s



Figure H.5 Control Panel with ABB Inverter Attached



Figure H.6 Thermocouple Scanner

Table H.4 Thermocouple Scanner Specification

Brand	Cole Palmer
Model	92000-05 Benchtop 230V
Input	12 Probes (Multiple Type)
Output	Printer, PC



Figure H.7 FEIMA Electric Motor

Table H.5 Electric Motor Specification

Rated Output	11 Kw
Rated Speed	2940 rpm (2 pole)
Efficiency	89.5%
Power Factor (Cos ϕ)	0.88
Rated Torque	36 Nm

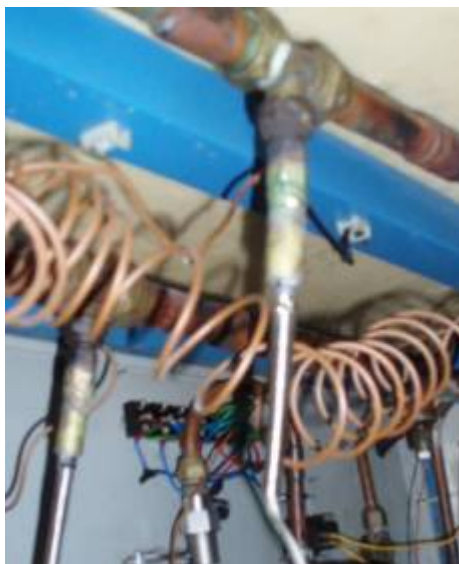


Figure H.8 Thermocouple Type-k with Probe



Figure H.9 Tachometer



Figure H.10 Attached Capillary Tube for Pressure Measurement



Figure H.11 Velocity Meter



Figure H.12 Air Temperature Sensor



Figure H.13 Inlet Air Mixture



Figure H.14 Evaporator Auxiliary Exhaust Fan

H.2 Equipment Calibration Data and Calculation

H.2.1 Flow Meter Calibration Data

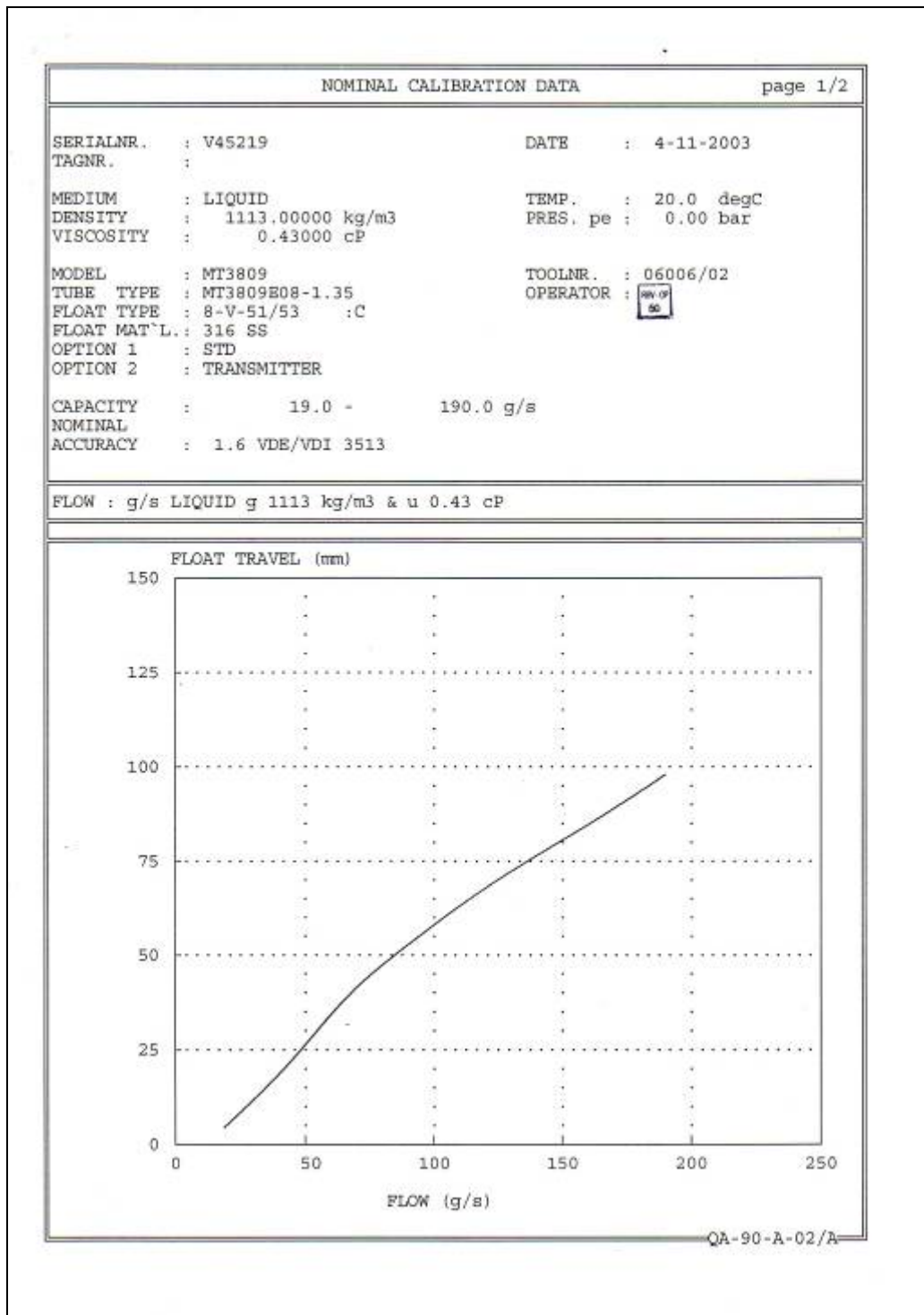


Figure H.15 Specification Data

NOMINAL CALIBRATION DATA								page 2/2
SERIALNR. : V45219				TAG NR. :				
FLOAT TRAVEL mm	FLOW g/s	FLOAT TRAVEL mm	FLOW g/s	FLOAT TRAVEL mm	FLOW g/s	FLOAT TRAVEL mm	FLOW g/s	
		26.0	50.1	51.0	87.3	76.0	139.7	
		27.0	51.3	52.0	89.2	77.0	142.1	
		28.0	52.6	53.0	91.1	78.0	144.5	
		29.0	53.8	54.0	93.0	79.0	147.0	
5.0	20.1	30.0	55.0	55.0	94.9	80.0	149.4	
6.0	21.6	31.0	56.3	56.0	96.8	81.0	151.9	
7.0	23.2	32.0	57.5	57.0	98.7	82.0	154.3	
8.0	24.7	33.0	58.8	58.0	100.7	83.0	156.7	
9.0	26.2	34.0	60.1	59.0	102.6	84.0	159.1	
10.0	27.8	35.0	61.4	60.0	104.6	85.0	161.5	
11.0	29.3	36.0	62.7	61.0	106.6	86.0	163.9	
12.0	30.8	37.0	64.1	62.0	108.6	87.0	166.2	
13.0	32.3	38.0	65.5	63.0	110.6	88.0	168.5	
14.0	33.8	39.0	66.9	64.0	112.7	89.0	170.8	
15.0	35.2	40.0	68.4	65.0	114.7	90.0	173.1	
16.0	36.7	41.0	69.9	66.0	116.8	91.0	175.4	
17.0	38.1	42.0	71.5	67.0	119.0	92.0	177.6	
18.0	39.5	43.0	73.1	68.0	121.1	93.0	179.9	
19.0	40.9	44.0	74.8	69.0	123.3	94.0	182.1	
20.0	42.3	45.0	76.5	70.0	125.6	95.0	184.3	
21.0	43.6	46.0	78.2	71.0	127.9	96.0	186.5	
22.0	44.9	47.0	80.0	72.0	130.2	97.0	188.7	
23.0	46.3	48.0	81.7	73.0	132.5	98.0	190.9	
24.0	47.6	49.0	83.6	74.0	134.9			
25.0	48.8	50.0	85.4	75.0	137.3			

FLOW g/s	FLOAT TRAVEL mm	FLOW g/s	FLOAT TRAVEL mm	FLOW g/s	FLOAT TRAVEL mm	FLOW g/s	FLOAT TRAVEL mm
		52.0	27.48	102.0	58.59	152.0	81.08
		54.0	29.07	104.0	59.60	154.0	81.90
		56.0	30.65	106.0	60.60	156.0	82.72
		58.0	32.23	108.0	61.60	158.0	83.54
		60.0	33.80	110.0	62.59	160.0	84.37
		62.0	35.34	112.0	63.58	162.0	85.21
		64.0	36.85	114.0	64.56	164.0	86.05
		66.0	38.32	116.0	65.52	166.0	86.91
		68.0	39.74	118.0	66.48	168.0	87.77
20.0	4.95	70.0	41.11	120.0	67.43	170.0	88.63
22.0	6.24	72.0	42.42	122.0	68.36	172.0	89.51
24.0	7.54	74.0	43.69	124.0	69.28	174.0	90.39
26.0	8.83	76.0	44.90	126.0	70.19	176.0	91.27
28.0	10.14	78.0	46.08	128.0	71.08	178.0	92.16
30.0	11.46	80.0	47.22	130.0	71.96	180.0	93.05
32.0	12.80	82.0	48.33	132.0	72.82	182.0	93.95
34.0	14.15	84.0	49.41	134.0	73.68	184.0	94.85
36.0	15.53	86.0	50.47	136.0	74.52	186.0	95.76
38.0	16.94	88.0	51.50	138.0	75.36	188.0	96.66
40.0	18.37	90.0	52.53	140.0	76.19	190.0	97.57
42.0	19.83	92.0	53.54	142.0	77.01		
44.0	21.31	94.0	54.56	144.0	77.83		
46.0	22.82	96.0	55.56	146.0	78.64		
48.0	24.35	98.0	56.58	148.0	79.46		
50.0	25.91	100.0	57.59	150.0	80.27		

QA-90-A-02/B

Figure H.16 Calibration Data

H.2.2 Pulley Ratio Calculation

Theoretically at 2000 rpm, the compressor would require;

$$P = \frac{n}{n-1} p_1 \dot{V} \left[\left(\frac{p_2}{p_1} \right)^{\frac{n-1}{n}} - 1 \right]$$

$$= \frac{1.14}{1.14-1} \times 3 \times 10^5 \times 0.0103 \left[\left(\frac{18}{3} \right)^{\frac{1.14-1}{1.14}} - 1 \right]$$

$$= 6192.92 \text{ watt}$$

Assuming compressor efficiency at 70%

$$P_{act} = 6192.92 \times \frac{100}{70}$$

$$= 8847.03 \text{ watt}$$

$$P = T\omega$$

$$T = \frac{P \times 60}{2\pi N}$$

$$= \frac{8847.03 \times 60}{2 \times \pi \times 2000}$$

$$= 42.24 \text{ N/m}$$

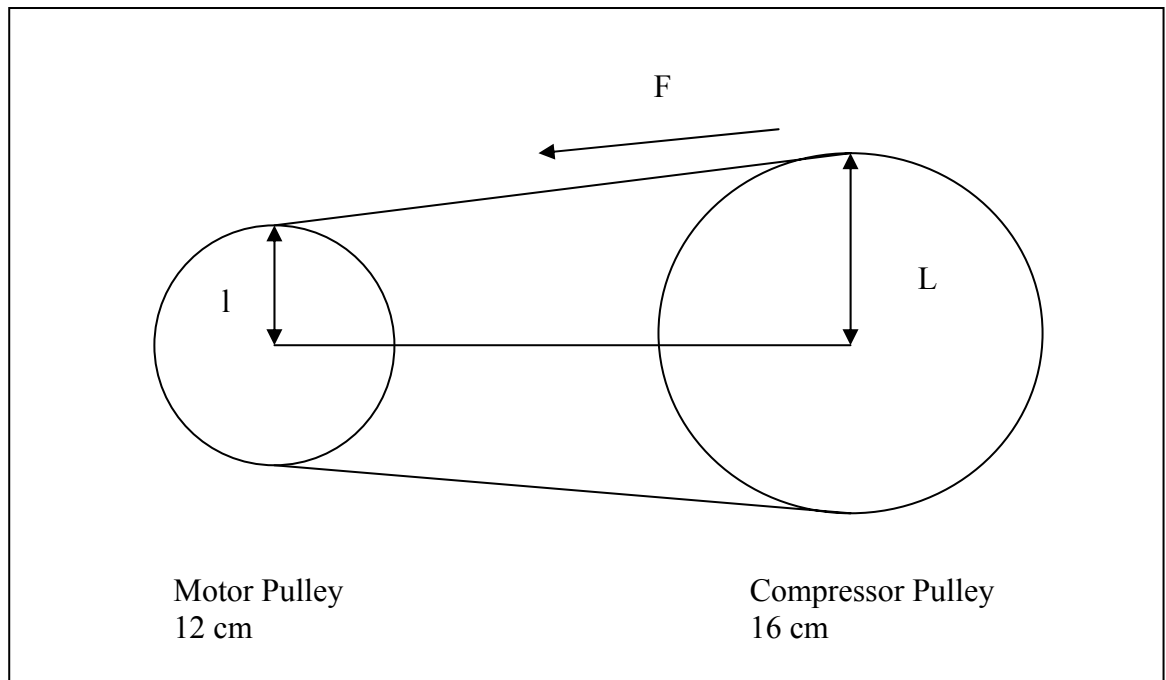


Figure H.17 Pulley Size and Arrangement

Since the maximum torque the motor can provide is 34 N/m at 3000 rpm. A step-down pulley is required to increase the torque provided. Using dimension provided in diagram.

$$T_m = Fl$$

$$F_m = \frac{T}{l}$$

$$= \frac{34}{0.12}$$

$$= 283N$$

$$T_c = FL$$

$$= 283 \times 0.16$$

$$= 45.28N$$

H.2.3 Test Rig Commissioning

Table H.6 Daily Recorded Pressure upon Charging the Test Rig

Gauge\Day	Day 1	Day 2	Day 3	Day 4	Day 5
Gauge 1 (Bar)	7.1	7.0	7.0	7.1	7.0
Gauge 2 (Bar)	7.1	7.0	7.0	7.0	7.0
Gauge 3 (Bar)	7.2	7.3	7.2	7.2	7.1
Gauge 4 (Bar)	7.3	7.2	7.2	7.1	7.1

Appendix H

Figures and Information of Experimental Setup and Equipments

I.1 Figures of Pressure Test Setup and Equipments

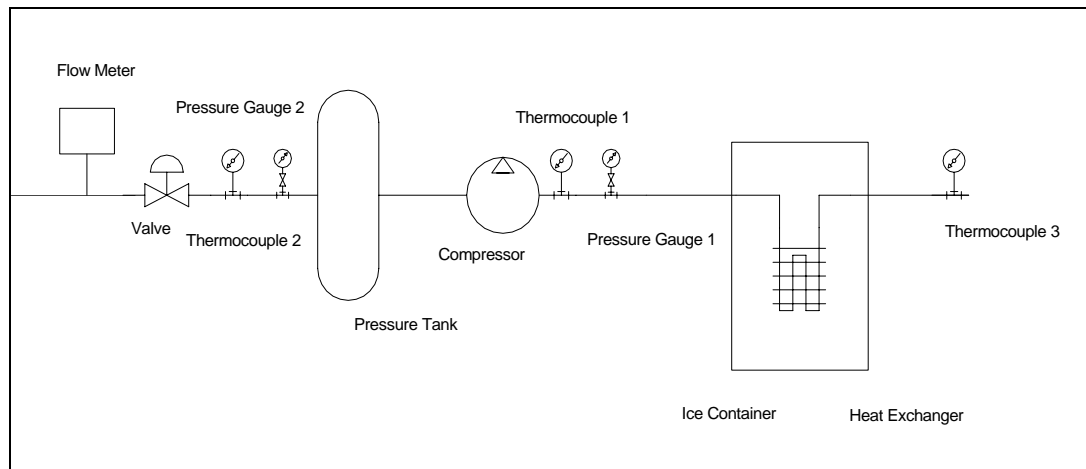


Figure I.1 Schematic Diagram of Pressure test rig



Figure I.2 Pressure Test Rig Setup



Figure I.3 Ice Container



Figure I.4 Pressure Tank



Figure I.5 (a): Pressure Gauge



(b): Thermocouple Display



Figure I.6 Air Flow Meter

I.2 Pressure Test Procedure



Figure I.7 Compressor Under Test

The following procedure was followed in executing the pressure test experiments.

- i. Ice Container is filled with ice to reduce the air inlet temperature
- ii. Record ambient temperature and pressure
- iii. Switched on motor and set the compressor speed to a designated value
- iv. Adjust the valve until an increased in pressure is observed at the discharge tube
- v. Record pressure and temperature on designated points on the system after a stable readings is observed
- vi. Record the flow rate of discharge air
- vii. Record the voltage and current supplied to the motor
- viii. Each reading is to be recorded every 10 minutes up to three times

Appendix I

Figures and Information of Pressure Test Setup and Equipments

J.1 Experimental Results for DKS-32

Date	:15 Jan 05	Ambient Pressure	: 1.016 bar
Time	: 1000 am	Ambient Temperature	29 OC

	RPM					
	800	1000	1200	1400	1600	1800
Suction Pressure, Ps (Bar)						
	3.8	3.8	3.8	3.8	3.8	3.8
Suction Temperature, Ts (OC)						
	21.5	19.3	17.2	16.2	14.2	11.2
Discharge Pressure, Pd (bar)						
	13.4	14.9	16.2	17.2	18.8	19.8
Discharge Temperature, Td (OC)						
	74	75	76	76.7	79	80
Condenser Pressure, P kond (Bar)						
	13.2	14.7	15.9	16.9	18	19.2
Condensor Temperature, T kond (OC)						
	62.5	59.2	57	54.8	52.1	48
Txv Pressure, P txv						
	4.3	4.6	5	5.2	5.6	6.1
Txv Temperature, T txv						
	11.5	12.8	12.1	12	10.7	9.5
T evap	11.5	19.3	17.2	16.2	14.2	11.2
T kond	50	53	57	54.8	52.1	48
ma	51	64	78	92	100	111
Enthalphy, h						
h1 (kj/g)	250.00	248.00	246.10	245.20	243.30	240.60
h2 (kj/kg)	285.00	283.50	282.40	281.30	281.10	280.40
h3	105.80	110.50	112.00	113.20	108.90	102.50
h4	105.80	110.50	112.00	113.20	108.90	102.50
Evap. Load	7.35	8.80	10.46	12.14	13.44	15.33
Volt, V	254.08	297.19	361.21	421.70	494.00	555.01
Current, I	12.60	13.90	14.37	15.00	15.47	15.70
Motr Pwr, Pc	2521.48	3253.52	4087.23	4981.95	6019.01	6862.89
Shft Pwr, Ps	2395.40	3090.84	3882.87	4732.85	5718.06	6519.74
Comp Power	1785.00	2272.00	2831.40	3321.20	3780.00	4417.80
COPa	4.12	3.87	3.69	3.66	3.56	3.47
Vol. Eff.	0.71	0.70	0.71	0.71	0.67	0.65
Mech. Eff.	74.52	73.51	72.92	70.17	66.11	67.76
Pressure Ratio	3.53	3.92	4.26	4.53	4.95	5.21

J.2 Experimental Result for New Symmetrical Compressor

Date : 15 Okt 05
Time : 1000 am

Ambient Pressure : 1.016 bar
Ambient Temperature : 29 °C

	Time					
	5	10	15	20	25	30
	RPM					
	700	700	800	800	900	900
	Suction Pressure, Ps (Bar)					
	4.7	4.4	4.3	4.2	4	4
	Suction Temperature, Ts (OC)					
	23.1	20.3	18.9	17.4	16.3	16.5
	Discharge Pressure, Pd (bar)					
	11.5	12	12	12	12	12
	Discharge Temperature, Td (OC)					
	56.6	60.6	60.3	59.4	61	61.7
	Condenser Pressure, P kond (Bar)					
	11	11.5	11.5	11.5	11.5	11.8
	Condensor Temperature, T kond (OC)					
	40.9	43.6	44.5	44.5	44.2	44.3
	Txv Pressure, P txv					
	4.9	4.8	4.8	4.8	4.8	4.8
	Txv Temperature, T txv					
	14.6	15.2	15.6	15	14	14.1
T evap	23.1	20.3	18.9	17.4	16.3	16.5
T kond	40.9	43.6	44.5	44.5	44.2	44.3
ma	nil	nil	nil	nil	nil	nil
	Enthalphy, h					
h1 (kj/g)	249.5	247.5	246.5	245.3	244.8	245
h2 (kj/kg)	269.2	272.6	272.3	271.3	273.1	273.9
h3	91.93	96	96	97.37	96.91	97.06
h4	91.93	96	96	97.37	96.91	97.06
Evap. Load	nil	nil	nil	nil	nil	nil
Volt, V	180.37	169.92	187.88	179.95	196.29	189.77
Current, I	12.60	13.90	14.37	15.00	15.47	15.70
Motr Pwr, Pc	1789.99	1860.19	2125.93	2125.93	2391.67	2346.54
Shft Pwr, Ps	1700.49	1767.18	2019.63	2019.63	2272.09	2229.22
min shaft	1733.83	2019.63	2250.65			
Comp Power	nil	nil	nil	nil	nil	nil
COPa	8.00	6.04	5.83	9.43	5.23	5.12
Vol. Eff.	nil	nil	nil	nil	nil	nil
Mech. Eff.	nil	nil	nil	2.86	nil	nil
Pressure Ratio	2.45	2.73	2.79	2.86	3.00	3.00

Appendix J

Experimental Results For DKS 32 and New Compressor

Appendix K

Results and Performance Characteristic of Swash Plate Compressor Model (ZEXEL)

K.1 Performance Test Result

The ZEXEL compressor was tested at six different speeds, 800 rpm to 1800 rpm. The parameters used for analysis were obtained from the average values at steady state during each operating speed. A number of test sets were conducted in order to obtain consistent result, an experiment set was then selected based on the consistency of the result between each experiments. The results are presented in Figure K.1 through Figure K.5.

Figure K.1 shows coefficient of performance (COP) of the air conditioning system with respect to compressor speed. It shows that the COP decreases as the compressor speed is increased. This means that the increase of power consumption and refrigerating capacity are inversely proportional. In fact, the compressor power consumption increases at faster rate than the refrigerating capacity.

Figure K.2 shows the volumetric efficiency with respect to compressor speed. The figure shows that the volumetric efficiency of the compressor is almost constant at 70% in the test range (800 rpm to 1800 rpm). Theoretically, the volumetric efficiency should be lower at higher speed which is why if observed closely at 1800 rpm, the efficiency recorded is lower than that at 1600 rpm.

Figure K.3 shows the shaft power consumption with respect to the compressor speed. The graph shows that the shaft power consumption increases from 2.36 kW at 800 rpm to 5.98 kW at 1800 rpm. Such characteristic is anticipated as an increase in speed ultimately increases the compressor power consumption.

Figure K.4 shows the refrigerating capacity of the air conditioning system with respect to compressor speed. It is shown that the refrigerating capacity is 7.11 kW at 800 rpm and increases to 13.99 kW at 1800 rpm. The increase in refrigerating capacity is caused by the increase of mass flow of refrigerant due to compressor speed increment.

Figure K.5 shows the pressure ratio of the compressor with respect to speed. In the experimental setting the suction pressure was to be maintained at 3.8 bar at all time. Such measure requires the evaporator air flow mixture to be adjusted accordingly at different speeds and the change in refrigerating capacity is recorded as discussed previously. The discharge pressure also increases in tandem with the refrigerating capacity where at the highest recorded speed of 1800 rpm the pressure ratio of 5.29 is achieved.

Figure K.6 shows the mechanical efficiency of the compressor with respect to speed. It shows that at lower speed, the compressor have a good efficiency averaging at 70%. However, the compressor efficiency is reduced at higher speed, falling to 60% at 1800 rpm. For a piston compressor, the efficiency behavior is quite normal due to an increase in frictions caused by the high speed moving components.

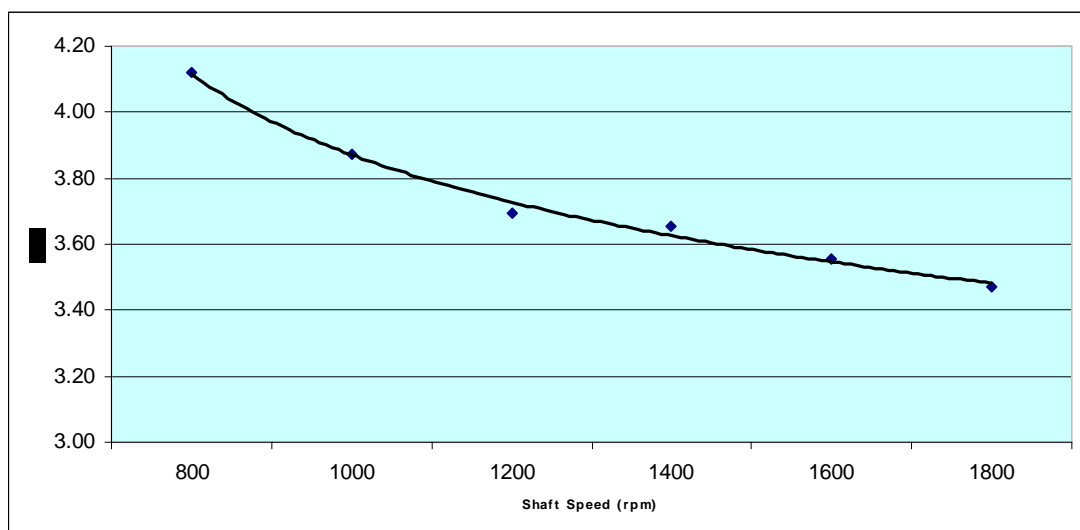


Figure K.1 Coefficient of Performance vs Compressor Speed

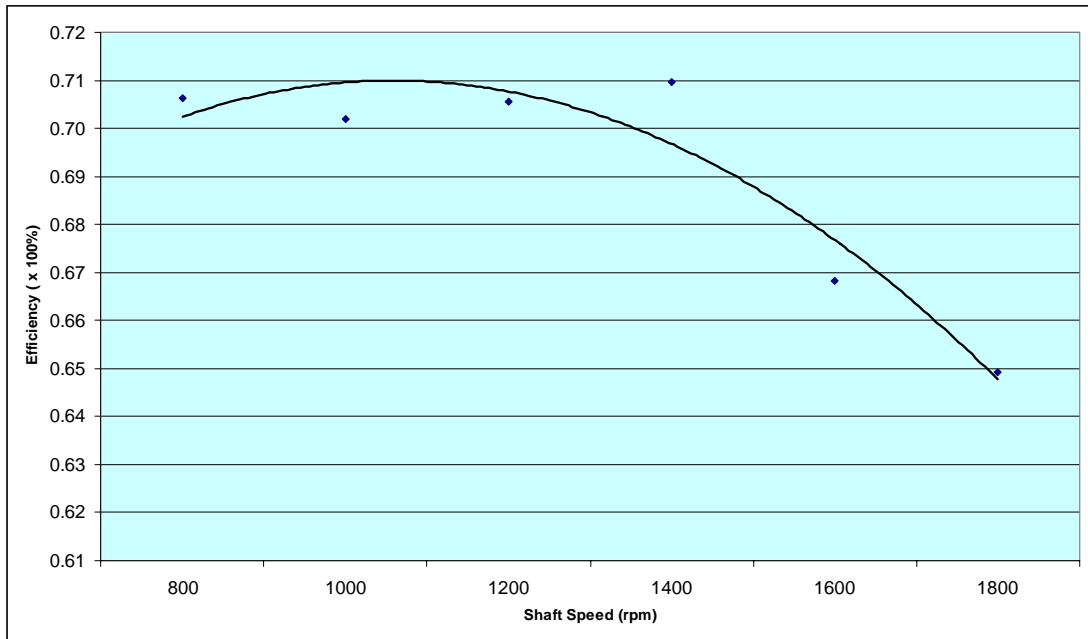


Figure K.2 Volumetric Efficiency vs Compressor Speed

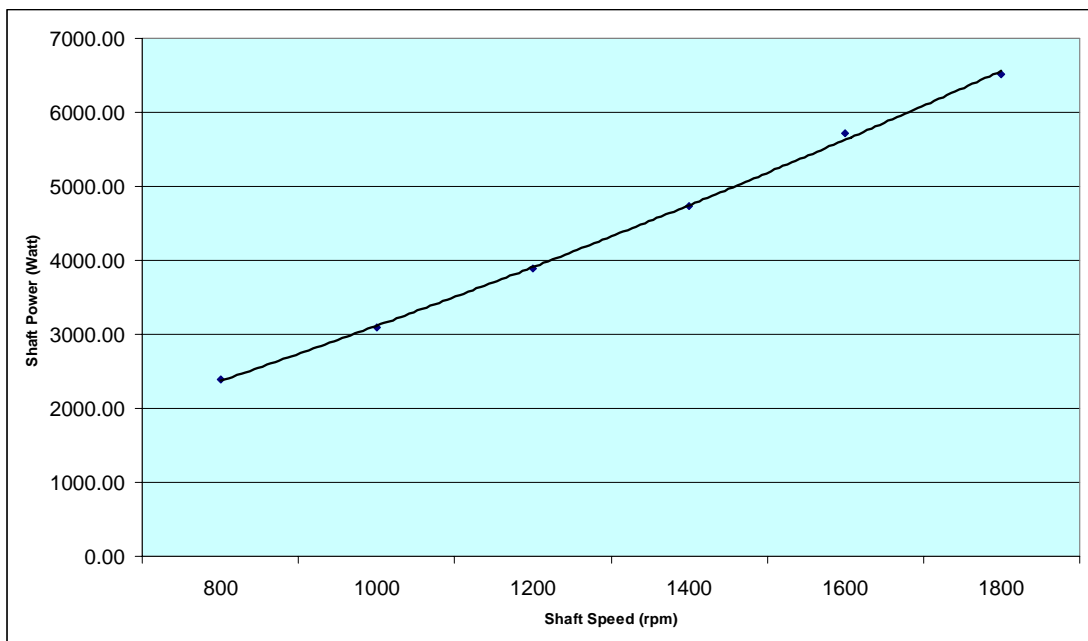


Figure K.3 Shaft Power Consumption vs Compressor Speed

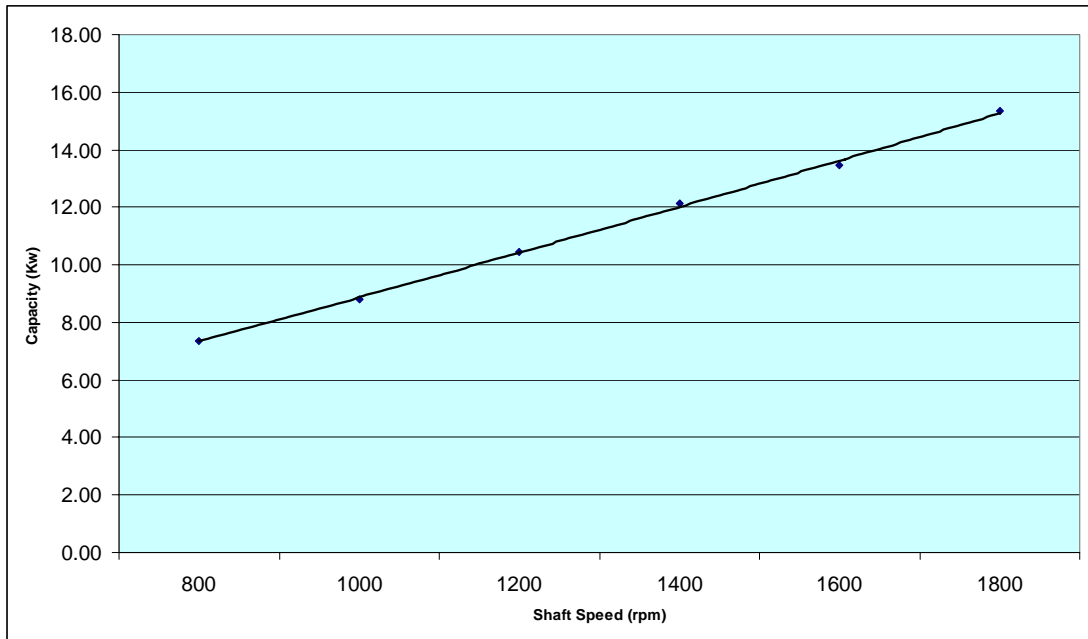


Figure K.4 Refrigerating Capacity vs Compressor Speed

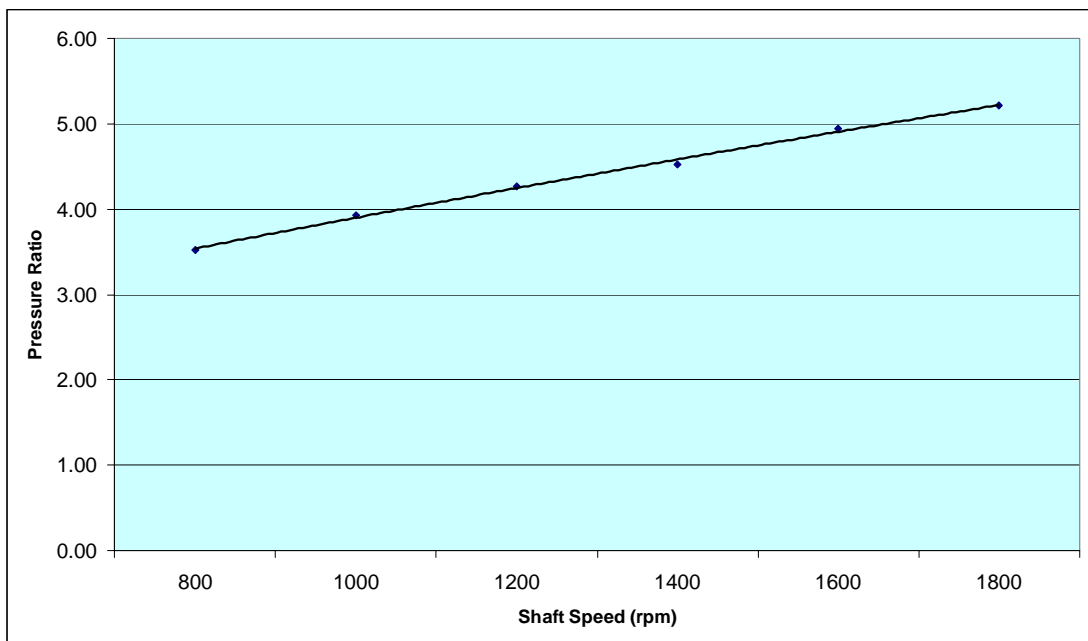


Figure K.5 Pressure Ratio vs Compressor Speed

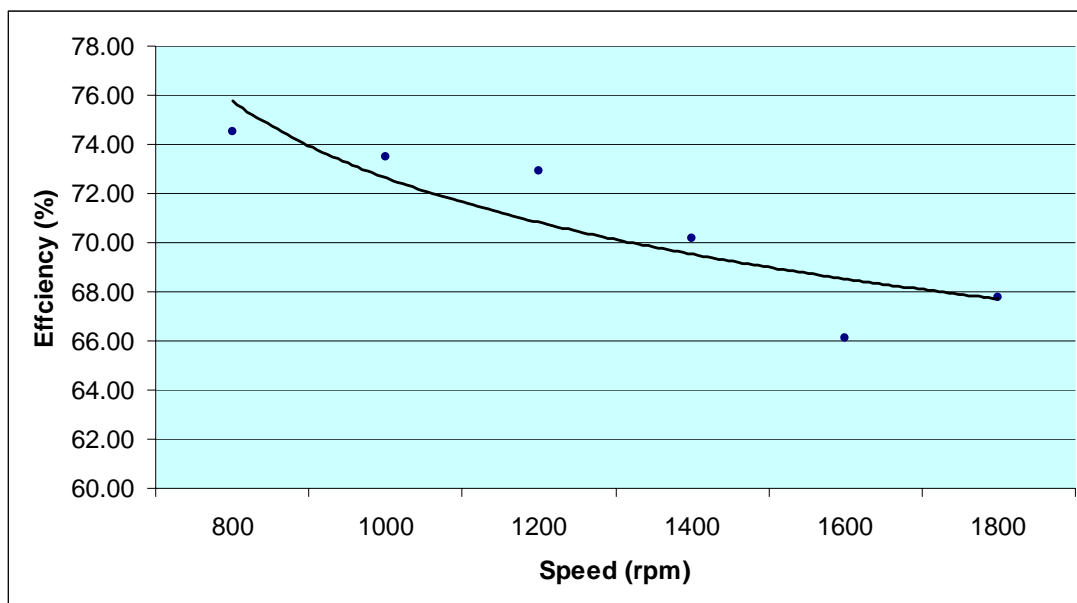


Figure K.6 Mechanical Efficiency Versus Compressor Speed

Appendix L

Parts Figures of New Compressor after Test

L.1 Damage Components

Figure L.1, L.2 and L.3 shows scrubbing that occurs on the prototype which caused the prototype to stall.



Figure L.1 Scrubbing on Ball Mount Surfaces



Figure L.2 Scrubbing on Shaft Surface

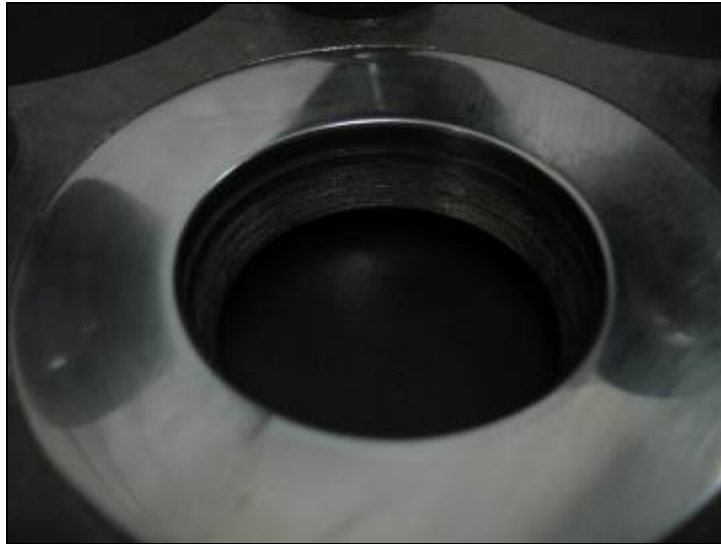


Figure L.3 Scrubbing Marks on Ball Mount Adaptor at Wobble Plate

L.2 Contaminated Lubrication Oil



Figure L.4 Lubrication Oil After test

Figure L.4 shows the lubrication oil after running test, it clearly shows the oil is contaminated both with black residue from piston rings and aluminum chips originated mostly from mating surfaces such as ball joints.

M.1 List of Papers

Misran, M. S and Musa, M. N. Development of experimental Rig for Bus Air Conditioning System. Fuel Cell Retreat Seminar. 2004. Port Dickson. UKM. 2004.

Misran, M. S, Sairaji, I. and Musa, M. N. Lubrication System for a New Symmetrical Wobble Plate Compressor. RIVET. 3-5, July 2006. Kuala Lumpur. UTM. 2004.

Misran, M. S, Sairaji, I. and Musa, M. N. Development of Symmetrical Double Sided Linear Wobble Plate Compressor for Bus A/C System. RPCES. 26-27, July 2006. Kuala Lumpur. UTM. 2004.

Appendix M

List of Papers

Developing of Bus Air-Conditioning System that Responds to a Variation in Cooling Load

(Keywords: roof-top bus air-conditioning system, simulation model, heat exchanger design, control strategy)

A newly developed bus air-conditioning system has been proposed to improve energy efficiency and enhance thermal comfort based on that of an existing roof-top bus air-conditioning system. The principle innovation of this proposed system is that it is split into two identical refrigeration circuits. Each circuit consists of a compressor, thermostatic expansion valve, condenser, receiver dryer, and an evaporator. A theoretical model of each component has been developed to analyze its thermal performance. The results obtained are being verified with those obtained from various references and the comparison in general gives a satisfactory agreement.

A steady state computer model has also been developed to simulate the thermal performance of the proposed system at different operating modes. Experiments were carried out to verify the simulation model and in general the deviation is less than 10%. A novel control strategy has been developed to provide a control algorithm for a digital temperature controller. A performance comparison between the developed system and the conventional one has been conducted in terms of energy saving and thermal comfort. The potential energy savings of the proposed system reach 31.6% when the set-point temperature of the controller is 21°C. Further analysis on the developed system has shown a significant enhancement in thermal comfort where neither undercooling nor overcooling conditions occurs.

This study presents another method to enhance the system's COP and to reduce its energy consumption. This method is based on thermoeconomic optimization of the system condenser. Comparing with the existing design, it was found in this study that the system COP can be improved from 2.46% to 6.6%. Although this enhancement is superficially not considerable, the saving in the annual fuel consumption for the bus engine will be in the range of 239 to 617 liter/year.

Key researchers :

Prof. Dr. Mohd Nor Bin musa (Head)

Prof. Dr. Mat Nawi wan Hassan

Mr. Mohamed khamis Mohd Mansour

Mr.

Mr.

Mr.

Mrs.

E-mail : mdnor@fkm.utm.my

Tel. No. : 07-5534567

Vote No. : 74522

Developing of Bus Air-Conditioning System that Responds to a Variation in Cooling Load

(Keywords: roof-top bus air-conditioning system, simulation model, heat exchanger design, control strategy)

Satu sistem baru pendingin-udara bus telah dicadangkan untuk meningkatkan kecekapan tenaga dan memantapkan keselesaan termal berasaskan kepada sistem pendingin-udara jenis atas atap bus yang sedia wujud. Inovatif utama sistem yang dicadangkan ini ialah ianya berbentuk gabungan sepasang litar penyejukan. Setiap litar mengandungi pemampat, injap pengembangan termostatik, pemeluwap, pengering dan penyejat. Model teoritikal setiap komponen ini telah dibangunkan untuk menganalisa prestasi termal setiapnya. Hasil yang diperolehi adalah disahkan oleh hasil-hasil yang diperolehi dari beberapa rujukan dan perbandingan secara am memberikan persetujuan yang memuaskan.

Satu model komputer berkeadaan mantap juga telah dibangunkan untuk mesimulasi prestasi termal sistem yang dicadangkan, dalam keadaan mod operasi yang berbeza-beza. Eksperimen telah dilakukan untuk mengesah ketepatan model dan secara amnya perselisihan antara kedua-dua hasil, adalah kurang dari 10%. Satu strategi kawalan yang novel telah dibangunkan untuk menyediakan algorithma kawalan bagi pengawal suhu digital. Perbandingan prestasi antara sistem yang dibangunkan dengan sistem konvensional dalam aspek penjimatan tenaga dan keselesaan termal, telah dilakukan. Potensi penjimatan tenaga oleh sistem yang dicadangkan mencapai 31.6% ketika suhu pengawal diset pada 21°C. Analisa seterusnya pada sistem yang dibangunkan menunjukkan pemantapan signifikan terhadap keselesaan termal dimana tidak berlaku samada terkurang atau terlampau sejukan.

Kajian ini menawarkan satu lagi kaedah untuk memperkasakan pekali prestasi sistem dan mengurangkan penggunaan tenaga. Kaedah ini berasaskan optimisasi termoekonomik pemeluwap sistem. Berbanding dengan rekabentuk sediaada, adalah didapati dalam kajian ini bahawa pekali prestasi sistem boleh ditingkatkan dari 2.46% kepada 6.6%. Walaupun peningkatan ini adalah tidak seberapa, namun penjimatan setahun penggunaan bahan bakar untuk enjin bus akan berada antara 239 dan 617 liter/tahun.

TABLE OF CONTENTS

CHAPTER	TITLE	PAGE
	Declaration Statement	ii
	Dedication	iii
	Acknowledgment	iv
	Abstract	vi
	Abstrak	viii
	Table of Contents	viii
	List of Tables	ix
	List of Figures	xix
	List of Abbreviations	xxv
	List of Symbols	xxvi
	List of Appendices	xxviii
1	INTRODUCTION	1
	1.1 Introduction	1
	1.2 Conventional roof-top bus air-conditioning system Layout	6
	1.3 Refrigerant-side flow diagram of the conventional Model	8
	1.4 Research objectives	10

1.5	Research scope	10
1.6	Thesis synopsis	11
2	LITERATURE REVIEW	13
2.1	Introduction	13
2.2	Cooling load calculation	14
2.3	Thermal analysis of the evaporator and condenser	15
2.4	Control methods in automotive air-conditioning system	18
2.5	Automotive air-conditioning system simulation	20
2.6	Heat exchanger thermoeconomic optimization design	23
3	COOLING LOAD AND PROPOSED AC SYSTEM DESCRIPTION	27
3.1	Introduction	27
3.2	Conduction heat load through body walls and glasses	29
3.2.1	Sol-air temperature	30
3.2.2	Determination of short wave radiation incident on a surface	33
3.3	Heat gain through glazing surfaces	36
3.3.1	Transmitted radiation	37
3.3.2	Fraction of absorbed radiation which flows inwards	37
3.3.3	Heat gain due to the difference between the outdoor and indoor air temperatures alone	38
3.4	Heat conduction through the motor compartment	39
3.5	Heat gain from ventilation	39
3.6	Passenger heat load	40
3.7	Heat gain from lights	41

3.8	Heat gain from power equipment	41
3.9	Passenger compartment climate characteristics	41
3.9.1	Dry air and vapor mass balance equations for passenger cabin	42
3.9.2	Air energy balance equation for passenger cabin	44
3.9.3	Determination of inlet air conditions to the AC system	45
3.10	Model technique and validation	46
3.11	Case study	50
3.12	Design philosophy of the proposed air-conditioning system	52
3.13	Conclusion	56
4	EXPERIMENTAL SET-UP AND RESULTS	58
4.1	Introduction	58
4.2	Description of experimental set-up	59
4.3	Measurements of physical parameters	63
4.3.1	Temperature measurement	63
4.3.2	Pressure gages	63
4.3.3	Hygrometer	64
4.3.4	Refrigerant flow meter	65
4.3.5	Air velocity transducer	65
4.3.6	Data acquisition “DAQ” system	66
4.4	Experimental components	69
4.4.1	Evaporator	69
4.4.2	Condenser	70
4.4.3	Compressor	72
4.4.4	Thermostatic expansion valve	74
4.4.5	Receiver-drier	75

4.4.6	Laboratory Simulated Passenger Cabin	75
4.4.7	Voltage regulator	76
4.4.8	Automatic controller	77
4.5	Experimental procedure	79
4.6	Thermodynamic analysis	82
4.7	Thermal comfort calculation	83
4.8	Experimental results and discussion	85
4.8.1	Effect of the cooling load variations on the system thermal performance for the three different operation modes	85
4.8.2	Effect of the cooling load variations on the the passenger's thermal comfort for different operation modes	89
4.9	Energy consumption analysis	92
4.10	Conclusion	95
5	EVAPORATOR AND CONDENSER MODELING	96
5.1	Introduction	96
5.2	Background	96
5.3	Model development	98
5.4	Air-side heat transfer coefficient and pressure drop	99
5.5	Refrigerant-side heat transfer coefficient and pressure drop for evaporator model	102
5.5.1	Superheated region	102
5.5.2	Evaporation region	104
5.5.3	Refrigerant-side heat transfer coefficient and Pressure drop for condenser model	105
5.6	Modelling scheme	106
5.7	Model Assumptions	107
5.8	Governing equations for evaporator model	108

5.9	Model calculation methodology	113
5.10	Governing equations for condenser model	114
5.11	Simulation implementation	117
5.12	Model validation	120
5.13	Conclusion	123
6	AC SYSTEM INTEGRATION AND SIMULATION	125
6.1	Introduction	125
6.2	Background	126
6.3	Mathematical model	127
6.3.1	Compressor modeling	127
6.3.2	Heat exchangers modelings	129
6.3.3	Thermostatic expansion valve modeling	130
6.3.2	Connecting lines and hoses modeling	132
6.4	Numerical procedure	133
6.5	Numerical results	139
6.6	Comparison between the results obtained from computer simulation model and those from the experimental work	142
6.6.1	Comparison in terms of the thermal performance for the first mode operation	142
6.6.2	Comparison in terms of the thermal performance for the second mode operation	143
6.6.3	Comparison in terms of the thermal performance for the third mode operation	145
6.7	Conclusion	147
7	CONTROL STRATEGY	148
7.1	Introduction	148

7.2	Control strategy concept	150
7.3	Comparison between the developed bus AC system and conventional bus AC system	157
7.3.1	Possible energy savings aspect	157
7.3.2	Costing aspect	159
7.3.3	Thermal comfort achievement	162
7.4	Conclusion	163

8 THERMOECONOMIC CONDENSER DESIGN OPTIMIZATION

8.1	Introduction	164
8.2	Background	165
8.3	Design optimization methodology	166
8.3.1	Exergy destruction calculations and its relationship with system COP	166
8.3.2	Condenser frontal area calculation	169
8.3.3	Cost calculation	170
	8.3.3.1 Capital investment Cost	170
	8.3.3.1.1 Material cost	170
	8.3.3.1.2 Compressor cost	171
	8.3.3.2 Running Cost	171
8.4	Parametric study	172
8.4.1	The effect of frontal velocity	173
8.4.2	The effect of saturation temperature	175
8.4.3	The effect of fin pitch	178
8.4.4	The effect of number of deep-rows	181
8.4.5	The effect of number of tube circuiting	183
8.4.6	The effect of vertical tube spacing	188
8.4.7	The effect of horizontal tube spacing	189
8.4.8	The effect of tube outside diameter	191

8.4.9	The instantaneous effect of the design parameters on system COP and frontal area	194
8.5	Comparison between the conventional condenser design and optimal one	200
8.6	Conclusion	203
9	CONCLUSIONS, CONTRIBUTIONS AND RECOMMENDATIONS	204
9.1	Conclusions	204
9.1.1	Conclusions related to the design of the developed AC system	205
9.1.2	Conclusions related to the optimization design of the condenser	206
9.2	Contributions	208
9.3	Recommendations	209
	REFERENCES	213
APPENDIX A	WEATHER DATA AND GEOMETRICAL CONFIGURATION FOR THE CASE STUDY	221
APPENDIX B	PHYSICAL QUANTITIES FOR THERMAL COMFORT CALCULATION	223
APPENDIX C	COMPUTER MODELS GRAPHICAL INTERFACES	231

APPENDIX D	CALCULATION OF FINNED-TUBE HEAT EXCHANGER GEOMETRIC CONFIGURATION	239
APPENDIX E	EXPERIMENTAL MEASUREMENTS DATA AND RESULTS	244
APPENDIX F	THERMAL COMFORT CALCULATION	262
APPENDIX G	CORRELATED FORMULAS AND ERROR ANALYSIS	271

ACKNOWLEDGEMNT

The work that went into this report was entirely supported by research grant from Malaysia Ministry of Science Technology and Innovation (MOSTI). We would like to express our sincere thanks and gratitude to the MOSTI for their funding and for giving us opportunity to work on the relevant industry problem. Many thanks to Universiti Tecknologi Malaysia Research Management Center for managing the fund.

We wish to thank from deepest heart SUTERA company members for their technical support and experience; We also do appreciate their patience and great efforts during the building up the experimental rig.

We also wish to thank the thermodynamics laboratory technicians for their help. Our deepest thanks to my colleagues and friends for their constructive support and comments.

CHAPTER 1

INTRODUCTION

1.1 Introduction

Energy crisis is becoming a global phenomenon. The increasing rate of the energy consumptions of the limited and non-renewable natural energy resources is aggravating this crisis. Energy consumption in Malaysia, which is moving fast towards its goal of a developed country, is increasing significantly every year. Rapid increase in energy demand has prompted the government to promote energy conservation and energy efficiency, both in supply and demand areas. This energy demand comes from several sectors; the important ones are transportation, industry, residential (households) and commercial as shown in Figure 1.1.

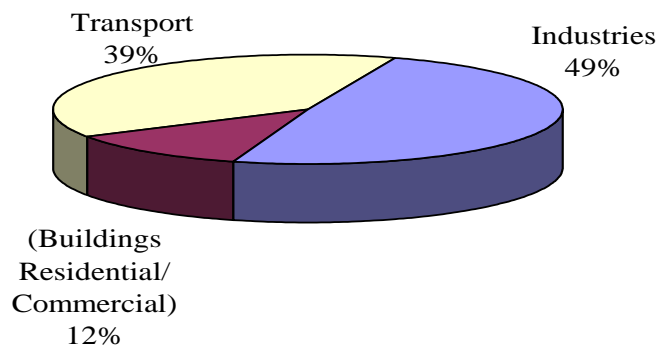


Figure 1.1 Energy consumption in Malaysia by sectors, (Mohd Zamzam,1999)

One sector where the energy consumption is increasing steadily is on space cooling. The use of air-conditioning (AC) system is crucial since Malaysia is a hot and humid, tropical country (except in the highlands) and the daily average temperature is around 29°C while the average humidity is about 78%. In general, the AC system consumes around 30% to 70% of the total energy in different energy consumption sectors in Malaysia (Hassan et al., 2001), particularly in the transport and residential sectors as shown in Figure 1.2. Furthermore, recently, there is a drastic instability in oil price due to the rapid development of the transportation and industrial sectors. All these factors contribute to make the issue of energy saving as imperative and indispensable.

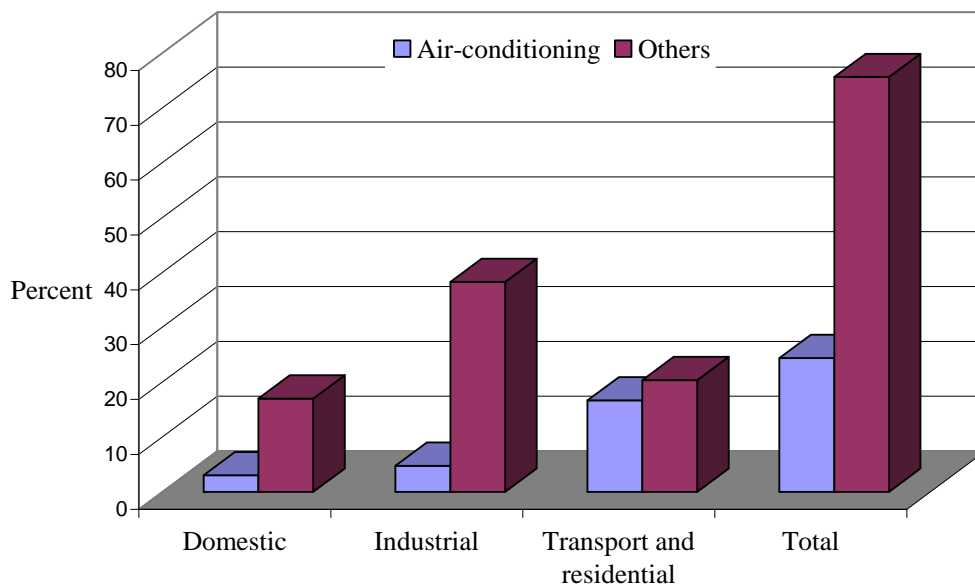


Figure 1.2 Different energy consumption sources in Malaysia, PTM (1999)

The use of roof-top passenger vehicle (buses or trains) AC system has been steadily growing not only in Malaysia but also in other countries experiencing hot and humid tropical climate. Train AC compressors are driven by electrical motors while a bus AC compressors are driven by an auxiliary engine which provides a constant speed operation. Still, there are many that are belt-driven by the main engine of the bus. An AC system is the second biggest energy consumer component

in either intercity or city buses. If the AC system is driven by the main engine, the driver can easily feel the drop in the vehicle power when the electromagnetic clutch is engaged.

In general, the bus AC system presents some peculiarities with respect to its commercial and industrial counterparts. On one hand, its operation is characterized by significant thermal load variations, which depend on several factors such as: opening of a door, changing of sun load through the windshield and side glass windows, and number of passengers on board. On the other hand, the refrigeration system must provide comfort under highly transient conditions and, at the same time, be compact and efficient. This requires a proper design and selection of AC system.

In tropical countries, the peak load which is between 12.00 noon to 3.00 pm, drives the AC system to operate at maximum capacity. However, at other times when the system experiences partial load conditions (low sensible heat load), especially at night or when it rains, it still operates at maximum capacity. This leads to an uncomfortable cold condition for passengers. The overcooling is due to the absence of any provision to modulate the system capacity to match the drastic reduction in the imposed cooling load. On the other hand, AC systems are often over-designed: first to ensure a fast response so that the cabin temperature drops quickly when the system is switched on, and second to overcome the irregular and rare conditions of extremely high humidity and high atmospheric temperature. Thus, under normal conditions, a lot of the energy is unnecessarily wasted (ASHRAE, 2000) and results in a higher consumption of fuel. Therefore, attention has been drawn towards designing energy-saving AC systems without sacrificing thermal comfort.

Most automotive air conditioners for small vehicles such as the car AC systems have on/off control or thermostat control. The compressor is disengaged from the vehicle engine when the set-point temperature has been reached. It will be

reengaged if the passenger cabin temperature increases. This type of comfort control technique is satisfactory for small AC systems. However, in larger vehicles such as a bus, this technique can be a quite difficult to be applied. The reason is that the compressor capacity is relatively large compared to those for the smaller vehicle AC systems. In this case, the AC system compressor will experience a high inertia torque when it is started suddenly from zero speed to a high speed. If the on/off action is frequently repeated during short intervals, the system is prone to behave in an erratic manner and the compressor could get damaged quickly.

In addition, the compressor of the bus AC system is located at the lowest point of the refrigeration cycle with respect to that of the evaporator and the condenser (see Figure 1.3). It is installed underneath the bus chassis and is connected to the shaft of the main or auxiliary engine by a coupling. When the system is off, the entire refrigerant charge is in liquid form and is collected inside the compressor which now acts like a sump. Every time the system is restarted, the liquid refrigerant will gradually damage the suction and discharge valves which are designed to control the flow of refrigerant in gaseous form. This will inevitably shorten the life cycle of the compressor and hence the passenger thermal comfort system.

To overcome this problem, most bus AC system manufacturers reject the idea of equipping the thermostat component in their AC systems. Usually they allow the compressor to work continuously without any attention to the energy consumption or thermal discomfort during partial load conditions. Consequently, the passengers are subjected to an unnecessary very low cooled temperature and they either have to wear thicker clothing or close the air duct louvers. Certainly, this freezing condition is not conducive to passenger's good will.

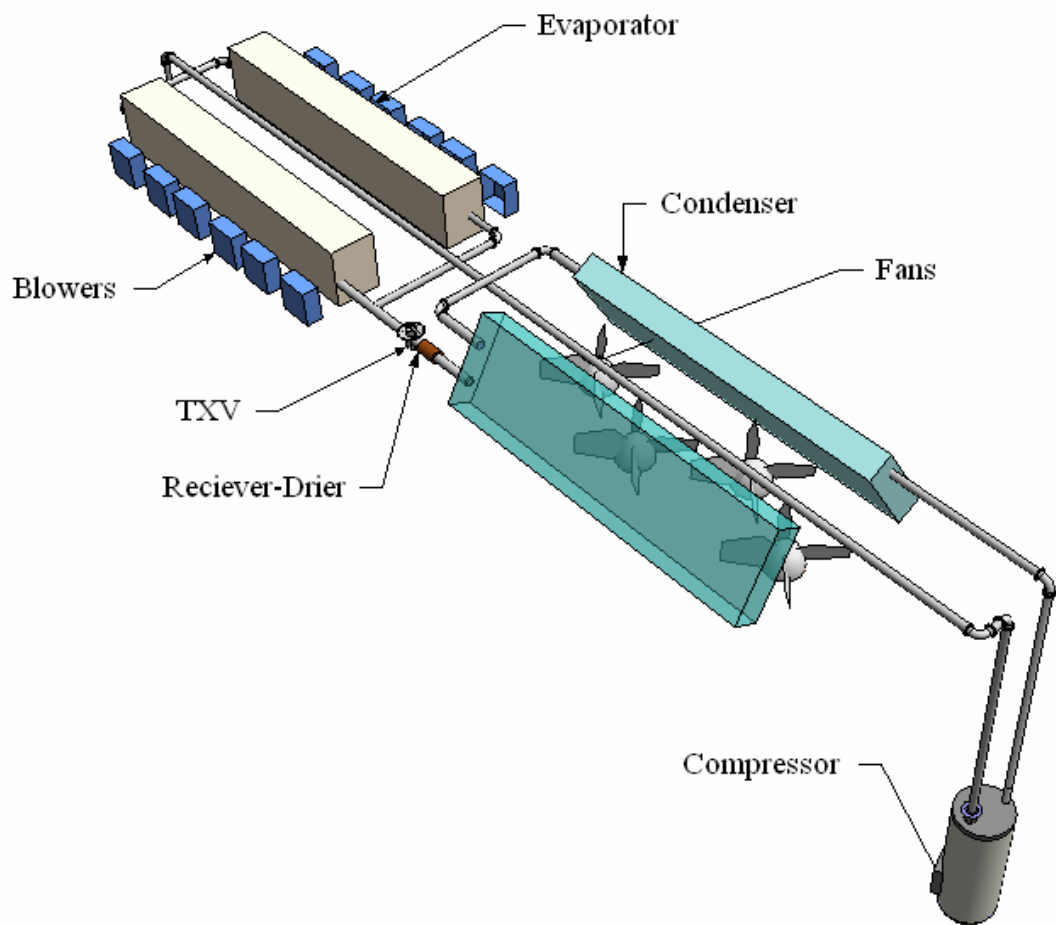


Figure 1.3 Layout of the roof package unit with compressor location

This picture of the current bus AC systems provides the motivation for researchers and manufacturers to develop new and more efficient bus AC systems. These systems may also be desired to provide an economical operation in terms of energy consumption along with thermal comfort at various system cooling loads.

In this work, an innovative bus AC system has been proposed to overcome the shortcomings of the existing system using multiple-circuit AC system (MCACS) approach. In such a system more than one unit can be used, each unit shares the evaporator surface area and this is called face-to-face evaporator control. The main advantages of the MCACS concept are of its simple installation and maintenance

together with the potential to conserve energy. Should one compressor fail to function the other circuit can still hold the load partially and supplies some cooled air to passengers until repairs can be performed. However, to reap these benefits of the MCACS, an efficient automatic controller has been developed.

1.2 Conventional roof-top bus air-conditioning system layout

Figures 1.4 and 1.5 show the arrangement of the existing roof-top bus AC system components. As it can be seen from these Figures, the system heat exchangers (the condenser and the evaporator), the receiver-drier, and the thermostatic expansion valve are located at the top of the roof. The compressor is mounted on the bus chassis connected by coupling to the shaft of an auxiliary engine. The thermostatic expansion valve (TXV) controls the flow of refrigerant into the evaporator; it has a capillary tube with a thermal bulb that controls the opening and the closing of the valve. The valve controls the flow of liquid refrigerant entering the evaporator in response to the superheat of the gas leaving it. It functions to keep the evaporator active without permitting liquid to return through the suction line to the compressor. The valve thermal bulb is installed at the outlet pipe of the evaporator. If insufficient refrigerant is flowing through the evaporator and causing a reduction in refrigeration effect, this bulb will sense it and automatically causes the valve to open more or vice versa. The evaporator is the heat exchanger that removes heat from the inside of the passengers' cabin and it is mounted on the bus roof-top as is depicted in Figure 1.5. It should be noted that the conventional bus AC system consists of two evaporators providing conditioned air to the two rows of the respective passengers' compartment, two-stage condensers (connected in series) and one compressor as shown in the Figures 1.5.

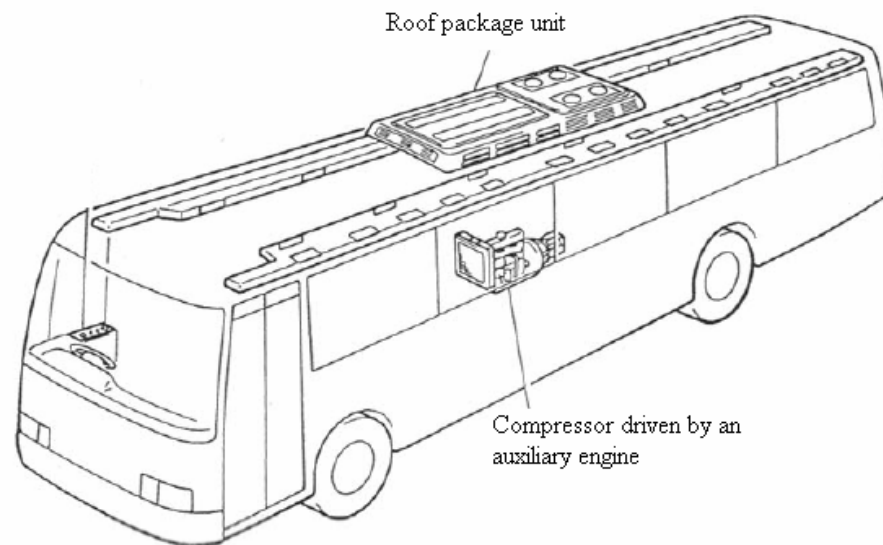


Figure 1.4 Layout of the roof package unit with sub-engine driven compressors



Figure 1.5 Evaporator and condenser arrangements in roof-top bus AC system

1.3 Refrigerant-side flow diagram of the conventional model

Figure 1.6 shows schematically the flow of refrigerant and how the existing AC system works. The hot pressurized gas is pumped from the compressor and passes via the discharge line to the air-cooled condenser which consists of two heat exchangers connected in series. The refrigerant starts its condensation process in the first heat exchanger and completes this process in the second one to exit as pressurized subcooled liquid which is then stored in the receiver-drier. There are four centrifugal fans providing the condensers with cooled air from the surrounding. The refrigerant liquid is expanded in the thermostatic expansion valve (TXV) to decrease the refrigerant temperature and pressure. The expanded refrigerant liquid is split into branches in order to feed the two evaporators in which the refrigerant is vaporized by absorbing the thermal load from the non-conditioned air. This air is induced by the blowers to pass across the evaporators and then supplied to the passenger cabin via air ducts. The two evaporators are each serviced by a set of six centrifugal blowers. Eventually the refrigerant vapour from the evaporators is combined and flows into a pipe and is sucked by the system compressor to complete the refrigerant cycle.

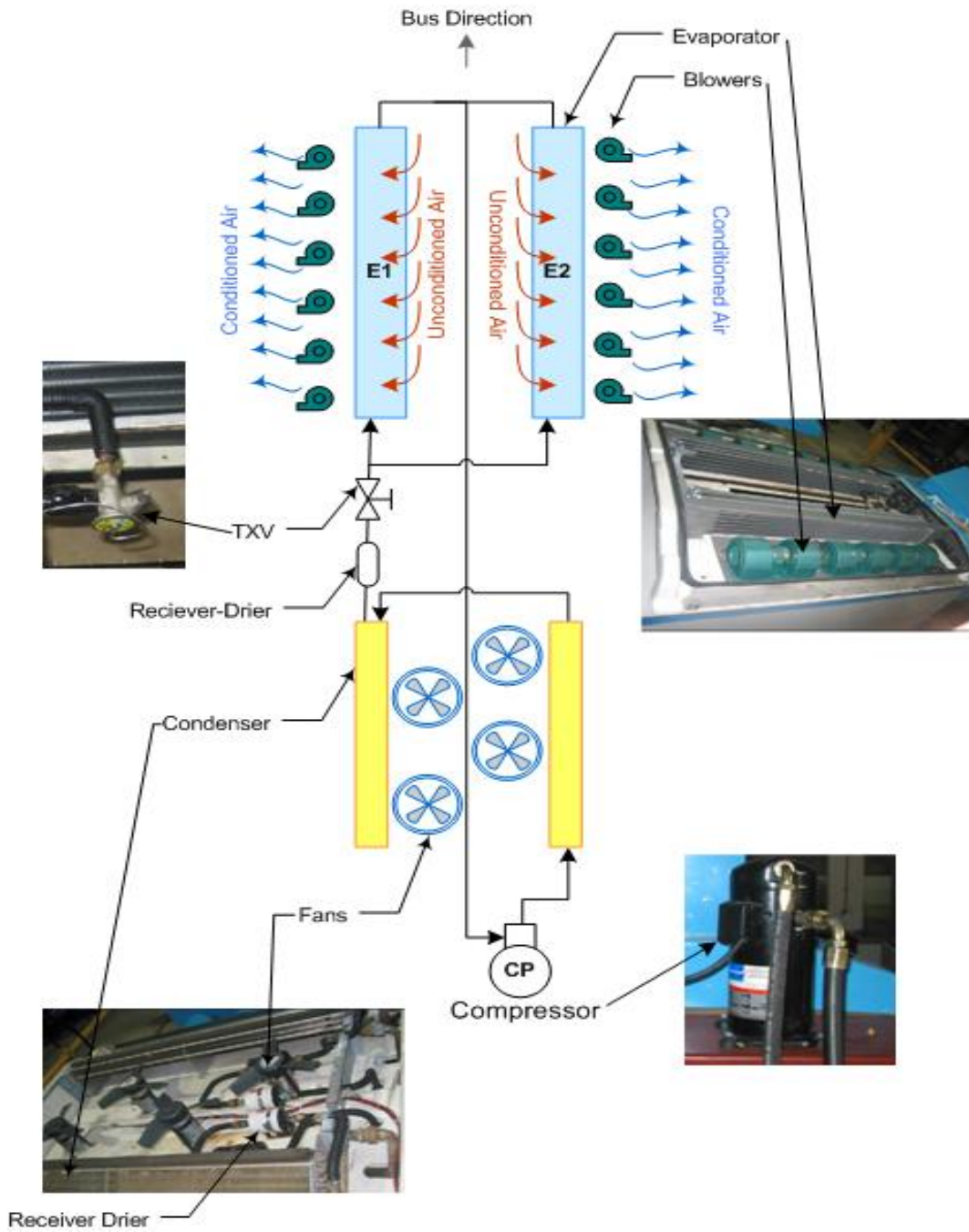


Figure 1.6 Schematic diagram of a conventional bus AC system

1.4 Research objectives

The following objectives of this research were addressed:

To design and optimize a new roof-top bus AC system through:

- 1) Development of a new roof-top bus AC conceptual design that will respond to the variation in cooling load imposed by tropical climates.
- 2) Development of a proper control strategy to achieve the optimal system operation, and
- 3) Optimization of the system condenser configuration which corresponds to a maximum AC system coefficient of performance (COP).

1.5 Research scope

The scope of the research involved three main parts i.e. designing, developing, and testing a new roof-top bus AC system. The work is divided into five phases:

- i- To study and develop a mathematical model to simulate the cooling load variation imposed on the bus compartment using the heat balance method.
- ii- To develop a mathematical model to simulate the thermal analysis of the heat exchangers (evaporator and condenser) by numerically solving the governing equations.
- iii- To develop a mathematical numerical model to simulate the vapour compression system in order to study its thermal performance during cooling load variations.

- iv- To construct an experimental test rig to verify the simulation of the theoretical work and to determine the proper control strategy for the temperature controller.
- v- To carry out a mathematical analysis to optimize the design parameters which have significant influence on the condenser design using thermoeconomic approach.

1.6 Report synopsis

The Report contains nine chapters. Chapter 1 introduces the project and its importance in the bus AC system industry. A review of applicable research works is presented in Chapter 2. Five related areas of research are reviewed. The first part is the cooling load calculation. The second part reviews the thermal analysis of the evaporator and condenser. The third part looks at the control methods which are used in automotive air conditioning system. The fourth part deals with the air conditioning simulation and computer programming. The last part discusses the methodology of the thermoeconomic optimization approach. Chapter 3 discusses the analytical model for cooling load calculation and describes the philosophy of the developed air-conditioning system while the experimental set-up and results are discussed in Chapter 4 and all instrumentation and system components are presented in this Chapter. Chapter 5 illustrates the analytical modelling of the evaporator and condenser. Chapter 6 describes the analytical simulation model for the air-conditioning system and verifies the theoretical results with those obtained from the experimental work. The control strategy of the automatic controller and the benefits of the developed system are discussed in Chapter 7. The air-cooled condenser of the air-conditioning system is optimized using the thermoeconomic optimization method. The new condenser design is compared with the conventional design to highlight the benefits of the thermoeconomic optimization for refrigeration system and this is

presented in Chapter 8. The conclusions, contributions, and recommendations for future development are given in Chapter 9.

CHAPTER 2

LITERATURE REVIEW

2.1 Introduction

It is unfortunate that the literature regarding automotive AC systems (AACS) particularly bus AC system is scarce due to the proprietary control of the knowledge and information. Nevertheless, the little literature available provides a fairly good review of studies concerning the theoretical and experimental performance of these systems. A number of studies in this area have been limited to either system components' analysis or system modellings or automatic controls. As aforementioned, the main purpose of the developed bus AC system in this research is to achieve energy conservation and thermal comfort during the period of operation. Therefore, the literature survey in this chapter will be classified into two categories; the first category is the system's theoretical simulation, and the second is the methodology of the system development. Each category is broken into pertinent topics. The first category involves reviewing: a) - the thermal analysis of system heat exchangers (evaporator and condenser) and b) - the methodology of the AC components integration. The second one reviews: a) - the bus cooling load calculation, b) - control methods which are used in automobile AC unit, and c) – Heat exchanger thermoeconomic optimization design.

2.2 Cooling load calculation

There is a substantial amount of work being carried out in this area but only that which is relevant to the present study is reviewed and presented in this section. Cited below are some of the most recent studies in this field by many researchers.

Kohler J. et al (1990) developed a simulation model to determine the time-dependent variations in temperature, humidity and the associated heat fluxes for bus or similar vehicle and verified with experimental works. They investigated the transient humidity and temperature responses for a bus with a capacity of 50 persons. The lumped AC system simulation model was integrated into their model and the rest of their research reported that the predictions and experiments were in good agreement. Their work claimed that it is possible to investigate the influences of the modifications of the vehicle structure and the components of the AC system installation on the interior climate. In addition, they concluded that the level of comfort in the interior of the vehicle is affected by glass coloured window and existence or number of occupants in the vehicle.

Stancanto F. and Onusic H. (1997) developed a mathematical simulation model and conducted the experiments to evaluate the conduction through walls, glasses, and the total cooling load of an intercity bus. The effects and influence of the direction, the time and colour of the walls and the tint of the glasses on the conduction and solar cooling loads of cabin were considered. The measured and calculated results showed good agreement with a small average difference.

Silva et al (1999) simulated the thermal behaviour of passengers' compartment with a numerical model to simulate mobile and immobile comfort conditions of passenger compartment. The validation of this model was done with a summer situation, when it was immobilized and running. The model reproduced well the experimental work to determine temperature and heat fluxes evolutions. However, the numeric

simulation showed the best agreement with the experimental results when the convection heat transfer coefficients, determined experimentally in this work, were used. It can be concluded that the numerical model is able to simulate the passenger compartment thermal behaviour when it is immobilized or running.

Akihiro Fujita et al (2001) developed a numerical simulation model to predict the thermal environment inside a car cabin under the influence of the outside environment. They verified their model through experiments with focus on thermal sensation evaluation for each part of the human body to determine the level of accuracy required for the simulation. The model also focused on the airflow inside the instrument panel, air leakage through gaps and direction of the artificial solar radiation lamps to enable a car cabin model to be created for the analysis and to provide the boundary conditions. The objective of the study was to predict the thermal environment inside a car cabin under the influence of the outside environment; over a wide temperature range and under various thermal load conditions. The calculated results were satisfactorily reproduced by the experimental results to confirm the validity of the proposed model and method.

2.3 Thermal analysis of the evaporator and condenser

Finned-tube direct-expansion coils are widely used in refrigeration and AC applications. The increasing interest in heat recovery from refrigeration systems and the application of new environment-friendly working fluids have created a need for a detailed analysis of the coils with R134a as a refrigerant. These heat exchangers consist of mechanically or hydraulically expanded round tubes in a block of parallel continuous fins. Several authors have investigated these heat exchangers for simulation and design purposes as described below.

Urbicain M. J. et al. (1981) presented the simulation of air-cooled finned-tube heat exchangers. They divided the transfer area of each tube into a finite number of

elements. The heat transfer rate equations and the energy balances corresponding to all the elements of all tubes constitute a system of linear equations which was solved iteratively.

Raymond D. Ellison et al. (1982) presented a computer model for an air-cooled refrigerant condenser. The model was intended for use in a detailed design analyses or in a simulation of the performance of existing heat exchangers that have complex refrigerant circulating or unusual air-side geometers. The model relied on a tube-by-tube computational approach calculating the thermal and fluid flow performance of each tube in the heat exchanger individually, using local temperature and heat transfer coefficients. The refrigerant circulating must be specified; the joining or branching of parallel circuits was accommodated using appropriate mixing expressions.

Fischer and Rice (1983) proposed an evaporator model as a part of a steady-state air-to-air heat pump design model. In the evaporator simulation model, the refrigerant flow in the tubes was divided into three regions that include the two-phase, liquid deficient (from dry-out to 100% vapor quality reached) and superheat regions. In the two-phase region, average refrigerant-side heat transfer coefficient was obtained by integrating local values determined from correlation equation.

Kempiak, and R.R. Crawford (1990) developed a simulation model for a mobile AC system condenser based on a least-squares analysis of experimental data. The inlet refrigerant mass flow rate, inlet air temperature, and airflow rate were all treated as independent variables in the model. The outlet temperature and pressure of refrigerant-side and the outlet air-side temperature were the dependent variables. The overall heat transfer coefficient for each of the three sections (desuperheating, condensing, and subcooling), expressed as a function of the air velocity across the condenser and the refrigerant mass flow rate, and the length of each section were determined using energy equations for each section. To include the pressure drop within the condenser model, a momentum equation was used to determine the friction factor as a function of the refrigerant mass flow rate for each section.

Oskarsson et al. (1996) presented three different models for evaporators, which may operate with dry, wet, and frosted finned surfaces. They developed a finite element model to study the local behaviour of heat transfer of fluids, as well as a three-region model and a parametric model.

Bensafi (1997) developed the computational model to separate plate-fin-tube-coil into tube elements and solved the associated governing equations of each element with local values of temperature, pressure, and heat transfer coefficient. The working fluids included water, R22, R134a, and some refrigerant mixtures. The coil geometry, circuitry, and operating parameters were chosen as input data and the computation algorithm started at the inlet tube and followed the refrigerant flow to the exit. Because of the presence of complicated circuits' arrangement in the evaporator coil, the refrigerant flow in each branch was calculated iteratively to yield the same pressure drop.

Vardhan and Dhar (1998) developed comprehensive simulation models of the individual finned-tube heat exchanger component with reasonable accuracy (~1% - 30% deviation) when compared to experimental data. Each of these models uses a nodal analysis approach and requires significant computation time to obtain performance results.

Theerakulpisut S. (1998) presented a modelling procedure for cooling coils with dehumidification based on the approach of Threlkeld. In order to verify the calculation results of the model, experiments were conducted with an aim to determine the outlet air conditions as well as some other parameters required as the inputs to the model. Comparison between the simulation and experimental results revealed that the model is accurate and suitable for predicting the performance of cooling coils with dehumidification.

Corberan J. M. et al. (2000) presented a model for heat exchangers working as evaporator or condenser of a refrigeration system, including a comparison between

calculated and actual results for a plate heat exchanger. The model was constructed based on discrete finite-difference method. The thermo hydraulic analysis for heat exchanger was calculated through the integration of the 1-D conservation equations. A full comparison of results on a fin-tube heat exchanger and a plate heat exchanger, both working as an evaporator and as a condenser was performed for two different refrigerants, showing a difference between measured and predicted values for the heat transferred typically lower than 6%.

Ge Y.T. et al. (2005) constructed a simulation model for air-cooled finned-tube condensers utilizing the modified lumped method. Within the model, the condenser was divided into four sections, a superheated section, two two-phase regions, and a subcooled section. The classification of the two-phase region was based on the experimental results of heat transfer behavior during condensation of refrigerant inside pipes. The proposed model was validated with test data and used to compare the performances of differently structured condensers using refrigerants R22 and R404A.

2.4 Control methods in automotive air-conditioning system

Controls play an important role in AC systems. Since the cooling load for a refrigeration system varies from time to time, the system capacity should be adjusted to match the cooling load, otherwise unsatisfactory operation conditions will result. This is the task of the controller which acts like an adaptor between the cooling load and the system capacity.

Controls may be energized in a variety of ways: pneumatic, electric, electronic or they may be even self-contained, where no external power is required. At the present time, the trend in AC systems is more oriented towards the use of electronic controllers, and interest is especially high in direct digital control (McQuiston and Parker, 1994).

In the following paragraphs, control methods for mobile air conditioners will be discussed. Clutch cycling (or on-off cycling) is the most common method whereas variable-displacement compressors and electronic expansion valve are less common. All of these control methods are also applicable to stationary systems. Another control strategy used in some prototype stationary systems is a variable-speed compressor. This strategy is not practical for mobile systems, (Tara, 1998). The high initial cost of this compressor and complexity of its installation have not attracted consumers as many as the manufactures expected. In addition, the long payback period for the initial cost often makes the customers reluctant to use it. Like the variable speed compressor, the electronic expansion valve (EEV) is characterized by a high expensive capital cost.

The electronic expansion valve operates with a much more sophisticated control design. EEV controls the flow of refrigerant entering a direct expansion evaporator in response to signals sent to it by an electronic controller, a microprocessor. A small motor is used to open and close the valve port. The motor is called a step or stepper motor. Step motors do not rotate continuously. They are controlled by an electronic controller and rotate a fraction of a revolution for each signal sent to them by the electronic controller. The electronic signals sent by the controller to the EEV are usually done by a thermistor connected to discharge airflow in the refrigerated case. EEV can perform effectively when it is installed with the variable speed compressor causing amplification in the system capital cost, as well the cost of the EEV controller and sophisticated sensors. In addition, if the current supply to the controller is cut off suddenly during system operation, the compressor is apt to the floodback phenomenon (refrigerant liquid enters the compressor) because the EEV retain its position of opening port as dictated by the stepper motor. The refrigerant liquid floods the evaporator and the compressor and unless there is a solenoid valve prior to the EEV, the compressor will likely to get damaged before long.

A variable-displacement compressor (VDC) changes its piston stroke length (or wobble plate angle), and consequently, the AC system will match the vehicle cooling demand. VDCs have the advantages of running continuously while responding to

cooling load variation. However, these compressors are more complex than constant displacement compressors and can be less reliable. Additionally, it promotes the system to have a tendency to cause hunting phenomenon particularly when the condensing pressure decreases excessively away from its design value which happens at low ambient temperature (e.g. at cloudy whether, in the night or in rainy time) (Changqing Tian, 2005). The hunting phenomenon is a term used to identify the erratic system behaviour or instability due to an abrupt or sudden change in refrigerant flow.

In this study, on-off cycling idea is used to control the system since it is simple and easy to manage. Since the on-off cycling has a restricted use in large equipments due to the harmful effect of cycling rates on compressor's life span, the idea of using on-off cycling in this research is different from the traditional on-off cycling. The current study presents a new control strategy by using a digital controller (a microcomputer controller) with a multiple-circuit AC system. This strategy can detect the cooling load variation and coordinates optimally the system driving actuators (compressors and blowers) to overcome the problems associated with the traditional on-off cycling. The description of the control strategy will be discussed later in Chapter 7.

2.5 Automotive air-conditioning system simulation

In 1972, Davis et al. presented a computer program for the performance analysis of separate automobile AC components as well as that for the performance simulation of the integrated AC system. Fin-and-tube type heat exchangers were used for evaporators and condensers in their model.

Kyle et al. (1993) carried out a performance simulation of an automobile AC system on the basis of the performance analysis program written for the residential heat pump model. The condenser was of fin-and-tube type and the evaporator was of plate-fin type. However, it is not clear whether they included a receiver drier in their system,

which is an important component of an automobile AC system using a thermostatic expansion valve.

Ronald et al. (1998) used a computer simulation model for steady-state operation of a mobile heat pump to study the effectiveness and performance of an automotive heat pump. Their prime concern was to improve the performance of cycle reversing using components currently employed in automotive AC systems.

Raman Ali (1999) developed a computer simulation program of the refrigeration circuit of an automotive AC system. His program included models of three different aluminium air cooled condensers and evaporators, a constant capacity reciprocating compressor, and a thermostatic expansion valve. Heat exchanger's modelling was accomplished by dividing the heat transfer area into regions associated to the phase of the refrigerant flowing in the channels. The resultant set of non-linear algebraic equations was solved by a successive substitution procedure.

Lee and Yoo (2000) analyzed each component of an R-134a automotive AC system and developed a simulation model for the whole system by combining the performance analysis programs of the separate components. Their program for the evaporator performance was based on experimental results, and the program for the condenser performance assumed no subcooling at the condenser outlet. Effects of several operational parameters over system performance were evaluated through the simulation program. They found that the agreement between the results of the simulation model for the whole system and the experimental results was within 17%.

Jabardo et al. (2003) developed a steady-state computer simulation model whereby the compressor displacement control was expressed with a simplified relationship between the suction pressure and discharge pressure from the experimental data. The model involved a micro-channel parallel flow condenser, a thermostatic

expansion valve, and a plate-fin-tube evaporator. The effects on system performance of such operational parameters as compressor rotary speed and air temperatures at the evaporator inlet and condenser inlet were simulated. They observed that the deviations between the simulated and experimental results for the cooling capacity, COP, and refrigerant mass flow rate as a function of compressor speed were within 5%. However, for the same performance parameters, as a function of the evaporator inlet air-temperature, the deviations of the simulated results with respect to the experimental ones were as high as 18%.

Tian and Li (2005) developed a mathematical model for an R-134a automotive AC system with a variable capacity compressor to simulate its steady state performance. Their model determined the effects of compressor speed, ambient temperature, and evaporator airflow rate on the evaporating pressure, condensing pressure, cooling capacity and indicated compressor power. They validated the model results on an experimental unit, reporting that the deviations between the simulated and measured parameters were within 11%.

Hosoz and Direk (2005) dealt with the performance characteristics of an R-134a automotive AC system with the feature of operating as an air-to-air heat pump. For this aim, they developed an experimental system and tested it in both AC and heat pump modes, varying the compressor speed and air temperatures at the inlets of the outdoor and indoor coils. They evaluated the performance of the integrated system in terms of cooling and heating capacities, COP, compressor discharge temperature, and the rate of exergy destroyed in each component of the system. They determined that the heat pump operation usually yielded a higher COP and a lower rate of exergy destruction per unit capacity compared to the AC operation, although it provided inadequate heating.

In addition, there are some studies carried out on experimental performance of the automotive AC systems. Rubas and Bullard (1995) presented an experimental analysis of the refrigerant circulating in an AC system and its general implications on the

coefficient of performance (COP). Lee and Loo (2000), Buck (1996), Kim et al. (2002) and Flavio et al. (2002) analyzed the performance of an AC system using different experimental methods. Ratts and Brown (2000) experimentally analyzed the effect of the R-134a refrigerant charge level on the performance of an automotive AC system. To this aim, they determined the individual component losses in an automotive AC system as a function of refrigerant charge using the second law. They found that the compressor and condenser were the components causing the largest percentage of total losses, while the evaporator and expansion device losses accounted for a smaller percentage of the total losses. Schwarz et al. (2002) studied the flow inside an accumulator of an automotive AC system, which is critical to system COP, lubrication, and safety of compressor.

Gu et al. (2003) experimentally determined the two-phase flow inside an evaporator and noticed its effect on the heat transfer performance of an evaporator. Wang and Gu (2004) measured two-phase flow inside an accumulator and its effect on the performance of automotive AC system. Kaynakli and Horuz (2003) analysed the experimental performance of an R-134a automotive AC system to find optimum operating conditions. They presented some performance parameters such as cooling capacity, compressor power, total power consumption, refrigerant mass flow rate, and COP as a function of condensing temperature, evaporator return air temperature, ambient temperature, and compressor speed.

2.6 Heat exchanger thermoeconomic optimization design

To increase the efficiency of AC system, it is necessary to improve the performance of the compressor itself and design the heat exchanger efficiently to reduce the pressure gap between the condenser and evaporator. As it is known, there are recent investigations to enhance the compressor performance and this is not the area of concern in this research. The finned-tube heat exchanger components, the condenser and evaporator, have the most potential for improvement in the design optimization of AC

systems (Susan, 2003). This motivates researchers to look deeply into the heat exchangers' design based on the maximum system efficiency COP. The task, however, can be quite complex, requiring the determination of no less than eight different finned-tube heat exchangers design interrelated parameters. In addition, there is a competing effect of increased heat transfer with increased air and refrigerant frictional pressure drop making it difficult to determine the relative goodness of a design. Therefore, the evaluation of the optimal trade-off between fluid friction and heat transfer irreversibility and the analysis of augmentation techniques to decrease frontal area at a specified thermal capacity, without causing a damaging increase in pumping power, are more significant. This leads to a thermoeconomic optimization exercise which combines economic and exergy/availability analysis.

Thermoeconomics can be considered as a new science which by connecting thermodynamics and economics provides tools to solve problems in complex energy systems that can hardly or not be solved using conventional energy analysis techniques based on the first Law of Thermodynamics (mass and energy balances). Energy (first law) analysis is still the most commonly used method in the analysis of thermal systems. The first law is concerned only with the conservation of energy, and it gives no information on how, where, and how much the system performance is degraded. Exergy analysis is a powerful tool in the design, optimization, and performance evaluation of energy systems. Identifying the main sites of exergy destruction shows the direction for potential improvements.

The concept of thermoeconomics, developed by El-Sayed and Evans (1970), in which the objective function is optimized, is subject to given economic and technical constraints. Thus, the purpose of thermoeconomics is to improve analyses of systems by introducing ways of concurrently suggesting improvements and hence thermoeconomic optimization is economic optimization in conjunction with thorough thermodynamic description of the system. Basically, vapor compression system is one of those energy systems which suffer from significant irreversibility owing to this system releasing large amounts of heat to the environment through a finite temperature difference. This heat

transfer mainly occurs in the condenser and evaporator. Therefore, both condenser and evaporator create some major irreversibility, Recep Yumnata (2002).

The technique of Entropy Generation Minimization (EGM) has been in use since the 1970's and is discussed in detail in Bejan (1982). According to Bejan & Pfister (1980), "the 'energy conservation' value of a heat transfer augmentation technique can be best measured in terms of the technique's ability to reduce the rate of entropy generation (irreversibility, exergy destruction) in the heat transfer device in which it is implemented." The central theme of the EGM method is that by minimizing entropy generation, performance is optimized. Bejan (1980, 1982 & 1996) gives many examples of situations in which EGM can be used to optimize performance; however most cases are very basic in nature and have constraints that make their application to a real world design problem impractical.

Klein & Reindl (1997) considered the effect of heat exchanger optimization in relation to an entire cycle. The work explores the optimum allocation of heat exchanger area for both the reverse Carnot and the vapor compression refrigeration cycle models and a comparison was made between using system performance and minimum entropy generation as the figure of merit. It was concluded that minimizing the total system entropy generation rate does not always result in the same design as maximizing system performance. However, Alefeld (1990) showed that COP and system entropy generation are directly related through fundamental equations. Additionally, Bejan (1996) suggests that the point of minimum system entropy generation should coincide with optimum system performance. It is believed that the discrepancies found in the Klein & Reindl's study are due to the evaporator cooling capacity not being fixed throughout the analysis.

Shiba and Bejan (2001) developed a model for optimizing geometric structure of counter flow heat exchanger which was a condenser of a vapor compression refrigeration system. The dimensionless ratio of the total power requirement (compressor and fan power) to the refrigeration load was selected as the objective function. Finally, with three degrees of freedom they performed the optimization procedure and obtained

diameter ratio of concentric tubes and the length of counter flow condenser. They also showed variations of the optimization results when the refrigeration load increased. It was described that the same results could be obtained in case of minimization of the total entropy generation of the system.

Susan (2003) optimized a set of 12 design parameters which produced the best figure of merit (maximizing the system COP or minimizing condenser entropy generation) for fixed frontal area or fixed material cost. Susan showed that isolating the condenser component and optimizing it independently by minimizing the entropy generation in the condenser component alone (also known as thermoeconomic isolation) did produce designs close in COP to those produced by using an entire system model to optimize the condenser design. The condenser saturation temperature was not taken as a controllable operational parameter in Susan's study despite of its significant effect on condenser thermoeconomic optimization as will be shown in the current study.

Massimo and Laura (2004) also investigated the design optimization of a tube-in-tube condenser of a conventional vapor compression heat pump. The inner tube diameter and saturation temperature were taken as the design variable parameters. The total annual cost involved the amortization and operating cost (depending on the overall exergy destruction rate in the system) was selected as the objective function. Massimo and Laura developed an approximate correlation to relate the local exergy destruction in the condenser to that of the entire system by a constant specified factor. This factor was obtained based on the results provided by a simulation program for conventional heat pump system for a small narrow range of the operating parameters.

CHAPTER 3

COOLING LOAD AND PROPOSED AC SYSTEM DESCRIPTION

3.1 Introduction

In Comparison with other AC systems, bus AC systems have some significantly particular features in the calculation of cooling load. Bus AC systems present challenges not normally encountered in those found in stationary AC systems, such as those used in AC systems for buildings. For example, the sun load through the windshield and side windows is much greater than that through buildings; it is almost 30% depending on the local weather solar radiation (ASHRAE, 1997). In this Chapter, a numerical computer code has been developed to calculate the cooling load variations in an intercity bus compartment (for example an intercity bus traveling from Johor Bahru to Kuala Lumpur and vice versa).

The main goal of the cooling load calculations is to determine the hourly cooling load behavior and magnitude of its fluctuations during the bus AC operation. On the basis of this hourly cooling load behavior, the proper number of units of the proposed multiple-circuit AC system can be identified.

In addition, the distribution of the temperature and relative humidity for the hourly inlet air to the AC system evaporators has been determined in this chapter for the

daytime operation. The description of the proposed AC system has also been presented in the last part of this Chapter.

The imposed cooling load on the bus compartment consists of the following parts:

- Conduction heat load through body walls and glasses.
- Solar radiation through glasses.
- Conduction heat load through the motor compartment panels.
- Heat gain from passengers.
- Heat gain from ventilation.
- Heat gain from lights.
- Heat gain from power equipment.

The cooling load components vary in magnitude over a wide range during a 24-h period. Since these cyclic changes in load components are often not in phase with each other, each component must be analyzed to establish the cooling load profile for the daytime operation. The heat balance method is more fundamental than the other methods because it invokes the first law of thermodynamics (ASHRAE, 1997). It is also more flexible because it requires fewer assumptions. Hence, this method has been chosen for this research work.

In order to commence the estimation of bus hourly cooling load profile the detailed vehicle design information and weather-data at selected design conditions are required. Generally, the following steps should be taken into account:

- a) The selection of day and month.
- b) Outside weather condition (temperature, relative humidity, and direct and diffuse solar radiation on horizontal plane).
- c) Inside design condition (temperature, relative humidity) which satisfies comfort condition for the space.
- d) Dimensions and thermal properties of material of the bus body.
- e) Occupancy data (number of passengers)

- f) Operating schedules of lighting and power equipment that contributes to the internal load.

3.2 Conduction heat load through body walls and glasses

To simplify the heat transfer calculations at the outside surface of a wall or roof, it is assumed that the sol-air temperature concept can be used. Furthermore, the using of sol-air temperature is a convenient way for heat gain calculations through surfaces, especially when the thermal storage effect is not taken into account. The automotive panels have low density-specific heat product compared with those for houses and buildings. This means that the thermal storage effect for bus cabin can be neglected with respect to the other thermal loads.

ASHRAE (1997) offers a method to calculate the heat gain through the walls, roof, and floor at steady-state condition. Assuming that the sol-air temperature represents the outdoor conditions, and that the outdoor and indoor convective heat transfer coefficients are constant at any given hour, then for a constant indoor temperature, the heat gain through a roof or wall (see Figure 3.1) is:

$$Q_{\tau} = \alpha_o A (t_{so} - t_{wo}) + \alpha_i A (t_{wi} - t_i) + \sum_{j=1}^{j=m} \frac{k}{\delta} A (t_{wo} - t_{wi}) = UA (t_{so} - t_i) \quad (3.1)$$

$$\text{Where, } U = \left[\frac{1}{\alpha_i} + \frac{1}{\alpha_o} + \sum_{j=1}^{j=m} \frac{\delta}{\kappa} \right]^{-1},$$

Q_{τ} = heat gain by conduction through a roof or wall at any given hour

A = indoor surface area of a roof or wall, m².

t_{so} = Sol-air temperature at any given hour, °C (discussed in section 3.2.1)

- t_{wo} = outside surface temperature at any given hour, °C
 t_{wi} = inside surface temperature at any given hour, °C
 t_i = inside design temperature and it is assumed 24°C (ASHRAE,1997)
 k = surface thermal conductivity, W/m.°C and it is assumed constant
 δ = a roof or wall material thickness
 α_i and α_o = indoor and outdoor heat transfer coefficients and are determined by using the correlations in Equations (3.5) and (3.6)

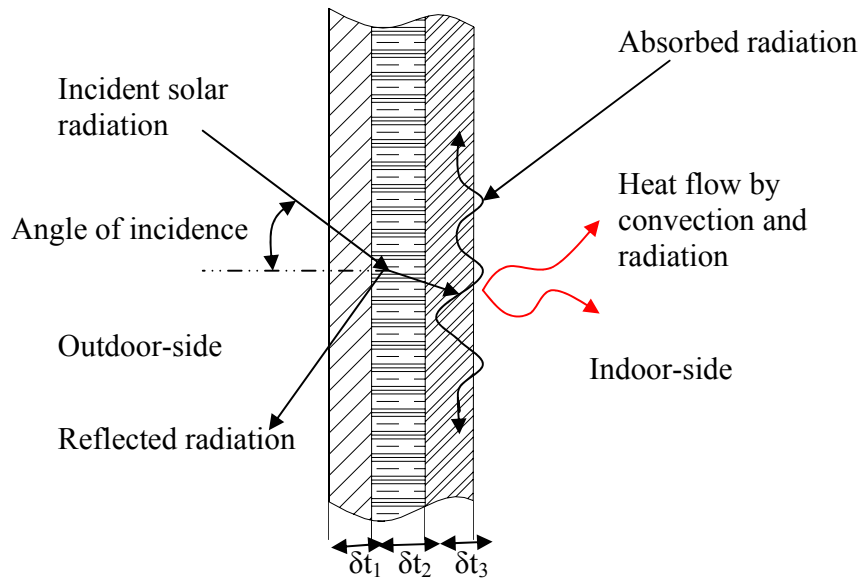


Figure 3.1 Heat balance for a sunlit opaque surface

3.2.1 Sol-air temperature

The sol-air temperature is defined as that temperature of the outdoor air which, in the absence of all radiation exchange, would give the same rate of heat entry into the surface as would exist with the actual combination of incident solar radiation, radiant energy exchange with the outdoor air. The sol-air temperature, t_{so} is given by the following expression, ASHRAE (1997):

$$t_{so} = t_o + \frac{(ab_s I_t - \varepsilon \Delta R)}{\alpha_o} \quad (3.2)$$

Where,

ab_s = surface absorptance for solar radiation (Table 3.1).

I_t = total solar radiation incident on the surface, W/m² (see section 3.3).

t_o = outdoor air dry bulb temperature at any given hour a 24-h period, °C
(Appendix A)

ε = hemispherical emittance of the surface (approximately 0.9 for non-metallic surfaces).

ΔR = the difference between the long wave radiation incident on the surface from the sky and surroundings, and the radiation emitted by a blackbody at outdoor air temperature, °K.

Pawelski (1979) used the following expression to determine the ΔR term:

$$\Delta R = \sigma \times [F_{s-sky} \times (T_o^4 - T_{sky}^4) + F_{s-sur} \times (T_o^4 - T_{sur}^4)] \quad (3.3)$$

Where,

σ = Stefan Boltzman's constant, 5.668×10^{-8} .

F_{s-sky} = view factor between the surface and the sky, ASHRAE (1997).

$$= \frac{(1 + \cos \phi)}{2}, \quad \phi \text{ is title angle of the surface, measured from the horizontal,}$$

degrees (Figure 3.2)

F_{s-sur} = view factor between the surface and surroundings, ASHRAE (1997).

$$= \frac{(1 - \cos \phi)}{2}$$

T_{sur} = temperature of surrounding objects, °K.

T_{sky} = sky temperature, °K.

T_o = outdoor air dry bulb temperature, °K

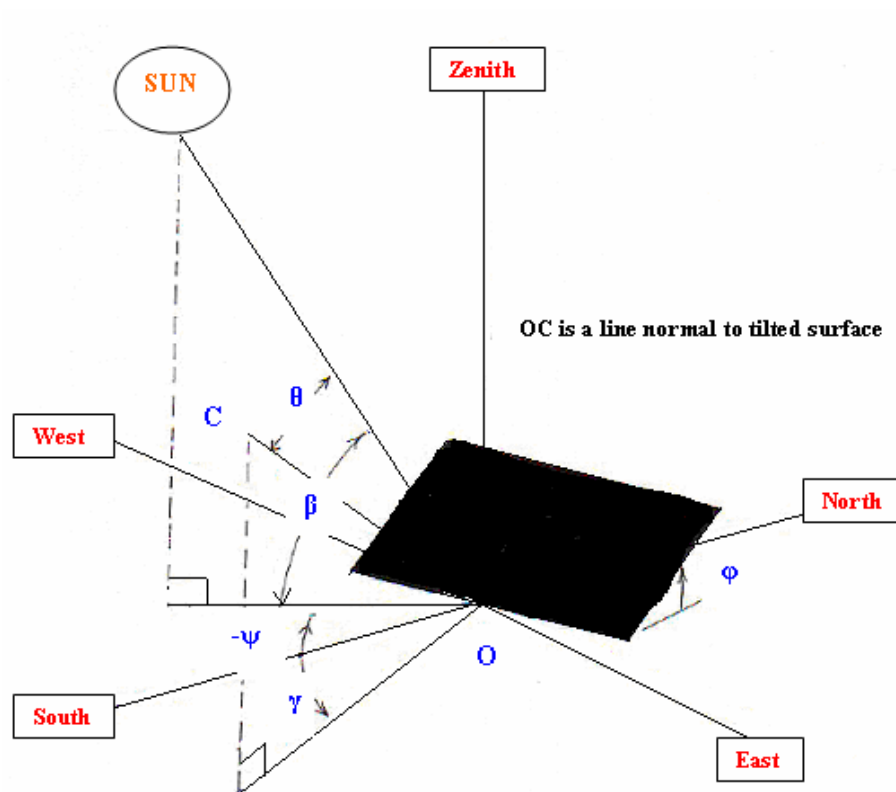


Figure 3.2 Solar angles for a tilted surface

- ϕ = Tilt angle of surface
- β = Solar altitude
- θ = Incidence angle
- γ = Surface azimuth angle
- ψ = Solar azimuth angle

During the daytime, surrounding objects absorb solar radiation and their surface temperature is higher than the ambient temperature. Pawelski (1979) assumed that T_{sur} was 10 °C above the ambient air dry bulb temperature. However, at night the temperature difference will be smaller. Thus, at night, the long wave radiation exchange between the surface and the surroundings will be neglected. For clear sky conditions, Duffie (1974) gives T_{sky} as:

$$T_{sky} = 0.0552 \times T_o^{1.5} \quad (3.4)$$

Chen et al. (1986) gives the heat transfer correlations for vertical and horizontal plates. Heat transfer coefficients are coupled by the expression that defines the Nusselt number under mixed convection (forced and natural convection) as follows:

For vertical plate,

$$Nu = 0.555 (Gr \times Pr)^{\frac{1}{4}} \left[1 + 6.26 \times \left(\frac{Re}{\sqrt{Gr}} \right)^{1.29} \right] = \frac{\alpha \times L_c}{k} \quad (3.5)$$

For horizontal plate,

$$Nu = 0.27 (Gr \times Pr)^{\frac{1}{4}} \left[1 + 4.3 \times \left(\frac{Re}{\sqrt{Gr}} \right)^{1.74} \right] = \frac{\alpha \times L_c}{k} \quad (3.6)$$

Table 3.1: Typical values of solar Absorptance for common bus construction material

Material	Solar Absorptance
Galvanized steel	0.40-0.65
Polished aluminium	0.10
Paints – blue, black	0.94- 0.97
Red, green	0.75
yellow	0.30-0.5
White	0.10-0.25

3.2.2 Determination of short wave radiation incident on a surface

The total short wave radiation incident on a terrestrial surface, I_t (W/m^2), can be expressed from ASHRAE (1997) as:

$$I_t = I_D \cos \theta + I_d + I_r \quad (3.7)$$

Where,

I_D = Direct solar radiation on a unit area normal to the solar rays, (W/m^2).

I_d = Diffuse sky radiation on a unit area of the surface, (W/m²).

I_r = Solar radiation reflected from surrounding surface and incident on a unit area of the surface, (W/m²).

θ = angle of incidence, defined as the angle between the incoming solar rays and a line normal to the surface, degrees (for $0 \leq \theta \leq 90$).

When hourly direct irradiation on a horizontal surface is known, I_D is calculated from:

$$I_D = I_{DH} / \sin \beta \quad (3.8)$$

I_{DH} = Direct solar radiation on a unit area of horizontal surface (Appendix A)

β = Solar altitude and is evaluated as follows (Iqbal, 1983).

$$\sin \beta = \sin l \sin \delta_s + \cos \delta \cos hr \cos l \quad (3.9)$$

Where,

l = Latitude of the location in degrees, positive in northern hemisphere.

δ_s = Solar declination angle, degrees is calculated from a simple expression by

Iqbal (1983):

$$\delta_s = 23.45 \times \sin \left[\frac{360 \times (d_n + 284)}{365} \right] \quad (3.10)$$

Where d_n is the day number of the year, ranging from 1 on the first day of January to 365 on the 31st. day of December. February is assumed to have 28 days. hr is the hour angle, noon zero and morning positive, is calculated from Iqbal (1983):

$$hr = \left[12 - LST - \frac{(Le - Ls)}{15} - \frac{E_t}{60} \right] \times 15 \quad (3.11)$$

Where,

LST = Local standard time, hours after midnight.

Ls = Standard longitude, negative if west of Greenwich, deg.

Le = Local longitude, negative if west of Greenwich, deg.

E_t = Equation of time in minutes as given by Iqbal (1983) as follows:

$$E_t = 0.0171 + 0.428 \cos \sigma - 7.351 \sin \sigma - 3.349 \cos 2 \sigma - 9.371 \sin 2 \sigma \quad (3.12)$$

Where σ in radians is given by: $\sigma = \frac{2 \pi \times (d_n - 1)}{365}$

The correction for daylight saving time can be made appropriately when calculating the hour angle. The angle of incidence, θ (Figure 3.2) is calculated from the following equation, for an arbitrarily oriented surface (Iqbal, 1983).

$$\begin{aligned} \cos \theta = & (\sin l \cos \phi - \cos l \sin \phi \cos \gamma) \sin \delta + (\cos l \cos \phi + \sin l \sin \phi \cos \gamma) \cos \delta \cos h \\ & + \cos \delta \sin \phi \sin \gamma \sin h \end{aligned} \quad (3.13)$$

ϕ = tilt angle of the surface, measured from the horizontal, degrees (Figure 3.2).

γ = Surface azimuth angle defined as the deviation of the normal to the surface (projected on the horizontal) with respect to the south direction, degrees (negative if west of the local meridian) (Figure 3.2).

Assuming that a surface can only “see” the sky and the ground cover and that the diffuse radiation is *isotropic* (perfectly diffused and uniform in all directions), a simple equation to calculate the diffuse sky radiation falling on any surface area is given by the following expression, ASHRAE (1997): I_{dh} is the sky diffuse radiation on a unit area of horizontal surface (Appendix A).

$$I_d = I_{dh} F_{ss} \quad (3.14)$$

The ground-reflected isotropic diffuse radiation incident on a unit area of a surface, I_r , may be estimated using the procedure described by Iqbal (1983) and is given by ASHRAE (1997):

$$I_r = I_D \rho_g F_{sg} \quad (3.15)$$

Where ρ_g is the reflectness of the foreground (Table 3.2) and F_{sg} is the view factor between the surface and the ground and is given by the following expression (ASHRAE, 1997):

$$F_{sg} = 1 - F_{ss} \quad (3.16)$$

Table 3.2: Typical values of solar reflectance for different types of ground covers

Ground cover	Solar reflectance
New concrete	0.32
Old concrete	0.23
Green grass	0.25
Crushed rock	0.20
Asphalt	0.10

3.3 Heat gain through glazing surfaces

The heat balance for a sunlit transport glass is shown in Figure 3.3. The total heat admission into the space can be written as (ASHRAE, 1997):

Total heat gain through glasses = transmitted radiation + fraction of absorbed radiation which flows inwards + heat gain due to the difference between the outdoor and indoor air temperatures alone.

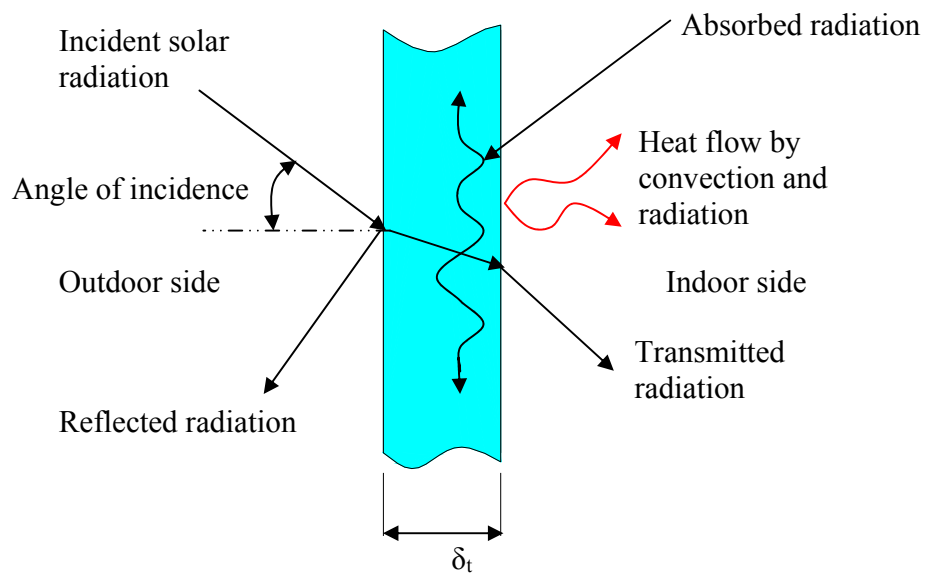


Figure 3.3 Heat balance for a sunlit transparent surface

3.3.1 Transmitted radiation

At any hour, when the window is sunlit, the direct component of transmitted radiation ITD , per unit fenestration area is computed from the following equation, ASHRAE (1997):

$$ITD = I_{DN} \cos \theta \sum_{j=0}^{j=5} t_j (\cos \theta)^j \quad (3.17)$$

The transmitted diffuse radiation ITd , per unit area of glazing as calculated by ASHRAE (1997):

$$ITd = (I_d + I_r) \times 2 \sum_{j=0}^{j=5} \frac{t_j}{(j+2)} \quad (3.18)$$

3.3.2 Fraction of absorbed radiation which flows inwards

The absorbed direct radiation, IAD for a sunlit window is obtained from the following expression, ASHRAE (1997):

$$IAD = I_{DN} \cos \theta \sum_{j=0}^{j=5} a_j (\cos \theta)^j \quad (3.19)$$

And the absorbed diffuse radiation IAd is given by ASHRAE (1997) as:

$$IAd = (I_d + I_r) \times 2 \sum_{j=0}^{j=5} \frac{a_j}{(j+2)} \quad (3.20)$$

The values of t_j and a_j as given in Table 3.3 are for the ASHRAE (1997) standard reference glass.

Table 3.3: Typical values of solar reflectance for different types of ground covers

j	a _j	t _j
0	0.011	-0.008
1	0.776	2.712
2	-3.946	-0.620
3	8.578	-7.073
4	-8.381	9.759
5	3.011	-3.899

3.3.3 Heat gain due to the difference between the outdoor and indoor air temperatures alone

The conduction gain through the fenestration due to air-to-air temperature difference, $C_{g\tau}$ is computed by assuming that the glass plate has negligible heat capacitance. Thus,

$$C_{g\tau} = A_g U_g (t_{a,\tau} - t_i) \quad (3.21)$$

A_g is the glass area, U_g is the overall heat transfer coefficient for the glass, t_i is the reference space temperature or inside design temperature, and $t_{a,\tau}$ is the outdoor air dry bulb temperature at any given hour.

3.4 Heat conduction through the motor compartment

High temperature surfaces such as the exhaust system and the high temperature of the air within the motor compartment can cause harmful levels of superficial temperatures in the cabin. So the motor can be configured as one more heat source acting in the cabin. The superficial temperature of the panels near the high temperature

surface of the engine t_{sc} is almost around the range of 50 to 60°C, Kohler et al. (1990).

The thermal load of motor compartment Q_{mc} through the bus cabin can be expressed as:

$$Q_{mc} = \alpha_o A_{sc} (t_{sc} - t_i) + \alpha_r A_{sc} (t_{sc} - t_i) \quad (3.22)$$

Where

A_{sc} = surface area of the hot surface adjacent to the motor compartment, m².

α_r = linear radiative heat transfer coefficient, W/(m²·K),

$$\left[\alpha_r = \sigma \varepsilon A_{sc} (t_{sc} + t_i) (t_{sc}^2 + t_i^2) \right]$$

3.5 Heat gain from ventilation

Fresh air is introduced into the return air-stream at the evaporator entrance. Fresh air is usually taken from a grilled or louvered opening in the end or side of the evaporator box configuration. The amount of mechanical outdoor air ventilation is usually expressed as L/s per passenger on a full load continuous basis. In general, the ventilation air rate of 5 L/s per passenger is recommended in a bus (ASHRAE, 2000). This amounts to 225 L/s in an average of forty-five passengers in a large-sized intercity bus (blowers capacity 4500 m³/hr), which is approximately 20.0 percent of the total air circulation volume. The infiltration thermal load can be ignored with respect to the ventilation load owing to the sealed construction of the windows and the door. The instantaneous ventilation load Q_v can be expressed as follows:

$$Q_v = \frac{\dot{V}_{air}}{3600 \times v_o} [h_o - h_i] \times SCHI \quad (3.23)$$

V_{air}° is a fresh air flow rate, $SCHI$ is defined as the ratio of ventilation load at hour τ to the maximum ventilation load, h_o, h_i are the specific enthalpies for air at outside and inside conditions, and v_o is specific volume at outside conditions.

3.6 Passenger heat load

For a normal percentage of men, women, and children, an individual cooling load of 115 W is given for people seated at rest. For driving heavy vehicles, an individual cooling load of 375 W is given (ASHRAE, 1997). The instantaneous cooling load for passenger can be expressed as:

$$Q_p = [375 + (N_p \times 115)] \times SCHP \quad (3.24)$$

N_p is the number of passengers and $SCHP$ is defined as the ratio of the actual number of passengers in the space at time τ to the maximum possible number of them.

3.7 Heat gain from lights

Generally, the instantaneous rate of heat gain from electric lighting system in W can be computed from:

$$Q_L = (\text{light intensity (W/m}^2) \times A_f \times NL) \times SCHL \quad (3.25)$$

A_f is the floor area, NL is the number of lights and $SCHL$ is the ratio of average wattage in use between hour τ and the maximum used wattage in the space.

3.8 Heat gain from power equipment

The fans and their electric motors are also heat sources. For motors and fans inside the conditioned space the appropriate equation is:

$$Q_F = \left(\frac{\text{rating power}}{\% \text{ motor efficiency}} \right) \times SCHE \quad (3.26)$$

SCHE is defined as the ratio of equipment heat load at hour τ to the maximum equipment heat load.

3.9 Passenger compartment climate characteristics

In the following sections, the governing equations which will be used to determine hourly inlet air temperature and relative humidity (the entering air conditions to the AC system evaporators) will be presented. The main purpose of calculation of the inlet air conditions to the AC system is to determine the air temperature and humidity at the evaporator entrance. That will help in the experimental tests in Chapter 4. In an intercity bus AC system, the inlet evaporator air conditions are the product of mixing the returning air conditions (exits from the passenger cabin) with the fresh air. Therefore, the returning air properties should be first identified. In the present study, the variations of the temperature and relative humidity are calculated using lumped system approach. It is assumed that the temperature and humidity inside the passenger compartment is spatially uniform at any instant of time during the process. This assumption implies perfect mixing of the air inside the compartment at all time.

The flow of energy and air in and out of the passenger compartment are therefore described by three coupled equations which are based on:

- Dry air mass balance
- Vapour mass balance
- Air energy balance

The steady-state temperature and humidity inside the control volume that encompasses the entire vehicle are calculated from these equations.

3.9.1 Dry air and vapour mass balance equations for passenger's cabin

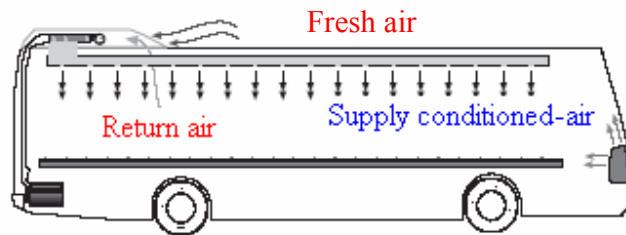


Figure 3.4 The air vents arrangement in an intercity bus air-conditioning system

Air enters the vehicle from two sources, infiltration (can be neglected in intercity bus as mentioned above) and the supply conditioned air, $\dot{m}_{a,S}$. Air exits the passenger space by return air vents $\dot{m}_{a,R}$ (see Figure 3.4). The air entering and exiting the vehicle carries with it a certain amount of moisture. While the moisture enters the vehicle through the conditioned air, moisture is also added to the system by passenger's perspiration and respiration. These sources provide the basis for mass balance of both dry air and vapour. As aforementioned in section 3.5, the recommended value for the ventilation rate is 20.0 % of the total air supplied. Therefore, the dry mass balance can be written as follows:

$$0.8 \times \dot{m}_{a,S} = \dot{m}_{a,R} \quad (3.27)$$

Assuming the specific volume for the supplied air is equal to that of the return air.

For vapour mass balance:

$$(\dot{m}_a w)_S + \dot{m}_{v,passenger} = (\dot{m}_a w)_R \quad (3.28)$$

Where \dot{m}_a is the dry air mass (kg/s) within the passenger compartment, W is the humidity ratio, and $\dot{m}_{v,passenger}$ is the vapour mass flow rate (kg/s) added to the interior air of the vehicle by the passengers. Although the air flow from the air registers can be controlled by the passengers, this analysis is only concerned when the AC system is turned on at its maximum flow rate. The vapour mass flow rate, $\dot{m}_{v,passenger}$, can be determined using (ASHRAE, 1997) as follows:

$$\dot{m}_{v,passenger} = \dot{m}_{res} + \dot{m}_{sw} + \dot{m}_{diff} \quad (3.29)$$

\dot{m}_{res} is the respiration rate under normal circumstances, and it is primarily a function of metabolic rate M , which is expressed empirically as follows (Fanger, 1970),

$$\dot{m}_{res} = 2.58 \times 10^{-6} \times M \quad (3.30)$$

The amount of metabolic heat production is related to several factors including height, weight, and activity being pursued. Tabulated values are provided by ASHRAE (1997) for the metabolism per square meter of skin surface area for average male performing different activities (Appendix B). In this study, passengers are defined as either resting quietly or driving. This produces metabolic rates of 58.2 W/m² and 87.3 W/m², respectively. The rate of regulatory sweat \dot{m}_{sw} depends on the difference between the water vapour pressure at the skin and in the ambient environment, and the amount of moisture on the skin:

$$\dot{m}_{sw} = \frac{0.006 \times (P_{sk,s} - P_a)}{h_{fg} \times (R_{e,cl} + 1/(f_{cl} h_e))} \quad (3.31)$$

Where

P_a = water vapour pressure in ambient air, kPa.

$P_{sk,s}$ = water vapour pressure at skin, normally assumed to be that of saturated water vapour at skin temperature (Appendix B), kPa.

h_e = evaporative heat transfer coefficient, W/(m².kPa) (Appendix B)

$$\begin{aligned}
 R_{e,cl} &= \text{evaporative heat transfer resistance of clothing layer,} \\
 & \quad (\text{m}^2 \cdot \text{kPa}) / \text{W} \quad (R_{e,cl} = 1 / h_e) \\
 h_{fg} &= \text{heat of vaporization of water} = 2430 \text{ kJ/kg at } 30^\circ\text{C} \\
 f_{cl} &= \text{clothing area factor, (Appendix B)}
 \end{aligned}$$

It is assumed that all sweat generated is evaporated, (Fanger, 1972). The rate of water vapour diffusion from the skin surface \dot{m}_{diff} is obtained by first calculating the diffusive heat loss \dot{E}_{diff} (Appendix B) and then dividing by the heat of vaporization of water λ at the skin temperature, $\dot{m}_{diff} = \frac{\dot{E}_{diff}}{h_{fg}}$.

3.9.2 Air energy balance equation for passenger cabin

The energy balance equation is derived using the first law of thermodynamics in rate form. It is assumed that the air kinetic and potential energies are negligible in this lumped analysis. The pressure inside the passenger's compartment is essentially constant. Therefore, the general energy balance rate equation reduces to the following form.

$$\dot{Q} = \sum_{out} (\dot{m}_a i) - \sum_{in} (\dot{m}_a i) = \left(\dot{m}_a i \right)_R - \left(\dot{m}_a i \right)_S \quad (3.32)$$

The heat loads on the control volume come from three main sources. They are solar radiation transmitted through windows, conduction/convection towards the cabin, and heat released from passengers, blowers' motors, and lights. Q is the instantaneous cooling load at a specified hour of the day time imposed on the passengers' compartment. To calculate the energy carried by conditioned and exit air from the cabin, a curve-fitting equation is adopted to evaluate the specific enthalpy i for an air-vapour mixture at temperature t ($^\circ\text{C}$) and humidity ratio w on the basis of a unit mass of dry air (ASHRAE, 1997),

$$i = 1.006 \times t + w \times (2501.0 + 1.805 \times t) \quad (3.33)$$

With the knowledge of the conditioned air temperature and humidity ratio at the air duct outlet registers and by plugging Equations (3.27), (3.28), and (3.33) back into Equation (3.32), the psychometric properties of the returning air (temperature and humidity ratio) can be determined.

3.9.3 Determination of inlet air conditions to the AC system

As abovementioned, the returning air from the passenger cabin is mixed with the outside air (fresh air) at the evaporator entrance; therefore, the air conditions entering the AC system are changed from the return air stream. The mixing process is schematized in Figure 3.5.

To determine the inlet air temperature and relative humidity to the air-conditioner, the heat and mass balance for the AC system should be performed first. From fundamental principles of mixing process for two moist streams (assuming adiabatic mixing), the heat and mass balance can be expressed as follows:

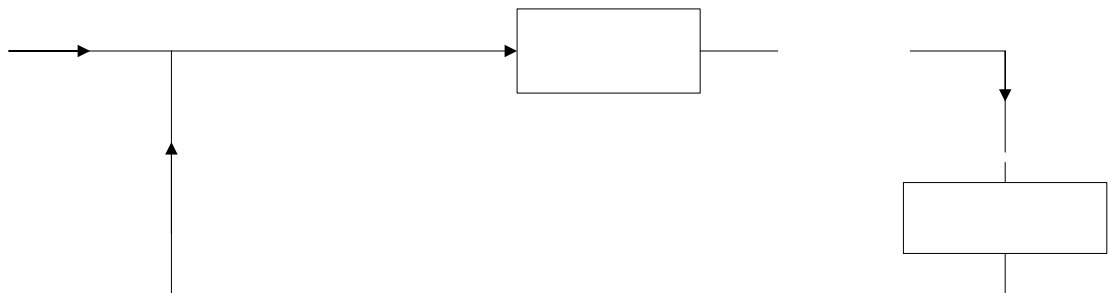


Figure 3.5 Schematic flow diagram for mixing air process

The heat balance equation is:

$$\left(\dot{m}_a i\right)_R + \left(\dot{m}_a i\right)_O = \left(\dot{m}_a i\right)_{in} \quad (3.34)$$

For dry mass balance,

$$\dot{m}_{a,R} + \dot{m}_{a,O} = \dot{m}_{a,in} = \dot{m}_{a,S} \quad (3.35)$$

While the vapour mass balance is:

$$\left(\dot{m}_a w\right)_R + \left(\dot{m}_a w\right)_O = \left(\dot{m}_a w\right)_{in} \quad (3.36)$$

By knowing the weather data for the typical design day and obtaining the values of the temperature and relative humidity profile for return air the inlet air psychometric properties to the air conditioner can be determined.

3.10 Model technique and validation

All the above equations and data tables are written in a computer code using Microsoft Visual Basic. The main purpose of the computer model is to create the graphical distribution of the cooling load imposed on the bus cabin at selected day and month in a year. In addition, the model is able to calculate hourly air temperature and humidity distribution inside the passenger cabin and inlet to the AC system evaporator. The computer model is featured by a graphical user interface, with freedom in choice of the selected design typical day and bus size. The computer code interface is presented in Appendix C.

The accuracy of a computer model can be tested by comparing program predictions with measured thermal energy consumption in a bus compartment. However, close monitoring of a bus thermal energy consumption over an extended period of time can be time and money consuming. For the unavailable measured consumption data,

another technique based on inter-model validation as described by Zaheer-Uddin et al. (1989) will be utilized. In this methodology, the program by Mohd Senawi (1992) is selected as a reference code after modifications to fit the bus cooling load calculation, SHEAP [*Simplified Hourly Energy Analysis package*].

To validate the presented simulation model, tests were carried out for a large intercity bus AC system with 28 kW cooling capacity and 45 passengers' seating capacity for a selected typical design day in March and April. The geometrical configuration and material construction of this bus are presented in Tables 3.4 to 3.7. This bus is considered the case study which serves as a reference point for the computer model validation and developing the new multiple-circuit AC system. As seen from Table 3.8, there is relative agreement between the presented and reference model predictions with minimum and maximum deviations of -13.08 % to +14.23%, respectively. It is believed that these discrepancies came from using different methodologies for cooling load calculations. The reference model used weighting factor method while the current work uses heat balance method. Although the maximum and minimum deviations are quite large between the two models, the cooling load trends of both models are quite similar as shown in Figure 3.6.

As aforementioned, the main purpose of the presented model is to predict the behaviour of the hourly cooling load variations and that is to determine the proper number of circuits to be used in the proposed AC system. Therefore, in light of this comparison, the present model is able to predict the hourly trend of the cooling load imposed on the passenger's cabin of bus.

Table 3.4: Geometrical configuration for the case study

Side	Dimension, m	Side	Dimension, m
Right and right-sides		Front and back-sides	
Bus length	7.12	Bus width	2.11
Bus height	3.17	Height	3.16
Glass length	4.38	Glass Width	2.0
Glass height	0.81	Glass height	2.1
Door height	1.73	Floor-side	
Door width	0.61	Length	6.25
Roof-side		Width	1.98
Length	7.12		
Width	2.18		

Table 3.5: Wall construction for the case study

Wall material	Thickness, mm	Thermal Conductivity, W/m.°C
Steel	6	43
Rubber	2.2	0.15
Glass wool	50	0.04
Fabric	5	0.064
Aluminium coated	4.6	210

Table 3.6: Roof construction for the case study

Roof material	Thickness, mm	Thermal Conductivity, W/m.°C
Steel	1	14.9
Air space	350	0.375
Rubber	2.5	0.15
Glass wool	30	0.04
Aluminium coated	1.5	177

Table 3.7: Floor construction for the case study

Floor material	Thickness, mm	Thermal Conductivity, W/m.°C
Steel	3	14.9
Ply wood	15	0.14
Fabric	40	0.064

Table 3.8: The comparison between the developed and the reference model for hourly cooling loads calculations

Day hours	Present model predictions for bus cooling load, kW	Reference model predictions for bus cooling load, kW	Difference (%)
1	5.88	5.76	+2.00
2	5.80	5.16	+11.00
3	5.60	5.14	+8.21
4	5.45	5.10	+6.42
5	5.30	4.97	+6.23
6	5.10	5.31	-4.20
7	9.52	9.41	+1.20
8	12.90	12.60	+2.00
9	15.40	17.00	-10.58
10	19.60	21.10	-7.47
11	23.20	26.30	-13.08
12	23.50	24.10	-2.36
13	24.60	26.60	-8.14
14	23.80	25.40	-6.87
15	23.20	25.10	-7.93
16	21.30	21.20	+0.42
17	17.40	19.50	-12.28
18	11.80	13.20	-11.95
19	11.50	12.80	-11.73
20	10.90	9.37	+14.22
21	10.60	9.13	+14.23
22	10.10	8.67	+13.94
23	9.24	8.28	+10.38
24	8.68	7.71	+11.20

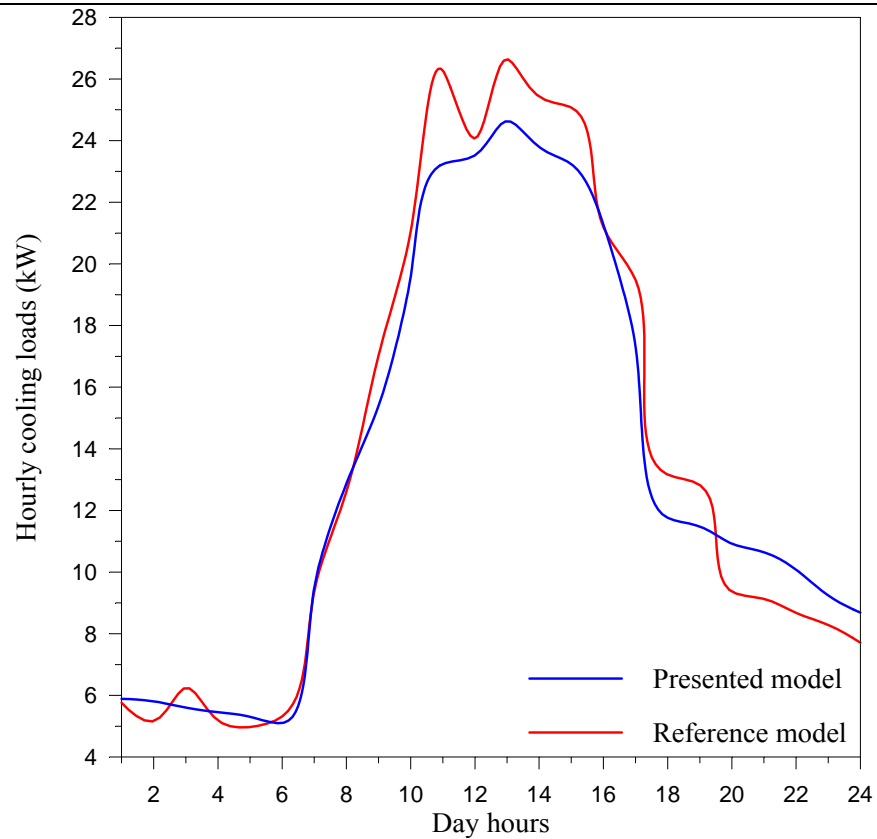


Figure 3.6 Hourly cooling load profiles of the present and reference models

3.11 Case study

As mentioned in section 3.10, an intercity bus AC system with 28 kW cooling capacity is selected as the case study. The conditioned air temperature and relative humidity at outlet of air duct register is 16°C, and 95% respectively. By the input of data to the computer code such as the bus walls and window's glasses areas and their material properties, and the typical design day, the bus hourly cooling load and evaporator inlet air properties are determined. The results for six typical days are shown in Figures 3.7 to 3.9.

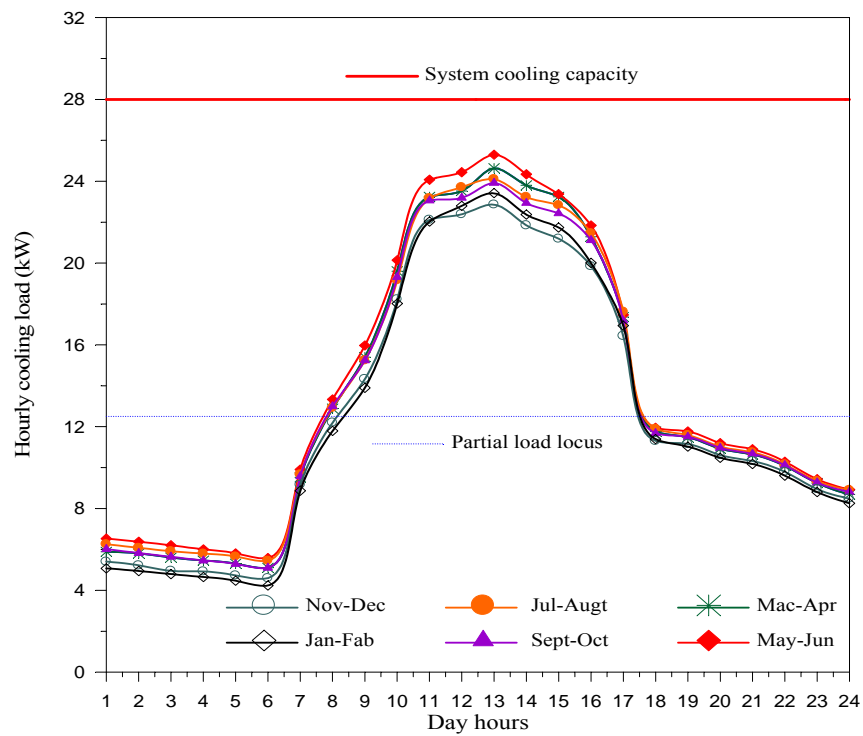


Figure 3.7 Hourly cooling load distribution at different typical day times

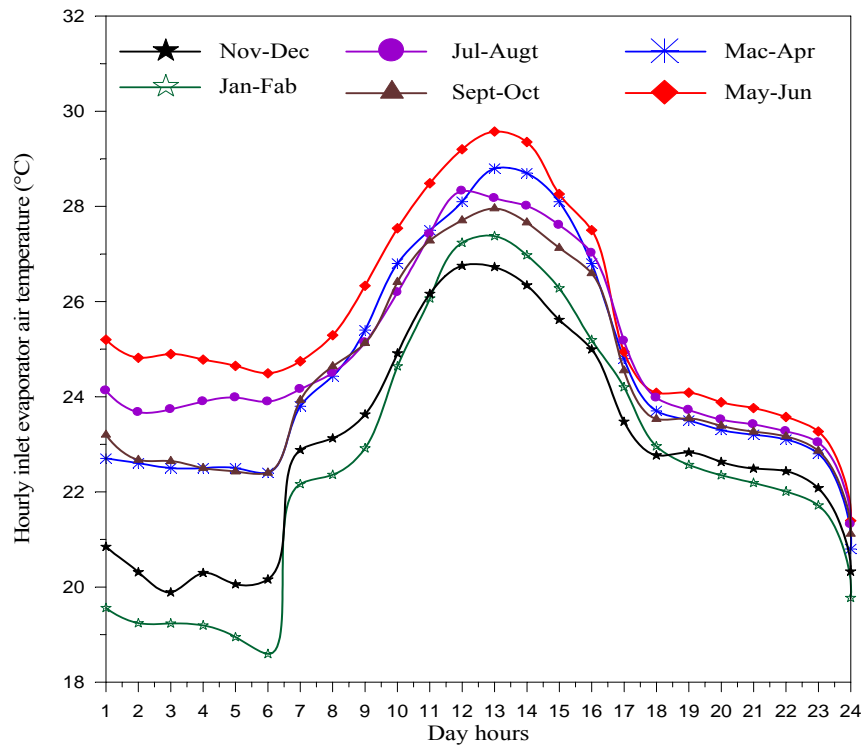


Figure 3.8 Variations of inlet air temperature to bus air-conditioning system along day times

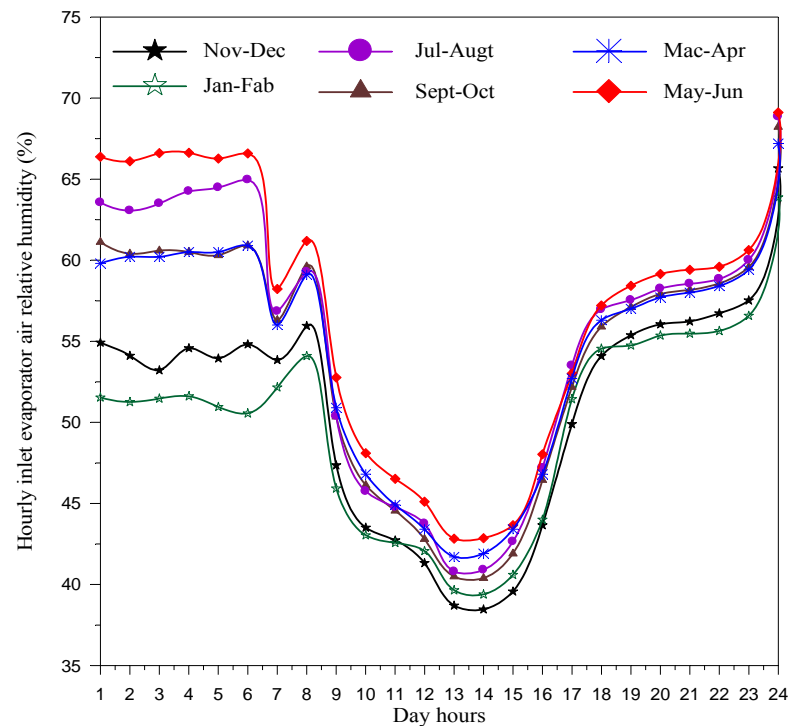


Figure 3.9 Variations of inlet air relative humidity to bus air-conditioning system along day times

3.12 Design's philosophy of the Proposed air-conditioning system

The schematic diagram of the existing AC system is given in Chapter 1 and it is repeated here in Figure 3.10 to highlight the differences between the structure of the existing AC and that of the proposed one.

Referring to Figure 3.7, it can be observed that the locus of the partial load (from 1 am to 7 am and from 6 pm to 12.00 pm) almost approaches 45 % of the system cooling capacity all year round. That means during partial loads, the bus AC system inevitably wastes unnecessary energy as a result of the AC system operation at maximum capacity. Therefore, the multiple-circuit approach is very practical from the energy saving point-

of-view. The principle of the multiple-circuit approach is to split the whole system into two small units, each unit is driven by a separate compressor e.g. one compressor capacity has 0.45 of the total system capacity and the other compressor for the reminder system capacity. However, for the sake of control simplicity and flexibility, it is suggested to split the whole system into two identical units (unit A and unit B, for example). Furthermore, using two identical units proves to be beneficial if one system becomes inoperative, the other system can rather hold the load until repairs can be performed.

Figure 3.11 shows the schematic diagram of the newly proposed AC system. The single evaporator is divided equally into separate “face-to-face” sections, so the half section of one evaporator is connected together with the half section of the other. Therefore, the proposed bus AC system is called a multiple-circuit AC system with face-to-face evaporator control. The two-stage condenser is also divided into two separate condensers where each unit has its own condenser.

To make the system respond automatically to the cooling load variation, an organizer or controller should govern how many compressors will be on service (one or two compressors work together). As mentioned in Chapter 1, the existing bus AC system contains 12 blowers; this can be exploited as another control actuator besides the number of compressors to enable the system to cope with the cooling load variations. The selection of optimum number of evaporator blowers at partial-load conditions is discussed in Appendix F. Therefore, the newly proposed AC system has now three different modes of operation.

- (i) Both units operate together, mode I.
- (ii) One unit idles and the other unit operates with all evaporator blowers running at full speed-operation, mode II.
- (iii) Mode II but with only partial capacity for the evaporator blowers running at full speed-operation, mode III.

It is obvious from the previous paragraph that the proposed AC system is able to operate in three different modes. Now, the question which may be raised is: what is the proper operating mode of the proposed system which makes the system perform efficiently in terms of energy saving and passenger's thermal comfort? The answer to this question will be elaborated in Chapter 7. The next paragraph describes the refrigerant flow and explains how the AC system works.

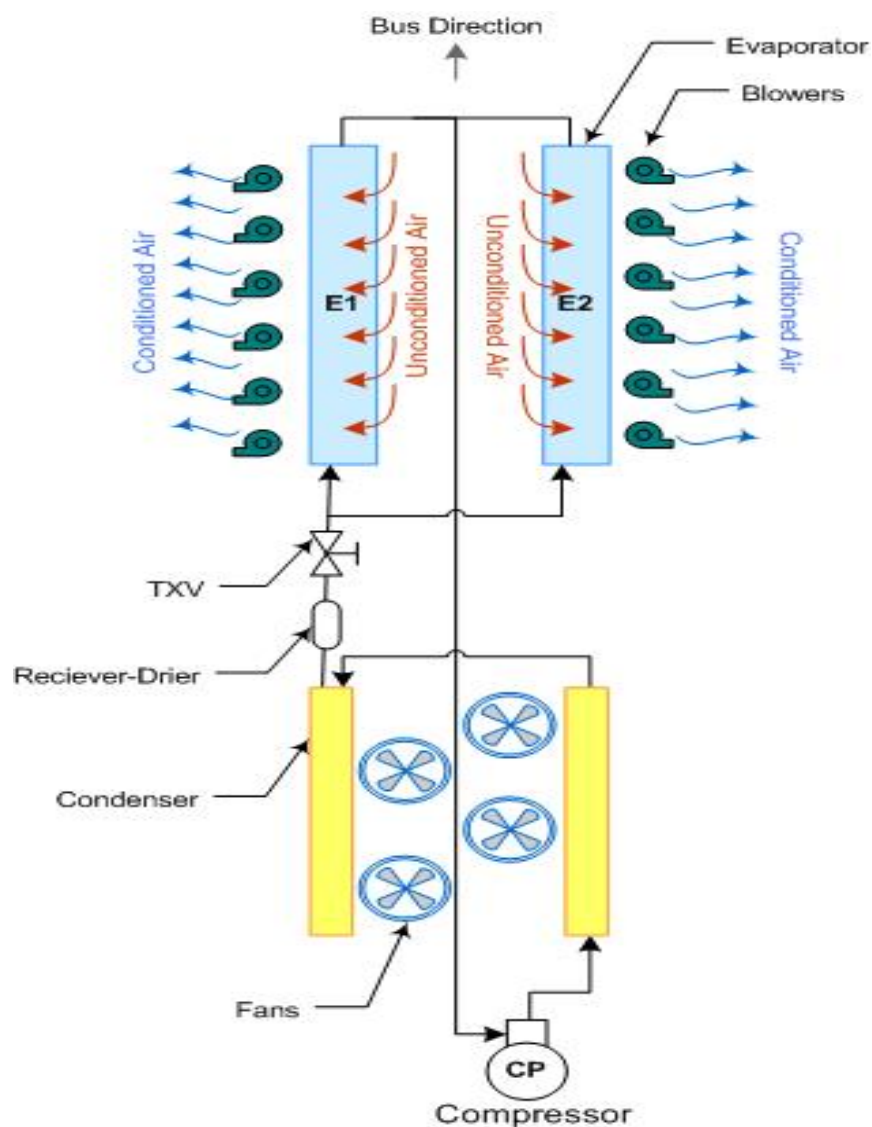


Figure 3.10 Schematic diagram for the conventional bus AC system

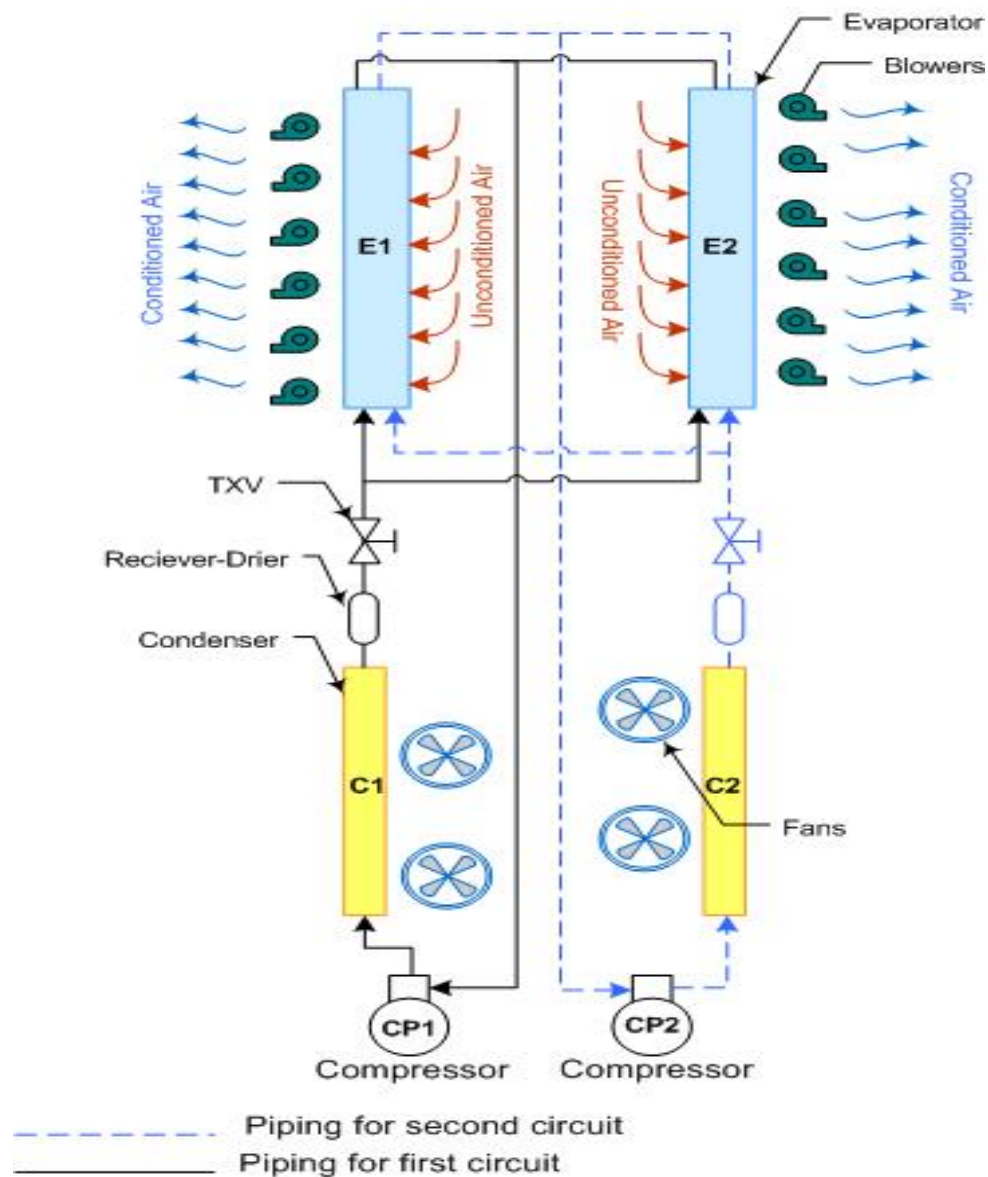


Figure 3.11 Schematic diagram for the proposed bus AC system

In the first mode of operation the two units work simultaneously. The hot pressurized gas is pumped from compressor A or B and passes via the discharge line to the individual air-cooled condenser of each unit. The refrigerant vapor is condensed into subcooled liquid and then it is stored in the unit receiver-drier. The refrigerant liquid is expanded in the unit's thermostatic expansion valve (TXV) to decrease the refrigerant temperature and pressure. The expanded refrigerant liquid is split into branches in order

to feed only the half part of each of the two evaporators. Therefore, each evaporator is fully supplied by the refrigerant liquid through the two units simultaneously. Then the refrigerant is vaporized in the evaporators by absorbing the thermal load from the non-conditioned air. This air is induced by the blowers to pass across the evaporators and then supplied to the two passenger rows inside the bus cabin via air ducts. The two evaporators are serviced by 12 centrifugal blowers; each evaporator has six blowers. Eventually, each half part of the evaporator discharges the vaporized refrigerant and it is collected together in one pipe and goes back to the unit compressor to complete the refrigerant cycle.

In the case of the second or third mode, one unit is idle and the other operates. However, the two passenger rows are still provided with the conditioned air since the two evaporators are supplied by the refrigerant liquid from the operated unit. This is the main benefit of using face-to-face evaporator control approach.

3.13 Conclusion

A mathematical simulation model has been developed to calculate the cooling loads in passenger's compartment of an intercity bus in tropical countries. The computer model has a capability to calculate the hourly cooling load imposed on the bus for any typical design day of the year. In addition, the model is able to determine the hourly inlet evaporator air conditions (temperature and humidity). The model is featured with a graphical user interface, freedom in choice of the typical design day of the six selected days of the year, and latitude. There is no restriction on area of each side for the bus glazed area, and number of passengers.

The validation of the model has been accomplished by comparing the output results of the model with the reference model results. It was found that there is quite an agreement between the presented and reference model predictions with minimum and

maximum deviations of -13.08 % to +14.23%, respectively. Although the maximum and minimum deviations are quite large between the two models, the cooling load trends of both models are quite similar.

CHAPTER 4

EXPERIMENTAL SET-UP AND RESULTS

4.1 Introduction

Proper experimental set-up is necessary before conducting actual experiments in order to achieve good results. In this chapter, the experimental set-up and settings for each component are described in detail. Operations of essential components are also mentioned. All instruments used in the experimental rig and the data acquisition DAQ system are discussed in detail. The physical quantities which act as a figure-of-merit to gauge the performance of the system are also discussed in this chapter. The experimental procedure is also described. The analytical model to evaluate the passenger's thermal comfort using Fanger (1972) method and thermodynamic analysis of the experimental results are also presented in this Chapter. In this study, the experimental test runs are categorized into two main groups. The purpose of the first group is to verify the theoretical model of the whole system simulation (discussed in detail in Chapter 6) while the purpose of the second group is to design the proper control algorithm for the automatic controller of the proposed system which is demonstrated in Chapter 7.

4.2 Description of experimental set-up

The experimental set-up shown in Figures 4.1 and 4.2 is mainly made up of original components from a bus AC system, arranged in such a way to emulate that of an actual bus. As aforementioned in Chapter 3, this newly developed system consists of two units, A and B. The 2-unit arrangements are displayed in Figures 4.1 and 4.2. Both the evaporator and condenser were maintained in their original plastic casing and mounted above the simulated passengers' compartment to simulate the actual bus AC system installation.

In order to simulate the cooling load imposed on the passengers' compartment, an electric heater was immersed in the main air duct upstream to the evaporators. The evaporator inlet air temperature was attained through the use of the electric heater controller to obtain the sensible cooling load while the latent load was achieved by mixing streams of external air with that of cooled air from the evaporator, as shown in Figures 4.1 or 4.2. In addition, four incandescent lamps of 400 W were installed inside the simulated passenger cabin conformed to ASHRAE Standard 16-61 (1961) in order to represent the relative amount of the passengers' radiant heat losses occurred in the actual bus cabin.

Motors for both the evaporator blowers and condenser fans motors were energized by a direct current power source with voltage and frequency adaptors to justify the actual power source of 24 volt with DC current for the blowers and fans motors. The reason for this is the evaporator and condenser's fan motors in the real bus AC system are driven electrically by the bus battery of 24 volts. Flexible rubber hoses were used to connect the evaporator and condenser with the compressor.

The air ducts were insulated by polyurethane foam with a thickness of 5 cm. The refrigerant lines of the system were made from copper tubing and insulated by elastomeric material. Temperature, pressure, and mass flow rate were measured at locations indicated in Figures 4.1 and 4.2. The refrigerant and air temperatures at various points of the system were detected by thermocouples. The thermocouples for the refrigerant temperatures were inserted inside the copper tubes.

The dry air bulb temperature and relative humidity of the air stream at the inlet and outlet of the evaporator were measured. The interior surface temperatures of the simulated passenger cabin were measured by attaching seven thermocouples to the interior cabin sides as shown in Figures 4.1 or 4.2. The pressures at various points of the refrigerant circuit were measured by pressure gauges. The refrigerant mass flow rate was measured using a refrigerant flow meter for R-134a. The detailed description of these instruments is presented in the following sections. The air mass flow rate passing over the evaporator was determined by measuring the average air velocity in the main air duct using an anemometer. The density of the air at the evaporator inlet was determined with the help of the dry temperature and relative humidity measurements and evaluating them in the continuity equation along with the flow area of the duct.

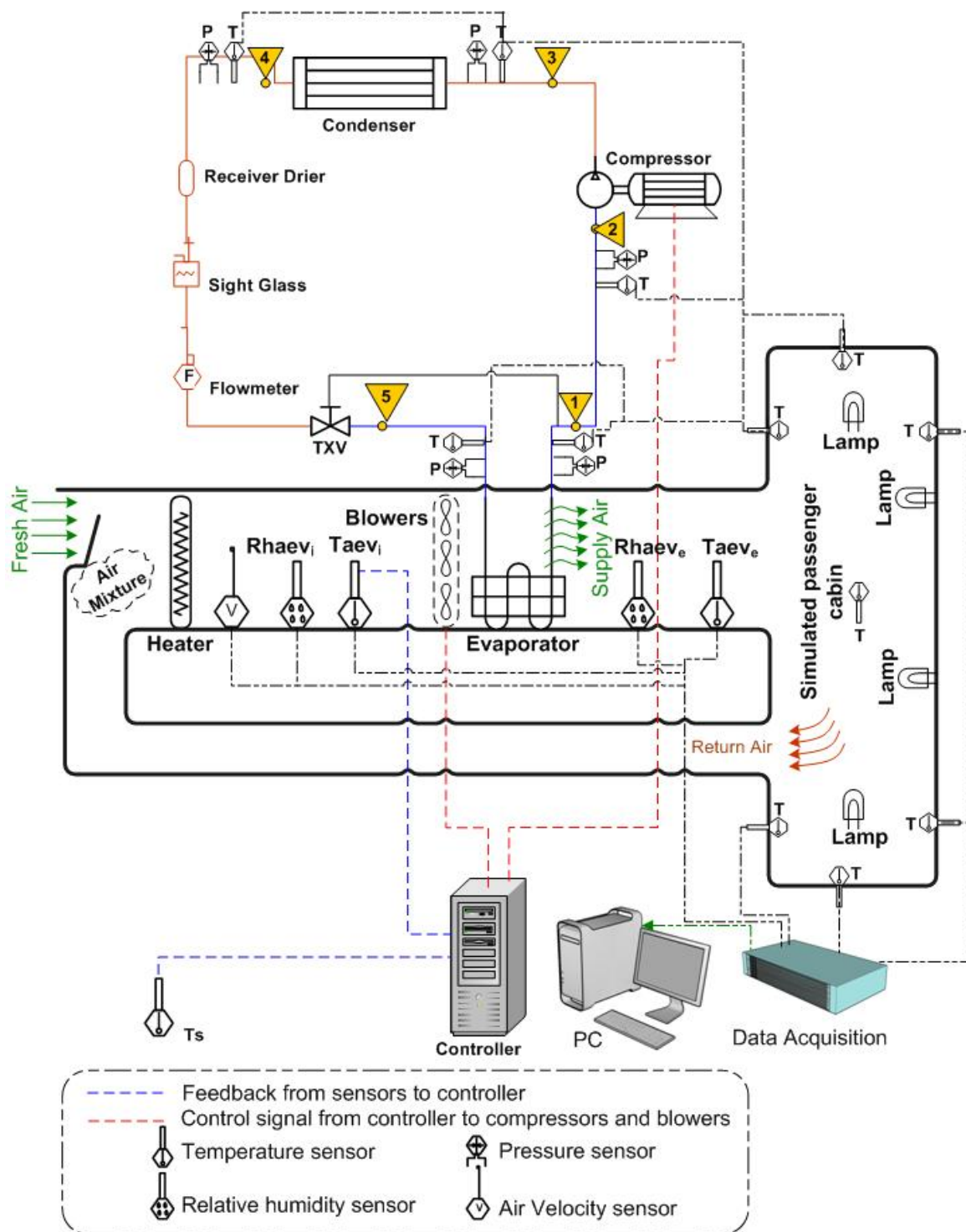


Figure 4.1 The apparatus schematic diagram of unit A

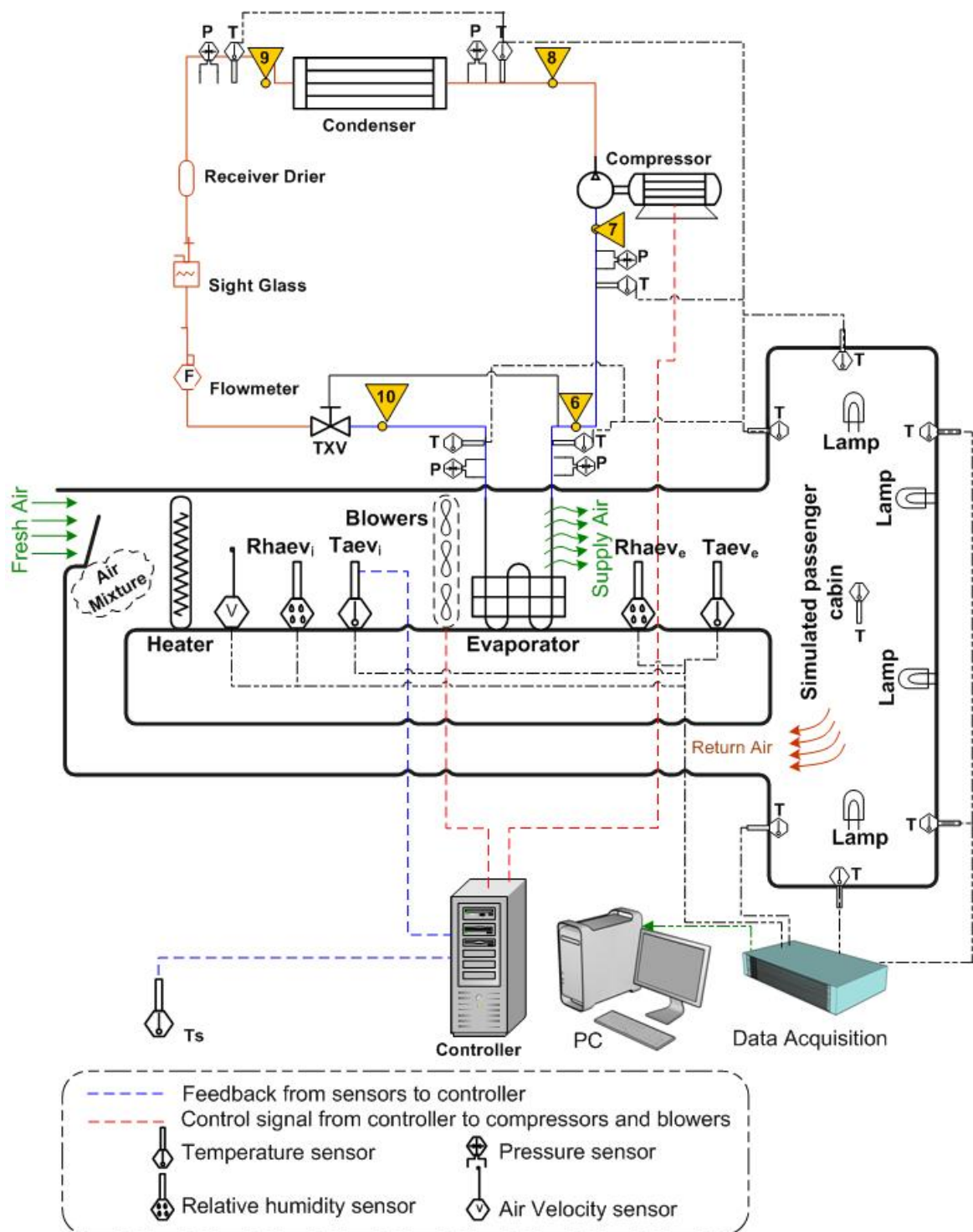


Figure 4.2 The Apparatus schematic diagram of unit B

4.3 Measurements of physical parameters

4.3.1 Temperature measurement

The temperatures were measured using thermocouples of "K" type. The thermocouple assembly sets were manufactured by *ChongWei* Electrical Singapore for a measurement range from -20°C to 200°C with an uncertainty of 0.3°C . The temperature measurement using this high quality thermocouple sets conformed to international standard ARI 1110-92 (2001). Nineteen thermocouples wires were installed of which ten thermocouples were placed at different locations throughout the two identical AC units to measure the refrigerant temperatures. Figure 4.1 shows the locations of five thermocouples for a sub-system of unit A while Figure 4.2 shows similar locations of the other five thermocouples for the sub-system of unit B. Two thermocouples were used to determine the inlet and outlet air temperatures from the evaporator and the installation of these two thermocouples in the duct air system conformed to the British Standards Institution BSI 5141 (1975). The remaining six thermocouples were used to measure the cabin interior surfaces temperatures. The thermocouple which is responsible about measuring of the inlet evaporator air temperature was insulated and shielded with balanced, low-pass filtered differential amplifiers (to avoid noise contamination and precision error)

4.3.2 Pressure gauges

The pressure gauges are technically divided into three different categories: standards, mechanical gauges, and electromechanical transducers (ASHRAE, 1997). For practical applications in HVAC, mechanical pressure gauges are generally the least expensive and the most common pressure instruments used. These instruments can achieve an accuracy of 0.01% of full scale or better when properly calibrated (ASHRAE, 1997). Doeblin (2004) can be referred for more details.

There are two common pressure values for HVAC application as obtained by the expansion valve and the compressor respectively. The low-pressure gauges are

located at the low-pressure side (after expansion valve, after evaporator and at compressor inlet) while the high-pressure gauges are placed at the high-pressure side (compressor discharge and sub-cooled liquid outlet of condenser). Pressures at the high-pressure side of the compressor discharge and exit of the condenser were measured by *OSAKA* pressure gauge from Japan, ranging from 0 to 25 bar gauge pressure with an accuracy of 50 kPa. The pressure gauges at low pressure side at suction and outlet of the expansion valve and inlet to compressor are capable of measuring pressure from 0 up to 10 gauge pressure with an accuracy of 10 kPa. The high side pressure gauge is of the type *BOURDAN SEDEME* Type MX5, EN837 from *France*.

4.3.3 Hygrometer

The most common hygrometer is the one that measures relative humidity. Other hygrometers measure moisture content and dew-point temperature. There are many kinds of hygrometers for HVAC applications (ASHRAE, 1997). The hygrometer used in this research project is shown in Figure 4.3. This humidity sensor is of model *Honeywell 4129* from *USA* with a high accuracy of $\pm 1.0\%$.



Figure 4.3 Humidity sensor

4.3.4 Refrigerant flow meter

The refrigerant flow meter type *KROHNE H250/RR/M9* model 2002 was used in the experiment. The flow meter is designed for installation in a vertical pipe run with flow from bottom to top. The flow meter is also designed to measure the refrigerant liquid of R134a. The scale is from 11 to 110 g/s with uncertainty of $\pm 1\%$. In the M9 indicator, the rotational movement of the follower magnet system is transmitted to the indicator.

4.3.5 Air velocity transducer

The model *TSI 8455* with accuracy $\pm 2.0\%$ of the reading was used as a transducer to measure the air velocity within the range of 0.1m/s to 50.0 m/s. The sensor is featured by fast response time of 0.2 second for air velocity measurement. The photograph of the velocity transducer is shown in Figure 4.4.



Figure 4.4 Velocity sensor

4.3.6 Data acquisition “DAQ” system

The DAQ system shown in Figure 4.5 consists of transducers, signal conditioner or signal amplifier, DAQ hardware, and software. Transducers sense changes in physical properties and provide electric signals that DAQ system receives such as those that come from the thermocouple, humidity, and velocity transducers. In each case, the electric signals produced are proportional to the physical parameters being monitored. The DAQ is being used to measure the signals from the nineteen thermocouples, which measure the temperature at different locations in the experiment, air velocity inside the supply duct, and the two relative humidity transducers, which detect air humidity before and after the evaporator.

The electric signal generated by the transducers (thermocouples or the humidity and velocity sensors) must be of high quality for the input range of DAQ board. Signal conditioning accessories can amplify low-level signals, and then isolate and filter them for more accurate measurements. The low-level signals should be amplified to increase the resolution and reduce noise. The temperature thermocouples connectors are connected to two PAD-TH10-K modules. Each module is able to handle ten input channels by using a connector block with ten k type thermocouples connectors. The humidity signals can be measured by using the hygrometer. The signals are first amplified before passing to the DAQ system by using DEWETRON amplifier which is classified under *DAQP-V-DSUB* type.

The whole modules were assembled in the DEWERACK-10 Channel Rack Housing. The data acquisition hardware comes in many physical formats. A common type is the plug-in card, which fits into a free expansion slot in the computer. The analog input specifications can give information on both the capabilities and accuracy of the DAQ product. Basic specifications, which are available on most DAQ products, indicate the number of channels, sampling rate, resolution, and input range. The DAQ card used in the present experiment is National Instrument DAQ hardware PCI-6023E type 267. The sampling rate determines how often conversions can take place. A faster sampling rate gets more points in a given time and can, therefore, offer a better representation of the original signal. The resolution is the

number of bits that the analog digital converter uses to represent the analog signal. The higher the resolution, the higher the number of division the range broken into, and therefore, the smaller the detectable voltages change from the modules. The DAQ card used up to 10 analog input channels, 200000 sample/sec, and 12-bit resolution.

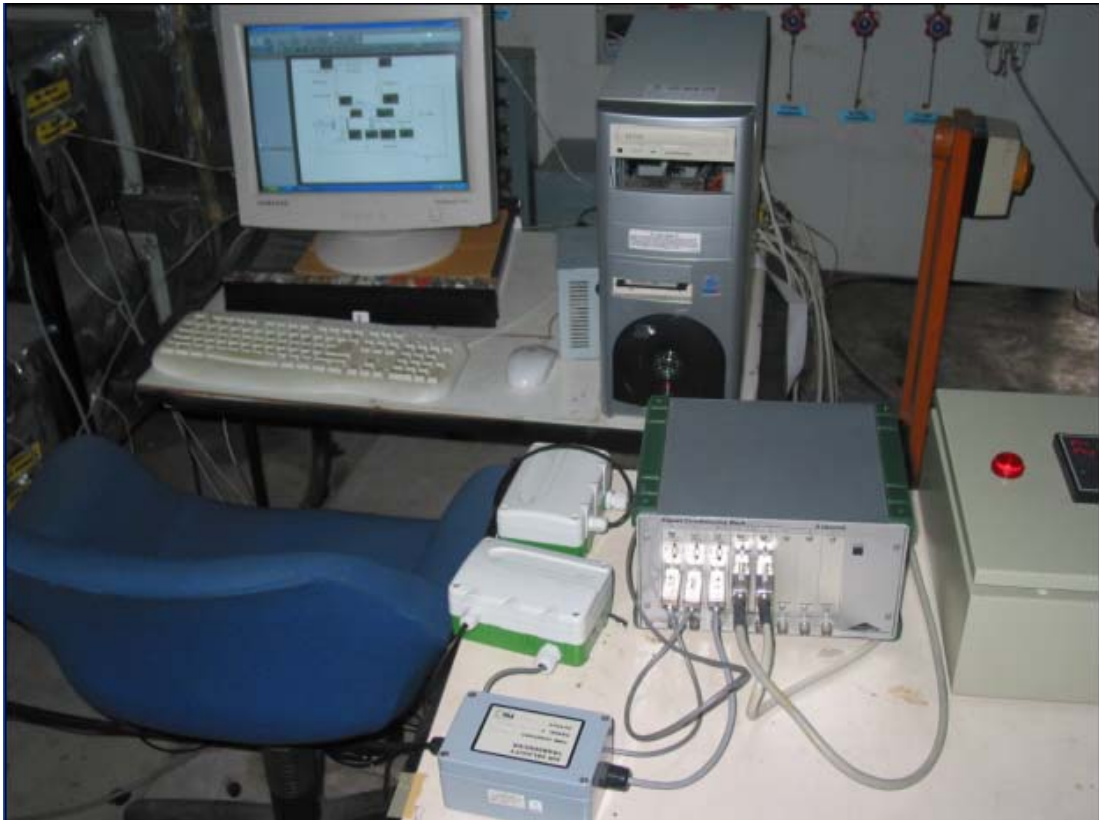


Figure 4.5 Data acquisition (DAQ) system

The driver software transforms the DAQ and PC into a complete DAQ, analysis, and display system. The majority of DAQ application uses driver software. The software manages the DAQ operation and its integration with the computer resources. The driver software for a DAQ board translates the binary code value of the analog digital converter to voltage by multiplying it by a constant. The software used in this system was DEWESOFT version 4.4. The selection of the software and DAQ hardware should be handled together for the reason that sometimes different companies develop hardware and software, which do not match or communicate with each other.

The software should be set first to inform the system the type of modules and hardware that are communicating with it. A general set up selection for display, sound, and sample rate selection can also be done in the software. The input channel can be activated and deactivated in the software. The input scaling and calibration for the modules should be set for the range and the filter setting. The display setting is available in the software to get an overview of the desired meter to be displayed. A sample of this display is shown in Figures 4.6 and 4.7.

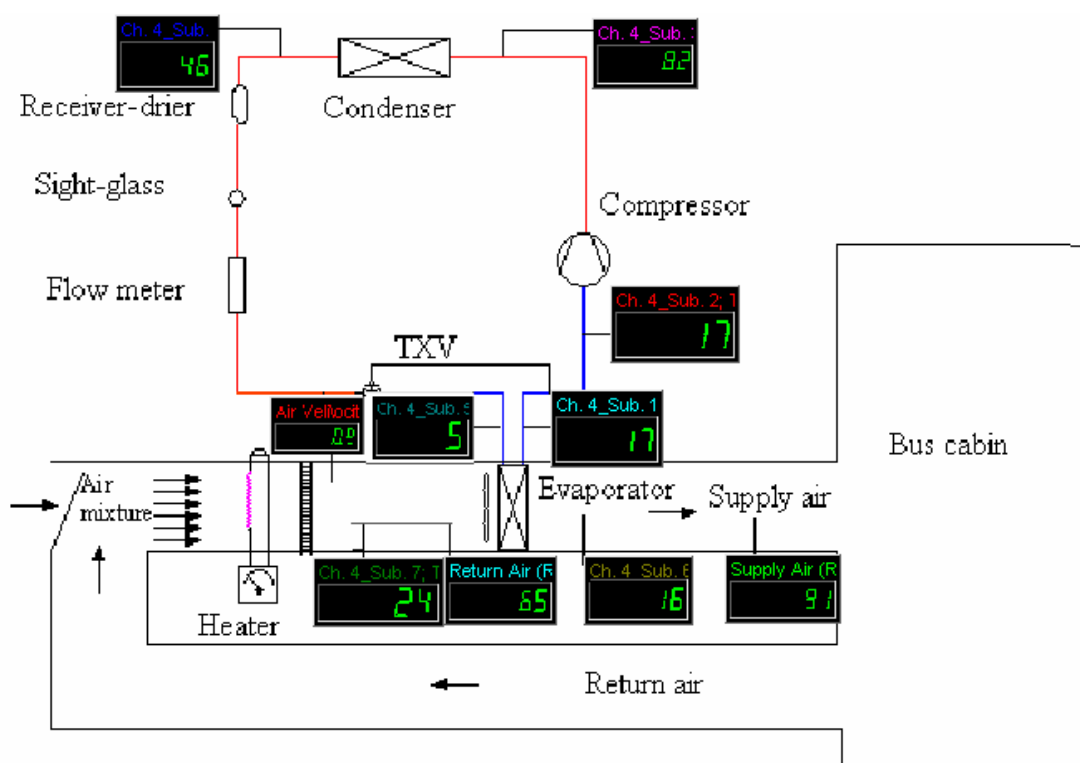


Figure 4.6 Sample of desired meter display for unit A of the whole system

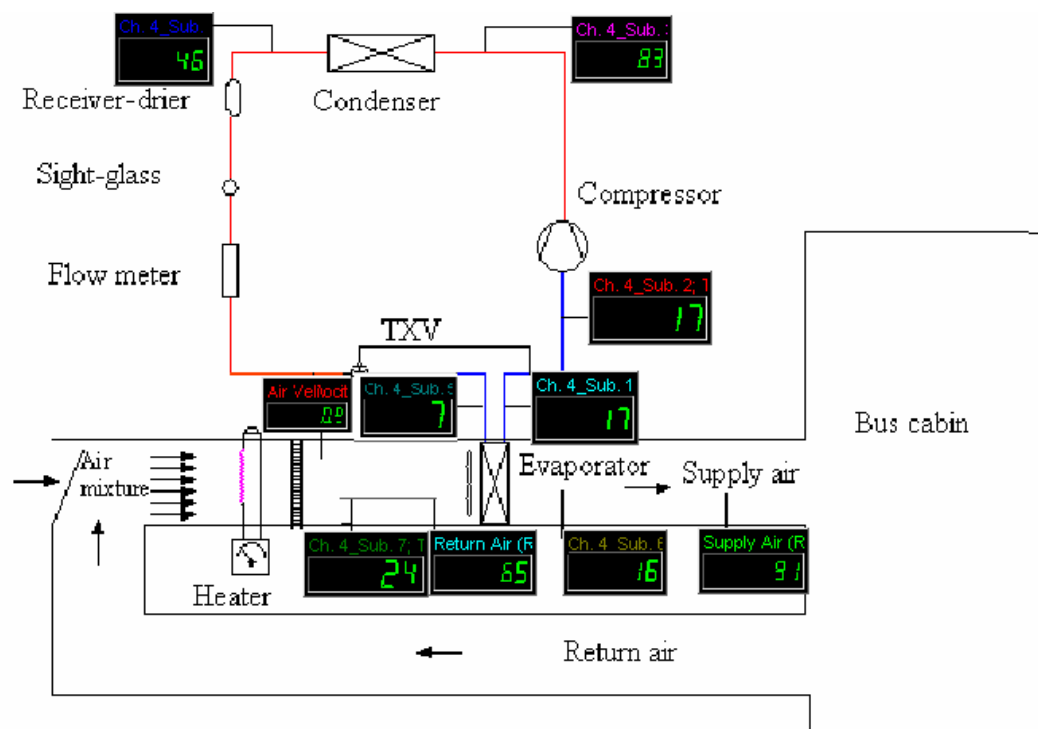


Figure 4.7 Sample of desired meter display for unit B of the whole system

4.4 Experimental components

4.4.1 Evaporator

The evaporator is a coil to remove the thermal load imposed on the AC system by transferring heat from the air in the conditioned space to the refrigerant. The evaporator used here is categorized under plain-finned-tube heat exchanger that is most commonly used in vapor compression AC system. The geometrical specifications are listed in Table 4.1. There are two sets of identical evaporator coils located in parallel with each other for supplying conditioned air to two passenger rows of the bus (see Figure 4.8). Each evaporator is serviced by three pairs of six blowers; each pair of these blowers is driven by one motor as seen in Figure 4.8.

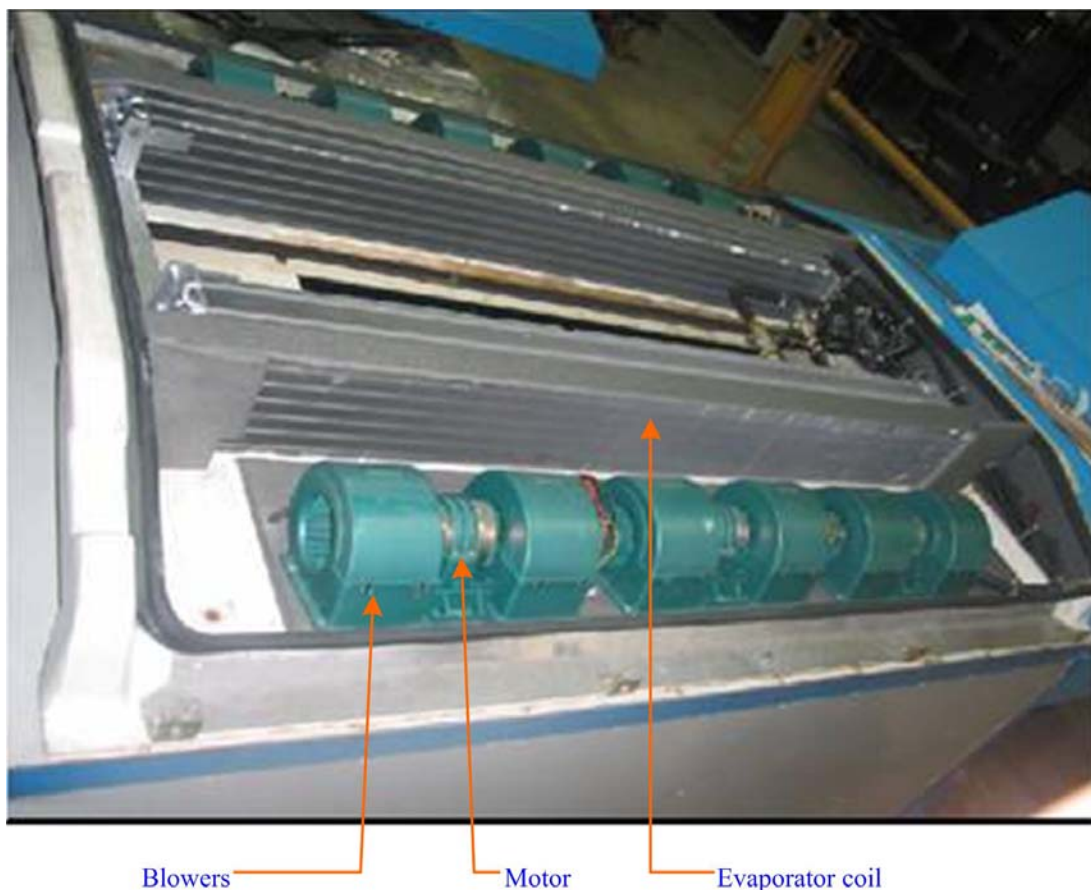


Figure 4.8 Evaporator coils arrangement

4.4.2 Condenser

The condenser is another type of a heat exchanger responsible for changing high pressure superheated refrigerant gas to that of high-pressure liquid state. Its purpose is to transfer heat from the refrigerant to the ambient air. The condenser used in the current experiment is also a finned-tube heat exchanger, with forced-draft fans. Similarly, there are two sets of identical condenser coils which are arranged in a parallel position to serve unit A and unit B respectively of the AC system. The condenser characteristics are stated in Table 4.1. The two condenser sets are forced-cooled by four radial centrifugal fans which are driven by their own motors as displayed in Figure 4.9.

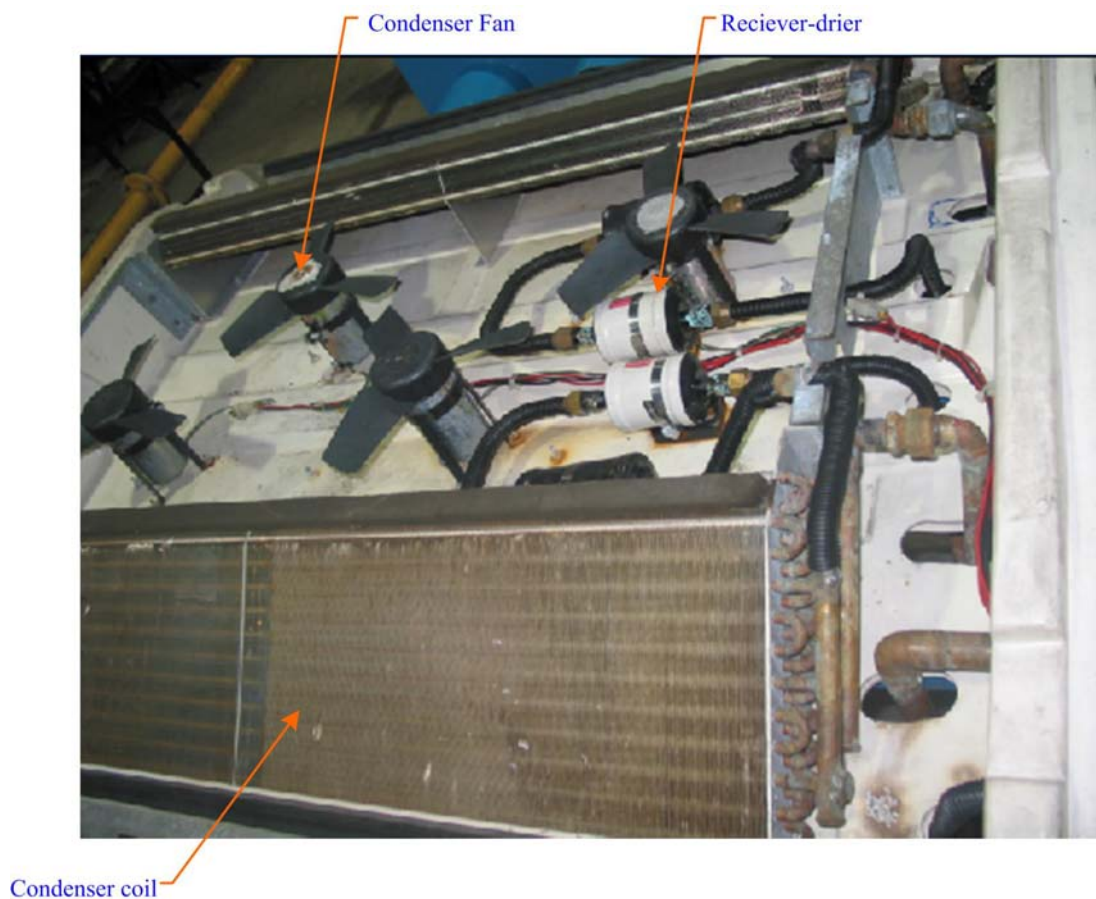


Figure 4.9 Condenser coils' arrangement

Table 4.1: The condenser and evaporator characteristics

Parameters	Condenser	Evaporator
Tube Spacing (mm×mm)	38.1×31.75	25.4×22.23
Tube inner diameter (mm)	15.67	8.865
Tube outer diameter (mm)	15.875	9.525
Height (mm)	457.2	177.8
Length (mm)	1250	1425
Fin pitch (fin/mm)	0.512	0.551
Number of rows	4	6
Number of circuits	6	3
Number of tubes per row	12	8
Fin thickness (mm)	0.15	0.15
Face air velocity (m/s)	2.5	2.25
Saturation temperature (°C)	55	10

4.4.3 Compressor

The compressor is the heart of the refrigeration system; it is responsible for pumping the refrigerant through the refrigeration cycle and increases the pressure of the incoming refrigerant gas. The compressors used in the experiment are of hermetic scroll type vertical model each integrated with a motor. The hermetic compressor is one in which the compressor and the motor are sealed and enclosed within the compressor's housing. Hence, the hermetic compressor does not need shaft couplings as in an open type thus avoiding the mechanical losses. Furthermore, the motor windings are cooled by the refrigerant vapor that is being drawn into the compressor from the suction line, thus providing extra protection to the windings from possible burn out.

Normally, the compressor frequently used in the bus AC system is of the open type driven by the main engine or sub-engine. However, it was intended in this research to use a horizontal hermetic scroll compressor (single-phase electrical power, and light in weight) to be compactly installed with the other components of the bus AC system on the roof-top of the bus. This will cut down the maintenance service time for the AC system. This will also avoid the problem of having refrigerant liquid inside the compressor during the non-operational period such as those occurring in the conventional AC system.

So far, the negotiations with the *COPELAND* Company that supplies the vertical model, are still open-ended because the commercial launches of the horizontal model is still pending, owing to some mechanical problems which the manufacturing company has made many attempts to overcome. Therefore, in order to save time and let the project proceed according to schedule, the available vertical type model was used which has the same specifications conformed to that of the horizontal type. It was decided to test the system using the horizontal type in the future work when this compressor is market ready.

The two identical compressors employed in the experiment here are *COPELAND* Model No. *ZR81KCE-TFD*, each with a displacement of 107.75 cc/rev. The compressor motor is a three-phase induction motor, with a frequency of 50 Hz, 4.75 kW, running at 2900 rev/min. The two compressors are installed in the same level with the evaporators and condensers (Figure 4.10). The two compressors are supplied with electrical power from an electrical box which has the possibility to drive each compressor separately by using a manual switch. Figures 4.11a and 4.11b show the exterior and interior construction of the electrical box.



Figure 4.10 Compressor arrangement



(a)



(b)

Figure 4.11 The image of the exterior and interior construction of the electrical box

4.4.4 Thermostatic expansion valve

The thermostatic expansion valve (TXV) controls the flow of liquid refrigerant entering the evaporator. It is actually a valve that modulates the refrigerant in order to allow the correct amount of refrigerant to enter the evaporator. The selection of the expansion device is particularly important for the operation of the refrigeration system. An expansion device, which is incorrectly sized, will inevitably result in operational difficulties and poor system performance. If the metering device supplies too much refrigerant to the evaporator, it might cause some liquid to enter the compressor, damaging the scroll. An undersized expansion valve will prevent sufficient refrigerant from flowing into evaporator causing reduction in the design cooling capacity of the system. As mentioned in Chapter 3, the main idea of the newly developed system is to split it into two identical units and each unit will require a separate TXV with a specific tubing arrangement as shown in Figure 4.12.

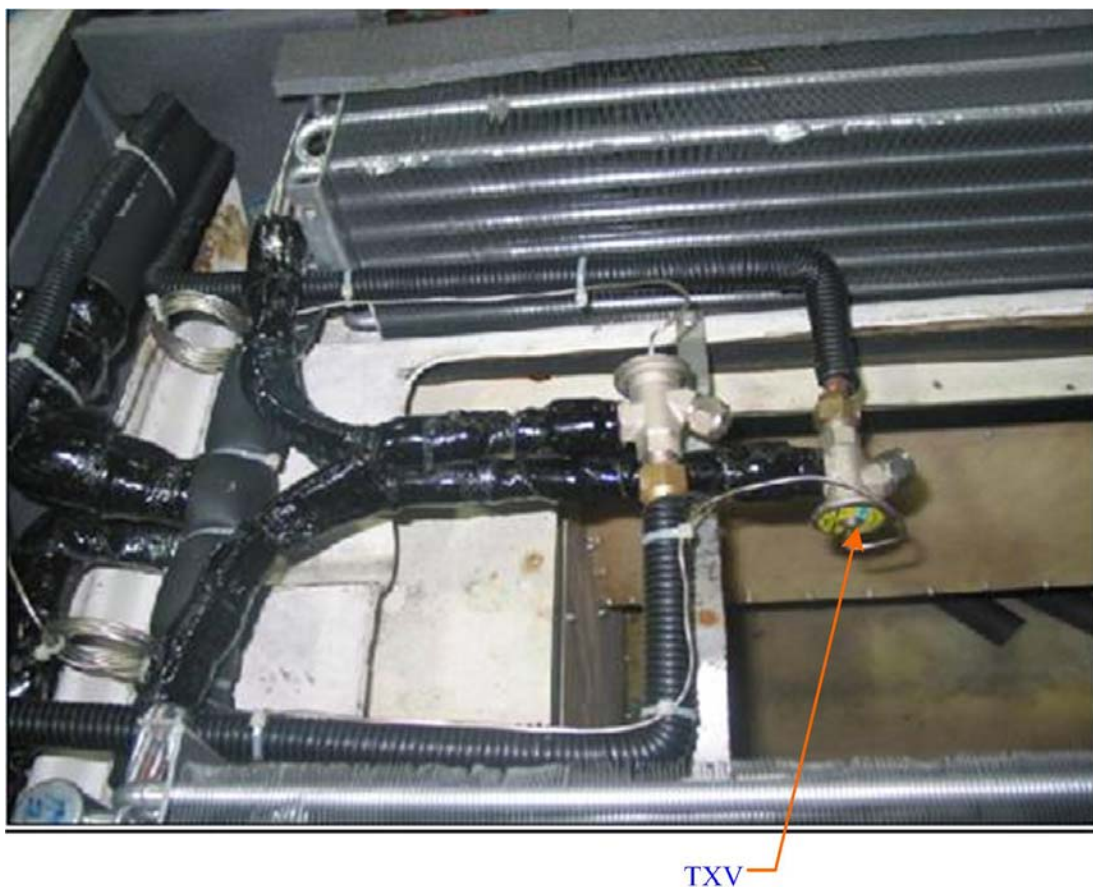


Figure 4.12 Expansion valves' arrangement

4.4.5 Receiver-drier

The receiver-drier is placed upstream to the expansion valve systems. Since this type of valve needs liquid refrigerant to function, a receiver is used to ensure that the valve gets the liquid it needs. This item provides three functions:

1. It is a tank that holds excess refrigerant and the refrigerant that leaves it usually flows up a pickup tube and past a sight glass. Under normal operating conditions, only liquid and no vapor bubbles should be visible in the sight glass.
2. It has a filter in it to remove any tiny debris that is caught by the flowing refrigerant in the cycle.
3. It has a chemical in it that treats the refrigerant by removing moisture and acid.

The capacity of the receiver drier used in the experiment is 1.2 liter with 300 gram of drying agent capacity in each unit. The assembly of the receiver-dryer is as shown in Figure 4.9.

4.4.6 Laboratory Simulated Passenger Cabin

The passenger cabin was fabricated using a fiberglass container of measurements 2100mm×1350mm×1600mm. The walls and roof were insulated with artificial insulator with a thickness of 20mm followed by 80mm of fiberglass. The cabin is located in the thermodynamic and air-conditioning laboratory of UTM. Since the environmental cabin itself is well insulated, effects of surrounding air on cabin temperature are assumed to be insignificant. Additionally, from many experiments conducted, it was found that the surrounding air was nearly constant around 29°C while the humidity was high, varying from 80 to 88% in a normal day. The photographs of the cabin's interior and exterior are shown in Figure 4.13.



Figure 4.13 The exterior and interior views of the simulated passenger cabin

4.4.7 Voltage regulator

The power input to the heater immersed in the duct was regulated by means of a voltage regulator. A Regavolt variable transformer with the following specifications was used: type 1225 EC, nominal voltage 240 V, loading rating 7.2 kVA, maximum current 30 A, output voltage at line voltage connection 0 to 100%, and over-voltage connection 0 to 155% of input. The voltage regulator was manufactured by *CLAUDE LYONS LTD, ENGLAND*. The electrical heater and voltage controller is displayed in Figure 4.14.



Heater controller ————— Electrical heater

Figure 4.14 Electrical heater is immersed in the air duct system and is connected to the heater controller

4.4.8 Automatic controller

The JCD-33A, By *SHINKO* Inc. is an Auto-Tuning (PID, PI, PD, P, ON/OFF) microcomputer based temperature indicating controller. It is featured by MIMO (Multiple Input-Multiple Output) option; the photograph of the controller is shown in Figure 4.15.

The main function of the automatic controller is to regulate the different operating modes of the newly developed AC system when required according to the thermal load imposed on the passenger compartment of bus. To switch on the AC system, the bus operator first switches on the controller which sends an electrical signal to activate one unit only to work regardless of the amount of the thermal load

imposed. During this transient stage, the controller allows all blowers to be operating. Then the controller is fully in charge of the system operation to match the system capacity with the cooling load by sensing the inlet air temperature to the evaporator.

In order to sense the increase or decrease of cooling load on the bus cabin, it is more precise to represent the cooling load by a difference in temperature instead of using a fixed temperature (inlet air temperature to the evaporator). In other words, the cooling load should be attributed to the difference between the evaporator inlet air temperature and any chosen set-point reference which is appropriate for achieving comfort condition inside the bus. Since the values of 21°C, 22°C, and 23°C are the most frequently used as set-point temperatures, experiments should be conducted to choose the proper temperature difference (the indoor temperature minus set-point temperature) that gives optimum comfort conditions (neither undercooling nor overcooling) while saving the energy. The thermal and electronic manipulation of the operation is discussed in detail in Chapter 7.



Figure 4.15 The automatic controller

4.5 Experimental procedure

As aforementioned, the experimental test runs are categorized into two main groups. The first group of experiments was conducted in order to verify the theoretical model of the whole system simulation. The main purpose of the second group is to design the proper control algorithm for the automatic controller of the proposed system.

It is to be noted that all these experiments were carried out throughout the deactivation of the automatic controller to simulate continuous operation of the AC system. However, another test was conducted during the activation of the controller after the controller settings were adapted by the proposed control strategy. The main purpose of this test was to check the quality of the controller function.

The first group of the experiments was conducted to analyze the effect of cooling load variations on the proposed system at the three different operating modes. The experimental tests were performed following the given procedure:

During testing of the AC system at the first operating mode, after the two compressors were switched on, adjustments were made during a preliminary run until the essential measurements required for the test were within the allowable limits of variations. The air was heated by controlling the voltage regulator at a desired inlet air temperature to the evaporator. The inlet air humidity was adjusted by allowing some fresh air to enter the air duct to reach the required air humidity. The adjustment of the humidity was accomplished by varying the angle of inlet air vane. When the pressure and temperature at various points remain constant for at least 15 minutes and the refrigerant flow meter indicates a constant flow rate, the steady working conditions were successively adjusted. The readings for the test period were taken at equal time intervals not exceeding 20 min, for a period of at least one hour during which at least four readings were taken. The arithmetic mean of the successive readings for each measurement is taken as the measurement value for the test. The same previous experimental procedure was repeated for the second and third operation modes of the AC system except one unit was idled and stoppage one-third

of the blowers' capacity for the 3rd mode operation. The set-up of the experimental test rig is presented in Figure 4.16.



Figure 4.16 The set-up of the whole experimental test rig

The experimental measurements are reported in Tables E.1 to E.7 of Appendix E. Under steady working conditions the following set of readings were taken:

- The absolute pressures and temperatures at the measuring points along the refrigerant path of the cycle were taken as depicted in Figure 4.1 or 4.2. Any pressure reading shall not vary more than $\pm 1\%$ throughout the test period while any of the temperature readings shall not vary more than $\pm 3\%$ throughout the test period.
- The inlet and exit air conditions (temperature and relative humidity) from the evaporator as well as the air velocity were taken. The locations of these measurement points are shown in Figure 4.1 or 4.2.
- Refrigerant mass flow rate reading of the flow meters were also taken.

The refrigerant temperatures at the different points of the cycle, inlet and exit air conditions, and air velocity were recorded using data acquisition and the software designated to read this quantities.

The second group of the experimental work consists of a series of experiments which were conducted at three set-point temperatures: 21°C, 22°C, and 23°C as these temperatures are typical conditioned space. The aim of these experiments was to provide a reference data for the control strategy design. . These experiments were conducted and controlled manually, with the controller disengaged, according to the following procedure:

1. Select the set-point temperature.
2. Heat the inlet evaporator air.
3. Turn on the developed system with a specified operating mode.
4. Record the required data and readings.
5. Determine the cycling on time taken for the inlet evaporator air temperature to decrease to the set-point temperature and the cycling off time.
6. Calculate the average system input power using the fundamental thermodynamic equations; then the energy consumption is calculated as will be discussed in section 4.9.

The previous procedure was repeated for the three different modes with the three different set-point temperatures. These experiments were conducted for a wide range of the inlet evaporator air temperatures to cover up the expected values for the air temperature entering the system evaporator. The measurements and results of the second group of the experimental work are reported in Tables B.1 to B.3 of Appendix B and Tables E.11 to E.14 of Appendix E, respectively.

In this study, the experimental results are represented by physical quantities such as cooling capacity, COP, evaluation of the thermal comfort for passenger's cabin, and energy consumption. To calculate these physical quantities, the thermodynamic analysis and thermal comfort calculation will be performed in the following sections.

4.6 Thermodynamic analysis

Referring to Figures 4.1 and 4.2, the cooling capacity of the experimental system can be expressed in terms of the mass flow rate and the enthalpies of the refrigerant stream at the inlet and outlet of the evaporator. That is,

$$\text{For the first mode, } Q_e = \left[\dot{m}_r \times (h_1 - h_5) \right]_A + \left[\dot{m}_r \times (h_6 - h_{10}) \right]_B \quad (4.1)$$

$$\text{For the respective second or third mode, } Q_e = \left[\dot{m}_r \times (h_1 - h_5) \right]_A \quad (4.2)$$

$$\text{or, } Q_e = \left[\dot{m}_r \times (h_6 - h_{10}) \right]_B \quad (4.3)$$

Assuming that the compression process is adiabatic, the compressor power input can be evaluated as

$$\text{For the first mode, } W_{cp} = \frac{\left[\dot{m}_r \times (h_3 - h_2) \right]_A + \left[\dot{m}_r \times (h_8 - h_7) \right]_B}{\eta_{motor}} \quad (4.4)$$

For the respective second or third mode,

$$W_{cp} = \frac{\left[\dot{m}_r \times (h_3 - h_2) \right]_A}{\eta_{motor}} \quad (4.5)$$

$$\text{or, } W_{cp} = \frac{\left[\dot{m}_r \times (h_8 - h_7) \right]_B}{\eta_{motor}} \quad (4.6)$$

A typical motor efficiency η_{motor} is equal to 85% (Hendricks et al., 2001) for all modes of system operation. The ratio of the cooling capacity to the total system input power (compressor power + electrical power input to the blowers and fans) gives the overall performance of the system in the AC system. That is,

$$COP_v = \frac{Q_e}{W_{cp} + W_{fans} + W_{blowers}} \quad (4.7)$$

The input power of the motor to either the condenser fan or evaporator blower is 140 W. Therefore, the four fans' (or four motors) input power, W_{fans} is 560 W and that for twelve blowers (or six motors), $W_{blowers}$ is 840 W.

The ratio of the cooling capacity to the compressor power yields the thermodynamic performance of the AC system which is,

$$COP = \frac{Q_e}{W_{cp}} \quad (4.8)$$

4.7 Thermal comfort calculation

The human sense of thermal comfort is very complex. It is related to both physiological and the psychological states of a person under specific environmental conditions. To quantify thermal comfort in fabricated enclosures such as houses, offices, cars and ships, Fanger (1972) suggested, in his proposed thermal comfort equation which is in terms of "Predicted Mean Vote", that body activity, thermal resistance of clothing, air temperature, mean radiant temperature (Appendix B), local mean air velocity (Appendix F), and relative humidity are the most important variables. The details of this equation development are presented in Appendix F. While the thermal comfort equation provides the general degree of discomfort for a group of people, thermal sensation still varies from one individual to another. To quantify the thermal comfort, it is more reasonable and practical to indicate the percentage of persons who can be expected to be thermally comfortable. Therefore, in the present study, the "Predicted Percentage of Dissatisfied" (PPD) was used to evaluate thermal comfort. These indices were derived from research studies carried out with a large number of human subjects inside a climatic chamber. They were subjected to different climatic conditions and asked to express their thermal sensations on a conventional seven-point scale (-3 = cold, -2 = cool, -1 = slightly cool, 0 = neutral, 1 = slightly warm, 2 = warm, 3 = hot). The environment is

considered comfortable if $-0.5 \leq \text{PMV} \leq 0$, which implies $\text{PPD} \leq 10\%$ for cooling purposes.

The relationship between PMV and PPD is shown in Figure 4.17 and can also be used to calculate PPD, if the value of PMV is known. In order to determine the PMV, there are some parameters that should be measured directly or calculated from other measurements and other parameters that should be quantified from Tables provided by ASHRAE (1997).

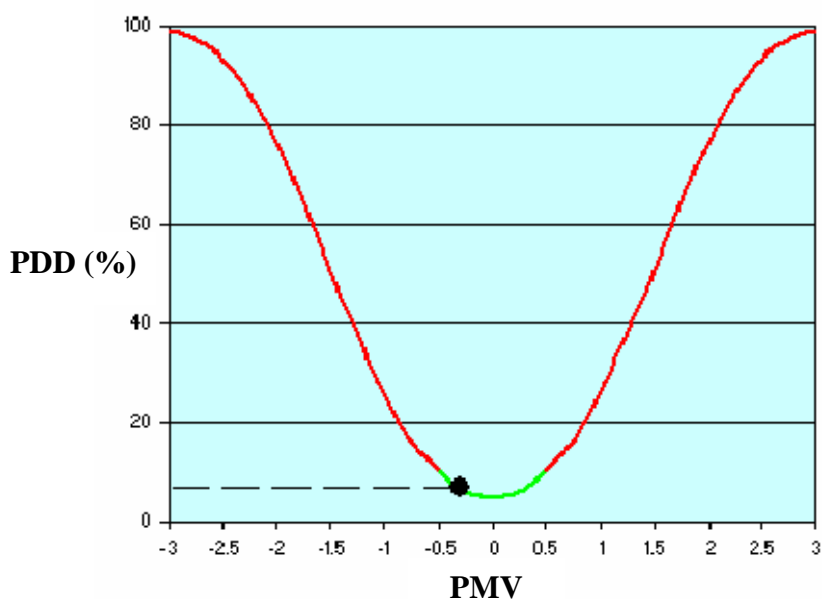


Figure 4.17 Curve to determine PPD as a function of PMV

The measuring parameters or calculated parameters are the space or return air temperature, t_r , mean radiant temperature, t_{mrt} , local mean air velocity, v_r , and space air relative humidity, R_{hr} . While the quantified parameters or personal parameters such as the metabolic rate, M and the clothing thermal insulation, I_{cl} can be obtained from Tables B.4 and B.5 in Appendix B. In this study, passengers are defined as resting quietly with casual clothing. This produces a metabolic rate, M of 1 met and a clothing insulation of 0.8 clo. The space or return air temperature and relative humidity are calculated as discussed in Chapter 3. The determination of the mean radiant temperature and local air velocity are given in Appendices B and F, respectively.

When all the previous parameters are identified, the computer program is prepared to determine the PMV and PDD. The computer program is written in Microsoft Visual Basic and has a graphical user interface as shown in Figure 4.18.

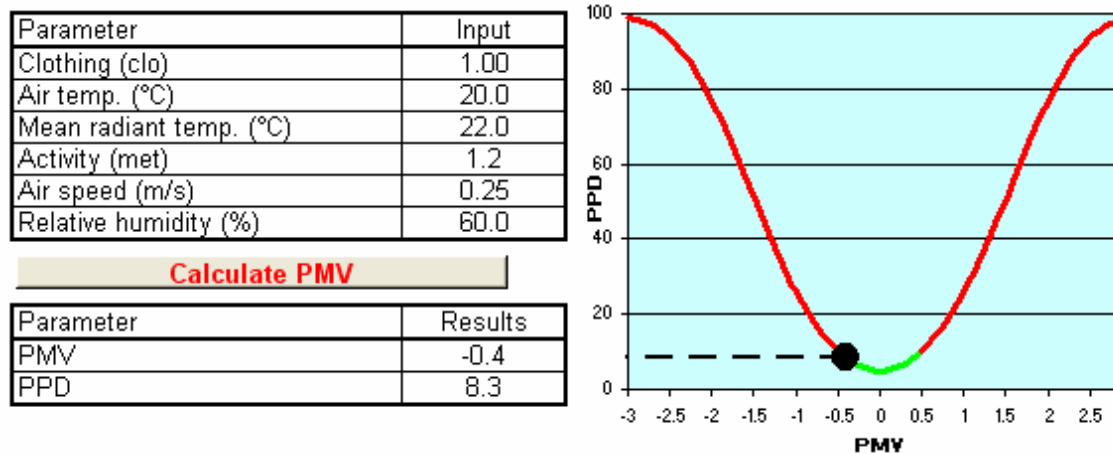


Figure 4.18 Computer program interface for PMV-PDD calculations

4.8 Experimental results and discussion

As aforementioned, the experimental test runs are grouped in two categories: the first one is related to the effect of cooling load variations on the proposed AC system's thermal performance and the second group is related to the control strategy design for the system controller. The main basis of the control strategy is to enable the controller to govern the AC system's operation for best performance which corresponds to adequate passenger's thermal comfort with an enhancement in system energy consumption. Therefore, section 4.8.1 discusses the effect of cooling load variations on the system thermal performance while section 4.8.2 and 4.8.3 discuss the effect of cooling load variations on the passenger's thermal comfort and system energy consumption, respectively.

4.8.1 Effect of cooling load variations on the system's thermal performance for different operating modes

The overall refrigeration system performance is strongly influenced by the cooling load variations. Tests were carried out in such a way as to allow for the evaluation of the effect of the cooling load variations on system performance. In addition, test data was being used to assess the quality of the computer simulation results which will be investigated in Chapter 6. In what follows, a summary of experimental thermal performance results for the three different operating modes of the proposed system will be presented along with the effect of the cooling load variations. The system thermal performance is represented by the system cooling capacity, compressor power, COP. The effect of cooling load variations on the exit evaporator air conditions (temperature and relative humidity) and passenger's cabin air conditions are also presented in the following graphs.

The refrigerating capacity is directly related to the evaporator's inlet air temperature; it increases with the increase in evaporating temperature. This behavior is clearly shown in Figure 4.19a. Extremely high and low values of air temperature were investigated for analysis purposes. It can be noted that as the temperature of the air increases, the compressor accommodates higher loads in order to increase the refrigerant mass flow rate through the cycle as shown in Figure 4.19b. The compression power increases with the inlet air temperature due to the increase in the refrigerant flow rate and the condensing pressure. Since the refrigerating capacity increases more than the compression power, the COP increases with increase in the evaporator inlet air temperature. This behavior can clearly be seen in Figure 4.20a.

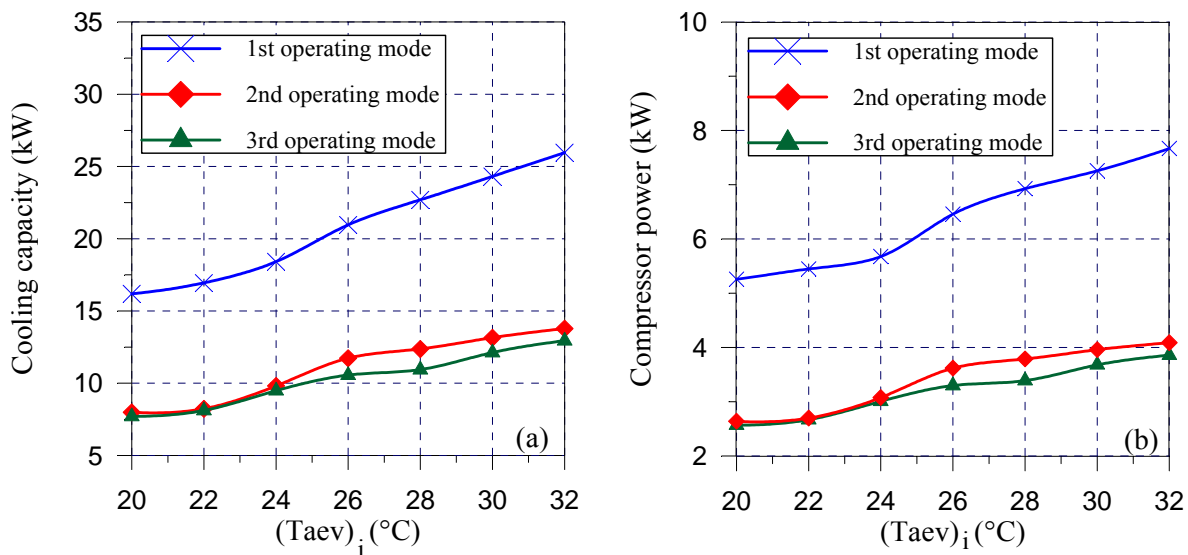


Figure 4.19 Effect of evaporator inlet air temperature on the system's (a) cooling capacity (b) compressor power for the three different modes of operation

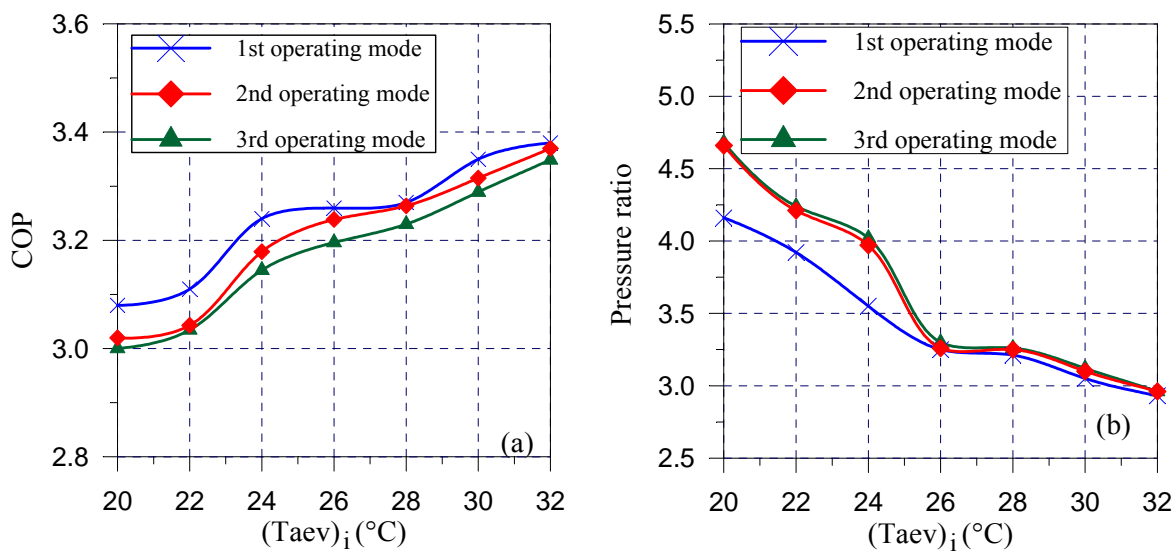


Figure 4.20 Effect of evaporator inlet air temperature on the system's (a) COP (b) pressure ratio for the three different modes of operation

As shown in Figure 4.19b, the system in the case of the second and third modes consumes lesser input power compared to the corresponding case in the first mode. That is an intuitive perception because the system at these modes has only one working compressor. One might expect that the system's compressor power in the second or third mode cases equals to half of the value of that for the first mode case. However, as revealed in Figure 4.19b, this is not true and the compressor power in the other modes is larger than the half of the value of that for the first mode. This behavior can be explained by taking into account that when one compressor of the system is stopped, the other compressor has to carry the same load and substitute the absence of the idling one. This leads to a slight increase in the compressor's pressure ratio as shown in Figure 4.20b and causes a drop in the compressor's isentropic and volumetric efficiencies. Accordingly, the compressor has to increase its consumed power to offset the shortcomings in its characteristic parameters' performance (isentropic and volumetric efficiencies). This also explains why there is a slight difference in the system COP for the three different modes of the AC system operation, as shown in Figure 4.20a.

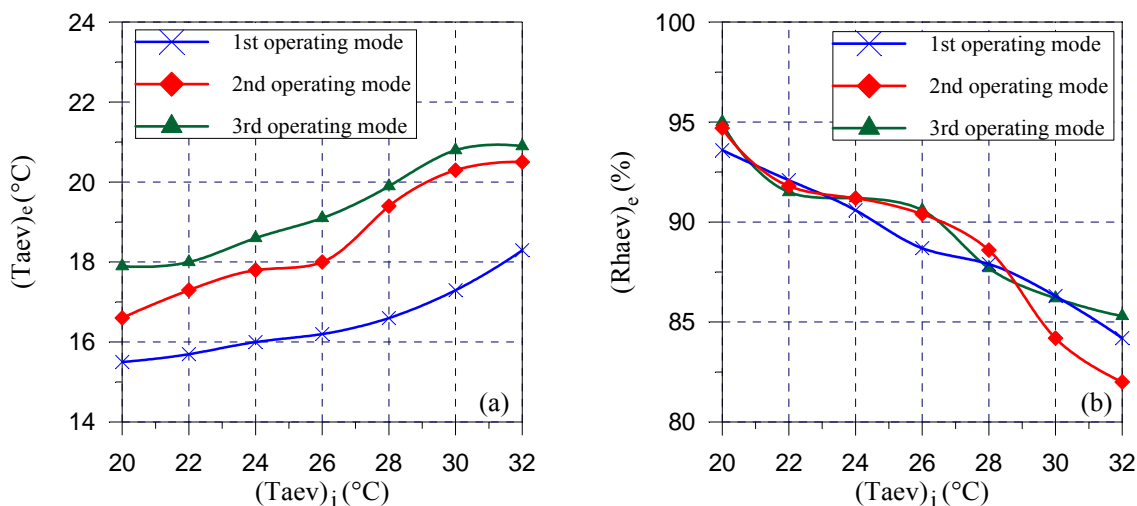


Figure 4.21 Effect of evaporator inlet air temperature on the system's (a) exit air temperature (b) exit air relative humidity for the three different modes of operation

As expected, the relationship between the air temperature and its relative humidity is distinguished by an opposing relationship i.e. the increase in air temperature results in a decrease in its relative humidity. This is demonstrated

graphically in Figures 4.21a and 4.21b. The increase in inlet evaporator air temperature causes the outlet air temperature of the evaporator to be increased and at the same time, the relative humidity is decreased.

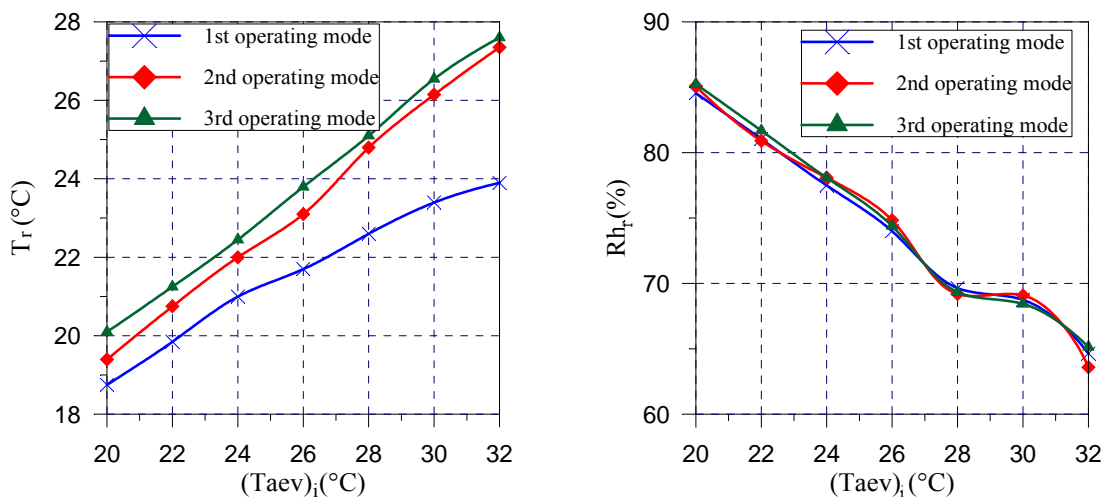


Figure 4.22 Effect of evaporator inlet air temperature on the system's (a) cabin or return air temperature (b) cabin or return air relative humidity for the three different modes of operation

As mentioned in Chapter 3, the calculation of the space or return air temperature and relative humidity are calculated by knowing exit evaporator air conditions (temperature and relative humidity) and the imposed cooling load on the space i.e. passenger's cabin. Accordingly, by using the previous model in Chapter 3 the effect of the cooling load variations on the passengers' cabin air conditions (temperature and relative humidity) can be presented in Figure 4.22.

4.8.2 Effect of cooling load variations on the passenger's thermal comfort for different operation modes

By identifying the input parameters to the computer code the passenger's thermal comfort is evaluated in terms of the comfort indices PMV and PPD. The input parameters and comfort indices are presented in Tables 4.2 to 4.4.

Figure 4.23 shows the thermal comfort in terms of PMV and PDD for the three different operating modes of the developed AC system. It can be seen from Figure 4.23 that the 1st mode operation of the system is favorable to provide adequate thermal comfort inside the bus compartment especially at high cooling load conditions (when $T_{ev,i} \geq 27^\circ\text{C}$). On other hand, the other operating modes causes discomfort conditions for the passengers inside the bus cabin ($\text{PMV} > 0$). At low cooling load conditions (when $T_{ev,i} < 27^\circ\text{C}$), the proposed system should operate on the 2nd or 3rd mode in terms of the thermal comfort point-of-view. However, the selection between the 2nd and 3rd operating mode should be accomplished on other decision parameters besides the thermal comfort conditions. These decision parameters are the saving in energy consumption and proper number of cycles per hour for the system compressors. This will be discussed in details in Chapter 7.

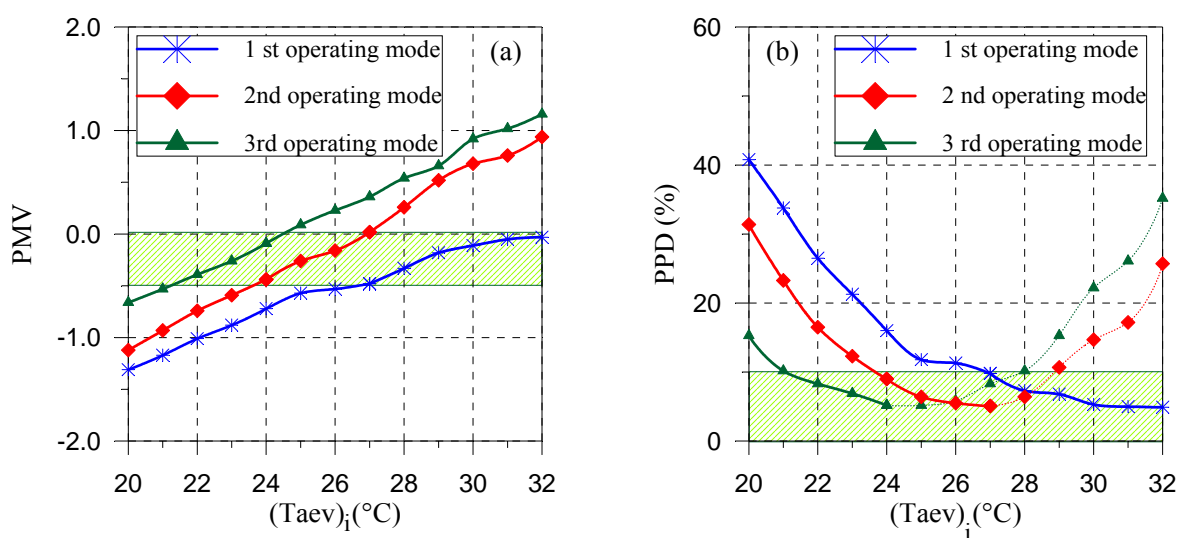


Figure 4.23 Evaporator inlet air temperature's effect on passenger's thermal comfort in terms of (a) PMV (b) PPD

Table 4.2: The input and output data of the computer program for the first mode operation [$v_r = 0.24$ m/s, Activity = 1.0 met, and Clothing = 0.8 clo]

Temperature	Input data			Output results	
Taev _i (°C)	tr(°C)	Rhr (%)	t _{mrt} (°C)	PMV	PPD (%)
20	18.75	84.55	23.87	-1.31	40.8
21	19.25	82.75	24.12	-1.17	33.8
22	19.85	81.05	24.42	-1.01	26.5
23	20.40	79.70	24.70	-0.88	21.3
24	21.00	77.50	25.00	-0.72	16.0
25	21.50	78.50	25.25	-0.57	11.8
26	21.70	74.00	25.35	-0.53	11.3
27	22.00	71.25	25.50	-0.48	9.8
28	22.60	69.65	25.80	-0.33	7.3
29	23.15	69.45	26.07	-0.18	6.8
30	23.40	68.75	26.20	-0.11	5.3
31	23.70	67.25	26.35	-0.05	5.0
32	23.90	64.65	26.45	-0.03	4.9

Table 4.3: The input and output data of the computer program for the second mode operation [$v_r = 0.24$ m/s, Activity = 1.0 met, and Clothing = 0.8 clo]

Temperature	Input data			Output results	
Taev _i (°C)	tr (°C)	Rhr (%)	t _{mrt} (°C)	PMV	PPD (%)
20	19.40	85.10	24.20	-1.12	31.4
21	20.10	83.65	24.55	-0.93	23.3
22	20.75	80.90	24.87	-0.74	16.5
23	21.35	80.00	25.17	-0.59	12.3
24	22.00	78.10	25.50	-0.44	9.0
25	22.55	78.50	25.77	-0.26	6.4
26	23.10	74.85	26.05	-0.16	5.5
27	23.80	70.35	26.40	+0.02	5.1
28	24.80	69.20	26.90	+0.26	6.4
29	25.55	69.20	27.27	+0.52	10.7
30	26.15	69.10	27.57	+0.68	14.7
31	26.80	66.65	27.90	+0.76	17.2
32	27.35	63.60	28.17	+0.94	25.7

Table 4.4: The input and output data of the computer program for the third mode operation [$v_r = 0.16$ m/s, Activity = 1.0 met, and Clothing = 0.8 clo]

Temperature	Input data			Output results	
Ta _{ev_i} (°C)	tr (°C)	Rhr (%)	t _{mrt} (°C)	PMV	PPD (%)
20	20.10	85.25	24.55	-0.66	15.3
21	20.65	83.55	24.82	-0.53	10.2
22	21.25	81.70	25.12	-0.39	8.3
23	21.80	80.20	25.40	-0.26	6.9
24	22.45	78.10	25.72	-0.09	5.2
25	23.20	76.80	26.10	+0.09	5.2
26	23.80	74.40	26.40	+0.23	5.8
27	24.40	71.35	26.70	+0.36	8.3
28	25.10	69.35	27.05	+0.54	10.2
29	25.60	69.30	27.30	+0.66	15.3
30	26.55	68.45	27.77	+0.92	22.2
31	26.95	66.90	27.97	+1.02	26.1
32	27.60	65.15	28.30	+1.16	35.2

4.9 Energy consumption analysis

Referring to Chapter 3, the evaporator inlet air temperature for the AC system changes of bus on an hourly basis as a result of the change in thermal load conditions. Thus, the quasi-steady-state concept is employed in order to calculate the energy consumption. However, the dynamic response of most systems is much more rapid than the one-hour-time's step used in thermal load calculations (Ayres and stamper, 1995). Quasi-steady-state refers to the steady-state operation at a certain hour, but it will be different in the next hour. As a result, the energy consumption can be calculated cumulatively from the start of the system using this relationship:

$$E_{n+1} = E_n + \frac{Wt_{av} \cdot \Delta t}{60} \times N_{cy} \quad (4.9)$$

Where,

Δt = running time of the compressor in minutes in one-hour step.

Wt_{av} = average system input power during the running time, kW

N_{cy} = number of compressor cycles per hour

At $n = 0$ (the starting of the system), $E_o = 0$, N_{cy} is determined by dividing 60 minutes (1 hour) by the sum of the running and off times. The hourly energy consumptions for a typical design day of March and April are listed in Table E.15 of Appendix E for the conventional system and the developed system with the three different operating modes. It should be noted that the conventional system has no cycling mode as a result of the continuous operating during all the operating hours. Therefore, the running time is one hour and thus the N_{cy} is equal to unity in this condition.

As it was observed in Chapter 3, the cooling load is varied along 24-hours. In fact, daily use of the bus AC system time is more than fifteen hours per day that is from 8 am to 11 pm (from Johor Baharu to Kuala Lumpur and vice versa). The daily energy consumption for both systems is shown in Figures 4.24 and 4.25. It should be noted that the conventional system has a continuous operation without stopping the system's compressor, so the daily energy consumption for this system is the same for any set-point temperature as shown in Figure 4.24. Figure 4.25 shows that the conventional system has the largest value of the daily energy consumption. If the developed AC system operates on the third mode only during all time of operation, the system will have the least possible daily energy consumption. However, the passenger's thermal comfort will be affected as a result of insufficient cooling of the AC system. The compromise between energy consumption, proper system operating mode and appropriate thermal comfort for the developed AC system operation will be discussed in detail in Chapter 7.

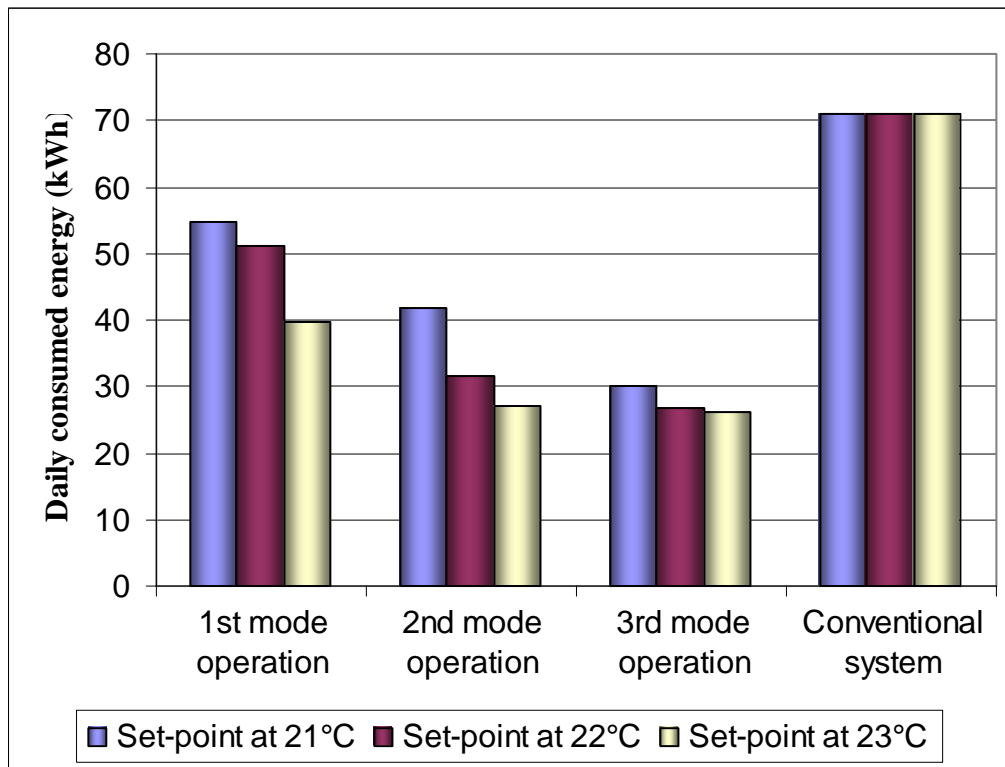


Figure 4.24 Daily energy consumption for both systems

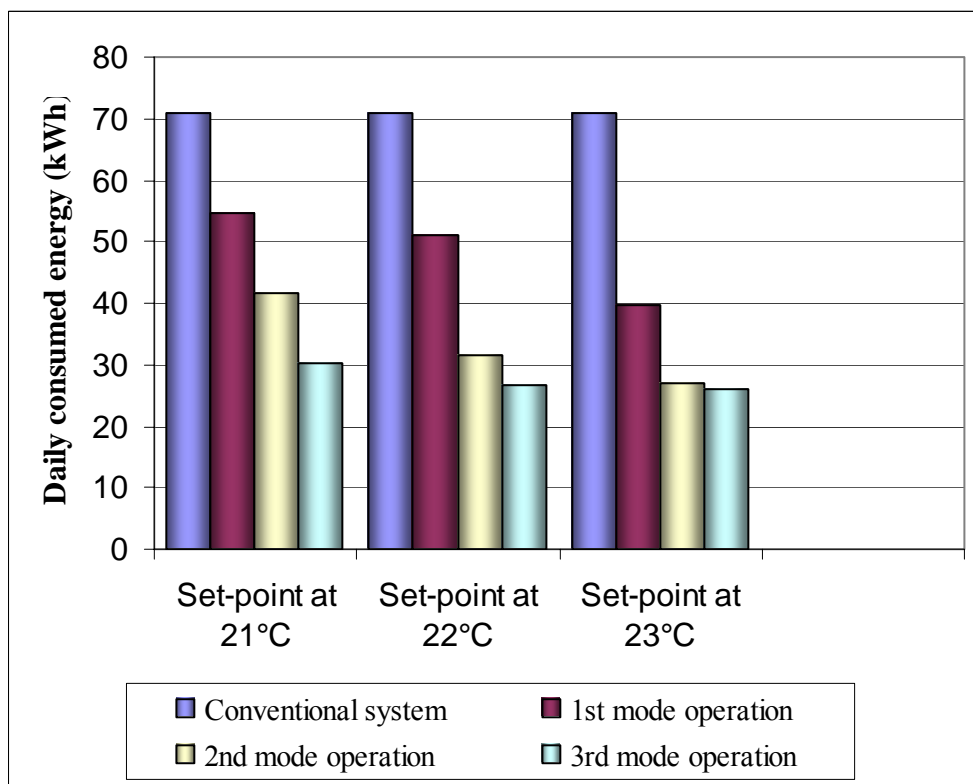


Figure 4.25 Daily energy consumption for both systems at different set-point temperatures

4.10 Conclusion

The impact of cooling load variations on the developed bus AC system's performance, the cooling capacity, compressor power, COP, and evaporator outlet air conditions (temperature and relative humidity) has been analyzed experimentally. In addition, the daily energy consumption for the conventional AC system and the developed one at the three different operating modes has been calculated for the three set-point temperatures of 21, 22, and 23°C.

The results indicate that the conventional AC system consumes the largest amount of energy when compared to the developed system at any operating mode. If the developed system operates on the third mode, it will consume the smallest amount of energy, but it will be established on the expense of passengers' thermal comfort. Therefore, combination of the three different modes will produce an efficient operation for the developed system coupled with achieving a satisfied thermal comfort for the passengers. This will be further investigated in the next Chapters.

CHAPTER 5

EVAPORATOR AND CONDENSER MODELING

5.1 Introduction

In this chapter, DX evaporator and air-cooled condenser models are proposed and validated for predicting their thermal analysis and design under different cooling capacities and various operating conditions. The main objective of these models is to provide a simplified and accurate analytical computer model for both heat exchangers' thermal analysis. Those computer models will be integrated in the AC system's simulation model.

5.2 Background

Evaporators are the heat exchangers that receive the refrigerant from the expansion device, which is in a two-phase and low temperature state. Heat transfer occurs from the high temperature unconditioned air to the low temperature refrigerant. Finned-tube direct expansion (DX) evaporators have been used widely in automotive AC systems since such kinds of evaporators require little maintenance, apart from easy cleaning of the air-side heat transfer surfaces, and have been known to operate

effectively and reliably. Similarly, a condenser is a heat exchanger which is designed to reject heat from the refrigerant to the ambient air. The condenser accepts hot, high-pressure refrigerant at superheated state from the compressor, and dissipates heat to a lower temperature ambient air. When the refrigerant exits the compressor, it enters the condenser as a superheated vapor and exits as a sub-cooled liquid. The configuration of an air-cooled condenser is mainly similar to the DX evaporator where both are classified in the finned-tube heat exchanger category. As shown in Figure 5.1, the air passes between the fin plates while the refrigerants flow through the tubes of the condenser or the evaporator.

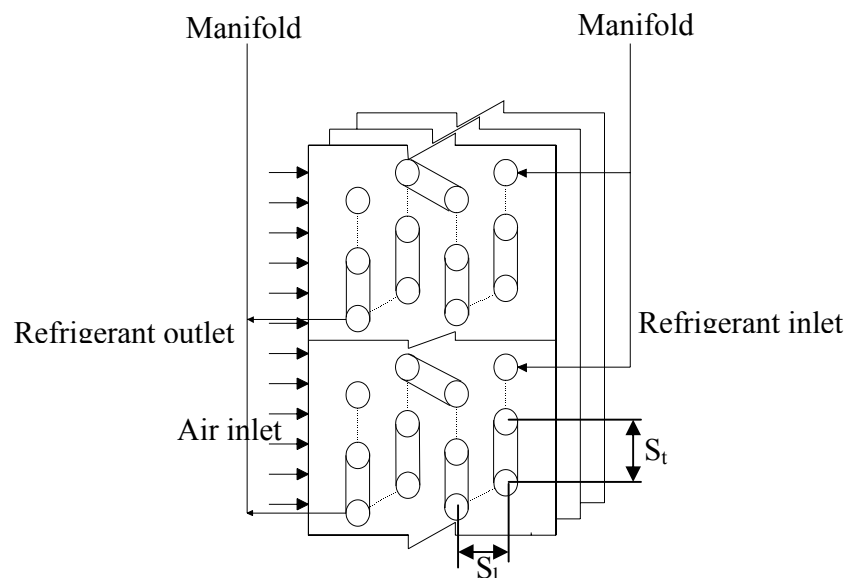


Figure 5.1 Finned-tube heat exchanger simple circuitry
(Shown: 4 rows, 2 circuits, 6 tubes per row)

Two possible approaches are usually taken when analyzing heat exchangers of this type. The first is a lumped method, in which the heat exchanger is analyzed as a single or several limited control volumes with two inlets and two outlets for each section (Fisher 1982, Kim 2002, and Jabardo 2002). The second technique is a local analysis, known as the distributed method, in which the heat exchanger is divided into segments or multiple control volumes, with the outlet of one control volume being the inlet to an

adjacent control volume, and vice versa. Efforts to develop simulation models based on the second method are ongoing (Liang 2001, and Bensafi 1997). Since the divided segments can be made small enough, the formulae for the calculation of local heat transfer coefficient (HTC) and pressure drop for fluids in the heat exchangers can be utilized directly and thus a higher degree of accuracy can be expected. Particularly, at the present time the computer-aided modeling and design techniques will be the drive motor of change for AC systems towards improving design systems, planning operation and control strategies. Furthermore, the rapid development of computer technologies and a deeper understanding of computing theory in engineering motivate the simulation to become more and more popular, and likely to replace much of the experimental work currently carried out. In this study, the second approach has been used in the AC heat exchangers thermal analysis.

5.3 Model development

Model descriptions are presented in the following manner. The calculations of heat transfer and pressure drop for both refrigerant and air sides are performed first. Then, the control volume analysis is introduced. Following that, model's assumptions and the model governing equations are presented. The thermodynamic properties of the refrigerant (R-134a) are determined using the software CATT (1994) while the thermophysical properties are obtained by using the McLinden M et al (1989) model. Both thermodynamic and thermophysical properties are typified in equation form by using the least-square method for curve-fitting of a set of numerical data. These correlated equations and their error analysis are reported in Appendix G.

The following section represents the calculation of the heat transfer coefficients and pressure drop for both the air and refrigerant sides on the basis of the correlations selected from the available literature.

5.4 Air-side heat transfer coefficient and pressure drop

To calculate the heat transfer coefficient and pressure drop on the air-side, several parameters need to be predetermined by direct calculation from the evaporator geometry. They are hydraulic diameter, minimum free-flow area, total heat transfer area, bare area, fin area, and fin efficiency. Appendix D provides details of the procedure for calculating these geometrical configurations.

The heat transfer coefficient and pressure drop have been computed from the experimental correlations derived from Kays and London (1964). The heat transfer parameter is written as Stanton number S_t times Prandtl number Pr to the 1/3 power. It is given as a function of Reynolds number, Re where the function was established through curve-fitting of a set of the experimental data:

$$S_t \times Pr^{\frac{2}{3}} = 0.11227 \times Re^{-0.261} \quad (5.1)$$

Where these three dimensionless parameters are defined as:

$$S_t = \frac{A_{\min} \times \alpha_a}{\dot{m}_a \times C_{pm}}, \quad Pr_a = \frac{C_{pm} \times \mu_a}{k_a}, \quad \text{and} \quad Re_a = \frac{\dot{m}_a \times Dh}{A_{\min} \times \mu_a}$$

Where,

α_a = heat transfer coefficient, (kW/m². °C)

\dot{m}_a = mass flow rate of air through the evaporator, (kg/.s)

A_{\min} = minimum free-flow air area, (m²)

C_{pm} = specific heat of moist air, (kJ/kg_{da}. °C)
= $C_{p,a} + W_{a,av} \times C_{p,v}$ (ASHRAE, 1997)

$W_{a,av}$ = average air humidity ratio, (kg_v/kg_{da})

- μ_a = dynamic viscosity of air (kg/m.s)
 k_a = thermal conductivity of air (W/m. °C)
 D_h = hydraulic diameter, (m) (Appendix D)

The specific heat of dry air $C_{p,a}$, and the specific heat of water vapour $C_{p,v}$ are obtained from the least squares regression of the data from Rogers and Mayhew (1982) as follows,

$$C_{p,a} = 1003.6 + 0.051 \times t_{a,av} \quad (\text{J/kg}_{\text{da}} \cdot ^\circ\text{C}) \quad (5.2)$$

$$C_{p,v} = 1857.2 + 0.284 \times t_{a,av} \quad (\text{J/kg}_v \cdot ^\circ\text{C}) \quad (5.3)$$

Equation 5.2 is valid for $t_{a,av}$ between 3°C to 52°C, while Equation 5.3 is valid when $t_{a,av}$ is between 3°C and 77°C. When the coil is wet, the air side convective heat transfer coefficient is computed from Myers (1967),

$$\alpha_{aw} = \alpha_a \times M_f \quad (5.4)$$

The correction factor M_f in Equation 5.4 is obtained from Myers (1967),

$$M_f = 1.0673 \times V_{fr}^{0.101}, \quad V_{fr} \text{ is air face velocity in m/s.} \quad (5.5)$$

The pressure drop associated with the air through the evaporator or condenser matrix consists of three components which include core friction, core acceleration, and entrance and exit losses. Kays and London (1964) gave a correlation to evaluate the total pressure drop for fluid flow across the heat exchanger matrix. In this study, the pressure change resulting from flow acceleration is neglected due to minimal density variation of

the air as it passes through the evaporator or condenser cores. The equation for calculating total pressure drop becomes:

$$\Delta P_a = \frac{Ga^2}{2 \times \rho_a} \times \left[\left(1 + k_c - \sigma^2 \right) + \left(f \cdot \frac{A_o}{A_{\min}} \right) + \left(1 - k_e - \sigma^2 \right) \right] \quad (5.6)$$

Where σ represents the ratio of the minimum free-flow area to the frontal area, Ga is the maximum air mass velocity ($\text{kg/m}^2 \cdot \text{s}$), ρ_a is the density at inlet, k_c and k_e are the flow contraction and expansion coefficients, respectively. Kays and London suggested the use of k_c and k_e curves for $\text{Re} = \infty$ to deal with the surfaces which have very frequent fin interruptions. Based on their experimental work (Kays and London, 1964), $k_c = 0.16$ and $k_e = 0.05$ for $\sigma = 0.566$.

The friction factor f for a dry process like the process in the condenser can be written as a function of Reynolds number through curve-fitting of a set of experimental data:

$$f = 0.68432 \cdot \text{Re}^{-0.278} \quad (5.7)$$

However, the friction factor is affected by the inlet air relative humidity at small fin pitch owing to the presence of water condensate for the evaporator case. Wang, C.C et al. (2000) developed a friction correlation to include the effect of the air moisture implicitly by using the condensate film Reynolds number, Re_{film} as follows.

$$f = 16.55 \text{Re}_{do}^{f1} (10 \times \text{Re}_{film})^{f2} \times \left(\frac{A_o}{A_{p,o}} \right)^{f3} \left(\frac{S_l}{S_t} \right)^{f4} \left(\frac{F_p}{d_h} \right)^{-0.5827} \left(e^{d_h/d_o} \right)^{-1.117} \quad (5.8)$$

The exponential factors $f1, f2, f3,$ and $f4$ are determined as a function of geometrical coil parameters through correlations proposed by Wang, C.C et al. (2000) and are listed in Appendix D.

5.5 Refrigerant-side heat transfer coefficient and pressure drop for evaporator model

In the evaporator model, two characteristic zones are considered: evaporation (or two-phase) and superheating (or single-phase). At the evaporator inlet, the refrigerant is almost always a mixture of liquid and vapour. Through the evaporation zone, the refrigerant is boiled and leaves the evaporator normally in the form of superheated vapour. Hence, the heat and/or mass transfer process in each section must be modeled separately. Equations for calculating the heat transfer coefficient and pressure drop of these regions are given in the following section.

5.5.1 Superheated region

The flow in the evaporator tubes always remains at high Reynolds number due to the relatively high fluid velocity through the small tubes diameter. Therefore, the heat transfer correlations for turbulent flow have been adopted in the analysis. Dittus and Boelter (1930) modified the Colburn equation and gave a correlation which could be used for both cooling and heating of the fluid:

$$\alpha_{sp} = \frac{k_r}{d_i} \times 0.023 \times \text{Re}_i^{0.8} \times \text{Pr}_i^n \quad (5.9)$$

Where $n = 0.4$ for heating and $n = 0.3$ for cooling. Once the Nusselt number has been computed from Equation 5.9, the heat transfer coefficient is then calculated by the expression that defines the Nusselt number.

The basic pressure drop equation was derived by applying the flow momentum balance to a control volume. The general form for steady-state single-phase flow in a

smooth tube shown below accounts for three applied forces which are pressure, gravity, and wall shear, respectively.

$$\Delta p + \rho \cdot g \cdot \sin \alpha - \frac{P \cdot \tau_w \cdot \Delta L}{A} = 0 \quad (5.10)$$

In Equation 5.10, τ_w (Pa) is the wall shear stress, P (m) is the tube periphery, and ΔL (m) is the tube length. For single-phase flow of a low-density vapour, the gravitational term due to a small change of elevation is not significant in comparison with the frictional loss. Therefore, for a circular pipe with the diameter d_i (m), the equation related to the wall shear becomes,

$$\Delta p_{sp} = \frac{4\tau_w \cdot \Delta L}{D} \quad (5.11)$$

And τ_w can be expressed in terms of friction factor

$$\tau_w = \frac{f}{8} \rho U^2 \quad (5.12)$$

Combing Equation 5.11 and Equation 5.12 gives the Darcy-Weisbach (1994) for calculating single-phase frictional pressure drop,

$$\Delta p_{sp} = \frac{f \cdot \Delta L}{D} \cdot \frac{\rho U^2}{2} \quad (5.13)$$

The friction factor f is determined by using Blasius (1993) correlation,

$$f = 0.079 \times \text{Re}_i^{-0.25} \quad (5.14)$$

5.5.2 Evaporation region

For the convective boiling conditions prevailing in the evaporator, the Wattlelet et al. (1992) correlation for the heat transfer coefficient has been adopted. It is to be noted that these correlations are local, in other words, dependent upon the quality.

$$\alpha_{tp} = 3.37 \times \alpha_l \cdot x_{tt}^{0.686} \quad (5.15)$$

Where x_{tt} is the Martinelli parameter, which is defined as a function in refrigerant vapor quality as follows:

$$x_{tt} = \left(\frac{1-x}{x}\right)^{0.9} \times \left(\frac{\rho_v}{\rho_l}\right)^{0.5} \times \left(\frac{\mu_l}{\mu_v}\right)^{0.1} \quad (5.16)$$

The subscripts l and v refer to the liquid and vapour phases, respectively. The liquid heat transfer coefficient for α_l is calculated by using Dittus and Boelter (1930).

Jung and Radermacher (1989) proposed a correlation to calculate the frictional two-phase pressure drop in a horizontal smooth tube. The calculation was based on the modification of the previous work of Lockhart and Martinelli (1949). The concept is to calculate the two-phase frictional pressure drop based on the single-phase frictional pressure drop multiplied by a two-phase friction multiplier, ϕ defined as:

$$\phi^2 = 30.79 \cdot x^{1.323} \cdot (1-x)^{0.477} \cdot Pr_i^{-0.732}$$

$$\text{And thus } \Delta P_{tp} = \Delta P_{sp} \times \phi^2 \quad (5.17)$$

Inertial effects over pressure drop in heat exchangers have been included only in those regions where there is a change of phase. In that case, the inertial component is determined from the following equation:

$$\Delta P_{it} = Gr^2 \times \left\{ \left[\frac{x_e}{\rho_v \cdot \gamma_e} + \frac{(1-x_e)^2}{\rho_l \cdot (1-\gamma_e)} \right] - \left[\frac{x_i}{\rho_v \cdot \gamma_i} + \frac{(1-x_i)^2}{\rho_v \cdot (1-\gamma_i)} \right] \right\} \quad (5.18)$$

Densities of saturated vapor and liquid are assumed constant throughout the two-phase flow regions. For refrigerant flowing inside the tubes of the evaporator, the exit quality, x_e , and void fraction, γ_e are equal to one and zero at the inlet of the change of phase region, so that Equation 5.18 can be simplified to the following form:

$$\Delta P_{it} = Gr^2 \times \left[\frac{1}{\rho_v} - \frac{1}{\rho_l} \right] \quad (5.19)$$

5.5.3 Refrigerant-side heat transfer coefficient and pressure drop for condenser model

The refrigerant enters the condenser as a superheated vapor, condenses inside the tubes, and exits as a subcooled liquid. Therefore, the condenser analysis will involve two characteristic zones which are desuperheating and subcooling (single-phase) and condensing (two-phase). The next paragraph exhibits the heat transfer and pressure drop correlations applied for the refrigerant-side as a single-phase and two-phase modes. The single-phase heat transfer coefficient for the refrigerant either in desuperheating or subcooling form is calculated similarly by using Dittus and Boelter (1930). Several correlations for the condensing heat transfer coefficient of refrigerants have been proposed in the last 20 years for conventional channel size. The correlation proposed by Shah (1979) for local condensing heat transfer coefficient has been employed in the present model due to its simplicity and relative accuracy.

$$\alpha_{tp}(x) = \alpha_l \times \left[(1-x)^{0.8} + \frac{3.8 x^{0.76} (1-x)^{0.04}}{Pr_l^{0.38}} \right] \quad (5.20)$$

The pressure drop for the refrigerant is calculated based on the procedure described for the evaporator as aforementioned. The work of Yang and Webb (1996) is used to evaluate frictional pressure drop for single and two-phase refrigerant respectively. The correlation for two-phase is represented as follows:

$$\Delta p_{tp} = C_{f_{eq}} \frac{2 \times Gr^2 \times L_{tp}}{\rho_r \times d_i} \quad (5.21)$$

Where,

$$\frac{C_{f_{eq}}}{C_f} = 0.435 \times Re_{eq}^{0.12} \quad , \quad Re_{eq} = \frac{G_{eq} d_i}{\mu_r} \quad , \quad C_f = 0.0676 \times Re_i^{-0.22} \quad ,$$

$$\text{and } G_{eq} = \left[(1-x) + x \left(\frac{\rho_l}{\rho_v} \right)^{0.5} \right]$$

5.6 Modeling scheme

For a given coil configuration, the simulation process begins with a set of input conditions for air and refrigerant. The refrigerant and air mass flow rates need to be estimated initially. The governing equations, the correlations for heat transfer coefficient, and pressure loss equations are applied to a control volume. Air and refrigerant properties at the exit of the control volume are calculated using an iterative procedure. It is suggested to divide the surface area of the coil into equal control volumes, each of an elementary area δA_0 and an elementary length δx as shown in Figure 5.2. Tubes are arranged parallel to the i direction, j is specified in the longitudinal direction. The airflow is parallel to the j direction and refrigerant flow is assumed in the counter-cross direction to the air for this sample. The selection of the number of control volumes in the i direction is arbitrary from unity to infinity. The accuracy of the model improves as the number of elements is increased. This improvement in accuracy must be paid for, however, with a considerable increase in computing time. The coordinate value i , is

allocated according to the number of control volumes selected by the model: j corresponds to the number of deep-rows starting from the air inlet. The pipes are numbered in order starting from the refrigerant inlet to the refrigerant outlet for each circuit. The modeling procedure requires the setting up of the conservation equations for each control volume and an efficient routine to solve these equations for each section. The first control volume is selected at the refrigerant outlet position and the computation is repeated for each successive control volume along the opposite direction of refrigerant flow until the refrigerant inlet position is reached.

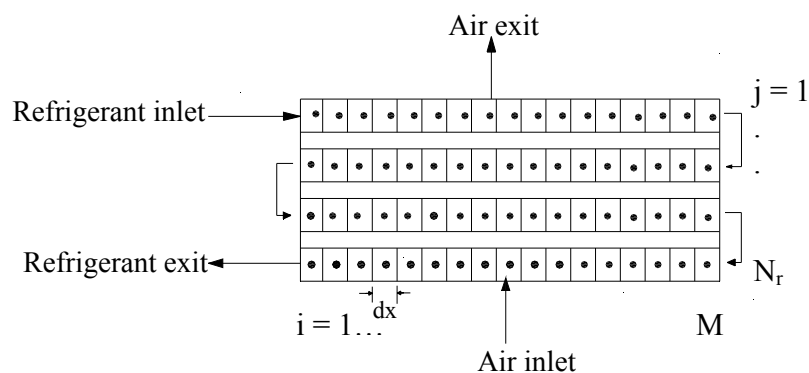


Figure 5.2 The mesh grids of the counter-cross flow evaporator in single circuitry

5.7 Model Assumptions

Prior to setting up the conservation equations for each section, some assumptions are proposed in advance. The major assumptions in the development of the heat exchangers model, either evaporator or condenser, are listed as follows:

1. Heat conduction in the direction of the pipe axis and nearby fins is neglected.
2. Only pure refrigerant is considered. No oil influence on heat transfer and pressure drop.

3. The thermodynamic properties of the air and the refrigerant are constant within an element.
4. No contact heat-resistance between the fin and pipe
5. Refrigerant at any point in the flowing direction is in thermal equilibrium.
6. Convection and radiation energy losses to the surroundings are neglected.
7. Changes in kinetic and potential energies are negligible.
8. Heat addition due to friction work on the control surface is negligible.

For the refrigerant side, the mass conservation is automatically satisfied because of the steady-flow assumption. The momentum equation can be represented by means of the calculation of pressure drop in each section. The energy equation can be simply expressed as shown in the next section. There are three elements in the model: circuit, tube and control volume. The basic element for computation in the model is the control volume, as shown in Figure 5.3.

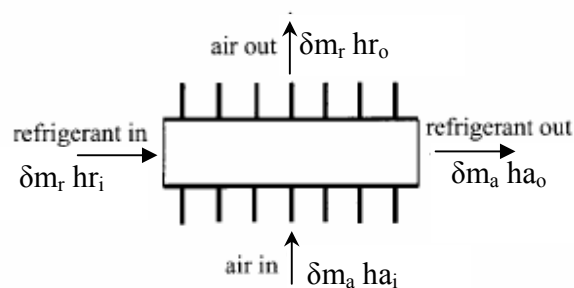


Figure 5.3 A control volume along a tube with fins

5.8 Governing equations for evaporator model

As illustrated graphically in Figure 5.4, moisture in air may condense on the cooling surface if the surface temperature of the tubes is below the dew point of the surrounding air, which results in simultaneous heat and mass transfer. In order to simulate the heat transfer mechanism from the moist air to refrigerant, it may be broken

down into two phases. The first phase is the heat transfer from the moist air to the tube surface and it can be expressed by “enthalpy potential” method (Threlkeld, 1972). While the second phase is the heat transfer from tube surface to the refrigerant-side and it is expressed normally by “temperature potential” concept. The calculations of the heat transfer in the first phase require coupling between the simultaneous heat and mass transfer. Using the heat and mass transfer analog, the mass transfer coefficient, α_m is related to the sensible heat transfer coefficient, α_{aw} by the Lewis number, Le .

$$\alpha_m = \frac{\alpha_{aw}}{Le.C_{pm}} \quad (5.22)$$

With the assumption that the leaving water temperature outside the tube is equal to the tube outer surface temperature, the incremental heat transfer from the moist air to the tube surface is obtained as follows:

$$\delta Q_{i,j} = \eta_s \alpha_{aw} \delta A_o (t_{a,i,jm} - t_{s,i,jm}) + \frac{\alpha_{aw} \eta_s}{Le.C_{pm}} h_{fg} \delta A_o (W_a - W_s) \quad (5.23)$$

The first term accounts for the sensible heat transfer while the last one accounts for the latent mode. The Lewis number approaches closely to a unity for most air-conditioning process, ASHRAE (1997). Substituting for $Le = 1$ and by using the primary definition of the specific enthalpy, h for moist air, the previous equation may be expressed in terms of the mean enthalpy difference as shown below:

$$\delta Q_{i,j} = \frac{1}{\partial R_o} \times (h_{a,i,jm} - h_{s,i,jm}) \quad (5.24)$$

Where,

$$h = C_{pm} t + W h_{fg} \quad , \text{ and } \partial R_o = \frac{C_{pm}}{\alpha_{aw} \eta_s \delta A_o}$$

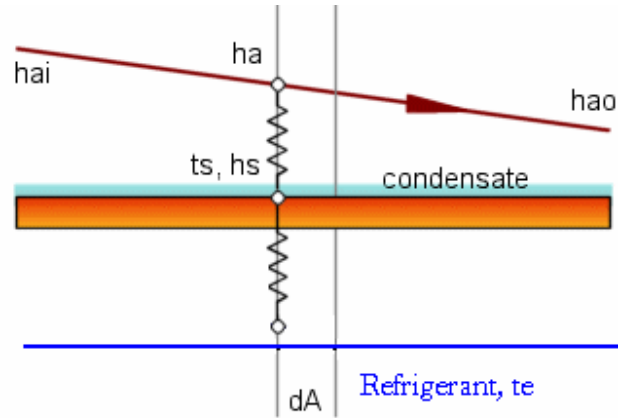


Figure 5.4 Thermal model of a wet DX-evaporator coil

The second phase (heat transfer from the tube surface via the refrigerant) is represented by the following equation:

$$\partial Q_{i,j} = \frac{1}{\partial R_i} \times [ts_{i,jm} - te] \quad (5.25)$$

The other equations for total heat transfer rates can be obtained by performing energy balances on the fluids entering and leaving a control volume, for the air-side and refrigerant-side, respectively.

$$\partial Q_{i,j} = \partial m_a \times [ha_{i,j} - ha_{i,j+1}] \quad (5.26)$$

$$\partial Q_{i,j} = \partial m_r \times [hr_{i,j} - hr_{i+1,j}] \quad (5.27)$$

Where,

$$\partial R_i = \frac{1}{\alpha_r} + \frac{r_{fi}}{\partial A_i} + \frac{\ln(d_o/d_i)}{2\pi k_t l}; \quad \partial R_o = \frac{C_{pm}}{\eta_s \alpha_a} + \frac{r_{fo}}{\partial A_o}, \quad \text{and } ha_{i,jm} = \frac{(ha_{i,j} + ha_{i,j+1})}{2}$$

r_{fi} and r_{fo} are the inner and outer fouling resistance for refrigerant and air respectively and are assumed in this study as 0.00035 and 0.004 m².°C/W. While η_s is the overall air side wet surface efficiency, and it is obtained from (Threlkeld, 1972) as follows:

$$\eta_s = 1 - \frac{A_f}{A_o} \times (1 - \eta_{fw}) \quad (5.28)$$

For a plate-fin-and-tube heat exchanger with multiple rows of staggered tubes, Schmidt (1945) proposed that the plates can be symmetrically divided into hexagonal shaped fins and they can be treated as circular fins by using an equivalent circular fin radius. Therefore, the wet fin efficiency for total heat transfer η_{fw} can be calculated from (McQuiston and Parker, 1994),

$$\eta_{fw} = \frac{\tanh(mr_o\phi)}{(mr_o\phi)} \quad (5.29)$$

Where,

$$m = \left(\frac{2\alpha_{aw}}{t_f k_f} \right)^{0.5} \quad (5.30)$$

r_o = is the outer radius of the evaporator tube, m.

ϕ = is the fin efficiency parameter for a circular fin and it is determined as:

$$\phi = \left(\frac{Re_q}{r_o} - 1 \right) \left(1 + 0.35 \ln \left(\frac{Re_q}{r_o} \right) \right) \quad (5.31)$$

Schmidt (1945) developed empirical correlations for the equivalent radius, Re_q as:

$$\frac{Re_q}{r_o} = 1.27\psi(\beta - 0.3)^{0.5} \quad (5.32)$$

$\psi = \frac{B}{r_o}$, $\beta = \frac{H}{B}$ for this analysis: $B = S_t$ if $S_l < 0.5S_t$, otherwise $B = 0.5S_t$

$$H = \frac{1}{2} \sqrt{\left(\frac{S_t}{2} \right)^2 + S_l^2} \quad (5.33)$$

Where S_t is the transverse tube spacing and S_l is the longitudinal tube spacing. α_{aw} can be obtained from the following expression (Threlkeld, 1972),

$$\alpha_{aw} = \frac{1}{\left(\frac{C_{pm}}{\alpha_a b_{wm}} + \frac{y_w}{k_w} \right)} \quad (5.34)$$

It is evident from Equation 5.34 that the evaluation of α_{aw} requires an estimation of y_w . Threlkeld has demonstrated that y_w/k_w is small in case of a water film and has recommended a water film thickness of 0.1016 mm (0.004 inches) as suggested by Myers (1967). The mean saturated air specific heat b_{wm} represents the slope of Equation 5.35 which signifies the saturation enthalpy of air as a function of tube surface temperature (neglecting the conductance of water film thickness).

$$hs_{i,jm} = 10.73 + 1.4 ts_{i,jm} + 0.046 ts_{i,jm}^2 \quad (5.35)$$

Equation 5.35 is curve fitted over the temperature range of 0°C to 50°C based on ASHRAE (1997). Thus, the mean saturated air specific heat b_{mw} can be computed by differentiation of Equation 5.35 which yields:

$$b_{mw} = 1.4 + 0.092 ts_{i,jm} \quad (5.36)$$

The above analysis gives a system of equations (5.24, 5.25, 5.26, 5.27, and 5.35) to be solved numerically. This system consists of a set of five finite difference equations with five unknowns ($\delta Q_{i,j}$, $hr_{i+1,j}$, $ha_{i,j+1}$, $hs_{i,jm}$, $ts_{i,jm}$). However, the reader should note that the calculation of the wet fin efficiency requires knowing the mean surface temperature first. Thus, at the start of the model solution, the second term in Equation 5.36 can be initially ignored. By solving the governing equations, the wet fin efficiency can be computed iteratively thereafter.

5.9 Model calculation methodology

The formulation of a control volume model presented previously has been implemented into a computer program written in MICROSOFT VISUAL BASIC language. The computer program solves the above Equations (5.24, 5.25, 5.26, 5.27, and 5.35) incrementally along the refrigerant and air flows direction. Before starting the solution methodology, these Equations should be reformulated in a simple form by eliminating $\delta Q_{i,j}$ from each equation as follows:

From Equations 5.27 and 5.25

$$hr_{i+1,j} = hr_{i,j} - \frac{1}{\partial mr \times \partial Ri} \times [ts_{i,jm} - te] \quad (5.37)$$

From Equations 5.26 and 5.25

$$ha_{i,j+1} = ha_{i,j} - \frac{1}{\partial ma \times \partial Ri} \times [ts_{i,jm} - te] \quad (5.38)$$

From Equations 5.24 and 5.25

$$\frac{1}{\partial Ro} \times [ha_{i,jm} - hs_{i,jm}] = \frac{1}{\partial Ri} \times [ts_{i,jm} - te] \quad (5.39)$$

Substituting Equations 5.34 and 5.38 into Equation 5.39 produces the following equation which is assorted in quadric form to simplify the solution:

$$A \times ts_{i,jm}^2 + B \times ts_{i,jm} + C = 0 \quad (5.40)$$

Where,

$$A = 0.046,$$

$$B = \left(1.4 + \left(\frac{\delta Ro}{\delta Ri} + \frac{1}{2 \times \delta ma \times \delta Ri} \right) \right)$$

$$C = \left[10.73 - \left(\frac{\delta Ro}{\delta Ri} + \frac{1}{2 \times \delta ma \times \delta Ri} \right) \times te - ha_{i,j} \right]$$

The previous quadric equation can be solved directly to obtain $ts_{i,jm}$ and then the other terms ($hr_{i+1,j}$, $ha_{i,j+1}$, $\partial Q_{i,j}$, and $hs_{i,jm}$) can be computed easily from Equations 5.37, 5.38, 5.26 or 5.27, and 5.35 respectively. The previous governing Equations, 5.24 up to 5.35, are appropriate to be used in the superheat region taking into account the single-phase heat transfer correlation and some modifications in Equation 5.25 to become as follows:

$$\partial Q_{i,j} = \frac{1}{\partial Ri} \times \left[ts_{i,jm} - \left(\frac{2te + \Delta tsh}{2} \right) \right] \quad (5.41)$$

Similarly, the single-phase governing equations are solved identically by the same technique which is used in the two-phase region.

5.10 Governing equations for condenser model

The total heat transfer rate in the condenser model is computed by using the method of a logarithmic mean temperature difference which can be approached as the arithmetic mean temperature difference. The approach is applicable owing to the infinitesimal size of the control volume. The equations associated with each control volume for the two-phase region are given below:

$$\partial Q_{i,j} = \partial m_a \times Cp_a \times \left(Ta_{i,j+1} - Ta_{i,j} \right) \quad (5.42)$$

$$\partial Q_{i,j} = \partial m_r \times \left(hr_{i+1,j} - hr_{i,j} \right) \quad (5.43)$$

$$\partial Q_{i,j} = U_{tp} \times \partial A_o \times \left(Tc - \left(\frac{Ta_{i,j} + Ta_{i,j+1}}{2} \right) \right) \quad (5.44)$$

Where,

$$\frac{1}{U_{tp}} = \frac{\partial A_o}{\alpha_{tp} \partial A_i} + \frac{1}{\alpha_o \times \eta_s} + \frac{\partial A_o \times (\ln (do/di))}{2\pi k \partial x} + \frac{r_{fi} \times \partial A_o}{\partial A_i} + r_{fo}$$

The above analysis gives a system of equations to be solved numerically. This system consists of a set of three finite difference equations with three unknowns ($\delta Q_{i,j}$, $hr_{i+1,j}$, $Ta_{i,j+1}$). The computer model is developed to solve the above system of equations. The system of equations are solved numerically and simultaneously, by eliminating $\delta Q_{i,j}$ from each equation as follows:

From Equation 5.42,

$$Ta_{i,j+1} = Ta_{i,j} + \frac{\partial Q_{i,j}}{\partial m_a \times Cp_a} \quad (5.45)$$

From Equations 5.42 and 5.44,

$$\delta Q_{i,j} = \frac{U_{tp} \times \partial A_o}{\delta m_r \times \left(1 + \frac{\delta NTU_a}{2}\right)} \times (Tc - Ta_{i,j}) \quad (5.46)$$

From Equations 5.45 and 5.48,

$$Ta_{i,j+1} = Ta_{i,j} + \frac{\delta NTU_a}{\left(1 + \frac{\delta NTU_a}{2}\right)} \times (Tc - Ta_{i,j}) \quad (5.47)$$

From Equations 5.43 and 5.46,

$$hr_{i+1,j} = hr_{i,j} + \frac{U_{tp} \times \partial A_o}{\delta m_r \times \left(1 + \frac{\delta NTU_a}{2}\right)} \times (Tc - Ta_{i,j}) \quad (5.48)$$

The governing equations for the single-phase zones are expressed as follows:

$$\partial Q_{i,j} = \partial m_a \times C p_a \times (T a_{i,j+1} - T a_{i,j}) \quad (5.49)$$

$$\partial Q_{i,j} = \partial m_r \times C p_r \times (T r_{i+1,j} - T r_{i,j}) \quad (5.50)$$

$$\partial Q_{i,j} = U_{sp} \times \partial A_o \times \left[\left(\frac{T r_{i,j} + T r_{i+1,j}}{2} \right) - \left(\frac{T a_{i,j} + T a_{i,j+1}}{2} \right) \right] \quad (5.51)$$

Where,

$$\frac{1}{U_{sp}} = \frac{\partial A_o}{a_{sp} \times \partial A_i} + \frac{1}{a_o \times \eta_s} + \frac{\partial A_o \times (\ln (d_o/d_i))}{2\pi k \partial x} + \frac{r_{fi} \times \partial A_o}{\partial A_i} + r_{fo}$$

Similarly, the single-phase region governing equations are re-equated and represented as follows:

From Equations 5.49,

$$T r_{i+1,j} = T r_{i,j} + \frac{\partial Q_{i,j}}{\partial m_r \times C p_r} \quad (5.52)$$

By substituting Equations 5.45 and 5.52 into Equation 5.51:

$$\partial Q_{i,j} = \frac{\partial NTU_r}{\left(1 + \frac{\partial NTU_a}{2} - \frac{\partial NTU_r}{2} \right)} \times (T r_{i,j} - T a_{i,j}) \quad (5.53)$$

Where $\partial NTU_r = \frac{U_{sp} \times \partial A_o}{\partial m_r \times C p_r}$, and $\partial NTU_a = \frac{U_o \times \partial A_o}{\partial m_a \times C p_a}$

From Equation 5.52 and 5.53

$$T r_{i+1,j} = T r_{i,j} + \frac{\partial NTU_r}{\partial m_r \times \left(1 + \frac{\partial NTU_a}{2} - \frac{\partial NTU_r}{2} \right)} \times (T r_{i,j} - T a_{i,j}) \quad (5.54)$$

From Equations 5.45 and 5.53,

$$Ta_{i,j+1} = Ta_{i,j} + \frac{\partial NTU_a}{\left(1 + \frac{\partial NTU_a}{2} - \frac{\partial NTU_r}{2}\right)} \times (Tr_{i,j} - Ta_{i,j}) \quad (5.55)$$

5.11 Simulation implementation

The developed model requires input data for coil configuration with specified physical parameters which consist of inside and outside diameter of tube, transverse and longitudinal tube spaces, number of fins per unit length, fin thickness, number of rows, and a specified coil height. Other input data includes cooling capacity, evaporating temperature, condensing temperature, degree of subcooling and degree of superheat.

The method of solution incorporated in the model is to calculate circuit-by-circuit across the heat exchanger, assuming more than one circuit exists in the evaporator. If each circuit can be assumed to exhibit the same behavior, it is thus only necessary for one circuit to be simulated. For each circuit, simulation begins with the refrigerant outlet pipe and carries on until the refrigerant inlet is reached. The heat transfer from each increment is summed in the refrigerant flow direction to get the total heat transfer rate. The logic diagram for the iteration process is shown in Figure 5.5 and Figure 5.6 for the evaporator and condenser respectively.

In the calculations, the refrigerant pressure drop and heat exchanger length are first guessed. The calculation associated with the exchanger length is repeated until the calculated total heat transfer matches the required cooling capacity or the heat rejection in the condenser case. The calculation associated with the refrigerant pressure drop is repeated until convergence is reached between the calculated refrigerant pressure drop and the iterated one. When the results converge with a specified tolerance of 0.1%, the

following data is printed: The exchanger size, blowers and fans input power, refrigerant and air pressure drop, and the exchanger outlet air properties.

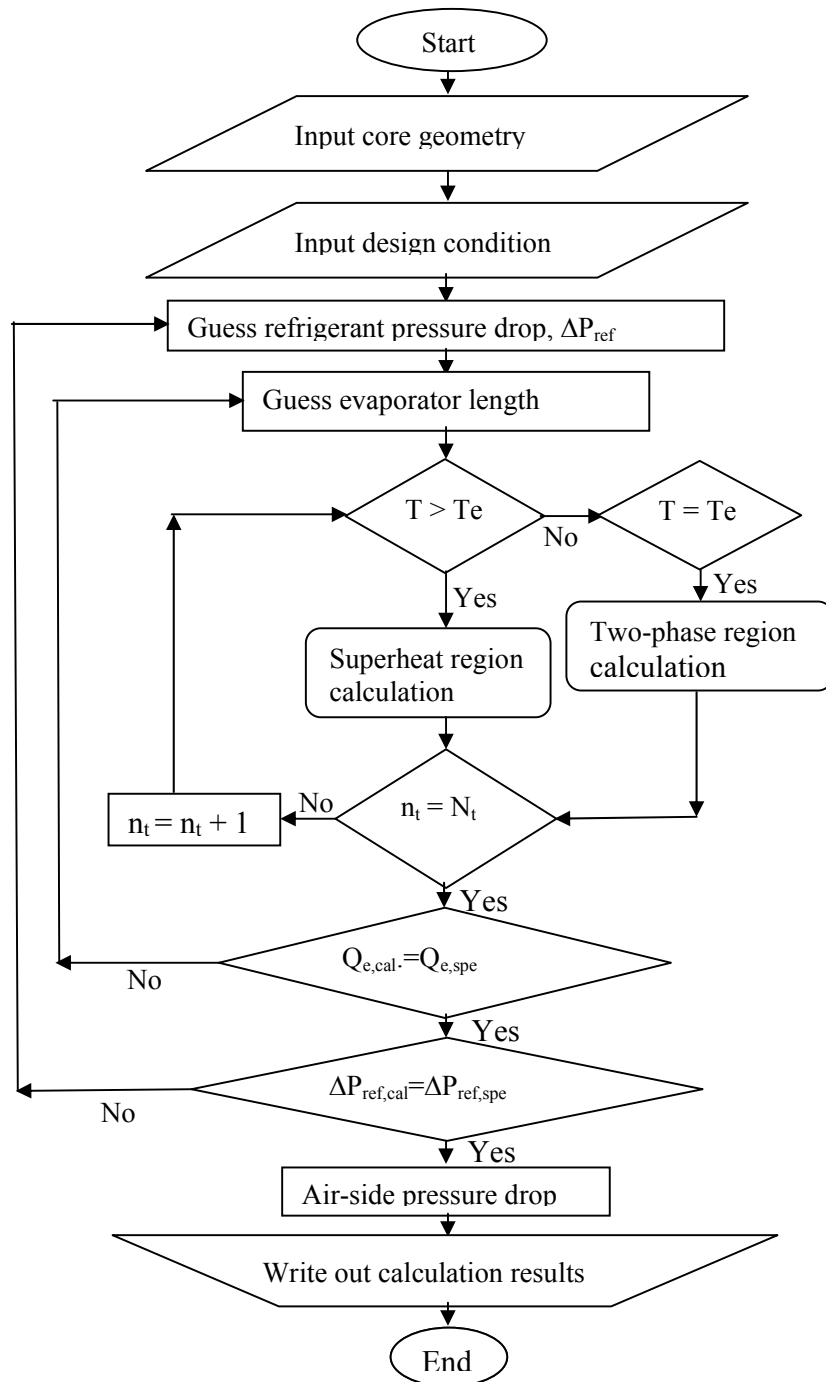


Figure 5.5 Flowchart of computer program for evaporator design

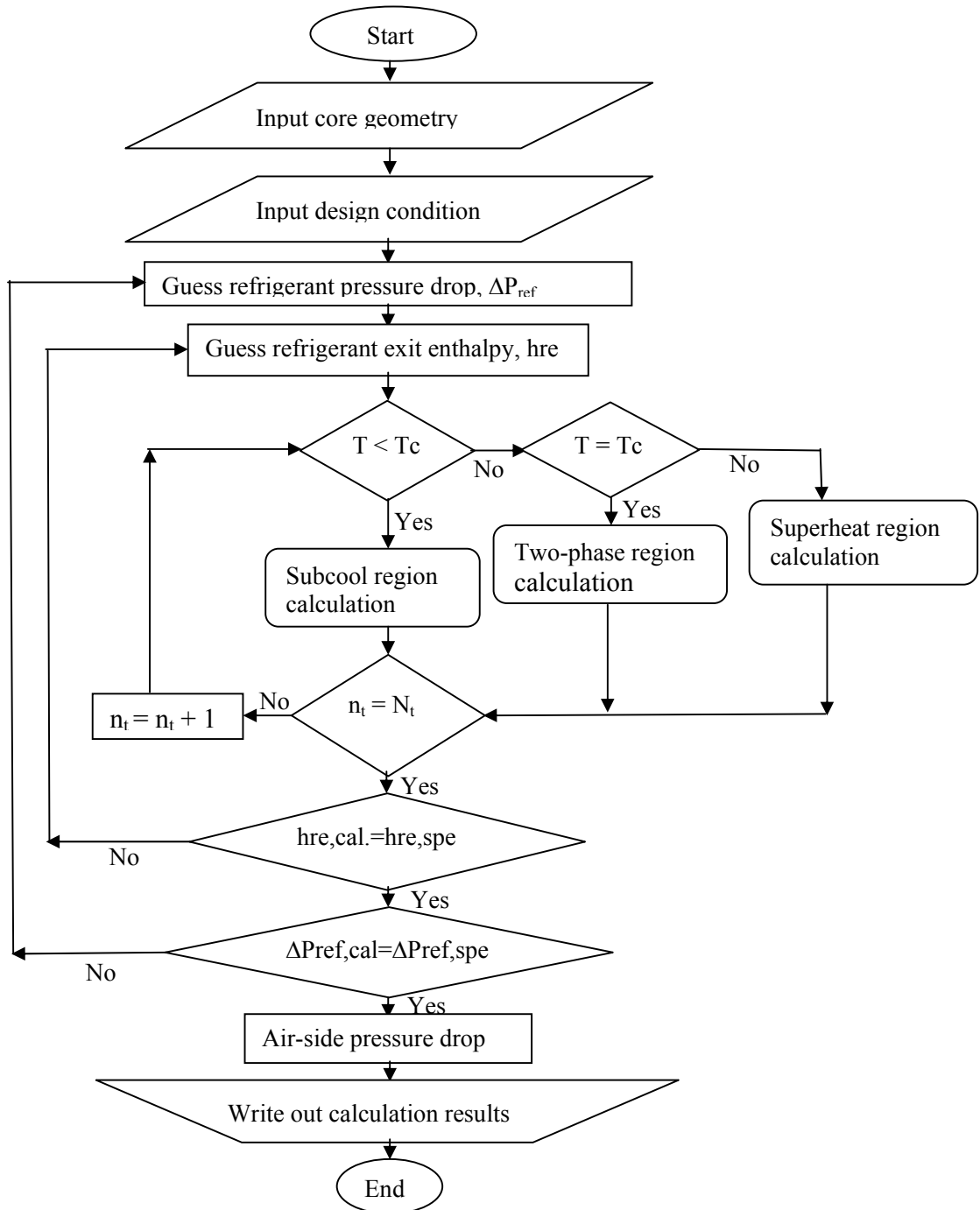


Figure 5.6 Flowchart of computer program for condenser design

The model for the condenser or evaporator is applicable for any geometrical configuration and flow arrangement with simple circuitry (see Figure 5.1). The model's validity will be investigated in the next section.

5.12 Model validation

When the computer model is completely described by its geometrical configuration, and its operational parameters, the model is able to be used as a code for finned-tube heat exchanger sizing or rating design. In order to prove the codes' reliability, it should be compared with experimental data or with the results of a commercially reliable computer software interface which is currently sold by some heat exchanger manufacturers. In this study, the comparison is accomplished in two ways.

The main purpose of the evaporator model is to be incorporated in the system simulation model. Therefore, the model should be assessed as a code for a rating design and this has been done by comparing its results with the experimental data of Horuz et al. (1998). However, for the condenser model, a commercial computer software interface (TechniSolve Software cc, 1985) is selected as a gauge for the code's feasibility for sizing and rating condenser design. The condenser model has two tasks; one is to complete the refrigeration cycle in the system simulation model and the other is to be used as a platform to carry out the thermoeconomic optimization for its design as described in Chapter 8. The condenser's computer code will be assessed as a rating and sizing code to accomplish its required tasks.

The specifications of the Horuz et al. (1998) evaporator coil are presented in Table 5.1. The rating assessment has been carried out by changing the frontal air velocity (from 0.6m/s to 2.4 m/s) for a prescribed frontal area of 0.065 m² and observing the impact on the cooling capacity variation. Table 5.2 represents the comparison between the experimental results and those which were predicted from the current study.

Table 5.1: Summary of physical data of coil (Horuz et al., 1998)

Geometric parameters	Values	Geometric parameters	Values
Tube spacing (mm×mm)	51×45	Fin pitch (fins/mm)	0.274
Tube inner diameter (mm)	12.7	Number of rows	4
Tube outer diameter (mm)	10.2	Number of circuits	1
Height (mm)	255	Number of tubes per rows	5
Length (mm)	255	Fin thickness, mm	0.25

Table 5.2: Comparison between present model prediction and the experimental data for evaporator model

Coil inlet air conditions	Horuz et al. (1978) $Q_{e_{exp}}$, kW	Present work $Q_{e_{sim}}$, kW	Deviation %
$v_{fr} = 0.60$ m/s $t_{ai} = 30.5$ °C $rh_i = 50.0$ %	1.50	1.53	+2.00
$v_{fr} = 1.00$ m/s $t_{ai} = 30.50$ °C $rh_i = 50.00$ %	1.70	1.57	-7.64
$v_{fr} = 1.40$ m/s $t_{ai} = 30.50$ °C $rh_i = 50.00$ %	1.80	1.75	-2.78
$v_{fr} = 1.80$ m/s $t_{ai} = 30.50$ °C $rh_i = 50.00$ %	1.88	1.70	-9.41
$v_{fr} = 2.60$ m/s $t_{ai} = 30.50$ °C $rh_i = 50.00$ %	2.00	1.80	-9.85

As can be seen from Table 5.2, the difference between the calculated results for the present code and those for experimental work is typically around -9.85 % to $+2.0$ % for the cooling capacity predictions. The difference shows that there is relatively good agreement between the results of the reference and the present model.

In order to compare the results of the computer code of the condenser model and the reference commercial computer interface, both were computed at the same geometrical and operating parameters. The computer model interfaces and the

commercial interfaces are presented in the Appendix C. In Tables 5.3 and 5.4, the calculated results for the present model and reference code are presented. The test has been performed using the commercial interface default which involves four rows of tubes, 8 tubes per row, and 4 identical circuits. The plain fins have a fin pitch of 2.12 mm made from aluminium. The tubes have an outer diameter of 16.586 mm and are made from copper. The vertical and horizontal spaces between the tubes are of 50.8 mm and 38.1 mm respectively.

Table 5.3: Comparison between the predictions of the present condenser model and the reference model for a sizing mode for the condenser model

Condenser heat capacity, kW	Reference interface A_{fr}, m^2	Present model A_{fr}, m^2	Discrepancy %
8.00	0.255	0.240	-5.88
10.00	0.297	0.310	+4.51
12.00	0.338	0.356	+5.10
14.00	0.382	0.400	+4.65
16.00	0.420	0.430	+2.38
18.00	0.462	0.481	+4.18

Table 5.4: Comparison between the predictions of the present condenser model and the reference model for a rating mode for the condenser model

Condenser saturation temperature, °C	Reference interface Q_c, kW	Present model Q_c, kW	Discrepancy %
40.0	5.98	5.55	+7.19
45.0	11.29	12.04	-6.64
50.0	16.18	15.43	+4.64
55.0	20.72	21.20	-2.32
60.0	24.91	26.92	-8.07
65.0	28.76	31.42	-9.25

For sizing design, the test data matrix is executed by varying the condenser heating capacity and calculating the condenser frontal area, A_{fr} as a result. For rating design, the condenser saturation temperature was varied for the same condenser frontal

area of 0.57 m^2 and ambient air of 35°C . The results of the reference model and the present model are listed in Tables 5.3 and 5.4 for rating and sizing purposes, respectively.

Tables 5.3 and 5.4 reveal that the difference between the computed results for the reference and the present code in terms of the frontal coil area is typically around -5.88% to $+5.1\%$ for the frontal area calculation. Furthermore, the present model gives satisfactory results and is consistent with the reference interface for the condenser heat capacity prediction with a maximum absolute deviation of approximately 9.25% at the maximum condensation temperature of 65°C . This result might be considered as reasonable since the higher deviation occurs at a saturation temperature considerably higher than that expected at typical operational conditions.

A low number of iteration is required for convergence. Typical values range from: 10-25 iterations for discretization of the heat exchanger length into one hundred control volumes. The model is always stable and convergence is always achieved.

5.13 Conclusion

A detailed steady-state simulation model for a finned-tube heat exchanger employed as an air-cooled condenser or a DX evaporator has been developed. The model used an explicit finite-difference scheme with LMTD-method. The hydraulic characteristics were taken into account and they were presented by the pressure drop in the refrigerant-side and air-side. The model is featured by a computer code interface, option to choose the number of circuits with simple circuitry type, number of rows, and geometry dimensions including tube diameter, coil height, tube spacing, fin thickness/pitch, and types of fins (flat and wavy pattern).

The model has been validated by comparing outputs from the model with the test data and results given in reference papers or available commercial program interface.

The model results show good agreement with those obtained from the references with a minimum and maximum deviation of -9.85% and $+2.0\%$ for the evaporator model. On the other hand, the condenser model has been assessed as a sizing and rating model and it was found that there was a discrepancy between the model's predictions and those obtained from the commercial interface which is around -5.88% to $+5.1\%$ for the sizing calculations and -9.25% to $+7.19\%$ for the rating calculations. The maximum absolute error is less than 10% which proves the validity and reliability of the analytical model for the condenser and the evaporator.

CHAPTER 6

AC SYSTEM INTEGRATION AND SIMULATION

6.1 Introduction

The simulation of the individual components of the bus AC system has been described in the previous Chapters. In this Chapter, the theoretical models of the system components will be combined into a steady-state system simulation model. The numerical technique of the computer model of the AC system's performance simulation is presented in this Chapter. The validation of the computer model is performed by comparing the simulated results with those obtained from the first group of the experiments in Chapter 4. The comparison is conducted in terms of the system's thermal performance for the three different modes of the system operation. The summary of the comparison results is presented in the last part of this chapter.

6.2 Background

The simulation program is based on a steady-state mathematical model of the components of the refrigeration circuit consisting of a compressor, two heat exchangers, thermostatic expansion valve, a receiver drier and connecting tubes, and hoses as shown in Figure 6.1. The individual components of the AC system are interdependent of each other. For example, a change in the evaporator inlet air temperature will cause alterations across the rest of the other components. As the passenger cabin temperature rises above the current steady-state operation, the warmer air input to the evaporator will not only yield higher exit air temperature but also higher refrigerant temperature leaving the evaporator. This phenomenon is known as increased load in practice. An increase in the heat load on the evaporator increases the temperature of the refrigerant gas leaving the evaporator. In turn, the bulb of the valve senses this increase and thus the valve throat opens wider to allow a larger amount of refrigerant liquid which has already settled in the volume of the receiver dryer to flow to the evaporator. This amount of refrigerant transfers to the evaporator and compensates the excess evaporation in the evaporator refrigerant flow rate. The increase in refrigerant vapor in the evaporator translates into an increase in compressor work, causing an increase in condenser pressure.

It is obvious from the above discussion that the refrigerant flow rate would have to be increased to increase the refrigerating cooling capacity in order to overcome the evaporator load increase. The refrigerant flow rate adjustments are limited to the amount of liquid present in the receiver dryer. Therefore, the refrigerant circuit can cope with higher load interactions only to a certain degree. A reverse process occurs when the evaporator load is decreased. The techniques for determining the balanced refrigeration loop and system performance, and the modeling of each component in the AC system are presented in the following sections.

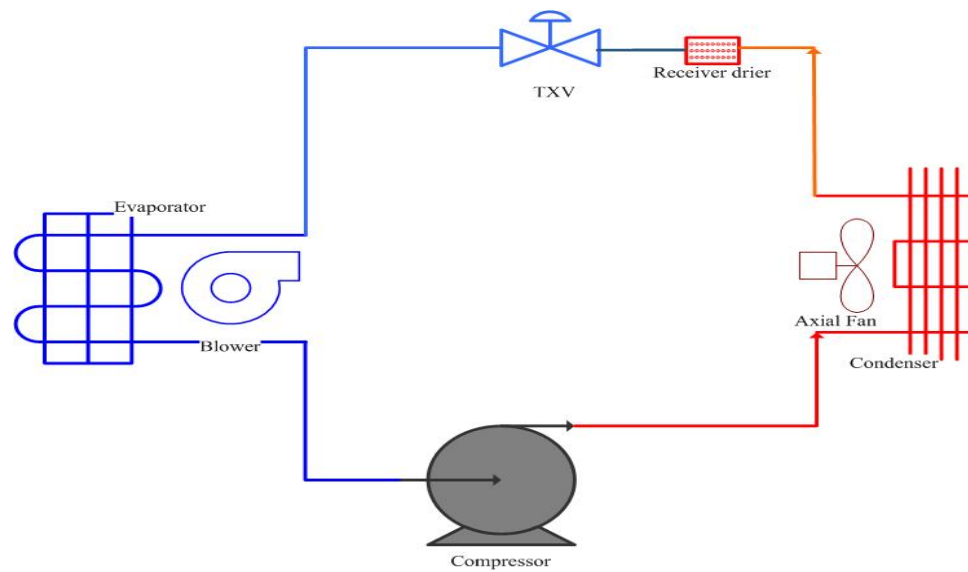


Figure 6.1 Schematic diagram of refrigeration cycle for automobile AC system

6.3 Mathematical model

The mathematical modeling for the individual components will be presented in the following sections. It should be noted that the mathematical models of some of the components such as the compressor and thermostatic expansion valve (TXV) are partially based on manufacturer's data. However, this procedure does not restrict the simulation program to a particular component model and manufacturer, since the adopted fitting procedure is general.

6.3.1 Compressor modeling

Scroll compressor is being used in residential and commercial air conditioning systems as well as in automotive AC system. The advantages of the scroll compressor are high efficiency, low torque variations, and low noise. An internal construction of this compressor is schematized in Figure 6.2.

In recent years, there has been a great deal of results and investigations concerning models elaborated to simulate the behavior of open or hermetic refrigeration compressors. Some of these models are very complex and take into account the refrigerant mass flow conditions through the inlet and outlet valves and the heat exchange in the various internal components of the compressor as in Yasuda (1983) and Parise (1983). Other models do not take into account the mass variation in the compressor, thus considering the same mass flow at the inlet and outlet as in Conde (1985). The latter type of model is adopted in this work in order to compute the mass flow and enthalpy at the compressor outlet.

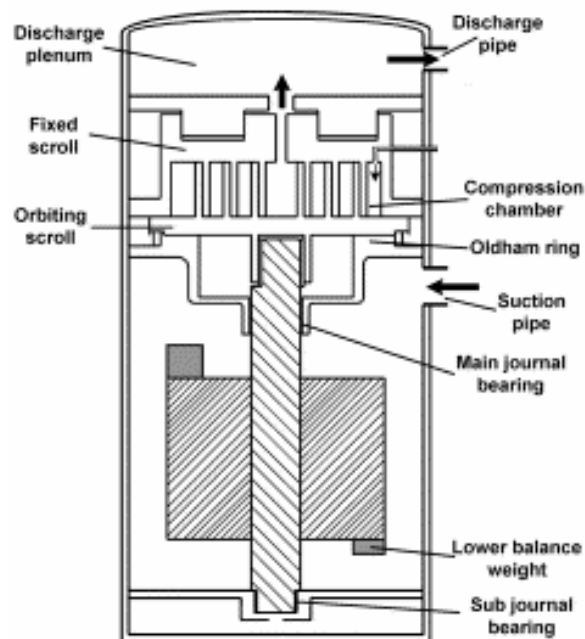


Figure 6.2 Schematic diagram of the scroll compressor

There are two required equations to characterize the behavior of the compressor: one for the mass flow rate, and the other for the power input. To calculate the refrigerant mass flow imposed by the compressor, the following equation is used:

$$\dot{m}_r = \frac{V_D \times \eta_v \times n}{v_s \times 60} \times 10^{-6} \quad (6.1)$$

Where V_D , η_v , v_s and n are the displacement volume, the volumetric efficiency of the compressor, specific volume for the refrigerant entering the compressor, and the rotational speed (rpm) respectively. The volumetric efficiency correlation can be obtained by curve-fitting the data of Park et al. (1999) for a R134a scroll compressor. It can be expressed by the following equation:

$$\eta_v = 0.82363 \times \left[1 - 0.09604 \times \left(r_p \frac{1}{\gamma} - 1 \right) \right] \quad (6.2)$$

Where,

r_p = compressor pressure ratio

γ = adiabatic index

The compressor power can be simply calculated from the energy equation for adiabatic compression process irrespective of the change in the kinetic and potential energies:

$$W_c = \frac{\dot{m}_r \left[\left(h_{cp} \right)_{dis} - \left(h_{cp} \right)_s \right]}{\eta_{is}} \quad (6.3)$$

Similarly, the isentropic efficiency, η_{is} correlation can be obtained by curve fitting the published experimental data of Park et al. (1999) and it can be expressed as:

$$\eta_{is} = 0.9343 - 0.04478 \times r_p \quad (6.4)$$

6.3.2 Heat exchangers' modelings

The condenser and evaporator are categorized as finned-tube-heat exchangers' type. The details of their modeling have been discussed in Chapter 5. The modeling has

been performed numerically by dividing the heat exchanger bundle into small control volumes taking into account the phase change of the refrigerant from region to region. In the condenser modeling, the desuperheated vapor, the condensation, and the subcooled liquid regions are considered, whereas the evaporator is divided into the evaporating and superheated vapor regions.

6.3.3 Thermostatic expansion valve modeling

The expansion device is one of the most important components of the refrigeration system. Its function is to reduce the pressure and to regulate the refrigerant mass flow rate. A widely utilized expansion device is the thermostatic expansion valves, TXV (see Figure 6.3). The thermostatic expansion valve is used for controlling the refrigerant flow by a sensor bulb placed in the evaporator discharge line and hence controls the mass flow rate by the degree of superheat. The expansion valve has a very small volume and thus, the expansion process can be considered as being adiabatic without any refrigerant mass variation inside it. It can be modeled as an orifice through which the liquid is expanded from condensing to evaporating pressures. Taking into account the negligible changes in kinetic and potential energies as well as the absence of production for mechanical work, the expansion process can be treated as isenthalpic. The flow rate through it can be correlated according to the following equation:

$$\dot{m}_r = C_v A_v \sqrt{2\rho_l \Delta p} \quad (6.5)$$

Δp is the pressure variation across the valve orifice. The flow coefficient C_v depends on the degree of opening of the valve. The maximum value of C_v is reached when the valve is fully open. A_v could be considered as a minimum flow area across the orifice, which, in general, does not coincide with the orifice cross sectional area. Both C_v and A_v are loosely defined and difficult to evaluate separately. Thus a parameter k_A is introduced such that:

$$K_A = \sqrt{2}C_v A_v \quad (6.6)$$

Data from several thermostatic expansion valve manufacturers have been analyzed in order to find a general correlation for K_A . It has been found that K_A depends linearly upon the evaporating temperature, as shown in the following equation (Jabardo et al, 2003):

$$K_A = A_v + B_v \times T_e \quad (6.7)$$

A_v and B_v were found to be equal to $6.745 \times 10^{-5} \text{ m}^2$ and $3.237 \times 10^{-7} \text{ m}^2 \text{ } ^\circ\text{C}^{-1}$ respectively for the valve used in the present study.

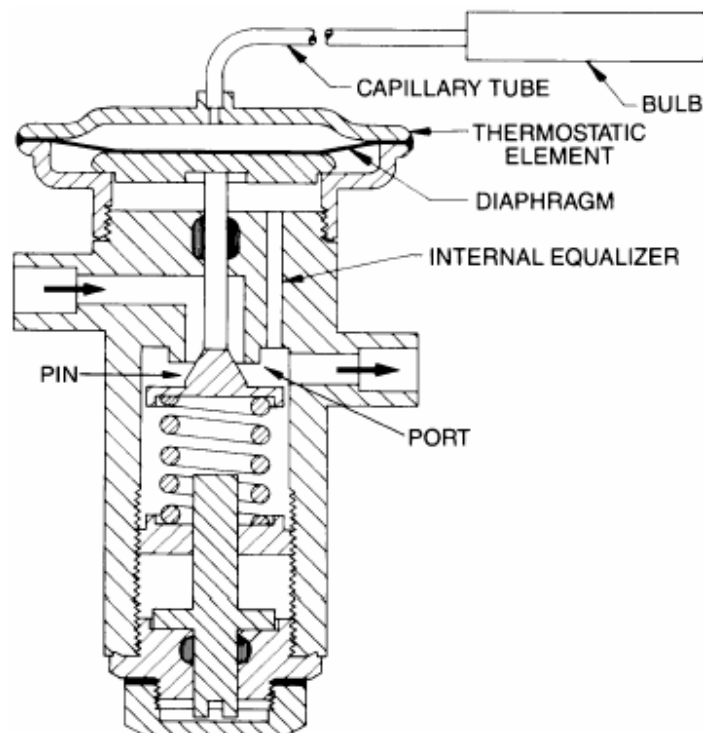


Figure 6.3 A typical thermostatic expansion valve

6.3.4 Connecting lines' and hoses' modeling

Pressure drop and heat transfer in the connecting lines and hoses have also been considered while developing the computer code. For that purpose, the external air temperature is assumed constant over the length of the particular tube or hose. Single phase heat transfer and pressure drop correlations have been used in the refrigerant side whereas in the air side, natural convection around cylindrical surfaces has been assumed. The heat transfer rate is thus given by:

$$Q_{lines} = (UA)_{lines} \Delta T_m \quad (6.8)$$

ΔT_m is the logarithmic average difference between the air and refrigerant temperatures, and $(UA)_{lines}$ is the product of the overall heat transfer coefficient and the heat transfer area.

The overall heat transfer coefficient can be computed from the following equation:

$$U = \frac{1}{\left(\frac{1}{\alpha_{p_i}} + \frac{A_i \cdot \ln(r_o/r_i)}{2\pi kL} + \frac{A_i}{A_o} \cdot \frac{1}{\alpha_{p_o}} \right)} \quad (6.9)$$

Where the heat transfer coefficient for forced convection, α_{p_i} , which flows through a horizontal circular cylinder is given by:

$$\alpha_{p_i} = \frac{4.3636 \times k p_i}{D_i} \quad (\text{in case of heating}) \text{ or}$$

$$\alpha_{p_i} = \frac{3.6568 \times k p_i}{D_i} \quad (\text{in case of cooling}) \text{ for } 0 < \text{Re}_i < 2000$$

$$\alpha_{p_i} = \frac{k p_i}{D_i} \cdot \frac{0.5 \times f \times (\text{Re}_i - 1000) \times p_{r_i}}{1 + 12.7 \times (0.5 \times f)^{0.5} \times (p_{r_i}^{2/3} - 1)} \quad \text{for } 2300 < \text{Re}_i < 5 \times 10^6$$

With

$$f = 0.054 + 2.3 \times 10^{-8} \times \text{Re}_i^{3/2} \quad \text{for } 2300 < \text{Re}_i < 4000$$

and,

$$f = 1.28 \times 10^{-3} + 0.1143 \times \text{Re}_i^{-0.311} \quad \text{for } 4000 < \text{Re}_i < 5 \times 10^6$$

α_{p_i} is used to express the heat transfer coefficient for the refrigerant inside the pipes, and α_{p_o} is the natural convection correlation outside a horizontal circular cylinder:

$$\alpha_{p_o} = \frac{k_a}{D_o} \times \left[0.6 + \frac{0.387 \times \text{Ra}^{1/6}}{\left(1 + (0.559 / \text{Pr}_a)^{9/16}\right)^{8/27}} \right]^2$$

$$\text{With } \text{Ra} = \frac{\beta \cdot g (T_a - T_w) \times D_o^3}{\nu^2} \times \text{Pr}_a$$

Pressure drop in pipes is obtained from Anon (1987) as follows:

$$\Delta p = f \frac{(L + L_{eq}) \rho u^2}{D_i} \frac{1}{2}$$

$$f = 64 / \text{Re}_i \quad \text{for } 0 < \text{Re}_i < 2200$$

$$f = 4 \times \left(0.0054 + 2.3 \times 10^{-8} \text{Re}_i^{2/3} \right) \quad \text{for } 2200 < \text{Re}_i < 4000$$

$$f = 0.184 \times \text{Re}_i^{-0.2} \quad \text{for } 4000 < \text{Re}_i < 2 \times 10^4$$

Where $L_{eq} = 0.7$ m for $D_i = 9.525$ mm, $L_{eq} = 0.8$ m for $D_i = 12.7$ mm, $L_{eq} = 0.9$ m for $D_i = 15.875$ mm, and $L_{eq} = 1.0$ m for $D_i = 19.05$ mm. L_{eq} means the equivalent length of a 90° curved pipe. The pressure drop in the receiver drier is also obtained from Anon (1987) and the value is 19.6 kPa. The specifications of the refrigerant pipelines used in the computer model are listed in Table 6.1.

Table 6.1: Refrigerant pipelines' specifications

Parameter	Suction line	Discharge line	Liquid line
Dout (mm)	38.310	15.875	19.500
Wall thick. (mm)	0.748	0.457	0.508
L (m)	21500	2150	1400.000
Insulation thick. (mm)	25.000	–	15.000
Kins (W/m.°C)	0.260	–	0.260

6.4 Numerical procedure

Performance simulation of the integrated AC system has been carried out by combining performance analysis programs of separate components to satisfy the laws of mass and energy conservation. The computer program is developed to couple the conservation equations of each component together and the system is simulated using Microsoft Visual Basic program. The computer program is capable of predicting the thermal performance for the developed AC system when it is operated with any of the three system modes mentioned in Chapters 3 and 4. It is featured by a user-friendly interface with an option to select the operating mode. The code interface is displayed in Figure 6.4.

Form1 [] [] [X]


Inlet Condition		Thermal Performance	
Taevi (°C) =	<input type="text" value="25"/>	Rhaevi (%) =	<input type="text" value="63"/>
Taci (°C) =	<input type="text" value="29"/>	Degree of superheat (K) =	<input type="text" value="5"/>
Hydraulic Performance		Thermal Performance	
mr (g / s) =	<input type="text" value="122.77"/>	Pressure ratio =	<input type="text" value="4.16161"/>
Vol. eff.(%) =	<input type="text" value="74.192"/>	Isent. eff.(%) =	<input type="text" value="82.6275"/>
Dpsuct (kPa) =	<input type="text" value="20.232"/>	Dpdis(kPa) =	<input type="text" value="0.23977"/>
Dpline (kPa) =	<input type="text" value="19.702"/>	DTsuct (K) =	<input type="text" value="0.049"/>
DTdis (°K) =	<input type="text" value="0.0421"/>	DTline (K) =	<input type="text" value="0.0447"/>
		T5 (°C) =	<input type="text" value="6.39400"/>
		T4 (°C) =	<input type="text" value="50.8236"/>
		Qe (kW) =	<input type="text" value="18.9375"/>
		Wc (kW) =	<input type="text" value="6.25881"/>
		COP =	<input type="text" value="3.02435"/>
		Qcond (kW) =	<input type="text" value="25.1964"/>
		T3 (°C) =	<input type="text" value="58.1183"/>
		<input type="button" value="Calculate"/>	<input type="button" value="End"/>
Air Conditions		Percentage off-blowers number is = <input type="text" value="zero off"/>	
Taevc (°C) =	<input type="text" value="16.44093"/>	Number of Operating Compressors = <input type="text" value="two compres"/>	
Rhaevc (%) =	<input type="text" value="96.69260"/>		
Tr (°C) =	<input type="text" value="20.31489"/>		
Rhr (%) =	<input type="text" value="50.90362"/>		
		<input type="button" value="Next>>"/>	<input type="text" value="14.42"/> %
			

Figure 6.4 The computer model interface

Table 6.2: Range of variable parameters input to the computer model

Parameters	Range of variations
Inlet evaporator air temperature (°C)	20.0 → 30.0
Inlet evaporator air humidity (%)	45.0 → 75.0
Inlet evaporator air velocity (m/s)	0.7 → 1.0

Table 6.3: The input parameters to the computer model

Compressor		Thermostatic expansion valve (TXV)	
Parameter	Value	Parameter	Value
RPM	2900.00	A_v (m ²)	5.637×10^{-5}
V_D (m ³ /min)	18.75	B_v (m ² °C ⁻¹)	1.358×10^{-7}
η_v	Equation (6.2)	K_v	(6.7)
η_{is}	Equation (6.4)	$c_v A_o$	(6.6)
γ	1.15	Degree of superheat	Specified by the user
Heat exchangers			
Parameters	Condenser		Evaporator
$S_t \times S_l$ (mm×mm)	38.10×31.75		25.40×22.23
d_i (mm)	15.67		8.86
d_o (mm)	15.87		9.52
H (mm)	457.20		177.80
L (mm)	1250.00		1425.00
N_{fin} (fins/mm)	0.51		0.55
N_r	4.00		6.00
N_{cr}	6.00		3.00
N_{tp}	12.00		8.00
t_f (mm)	0.15		0.15

The general flow chart in Figure 6.5 shows the principal steps used to integrate a complete AC system. The input data for the performance simulation program of the AC system is the inlet air temperature, relative humidity and flow rate for the evaporator, inlet air temperature for the condenser, compressor and expansion valve specifications, and superheat amount. The output data include evaporating capacity, COP, and evaporator exit air conditions (temperature and relative humidity). The input data is listed in Tables 6.2 and 6.3 while the output data is presented in details in section 6.5.

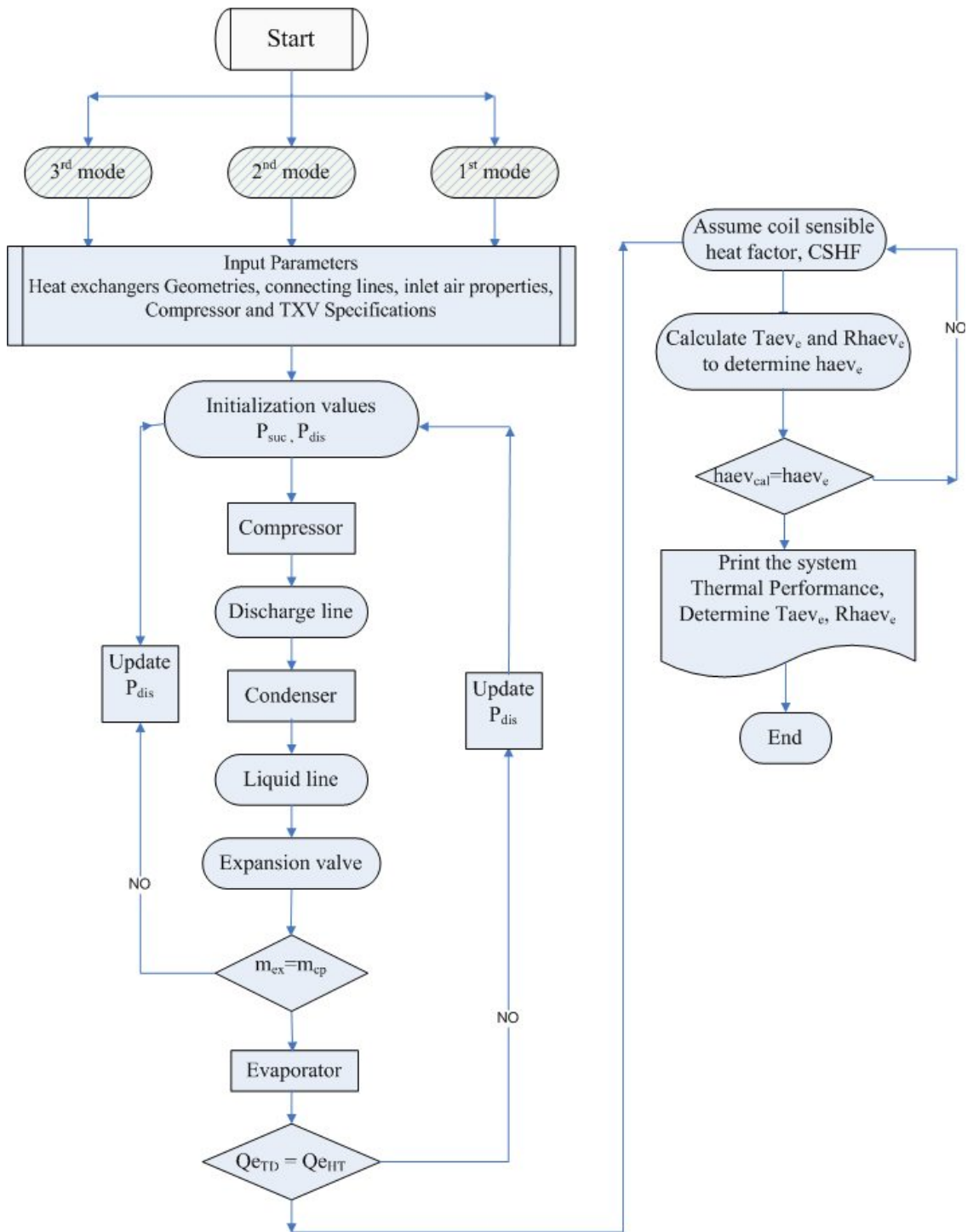


Figure 6.5 Block diagram of the numerical procedure

The compressor model first uses initial guesses of the discharge and suction pressures to calculate the refrigerant high-side flow rate, \dot{m}_h . The discharge line model calculates the inlet refrigerant state to the condenser. The refrigerant state leaving the condenser is then calculated from the performance analysis program of the condenser. The liquid line model estimates the inlet refrigerant state to the expansion valve. It is to be noted that the mean evaporator pressure is higher than the suction pressure by the evaporator pressure drop. The refrigerant pressure drop occurring in the evaporator is normally almost 10% of the mean evaporator pressure and this value was obtained experimentally. The expansion valve model then uses the inlet refrigerant state and the evaporator pressure to calculate the low-side flow rate, \dot{m}_l through the expansion valve. The discharge pressure is being updated until the two flow rates match to a specified tolerance. Then, the algorithm moves to the evaporator model. The evaporator model calculates the evaporator cooling capacity from the first law of thermodynamics and from the heat transfer equations for the evaporator. The estimate for the suction pressure keeps improving until convergence of the two cooling capacities is within an acceptable deviation of 0.1%.

The evaporator exit air psychometric properties can be determined using an iterative method. This method can be summarized as follows: assuming an initial value for the cooling coil sensible heat factor CSHF and by knowing the exit air enthalpy from the refrigeration cycle module, the exit air temperature and relative humidity can initially be identified and the exit air enthalpy can be recalculated with a new value. The CSHF is altered until the predetermined exit air enthalpy from the simulation module matches the new recalculated enthalpy. The air psychometric properties at the outlet of the cooling coil can then be obtained as demonstrated graphically in the logic chart.

6.5 Numerical results

Using the previous input parameters, the computer simulation model is capable of predicting the system's performance parameters, namely the cooling capacity, COP, evaporator exit air temperature and relative humidity for each mode of the system operation. Figures 6.6 to 6.8 display the trends of the numerical results with the cooling load variations while the numerical values of the computer model output have been listed in Table 6.4.

To validate the numerical model, the predicted results would be compared to those of the experimental work. In the following sections, the results of this comparison will be presented.

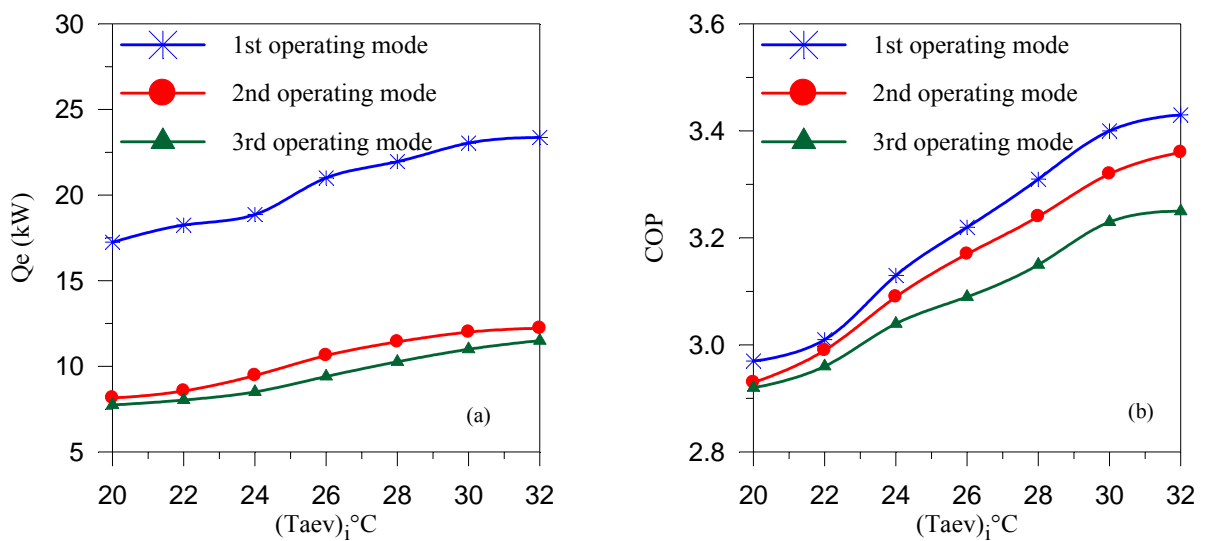


Figure 6.6 Effect of cooling load variations on the simulated results in terms of:

(a) Cooling capacity (b) COP

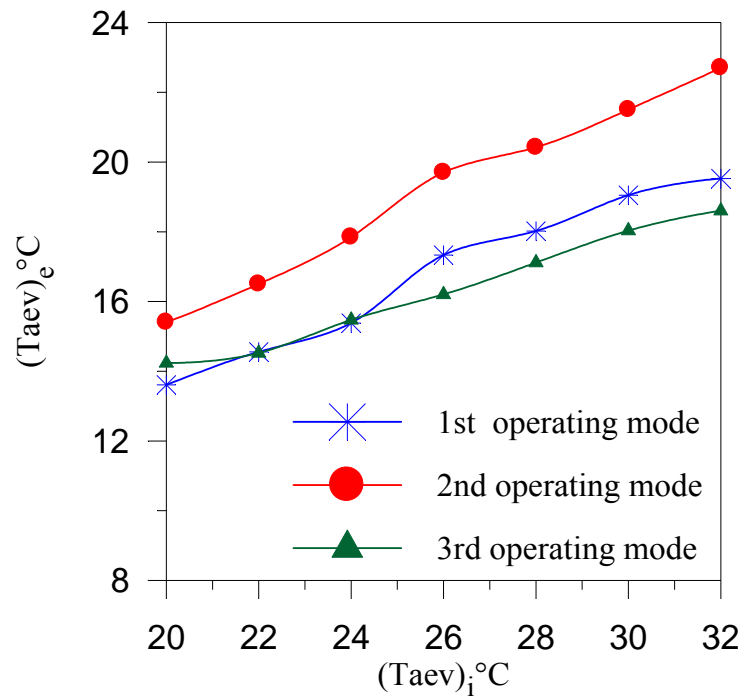


Figure 6.7 Effect of cooling load variations on the simulated results in terms of evaporator exit air temperature

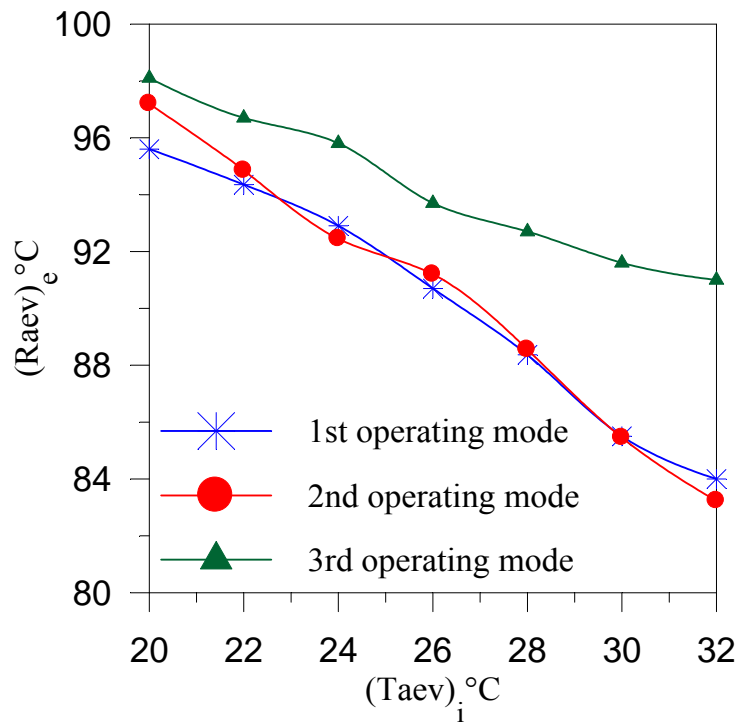


Figure 6.8 Effect of cooling load variations on the simulated results in terms of evaporator exit air relative humidity

Table 6.4: The output results of the computer simulation model for the three operating modes

Input parameters		Output parameters											
Cooling load		1 st system mode operation				2 nd system mode operation				3 rd system mode operation			
Taev _i °C	Rhaev _i (%)	Q _e (kW)	COP	Taev _e °C	Rhaev _e (%)	Q _e (kW)	COP	Taev _e °C	Rhaev _e (%)	Q _e (kW)	COP	Taev _e °C	Rhaev _e (%)
20.0	75.5	17.25	2.97	13.61	98.10	8.16	2.93	15.40	97.20	7.75	2.92	14.70	98.10
22.0	70.0	17.92	3.01	14.55	96.85	8.57	2.97	16.50	94.85	8.04	2.96	14.85	96.70
24.0	65.0	18.57	3.11	15.38	95.80	9.47	3.01	17.84	92.44	8.51	2.98	15.00	96.30
26.0	59.3	21.01	3.22	17.33	90.70	10.44	3.17	19.70	91.20	9.41	3.09	16.20	94.80
28.0	51.0	21.96	3.31	18.02	87.26	11.24	3.24	21.60	88.55	10.27	3.2	17.11	92.70
30.0	50.7	23.05	3.40	19.05	88.36	11.80	3.32	21.50	85.45	10.75	3.23	18.03	91.60
32.0	45.0	23.37	3.43	19.52	84.40	12.03	3.36	22.70	83.23	10.95	3.25	18.60	91.00

6.6 Comparison between the results obtained from the computer simulation model and those from the experimental work

The comparison between the analytical model and experimental one has been accomplished by varying the inlet air conditions to the system evaporators for the three different system operating modes. The simulated results are superimposed on those for experimental work and they are displayed graphically in Figures 6.9 to 6.14.

6.6.1 Comparison in terms of thermal performance for the first mode operation

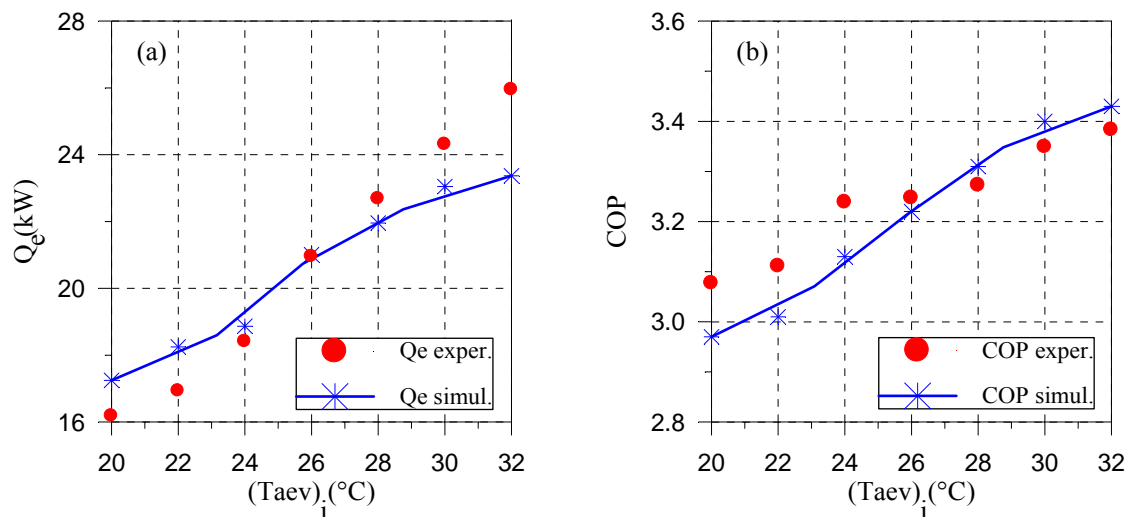


Figure 6.9 Evaporator inlet air temperature effects on: (a) refrigeration capacity (b) COP for the first mode operation of the multiple-circuit system

Figure 6.9 indicates that the computer model is able to predict the system's thermal performance when the cooling load is varied in the first mode of the system operation and these predictions are quite close to the results of the experimental tests. The maximum absolute deviations between the theoretical and experimental results are +9.9% and +4.0% for cooling capacity and COP predictions respectively. In addition,

the simulated results of evaporator exit air conditions (temperature and relative humidity) show good agreement with those of the experimental work as can be seen from Figure 6.10.

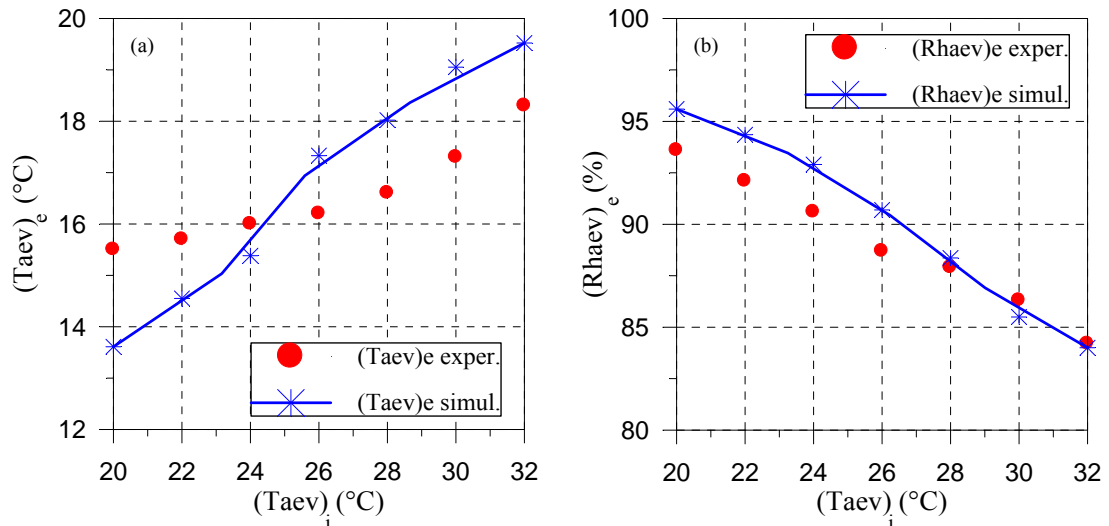


Figure 6.10 Evaporator inlet air temperature effects on (a) exit air temperature and (b) relative humidity for the first mode operation of the multiple-circuit system

6.6.2 Comparison in terms of the thermal performance for the second mode operation

As shown in Figures 6.11 and 6.12, the overall trend of the calculated thermal performance results and evaporator exit air properties which are obtained from the computer model is consistent with that of the experimental work in the second operation mode of the developed system. The minimum and maximum discrepancies for cooling capacity predictions are -12.6% and $+4.1\%$ respectively and for COP are -5.30% and $+0.30\%$, respectively. On the other hand, the theoretical exit air temperature and relative humidity trends deviate from the experimental ones within a range of -7.2% to $+11.3\%$ for air temperature predictions and -4.5% to $+7.6\%$ for air relative humidity.

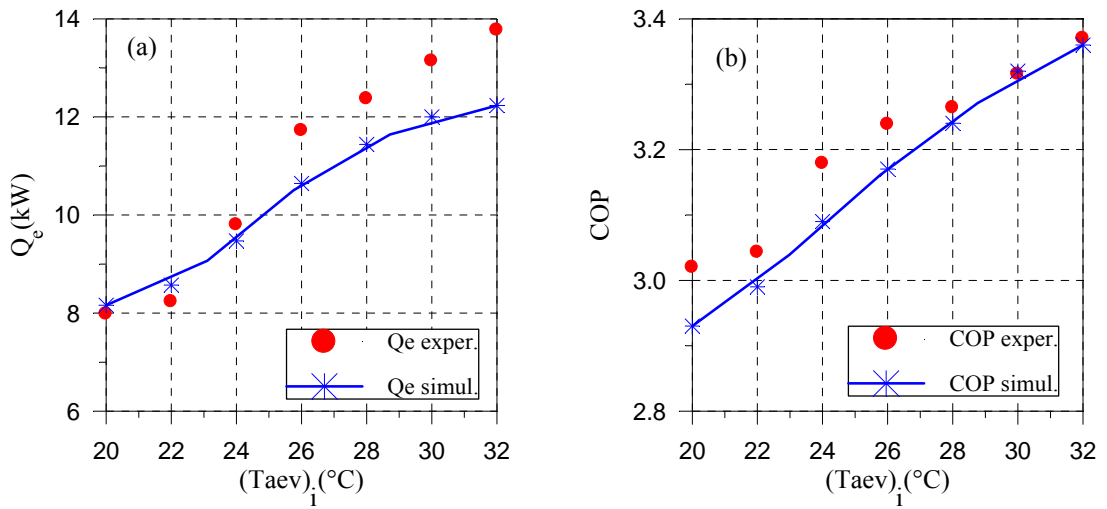


Figure 6.11 Evaporator inlet air temperature effects on: (a) refrigeration capacity (b) COP for the second mode operation of the multiple-circuit system

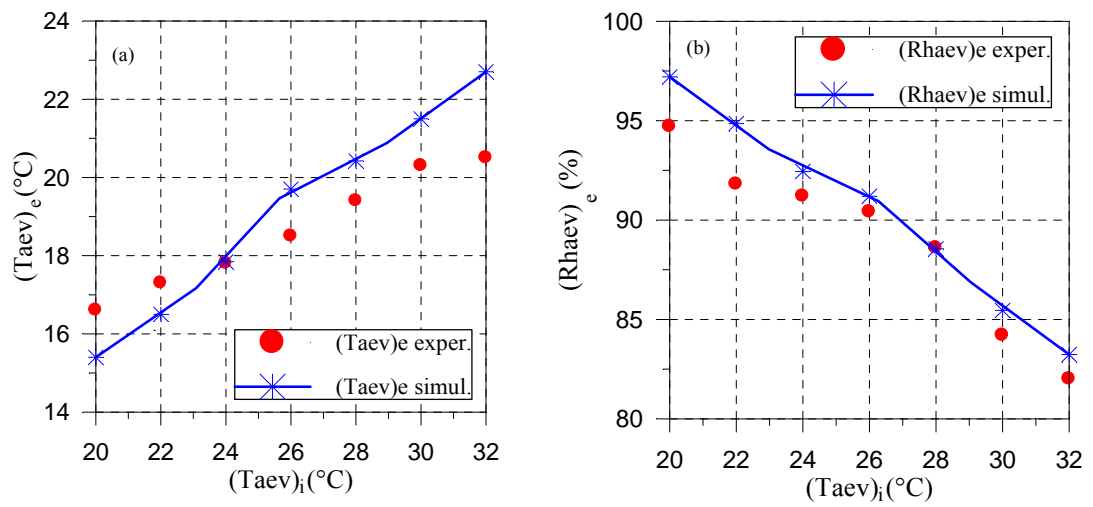


Figure 6.12 Evaporator inlet air temperature effects on (a) exit air temperature and (b) relative humidity for the second mode operation of the multiple-circuit system

6.6.3 Comparison in terms of thermal performance for the third mode operation

As noted from Figure 6.13, the computer model is still capable of simulating the thermal performance of the AC system at different operating modes. Here, the largest deviation between the simulated and experimental results occurred at a maximum of -15.4% for the system cooling capacity at the maximum inlet air temperature (32°C). This result might be considered reasonable since the higher deviations occur at an air temperature considerably higher than those expected at typical operational conditions. In addition, in the third mode operation, the blower's capacity is dropped to two-third of its full capacity owing to the stoppage of some of them. It is believed that an almost stagnant air zone is created between the stopped blowers and the evaporator surface area. The air in this zone ceases to reject completely its heat to the refrigerant inside the evaporator comparing to the air in the other zones as a result of the drop in the air velocity in this zone. Accordingly, the refrigerant saturation temperature in this zone drops drastically as compared to the rest of the evaporator surface making the average evaporation temperature to be smaller than expected. In turn, the system's cooling capacity is dropped further than is expected and an unexpected increment in the compressor power occurs as a result of the additional drop in the evaporator saturation temperature. The net outcome is that the experimental COP values are less than those for the simulated ones for the third mode operation i.e. the simulation model overpredicts the system thermal performance at the third mode operation as the cooling load is varied as clearly shown in Figure 6.13. On the other hand, there is another phenomenon which causes the experimental measurements of the evaporator exit air temperature to be larger than the computer model predictions as shown in Figure 6.14. Therefore, the simulation model here also underpredicts the behavior of the experimental measurements. The reason of such trend comes from the phenomenon related to the air in the stagnant zone.

As a result of the stoppage of some of the blowers, dead pockets for the air flow around the off blowers are produced. These dead pockets decelerate the air movement and thus deteriorate the air-side heat transfer coefficient leading to an insufficient cooling effect for the incoming air to the cooling coil. Accordingly, the air of this

stagnant zone exits almost unconditioned or inefficiently conditioned and mixes with the perfect conditioned air causing a slight warming in exit air temperature coupled with a decrease in air relative humidity. Therefore, the temperatures of the evaporator exit air at this operating mode obtained from the experimental tests are higher than it is expected theoretically resulting in a high relative discrepancy in the results between the experimental and simulation models.

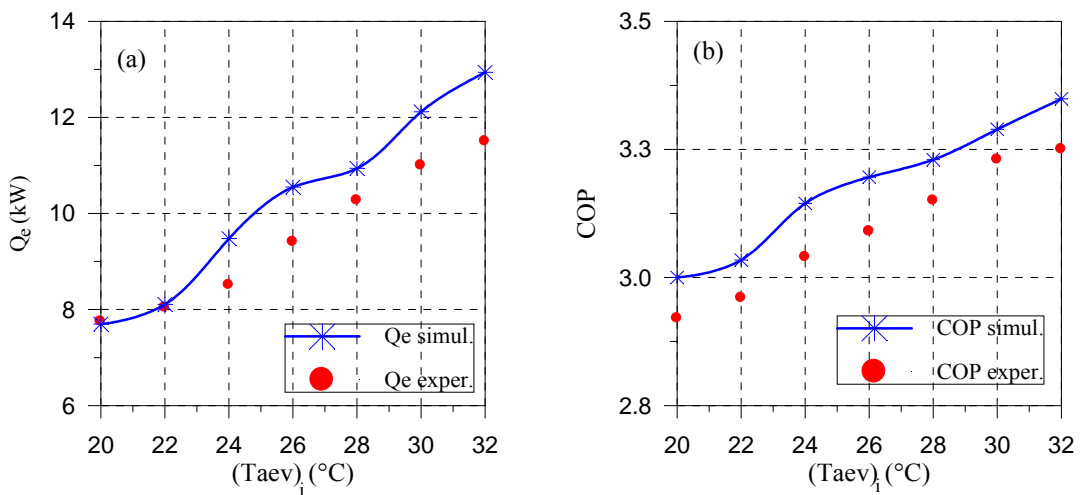


Figure 6.13 Evaporator inlet air temperature effects on: (a) refrigeration capacity; (b) COP for the third mode operation of the multiple-circuit system

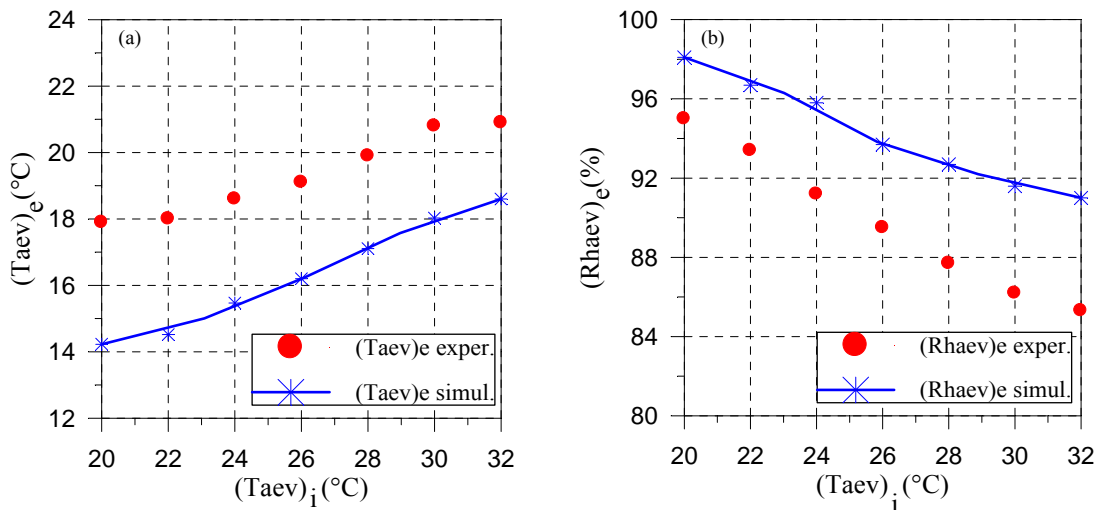


Figure 6.14 Evaporator inlet air temperature effects on (a) exit air temperature and (b) relative humidity for the third mode operation of the multiple-circuit system

6.7 Conclusion

In conclusion, the present analysis has shown that the simulated results are comparable to the experimental ones from both the qualitative and quantitative points of view. Table 6.5 shows the deviations of the simulated results from those obtained from the experiments under the same operational conditions. Maximum absolute deviations are within the range of 19.3%, though most of the deviations of the simulated results are within less than 10% range from the experimental ones, which proves the computer program's validity. In other words, the simulated results predict the system's performance with reasonable accuracy for return air temperatures within a typical range varying from 20 to 30°C.

Table 6.5: Deviations of simulated results from the experimental ones

Different operation modes of multiple-circuit AC system	Deviations (%)							
	Q _e		COP		(Ta _{ev}) _e		(Ra _{ev}) _e	
	Min	Max	Min	Max	Min	Max	Min	Max
1 st mode system operation	-9.9%	+7.00%	-4.0%	+1.5%	-12.2%	+10.1%	-5.7%	+6.4%
2 nd mode system operation	-12.6%	+4.10%	-5.3%	+0.3%	-7.2%	+11.3%	-4.5%	+7.6%
3 rd mode system operation	-15.4%	+1.54%	-7.9%	-0.9%	-19.3%	-11.0%	+3.3%	+6.7%

CHAPTER 7

CONTROL STRATEGY

7.1 Introduction

The thermal loads of a bus compartment are not constant, varying from time to time due to various reasons. Opening of a door, changing of the sun load through the windshield and side windows, and the number of passengers will change the load inside the bus cabin. The load also increases when the outdoor air becomes hotter and vice versa. Due to these changes, a controller is required to match the output of the AC system to the load imposed. Normally, an AC system is designed to meet the extremes in the demand, but most of the time it will experience partial load conditions. A properly designed control system will maintain good indoor air quality and comfort under all anticipated conditions with the lowest possible cost of operation.

As aforementioned in Chapter 3, the controlling actuators here in this developed system are the number of compressors and number of blowers which will be switched on or off. The main task of the automatic controller is to recognize the magnitude of the cooling load and adapt the system's capacity to match the imposed cooling load on the bus cabin. The main philosophy of the novel strategy is to represent the imposed cooling load on the passenger cabin by the temperature difference (TD) between the evaporator inlet air temperature, T_{aev_i} and the set-point temperature, T_s . This will facilitate the task

of the controller to recognize the value of the cooling load and select the proper system operating mode according to the TD value corresponding to the imposed thermal load.

The evaporator inlet air temperature is detected by the controller's temperature sensor and the set-point temperature can be determined by the controller's user (usually bus driver). With this information, it is easy for the controller to carry out its job through a prudent control strategy which will be discussed in this Chapter.

The prudent control strategy is defined as the strategy that enables the controller to govern the AC system's operation for best performance which satisfies passenger's thermal comfort with an improvement in system energy consumption. For this task, as mentioned in Chapter 4 the second group of the experiments were conducted at three set-point temperatures: 21°C, 22°C, and 23°C. These temperatures represent the typical temperatures of a conditioned space. The best TD for each temperature setting was determined by trial and error from the experiments that resulted in minimum energy consumption and passenger thermal comfort without impairing system's life time. This will be discussed in detail in this chapter. In the last part of this Chapter, a comparison between the conventional AC system and the developed one has been presented to highlight the main benefits of the developed system in terms of energy saving, costing, and thermal comfort achievement.

7.2 Control strategy concept

Figures 7.1 and 7.2 show the thermal comfort in terms of PMV and PDD for the three different operating modes of the proposed AC system at three set-point temperatures. It can be seen that the system in the first mode of operation is capable of providing a thermally comfortable condition inside the bus compartment only above the evaporator inlet air temperature of 27°C at any set-point temperature. Below that, the conditions inside the compartment are characterized by an overcooling environment which causes a high degree of expected dissatisfied occupants' percentage. On the other hand, the operation of the system in the second mode at a range below 27°C and above 23°C provides a comfortable condition inside the bus cabin for the three different set-point temperatures. As for the third mode of operation, the region below 25°C is characterized by a relatively thermal comfort condition inside the compartment for the different set-point temperatures. Therefore, the temperature of 27°C is the key point of switching the system from the first mode to the other modes and vice versa. However, there is another issue about the proper mode (2nd or 3rd) for the system to be operated when the evaporator inlet air temperature below 27°C . The issue is addressed in the following paragraph.

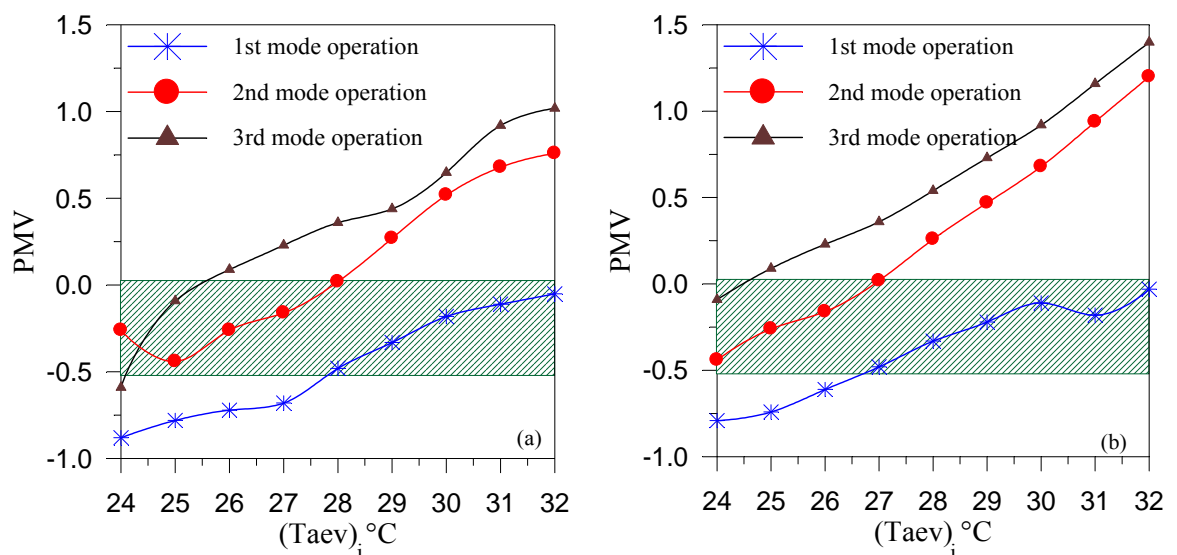


Figure 7.1 Evaporator inlet air temperature's effect on passenger's thermal comfort for set-point temperature of (a) 21°C (b) 22°C

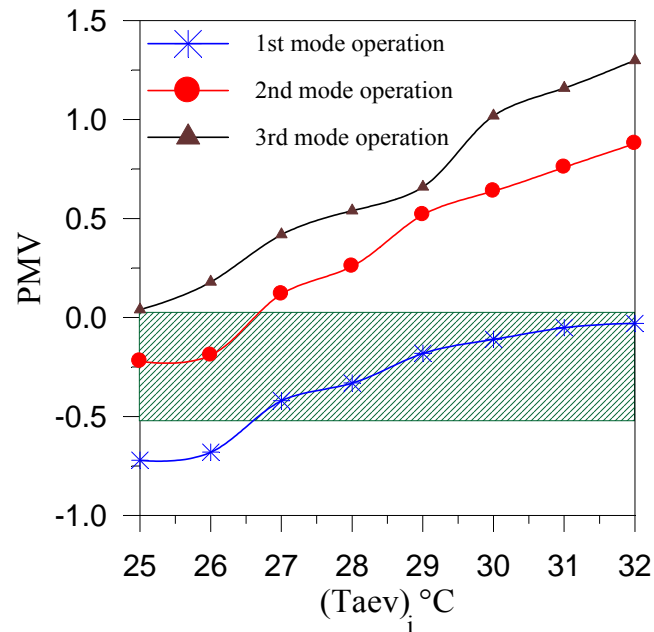
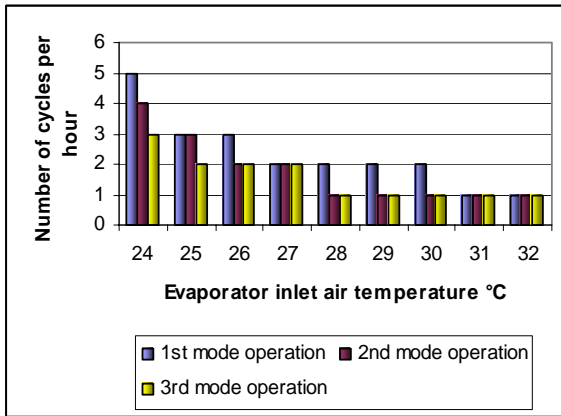
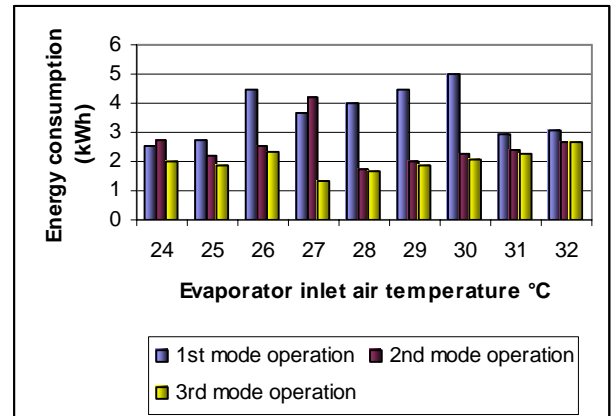


Figure 7.2 Evaporator inlet air temperature's effect on passenger's thermal comfort for set-point temperature 23°C

As aforementioned that the control strategy is established on basis of compromise between the thermal comfort and other decision parameters which are number of cycling per hour for the system compressors and energy consumption. Prior to see the effect of evaporator inlet air temperature on these parameters, it makes sense to demonstrate firstly the impact of these parameters on the system performance. The sum of cycling on and off times is called cycling rate and the common cycling rate recommended by compressor manufacturers for the large compressor capacity is 3 or 4 cycles/hour (Copeland, 1981). The less number of compressors cycling per hour the longer compressor life time, Copeland (1981). The experimental test runs were conducted at the set-point temperatures of 21, 22 and 23°C to determine the proper control logic which satisfies the appropriate cycling rate. The results of these experimental test runs are reported in E.11 to E.14 of Appendix E.

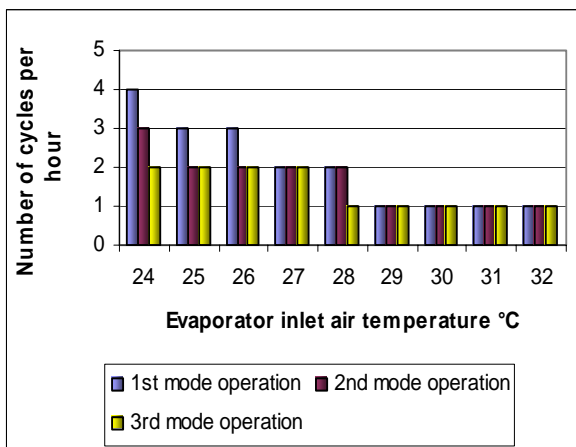


(a)

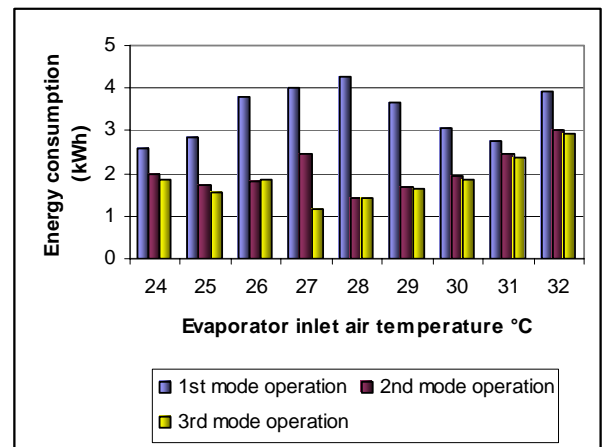


(b)

Figure 7.3 Effect of cooling load variations on a)- compressors cycling, and b)- energy consumption for set-point temperature of 21°C



(a)



(b)

Figure 7.4 Effect of cooling load variations on a)- compressors cycling, and b)- energy consumption for set-point temperature of 22°C

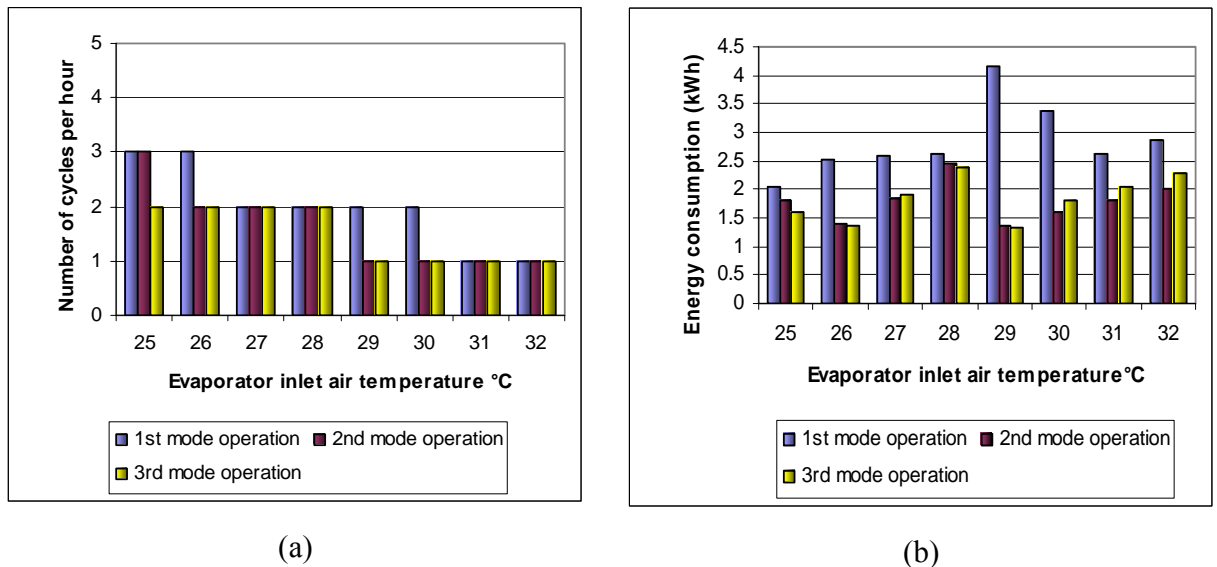


Figure 7.5 Effect of cooling load variations on a)- compressors cycling, and b)- energy consumption for set-point temperature of 23°C

Figures 7.3 to 7.5 show the summary of these experiments in terms of the effect of cooling load variations on the system cycling rate and energy consumption for the three different set-point temperature. As it is observed from these Figures that the 3rd mode operation has the less cycling rate when the evaporator inlet air temperature is less than 25°C at the set-point temperature of 21°C and 22°C. However, at the set-point temperature of 23°C the 3rd mode operation has the minimum cycling rate when the evaporator inlet air temperature equals to 25°C. In addition, the 3rd mode operation has the least energy consumption particularly when the evaporator inlet air temperature equals to or less than 25°C at any different set-point temperature. This emphasizes that the favourable working region for the 3rd operating mode is when the entering air temperature to the evaporator equals to or less than 25°C corresponding to the set-point temperature value. The region between the evaporator inlet air temperatures equals to or larger than 25°C and less than 28°C is recommended for the 2nd mode operation as the point-of-view of the energy consumption and thermal comfort level. The summary of the previous discussion is illustrated graphically in Figure 7.6. This Figure represents the control of the automatic controller. The proposed system and the automatic controller installation are displayed in Figure 7.7.

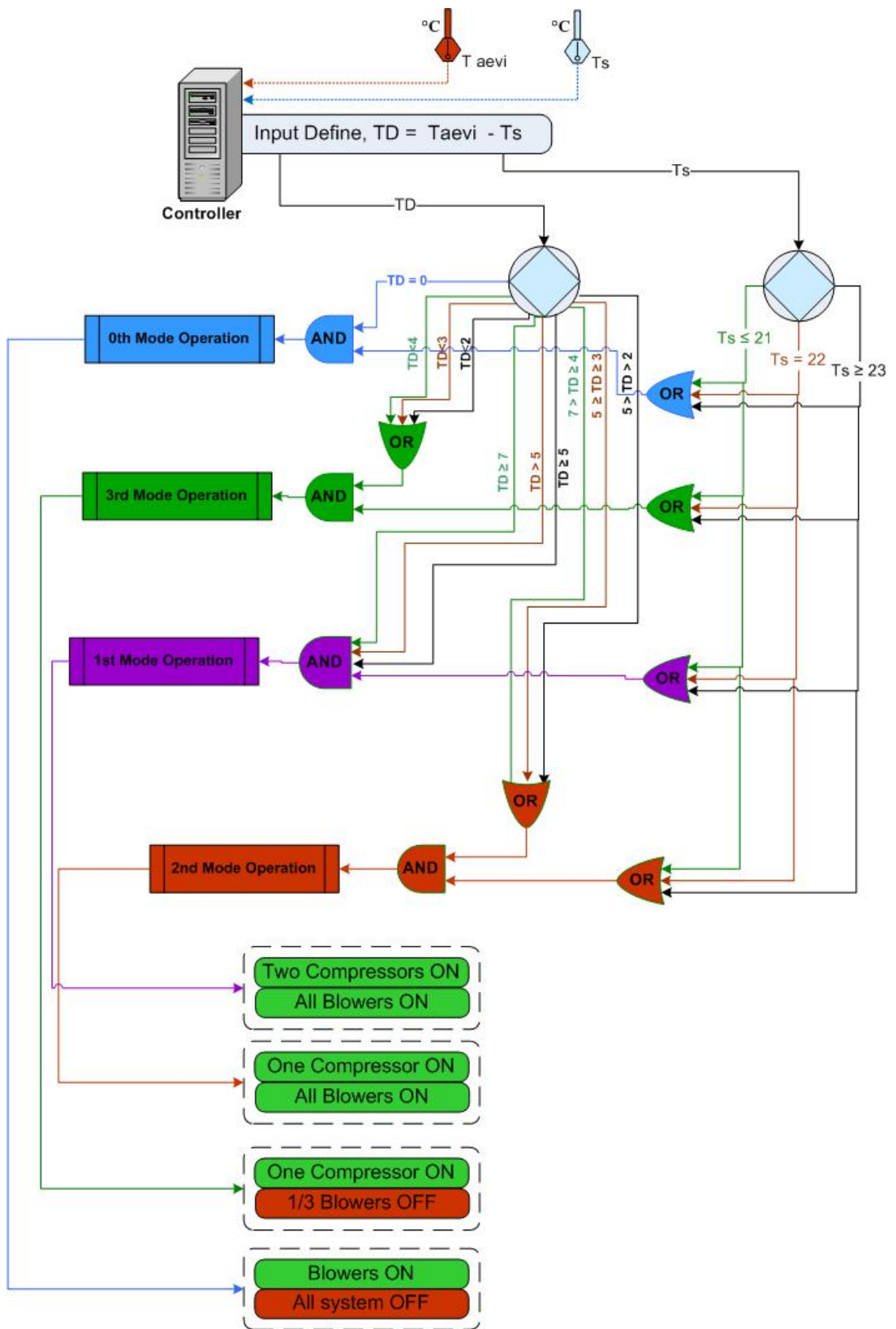


Figure 7.6 Control logic

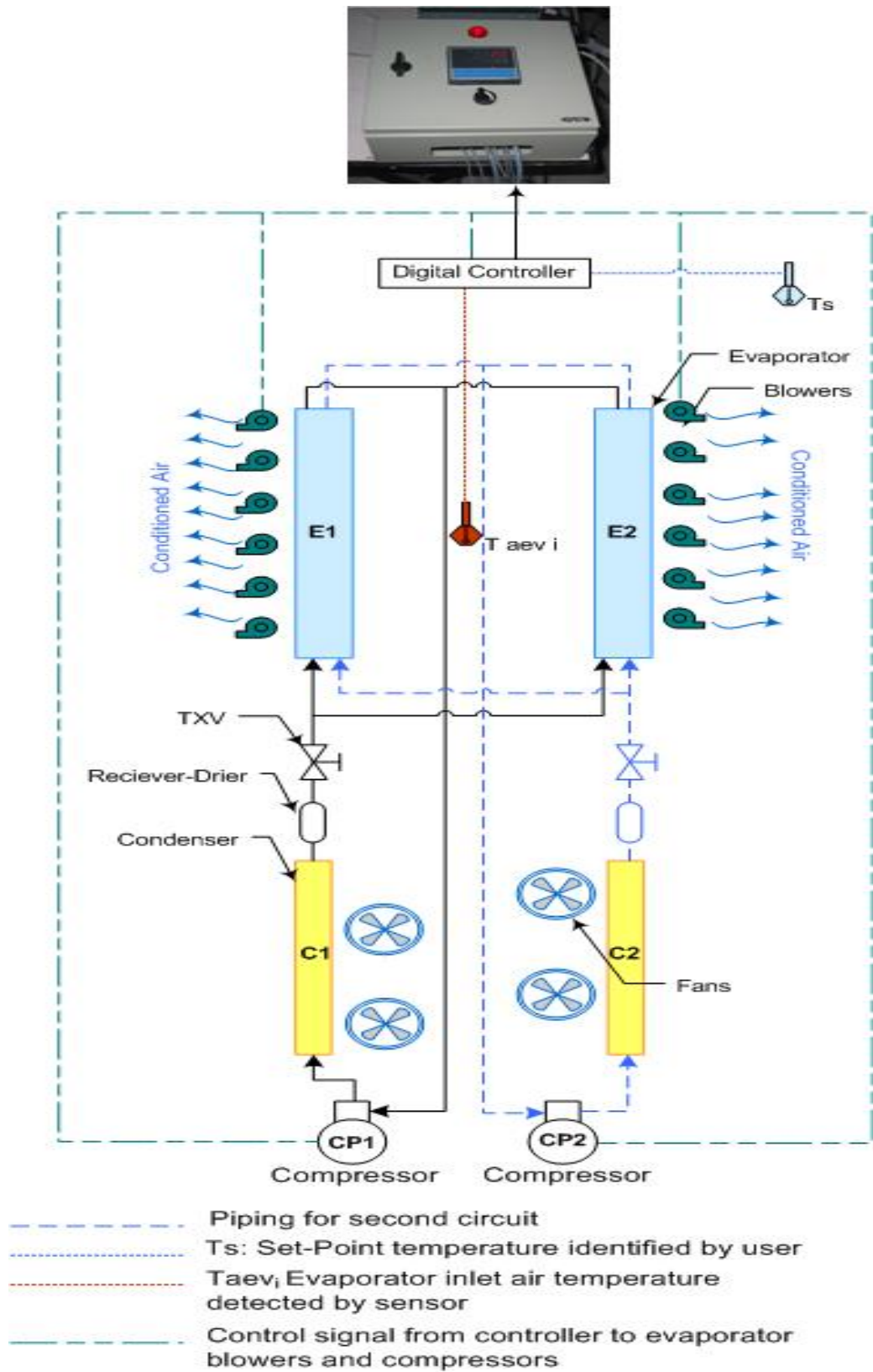


Figure 7.7 Schematic diagram for the developed AC system

When the bus driver turns on the controller button during start up, one compressor will commence to work with all blowers operating. The driver then selects a set-point temperature. The controller detects the evaporator inlet air temperature in milliseconds and by comparing the inlet evaporator air temperature and set-point temperature, the controller can recognize the cooling load and proceed with the decision making procedure. If the second compressor engagement is essential to cover the imposed cooling load, it will be on within one minute. The decision making process undertaken by the controller include the evaporator blowers as well; one third of the blowers is equipped to be independently off of the system, while all-blowers-on operation can be executed during 1st and 2nd operating modes. The control strategy shown in Figure 7.6 presents a distinct scenario for different set-point temperatures, and for different evaporator inlet air temperature. As an example for how the control strategy works; for a cooling load represented by a set-point temperature of 21°C and $DT < 4$ (i.e. $T_{\text{evai}} < 25$ °C) the controller shall keep one compressor on and one third of the blowers off (3rd mode). However, if a cooling load represented by $4 \leq TD < 7$ and the same set-point temperature of 21°C is recognized by the controller, all the evaporator blowers will be on while still keeping one compressor off (2nd mode). If the cooling load imposed exceeds the representation of $TD \geq 7$, the system will work with full capacity (1st mode). On the best cases, when the evaporator inlet air temperature equals the set-point temperature, all the system will be off, and the evaporator blowers will be on. The TD values are selected precisely to satisfy proper cycling rate for both compressors and also to avoid short-interval cycling.

7.3 Comparison between the developed bus AC system and the conventional bus AC system

The performance of the conventional AC system can be imitated by the performance of the first mode operation of the proposed system with continuous operating during all the operating hours. The following sections highlight the benefits of the developed AC system as compared to the conventional AC system from three aspects: possible energy saving, costing, and thermal comfort.

7.3.1 Possible energy saving

This section demonstrates possible energy saving when the developed AC system is used. Energy consumptions are calculated for the conventional and developed AC systems based on selected typical day of March-April. As aforementioned in Chapter 4, the daily use of the bus AC system is more than fifteen hours per day from 8 am to 11 pm (from Johor Bahru to Kuala Lumpur and vice versa). Assuming that the bus AC system runs 25 days a month, this means that its monthly operation is 375 hours. For one year, the total number of operation hours for the system is 4500 hours per year.

Table 7.1: Annual energy consumption for the conventional and developed bus AC system

Type of bus AC system	Set-point temperature, °C	Annual energy consumption, kWh	Percentage of Possible energy saving (%)
Conventional system	–	21273	–
Developed system	21	14544	31.6
	22	12453	41.5
	23	10347	51.4

The hourly energy consumption distribution for the selected typical day for the conventional system and the developed AC system at the temperature set-points of 21, 22, and 23°C is shown in Table E.16 of Appendix E. The possible annual energy saving of the developed AC system as compared to the conventional system at the three different temperature set-points is presented in Table 7.1. Figure 7.8 shows the annual energy consumption for the conventional system and the developed one at the three different set-point temperatures.

As can be seen from Figure 7.8 and Table 7.1, the potential saving in energy consumption for the developed AC system can be around 31.6% when the system is set at 21°C. On the other hand, if the developed system controller is set at 22°C or 23°C during the system operation time, the potential energy savings that can be obtained from the newly developed system are 41.5% and 51.4 % respectively.

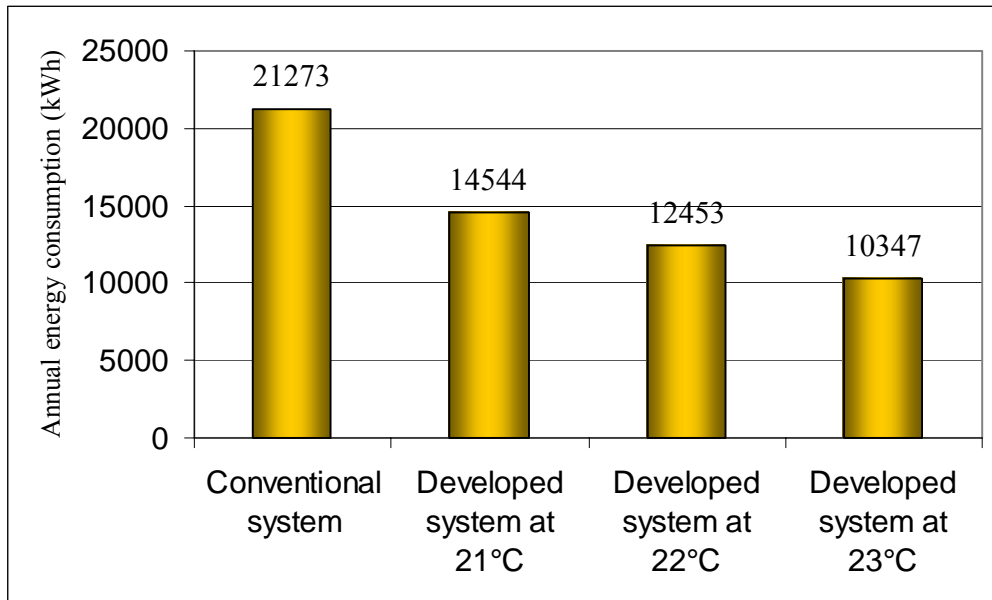


Figure 7.8 Comparison of annual energy consumption between the conventional and the developed AC system for the three set-point temperatures

7.3.2 Costing aspect

The economic merits of the developed AC system over the conventional cooling system can be evaluated by calculating and comparing the various economic indicators, such as life cycle cost, and payback period (PP). The calculation of these indicators involves two major cost categories: owing costs and operating costs. Owing costs comprise of initial costs, salvage value, property taxes, rents, and insurance. On the other hand, the annual system expenditures resulting from the actual use of the system are referred to as operating costs. Operating costs include costs for energy and maintenance. For the purpose of evaluating the new system, it is assumed that owing costs include initial (capital) costs only, whereas the operating costs involve costs for energy and periodic maintenance only. Thus, the effects of salvage value, property taxes, and insurance on owing costs are neglected. The total annual cost can be obtained by summing the annual operating cost, and adding the annual maintenance cost.

The payback method is the most commonly used economic analysis technique for evaluating energy alternatives (Spielvogel, 1984). It is defined as the capital cost of implementation divided by the annual cost savings at today's cost. The major advantages of the technique are simplicity, and that it is based on facts that are known today, not some future projections and assumptions. The life cycle cost (LCC) method is often used to promote and enhance expensive energy-related alternatives (Spielvogel, 1984). The capital cost (first cost) can be added to the present value of annual operating costs to yield the present value of life cycle cost for the system evaluated over the expected life. When comparing the two systems, the lowest present value is most desirable since it represents the minimum present cost of initial capital outlay and the sum of all future operating costs over the period of the economic analysis.

Table 7.2 and Figure 7.9 summarize the comparison between the cost of the two AC systems. As shown in Figure 7.9 and Table 7.2 that the initial cost for the proposed system is more expensive than that for the conventional one by 1100 USD as a result of replacing the big compressor with two identical capacity compressors and a new

automatic controller including installation and commission. However, the saving in energy consumption makes the new system profitable by an annual saving of 656 USD as a result of the reduction in the energy consumption by 31.6% when the set-point temperature is 21°C. That corresponds to a payback period of one year and five months. On the other hand, the payback period for a set-point temperature of 22°C is one year only while for a set-point temperature of 23°C is less than one year (eleven months). The newly developed system has a relatively short payback period (less than two years) for any of the three set-point temperatures. The combination of these set-point temperatures during the system operating hours will further shorten the payback period as a result of the considerable reduction in energy consumption.

Table 7.2: Costing study for the conventional and developed bus AC systems

Initial cost	Conventional system	Developed System	
Cost of equipment (\$)	10526	11526	
Cost of installation (\$)	300	400	
Total initial cost (\$)	10826	11926	<i>Difference = 1100 \$</i>
Annual operating cost			
Energy consumption (kWh)	21971	14544	<i>Energy saving = 30.8%</i>
Cost of Energy (\$)	2325	1539	<i>Difference = 785 \$</i>
Cost of maintenance (\$)	1000	1100	<i>Difference = 685\$</i>
Payback period and present value			
Interest = 5 % , life cycle time = 10 years , annuity = 0.1295			
Payback time	0	1.40	
Present value of annual operating cost (\$)	28272	19333	<i>Difference = 8939\$</i>
Life cycle cost (\$)	39098	31259	<i>Difference = 7839\$</i>

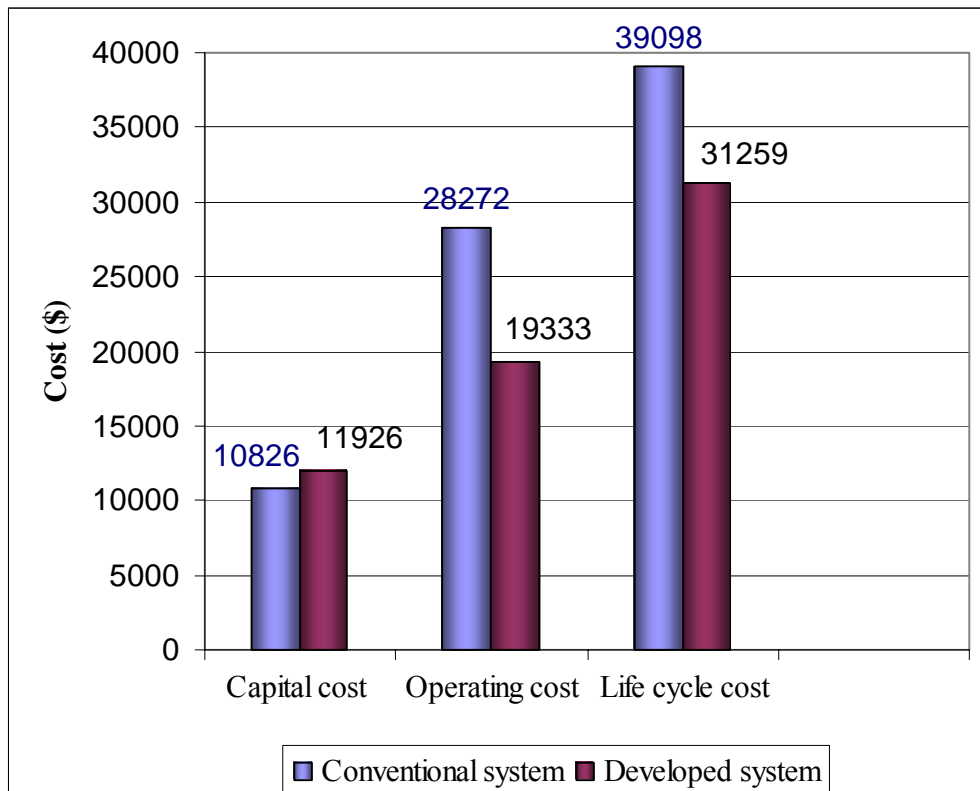


Figure 7.9 Comparison between the conventional and developed system in term of cost aspect

In order to determine the life cycle cost for the two systems, the life cycle time and investment rate should be firstly identified. Assuming that the life cycle time for both systems is 10 years and the investment interest is 5%, the resulting running cost for the new and existing systems are 19333 and 28272 USD respectively. This indicates the proposed system is more economical and has a lower life cycle cost as shown in Figure 7.9 to encourage the customers to accept the new system.

7.3.3 Thermal comfort achievement

As aforementioned, the operation of the conventional bus AC system could cause thermal discomfort to the passengers particularly during low sensible load as a result of overcooling condition inside the bus compartment. The developed bus AC system is able to match the imposed thermal load and thus prevents the condition of the thermal discomfort to the passengers. Figure 7.10 shows that the developed system is within the comfort zone ($-0.5 \leq \text{PMV} \leq 0$) and reduces the Predicted Percentage of Dissatisfied passengers PPD significantly. As shown in Figure 7.10a the operating range of the PMV for the developed system is from -0.66 to -0.07 corresponding to a PPD range of 15.3% to 5.1%. On the other hand, the operating range of the PMV for the conventional system is mostly away from the comfort level except above the evaporator inlet air temperature of 27°C as shown in Figure 7.10.

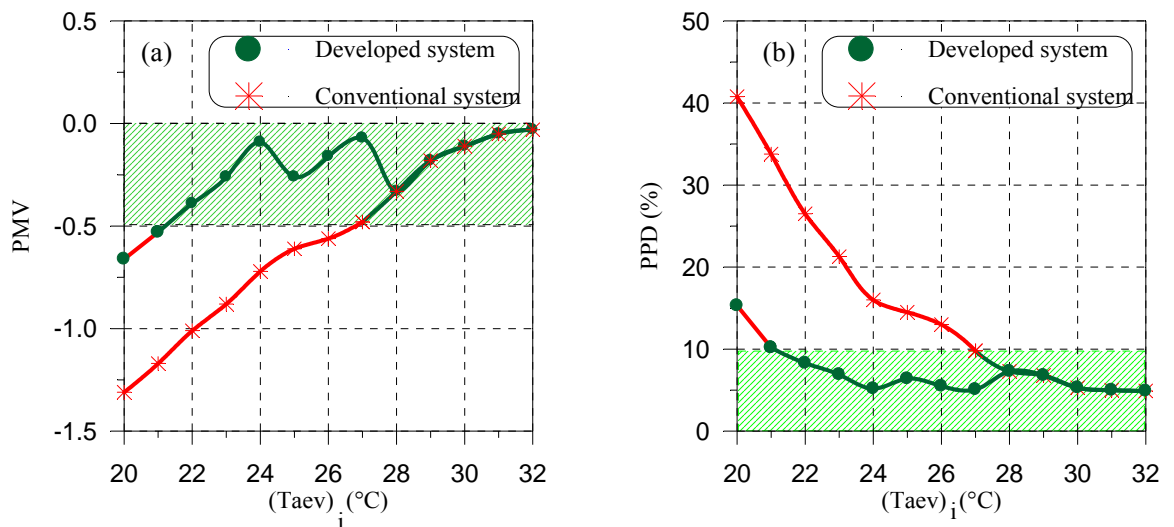


Figure 7.10 Effect of evaporator inlet air temperature on (a) PMV (b) PPD of the developed and conventional AC system

7.4 Conclusion

It may be concluded that the developed AC system is capable of providing thermal comfort to the passengers during all thermal loads. And it is able to operate economically as a result of a significant reduction in energy consumption of at least 31.6% for 4500 operation hours of the bus. Furthermore, an automatic controller relieves the bus driver of the responsibility for the proper functioning of the system and allows him to concentrate on his driving. Moreover, if one unit of the developed system is impaired or inoperative, the second unit can still provide conditioned air to the bus cabin.

CHAPTER 8

THERMOECONOMIC CONDENSER DESIGN OPTIMIZATION

8.1 Introduction

This Chapter investigates another method to reduce the energy consumption in the conventional bus AC system which is optimization of the system components' design i.e. evaporator, condenser, compressor, and thermostatic expansion valve. As it is known, a maximum value of the COP will result in the least energy consumed by the system. Therefore, the optimization should be carried out with a target of obtaining the optimal component configuration to achieve maximum COP without impairing the system or the component's capital cost. This approach is called thermoeconomic optimization. In this work, the component optimization is called a small-scale or process optimization while the modification in the system's (as whole) arrangements is called a large-scale or cycle arrangement optimization. The latter type of optimization was discussed in the previous Chapters 6 and 7 of this report while the former will be investigated here in this Chapter. The optimization approach has been applied to the condenser configuration of the AC system by investigating the effect of the condenser's design parameters on the AC system's COP, condenser's frontal area, and system's life cycle cost. In the last part of this Chapter, a comparison between the optimal condenser design and the conventional one in terms of the system's COP and costing is presented. The simulation model of Chapter 6 for the AC system was used for this task.

8.2 Background

Thermodynamic processes in refrigeration systems release large amount of heat to the environment. Heat transfer between the system and the surrounding environment takes place at a finite temperature difference, which is a major source of irreversibility or exergy destruction. The largest amount of heat transfer between the AC system and its surrounding occurs in the condenser. Thus, the condenser contributes a large part of the system exergy destructions. Therefore, in this study the condenser is selected as the system component which is employed as a platform for thermoeconomic optimization accomplishment. Irreversibilities cause the system performance to degrade (Recep et al., 2002). Alefeld (1990) showed that the COP and system irreversibility or exergy destruction are directly related through fundamental equations. Additionally, Bejan (1996) suggests that the point of minimum system exergy destruction should coincide with optimum system performance COP.

Unlike the residential AC systems, the roof-top bus AC system is subject to stringent space limitations and therefore the prime focus of the condenser's designer is the condenser frontal area taking into account its capital cost. Hence, the more compact the condenser, the more feasible and favorable is the design but the AC system's COP should also be considered. To sum up, the design optimization of a roof-top bus AC condenser should take into account the compromise between an economical compact condenser and an efficient system COP for the refrigeration cycle in which the condenser is one of its components. This can be quite complex since there is a continuous trade-off between increasing the heat transfer coefficient of the heat exchanger and increasing the frictional pressure drop on both the air-side and refrigerant side.

In this study, the design optimization is conducted by investigating the effect of the most important design parameters for the condenser configuration which have a significant influence on the objective functions of the design optimization (Susan, 2003). The design parameters are classified under two categories, geometrical and operational.

For this study, the selected operational parameters are frontal air velocity and saturation temperature at 35° C ambient temperature, while the number of deep-rows, fin pitch, tubes vertical and horizontal spaces, tube outside diameter and number of circuits are selected as the geometrical parameters. The objective functions in this work are the system's COP, condenser's frontal area, condenser's material cost, and system's life cycle cost.

8.3 Design optimization methodology

In order to determine the effects of the selected design parameters on the objective functions, the condenser coil of the conventional roof-top bus air-conditioning system is selected as the "base configuration". The geometric parameters of the tubes and fins are given in Chapter 4. The optimization scenario will be carried out by varying one of the selected parameters while the other parameters are kept at the same values as the base configuration parameters.

Again, the objective functions in this study are the system's COP or exergy destruction, condenser's frontal area, condenser's material cost, and system's life cycle cost. The relationship between the objective functions and the selected design parameters should first be determined before the optimization process can be carried out.

8.3.1 Exergy destruction calculations and its relationship with system's COP

Thermodynamic energy and second law analyses have been performed on each of the four major system components (an evaporator, a condenser, a compressor, and an expansion device) as shown schematically in Figure 8.1. Generally, the exergy losses can be grouped into two primary categories: (i) heat transfer (thermal) losses referred to

as ΔT -losses and (ii) frictional losses referred to as ΔP -losses. The equation used to compute the exergy destruction (ED) for the condenser coil (the focus of interest) and fan is:

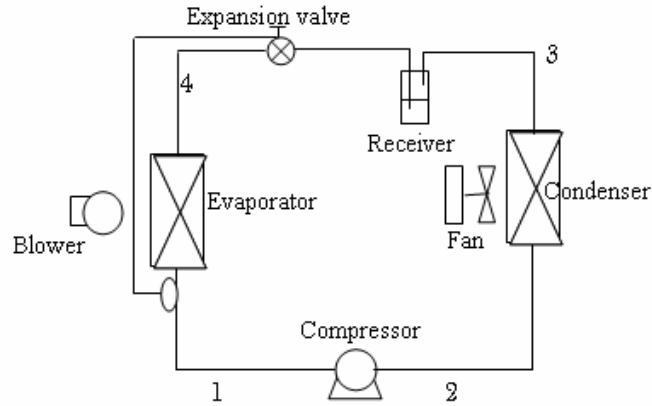


Figure 8.1 Schematic diagram of refrigeration cycle

$$ED_c = T_o \times \left[\dot{m}r(s_3 - s_2) + Q_c \right] + \left[\dot{m}_a c_{p,a} \ln \left(\frac{T_{ac,e}}{T_{ac,i}} \right) + \frac{\dot{m}_a \times \Delta P_a}{\rho_a} \right] \quad (8.1)$$

The first bracket accounts for the thermal and frictional losses for the refrigerant plus the irreversibility due to heat transfer Q_c over a finite temperature difference while the first term in the second bracket accounts for the thermal losses for the air stream over the condenser. On the other hand, the last term expresses the exergy losses due to the air flow friction. The exergy destruction associated with the air-side pressure drop comes entirely from the condenser's fan. Thus, the last term is almost equivalent to the value of the fan power, thus the Equation 8.1 can be rewritten as follows:

$$ED_c = T_o \times \left[\dot{m}r(s_3 - s_2) + Q_c \right] + \left[\dot{m}_{a,c} c_{p,a} \ln \left(\frac{T_{ac,e}}{T_{ac,i}} \right) + W_{fan,c} \right] \quad (8.2)$$

The exergy destruction can be calculated for an irreversible-adiabatic compression process as:

$$ED_{cp} = \dot{m}r T_o (s_2 - s_1) \quad (8.3)$$

The lost work produced in the expansion valve is obtained from the following equation:

$$ED_{ex} = \dot{m}r T_o (s_4 - s_3) \quad (8.4)$$

The evaporator's irreversibility can be expressed as:

$$\dot{E}D_e = \left[\dot{m}r T_o (s_1 - s_4) - \dot{Q}_e \times \frac{T_o}{T_s} \right] + \left[\dot{m}_{a,e} T_o c_{p,a} \ln \left(\frac{T_{aev,e}}{T_{aev,i}} \right) + W_{blower,e} \right] \quad (8.5)$$

By summing Equation 8.2, Equation 8.3, Equation 8.4, and Equation 8.5, the total exergy destruction of the refrigeration cycle can be expressed as follows:

$$\begin{aligned} \dot{E}D_t = & \left[\dot{m}_{a,e} c_{p,a} T_o \ln \left(\frac{T_{aev,e}}{T_{aev,i}} \right) + \dot{m}_{a,c} c_{p,a} T_o \ln \left(\frac{T_{ac,e}}{T_{ac,i}} \right) \right] + \left[Q_c - Q_e \frac{T_o}{T_s} \right] \\ & + \left[W_{blower,e} + W_{fan,c} \right] \end{aligned} \quad (8.6)$$

Where, $Q_c = Q_e + W_{cp}$

Where T_s and T_o are the conditioned space and ambient air temperatures and they are assumed to be 22°C and 35°C respectively. It should be noted that the evaporator blowers' power and the volume flow rate of air over the evaporator are fixed at 840 Watts and 4000 m³/hour of air flow respectively. It was found from the current study that the contribution of the thermal losses for air in the entire cycle irreversibility is very small comparing to that for the compressor and condenser fans. Accordingly, the term of air thermal losses (the first bracket in Equation (8.6)) can be ignored and thus, the cycle irreversibility is mainly varying with the variation in the compressor power and condenser's fan power as shown in Equation (8.6).

In order to clarify the relationship between the system's COP and the system's total exergy destruction, the definition for COP of a vapor compression cycle should be stated first. The COP is identified as the amount of cooling produced per unit work supplied.

Therefore, the COP is expressed according to the first law of thermodynamics as:

$$COP = \frac{Q_e}{PI} \quad (8.7)$$

And for a reversible refrigeration cycle, it can be expressed as:

$$COP_{rev} = \frac{Q_e}{PI_{rev}} = \frac{T_s}{(T_o - T_s)} \quad (8.8)$$

By combining the first and second laws of thermodynamics, the input system power can be determined as:

$$PI = PI_{rev} + ED_t = Q_e \times \left[\left(\frac{T_o}{T_s} - 1 \right) + \frac{ED_t}{Q_e} \right] \quad (8.9)$$

Thus, the cycle COP can be obtained from the following equation:

$$COP = \frac{1}{\left[\frac{1}{COP_{rev}} + \frac{ED_t}{Q_e} \right]} \quad (8.10)$$

It may be interesting to observe that the COP can be determined from two distinct equations, one comes from the first law, and the second comes from both (the first and second laws of thermodynamics). Almost similar results were obtained when both Equations 8.7 and 8.10 were used to calculate the COP.

8.3.2 Condenser's frontal area calculation

The calculation of the condenser's frontal area has been accomplished through the use of the computer program for condenser sizing discussed in Chapter 5. The roof-top AC standards state that the condenser height must be fixed at 18 inch (457.2 mm). Therefore; the change of the frontal area involves the change in condenser's length without any modification in its height.

8.3.3 Cost calculation

A system's life cycle cost is defined as the sum of two contributions:

- The sum of the capital investment cost of compressor and condenser's investment cost (material cost). It is found that varying all the design parameters except the condensation temperature does not produce a significant influence on the compressor's cost. Additionally, the condenser's fans cost and other system components cost (thermostatic expansion valve, liquid receiver, filter-dryer, piping network) are not significantly affected by the variation of the design parameters.
- The annual operating cost is the annual cost of the system's input power which is the sum of the compressor's power, condenser's fans power, and evaporator blowers' power. The system's input power is inversely proportional to the system efficiency COP for a fixed cooling capacity. It should be observed that the AC system's input power is considered as a part of the total consumed power from the power produced by the bus main engine or auxiliary engine. Therefore, the operating or running cost is represented by the annual fuel cost needed to produce the required input power to drive the AC system.

8.3.3.1 Capital investment Cost

8.3.3.1.1 Material cost

Heat exchanger price is typically based on a multiple of material cost assuming mass production. Therefore, the material cost for the condenser was calculated using the cost of copper (US\$1.76/kg) and aluminium (US\$1.54/kg) from the London Metals Exchange. The volume of each metal was calculated and multiplied by its density, annuity factor for material cost, and cost per kg to determine the material cost for each heat exchanger.

8.3.3.1.2 Compressor's cost

The compressor's capital cost is determined according to the equation suggested by Wall (1991):

$$C_{cp} = a_c k_c \left(\frac{\overset{o}{V}_s}{0.9 - \eta_{is}} \right) \times r_p \times \ln(r_p) \quad (8.11)$$

where a_c is the annuity factor for compressor, k_c is the cost per volumetric rate ($\overset{o}{V}_s$) and this value is taken as proposed by Wall (1991) to be 7000. The compression or pressure ratio is represented by r_p . The isentropic compressor efficiency, η_{is} can be obtained by curve fitting the published experimental data of Park et al. (1999) which is given as follows:

$$\eta_{is} = 0.9343 - 0.04478 \times r_p \quad (8.12)$$

Assuming that the interest rate is 5% and 10 years is the depreciation time, the resulting annuity factor is $a_1 = 0.1295 \text{ years}^{-1}$.

8.3.3.2 Running Cost

The operating or running cost is determined based on the price of fuel per liter (\$/liter). Therefore the annual operational cost, C_o is:

$$C_o = \dot{V}_{fuel} \times C_l \times H_{year} \quad (8.13)$$

H_{year} is the annual operational hours and this is assumed to be 4500 hr per year.

\dot{V}_{fuel} (liter/hour) is the volumetric fuel consumption per year to produce the required power to drive the compressor and fans. C_l is the price of diesel fuel and it is assumed to be 0.25 \$/liter. The required power for the fans is taken indirectly from the engine through the engine battery which is charged by the generator. The compressor may take its required power directly by engaging the engine or has a separate internal combustion engine. However, the following equation represents the relationship between the volumetric fuel consumption and AC system input power, PI .

$$\dot{V}_{fuel} = \frac{PI}{\eta_{engine} \times C.V \times \rho_{fuel}} \quad (8.14)$$

And the annual operational cost, C_o is given as:

$$C_o = \frac{Q_e}{\eta_{engine} \times C.V \times \rho_{fuel}} \times \left[COP_c + \frac{ED_t}{Q_e} \right] \times C_l \times H_{year} \quad (8.15)$$

It is expected from the previous analysis that the optimal point corresponds to a maximum COP and a minimum running cost. Intuitively, it can be deduced from Equations 8.10 and 8.15 that the minimum cycle irreversibility does produce maximum cycle efficiency (approaches closely to reversible efficiency) at minimum system operating cost.

8.4 Parametric study

The condenser model and the optimization search system are programmed in Microsoft Visual Basic to solve the non-linear equations for the optimization parameters. For a specified amount of condenser heat rejection, the refrigerant pressure drop and condenser length are iterated until convergence is approached. Then, the condenser design is incorporated to the simulation AC system module and all the objective functions are finally calculated. The logic chart for the iteration process and computer model interface are shown in Appendix C. The following sections present the effect of the selected design parameters on the objective functions.

8.4.1 The Effect of frontal velocity

As it might be expected, the increase in frontal air velocity results in an enhancement in the air-side heat transfer coefficient. Since the air-side thermal resistance is significantly more dominated than that of the refrigerant-side, small improvement in the air-side thermal resistance leads to a significant reduction in the frontal area until $v_{fr} = 2$ m/s as displayed in Figure 8.2a. Also, it is observed from the previous Figure that the reduction in frontal area becomes insignificant with the increase in frontal air velocity over 2 m/s indicating to the velocity augmentation becomes ineffective to reduce the frontal area significantly. Figure 8.3a shows that the frontal air velocity of 3 m/s is the optimal velocity consistent with the cycle exergy losses and COP. The reduction in frontal area with increasing in frontal air velocity causes a decrease in refrigerant pressure drop and thus the compressor entropic power is also decreased. Concurrently, the fanning entropic power is increased on account of the increase in frontal air velocity. Therefore, two competing effects are at work.

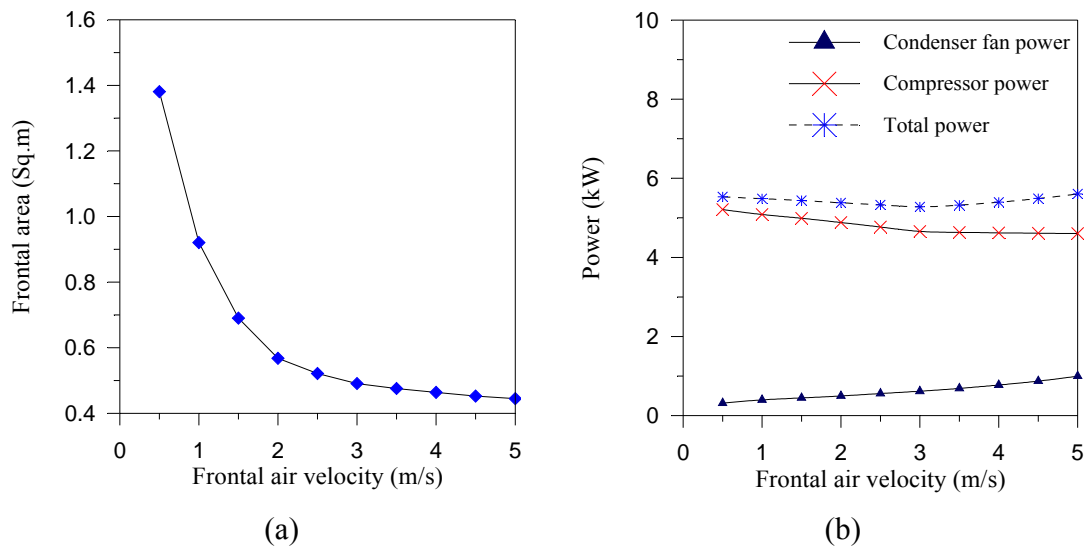


Figure 8.2: Effect of face air velocity on a) - Frontal area b) – Compressor power, condenser fan power, and total input power

The net product is demonstrated graphically in Figure 8.2b. At the beginning, the decrease in compressor power is outweighed by the increase in fan power because the decrease in frontal area and refrigerant pressure drop with increasing frontal air velocity are significant. Accordingly, the cycle input power is decreased until $v_{fr} = 3$ m/s. The cycle exergy losses decrease while the system COP is enhanced until $v_{fr} = 3$ m/s as depicted in Figure 8.3a. The change in compressor power then becomes insignificant as compared to the increase in condenser fan power (see Figure 8.2b) as a result of insignificant decrease in refrigerant pressure drop with increasing frontal air velocity. As such, the cycle input power is increased after $v_{fr} = 3$ m/s which causes an increase in the system irreversibility and hurts the system's efficiency as illustrated in Figure 8.3a. Figure 8.3b shows that the minimum running cost occurs at a frontal air velocity of 3 m/s in accordance with Equation 8.15. Therefore, it may be concluded that the optimal operating range for the frontal air velocity should not exceed over 3 m/s and should not be less than 2 m/s.

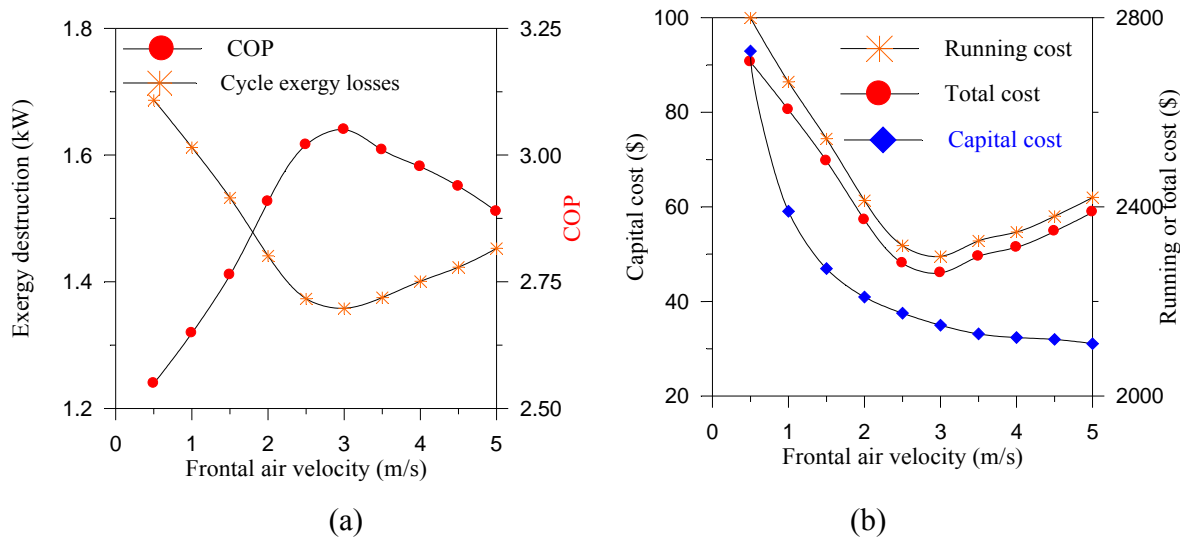


Figure 8.3 Effect of face air velocity on a) total cycle irreversibility and COP
b) annual cost

Comparing with the base configuration design, the system COP is enhanced by 6.55 % from $v_{fr} = 2.5$ m/s to the optimal point at $v_{fr} = 3$ m/s. Although this enhancement is superficially not considerable, there is some saving in the annual fuel consumption for the bus engine. As an example, if a condenser (with optimal design) is installed in an intercity bus with 4500 operating hours per year, the saving will be approximately 612 liter/year for one bus AC system. Suppose that there is accompany owns five buses in operation the fuel saving is 3060 liter/year which corresponds to USD 765 per year. Furthermore, due to the recent drastic instability in fuel prices the coil design optimization will be an added credit for energy saving.

8.4.2 The Effect of saturation temperature

The design of the condenser with a higher condensing temperature, T_c will create escalating in the potential temperature difference between the refrigerant and the air. This will result in a condenser that is more compact (smaller frontal area) and

cheaper in terms of condenser material cost as portrayed in Figure 8.4a. However, the system capital cost will be more expensive as a result of the increase in compressor's capital cost associated with the increase in pressure ratio (see Equation 8.11). Therefore, it can be deduced that the compressor's paid cost is more than the saving in condenser's material cost gained from the design with a higher condenser temperature. In turn, the design with a higher condensing temperature is attractive in terms of the material cost but is unprofitable in terms of the system capital cost point-of-view as shown in Figure 8.4b.

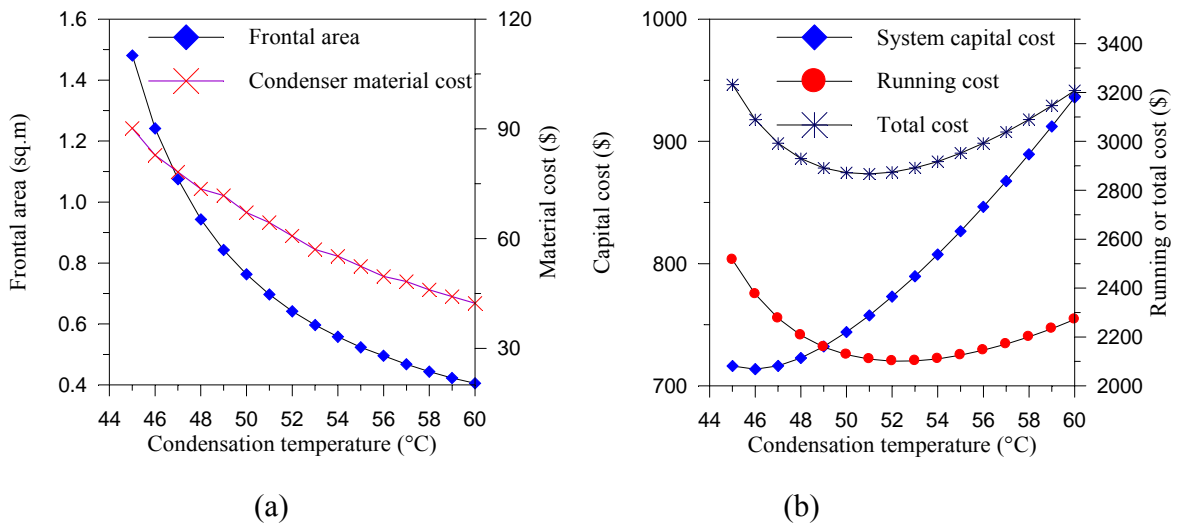


Figure 8.4 Effect of saturation temperature on a) Frontal area b) Annual cost

Again, the competing effect of the compressor's power and condenser's fan power is also repeated here. Theoretically, the design with a higher condensation temperature requires extra work by the compressor to compress vapor to a higher condensing pressure. Additionally, the increase in condensation temperature causes an increase in the enthalpy of refrigerant entering the evaporator. This causes an augmentation of the mass flow rate of the refrigerant required to maintain the evaporator's cooling capacity. Hence, the amount of the compressor's power is increased with the increase in condensation temperature. On the other hand, the reduction in the condenser's frontal area with increasing condensation temperature will result in the

selection of fans with smaller air flow rate and thus the fans' power is smaller. The net outcome is represented graphically in Figure 8.5 where it can be seen that the maximum COP is at a condensation temperature of 51°C. At $T_c = 51^\circ\text{C}$, it can be said that the increase in compressor power is equivalent to the decrease in the condenser's fan power. Beyond $T_c = 51^\circ\text{C}$, the increase in condensation temperature causes the increase in the compressor's power more than the decrease in condenser's fans power. This increases the system's irreversibility and decreases its efficiency as illustrated in Figure 8.5.

With respect to the running cost, it is noted earlier that the trend of the operating cost approximately follows the trend of the system's exergy losses as shown in Figure 8.4b. In conventional condenser design, the saturation condenser temperature is frequently taken as 20K over the ambient temperature. However, this study reveals that the increase in the condenser temperature difference, CTD (saturation condenser temperature – ambient temperature), over 16K can cause an adverse effect and hurt the system's efficiency. It may be concluded that the increase in the condenser temperature difference gives a positive result in terms of a smaller frontal area on the expense of an increase of running cost.

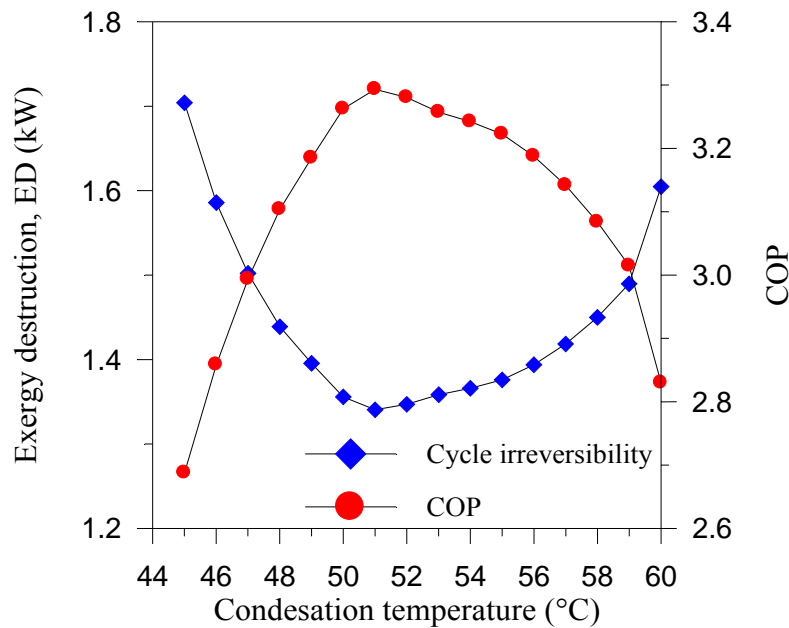


Figure 8.5 Effect of saturation temperature on cycle total irreversibility and COP

If the conventional condenser's design is changed from $T_c = 55^\circ\text{C}$ to 51°C (the optimal condensation temperature in the present study), the system's COP will be enhanced by 3.0 % which can be translated to an annual fuel consumption saving of 464 liter for the bus engine.

8.4.3 The Effect of fin pitch

For this investigation, the fin pitch is varied while the other design parameters are fixed to the values of the base configuration. As discussed earlier, there is competing effects of increased heat transfer with increased frictional pressure drop for air and refrigerant sides. Accordingly, the relationship between the thermal performance and the hydraulic performance of the heat exchanger design is of an opposing nature i.e. the upgrading in thermal performance (heat transfer coefficient) is built on the expense of the deterioration in hydraulic performance (pressure drop and pumping power). Figure 8.6a emphasizes the previous concept and reveals that the increase in fin pitch (number of fins per mm) leads to a decrease in frontal area due to a reduction in air flow area which is identified by the minimum passage area that allows the air to pass through, as given by Equation 8.16.

$$A_{flow} = (f - d_o) \times N_{tp} \times L \times (1 - N_f \times t_f) \quad (8.16)$$

This reduction in air flow area results in the acceleration of the air mass velocity and a decay in the thermal boundary layer. In turn, the frontal area trend is reduced drastically upon $N_f = 0.469/\text{mm}$ and the trend continues indicating that using a fin pitch of more than $0.469/\text{mm}$ has an ineffective influence on the frontal area trend as shown in Figure 8.6a.

One might expect that the design of a finned-tube heat exchanger with a high fin pitch will result in a more compact heat exchanger and hence its capital cost will be

lower. However, Figure 8.6b shows that this is correct up to $N_f = 0.391/\text{mm}$. Increasing the fin pitch further will lead to an increase in the condenser capital cost. This is because the condenser capital cost is dependent on two items (the tube material cost and fins material cost) and according to the magnitude of contribution of each item the condenser capital cost tendency will be formulated. At the beginning, the increase in fin pitch leads to a considerable reduction in frontal area (Figure 8.6a) and this, of course, will result in significant saving in tube material cost on the expense of an increase in the fins material cost. Therefore, at the beginning, the capital cost is decreased with the increase in fin pitch up to $N_f = 0.391/\text{mm}$. Increasing the fin pitch further will result in the increase in the fins's material cost and outweighing the saving in the tube material cost because the reduction in the frontal area is no longer significant as it was before $N_f = 0.391/\text{mm}$.

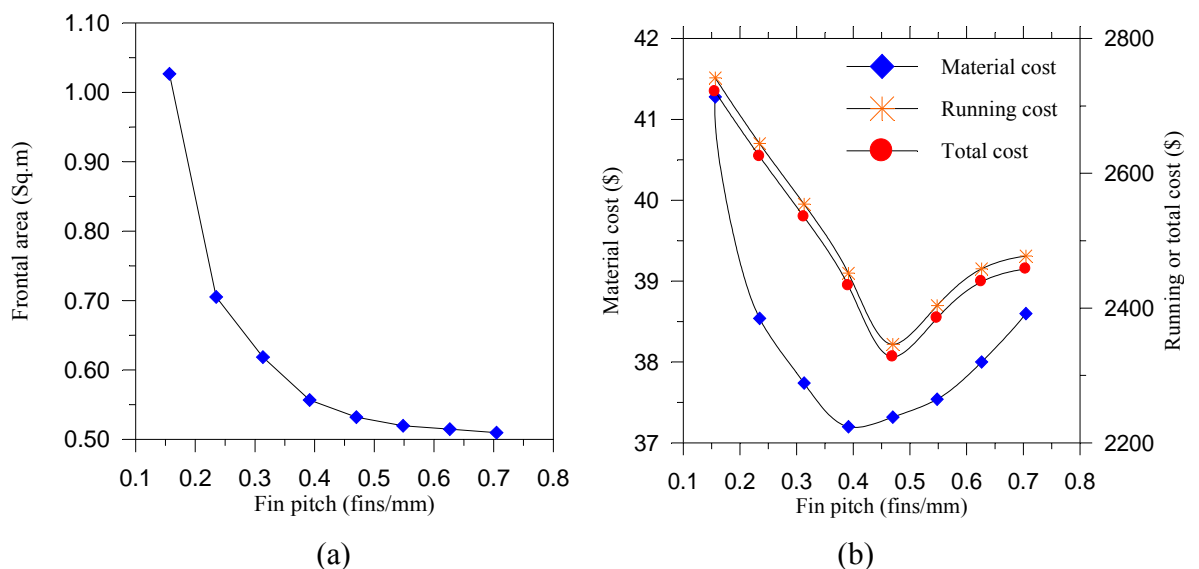


Figure 8.6 Effect of fin pitch on a) Frontal area b) Annual cost

The increase in fin pitch affects positively on the refrigerant frictional losses and negatively on the air frictional losses. The reason is that the increase in fin pitch shortens the tube length and reduces the refrigerant pressure drop and compressor power. On the other hand, the increase in fin pitch leads to an increase in air mass velocity causing high frictional losses in the air-side pressure and this has a negative effect on the fan entropic power as well. These phenomena are displayed in Figures 8.7a and 8.7b. The cycle

irreversibility and COP trends are dictated by the two competing effects of the decrease in compressor power and increase in condenser fan power as depicted in Figure 8.8. At the beginning, the increase in fin pitch results in a decrease in cycle irreversibility up to $N_f = 0.391/\text{mm}$ as a consequence of the decrease in compressor power which overbalances the increase in fan entropic power. Subsequently, further increase in the fin pitch over $0.391/\text{mm}$ reinforces the increase in fan power to outweigh the drop in compressor's power causing an increase in the cycle irreversibility with the increase in fin pitch as illustrated in Figure 8.8. The ultimate result is at the fin pitch of $0.469/\text{mm}$; the amount of decrease in compressor power is almost the same as that of the increase in fan power making $N_f = 0.469/\text{mm}$ as the optimal point from the cycle COP point-of-view.

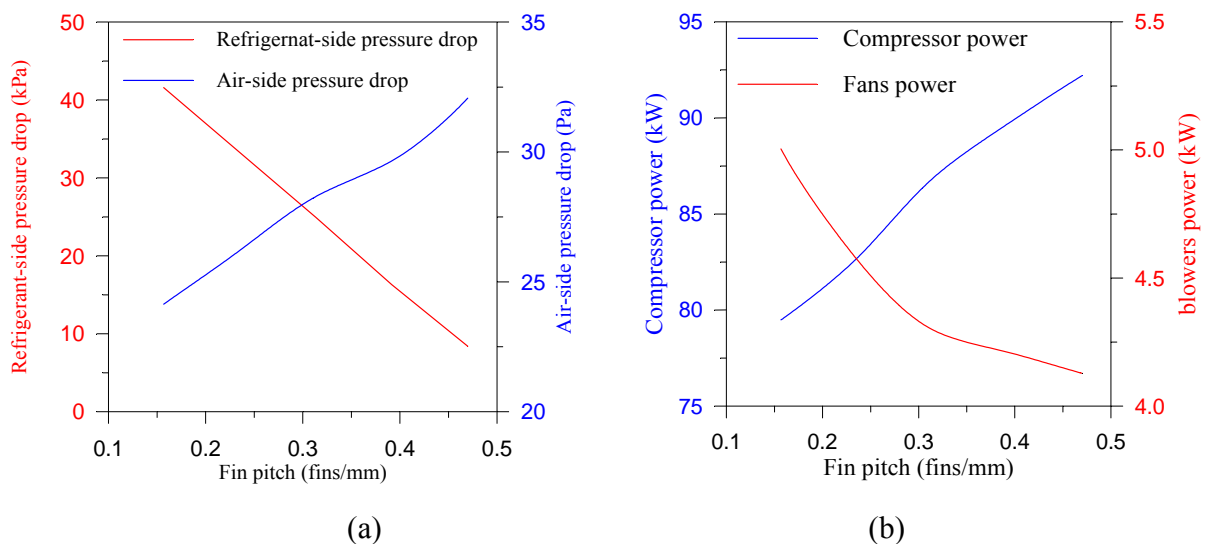


Figure 8.7 Effect of fin pitch on a) refrigerant and air sides pressure drop b) Compressor and condenser fan powers

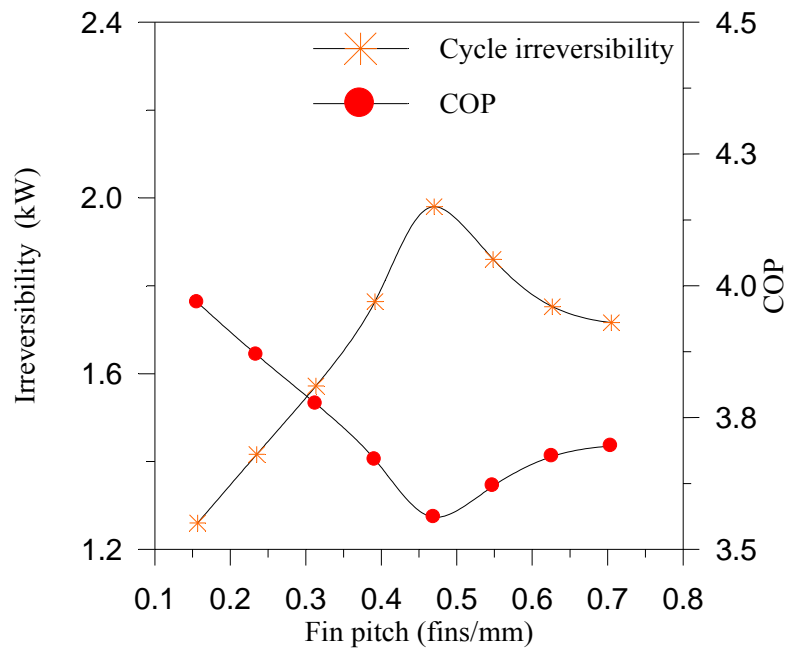


Figure 8.8 Effect of fin pitch on total cycle irreversibility and COP

Referring to the effect of fin pitch on the annual cost, Figure 8.6b displays its effect on the running and total cost. Increasing the fin pitch more than 0.469/mm will increase the running and total cost (material plus running costs) and this will add burden on the bus engine's annual fuel consumption. So, it may be commented that at higher fin pitch value of over 0.469/mm, the irreversibility in the system increases. Therefore, it is less profitable to invest money on greater fin pitch as the only benefit is an insignificant reduction in frontal area. Thus, optimal operating range for the fin pitch in the present study is from 0.391 (fins/mm) to 0.548 (fins/mm).

8.4.4 The Effect of number of deep-rows

As predicted, the increase in the number of rows of the condenser tubing, which defines the condenser coil depth, will lead to a compact condenser frontal area for the same cooling capacity. This production is verified by Figure 8.9a, which shows that as

the number of rows of tubes increases, the face area decreases. One would expect that a heat exchanger with only one long row of tubes and no tube bends, providing the largest heat exchanger frontal area possible, would yield the best performance. That is demonstrated in Figure 8.9b, which reveals that the decrease in number of rows is followed by an increase in system's COP. This is because decreasing the number of rows of tubing also decreases the number of tube bends. Furthermore, the number of rows governs the refrigerant flow path for the same number of tubes per row in a circuit, as well as the air flow path. Thus, the decreasing number of rows will lead to the decrease in the number of refrigerant and air flow paths. This results in reducing the refrigerant-side pressure drop by reducing the total flow length irrespective of the increase in condenser length in each individual tube. As a result, the required compressor work is reduced with the decrease in number of rows. Additionally, the decrease in number of rows will reduce condenser fan's power. This further contributes to the decrease in the system irreversibility and consecutively enhances the system's COP.

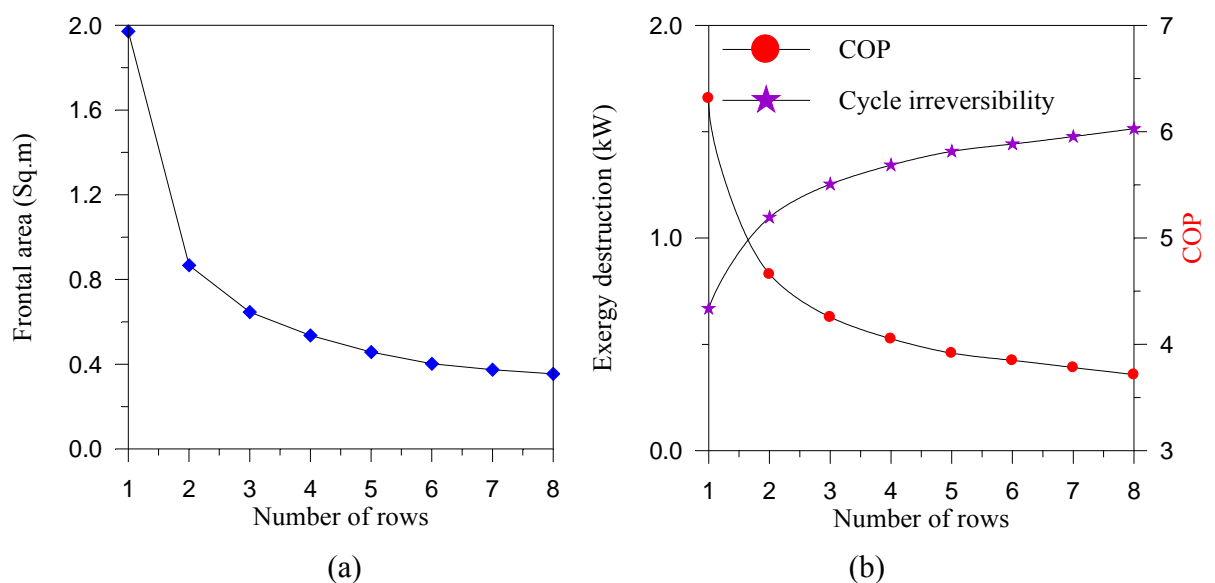


Figure 8.9 Effect of number of rows on a) Frontal area b) Total cycle irreversibility and COP

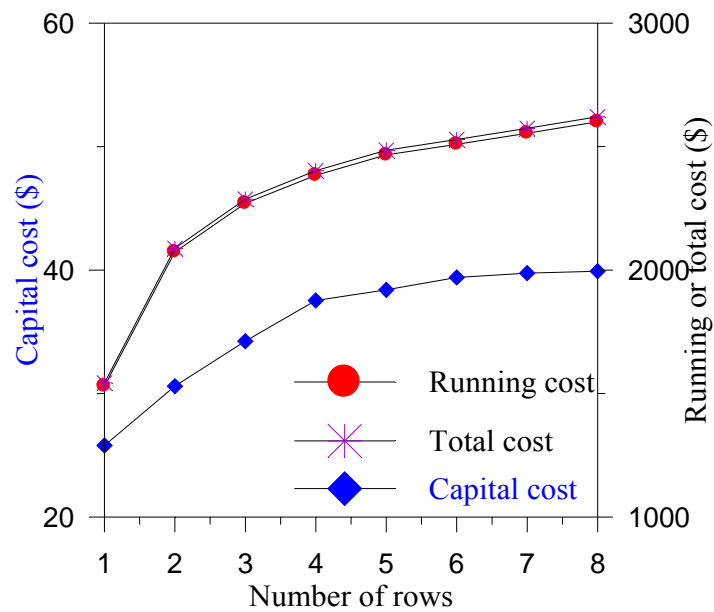


Figure 8.10 Effect of number of rows on annual cost

In accordance with Figure 8.9a, one might assume that the increase in number of rows will lead to a decrease in owing cost due to the reduction in condenser frontal area. However, Figure 8.10 shows that the trend of the owing cost is different from what is expected. More tubes rows increase the material cost regardless of the reduction in condenser length. Therefore, a smaller number of rows is recommended. However, when determining the number of rows of tubes, there should be a trade-off between space constraints and optimum performance if the condenser's designer encounters space constraints that prevent the use of a heat exchanger with a large frontal area.

8.4.5 The Effect of number of tube circuiting

For this investigation, the number of rows, tube diameter, tube spacing, the number of tubes per row and fin spacing were fixed to the values used for the base configuration. For the sake of simplicity in studying the effect of tube circuiting on the objective functions, the number of circuits is selected as an even number. This is because

the base configuration involves twelve tubes per row. This simplification will ease the investigation since each circuit will exhibit the same behavior. The refrigerant flow circuit configurations investigated for this study are summarized in Table 8.1. Figure 8.11 demonstrates the meaning of the tube circuiting.

Table 8.1: Condenser circuiting configurations

Number of Circuits	Tubes/Circuit
1	12
2	6
3	4
4	3
6	2
12	1

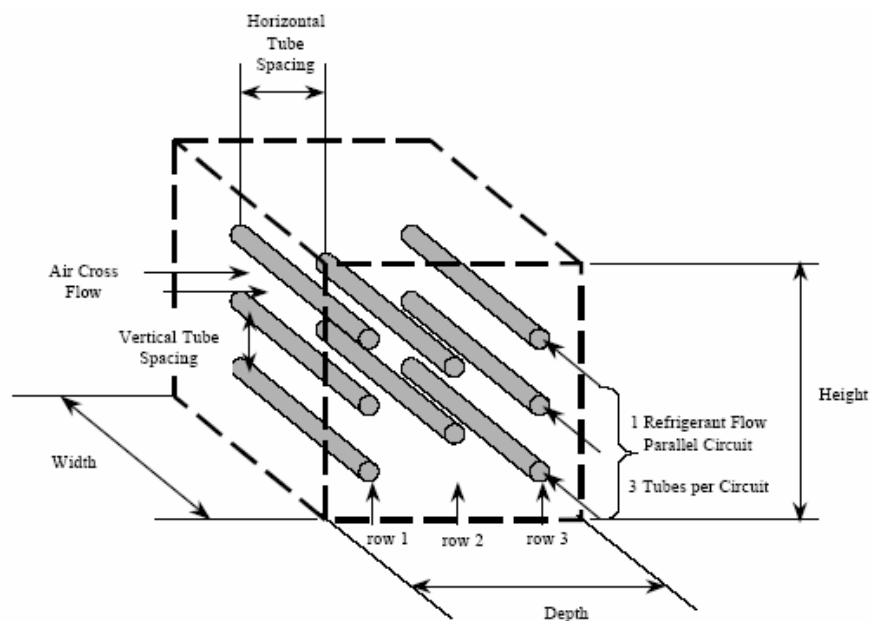


Figure 8.11 Tube circuiting configuration

The study of finned-tube heat exchanger (condenser or evaporator) is complicated by a number of factors. The main factor is the numerous possible refrigerant circuitry arrangements for a coil, which contributes to the complexity of the study. The

refrigerant circuitry without any refrigerant branch joining or splitting it is referred to as a simple refrigerant circuitry as shown in Figures 8.11 and 8.12, which is the area of focus in this study. The number of circuits determines the number of parallel tube passages in which the refrigerant mass flow rate is divided amongst by the manifold. It should be noted that the relation between refrigerant mass velocity and number of circuits is characterized by an opposing mode for a certain number of tubes per row. Equation 8.17 shows that the greater the number of circuits, the lesser the amount of the refrigerant mass flow rate that can be handled by the individual tube i.e. the smaller the refrigerant mass flux.

$$G_r = \frac{\dot{m}_r}{\frac{\pi}{4} d_i^2 \times N_{cr}} \quad (8.17)$$

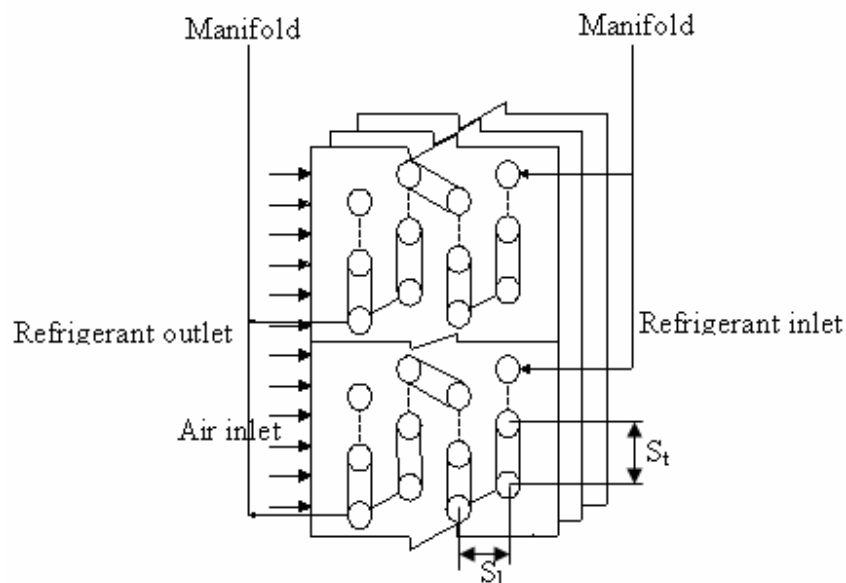


Figure 8.12 Finned-tube heat exchanger's simple circuitry
(Shown: 4 rows, 2 circuits, 6 tubes per row)

The heat transfer mainly depends on two factors: the convective heat transfer coefficient and the mean temperature difference between refrigerant and air. As it is obvious from Equation 8.17, the increase in circuits' number results in a decrease in the

refrigerant mass velocity and this will consequently lead to an enhancement in refrigerant pressure drop at the expense of a detriment in refrigerant heat transfer coefficient. The enhancement in refrigerant pressure drop translates to a small drop in condensation temperature and subsequently an increase in the mean temperature difference (heat transfer driving force) between air and refrigerant. Once again, two competing effects are at work. The deterioration in refrigerant heat transfer coefficient leads to enlarge the condenser size while the enhancement in driving force of heat transfer leads to a decrease in the condenser size. The net outcome is shown in Figure 8.13a which indicates that the design with more tubes' circuiting causes the condenser to have longer tubes for the same number of tubes. The possible explanation is that deterioration in the thermal performance is more significant than the enhancement in the hydraulic performance. Thus, as can be seen from Figure 8.13b, the heat exchanger is more expensive in this case because of the increase in its frontal area.

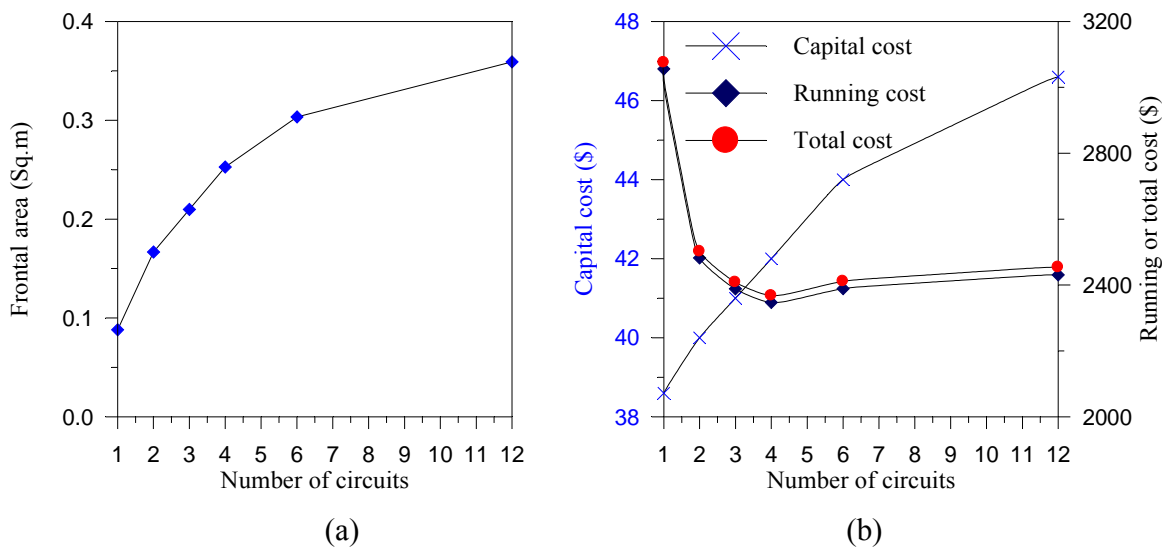


Figure 8.13 Effect of number of circuits on a) Frontal area b) Annual cost

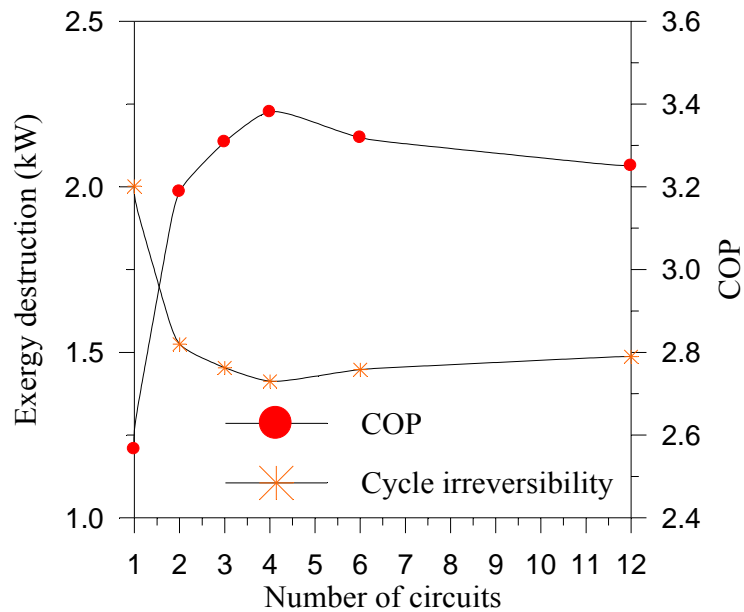


Figure 8.14 Effect of number of circuits on total cycle irreversibility and COP.

The increase in number of circuits means that the number of tubes per row in a circuit decreases as well. These effects reduce the refrigerant side pressure drop by reducing the total flow path regardless of the increase in individual tube length. That causes a decrease in the compressor power. Consequently, the condenser fan entropic power is increased to offset the increase in frontal area providing the condenser by appropriate air flow rate. Therefore, two opposing effects are working together. It can be deduced from Figure 8.14 that the decrease in compressor power no longer prevails over the increase in fan entropic power after $N_{cr} = 4$. As a result, the cycle COP begins to decrease as the number of circuits increases from 4 to 8 as shown in this Figure.

In conclusion, the condenser should be designed with quite a high number of circuits; at least equal to one-third of the total number of tubes per row ($N_{tp}/3$) for even number of tubes per row. Likewise, the number of circuits should be equal to one-third of the total number of tubes per row plus one ($(N_{tp} + 1)/3$) for the odd number of tubes per row taking into account that the number of tubes per parallel circuit will not be equal. This will result in different tubes' distribution between the circuits.

8.4.6 The effect of vertical tube spacing

The transverse pitch is the vertical space between the tubes in the normal direction of the air flow. The tube per row multiplied by the transverse tube spacing determines the condenser's height. This height should not be more than eighteen inches (457.2 mm) for a bus AC system. For a specified condenser height, the number of tubes per row is inversely proportional to the transverse pitch. The design with a wider vertical (transverse) space corresponds to a smaller number of tubes per row and this dictates the condenser to have a larger frontal area to offset the decrease in the number of tubes. Consequently, the design of the condenser with a wider tube space is distinguished by a large frontal area especially after $S_t = 31.75$ mm as shown in Figure 8.15a. Hence, it is difficult to predict the investment owing cost for the condenser. The increase in condenser frontal area prompts the owing cost to be high and at the same time, the decrease in number of tubes triggers to reduce it. Figure 8.15b shows that with increasing tube vertical spacing, the owing cost tends to decrease significantly till $S_t = 25.4$ mm and after that decreases slightly. This phenomenon can be explained by the fact that after $S_t = 25.4$ mm, the paid cost as a result of an increase in the frontal area offsets the saving due to the decrease in the number of tubes.

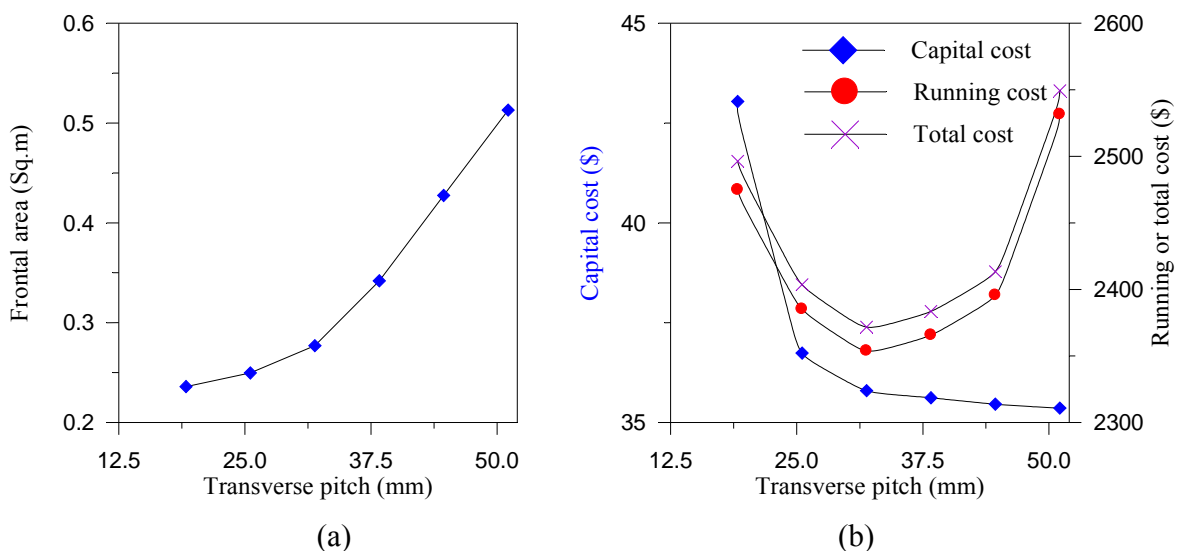


Figure 8.15 Effect of number of vertical tube spacing on a) Frontal area b) Annual cost

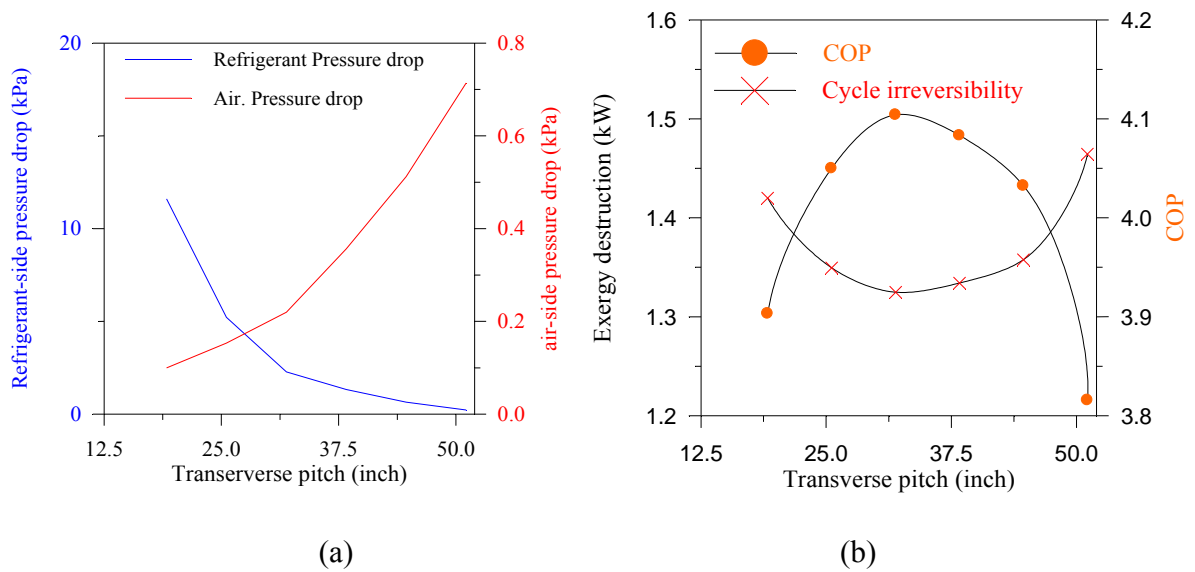


Figure 8.16 Effect of number of vertical tube spacing on: a) Refrigerant-side and air-side pressure drop b) Cycle irreversibility and COP

It is clear from Equation 8.16 that the air flow area is proportional to the number of tubes per row. Hence, the decrease in the number of tubes per row causes a reduction in the air flow area. Accordingly, the increase in tubes' transverse pitch is followed by a decrease in the number of tubes per row making the air flow area much smaller and increasing the air mass velocity. In turn, the air-side pressure drop is increased as shown in Figure 8.16a. The fan power is also increased to overcome the excessive increase in hydraulic resistance for the air-side. In contrast, the refrigerant pressure drop is decreased with the increase in the tube vertical spacing. This is because the decrease in the number of tubes per row will decrease the number of tubes per circuit as well. Thus, it will curtail the refrigerant flow path and causes a decrease in the frictional pressure drop.

It should be noted that the refrigerant pressure drop is also a function of the length of the individual tube itself and larger vertical space means longer individual tube for a specified height. The net outcome is that the refrigerant pressure drop is decreased regardless of the increase in tube length as shown in Figure 8.16a. Therefore, the increase in the tube vertical spacing has two adverse effects. The increase in tube

transverse pitch causes an increase in air-side pressure drop and the entropic fan power and concurrently causes a decrease in refrigerant pressure drop and compressor power. The net product, as shown in Figure 8.16b, indicates that refrigerant-side effect is more dominant resulting in a decrease in the cycle irreversibility up to $S_t = 31.75$ mm. For values of S_t greater than 31.75 mm, the air-side effect seems to be more dominant.

8.4.7 The Effect of horizontal tube spacing

The longitudinal pitch is defined by the horizontal tube space in a direction parallel to the air-flow. The condenser depth is the product of the number of rows and the longitudinal pitch. The effect of increasing the horizontal tube spacing on the air-side pressure drop is opposite to that of increasing the vertical tube spacing. In other words, the increase in horizontal tube spacing leads to a decrease in air-side pressure unlike the effect of increasing the vertical tube spacing. It can be explained by the longitudinal pitch (for the same number of rows) enlarging the air flow area and therefore decelerating the air mass velocity. The pressure drop for air-side will improve on the expense of its heat transfer coefficient. Poor air-side heat transfer coefficient means an increase in the condenser area. This will cause excessive pressure drop in the refrigerant side and put burden on the compressor's power to offset the refrigerant pressure drop. Therefore, the competition effect of the thermal and hydraulic performances will influence the trend of the objective functions as shown in Figures 8.17 and 8.18.

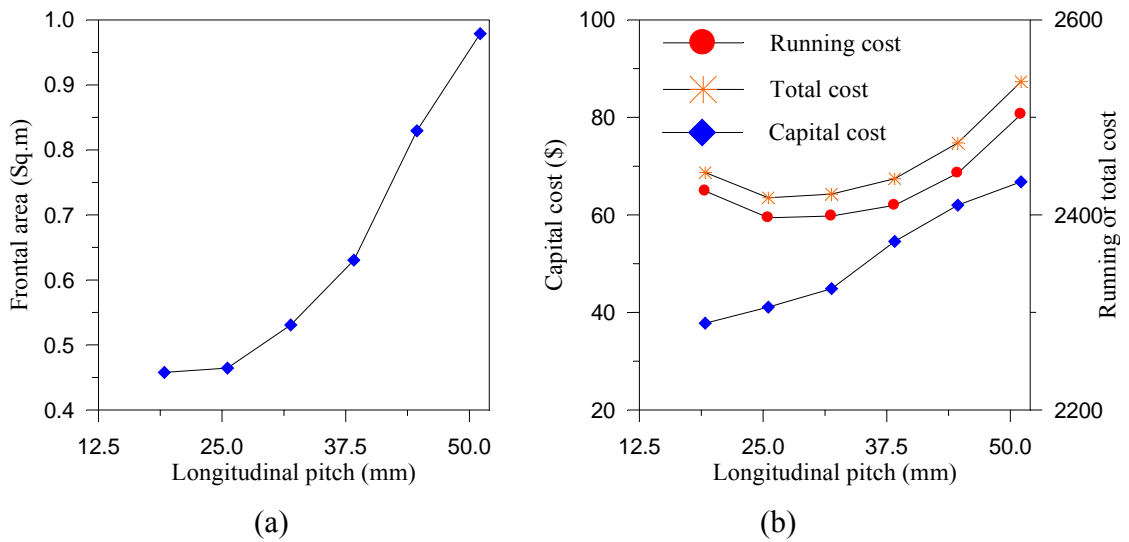


Figure 8.17 Effect of number of horizontal tube spacing on a) Frontal area b)

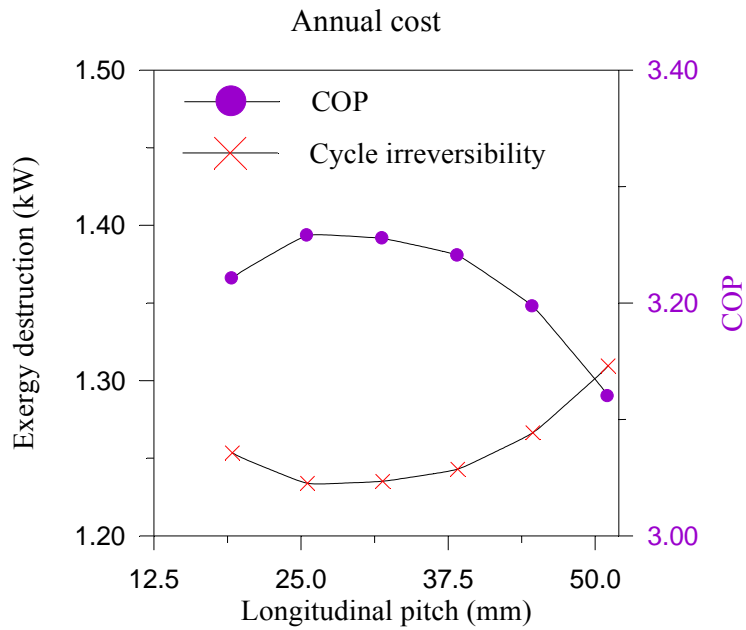


Figure 8.18 Effect of number of vertical tube spacing on cycle irreversibility and COP

8.4.8 The Effect of tube's outside diameter

Another geometric design parameter studied in this work is the condenser tube's diameter. The tube sizes considered for this study are taken from the AAON Heating and

Refrigeration Products Specifications (www.aeon.com). The dimensions of the tubes investigated are summarized in Table 8.2. For this investigation, the number of rows, number of circuits, tube spacing, and number of fins per mm were all maintained at the values used in the base configuration.

Table 8.2: Condenser tube dimensions (www.aeon.com, AAOP Heating and Air-Conditioning Products web site)

Outside Diameter (mm)	Inside Diameter (mm)	Wall Thickness (mm)
7.937	7.632	0.305
9.525	9.220	0.305
12.700	12.293	0.406
15.875	15.671	0.457
19.050	18.542	0.508

Increasing the tube diameter has a significant impact on many physical phenomena in the system. Increasing the tube diameter causes a decrease in the refrigerant-side pressure drop and a decrease in the refrigerant-side heat transfer coefficient as a result of the deceleration in refrigerant mass velocity. Both of these phenomena have two different impacts (positive and negative) on the objective functions. The frontal area and COP tends to increase. However, increasing the tube diameter also reduces the minimum air flow area, producing an increase in the air drag. As a result, the air-side pressure drop increases and the condenser fan's power also increases steadily. Furthermore, the air-side heat transfer is enhanced significantly. These phenomena have a negative impact on the COP while a positive impact on the frontal area in terms of enhancing air-side heat transfer coefficient. It may be interesting to note from Figure 8.19a that the frontal area is decreased with increasing tube diameter for the same number of tubes although the refrigerant heat transfer coefficient is diminished. This can be demonstrated from the fact that the air-side thermal resistance is more dominant than that for the refrigerant-side making up 85% or more of the total thermal resistance. Thus, any enhancement in air thermal resistance is translated directly to a reduction in the frontal area regardless of the amount of deterioration occurring in the refrigerant-side. Thus, it makes sense to expect the coil capital cost to be cheaper when using wider tube nominal diameter (for the same number of tubes) as a result of the smaller frontal area.

However, Figure 8.19b shows that the trend of the coil owing cost is not as expected. The coil investment cost is higher as the tube size is increased since the material cost for a wider tube is higher than the narrow tube.

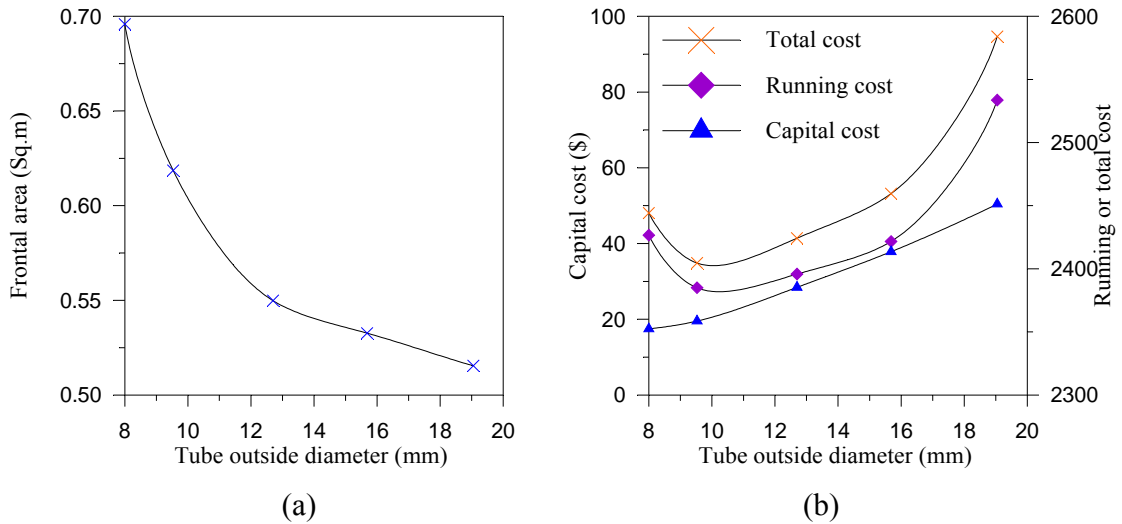


Figure 8.19 Effect of tube's outside diameter on a) Frontal area b) Annual cost.

The effect of tube's outside diameter on COP is shown in Figure 8.20. When the tube's diameter is increased from 7.9375 mm (5/16") to 9.53 mm (1/2"), the increase in the COP that results from the reduction in the refrigerant-side pressure drop and the decrease in the compressor work is larger than the reduction in the COP that results from the increased air-side pressure drop and increased condenser fan's power. Thus, as Figure 8.20 shows, the system COP increases when the diameter is increased from 7.9375 mm (5/16") to 9.53 mm (1/2"). However, when the tube diameter is further increased from 9.53 mm (1/2") to 19.05 mm (3/4"), the reverse effect is observed. Therefore, when the diameter is increased from 9.53 mm (1/2") to 15.875 mm (5/8"), the system COP decreases, as shown in Figure 8.20.

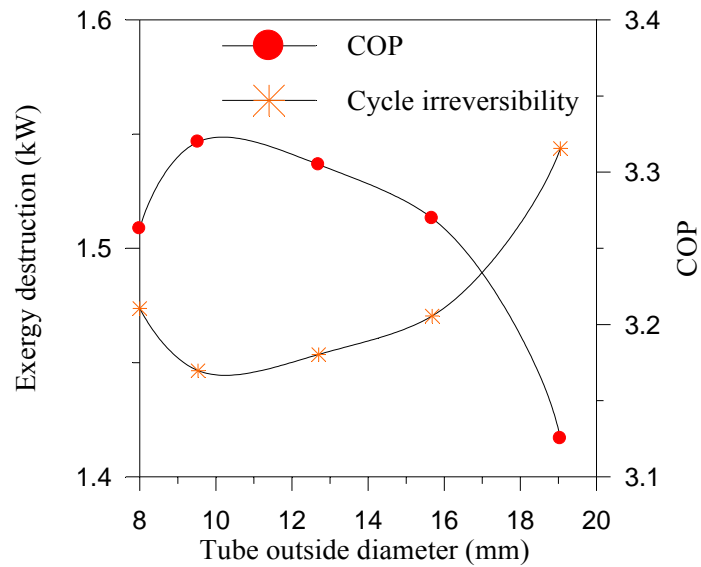


Figure 8.20 Effect of tube's outside diameter on cycle irreversibility and COP.

8.4.9 The instantaneous effect of the design parameters on system COP and frontal area

To study the influence of all the design parameters on the objective functions instantaneously is a complicated task and requires an extensive calculation. Thus, for the sake of simplicity, the parameters which have a significant influence on the optimization parameters should be selected first as decision variables. Based on the earlier results, it can be deduced that the most significant influence on the design comes from the frontal air velocity, saturation temperature, number of deep-rows, transverse pitch, number of tube circuiting, and tube's outside diameter. The saturation temperature and the frontal air velocity are mainly independent of the geometric parameters. Therefore, they can be taken at the optimal values of 51°C and 3.0 m/s respectively as the current study recommends. The number of tube circuiting is mainly related to the number of tubes per row and the present study of its effect shows that it should be one-third of the total number of tubes per row which is identified by the condenser height (fixed at 18 inches (457 mm)) divided by the transverse pitch. Additionally, the fin pitch and longitudinal

tube pitch may be recommended as 0.469 fins per mm and 25.54 mm respectively as mentioned before. The three decision variables selected are the number of deep-rows, transverse pitch, and tube's outside diameter. The following graphical charts (8.21 to 8.28) display both the effect of the number of deep-rows and transverse pitch on the system's COP and frontal area at different values of tube diameters.

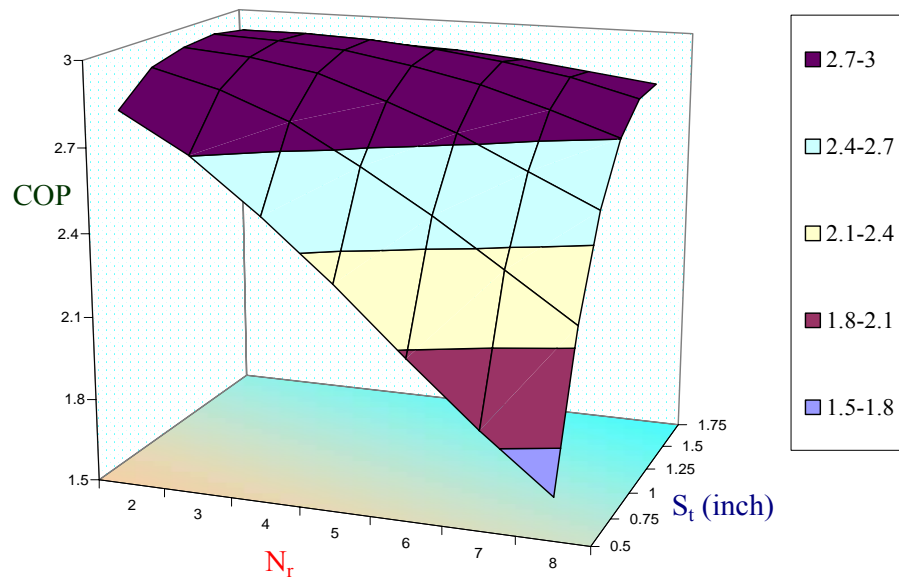


Figure 8.21 The system COP vs. number of deep-rows and transverse tube pitch at tube's outside diameter of 7.94 mm

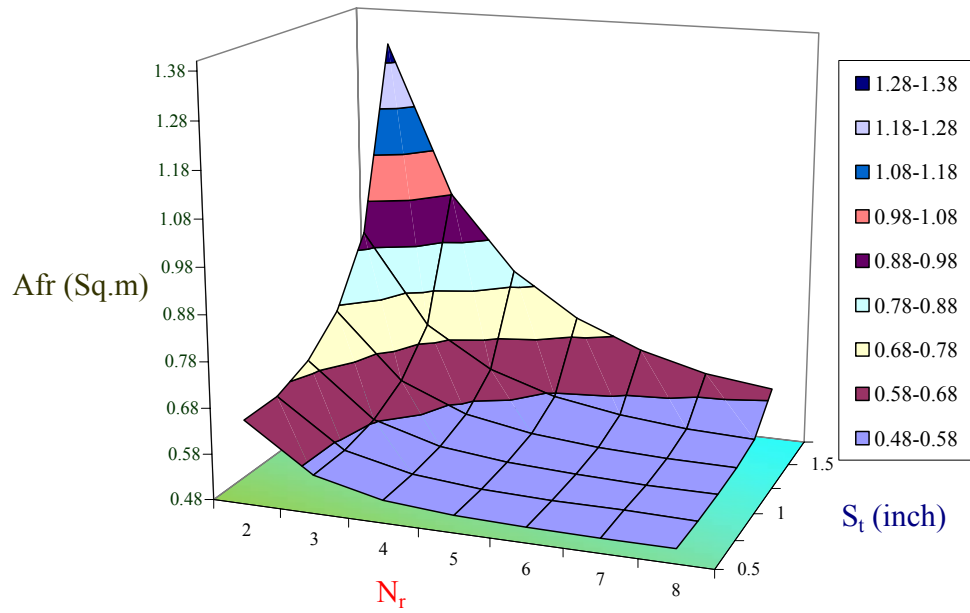


Figure 8.22 The frontal area vs. number of deep-rows and transverse tube pitch at tube's outside diameter of 7.94 mm

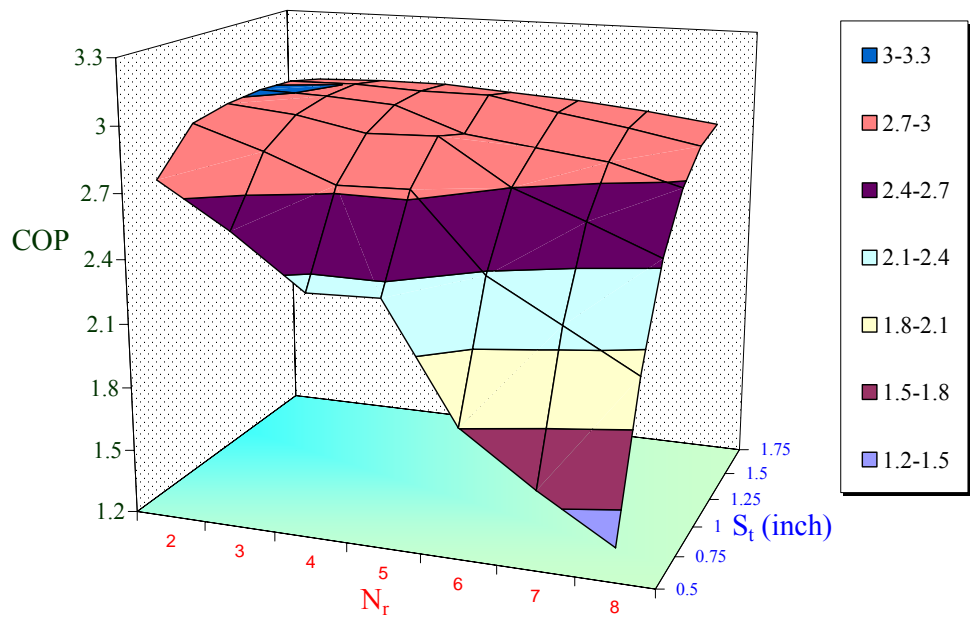


Figure 8.23 The system COP vs. number of deep-rows and transverse tube pitch at tube's outside diameter of 9.525 mm

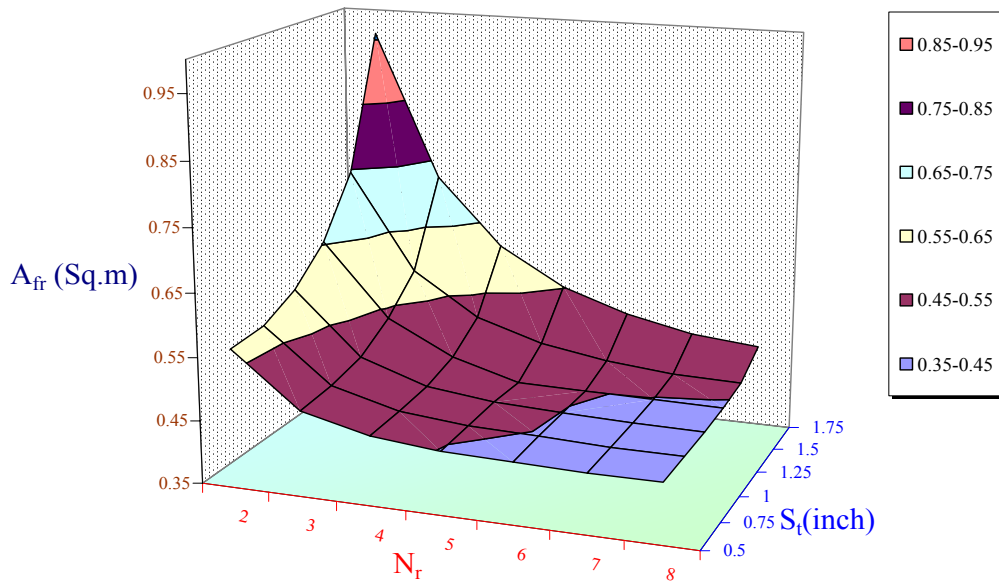


Figure 8.24 The frontal area vs. number of deep-rows and transverse tube pitch at tube's outside diameter of 9.525 mm

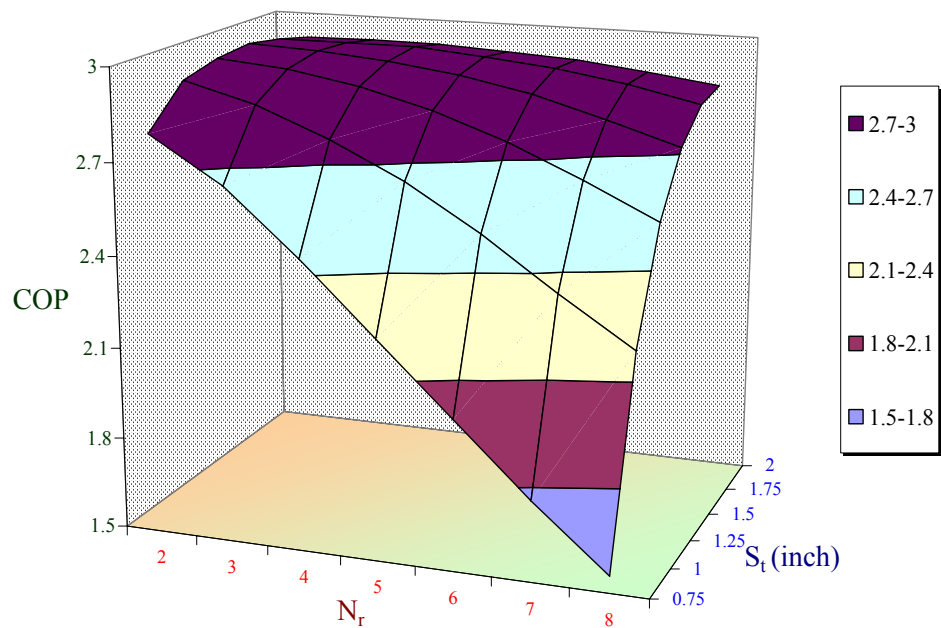


Figure 8.25 The system COP vs. number of deep-rows and transverse tube pitch at tube's outside diameter of 12.7 mm

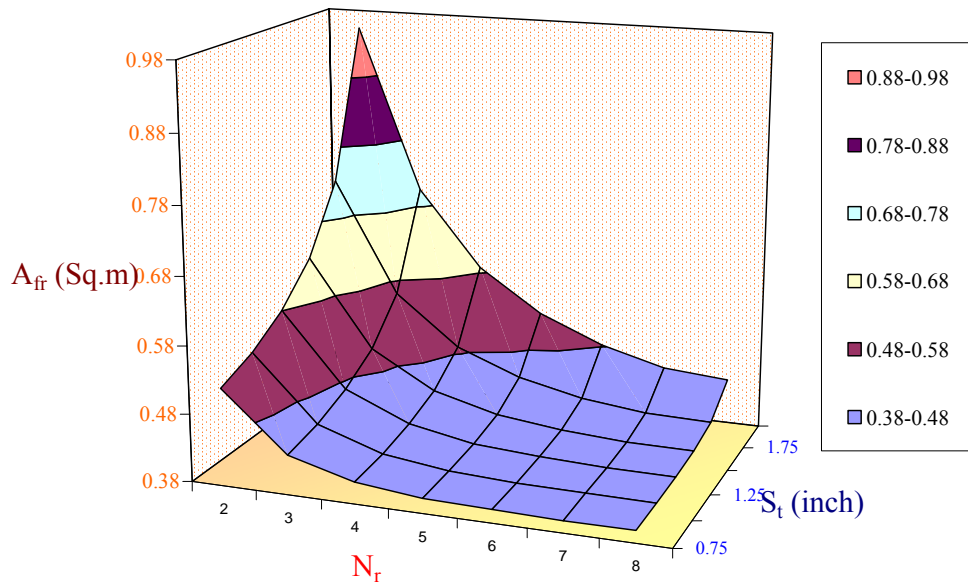


Figure 8.26 The frontal area vs. number of deep-rows and transverse tube pitch at tube's outside diameter of 12.7 mm

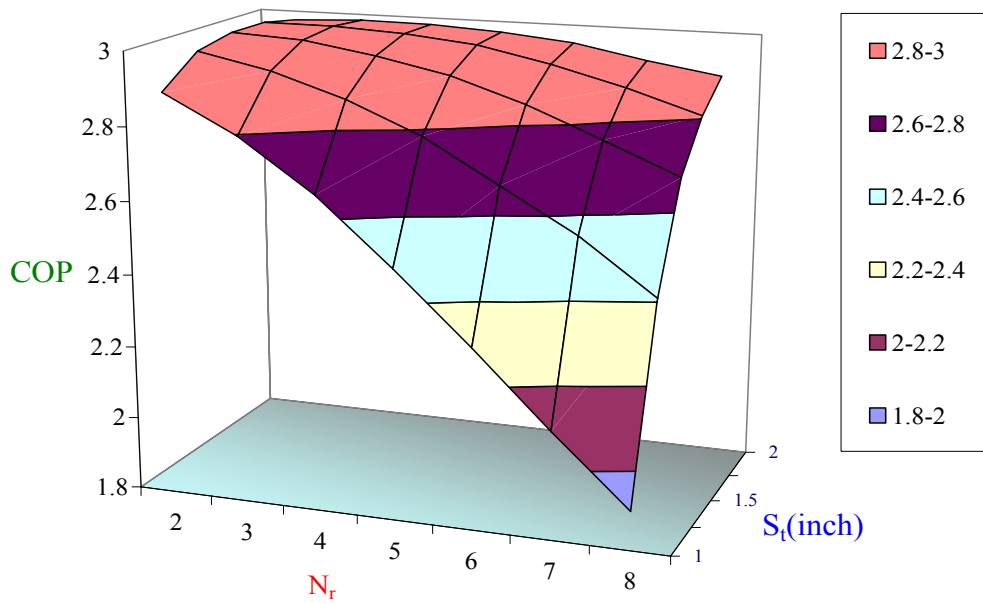


Figure 8.27 The system COP vs. number of deep-rows and transverse tube pitch at tube's outside diameter of 15.875 mm

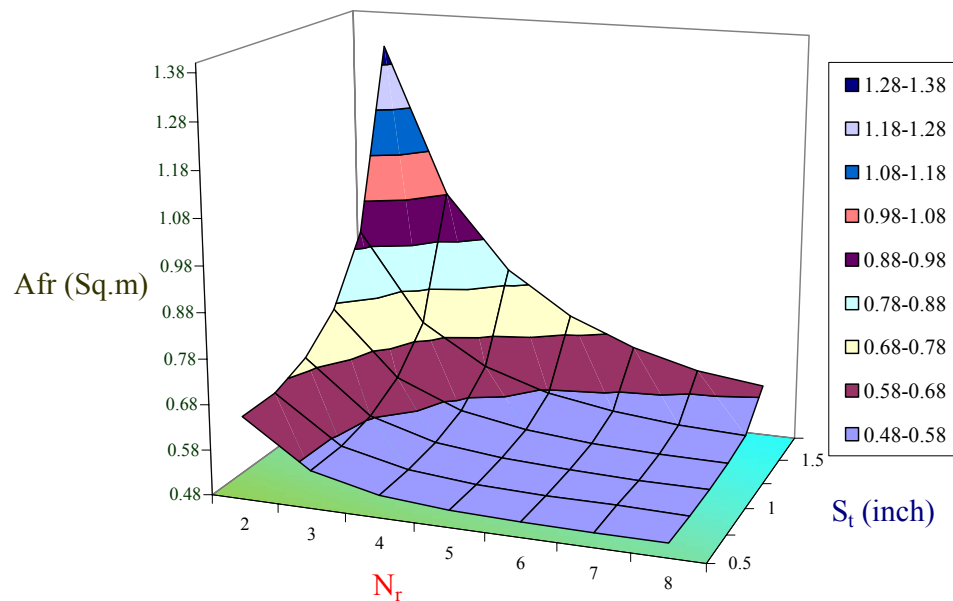


Figure 8.28 The frontal area vs. number of deep-rows and transverse tube pitch at tube's outside diameter of 15.875 mm

The graphs were plotted in order to determine the optimal configuration corresponding to the maximum COP by knowing the required frontal area and one of the three decision variables (number of rows, tube diameter, and tube transverse pitch). To demonstrate the use of the previous graphs to determine the optimal configuration of the condenser coil, the conventional condenser will be used as an example. Assuming that the condenser is to be designed with the same frontal area (0.524 m^2), four rows are selected and the other design parameters are then selected to give an optimal COP of 4.0 at these conditions. Referring to the previous graphs, it is found that the proper selection of tube diameter is 7.9375 mm and 1.25 inch (31.75 mm) for the tube transverse pitch while maintaining the values of the other parameters. The new configuration for the optimal design of the condenser and the conventional configuration for the commercial one are shown in Table 8.3.

Table 8.3: The conventional condenser and optimal condenser designs

parameters	Current design	Optimal design
Tube Spacing (mm×mm)	38.1×31.75	31.75×25.54
Tube inner diameter (mm)	15.67	7.6327
Tube outer diameter (mm)	15.875	7.9375
Height (mm)	457.2	457.2
Length (mm)	1250	1250
Fin pitch (fin/mm)	0.512	0.469
Number of rows	4	4
Number of circuits	6	5
Number of tubes per row	12	15
Fin thickness (mm)	0.15	0.15
Face air velocity (m/s)	2.5	3
Saturation temperature (°C)	55	51
Heat exchanger material cost (\$)	110	155

8.5 Comparison between the conventional condenser design and optimal one

The optimized condenser will be now used in the conventional system to show the effect of the optimal design on the AC system performance. The main idea of the thermoeconomic design is to reduce the heat transfer and pressure drop irreversibilities of the refrigeration cycle. This then reduces the pressure gap between the condenser and evaporator without an increase in the fans power. Figure 8.29a shows that the AC system with the optimal condenser design has less pressure ratio than that for the AC system with conventional condenser design. The enhancement in the AC system pressure ratio is an improvement of the AC system's thermal performance in terms of its COP and compressor isentropic and volumetric efficiencies as shown in Figures 8.29b, 8.30a, and 8.30b.

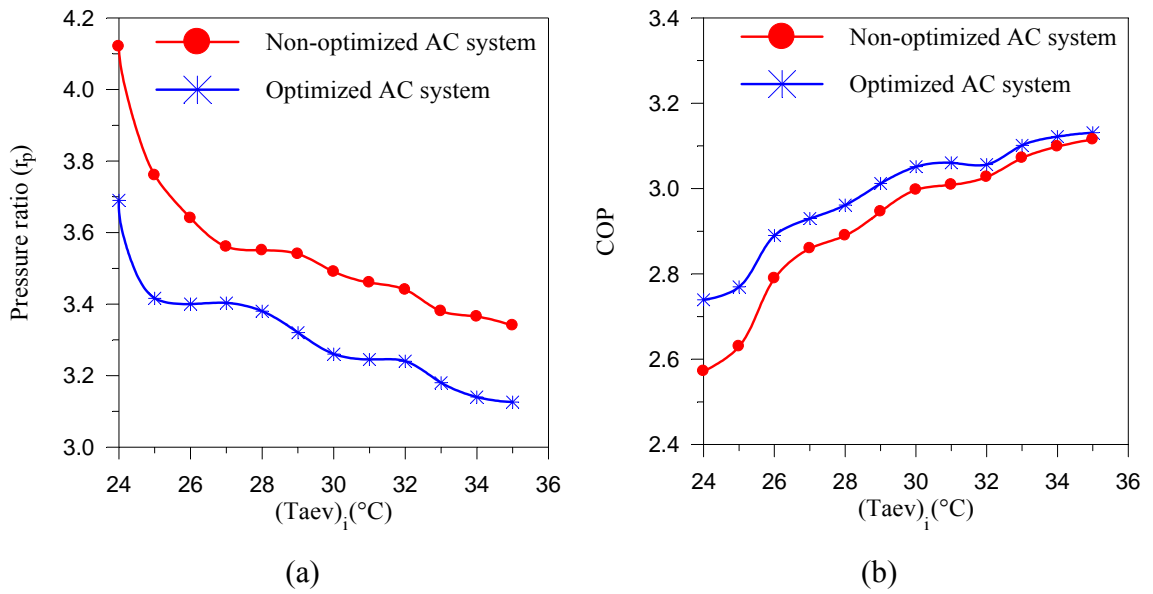


Figure 8.29: Comparison between AC system with conventional condenser design and AC system with optimal condenser design in terms of a) Pressure ratio b) COP

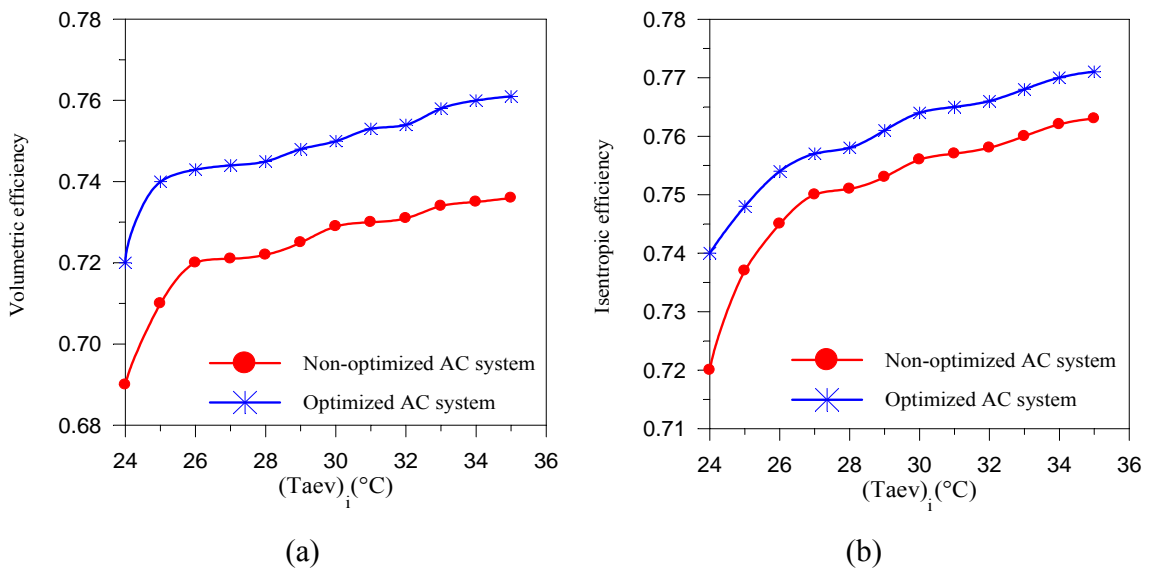


Figure 8.30: Comparison between AC system with conventional condenser design and AC system with optimal condenser design in terms of a) Volumetric efficiency b) Isentropic efficiency

Figure 8.31 shows that the system with the optimal condenser design consumes less amount of energy as compared to the system with the existing condenser design during the hours of bus operation. As shown in Figure 8.31, the energy saving that can be gained from the optimal design is almost 6.6% which leads to a fuel saving of 869.0 liter per year corresponding to USD 217.0 as saving in running cost. It may be interesting to note that although the capital cost of the optimized design is greater than that for the conventional design by USD 45, the saving in running cost can retrieve this excess amount in 3 months as payback period.

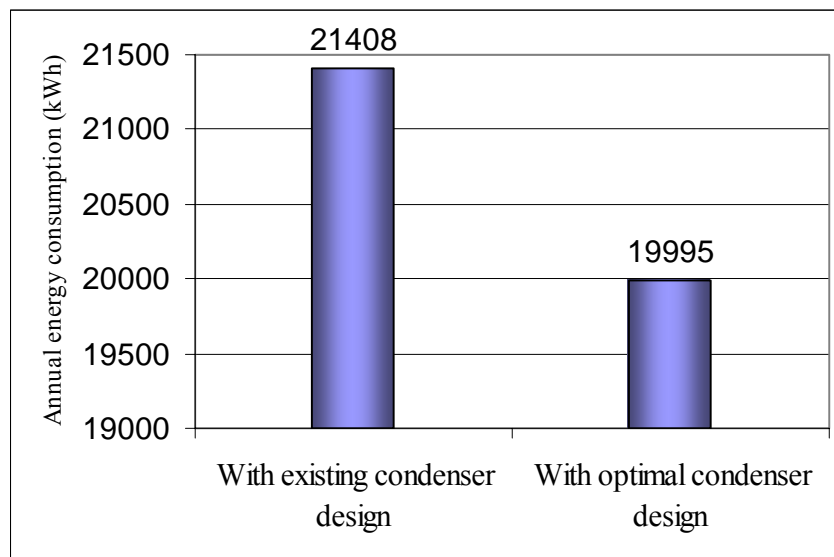


Figure 8.31 Annual energy consumption for bus AC system when it is installed with conventional condenser design and optimal condenser design

8.6 Conclusion

The thermoeconomic optimization of the condenser has been addressed in this chapter as a mean for energy saving. This approach involves investigating the influence of the selected design parameters on the condenser design. The potential saving in energy can be observed in the improvement of the system COP by reducing the gap between the condenser and evaporator pressures without impairing the fans' power. A comparison between the two AC systems, one with the existing condenser design and the other with the optimal configuration of the condenser design based on the thermoeconomic approach has been carried out. The result of the comparison is favorable for the second system in terms of energy consumption. The possible reduction in annual energy consumption is approximately 6.6% of that for the conventional system.

CHAPTER 9

CONCLUSIONS, CONTRIBUTIONS AND RECOMMENDATIONS

9.1 Conclusions

This research project involved designing, purchasing, commissioning, testing and retrofitting a newly developed bus AC system that responds to cooling load variations. The main concept of the new developed system is the use of multiple-circuit AC system employing two separate AC units sharing a common evaporator. The main result of the project is the implementation of a simple control strategy that is able to provide thermal comfort for bus passengers. The control strategy was constructed based on numerous experimental test runs to ensure the best operating conditions for the bus AC system in terms of energy saving, thermal comfort, and proper on/off cycling rates. The control algorithm of the microcomputer temperature based digital controller determines the system's operation by selecting the proper operating mode for the AC system. The selection of the AC system's operating mode is determined based on the desired set-point temperature and evaporator inlet air temperature.

This study also presents an optimization tool and design guidelines for a finned-tube air-cooled condenser by investigating the effect of the selected eight design parameters on the condenser's design. The optimization was carried out using the thermoeconomic approach with the objectives of achieving a maximum system COP and

compact condenser design. Therefore, the conclusions are classified into two categories: a) Conclusions related to the design of the developed AC system as a whole, and b) Conclusions related to the optimization design of the condenser as the system component.

9.1.1 Conclusions related to the design of the developed AC system

The existing roof-top bus AC system is generally oversized resulting in temperatures much lower than the temperatures required for thermal comfort. The cabin temperature can be as low as 18°C subjecting the passengers to overcooling. Furthermore, it consumes unnecessary energy at off-peak load conditions. There are specific benefits of the developed AC system which are listed below:

- The new proposed AC system is capable of saving at least 31.6% of energy for 4500 hours of operation per year corresponding to an annual saving of 617 USD. Moreover, the life cycle cost for the new AC system is lower by 20.0% than that for the existing one. The payback period for the investment is less than two years.
- The new proposed AC system is able to provide thermal comfort conditions for the passenger compartment at different loads particularly at low sensible loads. For an indoor temperature of 22°C, the PMV for the developed system is -0.39 (PPD of 8.3 %) while the PMV for the existing system is -1.01 % (PPD of 26.5%).
- By detecting the evaporator inlet air temperature and by selecting the desired set-point temperature, the AC system operation is automatically determined by the controller and this relieves the bus driver of the responsibility for the proper functioning of the system.

- The most vulnerable parts of the AC system are its control parts. Therefore, the developed system's controller is featured by the simplicity and reliability of its control algorithm with consistent satisfactory operation.
- The developed system has the ability to supply conditioned air should one of the two units fail to operate the other unit can still supply conditioned air to the passenger cabin until maintenance is performed.

9.1.2 Conclusions related to the optimization design of the condenser

This study also presents another method to enhance the thermal performance of the AC system and reduce its energy consumption through the use of thermoeconomic approach for condenser optimization of the conventional AC system with a cooling capacity of 14 kW. The optimal design configurations have been presented in the form of graphical charts. A figurative example has been given to show the reader how these charts are used. Conclusions drawn from this investigation are as follows:

- The study shows that varying the saturation temperature for the condenser has a significant effect on the system COP, annual cost, and frontal area. Comparing with the existing design, it was found that the system COP is improved by 3.68% while the fuel consumption in the bus engine is reduced by 3.55% of that for the existing design if the current saturation temperature is changed from 55°C to 51°C (the best operating point). The only pitfall for decreasing the saturation temperature is the enlargement in the frontal area and material cost for the condenser. The frontal area is increased by 11% and the increase in material cost is 16.67%. However, the reduction of system's capital cost (compressor + condenser material cost) by 10% can offset to some extent the increase in material cost.
- The optimum frontal air velocity, v_{fr} for the condenser design ranges from approximately 2.5 m/s to 3.5 m/s. In comparison with the base

configuration design, the system COP is enhanced by 6.55 % from the base configuration design at $v_{fr} = 2.5$ m/s to the optimal point at $v_{fr} = 3$ m/s.

- It is recommended from this study that the optimal range for fins pitch of plain finned-tube condenser is from 0.391 (fins/mm) to 0.548 (fins/mm). This will result in an increase of the system COP by 2.46% at the expense of an increase in the frontal area by 2.38%. The present study shows that the saving in fuel consumption is 2.41% (231 litres/year) for one bus. It was noted that although the frontal area is increased by 2.38 %, the material cost is decreased by 0.6% as a result of the decrease in fins' material cost.
- A single row condenser has the highest COP of 6.5 for unconstrained frontal area but this approach is not practical. Therefore, a smaller number of rows is recommended (from 4 to 6 rows) unless the space constraints are stringent.
- A condenser design with multi-tube simple circuiting will enhance the cycle COP for a certain limit since further increase in tube circuitry after the limit renders an adverse effect. In comparison with the base configuration design, the system COP is enhanced by 4.61 % from the base configuration design at $N_{cr} = 6$ to the optimal point at $N_{cr} = 4$.
- The best tube diameter for the condenser of an AC system according to the current study is 9.525 mm (3/8"). The improvement in system COP is 1.83% when the condenser tube diameter of 9.577 mm is used instead of 15.875. This will lead to a significant reduction in condenser material cost by 50% for the same total number of tubes for the current condenser design. However, this reduction in material cost is established on expense of the enlargement of the condenser frontal area by 19.0%.
- The optimal operating range for the vertical and horizontal tube spaces is from 25.54 mm (1.0") to 31.75 mm (1.25") and from 25.54 mm (1.0") to 38.1 (1.5"), respectively.

The comparison between the optimized condenser configuration and that for the conventional one reveals that the energy saving that can be gained from the optimal design is almost 6.6% leading to a fuel saving of 869.0 liter per year. It may be interesting to note that the extra material cost is USD 45 for the optimal design but the saving in running cost can outweigh this extra capital cost with a 3 months payback period.

9.2 Contributions

The contributions of this research are mainly in the area of analysis and development of energy saving roof-top bus AC system application in tropical countries. Some specific contributions can be summarized as follows:

- Development of a prototype of the newly developed roof-top bus AC system.
- Development of a theoretical simulation computer model for multiple-circuit AC system.
- Development of a new control strategy that achieves efficient system operation in terms of energy saving and passenger thermal comfort at off-peak conditions.
- Development of user-friendly and accurate computer models for a finned-tube air cooled condenser and DX evaporator design using numerical finite-difference technique.
- Design optimization of a system condenser using thermoeconomic approach by investigating the effect of the design parameters on the system COP and condenser sizing.
- Development of a user-friendly and accurate computer model to predict the variation of cooling load imposed on the passengers' compartment for a period of one year.

- Development of a computer model to evaluate the thermal comfort indices PMV and PPD using Fanger method.
- A comparison study between the newly developed AC system and the conventional one in terms of the annual energy consumption for systems, costing, and thermal comfort achievement during the cooling load variations.
- A comparison study between the optimized condenser and conventional one when both are installed in the existing AC system in terms of energy saving and economic aspects.

9.3 Recommendations

The research conducted in this project is by no means exhaustive. Further research could be carried out by testing the newly developed AC system and its controller in real bus compartment to check the system's reliability. The test experiments can be conducted to include a solar radiation and the some realistic conditions of the bus operation. In a laboratory, solar radiation was simulated using an electrical heater. A thermal manikin can be used to simulate a human body posture to the conditioned air. Additionally, further research can be conducted by using an internal combustion engine (ICE) as the prime mover of the AC system to simulate a typical conventional bus AC in which the compressor is underneath the engine carriage. In addition, if the two horizontal light compressors (single phase electrical connection) are available in the market, these compressors can be tested to work with the newly developed AC system.

As aforementioned in Chapter 1, the current conventional roof-top AC system experiences a problem of accumulation of the refrigerant in liquid form in the compressor during the off time of the AC system. Therefore, when the compressor is restarted, it pumps refrigerant in liquid form instead of the gaseous form. This accelerates the failure of the compressor valves. To overcome this problem, the present study proposed further modifications of the developed system as shown in Figure 9.1.

This proposal can be investigated for conducting further research in future. The modifications involve the installation of a solenoid valve in the liquid line after the thermostatic expansion valve and an accumulator in the suction line before the compressor.

As shown in Figure 9.1, the main principle of the proposed system is when the controller has a need to stop any compressor unit, it breaks the solenoid circuit, thereby deenergizing the solenoid and interrupting the flow of liquid refrigerant to the evaporator. Continued operation of the compressor causes evacuation of the refrigerant from that portion of the system beyond the point where the refrigerant flow is interrupted by the solenoid valve. When the pressure in the evacuated portion of the system is reduced to the cut-out pressure of the low pressure control, the low pressure control breaks the compressor magnetic clutch circuit and stops the compressor. When the controller requires the compressor to work, the controller closes the solenoid circuit and energizes the solenoid valve, thereby opening the liquid line and permitting liquid refrigerant to enter the evaporator. Since the evaporator is warm, the liquid entering the evaporator vaporizes rapidly so that the evaporator pressure rises immediately to the cut-in pressure of the low-pressure control. At this point, the low-pressure control closes the compressor clutch circuit and starts the compressor. The accumulator acts like a store or sump to hold any excess amount of refrigerant that might enter the compressor during the compressor off time and to ensure that the refrigerant entering the compressor is in gaseous form during the compressor's running time.

Thus, through these modifications, the AC system's compressor is highly protected from any floodback of a liquid refrigerant to the compressor during the on or off cycling times. At the same time, the AC system can reap the benefits of the newly developed system. In addition, the system can switch from automatic control to manual control by the additional electrical circuit which composes of a photodiode and a magnetic relay (normally open). The photodiode acts like a non-return valve in the mechanical arrangement. This circuit adds security for a continuous operation of the AC system even though its vulnerable part (automatic controller) is inoperative or impaired.

The optimal condenser configuration which is obtained from the present study can be utilized as an alternative for the conventional condenser configuration and some experiments could be conducted to compare the system thermal performance of the conventional condenser configuration and the optimal one. The developed AC system is designed to operate in cooling mode only because the weather of the tropical countries is hot and humid. However, the system can be adapted to operate in a heating mode by the incorporation of a reheater such as using the engine cooling system's water to heat the air entering the bus compartment. Therefore, future work can involve the addition of a reheater to the developed AC system for completion purpose and for the relative humidity control. The control algorithm can be extended to include relative humidity adjustment.

It is also recommended from this research to study the effects of non-uniform air-velocity over the condenser in the model since the typical condenser is tilted in its position which results in an uneven coolant air distribution over the condenser's frontal area. It is also recommended to investigate the effect of non-uniform air distribution over the evaporator surface during idling of some evaporator blowers at part-load conditions. This will give a clear theoretical explanation of the increase in the evaporator exit air temperature during the third operation mode of the AC system.

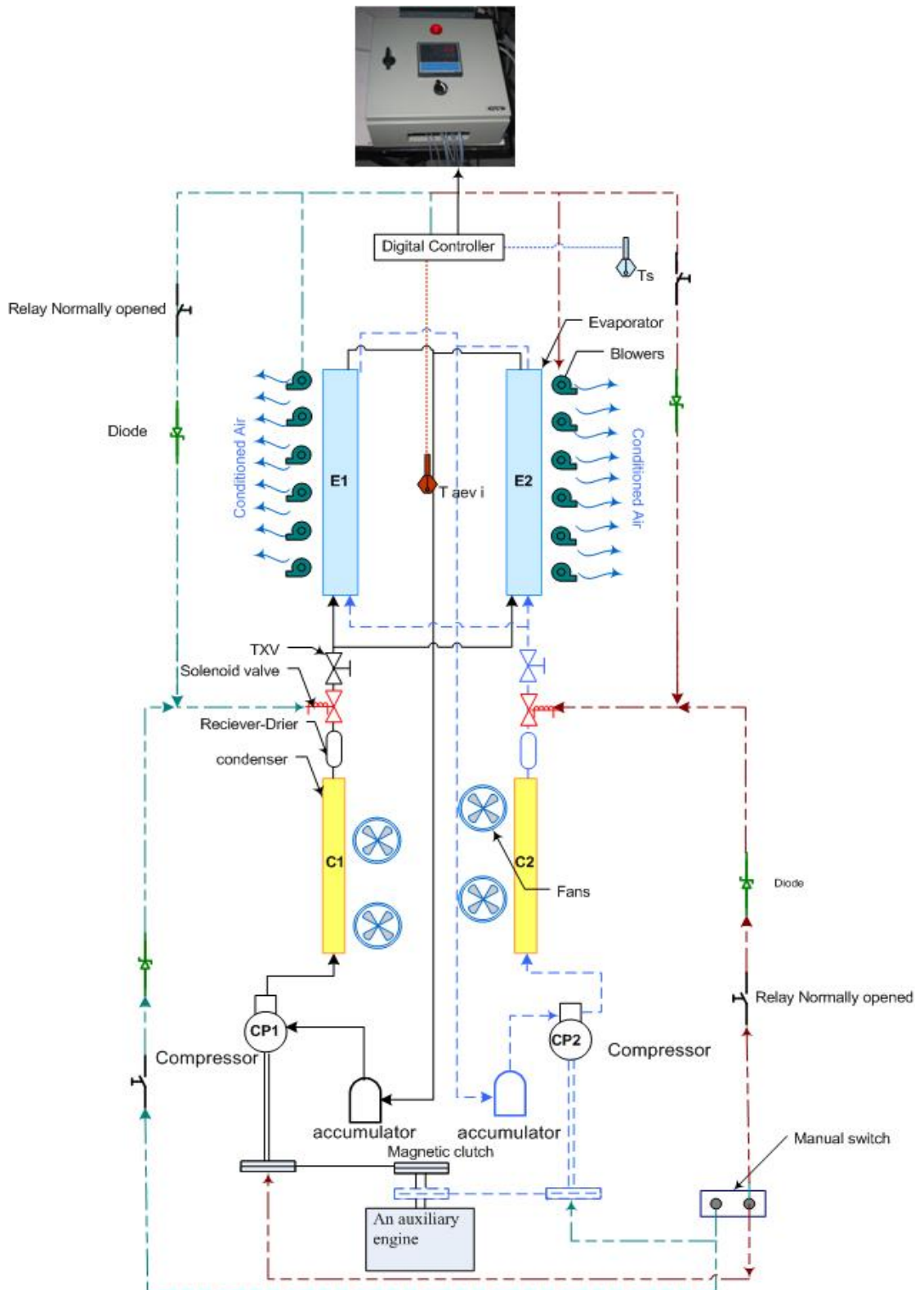


Figure 9.1 Schematic diagram for the future proposed system

REFERENCES

- Akihiro Fujita (2001). "Simulation Method to Predict the Thermal Environment inside a Car Cabin." *Society of Automotive Engineers of Japan (JSAE)*. (22); 39 – 47.
- Alefeld, G. (1990). *What are Thermodynamic Losses and How to Measure Them? A Future for Energy*, Proceedings of the World Energy Symposium, Italy, May 1990.
- Anon (1986). *Refrigeration Technical Data*. Japan Refrigeration Association.
- ARI (*Air-Conditioning Refrigeration Institute*) 1110-92. (2001). Mechanical Transport Refrigeration Units Standard
- ASHRAE (1961) Standard 16-61. Methods of testing for rating room air conditioners. New York: ASRHAE, Inc.
- ASHRAE (1997). *Handbook of Fundamental*. New York: ASRHAE, Inc.
- ASHRAE (2000). *Handbook of Systems and Equipment*. New York: ASRHAE, Inc.
- ET_AEE (2000). http://ktlabo.cm.kyushu-u.ac.jp/e/AT_EEE/ExplanationE.htm
- Ayres, J.M. and Stamper, E.(1995). "Historical Development of Building Energy Calculations." *ASHRAE Transactions*.101 (1).841-849.
- Barbusse S, Clodic D, Roume'goux JP (1998). Automobile air-conditioning. Effect in terms of energy and the environment, vol. 60. Elsevier Science;. p.3-18.
- Bejan, A. (1982). *Entropy Generation through Heat and Fluid Flow*. Wiley, New York.
- Bejan, A. (1996). *Entropy Generation Minimization, The Method of Thermodynamic Optimization of Finite-Size Systems and Finite-Time Processes*. CRC Press, New York.
- Bejan, A. and Pfister, P.A. (1980). Evaluation and heat transfer augmentation techniques based on their impact on entropy generation. *Letters in heat and mass transfer*, Vol. 7, pp. 97-106.

- Bensafi, A., Borg, S., and Parent, D. (1997). CYRANO: A Computational Model for the Detailed Design of Plate-Finned-Tube Heat Exchangers Using Pure and Mixed Refrigerants". *International Journal of Refrigeration*, Vol.20, No.3, pp. 218-228.
- Bhatti MS (1999). Enhancement of R-134a Automotive Air-Conditioning System. *SAE Technical Papers, Paper No. 1999-01-0870. Society of Automotive Engineers.*
- BSI (*British Standard Institution*) 5141:part1 (1975). Specification for Air Heating and Cooling Coils Standard.
- Buck W.C (1996). Measurements of Short-Term Flow Processes in Refrigerating Systems. *International Journal of Refrigeration* 19 (3) 181–186.
- Cavallini, A., Del Col, D., Doretti L., Longo G.A., and Rossetto, L. (2000). Heat Transfer and Pressure Drop During Condensation of Refrigerants Inside Horizontal Enhanced Tubes. *International Journal of Refrigeration*. 23 (1) 4–25.
- CATT: G.J. Van Wylen, R.E. Sonntag, C. Borgnakke (1994): *Computer-Aided Thermodynamic Tables: Fundamentals of Classical Thermodynamics*, 4_{th}, Intellipco, Inc.
- Changqing Tian, and Xianting Li (2005). Numerical Simulation on Performance Band of Automotive Air-Conditioning System with A variable Displacement Compressor. *Energy Conversion and Management* 46, 2718–2738.
- Chen, H. H. S. and Churchill, S.W. (1986). Correlating Equations for Laminar and Turbulent Free Convection from a Vertical Plate. *International Journal of Heat and Mass Transfer*. Vol.18, pp 1323-1329.
- Conde M.R. (1985). *A steady State Mathematical Simulation Model for Air-To-Water Heat Pumps (Report NEFF)*. Zurich: Swiss Federal Institute of Technology, P.236.
- Corberan, J. M., and Melon M.G. (1998). Modeling of Plate Finned Tube Evaporators and Condensers Working with R134a. *International Journal of Refrigeration*, Vol. 21, No.4, pp. 273-284.
- Copeland (1981). *Compressor short cycling an unrecognized problem*. Application Engineering Bulletin AE.17-1262.
- Corberan, J. M., and Melon M.G. (1998). Modeling of Plate Finned-Tube Evaporators and Condensers Working with R134a. *International Journal of Refrigeration*, Vol. 21, No.4, pp. 273-284.

- Davis GL, Chianese Jr. F, Scott TC (1972). Computer simulation of automotive air conditioning-components, system, and vehicle. *Society of Automotive Engineers*, (paper 720077).
- Dittus S.J, Boelter L.M.K. (1930). *University of California Publications on Engineering*; 2:443.
- Doebelin, E.O. (2004). *Measurement systems: Application and Design*. 5th ed. New York: McGraw-Hill book Co.
- Dossat, R.J. (1978), *Principles of Refrigeration*. 2nd Edition, John Wiley and Sons Inc.
- Duffie, J.A., and Beckman, W. A (1980). *Solar Energy Thermal Processes*. New York: John Wile & Sons.
- El-Sayed Y.M. and Evans R.B., (1970). *Engineering and Power*: ASME-J.92, 27-34
- Fanger, P.O. (1970). *Thermal Comfort Analysis and Applications in Environmental Engineering*. McGraw-Hill, New York.
- Fisher, R.D, Ellison, F., Creswich, A., Stevn K., and William L. (1982). A computer Model for Air-Cooled Refrigerant Condensers with Specified Refrigerant Circuiting. *ASHRAE Transactions 88 (1)*.
- Flavio A.S.F., Alex A.S.H., and Otavio D.M.S (2002). Experimental Analysis of Refrigerant Mixtures Flow Through Adiabatic Capillary Tubes. *Experimental Thermal and Fluid Science 26 (5) 499–512*.
- Ge Y.T and Cropper R (2005). Performance Evaluations of Air-Cooled Condensers using Pure and Mixture Refrigerants by Four-Section Lumped Modeling Methods. *Applied Thermal Engineering 25:1549–1564*
- Gu J., Kawaji M., Smith-Pollard T., and Cotton J (2003). Multi-Channel R134a Two-Phase Flow Measurement Technique for Automobile Air-Conditioning System. 4th ASME/FED & JSME Fluids Engineering Division Summer Meeting, Honolulu, Hawii, USA, July 6–10.
- Hassan, M.Y., Rahman, H.A., Majid, M.S. and Kannan, K.S. (2001). Standardization and Labeling of Electrical Appliance in Malaysia. *Energy Efficiency in Household Appliances and Lighting Berlin:Springer-Verlag*.

- Hendricks T. J. (2001). "Multi-Variable Optimization of Electrically-Driven Vehicle Air Conditioning Systems Using Transient Performance Analysis". *National Renewable Energy Laboratory, Golden, CO. C599-061*
- Horuz, E. K, and Yamankaradeniz, R. (1998). Experimental and Theoretical Performance Analysis of Air-Cooled Plate-Finned-Tube Evaporators. *International Communications in Heat and Mass Transfer, Volume 25, Issue 6, Pages 787-798.*
- Hosoz M, and Direk M. (2005). Performance Evaluation of An integrated Automotive Air Conditioning and Heat Pump System. *Energy Conversion and Management, in press.*
- Iqbal, M (1983). *An Introduction to Solar Radiation*. New York: Academic Press.
- Jabardo J.S, Mamani W.G, Ianella M.R (2002). Modelling and Experimental Evaluation of An automotive Air-Conditioning System with A variable Capacity Compressor. *International Journal of Refrigeration; 25:1157-73.*
- Jung D, and Radermacher R. (1989). Predication of Pressure Drop during Horizontal Annular Flow Boiling of Pure and Mixed Refrigerants. *International Journal Heat and Mass Transfer 32(9), pp. 2435-2446.*
- Kaynakli O, Horuz I. (2003). An Experimental Analysis of Automotive Air Conditioning System. *International Communications Heat Mass Transfer; 30:273-84.*
- Kays, M, London, AL. (1964). *Compact Heat Exchangers*. 3rd Ed. New York: McGraw-Hill, Raymond.
- Kempiak, and R.R. Crawford (1990). Three-Zone, Steady-State Modelling of A mobile Air-Conditioning Condenser. ASHRAE Transactions.
- Kim S.G., Kim M.S., and Ro S.T. (2002). Experimental Investigation of the Performance of R22, R407C and R410A in Several Capillary Tubes for Air-Conditioners. *International Journal of Refrigeration 25 (5) 521-531.*
- Klein, S. A. and Reindl, D. T. (1997). The Relationship of Optimum Heat Exchanger Allocation and Minimum Entropy Generation for Refrigeration Cycles. *Proceedings of the ASME Advanced Energy Systems Division, Vol. 37, pp.87-94.*

- Kohler, J., Kuhn B., and Beer H (1990). "Numerical Calculation of the Distribution of Temperature and Heat Flux in Buses under Influence of the Vehicle Air-Conditioning System. *ASRHAE Transaction*. 96. (part 1): pp.432-446.
- Kohler, J., Kuhn, B., and Beer, H. (1990). Numerical Calculation of the Distribution of Temperature and Heat Flux in Buses under Influence of the Vehicle Air-Conditioning System. *ASRHAE Transaction*. 96. (part 1): pp.432-446.
- Kyle D.M, Mei V.C, and Chen F.C (1993). An Automobile Air-Conditioning Design Model. *Society of Automotive Engineers*, (paper 931137).
- LABFIT curve fitting software (1999). <http://www.angelfire.com/rnb/labfit/index.htm>
- Lee G.H. and Loo J.Y (2000). Performance Analysis and Simulation of Automobile Air Conditioning system, *International Journal of Refrigeration* 23: 143–254.
- Lockhart, R.W., and Martinelli R.C. (1949). Proposed Correlation of Data for Isothermal Two-Phase, Two-Component Flow in Pipes. *Chemical Engineering Progress* 45(1):39-48.
- Liang, S., Wong, T., and Nathan, G. (2001). "Numerical and Experimental Studies of Refrigerant Circuitry of Evaporator Coils". *International Journal of Refrigeration*, Vol.24, pp.287-293.
- Mahmoud G (1999). An investigation of R-152a and Hydrocarbon Refrigerants in Mobile Air Conditioning. *SAE Technical Papers*, Paper no. 1999-01-0874. *Society of Automotive Engineers*.
- Massimo, D.A, and Vanoli L. (2004). Thermoeconomic Optimisation of the Condenser in A vapour Compression Heat Pump. *International Journal of Refrigeration* 27: 433-441.
- McLinden M., Gallagher J., Webber L., Morrison, G., Ward D., Goodwin A. (1989). Measurement and Formulation of the Thermodynamic Properties of Refrigerants 134a. *ASHRAE Transactions*.
- McQuiston F.Y and Parker J.D. (1994). *Heating, Ventilating, and Air Conditioning*. New York: John Wiley & Sons, Inc.
- Mohd Yusoff Senawi (1992). *Software Development for Building Energy Analysis*. Universiti Teknologi Malaysia: Masters Thesis.

- Mohd. Zamzam Jaafar, Wong Hwee Kheng, Norhayati Kamaruddin (2003). *Greener Energy Solutions for A sustainable Future: issues and challenges for Malaysia*. Energy Policy 31, 1061–1072
- Myers R.J. (1967). *The Effect of Dehumidification on the Air-Side Heat Transfer Coefficient for a Finned-Coil*: Master's Thesis, University of Minnesota.
- Omar Hartini. (1997). *Analysis of Energy Consumption in Building using SHEAP (Simplified Hourly Energy Analysis Package)*. UTM: Master Thesis.
- Oskarsson S.P., and Karakow K.L., and Lin. S. (1990). Evaporator Models for Operating with Dry, Wet and Frosted Finned Surfaces. *Part I: Heat transfer and fluid flow theory*. ASHRAE Trans.96 (1) 373-380.
- Parise, J.R. (1983). *Theoretical and Experimental Analysis of A diesel Driven Heat Pump*: PhD thesis, University of Manchester, UK.
- PTM: Pusat Tenaga Malaysia (1999), <http://www.managenergy.net>.
- Park Y.C, McEnaney R.(1999): Steady State and Cycling Performance of A typical R134a Mobile A/C System. *SAE International Congress and Exposition, Detroit, Michigan, Paper No. 1999-01-1190*.
- Pawelski M.J.(1979) “Transfer Function for Combined Walls and Pitched Roofs.” *ASHRAE Transactions*, 85(2); pp. 307-318.
- Raman Ali A (1999). Modelling of Condensers, Evaporators and Refrigeration Circuit in Automobile Air-Conditioning Systems. *SAE Technical paper series*.
- Ratts E.B., and Brown J.S. (2000). An Experimental Analysis of Cycling in An Automotive Air Conditioning System. *Applied Thermal Engineering 20: 1039–1058*.
- Recep Yumruta, Mehmet Kunduz, and Mehmet Kanoglu (2002). Exergy Analysis of Vapor Compression Refrigeration Systems. *Exergy, an International Journal 2: 266–272*.
- Ronald E.D, Mei V.C, and Chen F.C (1998). Simulation of An Automotive Heat Pump. *ASHRAE Transactions; 291-296*.
- Rubas P.J. and Bullard C.W. (1995). Factors Contributing to Refrigerator Cycling Losses. *International Journal of Refrigeration 18 (3):168–176*.
- Schwarz T., Galluzzi M., Richardson D., Radermacher R., Dickson T., and McGregor I. (2002). Model to Investigate the Performance of Accumulators in Vapor

- Compression Systems, in: *9th International Refrigeration and Air Conditioning Conference at Purdue*.
- Shah M.M. (1979). A general Correlation for Heat Transfer During Film Condensation in Tubes. *International Journal Heat Mass Transfer*; 22(4): 547-56.
- Shiba T. and Bejan A. (2001). Thermodynamic Optimization of Geometric Structure in the Counter Flow Heat Exchanger for Environmental Control Systems. *Energy* (26) 493–511.
- Silva M.C.G (1999). A Computational Model to Simulate the Thermal Behaviour of the Passenger Compartment of Vehicles. *Society of Automotive Engineers Paper Series.. No. 1999-01-0778*.
- Spielvogel L.G. (1984). "Estimating Energy Consumption in New and Existing Buildings." In. Meckler, M. (Ed.), "Retrofitting of Commercial, Institutional, and Industrial Buildings for Energy Conservation." New York: Van Nostrand Reinhold Company, 67-88.
- Stancanto F., and Onusic, H. (1997). "Road Bus Heat Load Numerical and Experimental Evaluate." *Society of Automobile Engineers (SAE) Technical Paper series, Paper no.971825*.
- Susan W.S and Sam V.S. (2003). Finned-Tube Condenser Design Optimization Using Thermoeconomic Isolation. *International Congress of Refrigeration, Washington, D.C*.
- Tara Lynn Hemami (1998): *Development of transient model of mobile air-conditioning systems*, PhD thesis, University of Illinois at Urbana-Champaign.
- TechniSolve Software cc (1985): www.coolit.co.za. *Recoil Condenser Coil Selection*
- Theerakulpisut S. and Priprem S. (1998). Modelling Cooling Coils. *International Community Heat Mass Transfer, Vol. 25, No. 1, pp. 127-137*.
- Threlkeld J.L. (1972). *Thermal Environmental Engineering*. Prentice-Hall, Inc.
- Tian C, Li X. (2005). Numerical Simulation on Performance Band of Automotive Air Conditioning System with Variable Displacement Compressor. *Energy Conversion and Management*; 46:2718–38.

- Tojo K., Ikegawa M., Shiibayashi .M, Arai. A, and Uchikawa, N. (1984). A Scroll Compressor for Air Conditioners. *Proceedings of the 1984 Purdue compressor Technology conference*. 496-503.
- Urbicain M.J. and Paloschi. J. (1981). Simulation of Air-Cooled Heat Exchangers. *Computers and Chemical Engineering, Vol. 5*, 75-81.
- Vardhan A. and Dhar P.L (1998). A New Procedure for Performance Prediction of Air Conditioning Coils. *International Journal Refrigeration, Vol. 21, No.1*, pp.77-83.
- Wall.G (1991). On the optimization of Refrigeration Machinery. *International Journal of Refrigeration 14*,336-340.
- Wang, C.C, Lee, W.S and Sheu, W.J. (2000). An airside Correlation for Plain Fin-and-Tube Heat Exchanger in Wet Conditions. *International Journal of Heat and Mass Transfer 43*: 1869-1872.
- Wang S., and Gu, J. (2004). Experimental Analysis of an Automotive Air Conditioning System with Two-Phase Flow Measurements. In: Proceedings. *10th International Refrigeration and Air Conditioning Conference at Purdue University*.
- Wattelet J., Jabrado J.M., Chato J.C., Panek J.S. and Souza A.L., (1992). Experimental Evaluation of Convective Boiling of Refrigerants R-134a and R-12, Two-Phase Flow and Heat Transfer. *ASME, HTD- Vol.197*, pp.256-267.
- Yang CY, Webb RL (1996). Condensation of R-12 in Small Hydraulic Diameter Extruded Aluminum Tubes with and without Micro-Fins” *International Journal Heat Mass Transfer*; 39(4): 791–800.
- Yasuda H. T. and Machielsen C.M. (1983). Simulation Model of a Vapor Compression Refrigeration System. *ASHRAE Transactions*; 98 (2a):408-425.
- Zaheer-Uddin, M. (1989). Inter-Model Comparisons between Three PC Programs and Blast. *Energy and Buildings, 13*; 201-216.

APPENDIX A

WEATHER DATA AND GEOMETRICAL CONFIGURATION FOR THE CASE STUDY

A.1 Introduction

The cooling load calculation requires the use of weather data in estimating the main items of the cooling load such as the solar load, heat transmission and ventilation. In another word, the hourly weather data for a period of one year is required. However, in simplified calculation procedures, the calculations are often made for a number of typical days in a year, instead of every day of the year (Mohd Senawi, 1992). This approach greatly reduces computer run time and cost, although a slight loss in accuracy may result. In this study, the weather data for Singapore has been used because weather data for Johor Bahru could not be obtained. It has been assumed that the Singapore weather data can be used for Johor Bahru since it is located close to Singapore. In this appendix the weather data is compressed into six two-monthly seasons by Mohd Senawi (1992) as it is presented in Table A.1. Also the full description of the bus case study is presented here in this appendix.

Table A.1: Compressed weather data for six typical days

	<i>Time of day (hours past midnight)</i>																							
	1	2	3	4	5	6	7	8	9	10	11	12	13	14	15	16	17	18	19	20	21	22	23	24
<i>Typical day 1: frequency = 59 days (Jan/Feb)</i>																								
dbt _o	24	24	24	24	24	24	24	25	27	28	29	29	29	29	29	28	28	27	26	25	25	25	25	25
wbt _o	18	18	18	18	18	18	18	19	19	19	19	19	18	18	18	18	18	18	18	18	18	18	18	18
IDH	0	0	0	0	0	0	2	106	221	300	344	343	318	261	198	124	51	7	0	0	0	0	0	0
ldh	0	0	0	0	0	0	18	49	118	193	251	299	319	313	277	224	150	59	1	0	0	0	0	0
<i>Typical day 2: frequency = 61 days (Mar/Apr)</i>																								
dbt _o	26	25	25	25	25	25	25	26	28	29	30	30	30	30	30	29	28	28	27	26	26	26	26	26
wbt _o	19	19	19	19	19	19	19	20	20	20	20	20	20	20	20	19	19	19	19	19	19	19	19	19
IDH	0	0	0	0	0	0	3	132	236	312	345	341	300	232	165	96	32	4	0	0	0	0	0	0
ldh	0	0	0	0	0	0	32	58	128	199	251	292	310	298	269	213	130	41	1	0	0	0	0	0
<i>Typical day 3: frequency = 61 days (May/Jun)</i>																								
dbt _o	26	26	26	26	25	25	26	27	29	29	30	30	30	30	30	29	29	28	27	27	27	27	26	26
wbt _o	20	20	20	20	20	20	20	21	21	21	20	20	20	20	20	20	20	20	20	20	20	20	20	20
IDH	0	0	0	0	0	0	3	124	204	255	281	275	252	206	129	76	27	4	2	0	0	0	0	0
ldh	0	0	0	0	0	0	37	58	124	186	233	269	286	271	234	182	106	31	1	0	0	0	0	0
<i>Typical day 4: frequency = 61 days (Jul/Aug)</i>																								
dbt _o	26	26	26	26	25	25	26	27	28	29	29	29	30	29	29	29	29	28	27	27	27	26	26	26
wbt _o	20	20	20	20	19	19	20	20	20	20	20	20	19	19	19	19	19	19	19	20	20	20	20	20
IDH	0	0	0	0	0	0	3	101	173	244	284	286	263	212	163	96	42	7	1	0	0	0	0	0
ldh	0	0	0	0	0	0	26	55	122	184	242	278	292	288	263	215	142	48	1	0	0	0	0	0
<i>Typical day 5: frequency = 61 days (Sept/Oct)</i>																								
dbt _o	26	25	25	25	25	25	25	27	28	29	29	30	30	29	29	29	28	27	27	27	26	26	26	26
wbt _o	19	19	19	19	19	19	19	20	20	20	20	20	19	19	19	19	19	19	19	20	20	20	20	20
IDH	0	0	0	0	0	0	27	115	191	257	297	308	271	210	144	76	26	3	0	0	0	0	0	0
ldh	0	0	0	0	0	0	22	78	155	221	274	308	308	300	257	198	119	27	0	0	0	0	0	0
<i>Typical day 6: frequency = 61 days (Nov/Dec)</i>																								
dbt _o	25	25	24	24	24	24	25	26	27	28	28	29	29	28	28	28	27	26	26	25	25	25	25	25
wbt _o	19	19	18	18	18	18	19	19	19	19	19	19	19	19	19	19	19	19	19	19	19	19	19	19
IDH	0	0	0	0	0	0	20	104	191	236	252	229	197	139	103	57	20	3	0	0	0	0	0	0
ldh	0	0	0	0	0	0	21	70	140	204	260	291	289	265	230	167	95	23	0	0	0	0	0	0

Symbols/units:

dbt_o = outdoor air dry bulb temperature (°C)

wbt_o = outdoor air wet bulb temperature (°C)

IDH = direct solar radiation on horizontal plane (W/m²)

ldh = diffuse solar radiation on horizontal plane (W/m²)

APPENDIX B

PHYSICAL QUANTITIES FOR THERMAL COMFORT CALCULATION

B.1 Introduction

In this appendix, the physical elements to evaluate the thermal comfort inside the bus compartment are presented. These elements are mean radiant temperature, and some physical items to determine the rate of respiration for the passengers such as evaporative heat transfer coefficient, clothing area factor, metabolic heat production, and diffusive heat loss.

B.2 Mean radiant temperature, t_{mrt}

The mean radiant temperature is that uniform temperature of an imaginary black enclosure which results in the same heat loss by radiation as the actual enclosure. It can be calculated from measured values of the temperature of the surrounding walls and surfaces and the relative position of the person with respect to these surfaces. As most enclosure materials have a high emittance (ε), all the surfaces in the enclosure can be assumed to be black, which enables us to use the following equation to calculate the mean radiant temperature with respect to a person placed in a enclosure consisting of n

isothermal surfaces (with temperatures t_1, t_2, \dots, t_n and angle factors between the person and the surfaces $(F_{p-1}, F_{p-2}, \dots, F_{p-n})$):

$$t_{mrt}^4 = t_1^4 \cdot F_{p-1} + t_2^4 \cdot F_{p-2} + \dots + t_n^4 \cdot F_{p-n} \quad (\text{B.1})$$

The angle factors between the person (point) and the surfaces $(F_{p-1}, F_{p-2}, \dots, F_{p-n})$ can be calculated from public domain software named ET_AEE (2000), the photograph of this software interface is shown in Figure B.1:

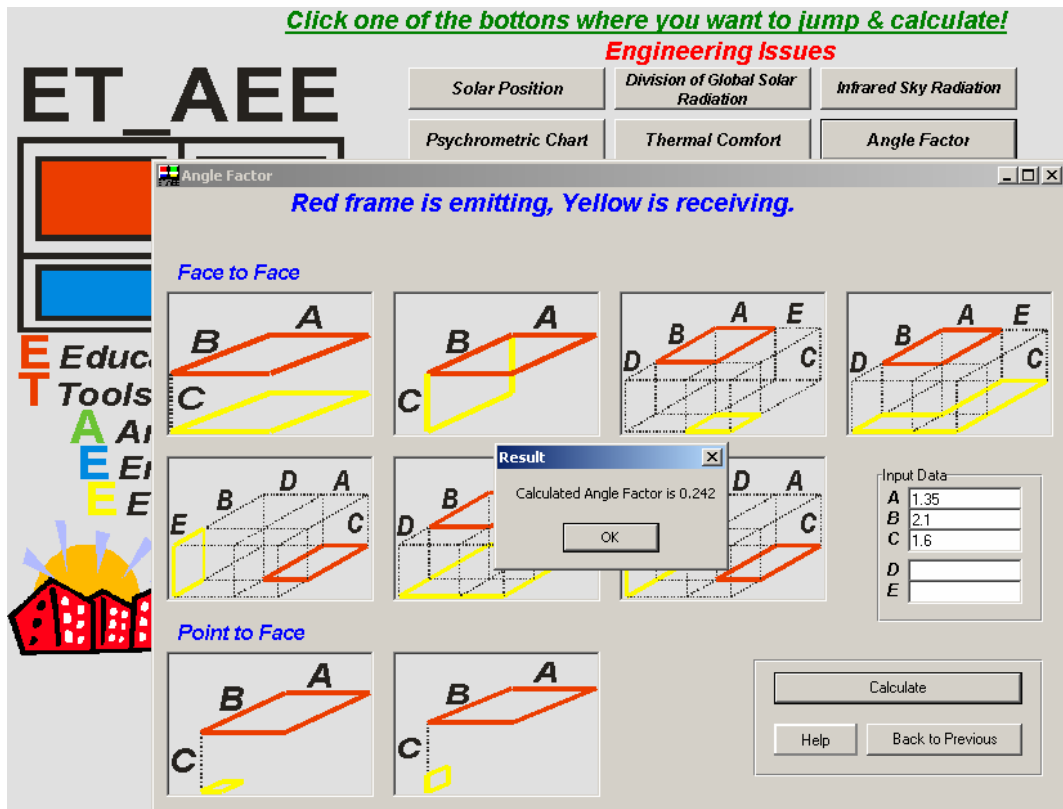


Figure B.1 Angle factor calculation by using ET_AEE (2000)

By applying ET_AEE software for the simulated passenger cabin (see Figure B.2) the view factors from the heat source to the surrounded sides are

$$\left(F_{p-1} = F_{p-3} = 0.154, F_{p-2} = F_{p-4} = 0.242, F_{p-5} = 0.098 \right).$$

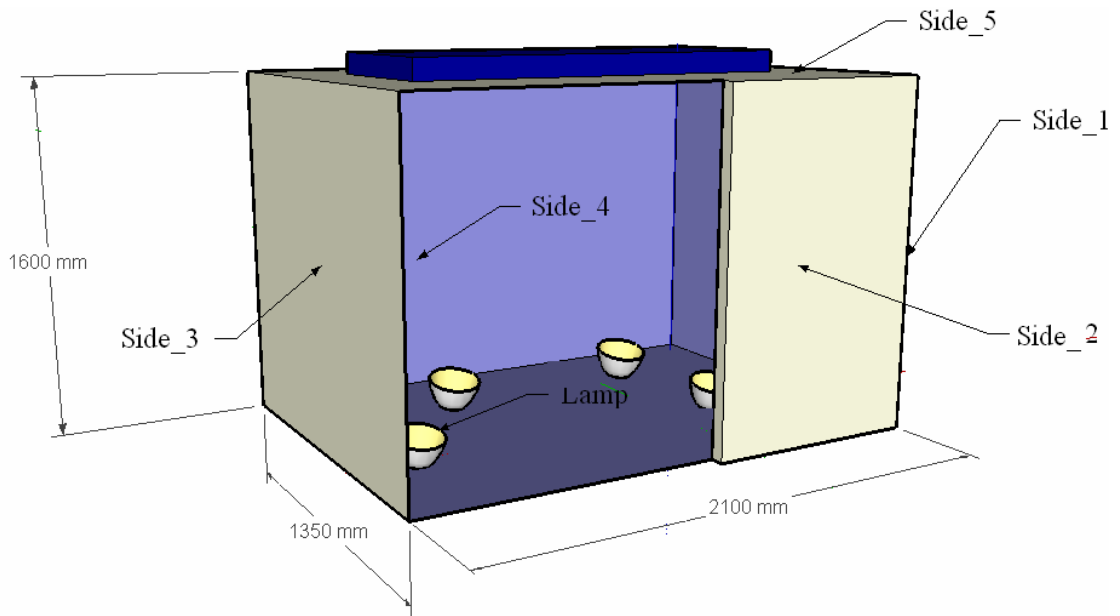


Figure B.2 Schematic diagram of the simulated passenger cabin

Tables B.1 to B.3 exhibit the measurements of the simulated cabin interior surfaces temperatures and calculated mean radiant temperatures according to the variation in cooling loads:

Table B.1: The measurement data of the simulated cabin interior surfaces temperatures for the first mode operation

Taev _i (°C)	Side_1	Side_2	Side_3	Side_4	Side_5	t _{mrt} (°C)
20	26.1	26.3	26.1	25.6	20.6	23.87
21	26.1	26.3	26.6	25.8	20.6	24.12
22	26.2	26.5	26.8	25.8	20.5	24.42
23	26.5	26.5	26.8	26.1	20.7	24.70
24	26.7	27.1	27.1	26.5	20.8	25.00
25	26.6	27.1	27.4	26.8	20.8	25.25
26	26.8	27.4	27.1	26.8	20.8	25.35
27	26.9	27.2	27.4	27.0	21.0	25.50
28	27.2	27.4	27.5	27.2	21.0	25.80
29	27.6	28.1	27.4	27.0	21.2	26.07
30	27.5	27.5	27.5	27.6	21.5	26.20
31	27.8	27.8	27.9	27.5	21.3	26.35
32	28.2	28.2	28.0	27.5	21.5	26.45

Table B.2: The measurement data of the simulated cabin interior surfaces temperatures for the second mode operation

Taev _i (°C)	Side_1	Side_2	Side_3	Side_4	Side_5	t _{mrt} (°C)
20	26.4	26.6	26.4	25.9	20.9	24.20
21	26.5	26.7	27.0	26.2	21.0	24.55
22	26.6	26.9	27.2	26.2	20.9	24.87
23	26.9	26.9	27.2	26.5	21.1	25.17
24	27.2	27.6	27.	27.0	21.3	25.50
25	27.1	27.6	27.9	27.3	21.3	25.77
26	27.5	28.1	27.8	27.5	21.5	26.05
27	27.8	28.1	28.3	27.9	21.9	26.40
28	28.3	28.5	28.6	28.3	22.1	26.90
29	28.8	29.3	28.6	28.2	22.4	27.27
30	28.8	28.8	28.8	28.9	22.8	27.57
31	29.3	29.3	29.4	29.0	22.8	27.90
32	29.9	29.9	29.7	29.2	23.2	28.17

Table B.3: The measurement data of the simulated cabin interior surfaces temperatures for the third mode operation

Taev _i (°C)	Side_1	Side_2	Side_3	Side_4	Side_5	t _{mrt} (°C)
20	26.7	26.9	26.7	26.2	21.2	24.55
21	26.8	27.0	27.3	26.5	21.3	24.82
22	26.9	27.2	27.5	26.5	21.2	25.12
23	27.2	27.2	27.5	26.8	21.4	25.40
24	27.4	27.8	27.8	27.2	21.5	25.72
25	27.4	27.9	28.2	27.6	21.6	26.10
26	27.8	28.4	28.1	27.8	21.8	26.40
27	28.1	28.4	28.6	28.2	22.2	26.70
28	28.4	28.6	28.7	28.4	22.2	27.05
29	28.8	29.3	28.6	28.2	22.4	27.30
30	29.1	29.1	29.1	29.1	23.0	27.77
31	29.4	29.4	29.5	29.1	22.9	27.97
32	30.0	30.0	29.8	29.3	23.3	28.30

B.3 Evaporative Heat Transfer Coefficient, h_e

The evaporative heat transfer coefficient h_e for the outer air layer of a nude or clothed person can be estimated from the convective heat transfer coefficient using the Lewis relationship given in Equation B.1. The Lewis relation describes the relations between convective heat transfer and mass transfer coefficients for a surface and it can be used to relate convective and evaporative heat transfer coefficients according to:

$$h_e / h_c = LR \quad (\text{B.1})$$

Where LR is referred to as the “Lewis ratio” and, at typical indoor conditions, equals approximately $16.5^\circ\text{C}/\text{kPa}$. h_c is the convective heat transfer coefficient is usually caused by air movement within the living space or by body movements and it is calculated from correlation proposed by Mitchell (1974) as follows:

$$\begin{aligned} h_c &= 8.3 V^{0.6} & 0.2 < V < 4.0 & \text{Seated with moving air} \\ h_c &= 3.1 & 0 < V < 0.2 & \end{aligned}$$

Where V is the velocity of the moving air in m/s.

B.4 Clothing area factor, f_{cl}

It is the ratio between closed body area to the surface body area, and it can be estimated by the correlation developed by (McCullough and Jones, 1984):

$$f_{cl} = 1.0 + 0.3I_{cl} \quad (\text{B.2})$$

Where I_{cl} ($\text{m}^2 \cdot \text{K}/\text{W}$) is the clothing thermal resistance, it is given in Table B.4, and it is usually expressed in clo units. 1.0 clo is equivalent to $0.155 \text{ m}^2 \cdot \text{K}/\text{W}$. Normally for the passengers commute the intercity bus their clothing thermal resistance between 0.80 and 0.91 clo, ASHRAE (1997).

Table B.4: Typical Clo Values for Typical Clothing Ensembles

Ensemble Description	Clothing thermal resistance (I_{cl}) [clo]
Walking shorts, short-sleeve shirt	0.36
Trousers, short-sleeve shirt	0.57
Trousers, long-sleeve shirt	0.61
Trousers, long-sleeve shirt, plus suit jacket	0.96
Trousers, long-sleeve shirt, long sleeve sweater, T-shirt	1.01
Same as above, plus suit jacket and long underwear bottoms	1.30
Sweat pants, sweat shirt	0.74
Long-sleeve pajama top, long pajama trousers, short 3/4 sleeve robe, slippers (no socks)	0.96
Knee-length skirt, short-sleeve shirt, panty hose, sandals	0.54
Knee-length skirt, long-sleeve shirt, full-slip, panty hose	0.67
Knee-length skirt, long-sleeve shirt, half-slip, panty hose, suit jacket	1.04
Ankle-length skirt, long-sleeve shirt, panty hose, suit jacket	1.10
Overalls, long-sleeve shirt, T-shirt	0.80

B.5 Metabolic heat production

It is the energy released by metabolism and it depends on muscular activity. The Metabolism is measured in met (1 Met=58.15 W/m² body surface), this is for Body surface for normal adult is 1.72 m² with the heat loss from his body of 100 W during his sitting in thermal comfort. Passengers are defined as resting quietly, this produces a metabolic rate, M of 1 met, ASHRAE (1997). The other values of M are listed in Table B.5.

Table B.5: Metabolic rate (W/m^2) as a function of the activity

Activity	Metabolic Rate, Met	
	W/m^2	Met ^a
Sleeping	40	0.68
Seated, quiet	60	1.03
Standing, relaxed	70	1.20
Walking (4.8 km/h)	150	2.58
Cooking	115	1.98
Washing by hand / ironing	210	3.61
Office work	80	1.37
Teaching	95	1.63
Digging trenches	300	5.16
Dancing	255	4.38
Gymnastics	230	3.95
Tennis	270	4.64
Basketball	440	7.57

B.6 Diffusive heat loss

It is rate of total evaporative heat loss from skin, W/m^2 , and it depends on the difference between the water vapor pressure at the skin and in the ambient environment, and the amount of moisture on the skin as follows:

$$\dot{E}_{diff} = \frac{0.06 \times (P_{sk,s} - P_a)}{(R_{e,cl} + 1/(f_{cl} h_e))} \quad (B.3)$$

P_a = water vapor pressure in ambient air, kPa.

$P_{sk,s}$ = water vapor pressure at skin, normally assumed to be that of saturated water vapor at skin temperature, t_{sk} (see Equation (B.4)), kPa.

h_e = evaporative heat transfer coefficient, $W/(m^2.kPa)$

$R_{e,cl}$ = evaporative heat transfer resistance of clothing layer,
($m^2.kPa)/W$ ($R_{e,cl} = 1/h_e$)

f_{cl} = clothing area factor

$$tsk = 35.7 - 0.028M \quad (B.4)$$

APPENDIX C

COMPUTER MODELS GRAPHICAL INTERFACES

C.1 Cooling loads computer model interfaces

The screenshot displays a software window titled "Bus material constructions" with a light blue background. It is divided into four main sections: "Wall Constructions", "Roof", "Floor", and "Glass Properties". Each section contains a table of material options with input fields for thickness and thermal conductivity (K).

Wall Constructions		
Wall Material	Thickness (mm)	K (W/m. °C)
Steel	6	43
Rubber	2.2	0.15
Glass wool	50	0.04
Fabric	5	0.064
Aluminum Coated	4.6	210

Roof		
Roof material	Thickness (mm)	K (W/m. °C)
Steel	1	14.9
Air space	350	0.375
Rubber	2.5	0.15
Glass wool	30	0.04
Aluminum	1.5	177

Floor		
Floor material	Thickness (mm)	K (W/m. °C)
Steel	3	14.9
Ply wood	15	0.14
Fabric	40	0.064

Glass Properties	
Thickness (mm)=	35
Thermal Conductivity =	0.8 W/m.°C
Transmissivity for diffusion radiation =	0.79
absroptivity =	0.6

Figure C.1 Cooling load model interface (form1)

Bus body areas

Right wall =	<input type="text" value="22.622"/>	m2	Right glass =	<input type="text" value="3.47"/>	m2
Left wall =	<input type="text" value="18.423"/>	m2	Windshield =	<input type="text" value="4.126"/>	m2
Back wall =	<input type="text" value="6.533"/>	m2	Back Glass =	<input type="text" value="1.504"/>	m2
Front wall =	<input type="text" value="6.667"/>	m2	Door area =	<input type="text" value="1.043"/>	m2
Roof =	<input type="text" value="15.533"/>	m2			
Floor =	<input type="text" value="12.379"/>	m2			
Left glass =	<input type="text" value="3.155"/>	m2			

Figure C.2 Cooling load model interface (form2)



Figure C.3 Cooling load model interface (form3)

C.2 Evaporator computer model interfaces

Coil

File Coil

Evaporator Design

Tube-Side

Te = 10 °C

Tc = 45 °C

Qe = 6 kW

Air-Side

dbto = 26.67 °C

Rh = 75 %

Face Velocity = 2.54 m/s

Specifications

Tube Material/Fins Material
Copper / Aluminum

Fins Type
Wavy fin

Heat Exchanger Configuration

do = 16.5862 mm

di = 15.7226 mm

St = 50.8 mm

Sl = 38.1 mm

Nfins = 12 /in

tf = 0.2 mm

Ncr = 4

Nr = 4

Heat Exchanger Size

Length (Width) = 288.860000 mm

Depth = 152.4 mm

Height = 406.4 mm

Figure C.4 Evaporator model interface (form1)

The analysis

Length = 288.8600 mm

Dt = 18.7208796 °C

Depth = 152.4 mm

Fins Thickness = 0.2 mm

Height = 406.4 mm

Power of Fan = 248.424911 W

do = 16.5862 mm

Dprefrigerant = 0.20818105 kPa

di = 15.7226 mm

Dpair = 135.385977 Pa

St = 50.8 mm

Tubes/ Row = 8

Sl = 38.1 mm

hi = 2189.751 W/m2. °C

Eitaf = 0.855

ho = 175.6149 W/m2. °C

Nrows = 4

Ncircuits = 4

Nfins = 12

Show

Next>>

<<Back

Figure C.5 Evaporator model interface (form2)

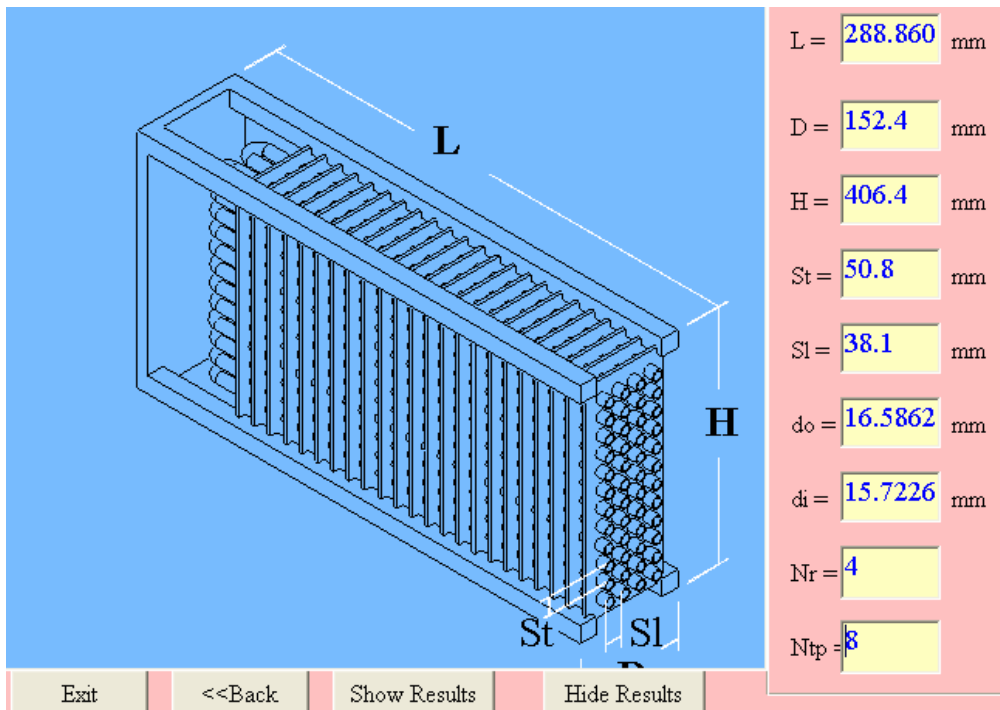


Figure C.6 Evaporator model interface (form3)

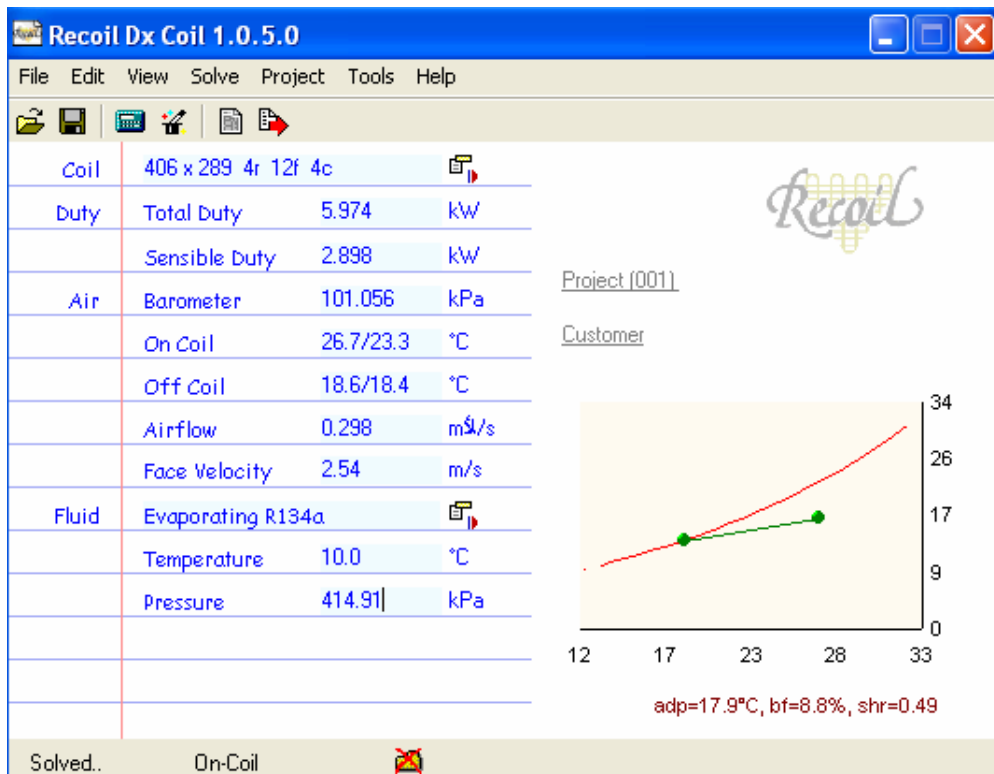


Figure C.7 Commercial model interface

C.3 Condenser computer model interfaces

Form1
file Coil

Condenser Design

Condenser size

Length = 2321.100000 mm
Depth = 132.08 mm
Height = 304.8 mm

Tube-side

Q_c = 20 kW
 T_e = 10 °C
 T_c = 45 °C

Air-side

Amb. temperature = 35 °C
Face velocity = 2.54 m/s

Specifications

Tube Material/Fins Material: Copper / Aluminum
Number of nodes = 100
Fins Type: Wavy fin

Condenser configuration

do = 15.875 mm Ncircuit = 2
di = 15.367 mm Nrows = 4
st = 38.1 mm Nfins = 12 / in
sl = 33.02 mm tf = 0.254 mm

Figure C.8 Condenser model interface (form1)

The analysis

Length = 2321.100 mm D_t = 1.67508412 °C
Depth = 132.08 mm Fins Thickness = 0.254 mm
Height = 304.8 mm Power of Fan = 718.739850 W
do = 15.875 mm Dprefrigerant = 515.55 kPa
di = 15.367 mm Dpair = 259.981563 Pa
St = 38.1 mm Tubes/ Row = 8
Sl = 33.02 mm Eitaf = 0.846
hi = 5983.900 W/m². °C Nrows = 4
ho = 62.74841 W/m². °C Nfins = 12
Ncircuits = 2

Show Next>> <<Back

Figure C.9 Condenser model interface (form2)

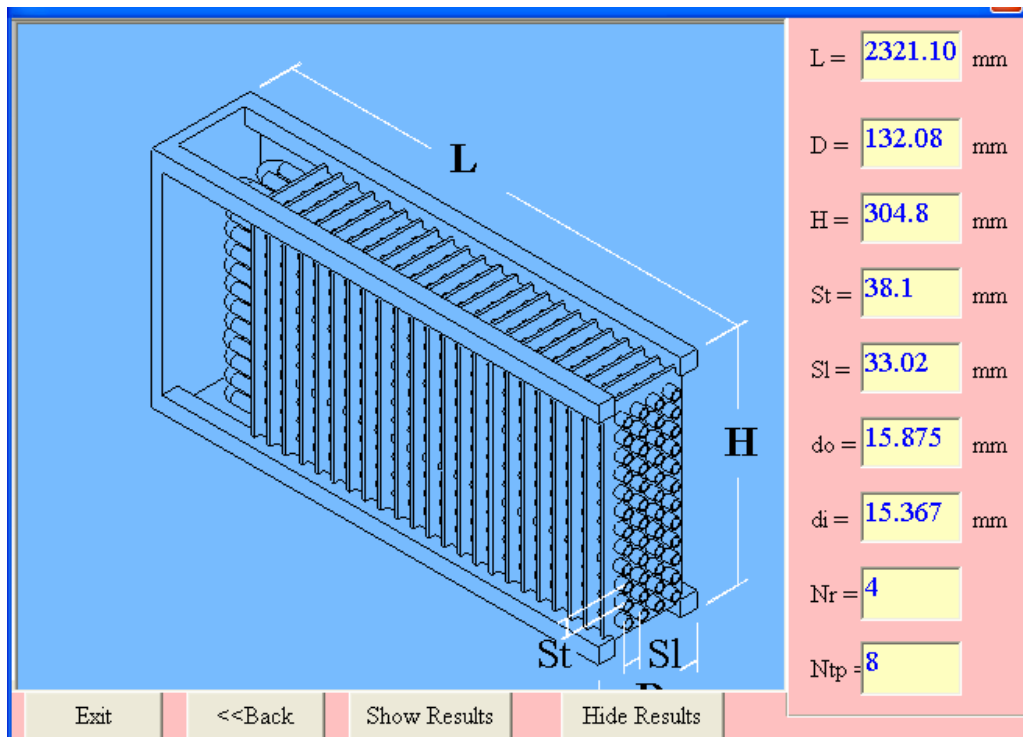


Figure C.10 Condenser model interface (form3)

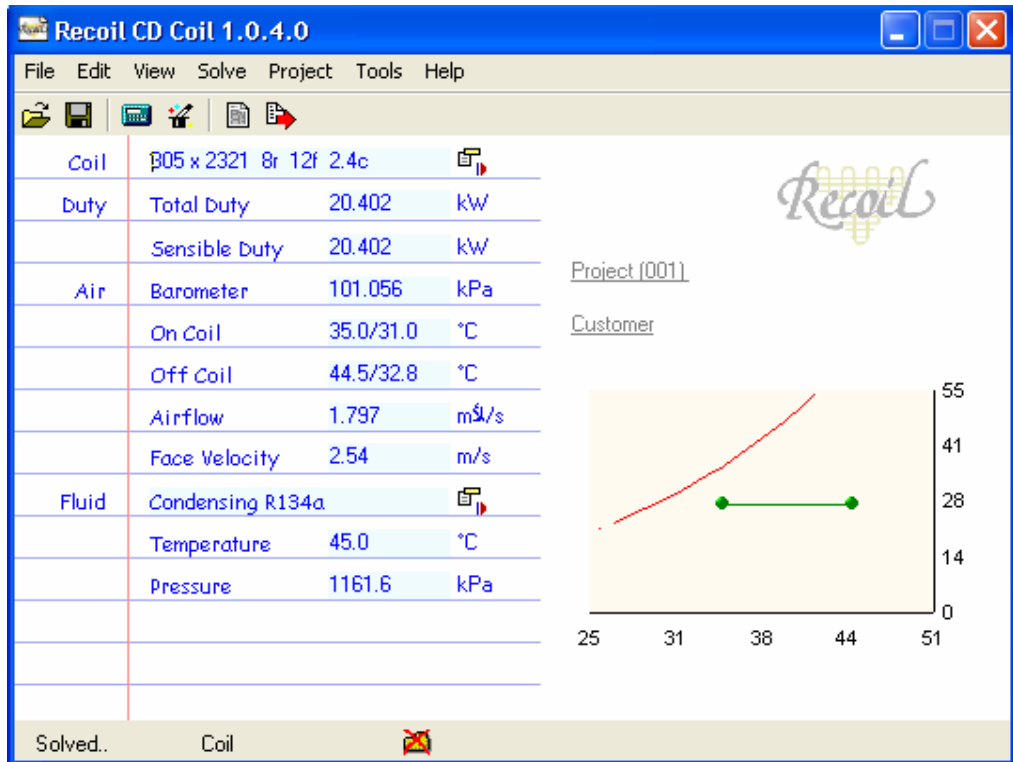


Figure C.11 Commercial model interface

C.4 Optimization computer model interface and flow chart

The screenshot shows a software interface for condenser optimization. It is divided into several sections:

- File:** Contains 'Calculate' and 'End' buttons.
- Input data:**
 - Length = 1.742299 m
 - Depth = 6.51385 m
 - Height = 0.2 m
 - Afr = 0.348459 Sq.m
 - dbt = 33 °C
 - te = 10 °C
 - Vair = 2.5 m/s
 - tc = 45 °C
 - Q = 12 kW
- Heat exchanger configuration:**
 - do = 9.525 mm
 - di = 8.8 mm
 - St = 25 mm
 - Sl = 21.59 mm
 - tf = 0.15 mm
 - Np/Circuit = 8
 - Nrows = 8
 - Nfins = 16
- The objective functions:**
 - F.c = 21.50937 \$
 - R.c = 596.2714 \$
 - Iap = 2.484464 kW
 - T.c = 617.7808 kW
 - EDT = 1.944066 kW
 - IXV = 0.424360 kW
 - Iref = 0.149689 kW
 - Iat = 1.374594 kW
 - ICD = 1.638009 kW
 - COP = 2.866784
 - Icomp = 1.185731 kW
 - IEV = 0.077566 kW

Figure C.12 Condenser optimization model interface

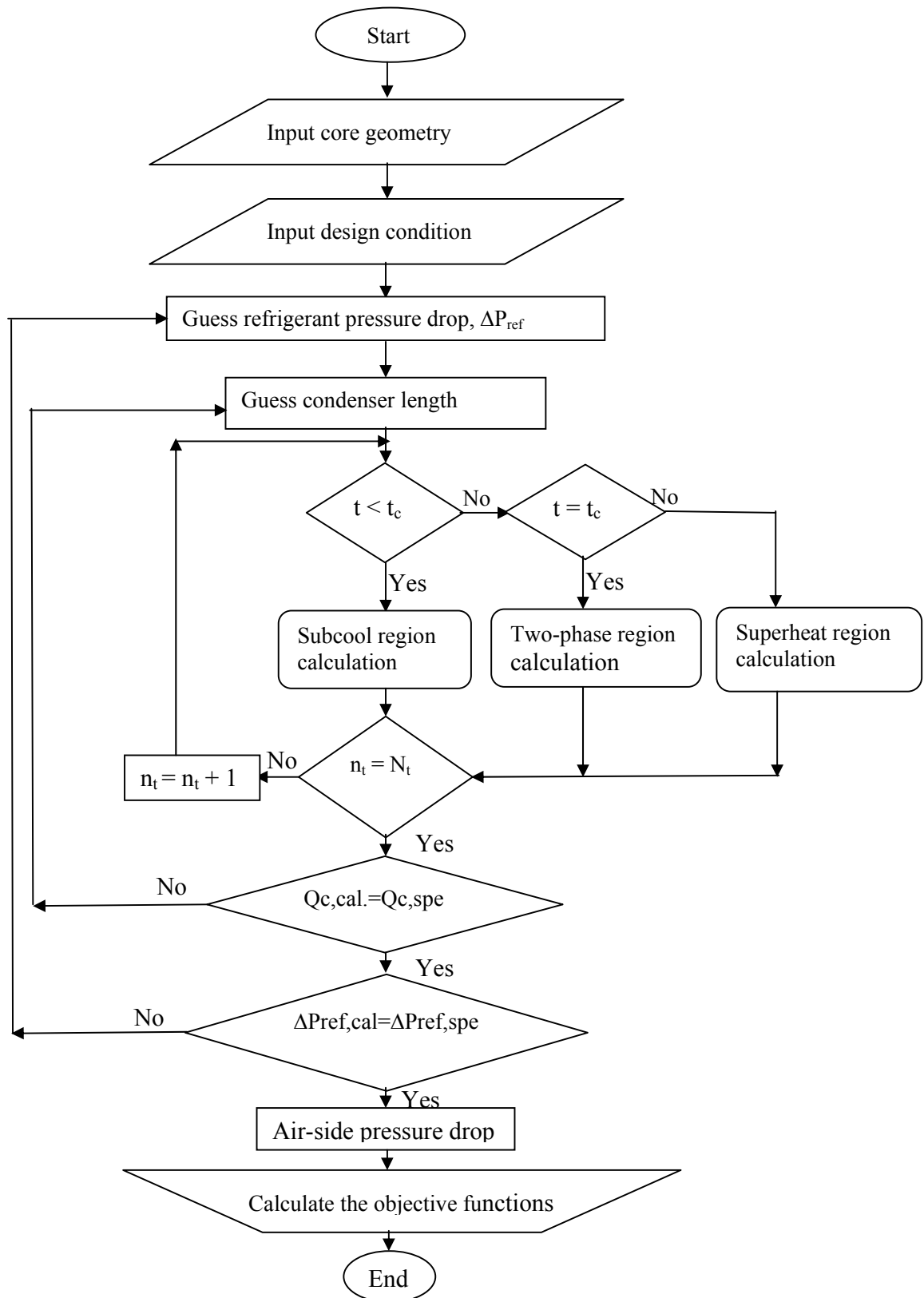


Figure C.13 Logic chart of optimization condenser model

APPENDIX D

CALCULATION OF FINNED-TUBE HEAT EXCHANGER GEOMETRIC CONFIGURATION

D.1 Introduction

A plate-fin type of evaporator or condenser is applied in the current AC systems simulation model. In this appendix, the calculation of either evaporator or condenser geometric and flow parameters are presented. These parameters are required for the evaluation of heat transfer coefficients on both the air and refrigerant sides. In addition, the over surface efficiency for the plate fins are determined in this appendix.

D.2 Geometric configuration areas

When plate fins are attached to a circular tube array, as shown in Figure D.1 with in staggered tube arrangement, to perform the heat exchanger analysis it is important to define the different coil areas expressing in terms of coil geometry and layout.

$$\text{Inside areas,} \quad A_i = \pi \times d_i \times L \times N_t \quad (\text{D.1})$$

$$\text{Finned area,} \quad A_{fins} = 2 \times \left[H \times Dt - \frac{\pi}{4} \times d_i^2 \times N_t \right] \times N_{fins} \times L \quad (\text{D.2})$$

$$\text{Unfinned area,} \quad A_{unfinned} = \pi \times d_o \times L \times \left(1 - N_{fins} \times t_f \right) \times N_t \quad (\text{D.3})$$

Total surface area, $A_o = A_{fins} + A_{unfinned}$ (D.4)

Bare area, $A_p = \pi \times d_o \times L \times N_t$ (D.5)

Minimum flow area, $A_{flow} = (f - d_o) \times N_{tp} \times L \times (1 - N_{fins} \times t_f)$ (D.6)

Where for staggered arrangement, $f = \sqrt{\left(\frac{S_t}{2}\right)^2 + S_l^2}$ (D.7)

Frontal area, $A_{fr} = L \times H$ (D.8)

Where L , H , and Dt are the heat exchanger length, height, and depth respectively as it is shown in Figure D.2.

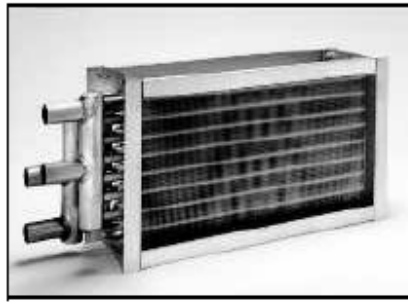


Figure D.1 Typical plate finned-tube heat exchanger

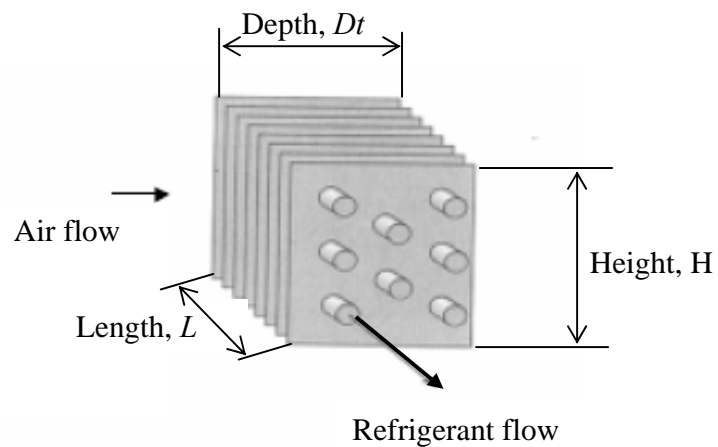


Figure D.2 Heat exchanger layout

D.3 Fin efficiency

In order to determine the overall surface efficiency for a finned-tube heat exchanger, it is first necessary to determine the efficiency of the fins as if they existed alone. For a plate fin-and-tube heat exchanger with multiple rows of staggered tubes, the plates can be evenly divided into hexagonal shaped fins as shown in Figure D.3. Schmidt (1949) analyzed hexagonal fins and determined that they can be treated as circular fins by replacing the outer radius of the fin with an equivalent radius. The empirical relation for the equivalent radius is given by:

$$\frac{R_t}{r} = 1.27 \times \psi \times \sqrt{(\beta - 0.3)} \quad (\text{D.9})$$

Where r is the outside tube radius. The coefficients ψ and β are defined as

$$\psi = \frac{S_t}{2r} \quad \text{and} \quad \beta = \frac{1}{S_t} \times \left(\frac{S_t^2}{4} + S_l^2 \right)^{1/2}$$

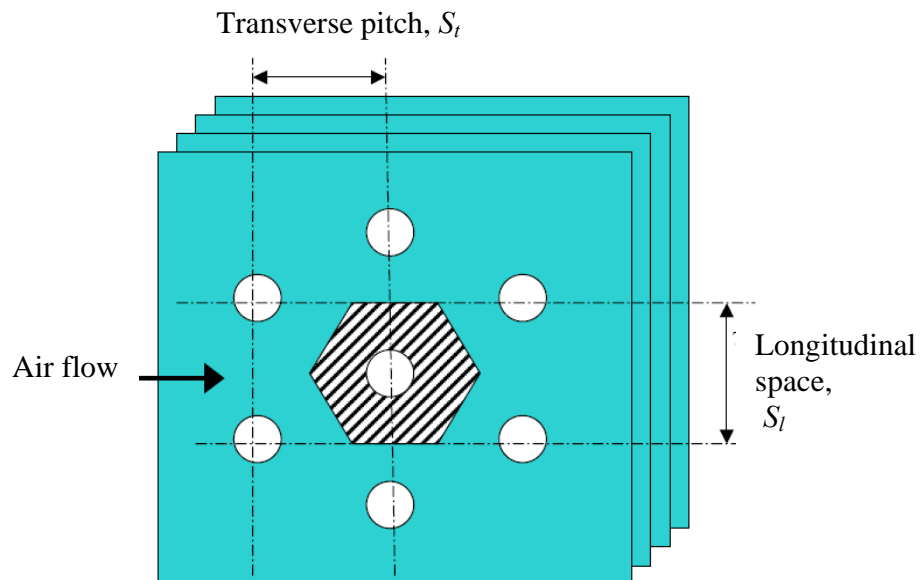


Figure D.3 Hexagonal fin layout and tube array

Where S_l is the tube spacing in the direction parallel to the direction of air flow, and S_t is the tube spacing normal to the direction of air flow. Once the equivalent radius has been determined, the equations for standard circular fins can be used. For this study, the length of the fins is much greater than the fin thickness. Therefore, the standard extended surface parameter, m_{es} can be expressed as,

$$m_{es} = \sqrt{\frac{2 \times \alpha_o}{k_f \times t_f}} \quad (D.10)$$

Where α_o is the air-side heat transfer coefficient, k_f is the thermal conductivity of the fin material, and t_f is the thickness of the fin. For circular tubes, a parameter ϕ can be defined as:

$$\Phi = \left(\frac{R_t}{r} - 1 \right) \times \left[1 + 0.35 \times \ln \left(\frac{R_t}{r} \right) \right] \quad (D.11)$$

The fin efficiency, η_f for a circular fin is a function of m_{es} , R_t , and ϕ can be expressed as:

$$\eta_f = \frac{\tanh(m R_t \phi)}{m R_t \phi} \quad (D.12)$$

The total surface efficiency of the fin, η_s is therefore expressed as

$$\eta_s = 1 - \frac{A_{fins}}{A_o} \times (1 - \eta_f) \quad (D.13)$$

D.4 Exponential factors for wet-coil friction coefficient

This paragraph describes the exponential factors f_1, f_2, f_3 , and f_4 of the friction coefficient correlation for wet-coil which was presented in Chapter 5. These factors are determined as function in geometrical coil parameters as:

$$f1 = -0.7339 + 7.187 \left(\frac{F_p}{S_l} \right)^{2.5} \left(\ln(9 \times \text{Re}_{film}) \right) \quad (\text{D.14})$$

$$f2 = -0.5417 \ln \left(\frac{A_o}{A_p} \right) \times \left(\frac{F_p}{d_o} \right) \quad (\text{D.15})$$

$$f3 = 0.02722 \ln(6 \times \text{Re}_{film}) \times \left(\frac{S_l}{S_t} \right)^{3.2} \times \ln(\text{Re}_{do}) \quad (\text{D.16})$$

$$f4 = 0.2973 \ln \left(\frac{A_o}{A_p} \right) \times \ln \left(\frac{D_h}{d_o} \right) \quad (\text{D.17})$$

Where F_p is the fin pitch (mm), $\text{Re}_{film} = \frac{2\rho_a v_{fr} A_{fr} (W_i - W_o)}{N_{tp} \times H \times \mu_a}$, W_i and W_o

are the air humidity ratio inlet and outlet from the coil. While $\text{Re}_{do} = \frac{\dot{m}_a \times d_o}{A_{flow} \times \mu_a}$ and

$$D_h = \frac{4A_{flow} D_t}{A_o}.$$

APPENDIX E

EXPERIMENTAL MEASUREMENTS DATA AND RESULTS

Introduction

This appendix shows the measurements which were obtained from the experimental work and were used to verify the simulation model and to be used in control strategy design. The measurements include the pressure and temperature for the refrigerant at different points in the two units of the system as it was described in Chapter 4. In addition, the psychometric properties (temperature and relative humidity) at inlet and exit from the evaporators plus the inlet air velocity to the AC system were measured. The refrigerant mass flow rate was also measured. In this appendix, the measurements are categorized into two groups. The first group of the experiments was conducted to analyze the effect of cooling load variations on the developed system at the three different operating modes. The measurements of this group are listed in Tables E.1 to E.7 corresponding to the three different modes of the developed system operation. Again, the three different system modes are:

- (i) Both units operates completely and simultaneously-operation, mode I.
- (ii) One unit idles and the other unit operates with all evaporators blowers run at full speed-operation, mode II.
- (iii) Mode II but with only partial capacity for the evaporator blowers runs at full speed-operation, mode III.

In addition, experimental results are also reported in this Appendix and they are compared with those obtained from the system simulation model and are tabulated in tables from E.8 to E.10. The second group of the experimental work consists of a series of experiments were conducted at three set-point temperatures: 21°C, 22°C, and 23°C as these temperatures are typical conditioned space. The results of the second group of the experimental work are listed in Tables E.11 to E.14. In addition, the hourly energy consumption for the conventional bus AC system and developed one for a typical design day is presented here in this appendix in Table E.16.

As aforementioned, the newly developed system consists of two units A and B, each unit has instruments to measure the physical properties of the refrigerant and the air-sides. Figures E.1 and E.2 show the measured points' location for the refrigerant-side on the P-H diagram for both units.

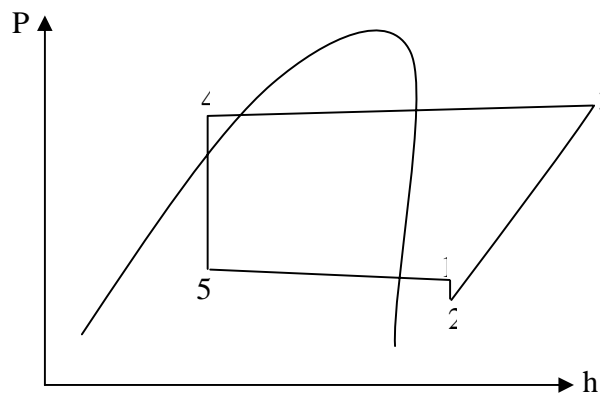


Figure E.1 P-h diagram for unit A

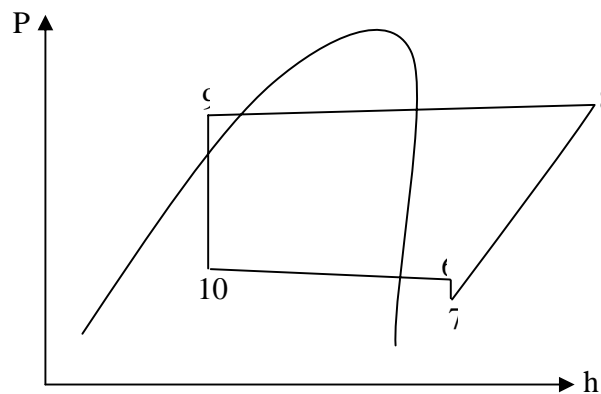


Figure E.2 P-h diagram for unit B

Table E.2: The measurements for the unit B at the first mode at $V_i = 1.0$ m/s

Taev _i °C	Rhaev _i %	P ₆ bar	P ₇ bar	P ₈ bar	P ₉ bar	P ₁₀ bar	T ₆ °C	T ₇ °C	T ₈ °C	T ₉ °C	T ₁₀ °C	m _{rB} g/s	Pressure ratio
20.0	75.5	3.85	3.16	13.20	12.90	4.10	16.0	16.2	76.8	44.1	5.2	55.2	4.18
21.0	73.0	4.10	3.28	13.45	13.40	4.25	16.1	16.4	76.9	44.8	5.8	57.5	4.10
22.0	70.0	4.25	3.34	13.30	13.2	4.30	16.3	16.5	79.3	45.4	6.4	58.8	3.98
23.0	68.0	4.40	3.43	13.40	13.30	4.35	16.7	16.6	80.6	45.6	6.7	59.3	3.91
24.0	65.0	4.80	3.76	14.40	14.20	4.50	16.9	17.1	82.8	46.2	7.3	63.7	3.83
25.0	63.0	4.90	3.99	15.20	15.10	5.45	17.3	17.5	83.6	47.1	7.4	67.1	3.81
26.0	59.3	5.10	4.12	15.40	15.10	5.65	17.3	17.5	84.2	48.2	7.6	71.3	3.74
27.0	54.0	5.10	4.23	15.50	15.20	5.75	17.5	17.7	84.8	48.7	7.7	74.8	3.66
28.0	51.0	5.15	4.30	15.60	15.5	5.85	17.8	17.9	85.4	49.4	7.8	76.0	3.63
29.0	51.2	5.20	4.66	15.90	15.60	5.85	18.3	18.4	85.6	49.7	8.0	79.8	3.41
30.0	50.7	5.25	4.94	16.40	16.00	5.85	18.5	18.5	86.8	50.5	8.3	82.1	3.32
31.0	48.0	5.30	5.16	16.80	16.50	4.55	19.1	19.0	87.6	51.3	8.6	84.6	3.15
32.0	45.0	5.35	5.15	17.20	16.90	4.60	19.4	19.4	88.2	51.6	8.8	88.3	3.00
33.0	45.0	5.45	5.14	17.50	17.25	4.65	19.6	19.5	89.1	51.8	9.0	89.3	2.98
34.0	42.5	5.45	5.00	17.80	17.50	4.70	19.8	19.8	90.2	52.2	9.1	90.3	2.96
35.0	42.2	5.50	5.00	18.20	17.80	4.85	20.3	20.4	90.8	52.6	9.3	91.7	2.91

Table E.3: The experimental results for the developed AC system at the first mode at $V_i = 1.0$ m/s

Taev _i °C	Rhaev _i %	h ₁ kJ/kg	h ₂ kJ/kg	h ₃ kJ/kg	h ₄ kJ/kg	h ₅ kJ/kg	h ₆ kJ/kg	h ₇ kJ/kg	h ₈ kJ/kg	h ₉ kJ/kg	h ₁₀ kJ/kg	Q _e kW	W _c kW	Wfans kW	COP	COP _v
20.0	75.5	351.7	420.5	456.0	264.2	206.4	353.3	420.9	454.7	262.7	207.0	16.18	5.26	1.40	3.08	2.43
21.0	73.0	349.1	422.8	457.0	264.5	206.4	350.2	422.7	455.4	263.8	207.9	16.46	5.33	1.40	3.09	2.44
22.0	70.0	351.2	424.1	458.0	265.1	206.5	351.7	424.1	457.2	264.8	208.7	16.93	5.45	1.40	3.11	2.47
23.0	68.0	354.4	423.4	457.6	265.4	206.6	354.8	424.3	458.5	265.0	209.1	17.43	5.54	1.40	3.15	2.51
24.0	65.0	353.6	426.8	459.1	265.9	206.8	352.9	427.0	459.4	265.9	209.9	18.41	5.68	1.40	3.24	2.60
25.0	63.0	354.8	426.8	458.4	266.5	206.9	355.8	425.9	459.1	267.2	210.0	19.77	6.11	1.40	3.24	2.64
26.0	59.3	355.9	427.2	458.5	266.8	207.5	355.9	426.3	459.5	268.9	210.3	20.96	6.46	1.40	3.25	2.67
27.0	54.0	354.5	428.2	459.5	267.1	207.7	355.1	427.3	460.0	268.2	210.5	21.85	6.71	1.40	3.26	2.69
28.0	51.0	358.2	427.8	459.4	270.2	208.1	358.5	427.0	460.5	270.8	210.6	22.68	6.93	1.40	3.27	2.72
29.0	51.2	356.6	429.6	459.6	270.6	208.2	357.4	427.8	460.3	271.3	210.9	23.61	7.11	1.40	3.32	2.78
30.0	50.7	357.2	429.9	459.8	270.9	208.4	357.9	428.4	460.9	272.5	211.3	24.31	7.26	1.40	3.35	2.81
31.0	48.0	359.2	430.9	460.8	271.1	208.5	360.3	428.9	461.2	273.7	211.7	25.42	7.52	1.40	3.38	2.85
32.0	45.0	356.2	431.7	461.6	271.4	208.7	357.4	430.1	461.3	274.2	212.0	25.95	7.67	1.40	3.38	2.86
33.0	45.0	358.1	432.5	463.4	271.9	208.8	358.9	431.1	461.9	275.1	212.3	16.18	7.80	1.40	3.40	2.88
34.0	42.5	358.6	433.4	464.0	273.3	209.8	359.5	431.9	462.7	275.7	212.4	16.46	7.86	1.40	3.41	2.89
35.0	42.2	360.6	433.8	465.8	273.6	210.2	361.4	433.0	462.8	275.7	212.7	16.93	7.94	1.40	3.47	2.95

Table E.4: The measurements for the developed AC system at the second mode at $V_i = 1.0$ m/s

Taev _i °C	Rhaev _i %	P ₁ bar	P ₂ Bar	P ₃ bar	P ₄ bar	P ₅ bar	T ₁ °C	T ₂ °C	T ₃ °C	T ₄ °C	T ₅ °C	m _r g/s	Taev _e °C	Rhaev _e %
20.0	75.5	4.00	2.90	13.50	13.30	4.20	15.70	16.10	83.80	46.20	4.40	55.0	16.60	94.70
21.0	73.0	4.30	3.25	13.70	13.50	4.40	16.40	16.60	84.00	45.90	4.80	57.0	17.00	94.30
22.0	70.0	4.50	3.35	14.10	13.90	4.65	16.70	16.70	84.30	50.10	4.90	58.0	17.30	91.80
23.0	68.0	4.65	3.55	14.30	14.00	4.75	16.30	16.90	84.80	50.20	5.15	60.0	17.50	92.00
24.0	65.0	4.85	3.70	14.70	14.30	4.90	17.00	17.20	86.00	50.50	5.30	67.5	17.80	91.20
25.0	63.0	5.15	3.90	15.00	14.80	5.35	17.20	17.60	86.60	50.80	5.35	72.0	17.90	94.00
26.0	59.3	5.20	4.70	15.30	15.00	5.40	17.40	17.90	87.00	51.10	5.55	77.2	18.00	90.40
27.0	54.0	5.25	4.90	15.60	15.30	5.50	17.60	17.90	87.25	51.30	5.70	82.5	18.40	84.20
28.0	51.0	5.25	4.95	15.70	15.40	5.65	17.50	17.80	87.40	51.25	5.75	84.0	19.40	82.30
29.0	51.2	5.35	5.10	15.85	15.60	5.70	17.80	17.90	87.60	51.40	5.80	87.5	19.90	89.50
30.0	50.7	5.35	5.25	15.90	15.70	5.75	18.00	18.20	87.80	51.40	6.10	90.0	20.10	87.70
31.0	48.0	5.40	5.45	16.00	15.80	5.80	18.30	18.50	88.00	51.70	6.30	92.0	20.40	84.00
32.0	45.0	5.45	5.60	16.25	16.10	5.90	18.50	18.70	88.30	51.90	6.40	95.4	20.50	82.20

Table E.5: The experimental results for the developed AC system at the second mode at $V_i = 1.0$ m/s

Taev _i °C	Rhaev _i %	h ₁ kJ/kg	h ₂ kJ/kg	h ₃ kJ/kg	h ₄ kJ/kg	h ₅ kJ/kg	Q _e kW	W _c kW	Wfans kW	COP	COP _v	r _p
20.0	75.5	351.1	421.1	461.90	265.90	206.00	7.98	2.64	1.40	3.02	1.77	4.66
21.0	73.0	349.0	421.8	461.80	265.40	206.50	8.12	2.68	1.40	3.03	1.78	4.52
22.0	70.0	348.5	421.9	461.50	272.00	206.60	8.23	2.70	1.40	3.04	1.80	4.21
23.0	68.0	347.8	422.7	461.80	272.10	207.00	8.45	2.76	1.40	3.06	1.82	4.16
24.0	65.0	352.4	423.7	462.50	272.60	207.20	9.80	3.08	1.40	3.18	1.95	3.97
25.0	63.0	361.2	422.2	462.80	273.00	207.30	11.08	3.44	1.40	3.22	2.03	3.48
26.0	59.3	359.3	422.9	462.80	273.50	207.50	11.72	3.62	1.40	3.24	2.07	3.26
27.0	54.0	352.4	438.2	476.10	273.80	207.70	11.94	3.68	1.40	3.25	2.09	3.25
28.0	51.0	355.1	424.2	462.60	273.70	207.80	12.37	3.79	1.40	3.26	2.11	3.25
29.0	51.2	354.2	424.7	462.70	273.90	207.90	12.84	3.91	1.40	3.28	2.14	3.15
30.0	50.7	354.3	425.4	462.80	273.90	208.30	13.14	3.96	1.40	3.32	2.17	3.10
31.0	48.0	355.4	425.9	462.90	274.40	208.60	13.51	4.01	1.40	3.37	2.21	3.00
32.0	45.0	353.0	426.5	462.90	274.70	208.70	13.77	4.09	1.40	3.38	2.22	2.96

Table E.6: The measurements for the developed AC system at the third mode at $V_i = 0.7$ m/s

Taev _i °C	Rhaev _i %	P ₁ bar	P ₂ Bar	P ₃ bar	P ₄ bar	P ₅ bar	T ₁ °C	T ₂ °C	T ₃ °C	T ₄ °C	T ₅ °C	m _r g/s	Taev _e °C	Rhaev _e %
20.0	75.5	3.90	2.93	13.70	13.50	4.25	17.50	17.60	84.90	46.40	5.40	54.0	17.9	95.0
21.0	73.0	4.25	3.03	13.80	13.65	4.60	17.70	17.75	84.90	46.40	5.85	55.2	18.0	94.1
22.0	70.0	4.55	3.38	14.35	14.15	4.75	17.70	17.90	85.20	46.72	6.00	56.4	18.2	93.4
23.0	68.0	4.60	3.46	14.50	14.35	4.90	19.00	19.10	85.30	46.85	6.10	58.5	18.3	92.4
24.0	65.0	4.75	3.69	14.85	14.65	5.15	20.10	20.3	85.30	46.80	6.25	65.0	18.6	91.2
25.0	63.0	5.10	4.63	15.97	15.25	5.55	20.30	20.35	85.70	46.75	6.25	70.0	19.1	90.6
26.0	59.3	5.15	4.92	16.25	15.75	5.60	20.60	20.60	86.10	47.25	6.30	76.3	19.3	89.5
27.0	54.0	5.15	5.05	16.50	15.90	5.65	20.63	20.50	86.10	47.50	6.30	80.0	19.5	88.7
28.0	51.0	5.10	5.14	16.75	16.25	5.80	20.50	20.52	86.50	47.53	6.35	81.0	19.9	87.7
29.0	51.2	5.30	5.44	17.30	16.55	5.90	20.61	20.53	86.80	47.65	6.40	84.3	19.9	87.4
30.0	50.7	5.33	5.59	17.45	16.75	5.90	20.70	20.65	86.80	47.74	6.42	86.0	20.8	86.2
31.0	48.0	5.34	5.69	17.65	17.10	5.95	20.92	20.95	87.30	47.81	6.45	87.0	20.6	85.8
32.0	45.0	5.34	6.01	17.80	17.25	5.95	21.20	21.4	87.93	47.85	6.54	90.0	20.9	85.3

Table E.7: The experimental results for the developed AC system at the third mode at $V_i = 0.7$ m/s

Taev _i °C	Rhaev _i %	h ₁ kJ/kg	h ₂ kJ/kg	h ₃ kJ/kg	h ₄ kJ/kg	h ₅ kJ/kg	Q _e kW	W _c kW	Wfans kW	COP	COP _v	r _p
20.0	75.5	349.9	416.6	457.0	266.2	207.3	7.75	2.65	1.12	2.92	2.05	4.68
21.0	73.0	348.8	422.9	462.6	266.2	207.9	7.90	2.70	1.12	2.93	2.07	4.55
22.0	70.0	351.9	421.9	462.2	266.7	208.1	8.04	2.72	1.12	2.96	2.1	4.24
23.0	68.0	350.4	422.4	462.1	266.9	208.3	8.17	2.75	1.12	2.97	2.11	4.19
24.0	65.0	354.3	422.2	461.6	266.8	208.5	8.51	2.86	1.12	2.98	2.14	4.02
25.0	63.0	353.5	421.4	460.3	266.7	208.5	9.10	2.99	1.12	3.04	2.21	3.45
26.0	59.3	346.9	423.5	460.3	267.4	208.6	9.41	3.05	1.12	3.09	2.26	3.30
27.0	54.0	344.4	424.0	460.0	267.8	208.6	10.07	3.23	1.12	3.12	2.32	3.27
28.0	51.0	343.7	424.9	460.4	267.9	208.6	10.27	3.21	1.12	3.20	2.37	3.26
29.0	51.2	345.8	423.4	459.3	268.0	208.7	10.51	3.26	1.12	3.22	2.4	3.18
30.0	50.7	349.6	422.9	459.3	268.2	208.7	10.75	3.33	1.12	3.23	2.42	3.12
31.0	48.0	353.2	422.7	459.5	268.3	208.8	10.79	3.33	1.12	3.24	2.42	3.10
32.0	45.0	352.7	423.5	460.0	268.3	208.9	10.95	3.37	1.12	3.25	2.44	2.96

In Tables from E.8 to E.10, the first group of experimental results is compared with those obtained from the numerical simulation model and the comparisons show that the numerical results give a good agreement with the experimental work. On the other hand, the second group of experimental results is presented in Tables E.11 to E.14.

Table E.8: The comparison between the theoretical and experimental results at the first mode of AC system operation

Tae _{v_i} °C	Rhaev _i (%)	Q _e kW		COP		Tae _e °C		Rhaev _e (%)		Difference (%)
		Exp.	Simu.	Exp.	Simu.	Exp.	Simu.	Exp.	Simu.	
20.0	75.5	16.18	17.25	3.08	2.97	15.5	13.61	93.6	98.10	-12.20
21.0	73.0	16.46	17.62	3.09	2.99	15.5	13.82	92.5	97.70	-10.80
22.0	70.0	16.93	17.92	3.11	3.01	15.7	14.55	92.1	96.85	-7.32
23.0	68.0	17.43	18.29	3.15	3.10	15.8	14.52	91.4	96.40	-8.10
24.0	65.0	18.41	18.57	3.24	3.11	16	15.38	90.0	95.80	-3.87
25.0	63.0	19.77	18.94	3.24	3.13	16	16.44	94.0	96.70	+2.75
26.0	59.3	20.96	21.01	3.25	3.22	16.2	17.33	88.7	90.70	+6.98
27.0	54.0	21.85	21.68	3.26	3.28	16.4	17.14	88.5	88.43	+4.51
28.0	51.0	22.68	21.96	3.27	3.31	16.6	18.02	88.3	87.26	+8.55
29.0	51.2	23.61	22.48	3.32	3.36	16.7	18.32	87.7	87.12	+9.70
30.0	50.7	24.31	23.05	3.35	3.40	17.3	19.05	86.8	88.36	+10.10
31.0	48.0	25.42	23.2	3.38	3.41	17.7	19.47	86.5	85.50	+10.00
32.0	45.0	25.95	23.37	3.38	3.43	18.3	19.52	84.3	84.40	+6.67

Difference (%)

Table E.9: The comparison between the theoretical and experimental results at the second mode of AC system operation

Taev _i	Rhaev _i	Q _e kW	Q _e kW	Difference	COP	COP	Difference	Taev _e °C	Taev _e °C	Difference	Rhaev _e (%)	Rhaev _e (%)	Difference
°C	(%)	Exp.	Simu.	(%)	Exp.	Simu.	(%)	Exp.	Simu.	(%)	Exp.	Simu.	(%)
20.0	75.5	7.98	8.16	+2.3	3.02	2.93	-2.98	16.60	15.40	-7.23	94.70	97.20	+2.64
21.0	73.0	8.12	8.36	+3.0	3.03	2.95	-2.64	17.00	16.00	-5.88	94.30	96.42	+2.25
22.0	70.0	8.23	8.57	+4.1	3.04	2.97	-2.30	17.30	16.50	-4.62	91.80	94.85	+3.32
23.0	68.0	8.45	8.74	+3.4	3.06	2.99	-2.28	17.50	17.37	-0.74	92.00	93.50	+1.63
24.0	65.0	9.80	9.47	-3.4	3.18	3.01	-5.34	17.80	17.84	+0.20	91.20	92.44	+1.36
25.0	63.0	11.08	10.02	-9.6	3.22	3.07	-4.66	17.90	18.77	+4.90	94.00	91.60	-2.55
26.0	59.3	11.72	10.44	-10.9	3.24	3.17	-3.67	18.00	19.70	+9.40	90.40	91.20	+0.88
27.0	54.0	11.94	11.13	-6.8	3.25	3.22	-0.78	18.40	20.23	+9.90	84.20	90.50	+7.48
28.0	51.0	12.37	11.24	-9.1	3.26	3.24	-0.78	19.40	21.60	+11.30	82.30	88.55	+7.59
29.0	51.2	12.84	11.53	-10.2	3.28	3.29	+0.26	19.90	20.69	+4.00	89.50	85.45	-4.53
30.0	50.7	13.14	11.80	-10.2	3.32	3.32	+0.25	20.10	21.50	+5.90	87.70	85.45	-2.57
31.0	48.0	13.51	11.88	-12.1	3.37	3.33	-1.01	20.40	21.78	+6.30	84.00	85.11	+1.32
32.0	45.0	13.77	12.03	-12.6	3.38	3.36	-0.37	20.50	22.70	+9.70	82.20	83.23	+1.25

Table E.10: The comparison between the theoretical and experimental results at the third mode of AC system operation

Taev _i	Rhaev _i	Q _e kW	Q _e kW	Difference	COP	COP	Taev _e °C	Taev _e °C	Difference	Rhaev _e (%)	Rhaev _e (%)	Difference	Difference
°C	(%)	Exp.	Simu.	(%)	Exp.	Simu.	Exp.	Simu.	(%)	Exp.	Simu.	(%)	(%)
20.0	75.5	7.75	7.70	-0.65	2.92	3.00	17.9	14.70	+2.67	95.0	98.1	-17.87	+3.26
21.0	73.0	7.90	7.78	-1.54	2.93	3.02	18.0	14.80	+2.98	94.1	98.0	-17.77	+4.14
22.0	70.0	8.04	8.11	+0.87	2.96	3.03	18.2	14.85	+2.53	93.4	96.7	-17.50	+3.53
23.0	68.0	8.17	8.31	+1.68	2.97	3.14	18.3	14.88	+5.41	92.4	97.7	-18.68	+5.74
24.0	65.0	8.51	9.48	+10.20	2.98	3.15	18.6	15.00	+7.98	91.2	96.3	-19.35	+5.59
25.0	63.0	9.10	10.15	+10.30	3.04	3.17	19.1	15.70	+6.54	90.6	95.8	-16.48	+5.74
26.0	59.3	9.41	10.55	+10.80	3.09	3.20	19.3	16.20	+3.27	89.5	94.8	-15.18	+5.92
27.0	54.0	10.07	10.86	+7.30	3.12	3.20	19.5	16.78	+2.50	88.7	93.7	-13.94	+5.64
28.0	51.0	10.27	10.94	+6.10	3.20	3.23	19.9	17.11	+0.94	87.7	92.7	-14.02	+5.70
29.0	51.2	10.51	11.56	+9.10	3.22	3.25	19.9	17.96	+0.92	87.4	92.2	-12.39	+5.49
30.0	50.7	10.75	12.12	+11.30	3.23	3.29	20.8	18.03	+1.26	86.2	91.6	-13.31	+6.26
31.0	48.0	10.79	12.56	+14.10	3.24	3.33	20.6	18.35	+4.08	85.8	91.3	-12.61	+6.41
32.0	45.0	10.95	12.94	+15.40	3.25	3.35	20.9	18.60	+3.58	85.3	91.0	-11.00	+6.68

Table E.11: The physical quantities which are used for the control algorithm construction for a first mode operation of the proposed system

Taev _i (°C)	Ts = 21°C						
	On/off times (min)/ N _{cy}	W _{t_{av}} (kW)	Consumed energy (kWh)	tr (°C)	Rhr (%)	t _{mrt} (°C)	PMV
23.0	4/8/5	7.42	2.47	19.30	75.42	23.37	-0.93
24.0	7/10/3	7.78	2.72	19.73	72.83	23.49	-0.83
25.0	11/11/3	8.08	4.44	20.10	73.40	23.61	-0.77
26.0	13/14/2	8.43	3.65	19.67	67.09	22.98	-0.75
27.0	14/18/2	8.54	3.98	19.59	63.46	22.71	-0.64
28.0	14/19/2	9.19	4.28	21.38	65.91	24.41	-0.35
29.0	17/21/2	8.82	4.99	21.76	65.27	24.50	-0.19
30.0	20/22/1	9.23	3.07	21.88	64.29	24.50	-0.12
31.0	21/26/1	8.85	3.09	21.49	60.97	23.89	-0.06
32.0	26/30/1	9.46	4.10	21.55	57.76	23.74	-0.03
Taev _i (°C)	Ts = 22°C						
	On/off times (min)/ N _{cy}	W _{t_{av}} (kW)	Consumed energy (kWh)	tr (°C)	Rhr (%)	t _{mrt} (°C)	PMV
23.0	3/8/6	7.40	2.22	19.72	77.07	23.89	-0.90
24.0	5/10/4	7.81	2.60	20.16	74.43	24.01	-0.81
25.0	7/11/3	8.15	2.85	20.60	75.24	24.20	-0.75
26.0	9/14/3	8.80	3.96	20.17	68.77	23.56	-0.73
27.0	14/18/2	8.62	4.02	20.16	65.30	23.37	-0.62
28.0	14/19/2	9.19	4.28	22.01	67.82	25.12	-0.33
29.0	18.5/20/1	9.22	2.85	22.39	67.16	25.21	-0.18
30.0	20/22/1	9.23	3.07	22.60	66.41	25.31	-0.11
31.0	18/23/1	9.27	2.78	22.20	62.99	24.68	-0.05
32.0	25/25/1	9.39	3.91	22.26	59.66	24.52	-0.03
Taev _i (°C)	Ts = 23°C						
	On/off times (min)/ N _{cy}	W _{t_{av}} (kW)	Consumed energy (kWh)	tr (°C)	Rhr (%)	t _{mrt} (°C)	PMV
24.0	3/8/6	7.81	2.34	19.90	77.75	24.10	-0.90
25.0	5/13/3	8.15	2.04	20.35	75.09	24.22	-0.81
26.0	6/13/3	8.43	2.53	20.73	75.68	24.34	-0.75
27.0	9/18/2	8.62	2.58	20.38	69.51	23.81	-0.72
28.0	9/19/2	8.80	2.64	20.30	65.74	23.53	-0.62
29.0	14/21/2	8.94	4.17	22.15	68.28	25.29	-0.34
30.0	16.5/22/1	9.18	2.52	22.54	67.62	25.38	-0.18
31.0	17/24/1	9.27	2.62	22.73	66.79	25.45	-0.11
32.0	17/24/1	9.39	2.66	22.33	63.35	24.82	-0.05

Table E.12: The physical quantities which are used for the control algorithm construction for a second mode operation of the proposed system

Taev _i (°C)	Ts = 21°C						
	On/off times (min)/ N _{cy}	W _{t_{av}} (kW)	Consumed energy (kWh)	tr (°C)	Rhr (%)	t _{mrt} (°C)	PMV
23.0	10.5/8/3	3.47	1.82	20.20	75.70	23.82	-0.62
24.0	15/10/2	3.74	1.87	20.67	73.40	23.96	-0.47
25.0	19/11/2	3.96	2.51	21.09	73.40	24.10	-0.28
26.0	20/14/3	4.19	4.19	20.94	67.86	23.62	-0.18
27.0	25/18/1	4.19	1.74	21.20	62.66	23.51	0.02
28.0	28/20/1	4.26	1.99	23.47	65.48	25.45	0.27
29.0	31/21/1	4.37	2.25	24.01	65.03	25.63	0.55
30.0	33/22/1	4.41	2.42	24.45	64.61	25.78	0.73
31.0	36/24/1	4.49	2.69	24.30	60.43	25.30	0.84
32.0	38.5/21/1	4.56	2.93	24.36	56.64	25.09	1.06
Taev _i (°C)	Ts = 22°C						
	On/off times (min)/ N _{cy}	W _{t_{av}} (kW)	Consumed energy (kWh)	tr (°C)	Rhr (%)	t _{mrt} (°C)	PMV
23.0	6.5/8/4	3.41	1.48	20.65	77.36	24.34	-0.61
24.0	10/10/3	3.75	1.87	21.13	75.01	24.49	-0.46
25.0	13/11/2	4.03	1.74	21.61	75.24	24.70	-0.27
26.0	14/14/2	4.19	1.95	21.47	69.56	24.21	-0.17
27.0	17.5/18/2	4.23	2.46	21.81	64.47	24.19	0.02
28.0	20/19/1	4.31	1.44	24.15	67.38	26.19	0.27
29.0	22.5/20/1	4.38	1.64	24.71	66.92	26.37	0.54
30.0	26/22/1	4.45	1.93	25.26	66.75	26.63	0.70
31.0	28/23/1	4.49	2.17	25.10	62.42	26.13	0.81
32.0	31/25/1	4.55	2.42	25.16	58.51	25.92	1.02
Taev _i (°C)	Ts = 23°C						
	On/off times (min)/ N _{cy}	W _{t_{av}} (kW)	Consumed energy (kWh)	tr (°C)	Rhr (%)	t _{mrt} (°C)	PMV
24.0	6.0/10/4	3.16	1.26	20.83	78.05	24.56	-0.60
25.0	9/13/3	3.72	1.67	21.32	75.67	24.71	-0.45
26.0	10/13/2	4.19	1.39	21.74	75.68	24.84	-0.27
27.0	13/18/2	3.91	1.69	21.70	70.31	24.47	-0.17
28.0	17/19/2	4.31	2.44	21.96	64.91	24.36	0.02
29.0	20.0/21/1	4.16	1.38	24.31	67.84	26.37	0.27
30.0	22.5/23/1	4.20	1.57	24.88	67.37	26.55	0.53
31.0	25.5/24/1	4.24	1.80	25.41	67.13	26.79	0.70
32.0	28/24/1	4.55	2.12	25.25	62.79	26.28	0.81

Table E.13: The physical quantities which are used for the control algorithm construction for a third mode operation of the proposed system

Taev _i (°C)	Ts = 21°C						
	On/off times (min)/ N _{cy}	W _{t_{av}} (kW)	Consumed energy (kWh)	tr (°C)	Rhr (%)	t _{mrt} (°C)	PMV
23.0	12.2/8/3	3.52	2.15	20.63	75.89	24.03	-0.27
24.0	15.5/10/2	3.56	1.84	21.10	73.40	24.17	-0.10
25.0	19.3/11/2	3.60	2.31	21.69	71.81	24.41	0.10
26.0	21.0/14/2	3.75	1.31	21.58	67.46	23.94	0.25
27.0	26.5/18/1	3.81	1.68	21.73	63.55	23.78	0.40
28.0	28.5/20/1	3.84	1.82	23.75	65.62	25.60	0.57
29.0	31.2/21/1	3.93	2.04	24.06	65.13	25.66	1.22
30.0	34.0/26/1	3.99	2.26	24.83	64.01	25.97	0.98
31.0	39.3/21/1	4.03	2.65	24.43	60.66	25.36	1.13
32.0	48.0/12/1	4.11	3.29	24.58	58.02	25.20	1.30
Taev _i (°C)	Ts = 22°C						
	On/off times (min)/ N _{cy}	W _{t_{av}} (kW)	Consumed energy (kWh)	tr (°C)	Rhr (%)	t _{mrt} (°C)	PMV
23.0	8.5/8/4	3.49	1.98	21.08	77.56	24.56	-0.27
24.0	10.5/10/3	3.56	1.86	21.56	75.01	24.70	-0.09
25.0	13.0/11/2	3.64	1.57	22.24	73.61	25.02	0.09
26.0	15.0/14/2	3.75	1.87	22.12	69.14	24.53	0.25
27.0	18.2/18/2	3.81	1.15	22.36	65.39	24.47	0.39
28.0	22.0/19/1	3.84	1.41	24.44	67.52	26.34	0.55
29.0	25.5/20/1	3.95	1.69	24.76	67.01	26.40	1.19
30.0	27.8/22/1	3.99	1.85	25.65	66.12	26.82	0.95
31.0	32.0/23/1	4.03	2.15	25.24	62.66	26.20	1.09
32.0	34.7/25/1	4.10	2.37	25.39	59.94	26.04	1.26
Taev _i (°C)	Ts = 23°C						
	On/off times (min)/ N _{cy}	W _{t_{av}} (kW)	Consumed energy (kWh)	tr (°C)	Rhr (%)	t _{mrt} (°C)	PMV
24.0	6.5/10/4	2.96	1.28	21.27	78.24	24.78	-0.27
25.0	9.5/13/3	3.40	1.61	21.75	75.67	24.92	-0.09
26.0	11.0/13/2	3.75	1.37	22.37	74.04	25.16	0.09
27.0	15.0/18/2	3.44	1.72	22.36	69.88	24.80	0.24
28.0	18.0/19/2	3.84	2.30	22.51	65.83	24.64	0.39
29.0	21.7/21/1	3.71	1.34	24.61	67.98	26.52	0.55
30.0	23.5/22/1	3.79	1.45	24.92	67.47	26.58	1.18
31.0	27.5/24/1	3.98	1.82	25.79	66.50	26.98	0.95
32.0	30.0/24/1	4.10	2.05	25.39	63.02	26.35	1.08

Table E.14: The energy consumption for the conventional AC system for set-point temperature of 21, 22, and 23°C

Taev _i (°C)	Ts = 21, 22 , and 23°C						
	N _{cy}	Wt _{av} (kW)	Consumed energy (kWh)	tr (°C)	Rhr (%)	t _{mrt} (°C)	PMV
23.0	1	3.88	3.88	19.30	75.42	23.37	-0.93
24.0	1	3.93	3.93	19.73	72.83	23.49	-0.83
25.0	1	3.97	3.97	20.10	73.40	23.61	-0.77
26.0	1	4.23	4.23	19.67	67.09	22.98	-0.75
27.0	1	4.64	4.64	19.59	63.46	22.71	-0.64
28.0	1	4.87	4.87	21.38	65.91	24.41	-0.35
29.0	1	5.10	5.10	21.76	65.27	24.50	-0.19
30.0	1	5.24	5.24	21.88	64.29	24.50	-0.12
31.0	1	5.36	5.36	21.49	60.97	23.89	-0.06
32.0	1	5.44	5.44	21.55	57.76	23.74	-0.03

Table E.15 The hourly energy consumption for the conventional system and the developed system at the three different operating modes for the three different set-point temperatures

Time (h)	Taev _i (°C)	Hourly energy consumption for 1 st mode operation (kWh)			Hourly energy consumption for 2 nd mode operation (kWh)			Hourly energy consumption for 3 rd mode operation (kWh)			Hourly energy consumption for Conventional system (kWh)			
		Set-up at 21 °C	Set-up at 22 °C	Set-up at 23 °C	Set-up at 21 °C	Set-up at 22 °C	Set-up at 23 °C	Set-up at 21 °C	Set-up at 22 °C	Set-up at 23 °C	Set-up at 21 °C	Set-up at 22 °C	Set-up at 23 °C	
8	26.0	4.44	3.79	2.53	2.31	1.85	1.39	2.31	1.83	1.38	2.31	1.83	1.38	4.23
9	26.5	4.47	3.95	2.55	2.35	2.25	1.67	2.26	1.56	1.61	2.26	1.56	1.61	4.44
10	27.0	3.65	4.02	2.58	4.19	2.46	1.83	1.31	1.15	1.9	1.31	1.15	1.9	4.64
11	28.5	3.98	3.82	3.25	1.82	2.21	1.55	1.71	1.44	1.42	1.71	1.44	1.42	5.04
12	29.0	4.49	3.67	4.17	2.01	1.68	1.38	1.85	1.63	1.34	1.85	1.63	1.34	5.10
13	29.5	4.55	3.04	3.39	2.21	1.93	1.59	2.04	1.85	1.82	2.04	1.85	1.82	5.14
14	29.5	4.55	3.04	3.39	2.21	1.93	1.59	2.04	1.85	1.82	2.04	1.85	1.82	5.14
15	28.0	2.95	3.75	2.64	1.77	1.44	2.44	1.7	1.41	2.38	1.7	1.41	2.38	4.87
16	27.5	3.95	3.72	2.6	4.22	2.33	2.31	1.29	1.27	2.21	1.29	1.27	2.21	4.83
17	25.0	2.72	2.85	2.04	2.2	1.74	1.81	1.84	1.57	1.61	1.84	1.57	1.61	3.97
18	24.0	2.53	2.6	1.96	2.76	1.99	1.68	1.97	1.86	1.55	1.97	1.86	1.55	3.93
19	24.0	2.53	2.6	1.96	2.76	1.99	1.68	1.97	1.86	1.55	1.97	1.86	1.55	3.93
20	24.0	2.53	2.6	1.96	2.76	1.99	1.68	1.97	1.86	1.55	1.97	1.86	1.55	3.93
21	24.0	2.53	2.6	1.96	2.76	1.99	1.68	1.97	1.86	1.55	1.97	1.86	1.55	3.93
22	23.5	2.48	2.55	1.95	2.73	1.96	1.82	1.95	1.82	1.51	1.95	1.82	1.51	3.90
23	23.0	2.42	2.5	0.84	2.71	1.93	0.84	1.95	1.8	0.84	1.95	1.8	0.84	3.88
Daily energy (kWh)		54.77	51.1	39.77	41.77	31.67	26.94	30.13	26.62	26.04	30.13	26.62	26.04	70.91

Table E.16: The hourly energy consumption for the conventional system and the developed system for the three different set-point temperatures

Time (h)	Taevi (°C)	Hourly energy consumption for developed system (kWh)			Hourly energy consumption for Conventional system (kWh)
		Set-up at 21°C	Set-up at 22°C	Set-up at 23°C	
8	26.0	2.31	1.85	1.39	4.23
9	26.5	2.35	2.25	1.67	4.44
10	27.0	4.19	2.46	1.83	4.64
11	28.5	3.98	3.82	3.25	5.04
12	29.0	4.49	3.67	4.17	5.10
13	29.5	4.55	3.04	3.39	5.14
14	29.5	4.55	3.04	3.39	5.14
15	28.0	2.95	3.75	2.64	4.87
16	27.5	4.42	3.72	2.6	4.83
17	25.0	2.95	2.85	1.61	3.97
18	24.0	1.97	1.86	1.55	3.93
19	24.0	1.97	1.86	1.55	3.93
20	24.0	1.97	1.86	1.55	3.93
21	24.0	1.97	1.86	1.55	3.93
22	23.5	1.95	1.82	1.51	3.90
23	23.0	1.91	1.8	0.84	3.88
Daily energy consumption (kWh)		48.48	41.51	34.49	70.91
Annually energy consumption (kWh)		14544	12453	10347	21273

APPENDIX F

THERMAL COMFORT CALCULATION

F.1 Introduction

This appendix exhibits the theoretical model for the thermal comfort calculations starting from the basic heat balance equation for human body in steady-state condition. In addition, the selection of optimum number of evaporator blowers at partial-load conditions has been discussed here in this Appendix.

F.2 Fanger's Steady-State Model

The steady-state model developed by Fanger (1970) assumes that the body is in a state of thermal equilibrium with negligible heat storage. The key assumption is that the body is in a state of thermal neutrality, i.e. there is no shivering, and vasoregulation is not considered because the core and skin are modeled as one compartment (ASHRAE 1997). At steady state, the rate of heat generation equals the rate of heat loss, and the energy balance is shown as:

$$M - W = Esk + Cres + Eres + (C + R) \quad (F.1)$$

Where

- M = rate of metabolic heat production, W/m^2
 W = rate of mechanical work accomplished, W/m^2
 E_{sk} = rate of total evaporative heat loss from skin, W/m^2
 C_{res} = rate of convective heat loss from respiration, W/m^2
 E_{res} = rate of evaporative heat loss from respiration, W/m^2
 $(C + R)$ = sensible heat loss from clothes (convection and radiation), W/m^2

Fanger used the following linear regression equations based on data from Rohles and Nevins_(1971) to calculate values of E_{sk} , C_{res} , E_{res} , and $(C+R)$ as follows:

$$E_{sk} = 3.05 \times 10^{-3} [5733 - 6.99 \times (M - W - Pa)] + 0.42 \times (M - W - 58.15) \quad (F.2)$$

$$C_{res} = 0.0014 \times M (34 - t_a) \quad (F.3)$$

$$E_{res} = 1.72 \times 10^{-5} \times M (5867 - Pa) \quad (F.4)$$

$$(C + R) = 3.96 \times 10^{-8} f_{cl} [(t_{cl} + 273)^4 - (t_{mrt} + 273)^4] + f_{cl} \times h_c (t_{cl} - t_{mrt}) \quad (F.5)$$

Where,

- Pa = water vapor pressure in ambient air, kPa
 t_a = ambient air temperature, °C
 f_{cl} = clothing area factor (Appendix B)
 t_{mrt} = mean radiant temperature, °C (Appendix B)
 h_c = convective heat transfer coefficient, $W/(m^2.K)$ (Appendix B)

t_{cl} = clothing mean temperature, °C and it can be determined by using iterative method for Equation F.6 which is derived from the phenomenon that the heat transfer from the skin surface to the clothes surface is equal to the heat transfer from the clothes to the surrounding environment.

$$\begin{aligned}
 t_{cl} = & 35.7 - 0.028(M - W) + f_{cl} h_c (t_{cl} - t_a) \\
 & - I_{cl} [3.96 \times 10^{-8} f_{cl} ((t_{cl} + 273)^4 - (t_{mrt} + 273)^4)] \quad (F.6)
 \end{aligned}$$

F.3 General Comfort Equation

Equation F.1 now can be rewritten in the following form after substituting Equation F.2 to Equation F.5. The following equation is known as the general comfort equation:

$$\begin{aligned}
 (M - W) = & 3.05 \times 10^{-3} [5733 - 6.99(M - W) - Pa] + 0.42[(M - W) - 58.15] \\
 & + 1.7 \times 10^{-5} M(5867 - Pa) + 0.0014M(34 - ta) + f_{cl} h_c (t_{cl} - t_a) \\
 & + 3.96 \times 10^{-8} f_{cl} \times \left[(t_{cl} + 273)^4 - (t_{mrt} + 273)^4 \right] \quad (F.7)
 \end{aligned}$$

For any type of clothing and any type of activity, Equation F.7 will be able to calculate all reasonable combinations of air temperature, air humidity, mean radiant temperature and air velocity which will create optimal thermal comfort for persons under steady state conditions (Fanger 1970). This equation assumes that all sweat generated is evaporated (eliminating clothing moisture permeability as a factor in the equation), which is valid for normal indoor clothing worn in typical indoor environment with low or moderate activity levels.

F.4 Predicted Mean Vote (PMV) and Predicated Percentage of Dissatisfied (PPD)

PMV predicts the mean value of thermal sensation votes of a large group of people and represents the statistical relation between physiological responses of the thermoregulatory system to the thermal sensation votes collected from more than 1300 subjects. Mathematically, it can be represented by Equation F.8. By setting $PMV = 0$, we can reduce Equation F.8 to Equation F.7 (general comfort equation).

$$\begin{aligned}
PMV = & (0.303e^{-0.036M} + 0.028)[(M - W) - 3.05 \times 10^{-3} \times [5733 - 6.99(M - W) - Pa]] \\
& - 0.42 \times ((M - W) - 58.15) - 1.7 \times 10^{-5} M(5867 - Pa) - 0.0041M(34 - t_a) \\
& - (3.96 \times 10^{-8} f_{cl}) \times [(t_{cl} + 273)^4 - (t_{mrt} + 273)^4] - f_{cl} h_c (t_{cl} - t_a)
\end{aligned} \tag{F.8}$$

The PMV-index predicts the mean value of the thermal votes of a large group of people exposed to the same environment but individual votes are scattered around this mean value and it is useful to predict the number of people likely to feel uncomfortably warm or cool. The PPD-index establishes a quantitative prediction of the number of thermally dissatisfied persons. In other words, it predicts the percentage of people who would be dissatisfied with the thermal environment i.e. those voting hot (+3), warm (+2), cool (-2) or cold (-3) on the 7-point thermal sensation scale.

$$PPD = 100 - (95 \times e^{-(0.02253PMV^4 + 0.2179PMV^2)}) \tag{F.9}$$

The relationship between PMV and PPD is shown in Figure F.1 and can also be used to calculate PPD, if the value of PMV is known. It should be noted to calculate the PMV it is proposed to know W (rate of mechanical work accomplished, W/m^2). The mechanical work done by the muscles for a given task is often expressed in terms of the body's mechanical efficiency $\mu = W/M$. It is unusual for μ to be more than 5 to 10%; for most activities, it is close to zero. The maximum value under optimal conditions (e.g., bicycle ergometer) is $\mu = 20$ to 24% (Nishi 1981). It is common to assume that mechanical work is zero for several reasons: (1) the mechanical work produced is small compared to metabolic rate, especially for office activities; (2) estimates for metabolic rates can often be inaccurate; and (3) this assumption results in a more conservative estimate when designing air-conditioning equipment for upper comfort and health limits.

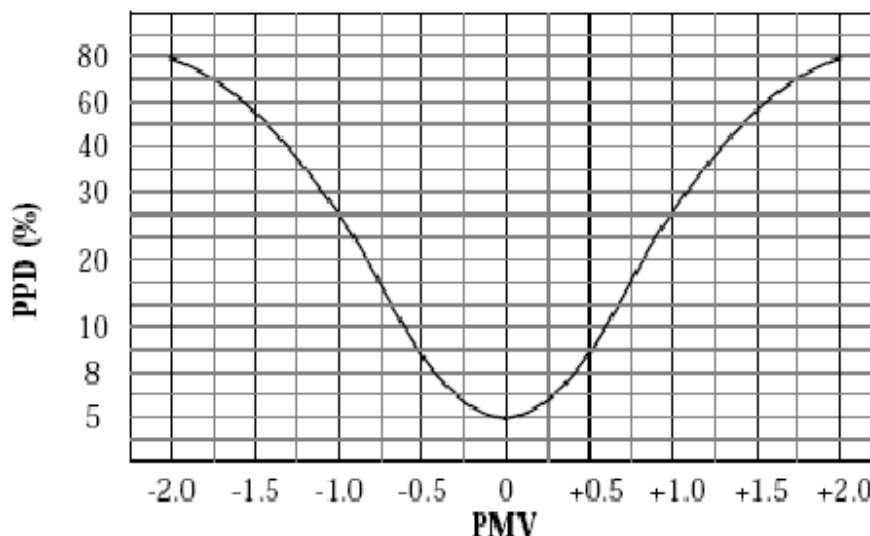


Figure F.1 Curve to interpolate PPD as a function of PMV

In order to determine the PMV there are some parameters should be measured directly or calculated from other measurements and other should be quantified from Tables provided by ASHRAE (1997). The measuring parameters or environmental parameters are the space or return air temperature, t_a , mean radiant temperature, t_{mrt} , local mean air velocity, v_r , and space air relative humidity, R_{ha} . While the quantified parameters or personal parameters such as the metabolic rate, M and the clothing thermal insulation, I_{cl} can be obtained from Tables B.1 and B.2 from Appendix B.

The air temperature and humidity can be measured directly by thermocouples and hygrometer respectively. Local mean air velocity is usually a difficult variable to measure, because it has vectorial characteristics and rapid and strong time fluctuations. The air local velocity value has a significant relation with the jet air velocity from the air duct outlet which is easy to measure and identify. Accordingly, A. Pitarma (2003) proposed numerically a graphical chart for one-dimension velocity distribution inside an empty enclosure (without any sedimentary objects); the graphical chart was introduced into non-dimensional velocity profile. The present study converts the graphical chart into algebraic polynomial equation (see Equation F.10) to be integrated to estimate the average air local velocity as function in jet air velocity which is measured of 4.65 m/s for

1st and 2nd modes and 3.0 m/s for 3rd mode in this study. The equation shows that the mean air local velocity is almost equal to 0.0531 of the air jet velocity.

$$V_r / V_j = 0.2312 \times \left(\frac{x}{L}\right)^3 - 0.049 \times \left(\frac{x}{L}\right)^2 - 0.3166 \times \left(\frac{x}{L}\right) + 0.1699, \quad R^2 = 0.9837 \quad (\text{F.10})$$

Where,

V_r = air relative velocity, m/s

V = air jet velocity, m/s

x = Local distance from the jet to the bottom of the enclosure, m

L = the enclosure height, m

By using the average theory, $\bar{V}_r / V_j = \frac{1}{L} \times \int_{x=0}^{x=L} \frac{V_r(x)}{V_j} dx$ thus $\bar{V}_r / V_j = 0.0531$

F.5 Optimization for number of non-operating blowers at part-load operation

Normally for large scale vehicle such as bus, the AC system consists of several blowers to provide the occupants by the proper amount of conditioned air. In conventional AC system the number of blowers are 12 (6 per a cooling coil), each pair of blowers are coupled by one motor to drive them as it can be seen in Figure F.3. The varying of blowers speed is complicated to be done automatically so to ease the controller job it is better to change the blowers' capacity by on/off operation.

The main reason of using on/off controlling for the blowers instead of using of varying the blower speed is to make the controller a simple and reliable. The most vulnerable parts of the air-conditioning system are its controls and nothing can be more aggravating than the failure of a system a couple of thundered kilometres from a maintenance garage, which failure is found later to be due to nothing more serious than a dirty contact on automatic switch. No matter how simple the cause of failure, if it occurs

on the highway on a hot day, it is a serious matter, certainly not conducive to passenger good will. It, therefore, behooves the designer to keep the controls as few and reliable as is consistent with satisfactory operation and it will be attractive for the customers as the initial cost view.

The question may be now imposed that how many number of blowers should be off at part-load condition. By using the simulation model for the whole system as in Chapter 6, it is found that when the load is dropped significantly the blower capacity should be decreased to the half to enable the AC system to fulfil the applied thermal load. However, as mentioned above that each pair of blowers are connected together by one shaft which is driven by one motor. So there is a decision must be taken either modify the current mass production of the blowers' arrangement in the market to another arrangement as it is shown in Figure F.4 or keeping it. Figures F.5 and F.6 are prepared in order to answer this question.

As it is obvious from these Figures that the difference in COP between the two suggestions is slight owing to the blower input power is inconsiderable comparing to that for the compressor. Despite the enhancement in comfort level is accounted for the using of one-half of the blowers capacity but it is not a substantial reason to apply the second suggestion in the market. It may be commented that the modification of the blowers' arrangement is not crucial where the benefits of that are insignificant.

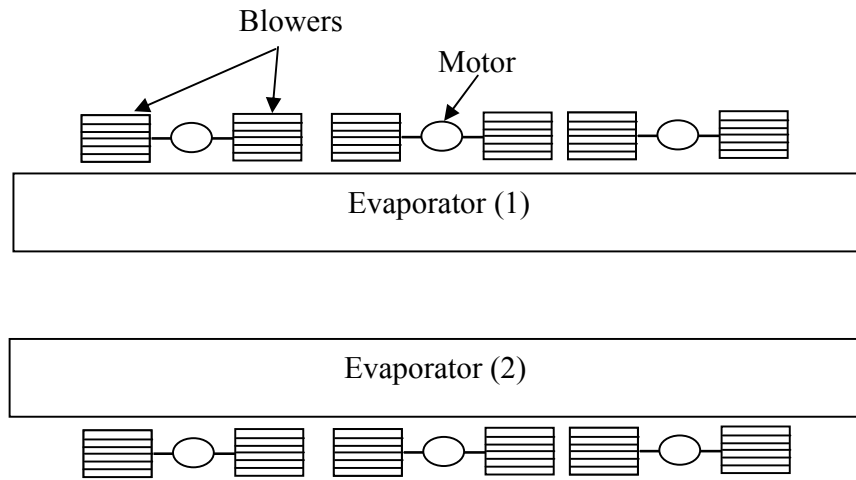


Figure F.2 the current arrangement of the evaporator blowers in the conventional bus AC system design

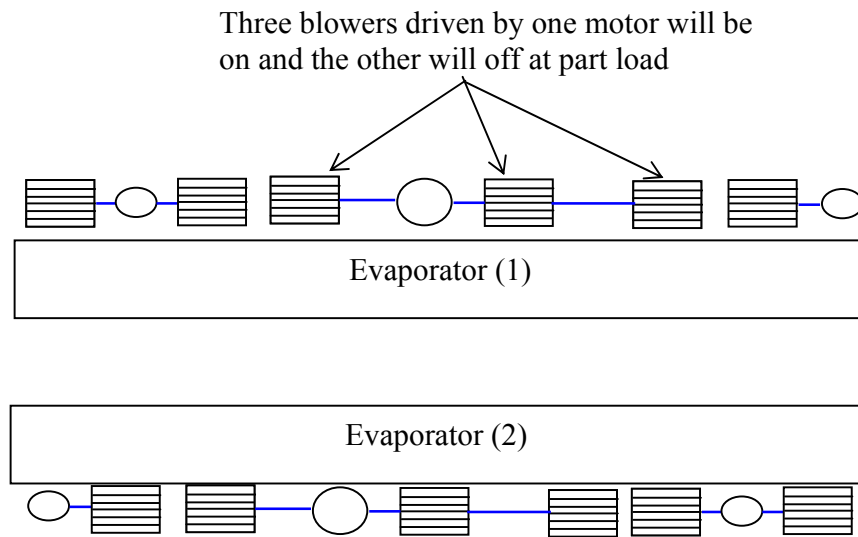


Figure F.3 the suggested arrangement of the evaporator blowers for the bus ACs design

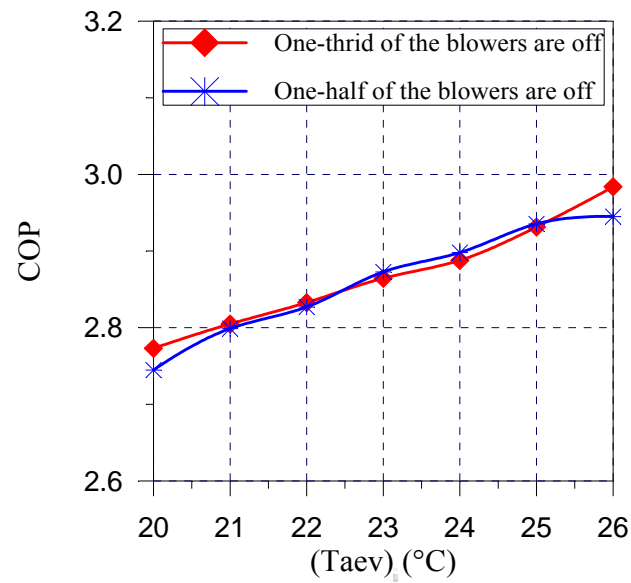


Figure F.4 Comparison between the current and suggested arrangement for the blowers in term of system COP

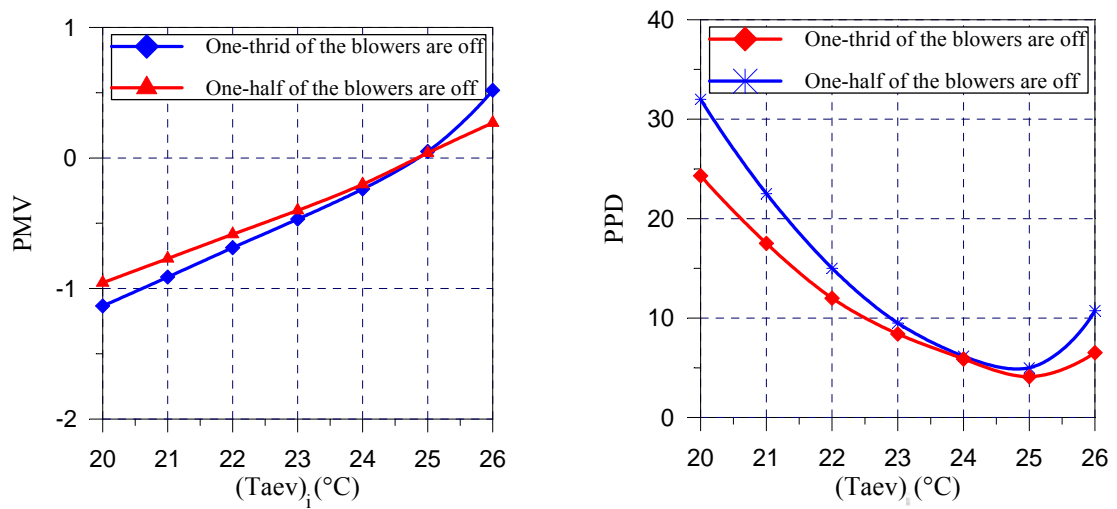


Figure F.5 Comparison between the current and suggested arrangement in terms of (a) PMV (b) PPD

APPENDIX G

CORRELATED FORMULAS AND ERROR ANALYSIS

G.1 Introduction

Thermodynamic and physical properties of R-134a needed for the analysis of the vapor compression cycle simulation in this study were calculated using mathematical formulas developed using the sum of least-square methods. These developed formulas have been incorporated in all the computer codes of this study to ease the calculation of the refrigerant properties when the computer program is activated. This appendix explains briefly the regression of some correlation equations that were developed and used in the simulation model. These equations were regressed using data from the software CATT (1994) and McLinden M et al (1989). In addition, in this appendix the calculation of the experimental results uncertainties have been discussed.

G.2 Formulas for thermodynamic properties of refrigerant

The vapor compression cycle consists of four state points as it is shown in Figure G.1. Given a set of thermodynamic data at each point, the best fit can be obtained for this data at which the sum of the squares of the residues is minimum. LABFIT software (1999) gives this facility to find out the proper curve-fitting of the data with lowest value

of the sum of the squares of the residues. Those equations regressed from thermodynamic data as follows:

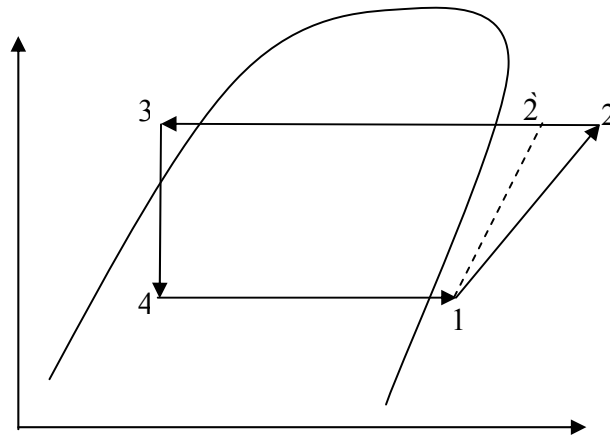


Figure G.1 A simple vapor compression refrigeration system

G.2.1 Thermodynamic properties of saturated liquid and saturated vapor

It is assumed that the enthalpies of saturated liquid, i_f and saturated vapor, i_g are a function of saturated temperature, T_e ($^{\circ}\text{C}$), the correlated equations are:

$$h_f = 1\text{E-}13 * T_e^2 + 1.35 * T_e + 200, \text{ (kJ/kg)} \quad (\text{G.1})$$

$$h_g = 0.0036 * T_e^2 + 0.5614 * T_e + 398.39, \text{ (kJ/kg)} \quad (\text{G.2})$$

The maximum absolute uncertainties of equations G.1 and G.2 are 0.015% and 0.012% respectively for temperature range from -2 to 20 $^{\circ}\text{C}$. The saturation evaporation pressure, P_e (mPa) and condensation pressure, P_c (mPa) are also directly function of saturation temperature, T_e ($^{\circ}\text{C}$) and T_c ($^{\circ}\text{C}$), respectively as follows:

$$P_e = 0.0003 * T_e^2 + 0.0029 * T_e + 0.4146 \quad (\text{G.3})$$

$$P_c = 0.0005 * T_c^2 + 0.0032 * T_c + 0.42 \quad (\text{G.4})$$

The calculated values for the saturation pressures from the two previous equations G.3 and G.4 deviate those obtained CATT software with a maximum absolute uncertainty of 0.013 %. The evaporation temperature range is -2 to 20°C and 40 to 65°C for condensation temperature.

G.2.2 Thermodynamic properties of superheat gas entering compressor

The superheat vapor entering the compressor is a function of the evaporator pressure, P_e (mPa) and the inlet vapor temperature, T_1 (°C) in the compressor suction line, the formula which is used for calculating enthalpy in (kJ/kg) is:

$$h_1 = 398.37 * P_e^{(-0.00165 * T_1)} \quad (G.5)$$

This formula is produced from curve-fitting method with a maximum absolute uncertainty of 0.25% and coefficient of determination of 0.988 for temperature range of 1 to 20°C and pressure of 0.291 to 0.42 mPa.

The correlated equation for the entropy (kJ/kg. °K)

$$S_1 = 1.73 * (P_e * T_1)^{-0.0000527} \quad (G.6)$$

The maximum absolute uncertainty of this equation is 0.052% and coefficient of determination of 0.998 for the same temperature and pressure ranges of Equation G.4.

The correlated equation for the specific volume (m^3/kg)

$$v_1 = P_e / (4.27 + 0.0257 T_1^2) \quad (G.7)$$

The maximum absolute uncertainty of this equation is 0.067% and coefficient of determination of 0.997 for the same temperature and pressure ranges of Equation G.4.

G.2.3 Thermodynamic properties of superheat gas entering condenser

The superheat vapor entering the condenser is a function of the condensation pressure, P_c (mPa) and specific entropy, S_1 (kJ/kg.°K) at the compressor entrance assuming isentropic compression process the formula which is used for calculating enthalpy in (kJ/kg) is:

$$h_2 = (5106.461 + 6972.256 * P_c - 2275.667 * P_c^2 - 5404.46 * S_1 + 1551.86 * S_1^2 - 8464.29 * P_c * S_1 + 2798.14141 * S_1 * P_c^2 + 2572.7 * S_1^2 * P_c - 858.59 * S_1^2 * P_c^2)/1000 \quad (G.8)$$

The temperature of the superheated vapor entering condenser can be computed from this equation:

$$T_2 = -14973.51 + 21650.8 * P_c - 7425.43 * P_c^2 + 16835.44 * S_1 - 4730.46 * S_1^2 - 24717.87 * P_c * S_1 + 8499.01 * S_1 * P_c^2 + 7073.947 * S_1^2 * P_c - 2435.17 * S_1^2 * P_c^2 \quad (G.9)$$

The maximum absolute uncertainty of the two previous equations G.7 and G.8 are 0.20% and 0.12% and coefficients of determination of 0.987 and 0.993 for temperature range of 40 to 65°C and pressure of 1.3 to 1.5 mPa.

G.2.4 Thermodynamic properties of subcooled liquid entering expansion valve

The subcooled liquid entering the thermostatic expansion valve is a function of the condensation pressure, P_c (mPa) and the subcooling temperature, T_3 (°C) calculating enthalpy in (kJ/kg) is:

$$h_3 = 258.1 * P_c^{(0.00276 * T_3)} \quad (G.10)$$

The maximum absolute uncertainty of this equation is 0.01% and coefficient of determination of 0.998 for temperature range of 35 to 60°C and pressure of 0.291 to 0.42 mPa. The summary of the maximum absolute uncertainties of the previous correlations is listed in Table G.1.

Table G.1: The summary of the maximum absolute uncertainties of the correlations used

Thermodynamic property	Equation number	Maximum absolute uncertainty (%)
h ₁	(G.5)	0.250
h ₂	(G.7)	0.200
h ₃	(G.9)	0.010
s ₁	(G.5)	0.052
v ₁	(G.6)	0.067
T ₂	(G.8)	0.120
h _f	(G.1)	0.015
h _g	(G.2)	0.012
Pe	(G.3)	0.013
Pc	(G.4)	0.013

G.3 Thermophysical properties of refrigerant-134a

The thermophysical properties have also correlated in equation form by regression data from McLinden M et al (1989) as function in temperature within a range of -2 to 65°C. The properties are specific heat at constant pressure, C_p (J/kg.°K) and dynamic viscosity, visc (N.s/m²), Prandtl number, Pr , and thermal conductivity K (W/m.°C) for both liquid and vapor phases.

$$C_{p_l} = 0.0298 * T^2 + 2.881 * T + 1335, \text{ with maximum absolute uncertainty of } 0.014\% \quad (\text{G.11})$$

$$C_{p_v} = 0.0294 * T^2 + 4.3523 * T + 883.02, \text{ with maximum absolute uncertainty of } 0.012\% \quad (\text{G.12})$$

$$\text{Visc}_l = (0.0243 * T^2 - 3.5485 * T + 287.4) * 10^{-6}, \text{ with maximum absolute uncertainty of } 0.023\% \quad (\text{G.13})$$

$$\text{Visc}_v = (0.0001 * T^2 + 0.0472 * T + 10.937) * 10^{-6}, \text{ with maximum absolute uncertainty of } 0.027\% \quad (\text{G.14})$$

$$\text{Pr}_l = -0.0156 * T^2 - 3.0439 * T + 1292.7, \text{ with maximum absolute uncertainty of } 0.018\% \quad (\text{G.15})$$

$$\text{Pr}_v = 0.0161 * T^2 + 0.1791 * T + 13.123, \text{ with maximum absolute uncertainty of } 0.015\% \quad (\text{G.16})$$

$$K_l = (0.00005 * T^3 - 0.0016 * T^2 - 0.4477 * T + 93.404) / 1000, \text{ with maximum absolute uncertainty of } 0.017\% \quad (\text{G.17})$$

$$K_v = (0.000004 * T^3 + 0.0001 * T^2 + 0.0857 * T + 11.789) / 1000, \text{ with maximum absolute uncertainty of } 0.019\% \quad (\text{G.18})$$

G.4 Error analysis

No matter how accurate a measurement is made, the result is never exact; it is always an approximation to the actual value, which is never known. So it is important to realize that every measurement always has some error related to it. A formula involving values that have errors will result in a certain error. This error may eventually propagate to such a magnitude, making the calculated formula deviate farther from the true value or the expected value.

A formula regressed from a set of data from measurement always has errors, too. However, we are not concerned with them. It is assumed that errors from established tables generated from the formula are sufficiently small for most applications that neglecting them would not lead to big errors for the result. If we instead produce a new correlation from the tables, the errors produced would concern us. We wish to know what the biggest error is if we apply the equation to a formula, say COP or work by the

compressor. Before going further to the problem, some basic understanding about errors will be useful.

If X^* is an approximation to a true value X , then error is defined as the difference between the approximation and the true value:

$$\text{Error} = \text{true value} - \text{approximation} \quad (\text{G-18})$$

$$E_t = X - X^* \quad (\text{G-19})$$

Here E_t is the exact value of the error. The subscript t designates that this the true error, which is in contrast to other cases where an approximated estimation of error must be employed. Often, it is more useful to compare the error relative to the true value. Here, the relative error E_r is defined by:

$$\text{Relative error} = \text{true error} / \text{true value} \quad (\text{G-20})$$

Provided that the true value is not equal to zero.

The relative error is often expressed in percent; this is obtained by multiplying Eq. (G-20) by 100%:

$$\varepsilon = (\text{true error} / \text{true value}) \times 100\% \quad (\text{G-21})$$

In many cases, we are often more interested in absolute error, which is simply defined by $|X - X^*|$. Using this definition, $X^* = X \pm \Delta X$ where ΔX is the error. Here, the relative error is given by $|X - X^*| / |X|$, provided that X is not zero. This definition is useful where the values are negative such as enthalpy of refrigerants below certain temperature.

If $X^* = X \pm \Delta X$ and $Y^* = Y \pm \Delta Y$ and $Z^* = X^* \text{ op } Y^*$ where op is one of mathematical operations $+$, $-$, \times or $/$, we then have the following relationships:

$$\text{Op} = \pm \rightarrow Z^* = (X \pm \Delta X) \pm (Y \pm \Delta Y) = X \pm Y \pm (\Delta X + \Delta Y) \quad (\text{G-22})$$

$$\text{Op} = \times \rightarrow Z^* = (X \pm \Delta X) \times (Y \pm \Delta Y) = XY \pm (Y \Delta X + X \Delta Y) \quad (\text{G-23})$$

$$\text{Op} = / \rightarrow Z^* = (X \pm \Delta X) \pm (Y \pm \Delta Y) = X/Y \pm (Y \Delta X + X \Delta Y)/X^2 \quad (\text{G-24})$$

The above equation can be compactly written as:

$$Z^* = Z \pm \Delta Z^{(i)} \quad (\text{G-25})$$

Where $\Delta Z^{(i)}$ is the error related to the i-th equation. So,

$$\Delta Z^{(1)} = \Delta X + \Delta Y \quad (\text{G-30})$$

$$\Delta Z^{(2)} = Y \Delta X + X \Delta Y \quad (\text{G-31})$$

$$\Delta Z^{(3)} = (Y \Delta X + X \Delta Y) / X^2 \quad (\text{G-32})$$

Actually, the above relation are derived from calculus as can be proved as follows,

$$Z = X \pm Y \rightarrow dZ = dX \pm dY$$

$$Z = X \times Y \rightarrow dZ = Y dX + X dY$$

$$Z = X/Y \rightarrow dZ = (XdY - Y dX) / X^2$$

But since we are interested in the bigger error, dX could be negative so we have

$$dZ = (XdY + YdX) / X^2$$

For approximation where all derivatives are sufficiently small,

$$dX \approx \Delta X, dY \approx \Delta Y \text{ and } dZ \approx \Delta Z$$

So, we have the relations from (G-30) to (G-31). More operations that are complicated are best treated using the use of derivatives from calculus.

As an illustration, let $X^* = 20.0 \pm 0.2$ and $Y^* = 5.0 \pm 0.1$. Here, $X = 20.0$, $Y = 5.0$, $\Delta X = 0.2$ and $\Delta Y = 0.1$. We then have $X_{\min} = 19.8$, $X_{\max} = 20.2$, $Y_{\min} = 4.9$ and $Y_{\max} = 5.1$. So,

$$\text{Addition: } Z = X + Y = 25.0; Z_{\min} = (X^* + Y^*)_{\min} = 19.8 + 4.9 = 24.7;$$

$$Z_{\max} = (X^* + Y^*)_{\max} = 20.2 + 5.1 = 25.3$$

$$\text{Subtraction: } Z = X - Y = 15.0; Z_{\min} = (X^* - Y^*)_{\min} = 19.8 - 5.1 = 14.7$$

$$Z_{\max} = (X^* - Y^*)_{\min} = 20.2 - 4.9 = 15.3$$

$$\text{Multiplication: } Z = X \times Y = 100; Z_{\min} = (X^* \times Y^*)_{\min} = 19.8 \times 4.9 \approx 97.0;$$

$$Z_{\max} = (X^* \times Y^*)_{\max} = 20.2 \times 5.1 \approx 103.0$$

$$\text{Division: } Z = X/Y = 4.0 \quad Z_{\min} = (X^*/Y^*)_{\min} = 19.8 / 5.1 \approx 3.9;$$

$$Z_{\max} = (X^*/Y^*)_{\max} = 20.2 / 4.9 \approx 4.1;$$

Here, for the addition,

$$\Delta Z_{\max} = 25.3 - 25.0 = 25.0 - 24.7 = 0.3$$

And for the subtraction,

$$\Delta Z_{\max} = 15.0 - 14.7 = 15.3 - 15 = 0.3,$$

For both operations, the maximum error is equal to $\Delta Z^{(1)} = 0.2 + 0.1 = 0.3$ as expressed from Eq. (H-30).

For the multiplication,

$$\Delta Z_{\max} = 103.0 - 100.0 = 100.0 - 97.0 = 3.0$$

From Eq. (A-10), the maximum error is equal to $\Delta Z^{(2)} = 5.0 \times 0.2 + 20.0 \times 0.1 = 3.0$

For the division,

$$\Delta Z_{\max} = 4.1 - 4.0 = 4.0 - 3.9 = 0.1$$

From Eq. (H-32), the maximum error is equal to $\Delta Z^{(3)} = (5.0 \times 0.2 + 20.0 \times 0.1)/5.0^2 \approx 0.1$. Note that in the multiplication and division, the results of the operations are retained in one decimal digit since both operands are only one decimal. It must also be pointed out that errors produced using the above formulas are maximum; the actual ones are often much lower. If ΔX and ΔY are both positive, both subtraction and division processes will reduce the resulting errors. However, since we often do not know the signs of the operands' errors, it is safer to adopt the same signs for them although they will likely produce higher errors.

Error analysis will be used to determine the maximum error produced in the computation of the COP, refrigeration effect, and compressor work. For simplicity, assume that the cycle is a simple one that is no pressure drops along the compressor, evaporator, and condenser lines as shown in Figure H.1.

For this system, COP is given by:

$$\text{COP} = \frac{\text{RE}}{W_c} = \frac{h_1 - h_3}{h_2 - h_1}$$

Values of enthalpies are calculated using aforementioned formulas from sections H.2.1 to H.2.4.

$$\text{Refrigerating effect: } \text{RE} = h_1 - h_3; \quad \text{RE}^* = \text{RE} \pm \Delta \text{RE}$$

$$\text{Work of compression: } W_c = (h_2 - h_1) / \eta_{\text{motor}}; \quad W_c^* = W_c \pm \Delta W_c$$

Coefficient of performance; $COP^* = COP \pm \Delta COP$

From Eq. (H-32):

$$\Delta COP = (W_c \Delta RE + RE \Delta W_c) / W_c^2$$

Here, $\Delta RE = \Delta h_1 + \Delta h_3$ and $\Delta W_c = (\Delta h_1 + \Delta h_2) / \eta_{motor}$

For an illustrative purpose, the following values are taken: $T_e = 10.0^\circ\text{C}$, $T_c = 52.0^\circ\text{C}$, $T_1 = 15.7^\circ\text{C}$, $T_2 = 65.0^\circ\text{C}$, $T_3 = 45.0^\circ\text{C}$, $P_e = 0.416 \text{ mPa}$, $P_c = 1.37 \text{ mPa}$, and $\eta_{motor} = 0.85$. For the analysis, we will take the average errors for all variables concerned. Using the correlated formulas given in sections G.2.1 to G.2.4, we then have:

$$h_1 = 405.82 \text{ kJ/kg}, h_2 = 441.5 \text{ kJ/kg}, \text{ and } h_3 = 268.62 \text{ kJ/kg}.$$

So, $RE = 137.2 \text{ kJ/kg}$, $W_c = 41.97 \text{ kJ/kg}$, and $COP = 3.26$

Errors for the enthalpies are taken as the average ones although they will likely to produce a higher error for the predicted ΔCOP . Here, $\Delta h_1 = 0.25\% = 1.01 \text{ kJ/kg}$, $\Delta h_2 = 0.20\% = 0.887 \text{ kJ/kg}$, $\Delta h_3 = 0.01\% = 0.0268 \text{ kJ/kg}$. So we have:

$$\Delta RE = \Delta h_1 + \Delta h_3 = 1.01 + 0.0268 = 1.03 \text{ kJ/kg} \text{ and } \Delta W_c = (\Delta h_1 + \Delta h_2) / \eta_{motor} = (1.01 + 0.88) / 0.85 = 2.22 \text{ kJ/kg}$$

Therefore,

$$\Delta COP = (W_c \Delta RE + RE \Delta W_c) / W_c^2 = (41.97 * 1.03 + 137.2 * 2.22) / 41.97^2 = 0.20 \text{ or about } 6.1\% \text{ from the computed COP}.$$

The actual error can be found as follow. From the ASHARE table and R-134a chart we have directly $h_1 = 406.3 \text{ kJ/kg}$, $h_2 = 443 \text{ kJ/kg}$, and $h_3 = 267.5 \text{ kJ/kg}$. $RE = 138.8 \text{ kJ/kg}$, $W_c = 43.2 \text{ kJ/kg}$, and $COP = 3.21$. So, $\Delta COP = |3.26 - 3.21| = 0.05$, or 1.53%. Clearly, the actual error of the COP is lower than the predicted one. It can then be concluded that the COP computed using the previous correlated equations would have error (uncertainty) less than 10%. The actual error of the COP for this example is only about 1.53%.